

# nature

## BUILT FOR LIGHT

Co-assembly of nanocrystals creates perovskite-style superlattices that show superfluorescence

### Coronavirus

Is it too soon to relax the rules on wearing face masks?

### Full cost of COVID

Account for long-term ill health, not just cases and deaths

### Cellular relations

A genetic family tree for fibroblasts in mice

# Nature.2021.05.29

[Sat, 29 May 2021]

- [This Week](#)
- [News in Focus](#)
- [Books & Arts](#)
- [Opinion](#)
- [Work](#)
- [Research](#)
- [Amendments & Corrections](#)

---

| [Next section](#) | [Main menu](#) |

---

# Donation

---

| [Next section](#) | [Main menu](#) |

# This Week

- **[Protect precious scientific collaboration from geopolitics](#)** [ 26 May 2021]  
Editorial • Rivalry between China and other countries could diminish global scientific collaboration — just when it is most needed.
- **[A patent waiver on COVID vaccines is right and fair](#)** [ 25 May 2021]  
Editorial • Wealthier countries must join the United States, Russia and China in recognizing that everyone benefits if vaccine manufacturing is distributed evenly around the world.
- **[Stem-cell guidelines: why it was time for an update](#)** [ 26 May 2021]  
World View • New oversight criteria aim to reassure the public and permit progress in contentious research, such as growing human embryos in the lab.
- **[Tapeworm infestation gives lowly ants long life](#)** [ 18 May 2021]  
Research Highlight • Parasite-ridden ants don't venture out of the nest, which might help to prolong their lives.
- **[Our radical changes to Earth's greenery began long ago — with farms, not factories](#)** [ 20 May 2021]  
Research Highlight • Humanity's imprint on plant species and abundance began roughly 4,000 years ago, when agriculture took off.
- **[Microbes teach a master class in how to clean polluted water](#)** [ 20 May 2021]  
Research Highlight • Chemists take a cue from bacterial enzymes that degrade perchlorate, a contaminant found in drinking water.
- **[The world's biggest seaweed patch sows doubt about a climate fix](#)** [ 19 May 2021]  
Research Highlight • Data from the Great Atlantic Sargassum Belt suggest that floating seaweed farms are no climate panacea.
- **[How a sugary, fatty diet threatens the gut's immune defences](#)** [ 18 May 2021]  
Research Highlight • Fed on the regimen known as the Western diet, intestinal microbes unleash changes that make the gut more prone to infection.

- **The secret origins of Van Leeuwenhoek's famous microscopes** [ 14 May 2021]  
Research Highlight • The father of microbiology surreptitiously relied on widely known formulae — including a protocol written by his arch-rival — when making lenses.
- **Why national attitudes about science matter for vaccine acceptance** [ 21 May 2021]  
Research Highlight • Views on vaccination are coloured by an individual's stance on science — and by their society's stance, too.

---

| [Next section](#) | [Main menu](#) | [Previous section](#) |

- EDITORIAL
- 26 May 2021

# Protect precious scientific collaboration from geopolitics

Rivalry between China and other countries could diminish global scientific collaboration — just when it is most needed.









Addressing challenges such as the COVID-19 pandemic demands scientific collaboration across national borders. Credit: Douglas Magno/AFP/Getty

The COVID-19 pandemic has provided striking demonstrations of the value of research cooperation across borders. From sharing SARS-CoV-2 genome sequences to piecing together how the virus behaves, international research teams have worked together to the benefit of all.

At the same time, there are signs that mounting geopolitical tensions — particularly between the United States and China — might be diminishing the exchange of people and knowledge between nations. As countries move to protect their own interests, effort is needed on all sides to strike an appropriate balance that safeguards the great rewards that flow from mutually beneficial cooperation between researchers.

The stakes could not be higher. Problems such as climate change, environmental degradation and infectious diseases cannot be addressed fully without global scientific collaboration. International research teams help lower-income countries to build the knowledge required to sustain progress;

they also help wealthier nations to pursue equitable, inclusive research based on diverse sources.

Regional collaborations — which are encouraged by the European Union and much-needed in Africa — are likewise crucial to collective science advancement.



### [Scientists in China say US government crackdown is harming collaborations](#)

An analysis<sup>1</sup> of more than 10 million papers tracked by Web of Science found that the number of internationally co-authored papers rose from 10.7% to 21.3% between 2000 and 2015. By 2015, some 200 countries were represented in the collaborative literature. But there is a risk that a golden era of open scientific cooperation is coming to an end.

In 2018, the FBI warned that China was exploiting the open research and development environment in the United States. A tsunami of investigations by the National Institutes of Health and other federal agencies identified hundreds of federally funded scientists suspected of breaking the rules on disclosing foreign ties. Although many were later exonerated, several were found guilty or are facing charges.

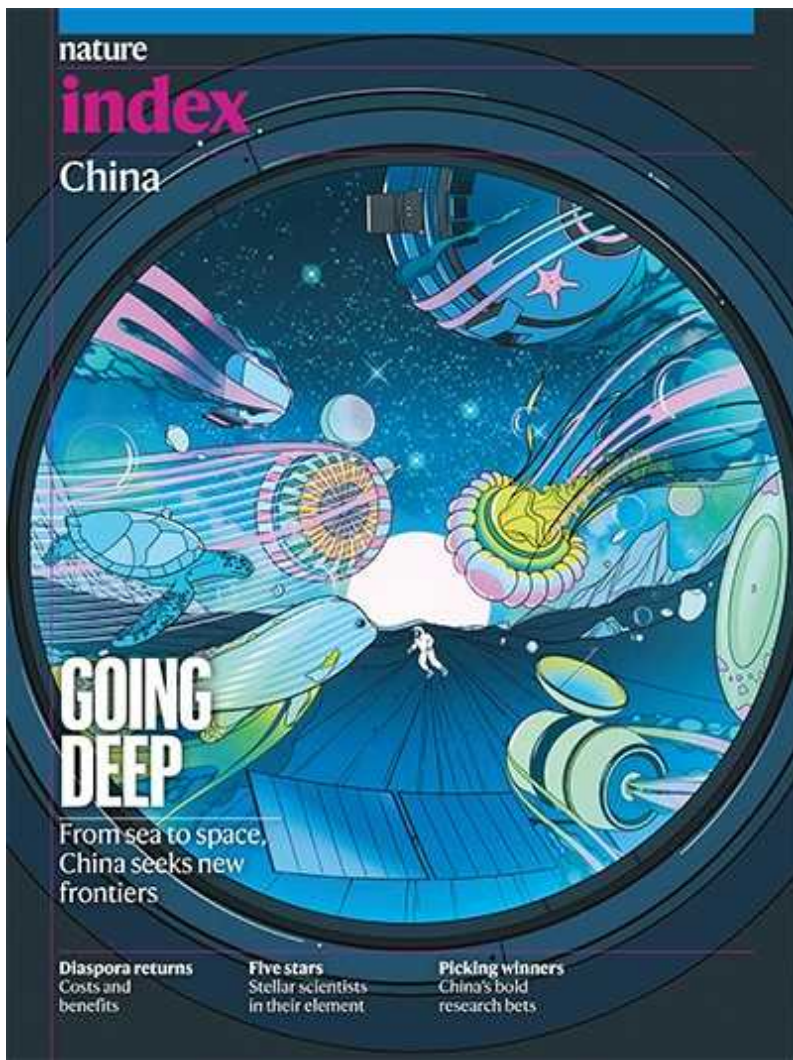
The United States is not alone. Japan, Australia, the United Kingdom, Germany and India have also increased their scrutiny of international

research relationships in the interests of protecting national security, with China widely understood to be the country of primary concern.

Research leaders are worried that researchers in Western nations are shying away from collaborations with those in China, partly for fear of being caught up in geopolitical tensions, and also because of the administrative burden of complying with beefed-up regulations.

In Australia, higher-education enrolments from China are down compared with pre-pandemic levels. In the United States, although student intake from China held steady in the 2019–20 academic year compared with the previous one, the number of scholars visiting from China on temporary visas fell.

Pandemic-related travel restrictions mean it is not possible to blame geopolitics alone. But the publication record also suggests that collaborations between the United States and China might be under threat.



## [Nature Index 2021 China](#)

An [analysis published in this issue](#) shows zero growth between 2019 and 2020 in US–China co-authored publications in the Nature Index, which tracks the author affiliations in 82 natural-sciences journals selected by reputation. By contrast, during the previous four years the growth was more than 10% annually. Publications co-authored by researchers in China and Germany, the United Kingdom, Australia and Japan all increased during the same period. (Nature Index is published by Springer Nature; *Nature* is editorially independent of its publisher.)

Studies that look at a broader swathe of journals also hint that collaborations between the United States and China are changing.

An analysis of science and engineering papers in the Scopus database shows that international collaboration on COVID-19-related research in the first five months of 2020 — including that between the United States and China — was higher than the average for the previous five years across all subjects<sup>2</sup>. On non-COVID-19 research, the proportion of China's collaborations that were with the United States was lower during those months compared with the previous five years, although this might be because collaborations with other countries rose, or because some collaborations switched to focus on COVID-19.



### [US universities call for clearer rules on science espionage amid China crackdown](#)

A later study shows that China–US collaborations in COVID-19 research dropped as the pandemic wore on<sup>3</sup>. This could be due to China's lower publication rate on the topic as infections there waned, political obstacles, or both.

As more data accumulate, researchers, institutions and governments must all play their part to guard against a chill in scientific collaboration. Countries erecting barriers need to set unified and consistent research-security guidelines to give researchers the confidence to collaborate across borders. China, meanwhile, could help to ease tensions by providing greater

transparency, in particular about the workings of Chinese science, its policy motivations and priorities, and how decisions are made.

In a landmark speech on science and technology in September, Chinese President Xi Jinping urged scientists to “adhere to the supremacy of the national interest”, but also highlighted the need for international cooperation. As China’s scientific strength grows, so, too, does the responsibility on all sides to retain a clear-eyed view of the global benefits of collaboration relative to any risks.

Nature **593**, 477 (2021)

doi: <https://doi.org/10.1038/d41586-021-01386-0>

## References

1. 1.

Ribeiro, L. C., Rapini, M. S., Silva, L. A. & Albuquerque, E. M. *Scientometrics* **114**, 159–179 (2018).

[Article](#) [Google Scholar](#)

2. 2.

Lee, J. J. & Haupt, J. P. *J. Higher Educ.* **92**, 303–329 (2020).

[Article](#) [Google Scholar](#)

3. 3.

Cai, X., Fry, C. V. & Wagner, C. S. *Scientometrics* **126**, 3683–3692 (2021).

[Article](#) [Google Scholar](#)

[Download references](#)

## Jobs from Nature Careers

- - - [All jobs](#)
    - - [Postdoctoral Training Fellow - Kassiotis Lab](#)  
[Francis Crick Institute](#)  
[London, United Kingdom](#)  
[JOB POST](#)
      - [Biological Safety Specialist](#)  
[Francis Crick Institute](#)  
[London, United Kingdom](#)  
[JOB POST](#)
      - [Post-doctoral Fellow - Autoimmune Pathogenesis](#)  
[Oklahoma Medical Research Foundation \(OMRF\)](#)  
[Oklahoma City, United States](#)  
[JOB POST](#)
      - [Research Technician / Research Assistant](#)  
[Oklahoma Medical Research Foundation \(OMRF\)](#)  
[Oklahoma City, United States](#)

## JOB POST

[Download PDF](#)

[Download PDF](#)

## Related Articles



- [US universities call for clearer rules on science espionage amid China crackdown](#)



- [Scientists in China say US government crackdown is harming collaborations](#)



- [US political crackdown spurs fears of Chinese brain-drain](#)

---

This article was downloaded by **calibre** from <https://www.nature.com/articles/d41586-021-01386-0>

- EDITORIAL
- 25 May 2021

# A patent waiver on COVID vaccines is right and fair

Wealthier countries must join the United States, Russia and China in recognizing that everyone benefits if vaccine manufacturing is distributed evenly around the world.









Katherine Tai, the US representative at the World Trade Organization, announced US support for a waiver on intellectual property for COVID vaccines on 5 May. Credit: Bill O'Leary/The Washington Post/Bloomberg/Getty

Every country should have the right to make its own vaccines during a pandemic. That's the principle underpinning the campaign to temporarily waive intellectual property (IP) protection on coronavirus vaccines. The campaign was initiated by India and South Africa, and is being backed by more than 100 countries, along with international organizations including the World Health Organization and the United Nations AIDS charity, UNAIDS. The goal is to reduce the barriers to countries producing their own vaccines — particularly for the lowest-income nations.

At present, the proposal does not have the support of the pharmaceutical industry, nor that of most high-income nations. Instead, these countries are pledging to share more of their own vaccines with low-income nations and

to provide more funding to charitable vaccine-provision schemes such as COVAX. However, in a surprising and welcome move earlier this month, the United States, Russia and China came out in support of an IP waiver on vaccines.

The significance of the US decision in particular cannot be overstated, because the country is the world's largest market for pharmaceuticals. For decades, US governments have worked with industry, universities and other research-intensive nations in setting — and enforcing — IP rules, most recently through the World Trade Organization (WTO), where the IP waiver proposal is being discussed. Even a few months ago, the mere idea of the United States taking this position would have been unthinkable. Now that it has done so, those countries still holding out — notably Japan, South Korea, the United Kingdom and European Union member states — need to follow suit.



### [How COVID spurred Africa to plot a vaccines revolution](#)

One of the biggest concerns about IP waivers is that they provide a short-cut to competitors looking to acquire expensive technology. Companies also say that IP relief will not accelerate vaccine manufacturing, because materials are in short supply and it can take several years to build up capacity from scratch.

Moreover, the governments opposing the waiver argue that current WTO rules already allow countries to apply for ‘compulsory licensing’ to override IP during emergencies. Right now, for example, Bolivia is applying to the WTO to use this process to allow it to manufacture Johnson & Johnson’s COVID vaccine. However, a group of researchers in the United Kingdom who study patent law point out in a draft paper on the waiver proposal that compulsory licences are extremely complex and time-consuming to apply for ([S. Thambisetty et al. Preprint at https://ssrn.com/abstract=3851737; 2021](https://ssrn.com/abstract=3851737)).

The EU has also pointed out that the United States has been blocking exports of COVID-19 vaccines and their components. It is right that this be called out. The easing of such restrictions is essential in a pandemic.

These are important arguments, and need to be addressed. But they are not, in themselves, reasons for denying IP relief. If anything, as the pandemic wears on, the reasons to allow a waiver grow stronger.

The core problem is that vaccine manufacturing, research and development is too heavily concentrated in a small group of high- and middle-income countries. Companies in these countries, which are also the main IP holders, have sold the majority of available vaccine doses to their own governments, and to governments of other high-income nations. Some 6 billion doses out of the 8.6 billion confirmed purchases so far have been pre-ordered by governments in high- and middle-income countries.



### It's time to consider a patent reprieve for COVID vaccines

According to pharmaceutical-industry data, the industry expects to have made a total of about ten billion vaccine doses by the end of 2021. But on the basis of current trends, this is unlikely to happen, according to researchers at the International Monetary Fund in Washington DC. In a paper published on 19 May, they report that the industry is likely to have produced around six billion doses by the end of 2021 (see [go.nature.com/2tchn13](https://go.nature.com/2tchn13)). This potential shortfall increases the risk that people in low-income countries will need to wait even longer for their first doses.

As *Nature* went to press, the number of vaccines given so far in Africa amounted to little more than one dose per person for some 2% of Africa's 1.2 billion people. This is, among other factors, because the continent currently imports 99% of its vaccines, and because African countries lack the pre-order purchasing capacity of richer nations. It is why the African Union has announced a plan for 60% of Africa's vaccines to be manufactured on the continent by 2040.

At the Global Health Summit in Rome last week, ahead of this week's World Health Assembly in Geneva, Switzerland, European nations promised to share more vaccine doses with low- and middle-income countries. European Commission president Ursula von der Leyen is also proposing to 'clarify'

and simplify' the existing ways in which countries can implement compulsory licensing. And there is a strong possibility that the G7 group of the world's biggest economies will pledge more funding for vaccination when member countries meet in the United Kingdom next month.

These commitments are crucial in the race to end the pandemic. But they do not deal with the systemic issue — countries backing the IP waiver are not asking for charity, but for the right to develop and make their own vaccines, free from the worry that they will be sued by patent holders.

Those backing the COVID IP waiver understand this core principle. The leaders of countries that are not currently in favour of the patent waiver must recognize it, too. As John Nkengasong, director of the Africa Centres for Disease Control and Prevention, says: they need to be on the right side when the history of the pandemic comes to be written.

Nature **593**, 478 (2021)

doi: <https://doi.org/10.1038/d41586-021-01242-1>

## Jobs from Nature Careers

- - - [All jobs](#)
    - - [Postdoctoral Training Fellow - Kassiotis Lab](#)  
[Francis Crick Institute](#)  
[London, United Kingdom](#)  
[JOB POST](#)
      - [Biological Safety Specialist](#)

[Francis Crick Institute](#)

[London, United Kingdom](#)

[JOB POST](#)

▪ [\*\*Post-doctoral Fellow - Autoimmune Pathogenesis\*\*](#)

[Oklahoma Medical Research Foundation \(OMRF\)](#)

[Oklahoma City, United States](#)

[JOB POST](#)

▪ [\*\*Research Technician / Research Assistant\*\*](#)

[Oklahoma Medical Research Foundation \(OMRF\)](#)

[Oklahoma City, United States](#)

[JOB POST](#)

[Download PDF](#)

[Download PDF](#)

## Related Articles



- [It's time to consider a patent reprieve for COVID vaccines](#)



- [How COVID spurred Africa to plot a vaccines revolution](#)



- [What it will take to vaccinate the world against COVID-19](#)

---

This article was downloaded by **calibre** from <https://www.nature.com/articles/d41586-021-01242-1>

| [Section menu](#) | [Main menu](#) |

- WORLD VIEW
- 26 May 2021

# Stem-cell guidelines: why it was time for an update



New oversight criteria aim to reassure the public and permit progress in contentious research, such as growing human embryos in the lab.

- [Robin Lovell-Badge](#) 0

## 1. [Robin Lovell-Badge](#)

1. Robin Lovell-Badge is a stem-cell and developmental biologist at the Francis Crick Institute in London.

[View author publications](#)

You can also search for this author in [PubMed](#) [Google Scholar](#)





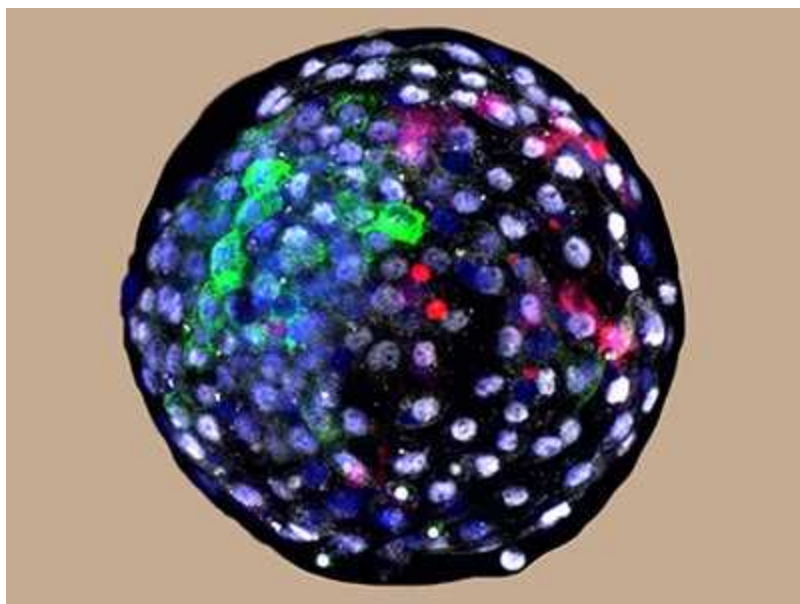
•

Over the past five years, researchers have kept human embryos alive in culture longer than once thought possible and cultured stem cells into structures that model embryos and organs with unprecedented sophistication. Perhaps most striking is the creation of animal–human chimaeras by injecting cells from one species into an early-stage embryo from another species. This might enable, for example, a pig to produce a human heart. Other techniques include making eggs and sperm from stem cells, editing genomes and replacing organelles. These approaches could one day help to treat or avoid human disease, and are already improving biological understanding.

Some find these scientific advances scary and uncomfortable. They raise complicated questions around ethics, beliefs, norms and values. Most scientists want clear boundaries delineating which experiments are acceptable, both legally and to society. And the public wants reassurance. That is why the International Society for Stem Cell Research (ISSCR) has updated its guidelines to reflect current science. These guidelines set standards that are consulted by researchers, policymakers, and funders, journals and others who review research.

The updated guidelines, published this week, are the product of a task force, which I chaired. It comprised 45 international experts, including scientists, clinicians, ethicists, lawyers and policy specialists. We deliberated over 18 months and more than 100 Zoom calls. We consulted relevant polls and public-engagement projects. The guidelines were then peer reviewed by a similar set of experts.

What changes did we recommend? Perhaps the most striking is relaxing the ‘14-day rule’, the limit to culturing intact human embryos in the laboratory, which has been written into law by some dozen countries, including the United Kingdom and Australia. Beyond this point, embryos must be destroyed. Fourteen days is shortly before the stage at which the first signs of the central nervous system appear (the first neurons appear at day 42).



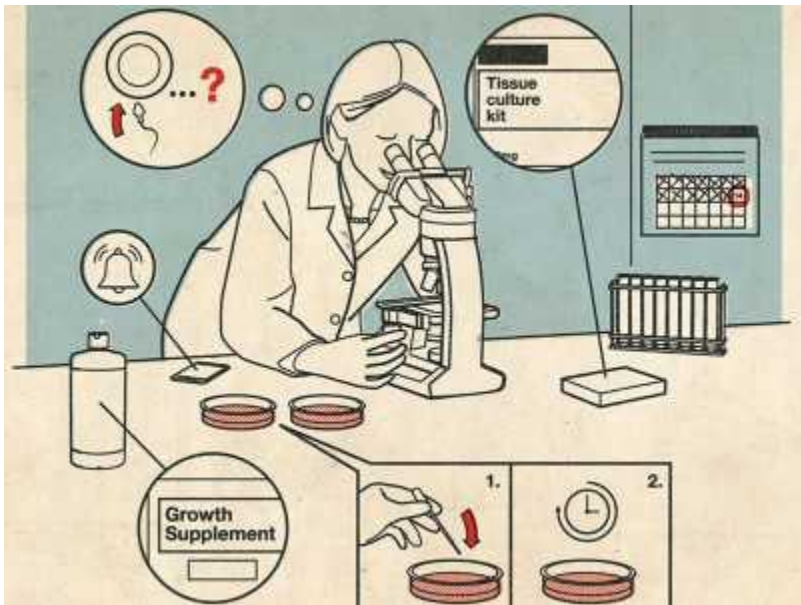
[First monkey-human embryos reignite debate over hybrid animals](#)

When the limit was proposed some 40 years ago, no one could culture human embryos much beyond 5 days, the time of implantation. Now, it prevents study of a critical period, between 14 and 28 days, when the beginnings of tissues are established. Processes that go awry during this time are thought to cause recurring miscarriages and congenital abnormalities, for example those of the heart and spine.

Researchers can also use stem cells to grow structures that are startlingly like embryos. These ‘embryo models’ almost certainly would not develop normally if implanted in a uterus; indeed, our guidelines ban doing so. Still, embryo models could inform us about the 14–28-day period. Comparing them with actual human embryos is the best way to assess their relevance and use them for experiments that might otherwise require embryos. Insights gained — for example, derivation of gametes *in vitro* — might address miscarriage and infertility and could be used to assess techniques, such as heritable genome editing, to avoid genetic disease.

Up to now, the 14-day rule has served science well. It has allowed research that is essential for many assisted-conception techniques to proceed in the face of strong opposition, notably from religious groups. Even scientists who saw value in experiments beyond 14 days, and viewed the time limit as arbitrary, were reluctant to discard a workable compromise made with public input.

The ISSCR’s solution is to require review and approval of proposals to study embryos beyond 14 days. (The approval process, whether by institution or national body, varies by country; all should have representation from specialists and lay members.) Importantly, each proposal should be judged individually, on whether the research is justifiable in terms of the value of the information obtained, whether there are alternative ways to obtain the information and so on. The more embryos that would be used, or the longer they would be kept in culture, the higher the bar.



### The labs growing human embryos for longer than ever before

Before approval could be given, it would require sufficient public support. This should be assessed quantitatively (using tools such as opinion polls) and qualitatively (using, for instance, citizen panels). Applying the guidelines will demand extensive public engagement, including consideration of social justice and whether experiments are an appropriate use of limited resources.

In past guidelines, the ISSCR recognized three broad categories of experiment: banned; permitted with dedicated review and oversight; and permitted generally. Now we have added nuance to these categories. We suggest that certain types of research, such as allowing animals with human gametes to breed, should not be permitted at all because they are ethically concerning, lack compelling scientific rationale or both. Other kinds (such as heritable genome editing) are not permitted now, but might be one day — with evidence about safety and efficacy, and public support.

The guidelines discourage premature commercialization of stem-cell-based interventions, and propose ways to curtail the activities of rogue clinics that offer untested, unsafe interventions with no basis in science.

Such oversight is more complicated but more valuable. Blanket bans enshrined in law appeal in their simplicity, yet leave the public worse off,

and are more vulnerable to dogma or instinct rather than evidence. Guidelines from international scientific societies can offer leadership in reassuring scientists and the public.

Nature **593**, 479 (2021)

doi: <https://doi.org/10.1038/d41586-021-01387-z>

## Competing Interests

The author declares no competing interests.

## Jobs from Nature Careers

- - - [All jobs](#)
    - - [Postdoctoral Training Fellow - Kassiotis Lab](#)  
[Francis Crick Institute](#)  
[London, United Kingdom](#)  
[JOB POST](#)
      - [Biological Safety Specialist](#)  
[Francis Crick Institute](#)  
[London, United Kingdom](#)  
[JOB POST](#)
      - [Post-doctoral Fellow - Autoimmune Pathogenesis](#)

[Oklahoma Medical Research Foundation \(OMRF\)](#)

[Oklahoma City, United States](#)

[JOB POST](#)

▪ [\*\*Research Technician / Research Assistant\*\*](#)

[Oklahoma Medical Research Foundation \(OMRF\)](#)

[Oklahoma City, United States](#)

[JOB POST](#)

[Download PDF](#)

[Download PDF](#)

## Related Articles



- [Research on embryo-like structures struggles to win US government funding](#)



- [Revisit the 14-day rule](#)



- [The labs growing human embryos for longer than ever before](#)



- **First monkey–human embryos reignite debate over hybrid animals**

---

This article was downloaded by **calibre** from <https://www.nature.com/articles/d41586-021-01387-z>

| [Section menu](#) | [Main menu](#) |



A *Temnothorax nylanderi* ant. Having a worm in the gut helps these ants to live to a ripe age. Credit: Shutterstock

Evolution

18 May 2021

## Tapeworm infestation gives lowly ants long life

Parasite-ridden ants don't venture out of the nest, which might help to prolong their lives.





•

A tapeworm infection benefits ant workers by extending their lives, allowing ordinary workers to survive as long as their queen does.

Susanne Foitzik at Johannes Gutenberg University in Mainz, Germany, and her colleagues placed 58 colonies of the ant *Temnothorax nylanderi* in observation nests. The team then checked on the ants every ten days.

In colonies that included ants infected with the tapeworm *Anomotaenia brevis*, no uninfected workers were alive when the experiment ended after three years, but half of the queens and infected workers were still kicking. The team is researching the mechanism behind this life extension, which

might involve extra activity by the same genes that help ant queens to reach old age.

Infected ants also never left the nest. This was probably due to the tapeworm's self-interested influence on its host's habits. For the parasite to complete its life cycle, it must be consumed by woodpeckers, which prey on ant nests. If the host ant stays at home, it's more likely to be eaten when a woodpecker comes knocking.

*R. Soc. Open Sci. (2021)*

- [Evolution](#)

---

This article was downloaded by **calibre** from <https://www.nature.com/articles/d41586-021-01323-1>

| [Section menu](#) | [Main menu](#) |



A nineteenth-century illustration of a harvest in ancient Greece. Farming intensified around 2000 BC, when the rate of change in Earth's plant life sped up. Credit: Docutres/Index/Heritage Images/Alamy

Ecology

20 May 2021

# Our radical changes to Earth's greenery began long ago — with farms, not factories

Humanity's imprint on plant species and abundance began roughly 4,000 years ago, when agriculture took off.





•

Human activity began to transform the number and variety of plant species on Earth thousands of years ago, long before the Industrial Revolution, and might have had an even greater impact on vegetation than did the last ice age.

Ice entombed much of the planet from roughly 115,000 to some 20,000 years ago. Then, massive glaciers around the world started to retreat and global temperatures rose, resulting in dramatic alterations to Earth's ecosystems.

To investigate how the abundance and composition of global vegetation changed after that thaw, Ondřej Mottl and Suzette Flantua at the University

of Bergen in Norway and their colleagues analysed 1,181 fossilized pollen samples from the past 18,000 years. The pollen came from all continents except Antarctica.

The researchers found that global vegetation has been transformed, first by the climate changes that accompanied the end of the last glacial period. However, starting about 4,000 years ago, when agriculture intensified, the pace of change in global vegetation accelerated, reaching or exceeding the rate of change at the end of the most recent ice age.

[Science \(2021\)](#)

- [Ecology](#)

---

This article was downloaded by **calibre** from <https://www.nature.com/articles/d41586-021-01336-w>

| [Section menu](#) | [Main menu](#) |



Drinking water in the United States and elsewhere has been contaminated with perchlorate, an ingredient of rocket fuel. A new material can break down the pollutant. Credit: Getty

Chemistry

20 May 2021

## Microbes teach a master class in how to clean polluted water

Chemists take a cue from bacterial enzymes that degrade perchlorate, a contaminant found in drinking water.





•

Bacteria that break down a harmful molecule have inspired chemists to build a material that does the same, potentially yielding benefits for humans on Earth and perhaps, one day, Mars.

Used in fireworks and rocket fuels, the explosive perchlorate ion ( $\text{ClO}_4^-$ ) disrupts thyroid function and often seeps into drinking water. Microbes living in oxygen-poor environments provide an idea for remediation: some of them breathe by splitting perchlorate into oxygen gas and harmless chloride ions.

The complex microbial machinery for this process includes an enzyme containing molybdenum atoms, which rip the first oxygen atom from perchlorate. Jinyong Liu at the University of California, Riverside, and his colleagues designed a material that also relies on molybdenum to strip oxygen from perchlorate. The researchers stabilized the molybdenum molecules by embedding them in the pores of a carbon powder, which also house palladium nanoparticles that power the entire oxygen-removal process.

Suspended in water, the powder completely degraded perchlorate in various concentrations at room temperature. The researchers hope that with further engineering, this process could help to supply oxygen on Mars, where perchlorates lace the soil.

[J. Am. Chem. Soc. \(2021\)](#)

- [Chemistry](#)

---

This article was downloaded by **calibre** from <https://www.nature.com/articles/d41586-021-01335-x>

| [Section menu](#) | [Main menu](#) |



*Sargassum* litters a beach on Saint Thomas, US Virgin Islands. A study of a *Sargassum* bloom that spread across the Atlantic Ocean in 2017 and 2018 casts doubt on seaweed farms' capacity to curb global warming. Credit: Alyson Myers

Biogeochemistry

19 May 2021

## The world's biggest seaweed patch sows doubt about a climate fix

Data from the Great Atlantic Sargassum Belt suggest that floating seaweed farms are no climate panacea.





•

Seaweed absorbs carbon dioxide from the atmosphere, but large seaweed farms in the ocean might not be the climate fix that many scientists have proposed.

To test seaweed farms' potential impact on climate, Lennart Bach at the University of Tasmania in Hobart, Australia, and his colleagues analysed a natural analogue: the Great Atlantic Sargassum Belt, a floating seaweed bloom in the north Atlantic Ocean. The team estimated the belt's carbon uptake during a major bloom in 2017 and 2018 and considered biological knock-on effects. For example, photosynthetic plankton that the bloom

displaced reduced their carbon intake, and microscopic animals that attached to the seaweeds increased their release of carbon dioxide.

The team's calculations suggest that these effects offset 20–100% of the 810,000 tonnes of carbon accumulated by the *Sargassum* bloom. The team also thinks that the bright *Sargassum* belt could affect climate by reflecting large amounts of solar radiation into space and by releasing organic matter into the atmosphere, thereby increasing cloud cover. The size of such effects is uncertain, raising questions about seaweed farming as a climate intervention strategy.

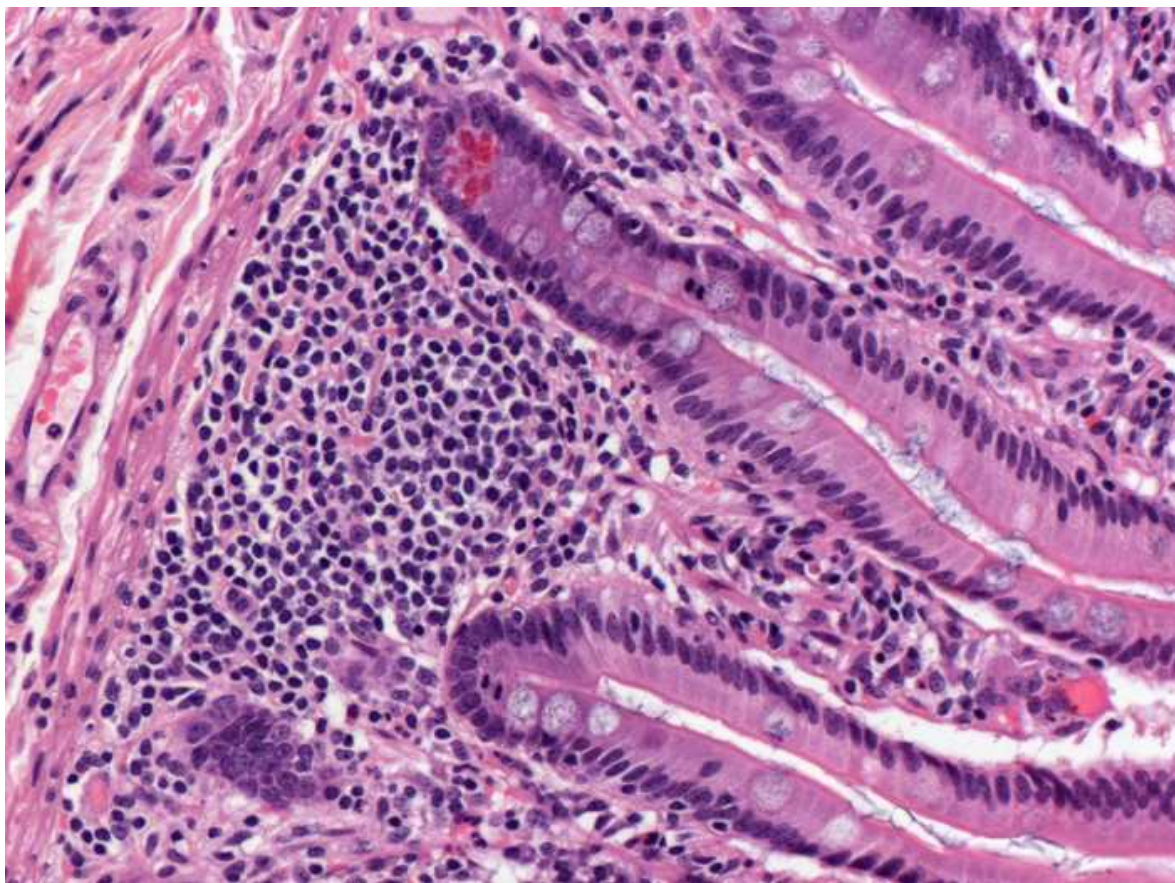
*Nature Commun.* (2021)

- [Biogeochemistry](#)

---

This article was downloaded by **calibre** from <https://www.nature.com/articles/d41586-021-01333-z>

| [Section menu](#) | [Main menu](#) |



The small intestine. Intestinal cells that secrete antibiotic compounds can malfunction in mice that subsist on unhealthy food. Credit: Alvin Telser/Science Photo Library

Metabolism

18 May 2021

## How a sugary, fatty diet threatens the gut's immune defences

Fed on the regimen known as the Western diet, intestinal microbes unleash changes that make the gut more prone to infection.





•

A diet high in fat and sugar impairs the immune defences of the gut by disturbing its resident bacteria.

Among the gut's guardians are its Paneth cells, which make and pump out antimicrobial molecules. Breakdown of these cells can raise the risk of small-intestine infections. Prior research has suggested a link between dysfunctional Paneth cells and the high-fat, high-sugar Western diet, which raises the risk of obesity.

Ta-Chiang Liu at Washington University School of Medicine in St. Louis, Missouri, Thaddeus Stappenbeck at the Cleveland Clinic in Ohio and their colleagues set out to understand the connections between malfunctioning

Paneth cells and both diet and obesity. The team examined Paneth cells from more than 400 people and found that participants with a higher body mass index, a proxy for obesity, tended to have more Paneth-cell defects.

The team then demonstrated that, in mice, a fat-laden diet could cause Paneth-cell impairment. Work in mice also revealed that a high-fat diet triggered resident gut bacteria to activate a signalling system that ultimately prompts immune cells to launch an attack against the Paneth cells.

*[Cell Host Microbe \(2021\)](#)*

- [Metabolism](#)

---

This article was downloaded by **calibre** from <https://www.nature.com/articles/d41586-021-01337-9>

| [Section menu](#) | [Main menu](#) |



These microscopes made by Antoni van Leeuwenhoek more than 300 years ago had magnifying powers of x118 (left) and x266. Credit: Tom Haartsen Fotografie, University Museum Utrecht

Microscopy

14 May 2021

# The secret origins of Van Leeuwenhoek's famous microscopes

The father of microbiology surreptitiously relied on widely known formulae — including a protocol written by his arch-rival — when making lenses.





•

Pioneering microbiologist Antoni van Leeuwenhoek made the best microscopes of the pre-industrial era with methods that he kept secret. But the first full-3D scans of two of his instruments reveal that he might have succeeded by perfecting his arch-rival Robert Hooke's techniques.

Tiemen Cocquyt at the Rijksmuseum Boerhaave in Leiden, the Netherlands, and his collaborators used a method called neutron tomography to image two of the roughly 10 surviving microscopes made by Van Leeuwenhoek (1632–1723). The neutron scans revealed the full structure of each instrument's lens, which is held by metal plates.

One lens has a lentil shape, achieved using a common glass-grinding technique, the team found. The other, in an instrument that is among the most powerful that Van Leeuwenhoek ever made, is a spherical glass bead. Hooke had previously described, in 1678, a simple technique to make such beads by melting the end of a glass needle — but it was Van Leeuwenhoek's unrivalled craftsmanship that honed this method to make microscopes that would not be surpassed until 150 years after his death, the authors conclude.

*[Sci. Adv. \(2021\)](#)*

- [Microscopy](#)

---

This article was downloaded by **calibre** from <https://www.nature.com/articles/d41586-021-01303-5>

| [Section menu](#) | [Main menu](#) |



A health-care worker gives an influenza jab in Milan, Italy. People in pro-science societies tend to have confidence in vaccines. Credit: Alessandro Bremec/NurPhoto/Getty

Human behaviour

21 May 2021

# Why national attitudes about science matter for vaccine acceptance

Views on vaccination are coloured by an individual's stance on science — and by their society's stance, too.





•

Ample evidence shows that people tend to trust vaccines if they also trust science in general. Now, survey data from 126 countries suggest that people also tend to trust vaccines if they live in countries where confidence in science is high.

Public-health officials around the world are struggling to overcome hesitance about vaccines that protect against COVID-19 and other diseases. To understand how societal attitudes influence individual hesitance, Patrick Sturgis at the London School of Economics and Political Science and his colleagues analysed data from more than 120,000 survey respondents to

assess each person's confidence in vaccines in the context of broader trust in science in their country.

The team found that individual vaccine confidence is highest in the countries with the greatest trust in science as a whole, regardless of a person's own opinions about science. This correlation is strongest when there is country-wide consensus that science and scientists are trustworthy.

The authors suggest that this insight could lead to new research into how societal consensus around trust in science can be used to promote effective vaccine strategies.

[Nature Hum. Behav. \(2021\)](#)

- [Human behaviour](#)
- 

This article was downloaded by **calibre** from <https://www.nature.com/articles/d41586-021-01334-y>.

| [Section menu](#) | [Main menu](#) |

# News in Focus

- **[Mars photos, COVID vaccine efficacy and dosing delays](#)** [ 26 May 2021]  
News Round-Up • The latest science news, in brief.
- **[India's neighbours race to sequence genomes as COVID surges](#)** [ 14 May 2021]  
News • From Sri Lanka to Nepal, scientists with limited resources are working feverishly to discover which variants are driving outbreaks.
- **[First nuclear detonation created 'impossible' quasicrystals](#)** [ 17 May 2021]  
News • Their structures were once controversial. Now researchers have discovered quasicrystals in the aftermath of a 1945 bomb test.
- **['It's a minefield': COVID vaccine safety poses unique communication challenge](#)** [ 21 May 2021]  
News • Poll on vaccine hesitancy demonstrates the extraordinary predicament researchers face in transmitting risk information during a pandemic.
- **[Open-access publisher PLOS pushes to extend clout beyond biomedicine](#)** [ 13 May 2021]  
News • The publisher will launch five new journals, and has introduced a new business model that aims to spread the cost of publishing more fairly.
- **[Prestigious European grants might be biased, study suggests](#)** [ 21 May 2021]  
News • Institutional affiliations of panellists seem to skew European Research Council decisions — especially in the life sciences.
- **[Mix-and-match COVID vaccines trigger potent immune response](#)** [ 19 May 2021]  
News • Preliminary results from a trial of more than 600 people are the first to show the benefits of combining different vaccines.
- **[The mini lungs and other organoids helping to beat COVID](#)** [ 26 May 2021]  
News Feature • Virologists have infected millions of miniature organs with SARS-CoV-2, to learn how the virus wreaks havoc and how to stop it.

- **What the science says about lifting mask mandates** [ 25 May 2021]

News Feature • With COVID rates dropping and vaccinations on the rise, the United States and other places are removing some requirements for face coverings. Are they moving too fast?

---

| [Next section](#) | [Main menu](#) | [Previous section](#) |

- NEWS ROUND-UP
- 26 May 2021

# Mars photos, COVID vaccine efficacy and dosing delays

The latest science news, in brief.









An image, taken from the front of Zhurong, shows the ramp deployed from its lander. The craft is ready to roll off and explore an invitingly flat plain. Credit: China National Space Administration

## First shots from China's Mars rover

The China National Space Administration (CNSA) has revealed the [first images from Mars taken by its Zhurong rover](#), which arrived on the planet's surface this month. Scientists say that the shots — which show its solar

panels unfurled and the ramp from its lander deployed — hint that it arrived at an ideal site from which it can explore.

“The first images show, first and foremost, a terrain that will be easy to drive over,” says Alfred McEwen, a planetary scientist at the University of Arizona in Tucson. He and other space scientists are thrilled to see that the site appears to be flat and largely free of obstructions, such as craters, rocks and boulders. From there, the craft will potentially travel long distances to features of interest seen in satellite imagery.

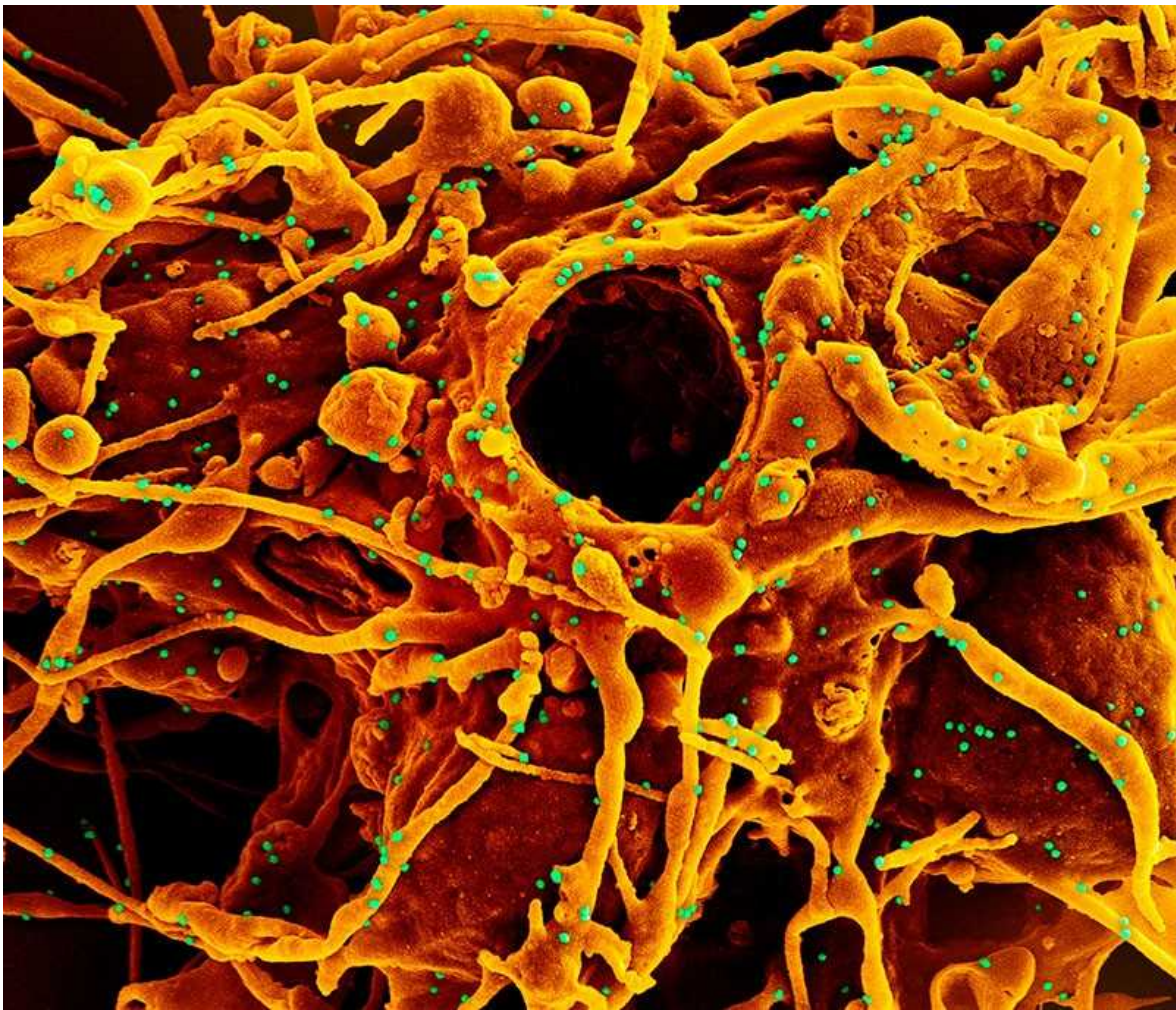
“We are very excited. But we are still waiting for more images with high resolution to come,” says Yuyan Zhao, a planetary geochemist at the Institute of Geochemistry, Chinese Academy of Sciences, in Guiyang.

A black-and-white image, taken from a forward-facing obstacle-avoidance camera with a wide-angle lens, shows a ramp descending from the landing platform, which Zhurong has now rolled off. A second image, in colour, showing the view from a navigation camera pointing towards the rear of the rover, reveals a deployed antenna and solar panels in the shape of butterfly wings.

The photographs are “clearly world-class quality and very exciting scientifically”, says Joseph Michalski, a planetary scientist at the University of Hong Kong. Researchers “will need a little time to dig into the details”, he adds. “But the images are enticing and encouraging.”

The flat landscape that can be seen is especially promising, scientists say, because it means Zhurong could reach features of geological interest that are several kilometres away. One land form of particular interest is a cone-shaped feature seen in aerial images, possibly a mud volcano, to the northeast.

Zhurong’s mission is expected to last three months, but the rover could survive for longer and tally up a considerable distance, as other solar-powered rovers have.



Particles of the SARS-CoV-2 coronavirus (blue-green; artificially coloured) infect a cell (orange). Credit: NIAID/NIH/SPL

## Scientists zero in on marker of COVID-vaccine efficacy

After people have been vaccinated against COVID-19, the levels of infection-blocking, or ‘neutralizing’, antibodies in their blood are a strong indicator of how much protection they’ve gained against the disease, according to a modelling study ([D. S. Khoury et al. \*Nature Med.\* <https://doi.org/gj3h47>; 2021\).](https://doi.org/gj3h47)

The research is the best attempt yet to define features of the immune response that can act as a proxy for protection against COVID-19, known as

a correlate of protection, says Daniel Altmann, an immunologist at Imperial College London (pictured, SARS-CoV-2 particles infecting a cell).

If researchers have a well-defined correlate of protection, they can predict from early trial data how effective a vaccine will be, says James Triccas, a medical microbiologist at the University of Sydney in Australia and a co-author of the study. This “alleviates the need to do larger, more expensive and time-consuming phase III trials”.

Triccas and his colleagues examined antibody data from trials of seven widely used vaccines. The team found a [strong link between neutralizing-antibody levels recorded in participants in early-stage trials and vaccine-efficacy results from late-stage trials](#).



A man in Tunis receives a dose of the Pfizer–BioNTech vaccine for COVID-19. Credit: Jdidi Wassim/SOPA Images/LightRocket via Getty

## Delaying second dose boosts vaccine response

At the end of 2020, the United Kingdom faced a limited supply of COVID-19 vaccines, so it delayed second doses to maximize the number of people who would be at least partially protected from hospitalization and death.

Now, a study suggests that [delaying the second dose of the Pfizer–BioNTech mRNA vaccine could boost antibody responses](#) after the second inoculation more than threefold in those older than 80 ([H. Parry et al. Preprint at medRxiv https://doi.org/gdhc; 2021](#)).

Published as a preprint, it is the first direct study of how such a delay affects coronavirus antibody levels, and could inform vaccine scheduling decisions in other countries, the authors say.

Gayatri Amirthalingam, an epidemiologist at Public Health England in London, and her colleagues studied 175 vaccine recipients older than 80 who received their second dose of the Pfizer vaccine either 3 weeks or 11–12 weeks after the first dose. Peak antibody levels were 3.5 times higher in those who waited 12 weeks for their booster shot than in people who waited only 3 weeks.

“This study further supports a growing body of evidence that the approach taken in the UK for delaying that second dose has really paid off,” says Amirthalingam.

Nature **593**, 483 (2021)

doi: <https://doi.org/10.1038/d41586-021-01388-y>

## Jobs from Nature Careers

- - - [All jobs](#)
    - - [Postdoctoral Training Fellow - Kassiotis Lab](#)  
[Francis Crick Institute](#)

[London, United Kingdom](#)

[JOB POST](#)

- [Biological Safety Specialist](#)

[Francis Crick Institute](#)

[London, United Kingdom](#)

[JOB POST](#)

- [Post-doctoral Fellow - Autoimmune Pathogenesis](#)

[Oklahoma Medical Research Foundation \(OMRF\)](#)

[Oklahoma City, United States](#)

[JOB POST](#)

- [Research Technician / Research Assistant](#)

[Oklahoma Medical Research Foundation \(OMRF\)](#)

[Oklahoma City, United States](#)

[JOB POST](#)

[Download PDF](#)

[Download PDF](#)

---

This article was downloaded by **calibre** from <https://www.nature.com/articles/d41586-021-01388-y>.

- NEWS
- 14 May 2021

# India's neighbours race to sequence genomes as COVID surges

From Sri Lanka to Nepal, scientists with limited resources are working feverishly to discover which variants are driving outbreaks.

- [Smriti Mallapaty](#)
  1. Smriti Mallapaty  
[View author publications](#)

You can also search for this author in [PubMed](#) [Google Scholar](#)









Health workers administer SARS-CoV-2 tests at a railway station in Sri Lanka's capital, Colombo. Credit: Xinhua/eyevine

In early April, Neelika Malavige shut down her laboratory in Sri Lanka for ten days to celebrate Sinhalese New Year. Malavige, an immunologist at the University of Sri Jayewardenepura in Colombo, runs the only lab in the nation that sequences SARS-CoV-2 genomes. But case counts had dipped, hotspots had started to receive vaccines, and her team needed the break.

When the researchers returned to work, however, what they found was dizzying. Of 78 samples that they sequenced from people with COVID-19 in late April, 66 contained the [highly transmissible B.1.1.7 variant](#). Since 17 April, the number of new COVID-19 cases in Sri Lanka — which hit 2,672 on 9 May — has been breaking records almost every day. Hospitals are filling up and Malavige is bracing for a looming wave of deaths. “The situation in Sri Lanka is looking very grim,” she says.

As India struggles [under the weight of a massive surge](#) of COVID-19, many of its neighbours in south and southeast Asia are experiencing some of their largest outbreaks yet (see ‘Asia’s growing outbreaks’). There are even surges in Bhutan, where 62% of the population has received at least one dose of a vaccine, and Laos, which has previously had very few cases — although these outbreaks are small compared with those in nearby nations.

## Spillover from India?

Researchers region-wide are embarking on a remarkable effort to quickly scale up their very limited sequencing capacities to identify whether India’s epidemic — [fuelled by variants such as B.1.617](#) — is spilling over into their communities, or if their outbreaks have origins elsewhere. In some cases, they are working around the clock and with insufficient resources. Specifically, they want to know whether worrying variants are circulating, so that they can assess the risks.



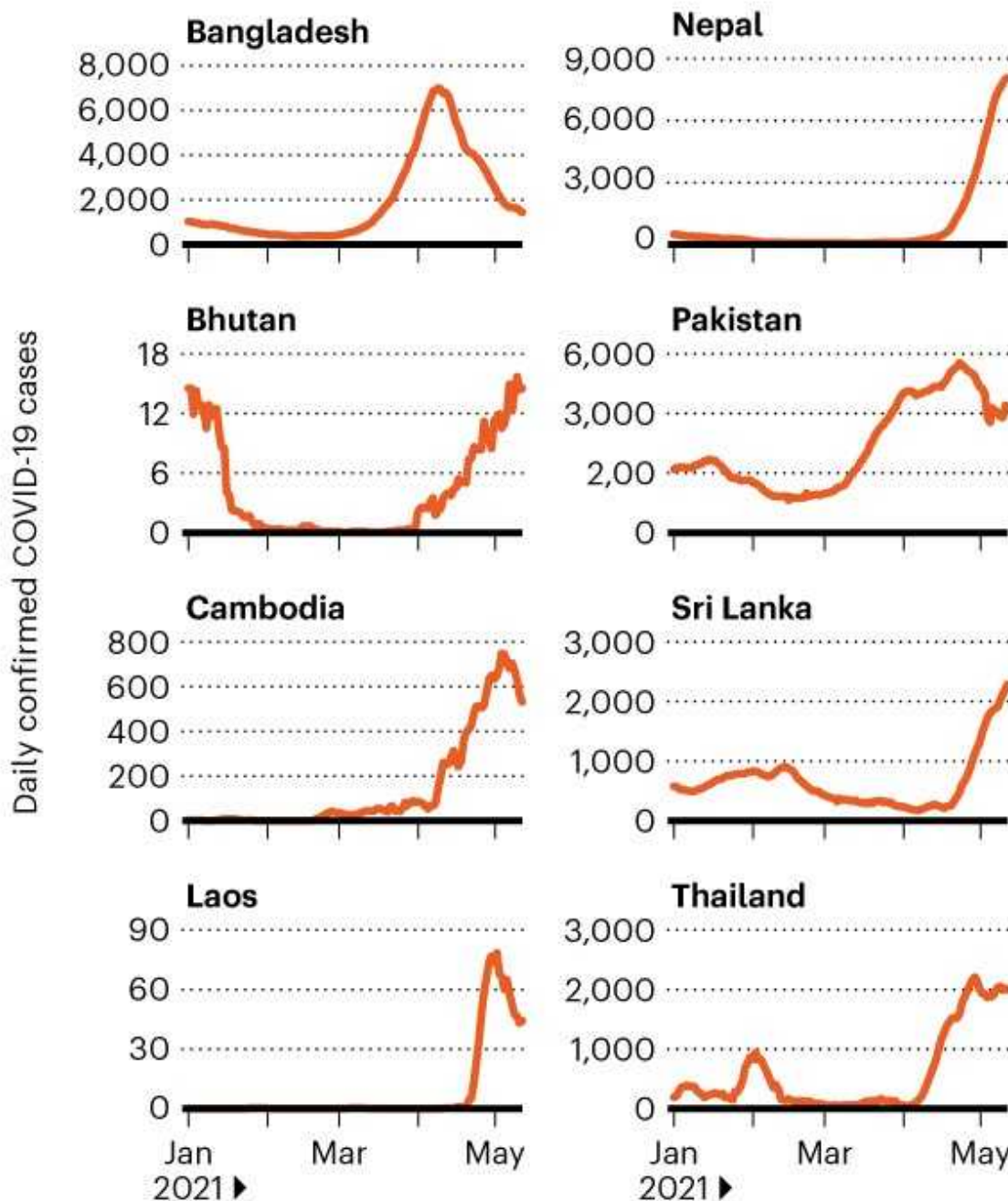
### [Coronavirus variants are spreading in India — what scientists know so far](#)

“It’s important to ramp up our sequencing to make sure we detect these variants in the community as soon as possible,” says Malavige, who, from May, is doubling the average number of samples sequenced each month, to nearly 200.

“We all have the question of why is it happening? Why is this wave now? And why is it so bad?” says Senjuti Saha, a molecular geneticist at the Child Health Research Foundation in Dhaka. New cases in Bangladesh reached more than 7,000 a day in mid-April. Numbers have fallen again since then, but Saha has noticed a big increase in sequences from the country shared on online genome databases and more labs are getting involved, which she puts down to concerns over the spread of variants.

# ASIA'S GROWING OUTBREAKS

Many of India's neighbours have experienced COVID-19 surges, with significant increases in numbers of new daily cases since early April.



Source: Our World in Data

Identifying worrying variants will help governments to make decisions about responses and restrictions, and whether more aggressive interventions are needed, says Dibesh Karmacharya, executive director of the Center for Molecular Dynamics Nepal, a non-profit organization in Kathmandu that sequences SARS-CoV-2 genomes.

Especially worrying is B.1.617, which was first identified in the Indian state of Maharashtra, and which the World Health Organization has said is probably highly transmissible. It is spreading fast through India and might have the ability to evade some immunity from previous infections or vaccination.

“Sequencing has always been important, but it is critical now, because we are getting to a stage where more and more new variants are cropping up,” says Gavin Smith, a viral evolutionary biologist at Duke–NUS Medical School in Singapore. “We need sequence data to see what is going on.”

## **Worrying variants**

Sequenced samples in south and southeast Asia still represent only a small fraction of cases. But they are beginning to reveal a mixed picture of variants driving outbreaks in the region.



### Why India must tackle a mutating virus head-on

In Bangladesh, for example, the surge has coincided with the widespread detection of B.1.351, a variant [first identified in South Africa](#), which has been linked to [reduced effectiveness](#) of the University of Oxford–AstraZeneca vaccine.

Saha first found the variant in her samples in February. In March, 28 of 36 genomes she sequenced were of B.1.351, as were more than 70% of 100 sequences shared by other groups in Bangladesh that month<sup>1</sup>. The variant has swept the country, and is especially worrying for Bangladesh, because most of the vaccines available there are Covishield, a version of the AstraZeneca vaccine produced in India.

The picture is different in Cambodia and Sri Lanka, where B.1.1.7 is predominant. Malavige wants to keep a close eye on its spread and evolution to see whether it develops a mutation known as E484K, which is present in some other variants and might allow it to evade immunity.

Cases in Cambodia have been rising steeply since early April. All 120 or so genomes sequenced there since then have been of B.1.1.7, says Erik Karlsson, a virologist at the Pasteur Institute of Cambodia in Phnom Penh, who runs the only lab in the country sequencing SARS-CoV-2.



People with COVID-19 receive oxygen outside an overwhelmed hospital in Kathmandu, Nepal. Credit: Navesh Chitrakar/Reuters

The lab has greatly increased its sequencing capacity during the pandemic, and can now process more than two dozen genomes a week, providing near real-time insights. COVID-19 has “revolutionized the way we use sequencing”, says Karlsson, who has been sleeping at the institute to continue his work since a lockdown was imposed in Phnom Penh in mid-April.

The researchers in Bangladesh, Sri Lanka and Cambodia say they have not yet detected B.1.617 in their communities, but it could have crept in without being detected, owing to the minimal sequencing. “We are surrounded by India, and people are coming in and out all the time,” says Saha, and fewer than 1% of confirmed cases in Bangladesh have been sequenced.

## Frightening picture

To the northwest, B.1.617 has definitely made its way to Nepal, which shares an extensive, largely open border with India. Reported cases of COVID-19 have shot up since mid-April — hitting a new record of 9,317 cases on 11 May. Relative to population size, that's more cases than in India.

In early May, Karmacharya's team sequenced 12 samples from people recently infected in the Kathmandu valley — including himself. Eleven of the sequences were of B.1.617, and one was of B.1.1.7. The results are only a tiny snapshot of what is circulating, but are still “a little scary”, says Karmacharya, who had received one shot of a COVID-19 vaccine before getting infected and has now recovered.

But although researchers recognize that more genomic surveillance would be useful, their ambitions are limited by resources. “The main problem is a lack of funds,” says Malavige.

Karlsson points out that sequencing reagents are in high demand globally. With reduced airline activity, getting supplies to Cambodia “is a fight”.

Sequencing takes time to process, says Malavige. As a shortcut, her lab uses real-time polymerase chain reaction (PCR) kits that can quickly detect three widely circulating variants of concern: B.1.1.7, B.1.351 and P.1. But kits that detect B.1.617 have only just been developed and they cannot identify newly emerging variants.

“We are at a critical point where we need to keep sequencing to identify anything as soon as possible,” she says. And with vaccines still in very short supply in much of the region, many people will remain at risk, say researchers.

Nature **593**, 485-486 (2021)

doi: <https://doi.org/10.1038/d41586-021-01287-2>

## References

1. 1.

Saha, S. *et al.* *BMJ Glob. Health* **6**, e006012 (2021).

[PubMed](#) [Article](#) [Google Scholar](#)

[Download references](#)

## **Jobs from Nature Careers**

- - - [All jobs](#)
    - - **[Postdoctoral Training Fellow - Kassiotis Lab](#)**
        - [Francis Crick Institute](#)
        - [London, United Kingdom](#)
        - [JOB POST](#)
      - **[Biological Safety Specialist](#)**
        - [Francis Crick Institute](#)
        - [London, United Kingdom](#)
        - [JOB POST](#)
      - **[Post-doctoral Fellow - Autoimmune Pathogenesis](#)**
        - [Oklahoma Medical Research Foundation \(OMRF\)](#)
        - [Oklahoma City, United States](#)
        - [JOB POST](#)

## **Research Technician / Research Assistant**

**Oklahoma Medical Research Foundation (OMRF)**

**Oklahoma City, United States**

### **JOB POST**

**Download PDF**

**Download PDF**

## **Related Articles**



- **Why India must tackle a mutating virus head-on**



- **India's massive COVID surge puzzles scientists**



- **India's COVID-vaccine woes — by the numbers**

---

This article was downloaded by **calibre** from <https://www.nature.com/articles/d41586-021-01287-2>

- NEWS
- 17 May 2021

# First nuclear detonation created ‘impossible’ quasicrystals

Their structures were once controversial. Now researchers have discovered quasicrystals in the aftermath of a 1945 bomb test.

- [Davide Castelvecchi](#)
  1. Davide Castelvecchi  
[View author publications](#)

You can also search for this author in [PubMed](#) [Google Scholar](#)









This sample of red trinitite was found to contain a previously unknown type of quasicrystal. Credit: Luca Bindi, Paul J. Steinhardt

Scientists searching for quasicrystals — so-called ‘impossible’ materials with unusual, non-repeating structures — have identified one in remnants of the world’s first nuclear bomb test.

The previously unknown structure, made of iron, silicon, copper and calcium, probably formed from the fusion of vaporized desert sand and copper cables. Similar materials have been synthesized in the laboratory and identified in meteorites, but this one, described in *Proceedings of the National Academy of Sciences* on 17 May, is the first example of a quasicrystal with this combination of elements<sup>1</sup>.

## Impossible symmetries

Quasicrystals contain building blocks made up of arrangements of atoms that — unlike those in ordinary crystals — do not repeat in a regular, brickwork-like pattern. Whereas ordinary crystal structures look identical after being translated (shifted along certain directions), quasicrystals have symmetries that were once considered impossible: for example, some have pentagonal symmetry, and so look the same if rotated by one-fifth of a full twist.

Materials scientist Daniel Shechtman, now at the Technion Israel Institute of Technology in Haifa, first discovered such an impossible symmetry in a synthetic alloy in 1982. It had pentagonal symmetry when rotated in each of various possible directions, something that would occur if its building blocks were icosahedral — that is, had a regular shape with 20 faces<sup>2</sup>. Many researchers initially questioned Shechtman’s findings, because it is mathematically impossible to fill space using only icosahedrons. [Shechtman ultimately won the 2011 Nobel Prize](#) in Chemistry for the discovery.

At around the same time, Paul Steinhardt, a theoretical physicist now at Princeton University in New Jersey, and his collaborators had begun to theorize the possible existence of non-repeating 3D structures. These had the same symmetry as an icosahedron, but were assembled from building blocks of several different types, which never repeated in the same pattern<sup>3</sup> — thus explaining why the mathematics of symmetrical crystals had missed them. Mathematical physicist Roger Penrose, now at the University of Oxford, UK, and other researchers had previously discovered analogous patterns in two dimensions, which are called Penrose tilings.

Steinhardt recalls the moment in 1982 when he first saw the experimental data from Shechtman’s discovery and compared it with his theoretical predictions. “I stood up from my desk and went and looked at our pattern, and you couldn’t tell the difference,” he says. “So that was kind of an amazing moment.”

In subsequent years, materials scientists synthesized many types of quasicrystal, expanding the range of possible forbidden symmetries. And Steinhardt and his colleagues later [found the first naturally occurring ‘icosahedrite’](#) in fragments from a meteorite recovered in Eastern Siberia, Russia. This quasicrystal probably formed in a collision between two

asteroids in the early Solar System, Steinhardt says. Some of the lab-made quasicrystals were also produced by smashing materials together at high speed, so Steinhardt and his team wondered whether the shockwaves from nuclear explosions might form quasicrystals, too.

## ‘Slicing and dicing’

In the aftermath of the Trinity test — the first ever detonation of a nuclear bomb, which took place on 16 July 1945 at New Mexico’s Alamogordo Bombing Range — researchers found a vast field of greenish glassy material that had formed from the liquefaction of desert sand. They dubbed this trinitite.

The plutonium bomb had been detonated on top of a 30-metre-high tower, which was laden with sensors and their cables. As a result, some of the trinitite that formed had reddish inclusions, says Steinhardt. “It was a fusion of natural material with copper from the transmission lines.” Quasicrystals often form from elements that would not normally combine, so Steinhardt and his colleagues thought samples of the red trinitite would be a good place to look for quasicrystals.

“Over the course of ten months, we were slicing and dicing, looking at all sorts of minerals,” Steinhardt says. “Finally, we found a tiny grain.” The quasicrystal has the same kind of icosahedral symmetry as the one in Shechtman’s original discovery.

“The dominance of silicon in its structure is quite distinct,” says Valeria Molinero, a theoretical chemist at the University of Utah in Salt Lake City. “However, after many quasicrystals have been synthesized in the lab,” she says, “what I find truly intriguing is that they are so scarce in nature.” Steinhardt says this might be because the formation of quasicrystals involves “unusual combinations of elements and unusual arrangements”.

Like most known quasicrystals, the trinitite structure seems to be an alloy — a metal-like material made up of positive ions in a sea of electrons. This is unusual for silicon, which typically occurs in rock in an oxidized form: reversing the oxidation would require extreme conditions, such as the

intense heat and pressure of a shockwave, says Lincoln Hollister, a geoscientist at Princeton.

Steinhardt suggests that quasicrystals could be used for a kind of nuclear forensic science, because they might reveal sites where a covert nuclear test has occurred. Quasicrystals might also form in other materials that were generated in violent conditions, such as fulgurite, the material made when lightning strikes rock, sand or other sediments. “The quasicrystal saga will continue!” says Hollister.

Nature **593**, 487 (2021)

doi: <https://doi.org/10.1038/d41586-021-01332-0>

## References

1. 1.

Bindi, L. *et al. Proc. Natl Acad. Sci. USA*  
<https://doi.org/10.1073/pnas.2101350118> (2021).

[Article](#) [Google Scholar](#)

2. 2.

Shechtman, D., Blech, I., Gratias, D. & Cahn, J. W. *Phys. Rev. Lett.* **53**, 1951–1953 (1984).

[Article](#) [Google Scholar](#)

3. 3.

Levine, D. & Steinhardt, P. J. *Phys. Rev. Lett.* **53**, 2477–2480 (1984).

[Article](#) [Google Scholar](#)

[Download references](#)

## Jobs from Nature Careers

- - - [All jobs](#)
    - - [Postdoctoral Training Fellow - Kassiotis Lab](#)  
[Francis Crick Institute](#)  
[London, United Kingdom](#)  
[JOB POST](#)
      - [Biological Safety Specialist](#)  
[Francis Crick Institute](#)  
[London, United Kingdom](#)  
[JOB POST](#)
      - [Post-doctoral Fellow - Autoimmune Pathogenesis](#)  
[Oklahoma Medical Research Foundation \(OMRF\)](#)  
[Oklahoma City, United States](#)  
[JOB POST](#)
      - [Research Technician / Research Assistant](#)  
[Oklahoma Medical Research Foundation \(OMRF\)](#)  
[Oklahoma City, United States](#)

## JOB POST

[Download PDF](#)

[Download PDF](#)

## Related Articles



- [Strange topological materials are popping up everywhere physicists look](#)
- [A simpler approach to Penrose tiling with implications for quasicrystal formation](#)
- [Quasicrystals: the thrill of the chase](#)



- [Impossible crystals snag chemistry Nobel](#)

---

This article was downloaded by **calibre** from <https://www.nature.com/articles/d41586-021-01332-0>

- NEWS
- 21 May 2021

# ‘It’s a minefield’: COVID vaccine safety poses unique communication challenge

Poll on vaccine hesitancy demonstrates the extraordinary predicament researchers face in transmitting risk information during a pandemic.

- [Ariana Remmel](#)

1. Ariana Remmel

[View author publications](#)

You can also search for this author in [PubMed](#) [Google Scholar](#)









The US roll-out of the Johnson & Johnson COVID-19 vaccination resumed in late April after a ten-day pause. Credit: Frederic J. Brown/AFP via Getty

Public confidence in the safety of COVID-19 vaccines dipped in the United States after government officials paused vaccinations with the Johnson & Johnson (J&J) shot last month, [according to a poll](#). During the ten-day hiatus, officials explored whether the vaccine was linked to a [rare type of blood clot](#), but they ultimately deemed the jab safe and gave the green light to resume its use. After the pause began, 7% of unvaccinated adults who were surveyed said that the news about blood clots made them less likely to want any COVID-19 shot, according to data published by the Kaiser Family Foundation (KFF).

The incident demonstrates the knife-edge that public-health authorities have been walking since COVID-19 vaccines became available late last year. Vaccines represent a way to end the COVID-19 pandemic and to protect individuals, so authorities would like people to sign up for them. But the [shots come with risks](#) that need to be communicated transparently, to maintain trust and uphold scientific ethics, says Hilda Bastian, an independent scientist who studies evidence-based medicine in Victoria, Australia.



## COVID vaccines and blood clots: five key questions

Public-health specialists must always strike a careful balance when communicating about vaccine safety, but the enormous scale of the COVID-19 vaccine roll-out means that safety data are evolving fast — so researchers are scrambling to share developments transparently and clearly with the public. And they worry that with the rise of anti-vaccination movements, their messages might be used or interpreted to fuel misinformation campaigns. Those who spoke to *Nature* say that because the stakes are so high for COVID-19, explaining vaccine risk has been especially fraught. “It’s a minefield,” says Bastian.

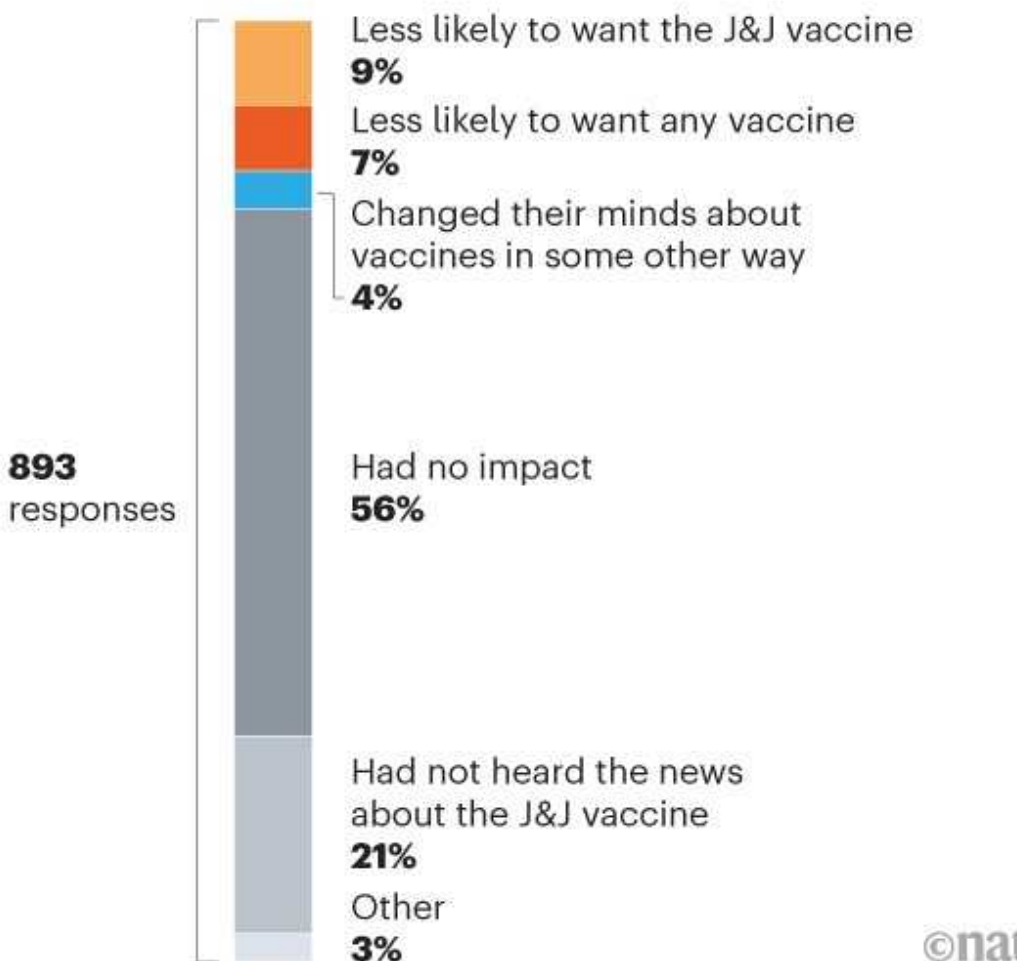
Kathryn Edwards, a vaccinologist at Vanderbilt University School of Medicine in Nashville, Tennessee, who has been a vaccine-safety consultant for 40 years, agrees. “I have not worked harder in my life,” she says.

## **The effects of a pause**

US officials paused inoculations with the J&J vaccine last month so that researchers at the US Centers for Disease Control and Prevention and the US Food and Drug Administration could evaluate 6 cases of a rare type of blood clot reported among 6.8 million people who had received a J&J jab. The pause followed an announcement by the European Medicines Agency that linked the Oxford–AstraZeneca COVID-19 vaccine to reports of a similar blood-clotting condition.

# NEW HESITANCY

After US inoculations with the Johnson & Johnson (J&J) shot were paused owing to worries over blood clots, unvaccinated Americans' hesitancy to get a COVID-19 jab increased, according to a survey.



©nature

Source: [Kaiser Family Foundation COVID-19 Vaccine Monitor](#)

By the end of the pause, US officials had identified 15 cases of a rare but severe condition called thrombosis with thrombocytopenia syndrome (TTS) in people who had received the J&J vaccine. The highly specific hallmarks of TTS are clots in unusual parts of the body, such as the brain or abdomen, combined with low blood-platelet levels. The cases occurred exclusively in women between the ages of 18 and 59. Still, officials decided that the benefit of protection against COVID-19 imparted by the vaccine outweighs the

remote risk of TTS, so they lifted the pause and asked health-care providers to update information provided with the J&J shot to include warnings about the condition.



### Why is it so hard to investigate the rare side effects of COVID vaccines?

During the pause and the week after it was lifted, the KFF, a non-profit health-policy organization based in San Francisco, California, polled around 2,100 adults across the United States about whether it had affected their stance on COVID-19 vaccines. Although 69% of respondents expressed confidence in the other two vaccines being administered in the country — the Pfizer–BioNTech and Moderna shots — only 46% said the same for J&J. Among the subset of respondents who had not yet been vaccinated, roughly 20% said that the pause had changed their view of at least one of the COVID-19 vaccines in some way (see ‘New hesitancy’).

Given the intense news coverage of safety concerns around J&J, “it’s not surprising that people might have questions”, says Katherine Schaff, who studies public-health communication at Berkeley Media Studies Group in California. She emphasizes that confidence in the other available COVID-19 vaccines remains high, and the J&J pause is ultimately evidence of vaccine safety-monitoring systems working as they should. But Schaff adds that the new hesitancy described in the KFF poll is evidence that more can be done to make sure people have access to transparent communication about their safety.

## Risk is not only a number

One challenge public-health authorities face is putting risk into context without seeming to dismiss people's worries, says Heidi Larson, an anthropologist at the London School of Hygiene & Tropical Medicine who specializes in risk and decision science. Even if authorities say the likelihood of a severe reaction is one in a million, she says, what people want an answer to is, "What does that one in a million mean for me or someone in my family?"



### COVID vaccines and safety: what the research says

Providing that context can be tricky because risk perception is highly subjective, says Alexandra Freeman, executive director of the Winton Centre for Risk and Evidence Communication at the University of Cambridge, UK. There are two elements of risk that people need to understand to make decisions, she says: the likelihood of something happening, and the impact of something happening. For example, the likelihood of severe, influenza-like symptoms after a vaccine injection might be one in ten, but if they happen, those symptoms could have a larger impact for a single parent without childcare support than for someone able to take time to recover.

Public-health specialists told *Nature* that the key to increasing public trust continues to be transparency. In a study of how communication about vaccine efficacy affected people's decisions to get a COVID-19 shot<sup>1</sup>,

Freeman and her colleagues found that being transparent about the uncertainties made no difference to whether or not a person got a vaccine. But, says Freeman, “we did find that people felt that they were more informed and felt more confident in their decision making when they were given more informative communication”.

Nature **593**, 488-489 (2021)

doi: <https://doi.org/10.1038/d41586-021-01257-8>

Additional reporting by Heidi Ledford.

## References

1. 1.

Kerr, J. R., Freeman, A. L. J., Marteau, T. M. & van der Linden, S. *Vaccines* **9**, 379 (2021).

[PubMed](#) [Article](#) [Google Scholar](#)

[Download references](#)

## Jobs from Nature Careers

- - - [All jobs](#)
    - - [Postdoctoral Training Fellow - Kassiotis Lab](#)
        - [Francis Crick Institute](#)
        - [London, United Kingdom](#)

[JOB POST](#)

- **Biological Safety Specialist**

Francis Crick Institute

London, United Kingdom

JOB POST

- **Post-doctoral Fellow - Autoimmune Pathogenesis**

Oklahoma Medical Research Foundation (OMRF)

Oklahoma City, United States

JOB POST

- **Research Technician / Research Assistant**

Oklahoma Medical Research Foundation (OMRF)

Oklahoma City, United States

JOB POST

Download PDF

Download PDF

## Related Articles

-  **Why is it so hard to investigate the rare side effects of COVID vaccines?**



- [\*\*COVID vaccines and blood clots: five key questions\*\*](#)



- [\*\*This COVID-vaccine designer is tackling vaccine hesitancy — in churches and on Twitter\*\*](#)



- [\*\*COVID vaccines and safety: what the research says\*\*](#)



- [\*\*The race to curb the spread of COVID vaccine disinformation\*\*](#)

---

This article was downloaded by **calibre** from <https://www.nature.com/articles/d41586-021-01257-8>

- NEWS
- 13 May 2021
- Clarification [14 May 2021](#)

# Open-access publisher PLOS pushes to extend clout beyond biomedicine

The publisher will launch five new journals, and has introduced a new business model that aims to spread the cost of publishing more fairly.

- [Holly Else](#)
  1. Holly Else  
[View author publications](#)

You can also search for this author in [PubMed](#) [Google Scholar](#)





•

Non-profit life-sciences publisher PLOS is gunning for a bigger share of science beyond the biomedical realm with the launch of five journals in fields where open science is less widely adopted. They will be its first new titles in 14 years. It is also piloting a new open-access business model, in a bid to spread the cost of publishing more equally among researchers.



## [A guide to Plan S: the open-access initiative shaking up science publishing](#)

The new business model is the first shake-up at the publisher for a while, and has been eagerly anticipated. “PLOS is a publisher that punches above its weight,” says Michael Clarke, managing partner at publishing consultancy Clarke & Esposito in Washington DC. “Since their inception, they have had an outsized influence on the industry. After a period of quiescence, it is good to see some long-overdue innovation,” he adds.

In the 20 years since its inception, PLOS has blazed a trail that many mainstream journals have followed, making papers free to read and drawing revenue from publishing charges rather than subscriptions. But some warn that other publishers might be less likely to adopt the new model — which requires institutions to sign up to long-term publishing agreements — owing to its complexity.

## **Open-access pioneer**

PLOS started life in 2001 as the Public Library of Science, in response to an open letter signed by almost 34,000 scientists calling for an online repository of life-sciences papers. In 2003, it launched its first journal, *PLOS Biology*, which was funded using an unconventional business model — asking authors to pay an article-processing charge to make their papers freely available for anyone to read.

Over the past 14 years, PLOS has maintained the same portfolio of seven life-sciences journals covering biology, medicine, computational biology, genetics and pathogens. Some of its more-selective journals, such as *PLOS Medicine* and *PLOS Biology*, ran at a loss, but the publisher generated more income by launching the mega-journal *[PLOS ONE](#)*, which accepts scientifically valid research from all disciplines.

The five new journals focus on water, climate, sustainability, global public health and digital health. Introducing non-life-sciences titles will allow PLOS to diversify, says Clarke. “This is significant in thinking about the possible future directions of the organization.” In the years since *PLoS ONE* was launched, he adds, other publishers have mimicked the mega-journal concept and eroded PLOS’s market share. [The publisher’s financial history is chequered](#). It first broke even in 2010. In recent years it has fallen into deficit, with 2019 the first year that it made an operating surplus since 2015.

## Spreading the cost

The journal launches come as PLOS continues to pilot a business model that it introduced last year. Under the scheme, known as Community Action Publishing, universities sign an agreement that gives their researchers unlimited publishing in *PLOS Medicine* or *PLOS Biology* for a fixed fee.



## Open-access journal eLife announces ‘preprint first’ publishing model

The membership fee for individual institutions varies from around US\$350 to almost \$40,000 for the three-year pilot scheme. The cost is based on the publishing history of an institution’s researchers over the past six years and takes into account whether scientists were corresponding or contributing authors. Profits are capped at 10%, with any revenue exceeding this being given back to members. Researchers publishing in these titles from institutions without an agreement will pay a non-member publishing fee — similar to an article-processing charge — that increases year-on-year.

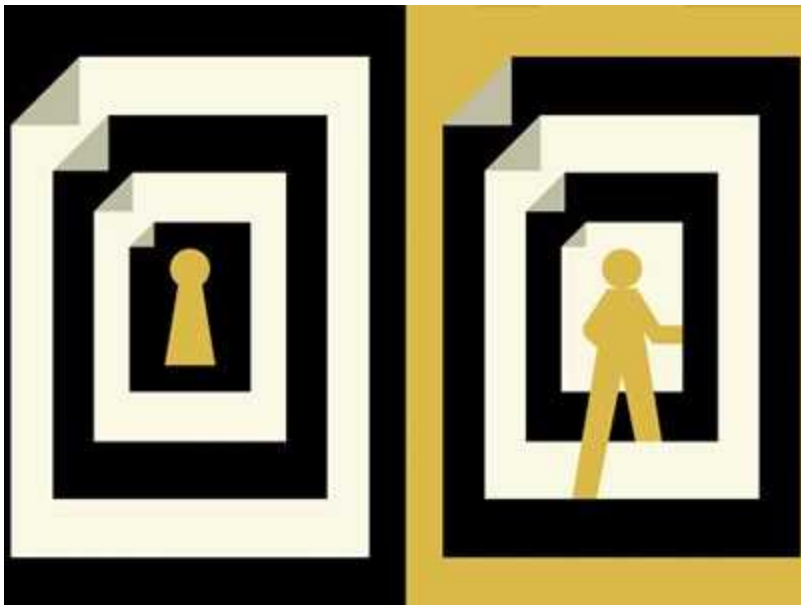
The idea behind the new model is that the cost of publishing a paper is spread more equally across all of the authors’ institutions, rather than the corresponding author’s institution or funder footing the bill, as is standard with an article processing charge. PLOS says that as more members join the scheme, it will become cheaper for researchers to publish papers. So far, more than 75 institutions in 8 countries have signed up.

PLOS’s chief publishing officer, Niamh O’Connor, says that PLOS hopes to circumvent the idea that open access moves the cost of publishing a paper from the reader to the author. “While the article-processing model has allowed open access to develop, we don’t see that as the future,” she says. “We are working to a future where those barriers are removed.”

Clarke says that Community Action Publishing is a “shrewd scheme”. Instead of collecting revenue from one-off transactions to publish individual papers, the partnership model locks institutions into longer-term financial agreements that give PLOS a predictable income across several years, which could put its journals in profit. “While 10% may be a modest profit margin, if the journals are operating at a loss now, the 10% target represents a substantial margin swing,” he says.

## **Acceptable profits**

As science grapples with how publishing will look in the future, there has been much debate about acceptable profit margins for publishers.



## Will the pandemic permanently alter scientific publishing?

Lisa Hinchliffe, a librarian at the University of Illinois at Urbana-Champaign, which is a member of the Community Action Partnership, says that if lots of institutions sign up to the PLOS scheme, it could indicate that a 10% profit margin is considered acceptable. She also cautions that, because the scheme takes into account all authors on a paper, it will be complicated to manage. “I believe that this complexity makes uptake by other publishers less likely,” she says.

O’Connor and her team are already thinking about how they can improve access to research without reinforcing existing hierarchies that exclude researchers in low- and middle-income countries. On 12 May, PLOS announced a partnership with a centre that teaches communication skills to scientists, which is based at the University of Nairobi in Kenya. The link is designed to ensure that the interests and values of African researchers are represented in the publisher’s policies and services.

“Our next phase of work is not just about being able to read or share an article: it’s about building a framework for equitable participation and distribution of knowledge,” O’Connor says.

doi: <https://doi.org/10.1038/d41586-020-01907-3>

## Updates & Corrections

- **Clarification 14 May 2021:** This article has been amended to clarify Lisa Hinchliffe's comments on the Community Action Publishing model.

## Jobs from Nature Careers

- - - [All jobs](#)
    - - **Postdoctoral Training Fellow - Kassiotis Lab**  
[Francis Crick Institute](#)  
[London, United Kingdom](#)  
[JOB POST](#)
      - **Biological Safety Specialist**  
[Francis Crick Institute](#)  
[London, United Kingdom](#)  
[JOB POST](#)
      - **Post-doctoral Fellow - Autoimmune Pathogenesis**  
[Oklahoma Medical Research Foundation \(OMRF\)](#)  
[Oklahoma City, United States](#)

## JOB POST

### **▪ Research Technician / Research Assistant**

Oklahoma Medical Research Foundation (OMRF)

Oklahoma City, United States

## JOB POST

Download PDF

Download PDF

## Related Articles



- A guide to Plan S: the open-access initiative shaking up science publishing



- Open-access journal eLife announces ‘preprint first’ publishing model



- Will the pandemic permanently alter scientific publishing?

- How a torrent of COVID science changed publishing – in seven charts

- The true cost of science publishing

---

This article was downloaded by **calibre** from <https://www.nature.com/articles/d41586-020-01907-3>

| [Section menu](#) | [Main menu](#) |

- NEWS
- 21 May 2021

# Prestigious European grants might be biased, study suggests

Institutional affiliations of panellists seem to skew European Research Council decisions — especially in the life sciences.

- [Diana Kwon](#) <sup>0</sup>

1. Diana Kwon

1. Diana Kwon is a freelance science journalist based in Berlin.

[View author publications](#)

You can also search for this author in [PubMed](#) [Google Scholar](#)









European Research Council grants are among the most highly coveted for researchers in the European Union and associated countries. Credit: Serhii Nemyrivskyi/Getty

Funding panels are more likely to give prestigious European Union early-career grants to applicants connected to the institutions of some of the panellists, a study of the 2014 funding round suggests.

The effect seems to be limited to the life sciences, social sciences and humanities, and the results have not yet been peer reviewed. But given the high profile of the grants administered by European Research Council (ERC), “the findings should be taken seriously”, says study co-author Peter van den Besselaar, a social scientist at the Free University of Amsterdam.

Although previous studies have found evidence of favouritism in funding in various European countries, “I was surprised that the phenomenon has been recorded at a level as high as the ERC grants”, says Giovanni Abramo, the technology research director at the National Research Council (CNR) of Italy in Rome.

The preprint<sup>1</sup> was posted on 9 March on the academic networking platform ResearchGate.

ERC ‘starting grants’ are among the most prestigious early-career funding schemes in academia, providing up to €1.5 million (US\$1.8 million) over five years. Van den Besselaar and Charlie Mom, a research consultant based in Amsterdam, conducted the latest study as part of a broader ERC-funded project to assess bias in funding allocations. It focused on the 2014 cycle, during which there were 3,207 applicants, of whom 375 received starting grants.

## Close to home

The authors examined something they called the ‘nearby panellist effect’ — the influence of a panellist from an applicant’s ‘home organization’, the university or research institution where they are currently based, or the ‘host organization’ where they plan to carry out the research.

Van den Besselaar and Mom discovered that, across all disciplines, applicants who shared both a home and a host organization with one panellist or more received a grant 40% more often than average. These were mainly cases in which an applicant planned to use the grant at the institution they applied from. The effect seemed to be discipline-specific: further analysis revealed that the success rate for connected applicants was approximately 80% higher than average in the life sciences and 40% higher in the social sciences and humanities, but there seemed to be no discernible effect in physics and engineering. It was also limited to certain countries, including Finland, Sweden, Italy, Germany and the United Kingdom, and more prevalent in applications from men than from women.

The presence of a nearby-panellist effect might not be evidence of favouritism, says Van den Besselaar, because the best applicants tend to be concentrated at certain institutions. To test this, the researchers evaluated whether applicants with an institutional connection to a panellist scored better on measures of academic performance, which they calculated using variables such as previous grants, citations and number of publications. Their analysis showed that successful and connected applicants scored

worse on these performance indicators than did funded applicants without such links, and even some unsuccessful applicants. “This nearby-panellist effect cannot be explained away by pointing at the performance of the applicants,” says Van den Besselaar.

By contrast, the connected applicants did seem to publish more often in high-impact journals and had more collaborations with researchers from high-ranking institutions. However, the authors classified these two measures as markers of reputation rather than performance.

According to ERC policy, if a panellist works in the same organization as an applicant, the ERC bars them — with some exceptions — from reviewing the proposal and requires them to leave meetings during which it is discussed. Van den Besselaar and Mom did not directly observe panels to monitor compliance with this rule.

In an e-mailed statement, the ERC said that it is unable to comment on the study, because it is not yet peer reviewed.

## Differences by discipline

One limitation of the authors’ method, Abramo notes, is that they lumped applicants from broad disciplines together, even though factors such as number of publications can vary drastically depending on subfield. For example, he says, blood-disease specialists publish much more frequently than vascular surgeons, so if you measure performance in these groups by the same factors, “you introduce an enormous bias”.

Another shortcoming, according to Natalia Zinovyeva, an economist at the University of Warwick, UK, relates to how Van den Besselaar and Mom interpreted some of their performance measures. In some fields, journal impact factor is a clear indicator of research quality, she says. “From my perspective as an economist, this evidence seems to indicate that connected applicants are much better.”

Zinovyeva adds that the applicants might have qualities that panellists can pinpoint but that are not accounted for in these types of quantitative measure. For this reason, she says, it is important to look not only at the past

success of grant recipients, but also at their future outputs. If a grant recipient who was connected to a panellist ended up performing worse than an unconnected applicant, that would indicate that something other than research quality had factored into the panellists' decisions.

"Measuring the quality of an applicant is extremely difficult," Zinovyeva says. These findings are "a warning that we should pay attention to", she adds, "but I think it requires deeper analysis".

Nature **593**, 490-491 (2021)

doi: <https://doi.org/10.1038/d41586-021-01362-8>

## References

1. 1.

Mom, C. S. & Van den Besselaar, P. Preprint at  
<https://www.researchgate.net/publication/344461606> (2021).

[Download references](#)

## Jobs from Nature Careers

- - - [All jobs](#)
    - 
    - [\*\*Postdoctoral Training Fellow - Kassiotis Lab\*\*](#)
      - [Francis Crick Institute](#)
      - [London, United Kingdom](#)
      - [JOB POST](#)

- **Biological Safety Specialist**

Francis Crick Institute

London, United Kingdom

JOB POST

- **Post-doctoral Fellow - Autoimmune Pathogenesis**

Oklahoma Medical Research Foundation (OMRF)

Oklahoma City, United States

JOB POST

- **Research Technician / Research Assistant**

Oklahoma Medical Research Foundation (OMRF)

Oklahoma City, United States

JOB POST

Download PDF

Download PDF

---

This article was downloaded by **calibre** from <https://www.nature.com/articles/d41586-021-01362-8>

- NEWS
- 19 May 2021

# Mix-and-match COVID vaccines trigger potent immune response

Preliminary results from a trial of more than 600 people are the first to show the benefits of combining different vaccines.

- [Ewen Callaway](#)
  1. Ewen Callaway  
[View author publications](#)

You can also search for this author in [PubMed](#) [Google Scholar](#)









Countries with fluctuating supplies of COVID-19 vaccines could benefit from using different vaccines for the first and second dose. Credit: Christof Stache/AFP/Getty

Vaccinating people with both the Oxford–AstraZeneca and Pfizer–BioNTech COVID-19 vaccines produces a potent immune response against the virus SARS-CoV-2, researchers conducting a study in Spain have found.

Preliminary results from the trial of more than 600 people — announced in an [online presentation](#) on 18 May — are the first to show the benefits of combining different coronavirus vaccines. A UK trial of a similar strategy reported<sup>1</sup> safety data last week, and is expected to deliver further findings on immune responses soon.



## Pfizer COVID vaccine protects against worrying coronavirus variants

Because of safety concerns, several European countries are already recommending that some or all people who were given a first dose of the vaccine developed by the University of Oxford, UK, and AstraZeneca in Cambridge, UK, get another vaccine for their second dose. Researchers hope that such mix-and-match COVID-19 vaccination regimens will trigger stronger, more robust immune responses than will two doses of a single vaccine, while simplifying immunization efforts for countries facing fluctuating supplies of the various vaccines.

“It appears that the Pfizer vaccine boosted antibody responses remarkably in one-dose AstraZeneca vaccinees. This is all around wonderful news,” says Zhou Xing, an immunologist at McMaster University in Hamilton, Canada.

## **Prime and boost**

Starting in April, the Spanish CombivacS trial enrolled 663 people who had already received a first dose of the Oxford–AstraZeneca vaccine, which uses a harmless chimpanzee ‘adenovirus’ to deliver instructions for cells to make a SARS-CoV-2 protein. Two-thirds of participants were randomly picked to receive the mRNA-based vaccine made by Pfizer, based in New York City, and BioNTech, in Mainz, Germany, at least eight weeks after their first dose. A control group of 232 people has not yet received a booster. The study was led by the Carlos III Health Institute in Madrid.

The Pfizer–BioNTech booster seemed to jolt the immune systems of the Oxford–AstraZeneca-dosed participants, reported Magdalena Campins, an investigator on the CombivacS study at the Vall d’Hebron University Hospital in Barcelona, Spain. After this second dose, participants began to produce much higher levels of antibodies than they did before, and these antibodies were able to recognize and inactivate SARS-CoV-2 in laboratory tests. Control participants who did not receive a booster vaccination experienced no change in antibody levels.



### [How can countries stretch COVID vaccine supplies? Scientists are divided over dosing strategies](#)

That is what researchers hoped for and expected from mixing different vaccines, a strategy known as a heterologous prime and boost, which has been deployed for vaccines against other diseases, such as Ebola. “These responses look promising and show the potential of heterologous prime–boost regimens,” says Dan Barouch, director of the Center for Virology and Vaccine Research at Beth Israel Deaconess Medical Center in Boston, Massachusetts.

Xing says the antibody response to the Pfizer boost seems to be even stronger than the one most people generate after receiving two doses of the Oxford–AstraZeneca vaccine, according to earlier trial data. But it is not clear how those responses compare with those seen in people who receive

two doses of mRNA vaccines such as Pfizer–BioNTech’s, which tend to trigger an especially potent antibody response after a second dose.

Making such comparisons is “apples and oranges”, says Daniel Altmann, an immunologist at Imperial College London. A strong immune response to the mix-and-match strategy is “entirely predictable from the basic immunology”, he adds.

Giving people first and second doses of different vaccines probably makes sense, says Altmann. But he wonders what will happen if people need a third dose to prolong immunity or protect against emerging coronavirus variants. Repeated doses of virus-based vaccines such as the Oxford–AstraZeneca one tend to be increasingly less effective, because the immune system mounts a response against the adenovirus. RNA vaccines, by contrast, tend to trigger stronger side effects with added doses. “I do think there’s a brave new world of vaccinology to be scoped in all of this,” Altmann says.

Last week, a UK study called Com-COV, which analysed combinations of the same two vaccines, found that people in the mix-and-match groups experienced higher rates of common vaccine-related side effects, such as fever, than did people who received two doses of the same vaccine<sup>1</sup>. In the Spanish CombivacS trial, mild side effects were common, and similar to those seen in standard COVID-19 vaccine regimens. None was deemed severe.

Nature **593**, 491 (2021)

doi: <https://doi.org/10.1038/d41586-021-01359-3>

## References

1. 1.

Shaw, R. H. *et al. Lancet* [https://doi.org/10.1016/S0140-6736\(21\)01115-6](https://doi.org/10.1016/S0140-6736(21)01115-6) (2021).

[Article](#) [Google Scholar](#)

[Download references](#)

## Jobs from Nature Careers

- - - [All jobs](#)
    - - **[Postdoctoral Training Fellow - Kassiotis Lab](#)**
  - [Francis Crick Institute](#)
  - [London, United Kingdom](#)
  - [JOB POST](#)
  - **[Biological Safety Specialist](#)**
  - [Francis Crick Institute](#)
  - [London, United Kingdom](#)
  - [JOB POST](#)
  - **[Post-doctoral Fellow - Autoimmune Pathogenesis](#)**
  - [Oklahoma Medical Research Foundation \(OMRF\)](#)
  - [Oklahoma City, United States](#)
  - [JOB POST](#)
  - **[Research Technician / Research Assistant](#)**
  - [Oklahoma Medical Research Foundation \(OMRF\)](#)

Oklahoma City, United States

JOB POST

[Download PDF](#)

[Download PDF](#)

## Related Articles



- [How can countries stretch COVID vaccine supplies? Scientists are divided over dosing strategies](#)



- [Who received the first billion COVID vaccinations?](#)



- [Pfizer COVID vaccine protects against worrying coronavirus variants](#)



- [What scientists do and don't know about the Oxford–AstraZeneca COVID vaccine](#)



- [J&J's single-dose COVID vaccine raises hopes for faster rollout](#)

---

This article was downloaded by **calibre** from <https://www.nature.com/articles/d41586-021-01359-3>

| [Section menu](#) | [Main menu](#) |

- NEWS FEATURE
- 26 May 2021

# The mini lungs and other organoids helping to beat COVID

Virologists have infected millions of miniature organs with SARS-CoV-2, to learn how the virus wreaks havoc and how to stop it.

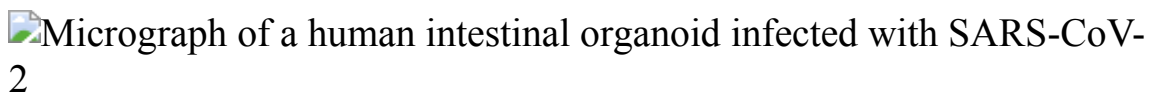
- [Smriti Mallapaty](#)
  1. Smriti Mallapaty  
[View author publications](#)

You can also search for this author in [PubMed](#) [Google Scholar](#)





- 



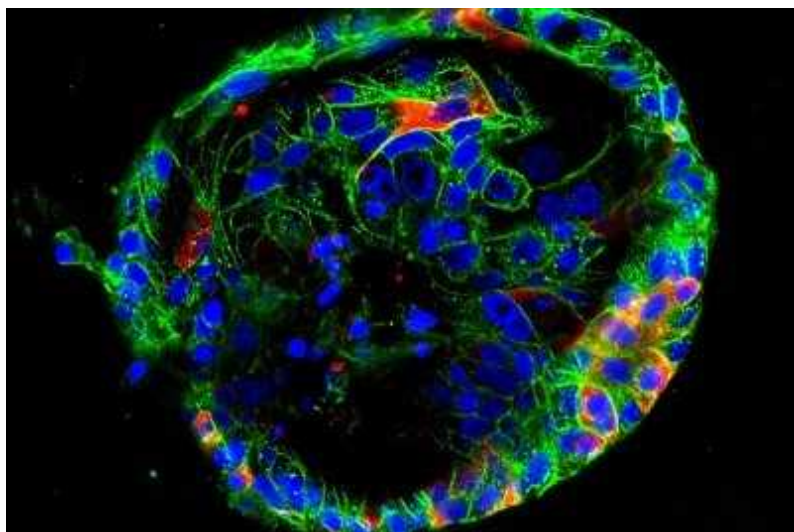
Human gut organoids infected with SARS-CoV-2 (white), the virus that causes COVID-19. Credit: Joep Beumer/Hubrecht Institute

Shuibing Chen spent close to two months tending to her mini lungs — some half a million of them. Each one looked like a tiny storm cloud, ensconced in a warm dish and protected by a jelly-like dome. Chen, a stem-cell biologist at Weill Cornell Medicine in New York City, and her team had nurtured them from clumps of human cells, adding nutrients every few days as they grew into 3D air sacs.

These lung organoids matured until they reached the size of a lentil. Then, the team packed them up and transported them just a few blocks away, to a laboratory authorized to work with SARS-CoV-2, the virus responsible for the COVID-19 pandemic. There, the organoids were drowned in virus and each was doused with one of 15,000 drugs. Almost all of the mini lungs died, but a few of the drugs stemmed the infection — representing a handful of possible treatments for COVID-19.

Chen is one of many cell biologists who have been driven by the pandemic to push the boundaries of organoid technology for studying infectious diseases. In the past year, researchers have created mini lungs, guts, livers, brains and more to study how SARS-CoV-2 infects organs. They have learnt which cells the virus targets, the speed of that attack and how the cells retaliate.

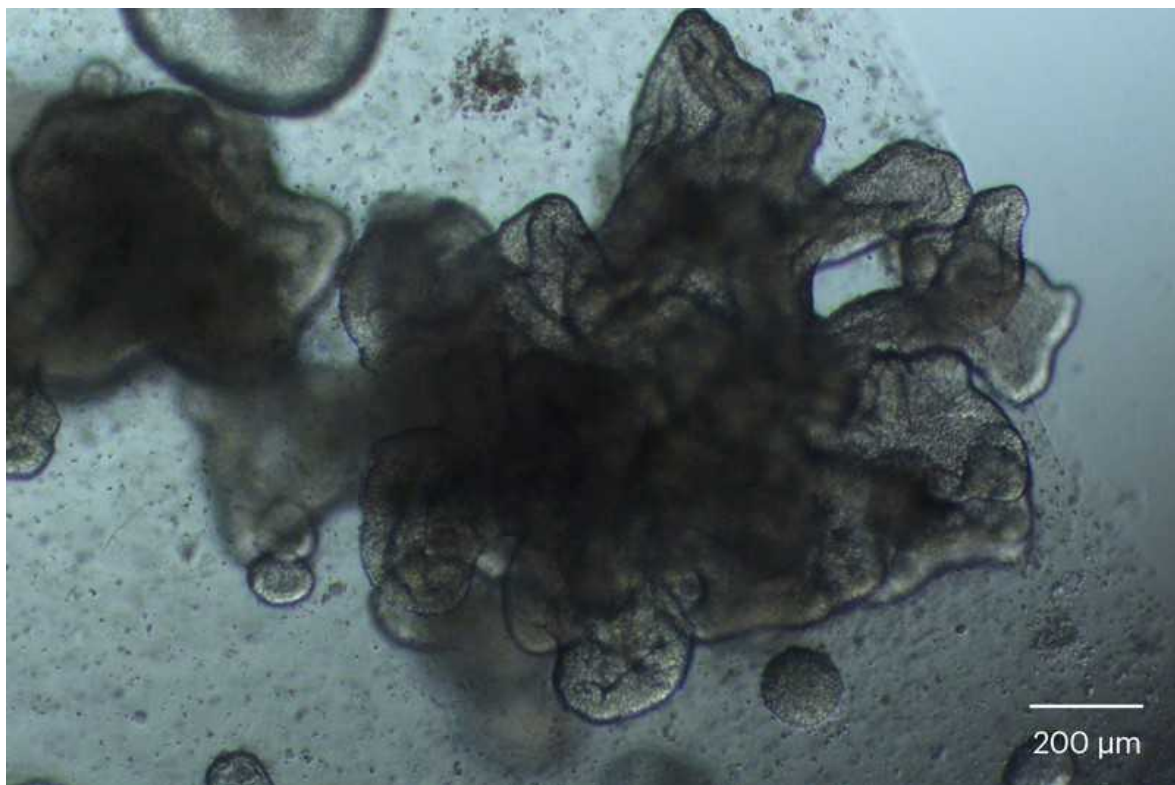
“Organoids have found their way into the toolbox of virologists,” says Hans Clevers, a developmental biologist at the Hubrecht Institute in Utrecht, the Netherlands. The technology had previously been used mainly to study basic human biology, development and related disorders, and cancers, with only a few labs using the models to study viruses and other infectious diseases. But the pandemic has brought organoids to centre stage, spurring high-impact papers and demonstrating their value for drug development, says Clevers.



[Mini organs reveal how the coronavirus ravages the body](#)

They are a welcome addition, because current methods of studying viruses have several limitations. The typical workhorse of virology is a cancerous cell line from the kidney of an African green monkey (*Chlorocebus sabaeus*), first extracted almost 60 years ago and dividing ever since. These cells, known as Vero cells, are excellent for growing viruses but don't reflect the human body's normal antiviral response. They are "really screwed up", says Elke Mühlberger, a virologist at Boston University in Massachusetts. Researchers also use some cancerous human cell lines but, similar to the Vero cells, they don't respond to infections in the way that normal cells would.

Although researchers have now established the potential relevance of organoids for studying new antiviral drugs, their work has not yet led to marketable treatments. "Organoid technology has benefited more from the pandemic than the treatment of COVID-19 has benefited from organoids, yet," says Clevers.



An organoid made from cells taken from the lung's air sacs, called alveoli, grows in a dish.Credit: Xuming Tang

To realize the technology's full potential, scientists still need to find ways of growing more complex systems, for example by adding immune cells and blood vessels. Researchers also need to streamline the production process to create thousands, if not millions, of uniform organoids, quickly and cheaply.

"The use of organoids to study viruses is only at its infancy," says Jie Zhou, a virologist at the University of Hong Kong.

## Unculturable viruses

Before she started working with organoids, virologist Mary Estes relied on a much messier way to study the highly contagious vomiting bug norovirus. Nobody could grow the virus in the laboratory. So instead, she would isolate it from the excrement of people who willingly ingested it — and suffered the consequences — for the sake of her research.

In 2011, she saw a paper by Clevers in which he grew mini guts from stem cells scraped off the villi, the tiny tentacles that line people's intestines<sup>1</sup>. Clevers had created the first organoids derived from adult stem cells, which grow almost indefinitely under the right conditions, and can build themselves into complex structures that reflect their organ of origin. (Organoids had already been made from embryonic stem cells or induced pluripotent stem (iPS) cells, which can develop into any cell type, but they typically reflect organs early in fetal development.)

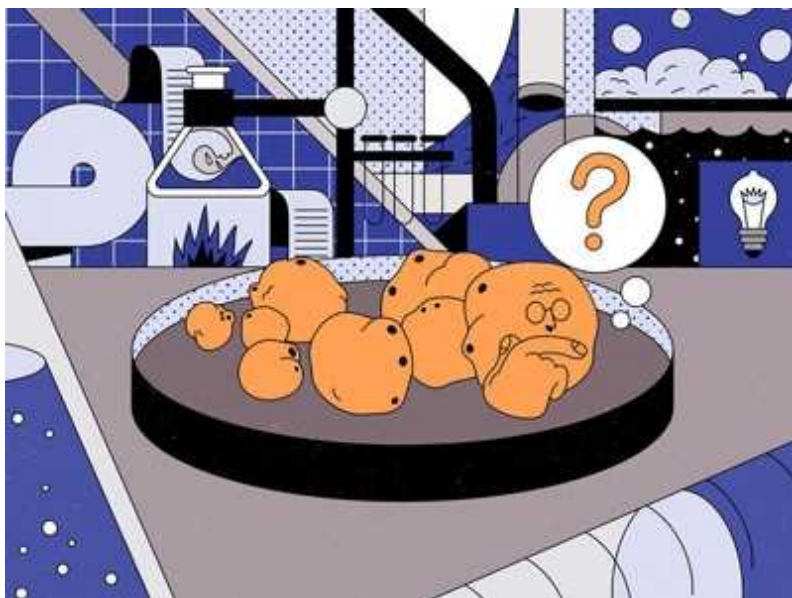
"I thought — well, that looks like a system we ought to try," says Estes, who is at Baylor College of Medicine in Houston, Texas. "Nobody else was using those cultures for virology at the time."

In 2016 — almost half a century after its identification — Estes became the first person to grow human norovirus in a dish in a way that could be reproduced, in an intestinal organoid<sup>2</sup>.

Her studies proved that organoids were a good model of disease in people. She discovered, for instance, that norovirus variants did not replicate at all in organoids made from the cells of people who typically don't get sick from the virus<sup>2</sup>.

Researchers have since used organoids to study many more viruses, including respiratory syncytial virus (RSV) — a common cause of lung infection in children — in airway organoids, and the rare and mysterious BK virus in kidney organoids.

In 2016, a team infected developing brain organoids with Zika virus and established a link between the infection in pregnant women and microcephaly<sup>3</sup>, a condition in which a fetus has an atypically small head. Ten days after being infected, the brain organoids were 40% smaller than the uninfected organoids. These neural progenitor cells are “fertile soil for Zika infection”, says Patricia Garcez, a neurobiologist at the Federal University of Rio de Janeiro in Brazil, who led the work.



### Can lab-grown brains become conscious?

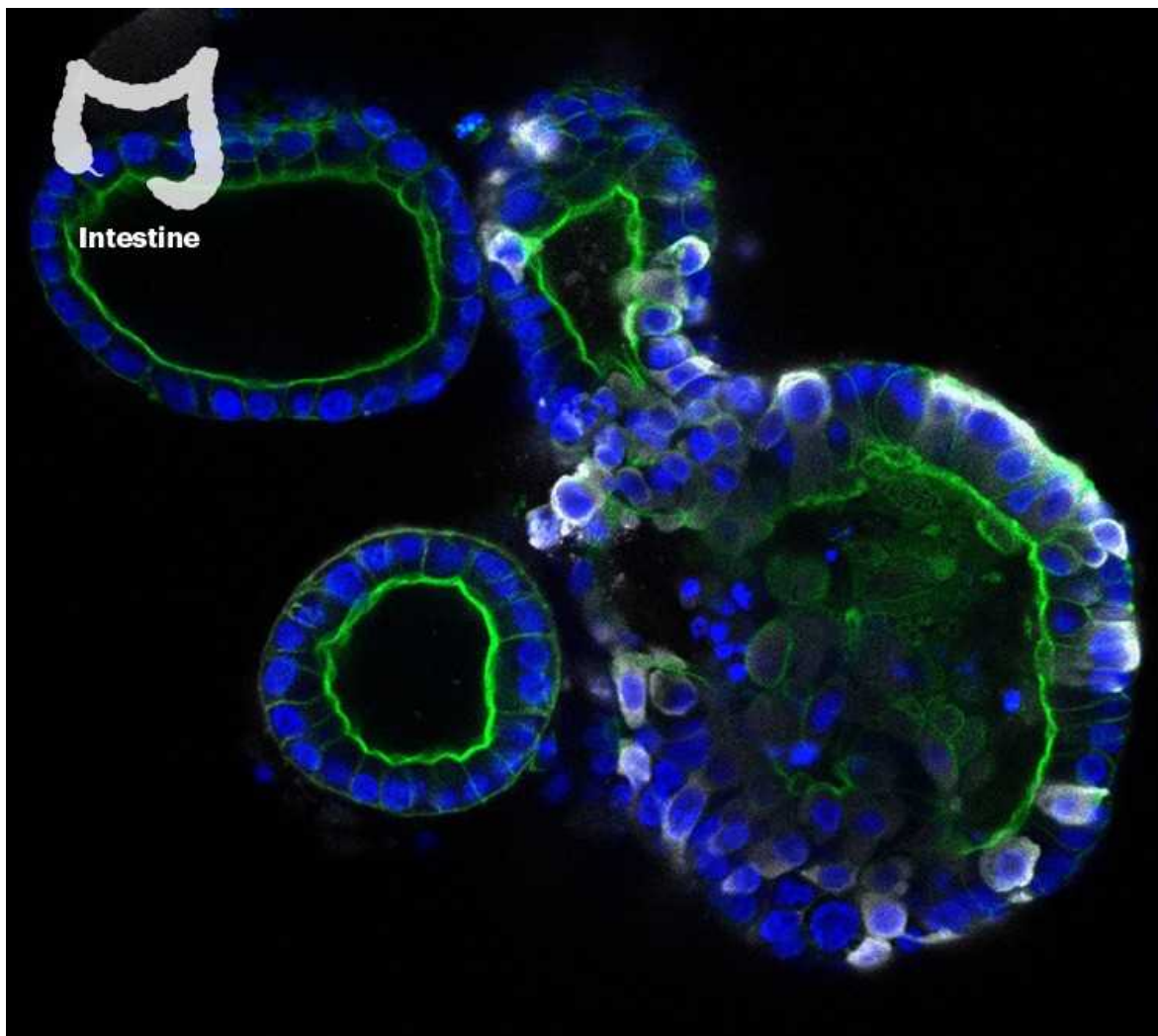
And in 2018, Zhou, Clevers and their colleagues developed a lung organoid that could be used to rapidly assess the infectiousness of an emerging flu virus<sup>4</sup>. Strains known to be highly infectious in people, including the one that caused the 2009 H1N1 influenza pandemic, replicated much faster in the organoids than did strains that typically infect pigs and birds.

Aside from these examples, few virologists had experimented with organoids when SARS-CoV-2 emerged and grabbed their attention.

It didn't take long for Clevers to recognize the potential of his organoid models for studying an unfamiliar virus in the middle of a pandemic. There were clear hints from the clinic that the virus could affect the gut, especially in children, says Clevers. He wondered whether he could use his intestinal organoids to see if the virus could infect gut tissue.

On 15 March 2020 — the day the Netherlands went into lockdown — he requested samples of SARS-CoV-2 from colleagues in Rotterdam. Within seven weeks, he and his colleagues published a paper in *Science* showing that SARS-CoV-2 readily replicated in mini guts, specifically targeting cells called enterocytes that line the intestines<sup>5</sup>. The study helped to explain why some people with COVID-19 have digestive problems, including diarrhoea and vomiting, and identified another possible route of transmission.

Researchers have since shown that SARS-CoV-2 can infect a host of mini organs, from the liver to kidneys to the brain — mimicking the multi-organ damage seen in some people with COVID-19.



Researchers have used organoids to explore how SARS-CoV-2 infects cells and to look for treatments. Here the virus (white) is shown infecting a gut organoid, which could explain why some people get gastrointestinal symptoms with COVID-19. Source: Ref. 5

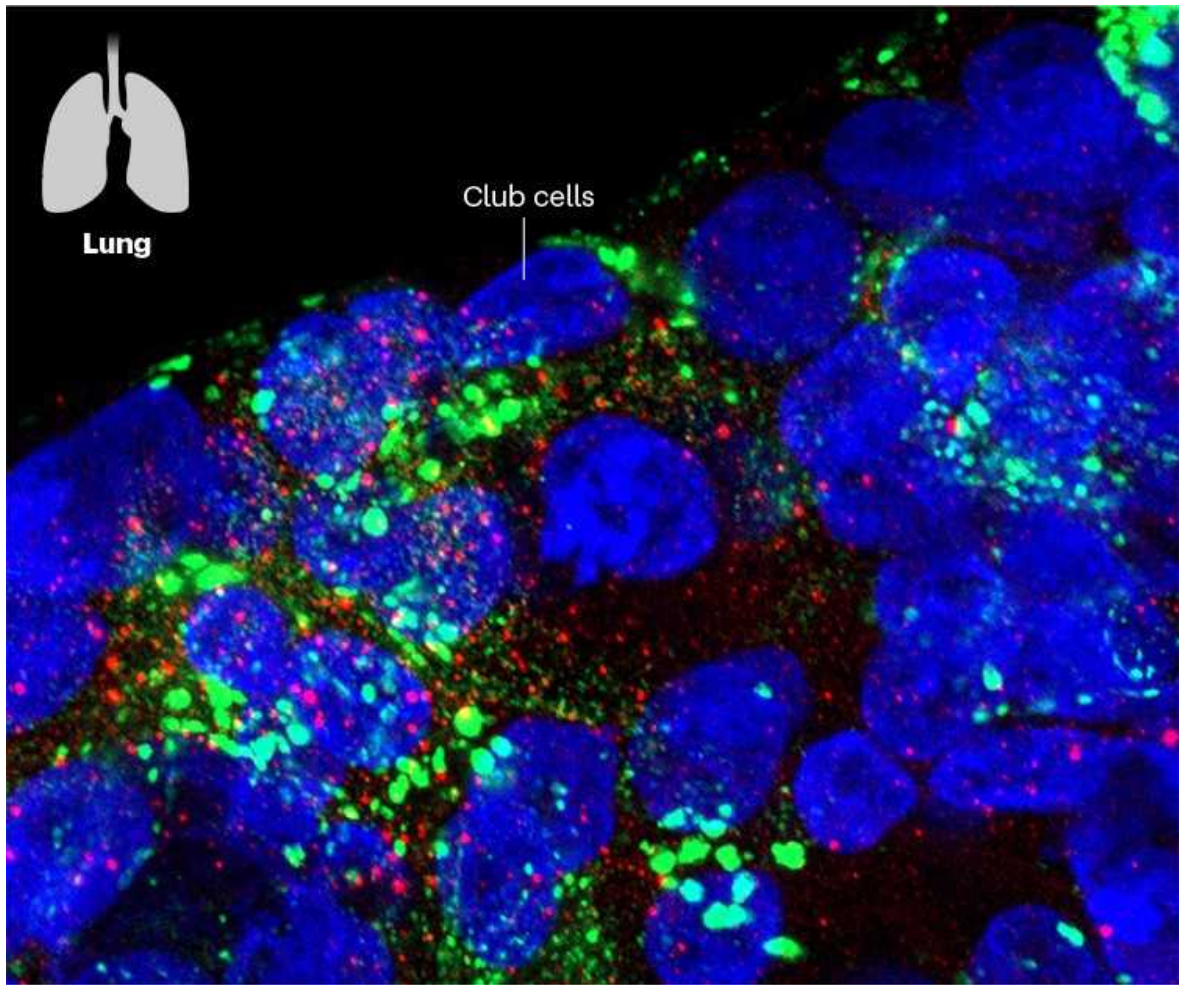
The organ that has received the most attention — for good reason — is the lung. Buried deep in the lungs are tiny air sacs called alveoli — the site of pneumonia in people with severe COVID-19. These cells are difficult to access and study. Catherine Blish, a viral immunologist at Stanford University in California, and her colleagues turned to cells that spontaneously form these air sacs to investigate the infection.

The researchers found that the virus ran riot in organoids made from alveoli and from cells in the tiny airways that feed them<sup>6</sup>. In the alveoli, SARS-

CoV-2 targeted the cells that cover the air-exposed surface, which are rich in the ACE2 receptor through which SARS-CoV-2 gains entry. The virus also affected cells in the airways that secrete a molecule for dealing with the constant stretching in the lungs, called club cells. “Without organoids, I don’t know that we would have discovered that club cells could support SARS-CoV-2 replication because nobody would have thought to put it on club cells,” says Blish.

Other studies in mini alveoli have revealed details of the battle that takes place between the virus and cells<sup>7</sup>. Young Seok Ju, a genome scientist at the Korea Advanced Institute of Science and Technology in Daejeon, found that it takes about a day for the cells to retaliate. A struggle ensues between the cells and the virus, and from day three, more than one-quarter of the cells begin to die.

Scientists also want to know more about how the virus gets into cells. In one study, researchers used the gene-editing technique CRISPR in gut organoids to identify two other proteins — TMPRSS2 and TMPRSS4 — that, together with ACE2, facilitate the virus’s entry<sup>8</sup>. Other labs are knocking out ACE2 entirely, to see whether the virus can still get in. “The more we study organoids, the more we realize that different types of cells use different mechanisms to support viral entry,” says Chen.



Lung organoids contain cells that are prime targets of SARS-CoV-2 (red), including club cells, which secrete a protective substance. Source: Ref. 6

Organoids have also been used to study emerging variants of SARS-CoV-2. In one preprint, Clevers and his colleagues studied human airway, alveolar and intestinal organoids and found that the B.1.1.7 variant, first identified in the United Kingdom, could produce larger amounts of infectious virus at later stages of infection than could previously circulating variants<sup>9</sup>, which might explain why B.1.1.7 is more transmissible.

## Tiny tonsils

A front-row view of the virus rattling through the body could help researchers to identify ways to stop it. Organoids help to fill the gap between watching the virus in cell lines, which lack the complexity of real tissue, and

in animal models, which mirror human infection poorly and are expensive, says Arinjay Banerjee, a coronavirus researcher at the University of Saskatchewan in Canada, who plans on using intestinal organoids in his work.

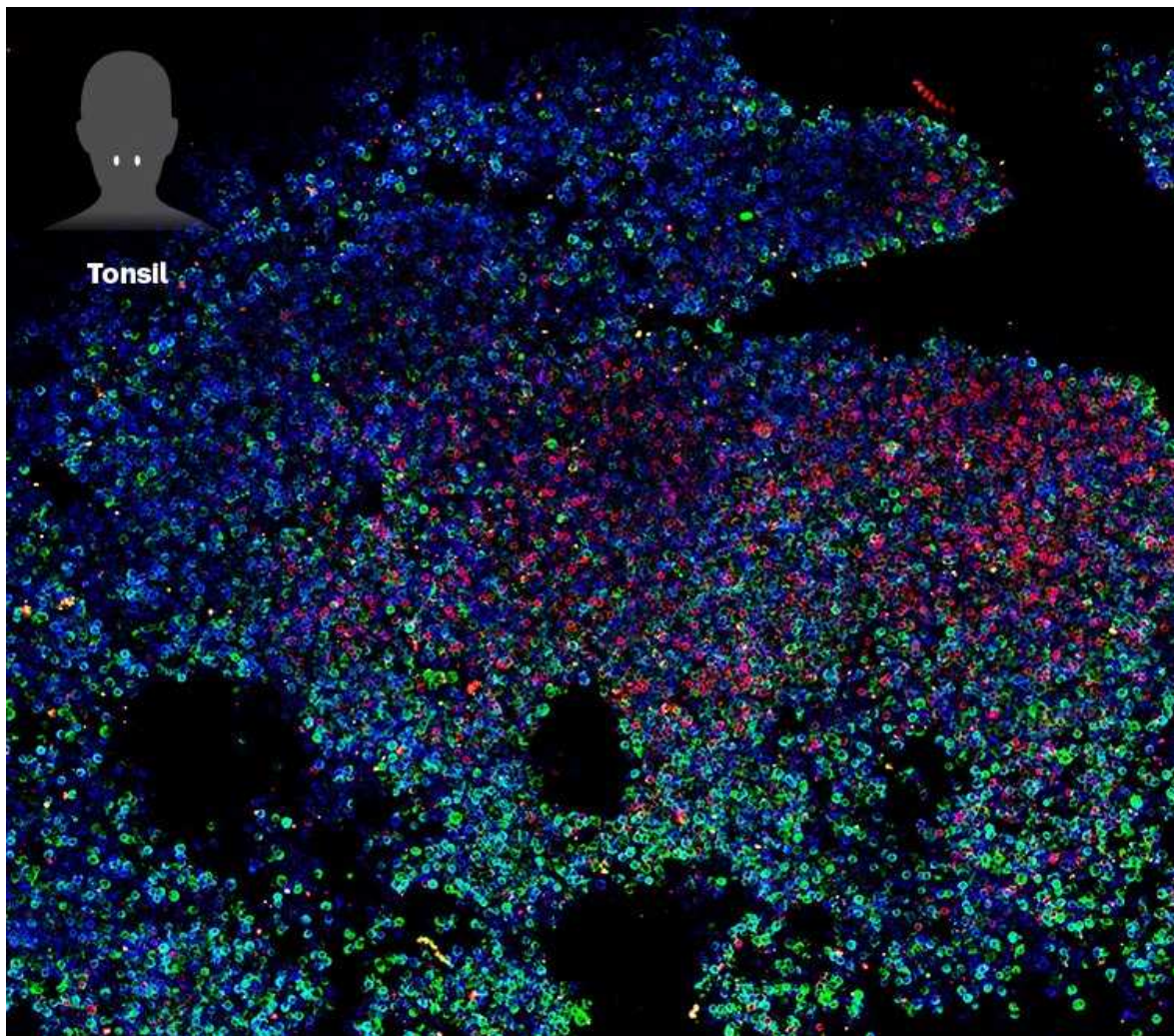
Many drug candidates that look promising in sheets of cells tend to fail in later stages, says Blish. One striking example is hydroxychloroquine, which was among the first drugs touted as a treatment for COVID-19. Studies in Vero cells suggested that chloroquine could block the virus, but later clinical trials showed that it had no protective effect. Clevers and others looked at how SARS-CoV-2 infects intestinal organoids, and found that the route it used to access them was different from the route it used to infect Vero cells. They discovered that hydroxychloroquine could block the virus's path in Vero cells but not in organoids<sup>10</sup>. "Had these original drug screens been done on organoids rather than on Vero cells, chloroquine would never have emerged as a promising candidate," says Clevers.

Many research groups are trying to realize the potential of organoids for drug discovery. Chen has tested around 1,000 drugs on mini colons and mini lungs, and has identified seven that look promising<sup>11</sup>, including the antiviral drug remdesivir, which had already been shown to have some benefit for participants in clinical trials. Chen sees her results as proving the utility of organoid screening.

The 15,000-drug-screen in lung organoids was her largest attempt yet. She spent weeks tweaking her methods to create organoids that are as similar to each other as possible. "We always worry about the variation between organoids, and comparing apples to oranges," says Chen. The screening is part of a larger project in which multiple labs are using different methods to study the same compounds, and comparing their results, she says.

Organoids have also been used to test vaccines. In January, researchers developed mini tonsils from snippets of discarded tissue taken during surgery. Tonsils play a key part in the body's defence; they're often the first organ to churn out immune cells against a pathogen to ensure long-lasting protection.

When researchers added a COVID-19 vaccine candidate, some of the tonsil organoids produced an immune reaction, generating killer T cells, as well as antibodies that could target the spike protein on the surface of the virus<sup>12</sup>. But much work needs to be done to understand whether what transpires in a dish reflects what will happen in the body.



Tonsil organoids include regions that nurture immune cells (red and green), and can mount a response when exposed to vaccines. Source: Ref. 12

Plus, organs in the body don't exist in isolation. To really understand what happens when a person is infected with SARS-CoV-2, and whether therapies will work, researchers need more complex systems that include immune cells and blood-vessel cells.

In unpublished work, Takanori Takebe, a clinician scientist and stem-cell biologist at Tokyo Medical and Dental University, grew blood-vessel cells on liver organoids and found that smaller capillaries and veins are more susceptible to SARS-CoV-2 infection than are larger vessels. And Chen has grown immune cells called macrophages on sheets of cardiac muscle cells<sup>[13](#)</sup>, and is doing the same for her lung organoids. These experiments, together with studies in animal models, could help to resolve a continuing debate about what it is that makes COVID-19 so deadly — the virus itself, or a hyperactive immune response.

Ideally, researchers want to be able to link organoids together. These systems could reveal, for example, how an infection that starts in the lung influences the heart or gut. “The dream for every virologist would be to have different organs connected to each other,” says Mühlberger. “The closer we can get to the human organ, the better it will be, the more we will learn about why viruses are so pathogenic.”

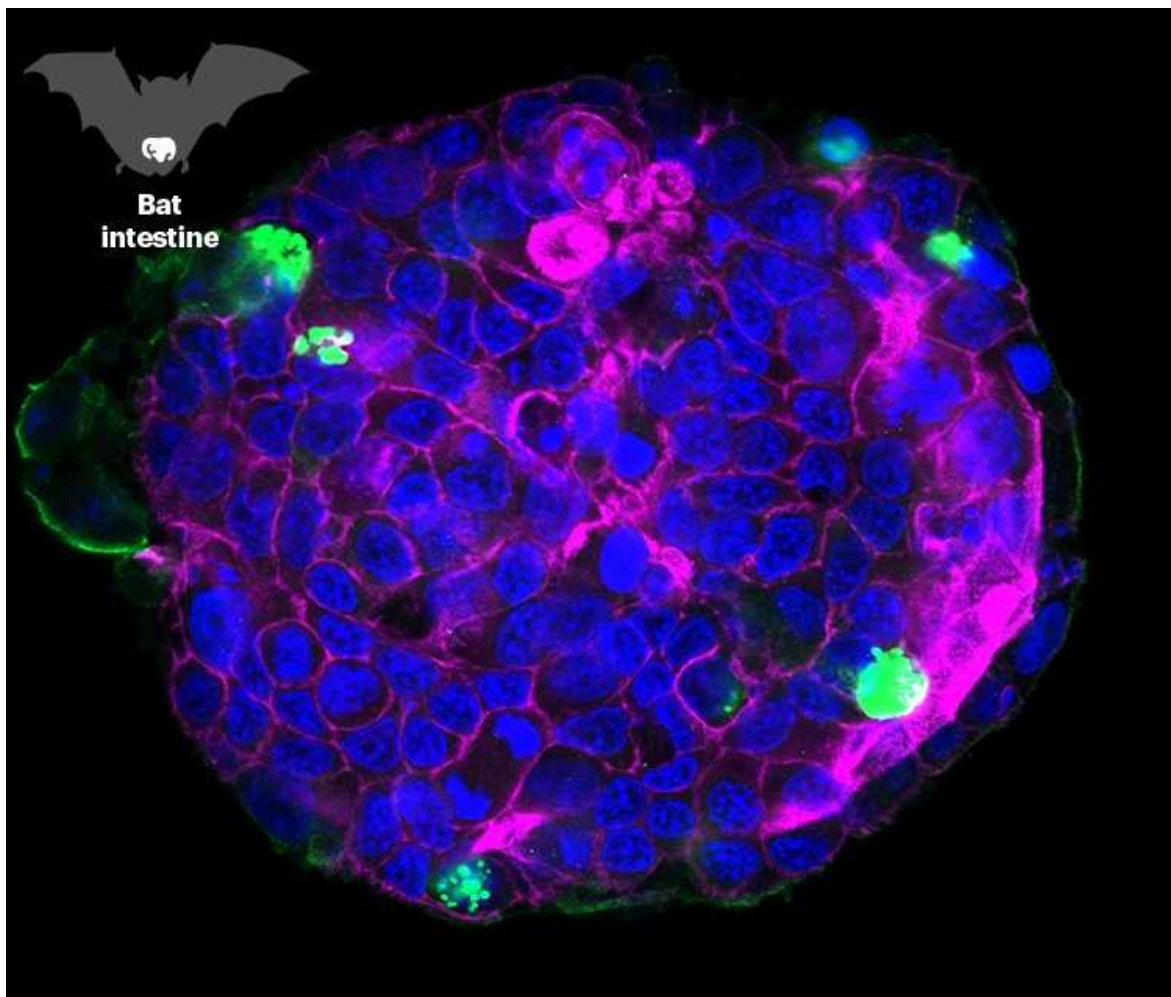
In 2019, Takebe connected liver, bile duct and pancreas organoids<sup>[14](#)</sup>, but so far, no teams have published papers using multi-organ models to study SARS-CoV-2.

## Next pandemic

The relationships formed between cell biologists and virologists will probably extend beyond COVID-19.

For every organoid Mühlberger has infected with SARS-CoV-2, she has run parallel experiments with Ebola virus, the cause of a deadly haemorrhagic fever for which there are very few models of infection. She has found that Ebola virus can infect almost every tissue, even reaching regions that SARS-CoV-2 cannot venture into. This ability could be what makes Ebola so deadly, she says.

As for predicting the next pandemic, some researchers are turning to organoids made from animal cells.



Organoids made out of tissue from bats, a known reservoir of viruses, can be infected with SARS-CoV-2 (green). Source: Ref. 15

In early 2020, Zhou reached out to Shi Zheng-Li, a virologist at Wuhan Institute of Virology in China, who helped to identify the closest known relative of SARS-CoV-2 — the bat coronavirus RATG13. Shi said she had sequenced hundreds of coronaviruses from bats but had been able to grow only a handful of them. Zhou wondered whether she could help by growing organoids from bat tissue. These could be used to test drugs that can target a wide range of viruses with the potential to infect people.

Zhou nipped fragments of gut from wild horseshoe bats (*Rhinolophus sinicus*), and created miniature bat intestines made of multiple cell types. SARS-CoV-2 grew well on the intestines<sup>15</sup> — the first experimental

evidence that the coronavirus could infect horseshoe bats, adding weight to the hypothesis that it originated in bats.

Studying viruses with organoids is still a new pursuit, but many consider them an exciting model for exploring interactions between human cells and viruses, and the technology could make the response to the next pandemic much faster, says Ju.

“These are magical cultures,” says Estes. “It’s just your imagination that limits where this field can go.”

Nature **593**, 492-494 (2021)

doi: <https://doi.org/10.1038/d41586-021-01395-z>

## References

1. 1.

Sato, T. *et al.* *Gastroenterology* **141**, 1762–1772 (2011).

[PubMed](#) [Article](#) [Google Scholar](#)

2. 2.

Ettayebi, K. *et al.* *Science* **353**, 1387–1393 (2016).

[PubMed](#) [Article](#) [Google Scholar](#)

3. 3.

Garcez, P. P. *et al.* *Science* **352**, 816–818 (2016).

[PubMed](#) [Article](#) [Google Scholar](#)

4. 4.

Zhou, J. *et al.* *Proc. Natl Acad. Sci. USA* **115**, 6822–6827 (2018).

[PubMed](#) [Article](#) [Google Scholar](#)

5. 5.

Lamers, M. M. *et al.* *Science* **369**, 50–54 (2020).

[PubMed](#) [Article](#) [Google Scholar](#)

6. 6.

Salahudeen, A. A. *et al.* *Nature* **588**, 670–675 (2020).

[PubMed](#) [Article](#) [Google Scholar](#)

7. 7.

Youk, J. *et al.* *Cell Stem Cell* **27**, 905–919 (2020).

[PubMed](#) [Article](#) [Google Scholar](#)

8. 8.

Zang, R. *et al.* *Sci. Immunol.* **5**, eabc3582 (2020).

[PubMed](#) [Article](#) [Google Scholar](#)

9. 9.

Lamers, M. M. *et al.* Preprint at bioRxiv  
<https://doi.org/10.1101/2021.05.03.441080> (2021).

10. 10.

Beumer, J. *et al.* Preprint at bioRxiv  
<https://doi.org/10.1101/2021.05.20.444952> (2021).

11. 11.

Han, Y. *et al.* *Nature* **589**, 270–275 (2021).

[PubMed](#) [Article](#) [Google Scholar](#)

12. 12.

Wagar, L. E. *et al.* *Nature Med.* **27**, 125–135 (2021).

[PubMed](#) [Article](#) [Google Scholar](#)

13. 13.

Yang, L. *et al.* *Circulation Res.*  
<https://doi.org/10.1161/CIRCRESAHA.121.319060> (2021).

[Article](#) [Google Scholar](#)

14. 14.

Koike, H. *et al.* *Nature* **574**, 112–116 (2019).

[PubMed](#) [Article](#) [Google Scholar](#)

15. 15.

Zhou, J. *et al.* *Nature Med.* **26**, 1077–1083 (2020).

[PubMed](#) [Article](#) [Google Scholar](#)

[Download references](#)

## [\*\*Jobs from Nature Careers\*\*](#)

- - - [All jobs](#)
    - - [\*\*Postdoctoral Training Fellow - Kassiotis Lab\*\*](#)

[Francis Crick Institute](#)

[London, United Kingdom](#)

[JOB POST](#)

▪ [Biological Safety Specialist](#)

[Francis Crick Institute](#)

[London, United Kingdom](#)

[JOB POST](#)

▪ [Post-doctoral Fellow - Autoimmune Pathogenesis](#)

[Oklahoma Medical Research Foundation \(OMRF\)](#)

[Oklahoma City, United States](#)

[JOB POST](#)

▪ [Research Technician / Research Assistant](#)

[Oklahoma Medical Research Foundation \(OMRF\)](#)

[Oklahoma City, United States](#)

[JOB POST](#)

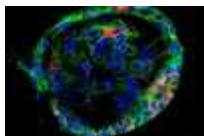
[Download PDF](#)

[Download PDF](#)

## **Related Articles**



- [Can lab-grown brains become conscious?](#)



- [Mini organs reveal how the coronavirus ravages the body](#)



- [The boom in ministomachs, brains, breasts, kidneys and more](#)

---

This article was downloaded by **calibre** from <https://www.nature.com/articles/d41586-021-01395-z>

| [Section menu](#) | [Main menu](#) |

- NEWS FEATURE
- 25 May 2021

# What the science says about lifting mask mandates

With COVID rates dropping and vaccinations on the rise, the United States and other places are removing some requirements for face coverings. Are they moving too fast?

- [Lynne Peeples](#) 0

1. Lynne Peeples

1. Lynne Peeples is a science journalist in Seattle, Washington.

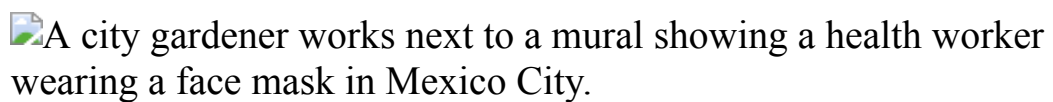
[View author publications](#)

You can also search for this author in [PubMed](#) [Google Scholar](#)





•



A mural promotes mask use while honouring health workers in Mexico City.  
Credit: Pedro Padro/AFP via Getty

A sign is still posted on the front door of the Wolfeboro Food Co-op that reads, “Face masks required.” Until recently, another sign had hung directly below it, explaining how the New Hampshire market was following federal policy.

Erin Perkins, manager of the shop, removed that second sign on 14 May — the day after the US Centers for Disease Control and Prevention (CDC) announced that fully vaccinated individuals, in most situations, no longer need to wear a mask. “We weren’t expecting that,” says Perkins. “It puts us in a precarious position. We were not about to start asking people if they are vaccinated or not.”

New Hampshire was the last state in New England to start mandating mask wearing in public to reduce the spread of the coronavirus SARS-CoV-2. And on 16 April, it became the first in the region to lift that mandate, joining several other states around the country that were loosening their pandemic-related restrictions. Cities and businesses in New Hampshire could still set their own policies, and Perkins wasn’t comfortable changing things right away. Even after the CDC announced its latest guidelines — just two weeks after communicating that vaccinated people should continue to mask up indoors — Perkins wasn’t personally comfortable with unmasked people in her shop. She also knows that several customers have immune systems that are compromised, and emerging research suggests that people in this group are still at risk even after vaccination.<sup>1</sup>.

“Until we feel better about the state of things — until the numbers make a little bit more sense to us, we have decided to wait,” she says, even if that means dealing with testy customers.

Anne Hoen, an epidemiologist at Dartmouth College in nearby Hanover, can understand Perkins’s caution. She says that both the state and federal moves were probably a little too early. Hoen works in New Hampshire but lives just across the border in Vermont, where a state-wide indoor mask mandate remained in force until mid-May, despite Vermont having a lower rate of hospitalizations than practically anywhere else in the country. In the wake of the CDC’s announcement, Vermont Governor Phil Scott relaxed the mandate for fully vaccinated individuals.

The weakening policies are out of step with those of many other countries. Germany strengthened its mask requirements at the end of April, for example. It was facing a slowdown in vaccination rates and a surge in cases. Spain tightened its requirements at the end of March.

The evidence is clear that [masks cut down on COVID-19 deaths](#), but nearly a year and a half into the pandemic and with vaccination coverage climbing in many places, public-health scientists and officials are still struggling to get people — particularly unvaccinated people — to wear masks at appropriate times. Average mask use across the United States has been declining since mid-February. Meanwhile, infection rates in some places have increased. A patchwork of policies and mixed messages from both politicians and public-health officials has resulted in confusion, consternation and a mess of data to interpret. “We’re all over the map,” says Monica Gandhi, an infectious-disease physician at the University of California, San Francisco. “That’s been the problem this entire pandemic. We’ve been making it up as we go along.”



### [How COVID is changing the study of human behaviour](#)

It wasn’t until late April, for example, that the US government finally distinguished between indoor and outdoor mask use in its recommendations, even though the science had been clear for months that the risk of transmission was much lower outdoors<sup>2</sup>. And now, after the CDC released its latest revision, agency director Rochelle Walensky noted that it could change its mask guidance yet again. Hoen and other epidemiologists warn that it is very difficult to reinstate a rule after it has been revoked.

Mask use will continue for this pandemic, and it's likely to become a common response to future outbreaks. So researchers are trying to get a handle on what the science says about how to encourage people to wear them. As the COVID-19 pandemic enters a new phase, scientists around the world are accessing the accumulated data and asking what makes some policies more effective than others, and probing when and how they need to change.

Gandhi is among those who emphasize that mask messaging should evolve in light of rising vaccination rates. Officials should begin relaxing restrictions to give people hope and to motivate vaccination, she says. But changes need to be made carefully.

Around the same time that New Hampshire rescinded its rule, for example, [COVID-19 cases in India began to surge](#). Strict mask mandates there had reined in the country's first wave of infections last September. But as COVID-19 numbers came under control, fewer people wore masks, and many attended large gatherings. The disease quickly gained the upper hand. The country is now scrambling to get people to vaccinate and to use masks again.

"Wearing masks should probably be one of the last things we stop doing," says Hoen, adding that she hopes no other countries are looking to the United States for guidance.

## Masks and mandates

The case for mask mandates was made relatively early in the pandemic. On 6 April 2020, the city of Jena, Germany, became one of the first communities in the world to require people to wear masks in public. Thomas Nitzsche, the town's mayor, says he was sleepless for two nights before the policy went into effect. "I didn't know if the public would comply," he says. "Luckily, they did."

Researchers estimate that new cases in the city, home to around 110,000 people, dropped by about 75% during the 20 days after the rule was brought in<sup>3</sup>.

But it wasn't as simple as flipping a switch one day and then reaping the rewards. Evidence is building that, although a mandate can be a powerful measure, effective messaging and role models are crucial for public uptake.



A sign about mask requirements goes up at a shop in Wales, UK, after regulations changed there in September. Credit: Matthew Horwood/Getty

In the days leading up to the order in Jena, city officials launched a campaign to give the local population an idea of what was to come. Posters around the city declared "*Jena zeigt Maske*" ("Jena shows mask"), and Nitzsche posed for photos on a city tram wearing a mask.

Making the case for masks, and making them obligatory early on, was a common-sense move for Nitzsche. Meanwhile, mask policies in most of the surrounding state of Thuringia and elsewhere in Germany lagged behind. There, officials generally adopted mandates only after case counts surged. Although there were no new COVID-19 cases in Jena five days after implementation of the mask mandate, for example, the virus continued to spread in nearby Erfurt, the state capital, and slowed only after a mask

requirement was imposed, according to a preprint study<sup>4</sup> by public-health leaders in Jena.

It was a similar story around the globe, with a few exceptions. China and other Asian nations quickly adopted mask policies that probably prevented large-scale spread of the disease. Nietzsche says he was personally inspired by the Czech Republic, which began requiring masks in certain public places in mid-March 2020.

Klaus Wälde, an economist at Johannes-Gutenberg University Mainz in Germany, says that the rest of the country should have followed Jena's lead. But the asynchronous mask mandates across Germany — and elsewhere — provided Wälde and others with a unique opportunity.

He and his colleagues used data from 401 regions in Germany to estimate the effect of mask mandates on SARS-CoV-2 transmission<sup>3</sup>. They took advantage of the regional variation to create artificial controls, and then estimated what would have happened had the intervention not been implemented. His team's conclusion: requiring people to wear face masks decreases the daily growth rate of reported COVID-19 cases by more than 40%. The economists' approach was "clever", says Hoen. "This adds to the body of evidence that masks work."



[Face masks: what the data say](#)

In a similar study in the United States, published this January<sup>5</sup>, researchers found that a national mandate for employees to wear face masks early in the pandemic could have reduced the weekly growth rate of cases and deaths by more than 10 percentage points in late April 2020. The study suggests that this could have reduced deaths by as much as 47% (or by nearly 50,000) across the country by the end of May last year. Another preprint, published in October, linked mask mandates with a 20–22% weekly reduction in COVID-19 cases in Canada<sup>6</sup>.

Still, US data suggest that regulation alone might not have been enough to produce a benefit from masks. In a survey of more than 350,000 people, published this March, self-reported mask wearing increased separately from government mask mandates<sup>7</sup>. The mandates do have an effect, “but when we looked at it, it was really the behaviour of the population that was a better metric”, says John Brownstein, an epidemiologist at Harvard Medical School in Boston, Massachusetts, and a co-author of the study. “There’s a difference between government policy and community buy-in.”

The research builds on evidence from hundreds of observational and laboratory studies, which find that [masks protect both the wearer and the people around them](#). Masks can block viral particles that hitch rides on droplets and aerosols. And a study from the US National Institutes of Health, published this February, further suggests that the humidity that builds up inside a mask could help to bolster the lungs’ defences against pathogens<sup>8</sup>.

Still, the debate over the effectiveness of masks, and whether or not they continue to be necessary, trundles on. What will it take to get people to wear masks in countries that still mandate them, and, in the United States, if infections surge again? What will motivate the unvaccinated everywhere to mask up, especially as pandemic fatigue continues to rise? Some researchers have looked to lessons from previous crises.

## Protective barriers

Early in the HIV–AIDS epidemic in the 1980s, public-health officials faced a major challenge in trying to slow the spread of the virus. The problem wasn’t necessarily convincing people that a physical barrier — in this case, a

condom — could prevent infection. “I don’t think the issue was so much about the level of protection as it was the perception of risk,” says Ronald Valdiserri, an epidemiologist at Emory University in Atlanta, Georgia. Whereas homosexual men on the east and west coasts of the United States couldn’t ignore the widespread deaths in the gay community early in the epidemic, many heterosexuals saw HIV–AIDS as a “gay disease”, and did not consider themselves at risk of infection, he says.

The early days of COVID-19 drew a tragic parallel in many places. “You had people thinking, ‘Well, you know, this is not something that’s going to affect my community, or my town, or my neighbourhood. So, why should I be wearing a mask?’” says Valdiserri, who co-authored a paper on how the lessons from research on promoting condom use during the early HIV epidemic could inform face-mask policy<sup>9</sup>. “Like any human behaviour, it’s more complex than saying, ‘Thou shalt do this.’”



A protester displays their displeasure with mask mandates in London. Credit: Henry Nicholls/Reuters

Public-health efforts to combat HIV–AIDS have revolved around tailoring the condom-use message and its delivery to different populations. Among sex workers in sub-Saharan Africa, peers have proved to be the best spokespeople. Popular footballers have successfully marketed condom use to men. When HIV swept through San Francisco and New York in the early 1980s, an effective campaign included an attractive gay man communicating to other gay men, and making condoms “fun and sexy”, says Susan Hassig, an infectious-disease epidemiologist at Tulane University in New Orleans.

But could face masks ever be made fun or sexy? Although there’s been no formal study on the effectiveness of mask marketing, the idea might not be far-fetched. Instructions for creating fun masks for children are easy to find, as are shops selling bedazzled masks for adults. At the Grammy Awards in Los Angeles, California, in March, stars drew attention with masks that matched their outfits.

Helene-Mari van der Westhuizen, a public-health scientist at the University of Oxford, UK, laments how early COVID-19 guidelines framed masks as “sterile and scary” — medical objects that required specific handling and use, including specific temperatures for washing. “Cloth masks and associated fashion brought playfulness and an everyday feeling to mask wearing. That contributed to its acceptability,” says van der Westhuizen, who co-authored a paper arguing that policies should consider masking as a social behaviour, not a medical one<sup>10</sup>.



## Why indoor spaces are still prime COVID hotspots

Balance and nuance are still important: masks need to work. “Masks with valves became really fashionable,” she adds, even though they allow virus particles from infected people to spread. “That’s an example of fashion gone awry,” says van der Westhuizen.

Further complicating mask use is the fact that masks are not all created equal. Simple cloth masks will “do a good job of protecting others from you, but don’t necessarily do a great job of protecting you from others”, says Jeremy Howard, a research scientist at the University of San Francisco, who co-authored a January review on face masks<sup>11</sup>. At the other extreme, medical-grade N95 masks might be overkill, he says. They are tested with much higher air pressures than what comes from normal breathing. Although they do protect the wearer, he instead recommends the widely available and more-comfortable KN95 masks.

“It’s time for nuanced messaging,” adds Gandhi, who co-authored a separate review on the effectiveness of various face masks in January<sup>12</sup>. She says that Germany did the right thing in specifying acceptable masks in its messaging. Cloth masks are no longer enough to comply with the mandate in Jena, or anywhere in the country. In January, Germany began requiring medical-grade or surgical masks in public spaces. The country, which has lagged behind the United States in vaccination rates, further upgraded its rule in April, mandating N95 or KN95 masks on public transport. The country is distributing masks to people who are at high risk of disease and those who can’t afford them. And leaders are enforcing their use. “If you’re not wearing a mask, you’ll get fined,” says Nitzsche. “Or people will start to stare at you.”

## Cultural change

South Korea is among the east Asian countries that had a head start on the West. A pre-existing culture of mask use bolstered quick and widespread adoption after the emergence of COVID-19 — a stark contrast to Western nations, where even public-health officials at the World Health Organization

and the US CDC were initially dissuading their use, describing them as unhelpful or even harmful.

The culture makes a difference, says Hong Bin Kim, who studies internal medicine and infectious disease at Seoul National University College of Medicine, and is author of a paper detailing mask use in South Korea<sup>13</sup>. Bin's work also highlights the importance of leaders serving as models for the public. Politicians and doctors filled that role in his country, much like Nitzsche and public-health officials did in Jena.

Although it's unlikely that the United States and other Western nations will adopt the same level of mask use beyond this pandemic, van der Westhuizen anticipates it will become much more common and acceptable than before. "It's truly remarkable how widespread this new habit has become," she says. "We have gained a valuable preventative tool."

She is referring to more than COVID-19 and its variants, or even influenza. Tuberculosis, for example, has been a leading cause of death in South Africa and a long-time focus of her research. Although data show that masks could help to control the spread of that disease, social norms and stigma have impeded their adoption<sup>14</sup>. When initial COVID-19 guidelines suggested only people with symptoms needed to wear masks, she says, her thoughts immediately went to tuberculosis, for which public-health officials have made similar concessions. Thankfully, mask recommendations evolved. "The pandemic has broken that previous stigma," says van der Westhuizen.

Hassig is reminded of other public-health interventions. The use of vehicle seat belts first arrived in the United States and United Kingdom as a recommendation, then became a law, for instance. Eventually, police began fining those who were non-compliant, and buckling up became the norm. "Very rarely does a public-health intervention wind up being widely accepted without some kind of enforcement mechanism," says Hassig, who still wears a mask despite being fully vaccinated, in part to encourage mask wearing.

Perkins, meanwhile, has to police her customers in rural New Hampshire — a challenging task without the backing of a state or federal mandate. At least once a day, she says, she gets a customer who asks why the shop still

requires masks. One man even chose to leave rather than put on the free mask she offered him. “People just keep asking ‘why, why, why?’ Some people have very strong feelings about it,” says Perkins. “I just keep telling people this is our policy at this time. It will change when we feel it is okay to do so.”

Nature **593**, 495-498 (2021)

doi: <https://doi.org/10.1038/d41586-021-01394-0>

## References

1. 1.

Boyarski, B. J. *et al.* *J. Am. Med. Assoc.* <https://doi.org/10.1001/jama.2021.7489> (2021).

[Article](#) [Google Scholar](#)

2. 2.

Bulfone, T. C., Malekinejad, M., Rutherford, G. W. & Razani, N. *J. Inf. Dis.* **223**, 550–561 (2021).

[PubMed](#) [Article](#) [Google Scholar](#)

3. 3.

Mitze, T. *et al.* *Proc. Natl Acad. Sci. USA* **117**, 32293–32301 (2020).

[PubMed](#) [Article](#) [Google Scholar](#)

4. 4.

Pletz, M. W. *et al.* Preprint at medRxiv  
<https://doi.org/10.1101/2020.09.02.20187021> (2020).

5. 5.

Chernozhukov, V., Kasahara, H. & Schrimpf, P. *J. Econom.* **220**, 23–62 (2021).

[PubMed](#) [Article](#) [Google Scholar](#)

6. 6.

Karaivanov, A. *et al.* Preprint at medRxiv  
<https://doi.org/10.1101/2020.09.24.20201178> (2021)

7. 7.

Rader, B. *et al.* *Lancet Digit. Health* **3**, e148–e157 (2021).

[PubMed](#) [Article](#) [Google Scholar](#)

8. 8.

Courtney, J. M. & Bax, A. *Biophys. J.* **120**, 994–1000 (2021).

[PubMed](#) [Article](#) [Google Scholar](#)

9. 9.

Valdiserri, R. O., Holtgrave, D. R. & Kalichman S. C. *Aids Behav.* **24**, 3283–3287 (2020).

[PubMed](#) [Article](#) [Google Scholar](#)

10. 10.

van der Westhuizen, H.-M. *et al.* *Br. Med. J.* **370**, m3021 (2020).

[Google Scholar](#)

11. 11.

Howard, J. *et al.* *Proc. Natl Acad. Sci. USA* **118**, e2014564118 (2021).

[PubMed](#) [Article](#) [Google Scholar](#)

12. 12.

Gandhi, M. & Marr, L. C. *Med* **2**, 29–32 (2021).

[PubMed](#) [Article](#) [Google Scholar](#)

13. 13.

Lim, S. *et al.* *J. Hosp. Infect.* **106**, 206–207 (2020).

[PubMed](#) [Article](#) [Google Scholar](#)

14. 14.

Driessche, K. V. *et al.* *Lancet Resp. Med.* **4**, 340–342 (2021).

[Article](#) [Google Scholar](#)

[Download references](#)

## [\*\*Jobs from Nature Careers\*\*](#)

- - - [All jobs](#)
    - - [\*\*Postdoctoral Training Fellow - Kassiotis Lab\*\*](#)
        - [Francis Crick Institute](#)
        - [London, United Kingdom](#)
        - [JOB POST](#)
      - [\*\*Biological Safety Specialist\*\*](#)
        - [Francis Crick Institute](#)

[London, United Kingdom](#)

[JOB POST](#)

▪ [\*\*Post-doctoral Fellow - Autoimmune Pathogenesis\*\*](#)

[Oklahoma Medical Research Foundation \(OMRF\)](#)

[Oklahoma City, United States](#)

[JOB POST](#)

▪ [\*\*Research Technician / Research Assistant\*\*](#)

[Oklahoma Medical Research Foundation \(OMRF\)](#)

[Oklahoma City, United States](#)

[JOB POST](#)

[Download PDF](#)

[Download PDF](#)

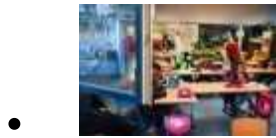
## Related Articles



- [How COVID is changing the study of human behaviour](#)



- [India's massive COVID surge puzzles scientists](#)



- **Why indoor spaces are still prime COVID hotspots**



- **Face masks: what the data say**

---

This article was downloaded by **calibre** from <https://www.nature.com/articles/d41586-021-01394-0>

| [Section menu](#) | [Main menu](#) |

## Books & Arts

- **[AI — the people and places that make, use and manage it](#)**

[ 26 May 2021]

Book Review • Two books offer complementary insights into how artificial intelligence is shaping society.

- **[A physicist goes in search of our origins](#)** [ 24 May 2021]

Book Review • CERN experimentalist offers sweeping history of the Universe, in science and culture.

---

- BOOK REVIEW
- 26 May 2021

# AI — the people and places that make, use and manage it

Two books offer complementary insights into how artificial intelligence is shaping society.

- [Virginia Dignum](#) 0
- 1. [Virginia Dignum](#)

1. Virginia Dignum is a professor in the department of computing science at Umeå University in Sweden.

[View author publications](#)

You can also search for this author in [PubMed](#) [Google Scholar](#)









A man sorts tin ore from sand in Indonesia. Many of the metals needed for semiconductors are mined at great human and environmental cost. Credit: Beawiharta/Reuters

**The Alignment Problem: Machine Learning and Human Values** *Brian Christian W. W. Norton* (2020)

**Atlas of AI: Power, Politics, and the Planetary Costs of Artificial Intelligence** *Kate Crawford* Yale Univ. Press (2021)

Artificial intelligence (AI) permeates our lives. It determines what we read and buy, whether we get a job, loan, mortgage, subsidies or parole. It diagnoses diseases and underlies — and undermines — democratic processes. Two new books offer complementary visions of how society is being reshaped by those who build, use and manage AI.

In *The Alignment Problem*, writer Brian Christian gives an intimate view of the people making AI technology — their aims, expectations, hopes, challenges and desolations. Starting with Walter Pitts's work on a logical

representation of neuron activity in the early twentieth century, he recounts the ideas, aims, successes and failures of researchers and practitioners in fields from cognitive science to engineering. *Atlas of AI*, from the influential scholar Kate Crawford, deals with how, practically, AI gets into and plays out in our lives. It shows that AI is an extractive industry, exploiting resources from materials to labour and information.

Both books parse how the power of, and over, the digital world is shifting politics and social relations. They nod to alternative approaches to these imbalances — state control in China, or the regulatory efforts of the European Union — but focus on the North American story. Together, they beg for a sequel: on ways forward.

## From prophecy to ubiquity

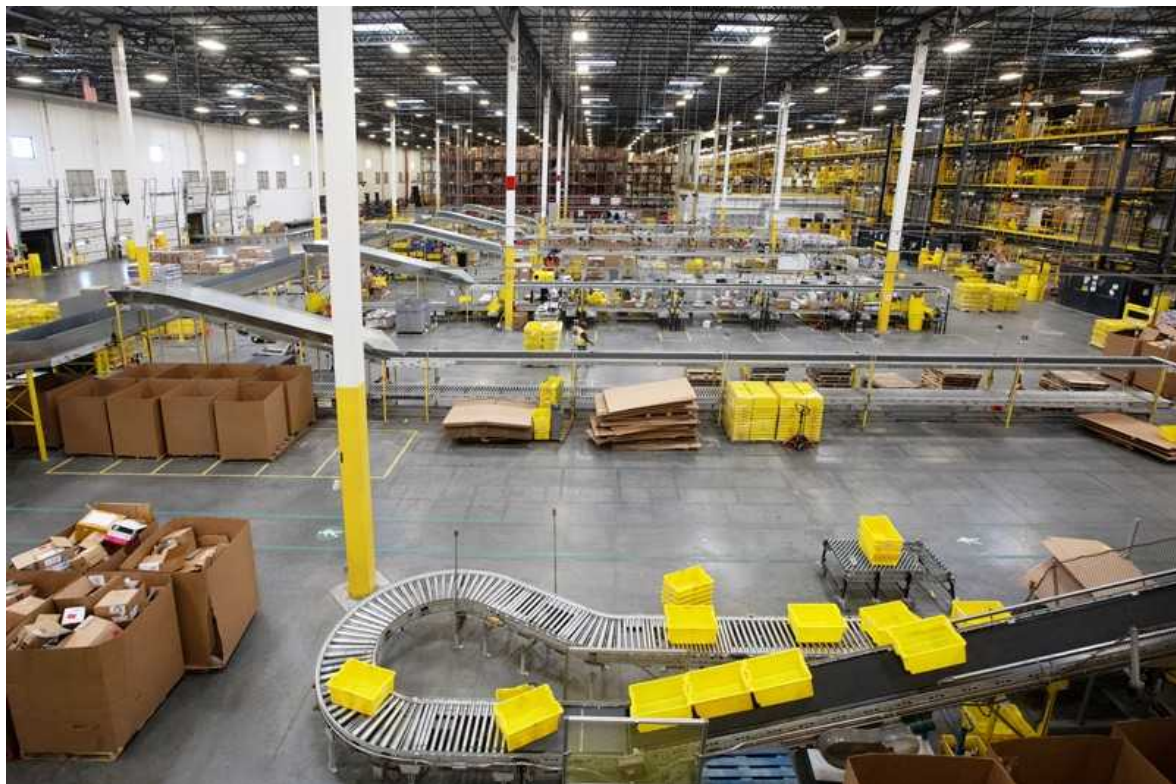
Christian tracks the evolution of AI technology, from prophecy to ubiquity. He shows how researchers try to get AI to interpret human values such as fairness, transparency, curiosity and uncertainty, and the challenges that stand in their way. Largely based on encounters with researchers and practitioners, the book charts a slow, steady, complex progress, with many lows and some incredible highs.



[Cooperative AI: machines must learn to find common ground](#)

We meet people such as Rich Caruana, now senior principal researcher at Microsoft in Redmond, Washington, who was asked as a graduate student to glance at something that led to his life's work — optimizing data clustering and compression to make models that are both intelligible and accurate. And we walk along the beach with Marc Bellemare, who pioneered reinforcement learning while working with games for the Atari console and is now at Google Research in Montreal, Canada.

Christian shows researchers' growing realization that AI developments are affected by societal values — and, more importantly, affect them. They come with a cost and can have profound impacts on communities. At its core, *The Alignment Problem* asks how we can ensure that AI systems capture our norms and values, understand what we mean and do what we want. We all have different conceptions of and requirements for what such systems should do. As mathematician Norbert Wiener put it in 1960: "We had better be quite sure that the purpose put into the machine is the purpose which we really desire."



Behind the scenes of the big-data economy: an Amazon fulfilment centre in New Jersey.Credit: Bess Adler/Bloomberg/Getty

Crawford's collection exposes the dark side of AI success. It traverses the globe exploring the relationships between places and their impact on AI infrastructure. From Nevada and Indonesia, where the lithium and tin central to semiconductors are mined at great human and environmental cost, we travel to an Amazon warehouse in New Jersey. Here, labourers bend their bodies to the will of robots and production lines, instead of the automation adapting to human tempo. In an uneasy reminder of Charlie Chaplin's 1936 film *Modern Times*, we witness the hardship of "fauxtomation" — supposedly automated systems that rely heavily on human labour, such as that of workers paid below minimum wage in data-labelling farms.

Crawford concludes with the arresting reminder that AI is not objective, neutral or universal. Instead, it is deeply embedded in the culture and economic reality of those who make it — mostly, the white, wealthy men of California's Silicon Valley.

Both books are strong in their exposition of the challenges and dangers of current use and development of AI, and what sets it apart from 'classic' computing. Reading them side by side highlights three core issues: over-reliance on data-driven, stochastic predictions; automated decisions; and concentration of power.

## Data dominance

As AI researcher Joy Buolamwini comments in the 2020 documentary *Coded Bias*, algorithmic decision-making is undoing decades of progress towards equal rights, reifying the very prejudices it reveals to be still deeply rooted. Why? Because using data to inform automated decisions often ignores the contexts, emotions and relationships that are core to human choices.

Data are not raw materials. They are always about the past, and they reflect the beliefs, practices and biases of those who create and collect them. Yet current application of automated decision-making is informed more by efficiency and economic benefits than by its effects on people.



### Time to regulate AI that interprets human emotions

Worse, most approaches to AI empower those who have the data and the computational capability to process and manage them. Increasingly, these are big tech corporations — private entities outside democratic processes and participatory control. Governments and individuals are the users, not the leaders. The consequences of this shift are enormous and have the potential to alter society.

So, what now? Besides efforts to debias the data and explain decisions algorithms make, we need to address the source of the bias. This will be done not through technological fixes, but by education and social change. At the same time, research is needed to address the field's perverse dependence on correlations in data. Current AI identifies patterns, not meaning.

Meticulously researched and superbly written, these books ultimately hold up a mirror. They show that the responsible — ethical, legal and beneficial — development and use of AI is not about technology. It is about us: how we want our world to be; how we prioritize human rights and ethical principles; who comprises this ‘we’. This discussion can wait no longer. But the key question is: how can all have a voice?

Nature **593**, 499-500 (2021)

doi: <https://doi.org/10.1038/d41586-021-01397-x>

## Competing Interests

The author declares no competing interests.

## Jobs from Nature Careers

- - - [All jobs](#)
    - 
    - [Postdoctoral Training Fellow - Kassiotis Lab](#)
      - [Francis Crick Institute](#)
      - [London, United Kingdom](#)
      - [JOB POST](#)
    - [Biological Safety Specialist](#)
      - [Francis Crick Institute](#)
      - [London, United Kingdom](#)
      - [JOB POST](#)
    - [Post-doctoral Fellow - Autoimmune Pathogenesis](#)
      - [Oklahoma Medical Research Foundation \(OMRF\)](#)
      - [Oklahoma City, United States](#)
      - [JOB POST](#)

▪ **Research Technician / Research Assistant**

Oklahoma Medical Research Foundation (OMRF)

Oklahoma City, United States

JOB POST

[Download PDF](#)

[Download PDF](#)

## Related Articles



- [Cooperative AI: machines must learn to find common ground](#)



- [Time to regulate AI that interprets human emotions](#)



- [Policies designed for drugs won't work for AI](#)



- [Don't ask if artificial intelligence is good or fair, ask how it shifts power](#)

-  **Halt the use of facial-recognition technology until it is regulated**
-  **AI can be sexist and racist — it's time to make it fair**

---

This article was downloaded by **calibre** from <https://www.nature.com/articles/d41586-021-01397-x>

| [Section menu](#) | [Main menu](#) |

- BOOK REVIEW
- 24 May 2021

# A physicist goes in search of our origins

CERN experimentalist offers sweeping history of the Universe, in science and culture.

- [Andrea Taroni](#) <sup>0</sup>

1. Andrea Taroni

1. Andrea Taroni is chief editor of *Nature Physics*. He is based in London.

[View author publications](#)

You can also search for this author in [PubMed](#) [Google Scholar](#)









Part of the Large Hadron Collider, where author Guido Tonelli worked on the Higgs boson, foundational to the structure of the Universe.Credit: Valentin Flauraud/AFP/Getty

### **Genesis: The Story of How Everything Began** *Guido Tonelli (transl. Erica Segre & Simon Carnell)* Profile (2021)

Physicist Guido Tonelli has spent decades constructing intricate instruments to probe the mysteries of matter. As part of one of the two main experiments at the Large Hadron Collider near Geneva, Switzerland, he vaulted to international attention in front of a packed auditorium in July 2012, when the group announced the discovery of the Higgs boson — the long-sought elementary particle that imparts mass to all others.

Now, Tonelli has turned his gaze from the very small to the very large — the history of the Universe. His ambition encompasses scientific insights, art, philosophy and religion. *Genesis* is not just a book about the cosmos as measured by giant telescopes and particle accelerators. It is also a story of humanity’s interpretations of the beginning and evolution of creation.

Many other physicists, from Stephen Hawking to Janna Levin, have explored this space in popular writing. Most cater to an Anglophone audience. Tonelli's contribution — a bestseller in his native Italy — has a different flavour. It combines the humanistic approach that underpins much Italian education with scientific facts gleaned from a career as a nuts-and-bolts experimentalist.



### [From Big Bang to cosmic bounce: an astronomical journey through space and time](#)

Tonelli argues that the search for the origins of the cosmos arises from humans' need to be rooted. His biblical title nods to the idea that current scientific understanding is part of a much wider cultural history. And the picture of creation built up by twenty-first-century science is as astonishing and mysterious as any ancient myth.

His starting point is Hesiod's *Theogony*, a poem from around 700 bc on the birth of the Greek gods. In the beginning, there was chaos. Tonelli uses 'chaos' in its original sense — a chasm or void so enormous that it could swallow and contain everything — rather than with its more modern connotation of disorder. Just as silence can be understood as a superposition of opposite-phase sound waves that cancel one another out, the void can host unlimited quantities of matter and antimatter, yet have a net energy of zero.

The Universe was born 13.8 billion years ago from a random quantum fluctuation in this void.

A sweeping description ensues. First came the unfathomably quick inflation through which the Universe ballooned in size. Next came cooling, in which hierarchies of forces, symmetries, particles, black holes, stars and galaxies emerged. Each chapter represents a ‘day’ in Tonelli’s genesis, capturing an important phase as the Universe acquired structure. Here lie phenomena such as baryogenesis (the mysterious process that led to the asymmetry between matter and antimatter); the primordial soup of quarks and gluons from which the building blocks of atoms were born; and the uncoupling of matter from radiation.

## Matter and mythology

Tonelli references all manner of mythology and literary sources. He is also scrupulous in explaining how scientists arrived at their conclusions. The chapter on the Big Bang describes the work of researchers including Albert Einstein, Georges Lemaître and Henrietta Swan Leavitt, and refers to the Hindu deity Shiva, the Buddhist doctrine of emptiness, or *Śūnyatā*, and Jorge Luis Borges’s 1945 short story ‘The Aleph’. Although fascinating, the conceptual leaps between scientific detail and cultural references are demanding to follow.



## [Crunch, rip, freeze or decay — how will the Universe end?](#)

The book's most vivid passages are its more scientific ones. The description of the Higgs boson, and its foundational importance in the development of the structure of the Universe and our understanding of it, is clearly home turf for Tonelli. He makes deep and lucid connections with concepts such as spontaneous symmetry breaking, the process through which a physical system enters its lowest-energy state by seemingly disregarding all the other possible states with the same symmetry. And the chapters examining the formation and structure of stars and galaxies are spellbinding – it would be a joy to listen to these while gazing at a starry sky.

Yet Tonelli leaves a gap between the very small and the very large. Considering that so much of his story pertains to the transformation of matter across phases, it is striking that he makes no explicit connection with branches of physics developed to understand these phenomena, such as the theory of phase transitions that explains the structural rearrangement when water becomes ice. This omission exposes a cultural gap in physics. But some pioneering physicists, such as Robert Brout, Murray Gell-Mann and Ken Wilson, have managed to connect high-energy particle physics with its ‘low-energy’ condensed-matter cousin. Tonelli misses a trick here.

Ultimately, however, his goal is to bridge a much wider gap — the one between science and the humanities. For Tonelli, everything in the evolution of the Universe, culture and the human condition follows from the need to understand our origins. Stories allow us to make sense of the void from which all things began. It is fitting that his own story is complex, mysterious and, at times, even messy — a bit like the Universe itself.

Nature **593**, 500-501 (2021)

doi: <https://doi.org/10.1038/d41586-021-01398-w>

## **Competing Interests**

The author declares no competing interests.

## Jobs from Nature Careers

- - - [All jobs](#)
    - - [Postdoctoral Training Fellow - Kassiotis Lab](#)  
[Francis Crick Institute](#)  
[London, United Kingdom](#)  
[JOB POST](#)
      - [Biological Safety Specialist](#)  
[Francis Crick Institute](#)  
[London, United Kingdom](#)  
[JOB POST](#)
      - [Post-doctoral Fellow - Autoimmune Pathogenesis](#)  
[Oklahoma Medical Research Foundation \(OMRF\)](#)  
[Oklahoma City, United States](#)  
[JOB POST](#)
      - [Research Technician / Research Assistant](#)  
[Oklahoma Medical Research Foundation \(OMRF\)](#)  
[Oklahoma City, United States](#)

## JOB POST

[Download PDF](#)

[Download PDF](#)

## Related Articles



- [From Big Bang to cosmic bounce: an astronomical journey through space and time](#)



- [A few words on infinity](#)



- [Crunch, rip, freeze or decay — how will the Universe end?](#)



- [A physicist probes the metaphysical](#)

---

This article was downloaded by **calibre** from <https://www.nature.com/articles/d41586-021-01398-w>

# Opinion

- **Count the cost of disability caused by COVID-19** [ 26 May 2021]  
Comment • Focusing only on cases and deaths hides the pandemic's lasting health burden on people, societies and economies.
- **Tissues, not blood, are where immune cells function** [ 25 May 2021]  
Comment • COVID has shown we must study immunity in the whole body — let's sort the logistics to acquire the right samples.
- **Vaccination: Brazil fails Indigenous people again with two-tier scheme** [ 25 May 2021]  
Correspondence •
- **Deploy international satellite monitoring to safeguard forests** [ 25 May 2021]  
Correspondence •
- **EU forest strategy: adapt, innovate, employ** [ 25 May 2021]  
Correspondence •
- **Trade resolution further threatens Brazil's amphibians** [ 25 May 2021]  
Correspondence •

- COMMENT
- 26 May 2021

# Count the cost of disability caused by COVID-19

Focusing only on cases and deaths hides the pandemic's lasting health burden on people, societies and economies.

- [Andrew Briggs](#) <sup>0</sup> &
- [Anna Vassall](#) <sup>1</sup>

## 1. [Andrew Briggs](#)

1. Andrew Briggs is professor of health economics in the Department of Health Services Research & Policy, London School of Hygiene & Tropical Medicine, UK.

[View author publications](#)

You can also search for this author in [PubMed](#) [Google Scholar](#)

## 2. [Anna Vassall](#)

1. Anna Vassall is professor of health economics in the Department of Global Health & Development, London School of Hygiene & Tropical Medicine, UK; and chair in global health at the Amsterdam Institute of Global Health and Development, University of Amsterdam, the Netherlands.

[View author publications](#)

You can also search for this author in [PubMed](#) [Google Scholar](#)









A person receiving dialysis. COVID-19 can leave people with lasting damage to their kidneys, among many other organs. Credit: Grant Hindsley/New York Times/Redux/eyevine

The COVID-19 pandemic is well into its second year, but countries are only beginning to grapple with the lasting health crisis. In March, a UK consortium reported that 1 in 5 people who were hospitalized with the disease had a new disability after discharge<sup>1</sup>. A large US study found similar effects for both hospitalized and non-hospitalized people<sup>2</sup>. Among adults who were not hospitalized, 1 in 10 have ongoing symptoms 12 weeks after a positive test<sup>3</sup>. Treatment services for the long-term consequences of COVID-19 are already having to be absorbed into health and care systems urgently. Tackling this requires a much clearer picture of the burden of the disease than currently exists.

Tracking disease cases and deaths has advantages in a health emergency — they are easily collated, and, to some extent, trends can be compared across

countries. But continuing the use of such simplified metrics heightens the risks of underestimating the true health impact on a population. It focuses policy and public discourse on the immediate prevention of deaths and on the economic impact of lockdown policies, ignoring the long-term disease-related disabilities that will also affect well-being and productivity.

To tackle the pandemic's inequitable impact, researchers must also count how COVID-19 contributes to ill health, and do so comprehensively. If scarce resources are allocated with only the death count in mind, low- and middle-income countries (LMICs) with younger populations might not receive their fair share. This could be devastating for countries that rely on the productivity of people of working age for economic development. Choosing the right metrics can also help to identify and address inequity within countries. Evidence from many nations suggest that members of minority ethnic communities are more likely to catch COVID-19 and die from it, as well as being more likely to die at a younger age<sup>4</sup> (see also [\*Nature\* 592, 674–680; 2021](#)).

Fortunately, metrics of illness exist. They inform much health policy — from cancer screening and treatment to attempts to eradicate tuberculosis. Called DALYs and QALYs (disability-adjusted life years and quality-adjusted life years), these measures capture the impact of ill health on a person's life course — combining the years of life lost because of premature death, and the years lived while experiencing the disabling consequences of disease.



## Will COVID force public health to confront America's epic inequality?

As health economists, we use these metrics to understand the global burden of disease. They help us to compare the effects of prevention, treatment and social action (such as education or housing initiatives) on tackling the HIV pandemic, for example. In a recent study<sup>5</sup>, we used these metrics to estimate that a death from COVID-19 results in around 5 QALYs lost, on average. We have previously used similar estimates to inform COVID-19 vaccine policy in the United Kingdom<sup>6</sup>.

Here we offer a very rough first estimate, based on simple assumptions, that as much as 30% of the COVID-19 health burden could be due to COVID-induced disability, not death. Much more needs to be done to improve such estimates so they can be acted on effectively. To design the right policies now, and invest well to deal with COVID-19 (and other pandemics) in the future, we need to use metrics that encapsulate all the consequences of a disease.

## **Long view**

Health comprises our social, mental and physical well-being. DALYs and QALYs are already used by global institutions and national governments to capture this holistic understanding of the burden of other diseases globally.

One DALY represents one year of healthy life lost because of illness, disability or early death. This metric has been developed and used widely by the World Bank, the World Health Organization (WHO) and the University of Washington's Institute for Health Metrics and Evaluation (IHME) in Seattle. The latter produces annual estimates of the global burden of disease (see, for example, ref. 7). DALYs are often used by governments in LMICs to set priorities across their health sectors. A 2020 estimate by Pakistan's health-services ministry found that the cost of a skilled attendant who can manage labour and delivery in low-risk pregnant women is just US\$2 for each DALY averted, for example<sup>8</sup>.

One QALY equates to one year of perfect health. This measure is mainly used by high-income countries (HICs), including the United States. That said, the US Affordable Care Act of 2010 outlawed the use of QALYs following lobbying<sup>9</sup>. In many countries, the metric is often used to assess the value of new technologies, such as population screening tests or innovative cell and gene therapies.

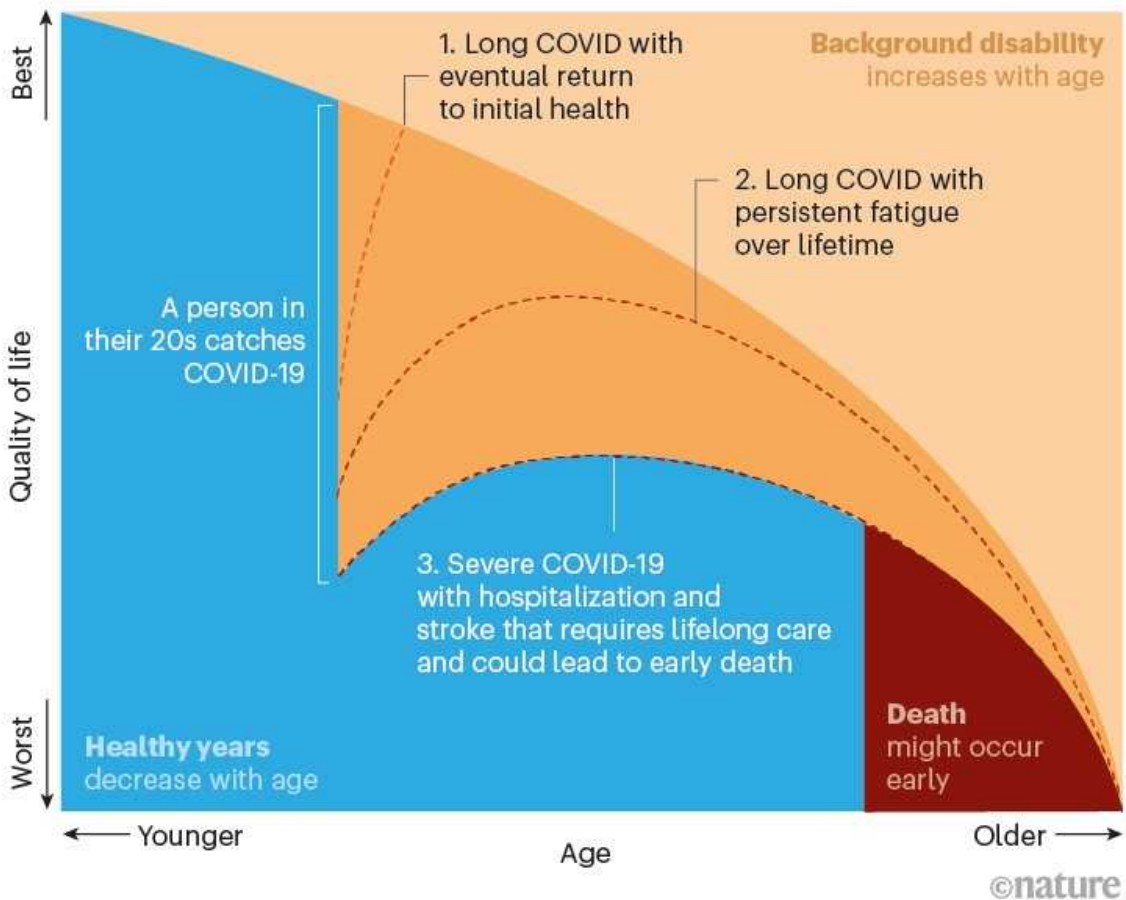
Each measure is calculated by considering the overall impact of different types of ill health — such as cancer or diabetes — during the course of a life. Although the detailed methods of calculating QALYs and DALYs differ, they can be considered functionally equivalent.

For instance, a person with a fractured limb might recover quickly if they are in their twenties. The same accident could leave a 70-year-old with reduced mobility for the rest of their life. More QALYs are lost and DALYs incurred in the second case. Likewise, the burden of HIV infection can be vastly reduced if effective drugs allow a person with the virus to live a full life.

The wide range of COVID-19 outcomes can lead to markedly different profiles (see ‘COVID casts a long shadow’). A mild case of the disease in an otherwise well person might lead to ‘long COVID’ — a sharp decrease in overall health that can resolve after months or last for more than a year. Some people with COVID-19 experience strokes or become diabetic. Weeks of treatment in intensive care can mean that a person never returns to their former health because of damage to the brain, heart or lungs, for example. More needs to be understood about all of these scenarios so that researchers can calculate disease burdens with confidence.

## COVID CASTS A LONG SHADOW

Conditions such as heart disease gradually decrease a person's quality of life (blue) and increase their disability burden (pale orange) over their lifetime. Catching COVID-19 adds an immediate disability burden (dark orange). The disease can have a wide range of outcomes; three illustrative scenarios are shown (dashed lines).



## COVID burdens

To illustrate how QALYs and DALYs can provide a more complete picture of COVID-19, we attempted a first rough estimate of the burden of the disease in two countries that have different demographics: Pakistan and the United Kingdom (see 'Life and health lost'). The population of Pakistan, in common with many LMICs, has a high proportion of younger age groups; the United Kingdom, like other HICs, does not. It should be noted that our sketch is illustrative only, because we extrapolated from UK data on the rates of hospitalized people needing long-term care. The two nations have differing health systems, pre-existing patterns of co-morbidity and so on;

and many people who are not hospitalized with COVID-19 also experience lasting effects.

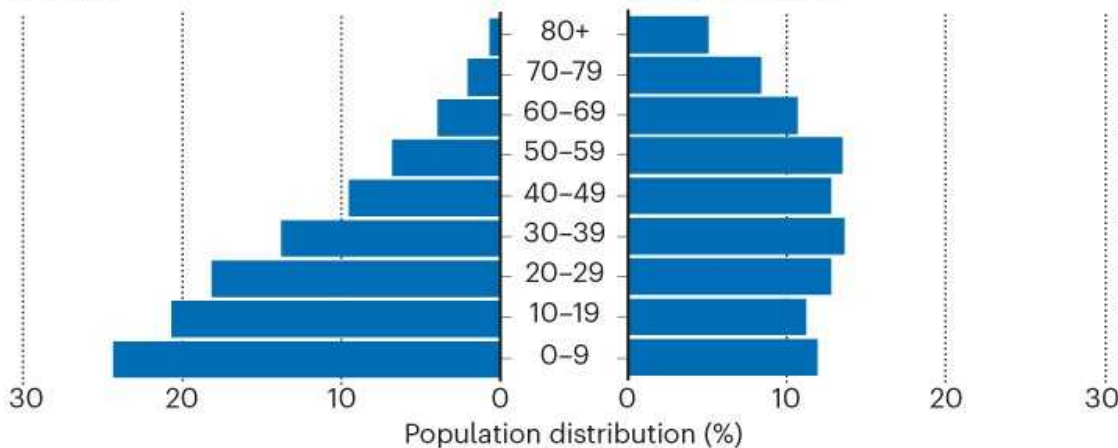
## LIFE AND HEALTH LOST

Metrics that capture the overall burden of ill health, rather than simply counting deaths, hint at how COVID-19 might affect populations in Pakistan and the United Kingdom in the long term.

### Different demographics

Pakistan's population is predominantly young; the United Kingdom's is more evenly distributed across age groups.

#### Pakistan



#### United Kingdom

### DALYs lost to COVID-19

Estimates using disability-adjusted life years (DALYs) suggest that, in Pakistan, most of the health burden of COVID-19 could fall on people aged 60 or under.

#### Pakistan

0.31 total

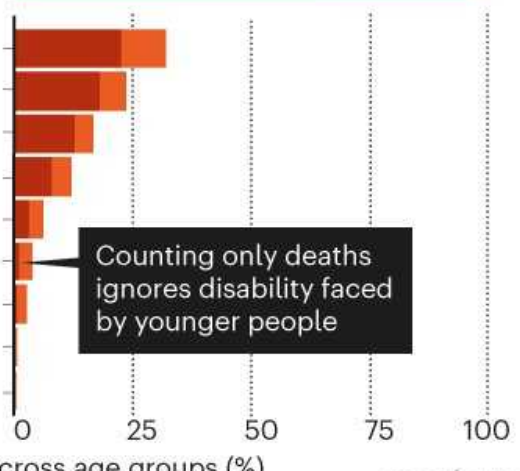
0.10 Deaths    0.22 DALYs per case

- Deaths
- Disability (from COVID-related conditions)

#### United Kingdom

0.26 total

0.17 Deaths    0.08 DALYs per case



Counting only deaths  
ignores disability faced  
by younger people

©nature

Sources: Population data: [www.populationpyramid.net](http://www.populationpyramid.net); DALYs lost: Authors' estimate

We approximate that the health burden due to COVID-induced disability across all age groups could be around 30% overall. We arrived at this crude figure using modest assumptions about the duration and severity of COVID-19-related disease (see Supplementary information). This number also assumes a loss of 0.5 DALYs for an average case of long COVID, regardless of age, and includes DALYs lost as a result of COVID-19 deaths, using standard methods<sup>5</sup>.

This exercise hints at how much of the long-term health impact we could be missing by counting only deaths.

We can also compare the DALYs lost across age groups. The demographics in Pakistan could place more of the estimated burden of sickness on people of working age. More research is needed to assess whether this is the case: death statistics, in particular, could be under-reported among older people in many countries.

In the United Kingdom, too, counting COVID disabilities gives a different picture of the impact of the pandemic. The steep increase in death rate with age means that deaths dominate the DALYs lost for the very old. But the share of cases is much flatter across the adult population. Younger people are much more likely to be left sick than dead by COVID-19. Metrics that consider a person's stage of life and disease could fundamentally shift both public understanding and the policy response to COVID-19.

## Metrics for policy

QALYs and DALYs enable governments to balance resources between lockdowns, quarantine, social distancing, ventilation, masking, vaccination, testing, treatment and long-term care for COVID-19. It is crucial to get these trade-offs right in LMICs such as Pakistan, where the public purse has only US\$15 per person to spend on health, according to World Bank data. The price of COVID-19 vaccination is considerable. The cost of administering

two doses of COVID-19 vaccine in Pakistan is estimated to be \$3.15 per person, without factoring in the cost of the doses themselves<sup>[10](#)</sup>.

As the market for COVID-19 vaccines and therapeutics becomes more crowded, using a common metric for disease burden and value assessment will become important for HICs, too. It seems self-evident that vaccines are a wise investment for wealthy nations, given the huge toll that the pandemic places on economies. Indeed, for this reason, we think it might be cost-effective for HICs to vaccinate the entire global population, not just their own citizens. But countries could have to decide, for example, whether the antibody cocktail casirivimab and imdevimab is a sensible use of health budgets, now that data are emerging on its potential effectiveness and before a price has been set (see [go.nature.com/3wh9kjy](https://go.nature.com/3wh9kjy)).



Indonesia is prioritizing vaccinations for people of working age (18–59-year-olds) to aid its economic recovery.Credit: Ulet Ifansasti/Getty

An estimated 6% of the global population is living with two or more conditions (co-morbidities) that put them at high risk of death or disability from COVID-19<sup>[11](#)</sup>. QALYs and DALYs can help governments to compare

interventions targeted at such co-morbidities with those that directly address COVID-19. For instance, managing non-communicable diseases such as diabetes requires substantial increases in funding globally<sup>12</sup>. Without a clear analysis of these factors, pressure to allocate scarce resources to COVID-19 could reduce the availability of services for non-communicable disease. This might worsen overall well-being in the long run<sup>13</sup>.

Improved measures of disease burden can help to map the impact of COVID-19 on vulnerable communities. In the United States, Black and Latinx people and Indigenous Americans are roughly three times more likely to be hospitalized with the disease than are white or Asian, non-Hispanic people (*Nature* **592**, 674–680; 2021).

Longer-term outcomes are also likely to be affected by underlying health disparities and unequal access to care and treatment. And for people without a social safety net, chronic disease can push them into poverty<sup>14</sup>.

Metrics that capture how ill health, disability, stigma and poverty interact with COVID-19 could prove pivotal in efforts to overcome the disease. Other infectious diseases, such as tuberculosis, commonly become entrenched in communities that are unable to fully protect themselves against risk, owing to social and economic barriers<sup>14</sup>. In the ongoing global HIV epidemic, countries that recognized and supported community action for vulnerable people<sup>15</sup> early on were able to prevent wider transmission over time.

## Next steps

It has always been difficult to assess the comprehensive burden of health and inequity. This is particularly hard in settings where disease surveillance and health-information systems are weak. The COVID-19 pandemic has shown the importance of these systems, and should drive a global effort to improve them.

Poorer nations are streets ahead of wealthy ones in their use of DALYs. The metric has highlighted emerging patterns of HIV in south India, for example, and has helped to identify the risk factors behind them<sup>16</sup>. They also inform

health planning. Ethiopia<sup>[17](#)</sup> and Pakistan both recently used DALYs to define the package of services required to roll out universal health care in their countries.



### Why the United States is having a coronavirus data crisis

On the basis of this infrastructure, global DALYs attributable to COVID-19 are likely to appear in the next burden of disease estimates from both the WHO and the IHME. Due to be released in the second half of 2021, these should be the first comprehensive assessments of the relative health burden from COVID-19 globally. They could support the change in measurement and perception that we are highlighting, but they are likely to suffer from a paucity of data, with estimates being highly uncertain.

These data gaps appear because many LMICs lack the reporting infrastructure required to calculate QALYs and DALYs. Apart from South Africa, most countries in sub-Saharan Africa have been unable to count excess deaths from COVID-19, for example, because of inadequate registration systems. Scaling up of testing remains one of the most urgent public-health needs. But it is challenging for governments to prioritize the gathering of information when they cannot afford essential medicines<sup>[18](#)</sup>. The scientific community and HICs should ramp up investment in health information systems to capture service use, morbidity and mortality.

Research funding to build a global picture of COVID-19-related disease is also needed. The full range of symptoms and consequences is not yet known. These might also depend on a person's underlying health status and access to care. Longitudinal studies, similar to those beginning to report in the United Kingdom<sup>1</sup> and other HICs<sup>19,20</sup>, should be initiated globally. These should assess the mental-health effects and long-term economic impacts of living with chronic diseases in the wake of COVID-19. Countries such as South Africa — which developed infrastructure to track populations over time for epidemics such as HIV — should lead the way.

Data on both deaths and disease in vulnerable groups is often the most challenging to collect, particularly where access to services is poor. But it can be done. Kenya, for instance, is already conducting surveys that can potentially feed into real-time models of COVID-19 transmission and impact<sup>21</sup>. These should be linked with burden-of-disease estimates.

As we count the devastating losses from COVID-19 — of loved ones, jobs, communities, security — the lasting loss of health must also be tallied. Without the right metrics, we can see, understand and respond to only a fraction of the problem.

Nature **593**, 502-505 (2021)

doi: <https://doi.org/10.1038/d41586-021-01392-2>

## References

1. 1.

PHOSP-COVID Collaborative Group. Preprint at medRxiv  
<https://doi.org/10.1101/2021.03.22.21254057> (2021).

2. 2.

Al-Aly, Z., Xie, Y. & Bowe, B. *Nature* <https://doi.org/10.1038/s41586-021-03553-9> (2021).

[Article](#) [Google Scholar](#)

3. 3.

National Institute for Health Research. *Living with COVID19: Second Review* [https://doi.org/10.3310/themedreview\\_45225](https://doi.org/10.3310/themedreview_45225) (NIHR, 2021).

4. 4.

Public Health England. *Disparities in the Risk and Outcomes of COVID-19* (PHE, 2020).

[Google Scholar](#)

5. 5.

Briggs, A. H. *et al. Health Econ.* **30**, 699–707 (2021).

[PubMed](#) [Article](#) [Google Scholar](#)

6. 6.

Sandmann, F. G. *et al. Lancet Infect. Dis.* [https://doi.org/10.1016/S1473-3099\(21\)00079-7](https://doi.org/10.1016/S1473-3099(21)00079-7) (2021).

[Article](#) [Google Scholar](#)

7. 7.

Vos, T. *et al. Lancet* **396**, 1204–1222 (2020).

[PubMed](#) [Article](#) [Google Scholar](#)

8. 8.

Ministry of National Health Services, Regulations and Coordination. *Universal Health Coverage Benefit Package of Pakistan* (Government of Pakistan, 2020); available at <https://go.nature.com/3upgx8t>

9. 9.

Neumann, P. J. & Weinstein, M. C. *N. Engl. J. Med.* **363**, 1495–1497 (2010).

[PubMed](#) [Article](#) [Google Scholar](#)

10. 10.

Griffiths, U. *et al.* *Costs of Delivering COVID-19 Vaccine in 92 AMC Countries: Updated Estimates from COVAX Working Group on Delivery Costs* (WHO, Gavi & UNICEF, 2021).

11. 11.

Clark, A. *et al.* *Lancet Glob. Health* **8**, e1003–e1017 (2020).

[PubMed](#) [Article](#) [Google Scholar](#)

12. 12.

Nugent, R. *Glob. Heart* **11**, 371–374 (2016).

[PubMed](#) [Article](#) [Google Scholar](#)

13. 13.

Abbas, K. *et al.* *Lancet Glob. Health* **8**, e1264–e1272 (2020).

[PubMed](#) [Article](#) [Google Scholar](#)

14. 14.

Puteh, S. E. W. & Almualim, Y. *Health Syst. Policy Res.* **4**, 1 (2017).

[Article](#) [Google Scholar](#)

15. 15.

Medley, G. F. & Vassall, A. *Science* **357**, 156–158 (2017).

[PubMed](#) [Article](#) [Google Scholar](#)

16. 16.

Vassall, A. *et al.* *Lancet Glob. Health* **2**, e531–e540 (2014).

[PubMed](#) [Article](#) [Google Scholar](#)

17. 17.

Verguet, S. *et al.* *Nature Med.* **27**, 380–387 (2021).

[PubMed](#) [Article](#) [Google Scholar](#)

18. 18.

Watkins, D. A. *et al.* *Lancet Glob. Health* **8**, e829–e839 (2020).

[PubMed](#) [Article](#) [Google Scholar](#)

19. 19.

Walle-Hansen, M. M., Ranhoff, A. H., Mellingsæter, M., Wang-Hansen, M. S. & Myrstad, M. *BMC Geriatr.* **21**, 199 (2021).

[PubMed](#) [Article](#) [Google Scholar](#)

20. 20.

Daugherty, S. E. & Guo, Y. *Br. Med. J.* **373**, n1098 (2021).

[Article](#) [Google Scholar](#)

21. 21.

Quaife, M. *et al.* *BMC Med.* **18**, 316 (2020).

[PubMed](#) [Article](#) [Google Scholar](#)

[Download references](#)

## Supplementary Information

## 1. Assumptions used to estimate COVID health burden

## Competing Interests

The authors declare no competing interests.

## Jobs from Nature Careers

- - - [All jobs](#)
    - 
    - [Postdoctoral Training Fellow - Kassiotis Lab](#)
      - [Francis Crick Institute](#)
      - [London, United Kingdom](#)
      - [JOB POST](#)
    - [Biological Safety Specialist](#)
      - [Francis Crick Institute](#)
      - [London, United Kingdom](#)
      - [JOB POST](#)
    - [Post-doctoral Fellow - Autoimmune Pathogenesis](#)
      - [Oklahoma Medical Research Foundation \(OMRF\)](#)
      - [Oklahoma City, United States](#)
      - [JOB POST](#)

▪ **Research Technician / Research Assistant**

Oklahoma Medical Research Foundation (OMRF)

Oklahoma City, United States

JOB POST

[Download PDF](#)

[Download PDF](#)

## Related Articles



- [Will COVID force public health to confront America's epic inequality?](#)



- [Why the United States is having a coronavirus data crisis](#)

---

This article was downloaded by **calibre** from <https://www.nature.com/articles/d41586-021-01392-2>

- COMMENT
- 25 May 2021

# Tissues, not blood, are where immune cells function

COVID has shown we must study immunity in the whole body — let's sort the logistics to acquire the right samples.

- [Donna L. Farber](#) 0

## 1. [Donna L. Farber](#)

1. Donna L. Farber is a professor of surgical sciences, microbiology and immunology at Columbia University Irving Medical Center in New York City, New York, USA.

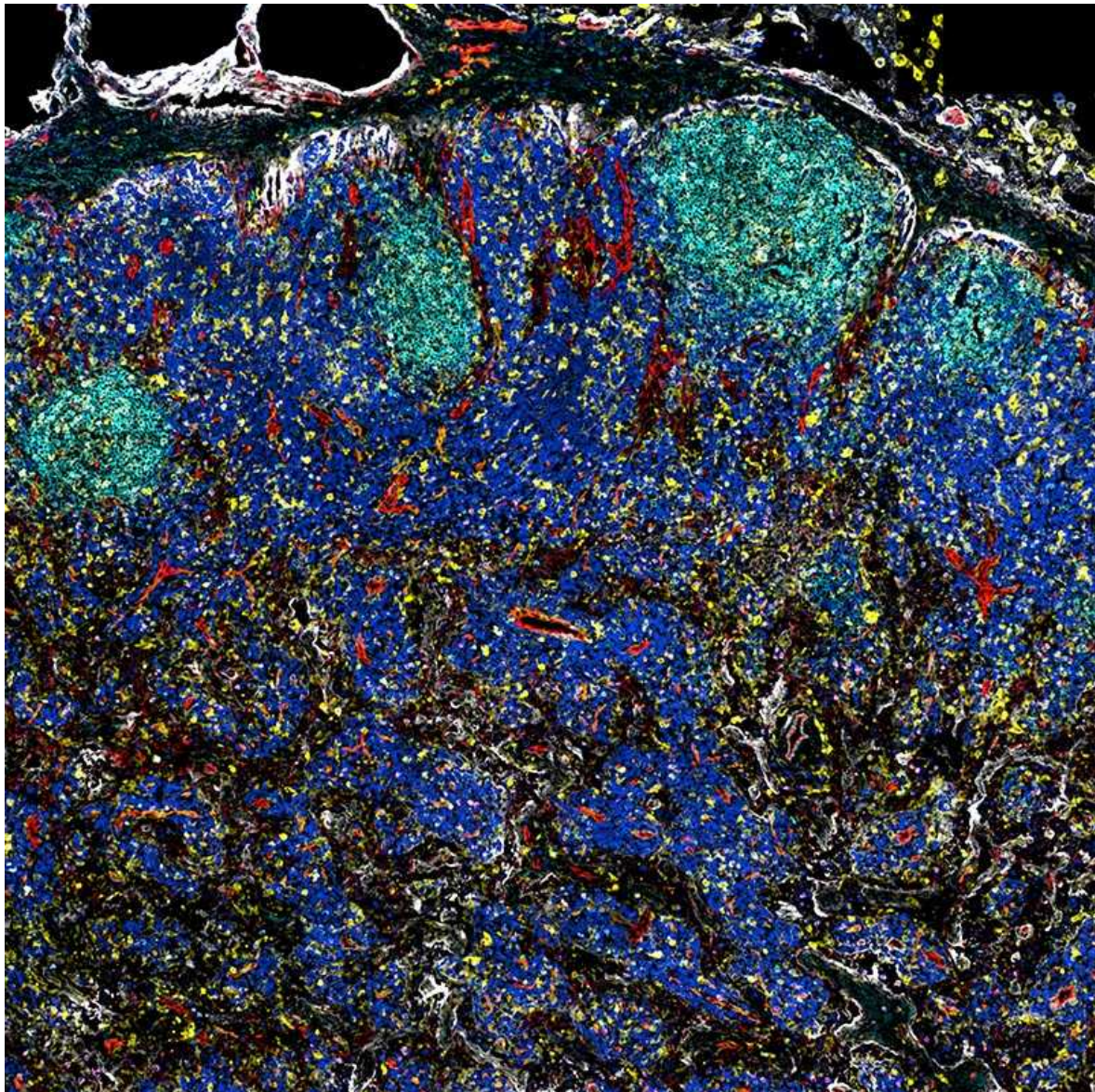
[View author publications](#)

You can also search for this author in [PubMed](#) [Google Scholar](#)









Immune cells have designated sites. In this lymph node, colours indicate cell types, such as B cells (light blue) and T cells (dark blue and green). Credit: Andrea Radtke

Early in the pandemic, my team spotted something surprising. When people were severely ill with COVID-19 and on a ventilator, the daily rinses of the plastic tubes in their windpipes contained immune cells from the airway. More surprisingly, what was in these airway samples was very different from what was found in the same patient's blood.

The airway cells were producing high levels of cytokines — factors that recruit immune cells such as T cells to a tissue site and promote inflammation. By contrast, the corresponding blood samples were low in T cells, but high in other immune cells called monocytes, which were displaying unusual patterns of cell-surface receptors. Lung samples from patients who had died showed monocytes and a further type of immune cell (macrophages) clustered in the lung's tiny air sacs; this is associated with the damage that typifies severe COVID-19. The unusual receptors suggested to us that monocytes circulating in the blood had been both altered and summoned by the cytokines produced in the airway<sup>1</sup>. Had we not collected both airway and blood samples, we would not have put these pieces together.

As this example shows, the pandemic has revealed major gaps in our understanding of the human immune system. One of the biggest is the reactions in tissues — at sites of infection and where disease manifests.

Immune cells are often referred to as white blood cells. But most, including more than 95% of T cells<sup>2</sup>, reside and function in tissues, particularly lymphoid organs — such as bone marrow, spleen and lymph nodes — and in barrier surfaces, such as the skin, gut and mucous membranes. Although infection with the SARS-CoV-2 coronavirus leads to virus-specific CD4<sup>+</sup> and CD8<sup>+</sup> T cells that are detectable in the blood for months or longer<sup>3</sup>, it is unclear what their presence in circulating blood means for tissue-based immunity in the lungs — or elsewhere.

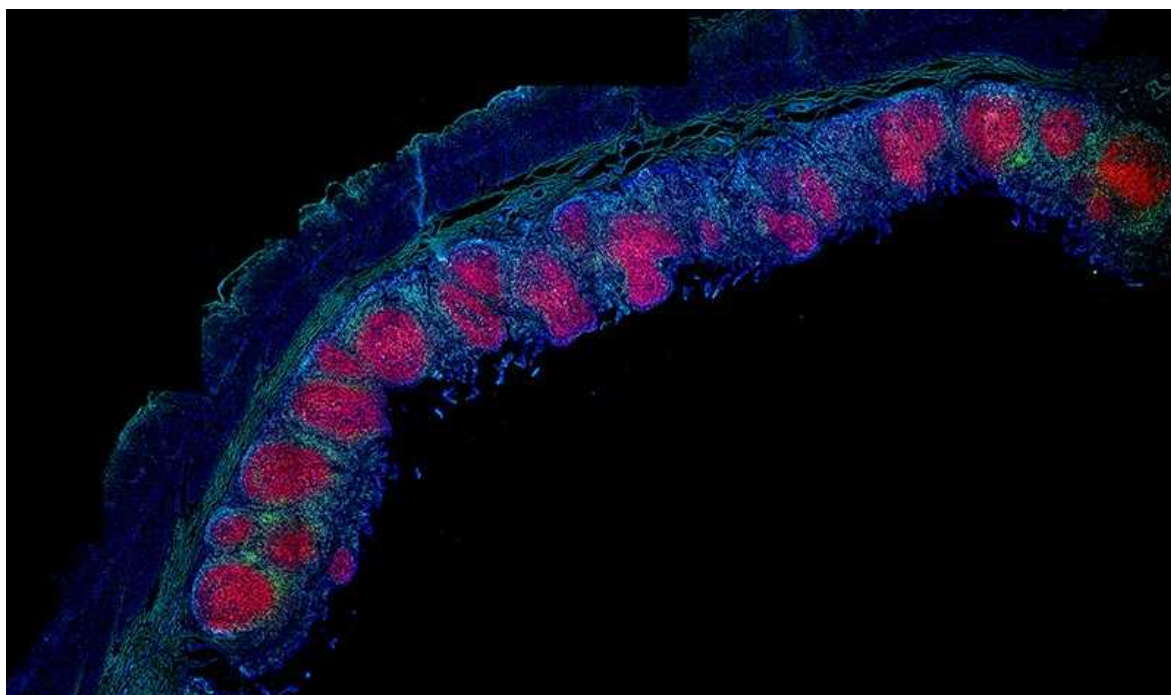
Some immune cells are never found in blood. (Or rather, in many cases, we don't know if they fail to enter the circulation or whether they change their properties when they do.) Some, such as macrophages, derive directly from fetal progenitor cells to mature in tissues such as the lungs, liver and spleen. Others, such as memory T cells, develop from activated T cells that migrate to tissues following priming in lymph nodes during an infection. These tissue-homing T cells take up long-term residence in tissues and can develop properties that are distinct in each.

To fully grasp the immune system, researchers need to understand respiratory, gut and skin immunity, and how each interacts with nearby lymph nodes. That means expanding support and infrastructure for obtaining tissues: forging alliances with clinicians, biobanks, hospitals and

procurement agencies for donor organs. Here I describe how to make such research happen and what can be learnt.

## Mouse models

Mouse models of infection, autoimmunity, cancer and inflammatory disease are extremely valuable for understanding the immune system. Mouse studies usually sample affected organs and associated lymph nodes, but rarely blood, owing to the tiny volumes involved. These site-specific studies have revealed fundamental processes — for instance, that respiratory infection with a virus prompts dendritic (antigen-presenting) cells to migrate from the lungs to adjacent lymph nodes, where they prime virus-specific T cells, such as CD4<sup>+</sup> T helper cells. This priming promotes B cells to differentiate and produce antibodies; cytotoxic CD8<sup>+</sup> T cells are also produced, and migrate to the lung to kill the infected cells and prevent viral spread. Once an infection is cleared, a small population of these virus-specific memory T and B cells persist in tissues, poised to launch protective responses rapidly if the pathogen is encountered again.



Immune cells in the intestine are organized spatially: antibody-producing B cells (red) are surrounded by T cells (light blue). Credit: Takashi Senda

Mouse studies have also shown that, for site-specific viruses such as influenza or human papillomavirus, immunological memory is maintained by dedicated sets of memory T cells at the relevant site. These ‘tissue-resident’ memory T cells are found in the lungs for respiratory viruses, in the skin for cutaneous pathogens or in the female reproductive tract for genital infections<sup>4</sup>. Furthermore, these resident memory cells can protect against infection and can be generated by vaccines that target specific tissues, such as intranasal flu vaccines<sup>5</sup>.

In humans, it is not practical to follow an immune response from the start of an infection to the development of immunological memory. It’s not always clear where an infection starts or when, and sampling the relevant tissue over time is not straightforward.

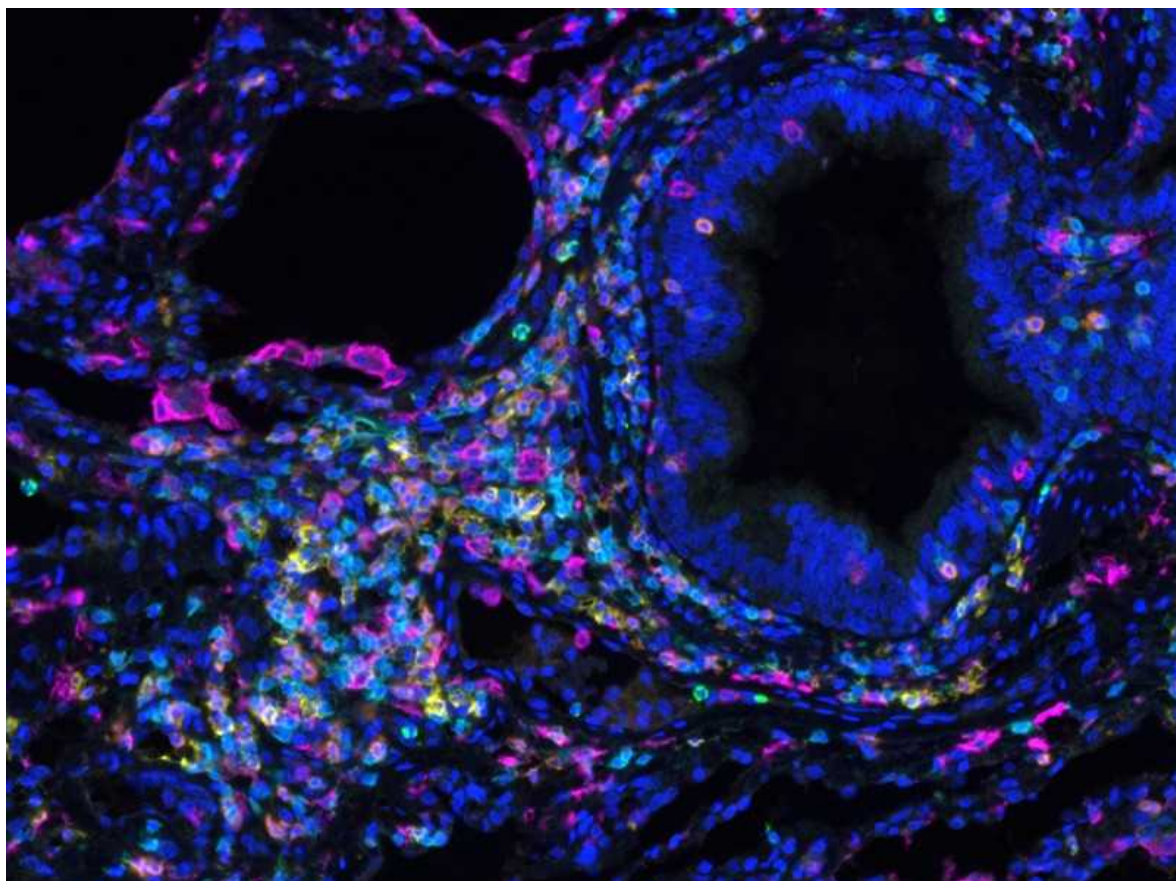
However, humans have ample blood, which can be collected regularly. Blood contains all major lineages of immune cells, plus circulating antibodies and secreted cytokines. This approach has been invaluable for monitoring immune responses in real time, and for understanding the formation and function of antibodies and inflammation.

For SARS-CoV-2, examining blood has helped to track responses to infection and vaccines, and to find correlates of severe disease. But much of the story is still unknown, because the bulk of the immune action is in the tissues.

## Lessons from tissues

Immune studies in tissues have led to therapies. In autoimmune diseases such as rheumatoid arthritis, a plethora of inflammatory markers become elevated in blood serum. When researchers looked specifically at the synovial fluid that fills the spaces between a person’s joints, they found high levels of the cytokine TNF- $\alpha$ , which was ultimately found to initiate this disease<sup>6</sup>. Now, anti-TNF- $\alpha$  blockers are among the most commonly prescribed medicines for rheumatoid arthritis and other inflammatory diseases, and are tremendously effective at treating symptoms.

Similarly, examination of immune cells in tumours that have been surgically excised or biopsied revealed functionally inactive T cells that failed to remove diseased cells<sup>7</sup>. This has led to the idea that many cancers can avoid immune defences. Such studies provided the rationale for the tumour immunotherapies that have revolutionized treatments for some breast, lung, colon and other cancers.



Spatial organization of immune cells in the lung. T cells (blue and orange) cluster around the major airway on the right, but not around the tiny air sacs where gases are exchanged in the blood.Credit: Stuart Weisberg

Our work and that of others indicates that the composition of immune cells is distinct in different tissues, with tissue-specific variation in gene expression, metabolic pathways and functional regulation<sup>8</sup>. Defining these properties could target therapies to tissue immune responses — but that requires first looking at the tissues.

Many tissue samples from living individuals can be collected during routine medical care. For instance, biopsies and elective surgeries allow collection of diseased and healthy tissue (see ‘Human tissues for immunology’). In surgeries from tonsillectomies to tumour removals, lymph nodes are removed and discarded. Cardiac surgeons typically remove and discard the thymus. Procedures to bypass the stomach and intestines remove gut tissues that are rich in immune cells and lymph nodes associated with the intestines. Such samples are particularly useful in showing the spatial organization of immune cells in these tissues, which can suggest how cell types communicate with and influence each other.

## Human tissues for immunology

Source	How tissue obtained	Material available
Deceased individuals (multiple sites, one time point)	Autopsies (fixed tissues, no viable cells)	Many and variable: brain, liver, lungs, intestines, kidney, pancreas
Deceased individuals (multiple sites, one time point)	Organ donors (living cells that can be cultured and analysed for function)	Lungs, intestines, spleen, lymph nodes, bone marrow, pancreas, salivary glands, skin, thymus
Living individuals (single sites, single time point)	Surgery (tumour removal, gastric bypass, organ transplant, cosmetic surgery, gender reassignment)	Blood vessels, tumours, lungs, intestines, tonsils, skin, reproductive organs

<b>Source</b>	<b>How tissue obtained</b>	<b>Material available</b>
Living individuals (single sites, single time point)	Clinical biopsies (for assessing cancer, infection, organ damage, monitoring a transplant)	Intestines, lungs, lymph nodes, pancreas, skin, breast, kidney
Living individuals (single sites, single time point)	Fine-needle aspirates (to assess cancer, infection)	Breast, liver, lymph node
Living individuals (single sites, multiple time points)	People treated for infections or respiratory distress; recipients of organ transplants	Respiratory washes from airway tubes, bronchoalveolar washes, biopsies (heart, liver, intestines)
Living individuals (single sites, multiple time points)	Healthy people, and people with infections, asthma, chronic lung diseases	Nasal washes, sputum, nasal swabs

Ten years ago, my team set up a new type of tissue resource to obtain samples from organ donors. We reached out to a local non-profit organization in New York City called LiveOnNY, which coordinates organ donation and collaborates with researchers and consenting families. As part of this collaboration, my team has an on-call surgeon ready to respond when the transplant coordinator alerts them that a potential donor has died.

After clinical teams obtain the person's organs for transplantation, our surgeon collects tissues for research — including the intestines, lungs, many lymph nodes, the thymus, spleen, bone marrow, skin, tonsils and salivary glands — and brings everything directly back to the laboratory for processing and sample storage. Linking tissue collection with organ donation is the best way to preserve the most tissue and the most-viable samples. So far, results from these tissues match those of tissue from living patients<sup>9</sup>, although side-by-side comparisons are not always feasible.

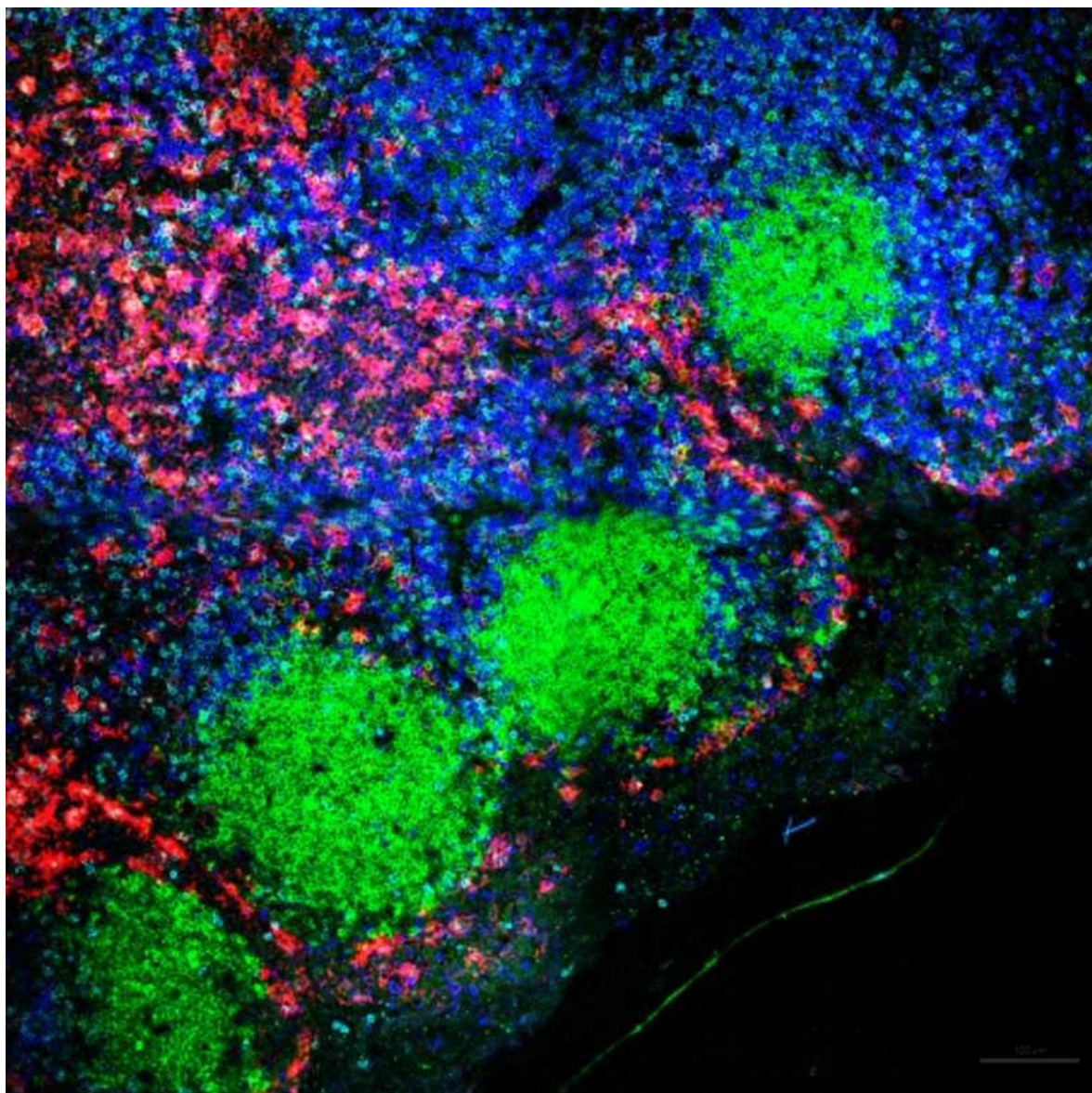
We have so far obtained tissues from more than 500 donors. We have shared samples with many collaborating investigators and are profiling them as part of the [Human Cell Atlas](#), which aims to create comprehensive reference maps of all human cells.

Research teams at the Wellcome Sanger Institute in Hinxton, UK, and the Karolinska Institute in Stockholm have set up similar programmes to obtain tissue samples. The University of Florida in Gainesville has established collaborations with many organ-procurement organizations, originally to obtain pancreas samples for type 1 diabetes research (the nPOD programme<sup>10</sup>).

Technological advances mean that RNA transcripts, protein content and gene modifications can be pinpointed even for single cells. Combined with computational analyses, these measurements allow the simultaneous identification of immune-cell composition, lineage and functional states. When applied to cells in blood, this detailed profiling has revealed immune signatures for certain infections and vaccines<sup>11</sup>, from flu to SARS-CoV-2.

My team and others have compared distinct tissues in hundreds of individual donors to map the different types of innate and adaptive immune cell in each<sup>8</sup>. Our ongoing studies include determining how tissue immune profiles correlate with factors such as sex and age.

Still, organ-donor samples provide snapshots of immune status at only a single point in time. One of the greatest challenges is to follow an immune response to infection, vaccination or other immune-based therapies in specific tissues. This would let us explore, for instance, the changes that occur with age or declining health status.



Immune cells in tissue are found at specific sites in the lymph node: antibody-producing B cells (green) are in circular follicles, partially surrounded by T cells (blue) with macrophages (red) on the periphery. Credit: Basak B. Ural

## Three steps

What can researchers, institutions and funders do to advance work in human tissue immunity? I have three recommendations.

**Promote paired sampling.** Clinicians and immunologists should find more opportunities to pair the collection of blood and tissue, such as by obtaining respiratory washes from intubated patients or nasal washes from children and adults who have a respiratory disease. (Nasal washes are sufficiently non-invasive that they could also be used in matched healthy controls.) Paired samples could be taken from people undergoing diagnostic biopsies (such as during colonoscopy of the intestines) or research biopsies using fine-needle aspiration (such as from skin and lymph nodes).

These studies establish how immune parameters in blood and the relevant tissue correlate with each other, as well as with disease and disease outcome. For example, researchers studying a hepatitis B vaccine collected samples of lymph nodes near the injection site to compare the responses of immune cells there with what is in the blood<sup>12</sup>. A study of varicella zoster virus, which causes chickenpox and can reactivate to cause shingles, looked at T cells in the skin near the site of injection with a virus antigen<sup>13</sup>.

Approaches developed during the current pandemic mean that samples that it was not possible to analyse even a year ago can now supply in-depth data. This includes the nasal swabs used in SARS-CoV-2 testing, which contain enough cells for highly sensitive single-cell profiling. Gene expression can be measured in individual cells to help piece together the immune response. Those techniques can be applied to other sampling sites in other types of infection and disease, so that routine care can provide material for immune-based studies.

**Adapt collections for biobanks.** There are dozens of biobanks throughout the world; the largest contain samples from hundreds of thousands of people. Generally, however, these samples are not useful for immunologists. Instead of preserving samples chemically for pathology, or storing only DNA, plasma or serum, biobanks should also store frozen tissues and secretions full of immune cells and soluble factors. For example, studies of asthma and other chronic lung diseases have created biobanks of different respiratory secretions, including sputum, saliva, nasal swabs and bronchial brushings<sup>14</sup>. Studying the preserved immune cells in these samples could advance our understanding of mucosal immunity.

**Support and streamline collaborations.** Currently, an individual immunologist needs to connect with clinicians on a case-by-case basis to acquire tissue samples for research. Many institutions and centres have set up central cores for obtaining ethical or institutional-review-board approval, using clinical coordinators to get patients' consent to take samples. However, these centres tend to be affiliated with clinical departments, not basic-science ones.

In the past, immunological research was conducted in pathology departments that received all clinical specimens, and distributed them to researchers. It is time to reinvigorate these old alliances and establish more and deeper connections between immunologists and clinicians who work with patients. Immunologists should pursue joint appointments in clinical departments. Clinician-scientists should train in immunology laboratories. Joint projects between the two fields should become common, and extend far beyond acquiring samples. There should be funding and programmes for immunologists to work with geriatricians to learn what leads to immune-system decline. Paediatricians and immunologists should be collaborating not just on childhood allergies, but also on understanding child immunity and the development of the immune system. Immunology should be pulled into many other disciplines not normally associated with it, such as neurology.

As SARS-CoV-2 continues to devastate the world, there is a new urgency to establish collaborations that can tackle intractable questions in human immunology. To move the field forward and translate findings to cures, immunologists must explore the whole body.

Nature **593**, 506-509 (2021)

doi: <https://doi.org/10.1038/d41586-021-01396-y>

## References

1. 1.

Szabo, P. A. *et al. Immunity* **54**, 797–814 (2021).

[PubMed](#) [Article](#) [Google Scholar](#)

2. 2.

Kumar, B. V., Connors, T. J. & Farber, D. L. *Immunity* **48**, 202–213 (2018).

[PubMed](#) [Article](#) [Google Scholar](#)

3. 3.

Dan, J. M. *et al.* *Science* **371**, eabf4063 (2021).

[PubMed](#) [Article](#) [Google Scholar](#)

4. 4.

Szabo, P. A., Miron, M. & Farber, D. L. *Sci. Immunol.* **4**, eaas9673 (2019).

[PubMed](#) [Article](#) [Google Scholar](#)

5. 5.

Zens, K. D., Chen, J.-K. & Farber, D. L. *J. Clin. Invest. Insight* **1**, e85832 (2016).

[Article](#) [Google Scholar](#)

6. 6.

Feldmann, M. & Maini, R. N. *J. Immunol.* **185**, 791–794 (2010).

[PubMed](#) [Article](#) [Google Scholar](#)

7. 7.

Crespo, J., Sun, H., Welling, T. H., Tian, Z. & Zou, W. *Curr. Opin. Immunol.* **25**, 214–221 (2013).

[PubMed](#) [Article](#) [Google Scholar](#)

8. 8.

Weisberg, S. P., Ural, B. B. & Farber, D. L. *Cell* **184**, 1517–1529 (2021).

[PubMed](#) [Article](#) [Google Scholar](#)

9. 9.

Snyder, M. E. *et al.* *Sci. Immunol.* **4**, eaav5581 (2019).

[PubMed](#) [Article](#) [Google Scholar](#)

10. 10.

Pugliese, A. *et al.* *Pediatr. Diabetes* **15**, 1–9 (2014).

[PubMed](#) [Article](#) [Google Scholar](#)

11. 11.

Pulendran, B. & Davis, M. M. *Science* **369**, eaay4014 (2020).

[PubMed](#) [Article](#) [Google Scholar](#)

12. 12.

Ben-Othman, R. *et al.* *Front. Immunol.* **11**, 580373 (2020).

[PubMed](#) [Article](#) [Google Scholar](#)

13. 13.

Vukmanovic-Stejic, M. *et al.* *J. Invest. Dermatol.* **135**, 1752–1762 (2015).

[PubMed](#) [Article](#) [Google Scholar](#)

14. 14.

Backer, V. *et al. Eur. Clin. Respir. J.* **7**, 1736934 (2020).

[PubMed](#) [Article](#) [Google Scholar](#)

[Download references](#)

## Competing Interests

The author declares no competing interests.

## [\*\*Jobs from Nature Careers\*\*](#)

- - - [All jobs](#)
    - - [\*\*Postdoctoral Training Fellow - Kassiotis Lab\*\*](#)
        - [Francis Crick Institute](#)
        - [London, United Kingdom](#)
        - [JOB POST](#)
      - [\*\*Biological Safety Specialist\*\*](#)
        - [Francis Crick Institute](#)
        - [London, United Kingdom](#)
        - [JOB POST](#)
      - [\*\*Post-doctoral Fellow - Autoimmune Pathogenesis\*\*](#)

[Oklahoma Medical Research Foundation \(OMRF\)](#)

[Oklahoma City, United States](#)

[JOB POST](#)

▪ [\*\*Research Technician / Research Assistant\*\*](#)

[Oklahoma Medical Research Foundation \(OMRF\)](#)

[Oklahoma City, United States](#)

[JOB POST](#)

[Download PDF](#)

[Download PDF](#)

## Related Articles



- [How kids' immune systems can evade COVID](#)



- [Measles erases immune 'memory' for other diseases](#)



- [Rogue antibodies could be driving severe COVID-19](#)

---

This article was downloaded by **calibre** from <https://www.nature.com/articles/d41586-021-01396-y>.

| [Section menu](#) | [Main menu](#) |

- CORRESPONDENCE
- 25 May 2021

# Vaccination: Brazil fails Indigenous people again with two-tier scheme

- [Ana Carla dos Santos Costa](#) <sup>0</sup>,
- [Shoaib Ahmad](#) <sup>1</sup> &
- [Mohammad Yasir Essar](#) <sup>2</sup>

1. [Ana Carla dos Santos Costa](#)

1. Federal University of Bahia, Salvador, Bahia, Brazil.

[View author publications](#)

You can also search for this author in [PubMed](#) [Google Scholar](#)

2. Shoaib Ahmad

1. Punjab Medical College, Faisalabad, Pakistan.

[View author publications](#)

You can also search for this author in [PubMed](#) [Google Scholar](#)

3. Mohammad Yasir Essar

1. Kateb University, Kabul, Afghanistan.

[View author publications](#)

You can also search for this author in [PubMed](#) [Google Scholar](#)





•

Brazil included Indigenous people in its first vaccination group against COVID-19 because of their greater vulnerability to infection (see [go.nature.com/3uigjgu](https://go.nature.com/3uigjgu)). However, only those living on legally demarcated territories were vaccinated. The Supreme Federal Court later extended immunization to the 500,000 or so Indigenous people living elsewhere (see [go.nature.com/3wj8fkt](https://go.nature.com/3wj8fkt)). In practice, many in that group were excluded because they did not have access to the country's unified health system.

This vaccination scheme is another example of the dearth of meaningful public-health policies aimed at the Indigenous population (see also [R. Santunes et al. \*Nature\* 584, 524; 2020](#); [E. Benites et al. \*Nature\* 591, 369](#);

[2021](#)). It exposes a lack of coordination between the government entities that drafted it. And it stokes discrimination and segregation.

The Brazilian constitution mandates the special protection of Indigenous peoples by the state. There is therefore an urgent need for a more robust vaccination plan that is tailored to the health and social determinants of these people.

Nature **593**, 510 (2021)

doi: <https://doi.org/10.1038/d41586-021-01409-w>

## Competing Interests

The authors declare no competing interests.

## Jobs from Nature Careers

- - - [All jobs](#)
    - - [Postdoctoral Training Fellow - Kassiotis Lab](#)
        - [Francis Crick Institute](#)
        - [London, United Kingdom](#)
        - [JOB POST](#)
      - [Biological Safety Specialist](#)
        - [Francis Crick Institute](#)
        - [London, United Kingdom](#)

JOB POST

- **Post-doctoral Fellow - Autoimmune Pathogenesis**

Oklahoma Medical Research Foundation (OMRF)

Oklahoma City, United States

JOB POST

- **Research Technician / Research Assistant**

Oklahoma Medical Research Foundation (OMRF)

Oklahoma City, United States

JOB POST

Download PDF

Download PDF

## Related Articles

- **See more letters to the editor**

---

This article was downloaded by **calibre** from <https://www.nature.com/articles/d41586-021-01409-w>

- CORRESPONDENCE
- 25 May 2021

# Deploy international satellite monitoring to safeguard forests

- [Ricardo M. O. Galvão](#) 0
  - 1. [Ricardo M. O. Galvão](#)
    - 1. University of São Paulo, Brazil.

[View author publications](#)

You can also search for this author in [PubMed](#) [Google Scholar](#)





•

I contend that an internationally coordinated satellite monitoring system is urgently needed to safeguard forests against governments that deny climate change. Earth-observation and image-processing techniques have improved since the move was proposed eight years ago ([J. Lynch et al. Nature 496, 293–294; 2013](#)). Moreover, the cost of remote-sensing missions is falling.

Many international institutions and countries, including Australia, Brazil, China and India, have modern systems for monitoring forests. However, there are no agreed protocols on how forest data should be produced, verified, stored and made freely available. Neither is there an international warning system for illegal deforestation and forest degradation.

Such a system would need to be effective, comprehensive and properly coordinated and supervised. It could use a real-time early-warning mechanism, such as that of the Brazilian satellite-based DETER, for environmental monitoring and law enforcement ([\*S. J. Goetz et al. Environ. Res. Lett. 10, 123001; 2015\*](#)). DETER led to a decline in Amazon deforestation: the rate fell from more than 27,000 square kilometres in 2004 to about 10,000 square kilometres in 2019 (see [go.nature.com/3fbhkys](https://go.nature.com/3fbhkys)).

Nature **593**, 510 (2021)

doi: <https://doi.org/10.1038/d41586-021-01410-3>

## Competing Interests

The author declares no competing interests.

## Jobs from Nature Careers

- - - [All jobs](#)
    - - [\*\*Postdoctoral Training Fellow - Kassiotis Lab\*\*](#)  
[Francis Crick Institute](#)  
[London, United Kingdom](#)  
[JOB POST](#)
      - [\*\*Biological Safety Specialist\*\*](#)  
[Francis Crick Institute](#)  
[London, United Kingdom](#)

JOB POST

- **Post-doctoral Fellow - Autoimmune Pathogenesis**

Oklahoma Medical Research Foundation (OMRF)

Oklahoma City, United States

JOB POST

- **Research Technician / Research Assistant**

Oklahoma Medical Research Foundation (OMRF)

Oklahoma City, United States

JOB POST

Download PDF

Download PDF

## Related Articles

- **See more letters to the editor**

---

This article was downloaded by **calibre** from <https://www.nature.com/articles/d41586-021-01410-3>

- CORRESPONDENCE
- 25 May 2021

# EU forest strategy: adapt, innovate, employ

- [Marc Palahí](#) 0

1. [Marc Palahí](#)

1. European Forest Institute, Joensuu, Finland.

[View author publications](#)

You can also search for this author in [PubMed](#) [Google Scholar](#)





•

European forests are crucial to achieving the European Green Deal — a socially and territorially fair transition to a circular bioeconomy, in which resources are renewable, biologically based, sustainably managed and reused whenever possible ([M. Palahi et al. <https://doi.org/10.36333/k2a02>; 2020](https://doi.org/10.36333/k2a02)). The European Union Forest Strategy currently being drawn up needs actionable vision as climate change and natural disturbances erode forests' capacity to provide key ecosystem services. It could also generate a range of renewable options to replace fossil-based products.

In my view, we should increase the ecological, economic and social value of EU forests simultaneously. The Forest Strategy needs to catalyse a deal

that is rooted in interconnected plans for adaptation–restoration, innovation and employment.

The adaptation–restoration plan would implement dynamic conservation and integrated management to foster biodiversity at different spatial scales (see [go.nature.com/2ryt](https://go.nature.com/2ryt)). The innovation plan would use forest resources to stimulate new business models that decarbonize important industrial sectors, such as textiles, construction and packaging. And the employment plan would ensure a green transition that is fair by investing in upgrading the skills of new and existing workers based in forests.

Nature **593**, 510 (2021)

doi: <https://doi.org/10.1038/d41586-021-01411-2>

## Competing Interests

The author declares no competing interests.

## Jobs from Nature Careers

- - - [All jobs](#)
    - - [Postdoctoral Training Fellow - Kassiotis Lab](#)  
[Francis Crick Institute](#)  
[London, United Kingdom](#)  
[JOB POST](#)
      - [Biological Safety Specialist](#)  
[Francis Crick Institute](#)

[London, United Kingdom](#)

[JOB POST](#)

▪ [\*\*Post-doctoral Fellow - Autoimmune Pathogenesis\*\*](#)

[Oklahoma Medical Research Foundation \(OMRF\)](#)

[Oklahoma City, United States](#)

[JOB POST](#)

▪ [\*\*Research Technician / Research Assistant\*\*](#)

[Oklahoma Medical Research Foundation \(OMRF\)](#)

[Oklahoma City, United States](#)

[JOB POST](#)

[Download PDF](#)

[Download PDF](#)

## Related Articles

- [\*\*See more letters to the editor\*\*](#)

---

This article was downloaded by **calibre** from <https://www.nature.com/articles/d41586-021-01411-2>

- CORRESPONDENCE
- 25 May 2021

# Trade resolution further threatens Brazil's amphibians

- [Joice Ruggeri](#) <sup>0</sup> &
- [Lucas Rodriguez Forti](#) <sup>1</sup>

1. [Joice Ruggeri](#)

1. University of Campinas, Brazil.

[View author publications](#)

You can also search for this author in [PubMed](#) [Google Scholar](#)

2. Lucas Rodriguez Forti

1. Federal University of Bahia, Salvador, Brazil.

[View author publications](#)

You can also search for this author in [PubMed](#) [Google Scholar](#)





•

In March, Brazil's Ministry of Agriculture took an alarming step to boost trade of artisanal animal products across states (see [go.nature.com/3by9](https://go.nature.com/3by9)). It added reptiles and amphibians — already the most threatened vertebrates on Earth — to the list permitting the capture of fishes, crustaceans and molluscs for human consumption.

Brazil has the fastest rate of decline of amphibian populations in South America, owing to habitat loss and infectious diseases ([B. C. Scheele \*et al.\* Science 363, 1459–1463; 2019](https://science.sciencemag.org/content/363/6425/1459)). If the policy takes effect in its current form, trade of amphibians will increase — compounding the spread of lethal pathogens such as *Batrachochytrium* species and ranavirus.

We urge the government to align its policy with the Convention on Biological Diversity and other international commitments that are backed by substantial scientific evidence.

Nature **593**, 510 (2021)

doi: <https://doi.org/10.1038/d41586-021-01412-1>

## Competing Interests

The authors declare no competing interests.

## Jobs from Nature Careers

- - - [All jobs](#)
    - - [Postdoctoral Training Fellow - Kassiotis Lab](#)  
[Francis Crick Institute](#)  
[London, United Kingdom](#)  
[JOB POST](#)
      - [Biological Safety Specialist](#)  
[Francis Crick Institute](#)  
[London, United Kingdom](#)  
[JOB POST](#)
      - [Post-doctoral Fellow - Autoimmune Pathogenesis](#)

[Oklahoma Medical Research Foundation \(OMRF\)](#)

[Oklahoma City, United States](#)

[JOB POST](#)

▪ [\*\*Research Technician / Research Assistant\*\*](#)

[Oklahoma Medical Research Foundation \(OMRF\)](#)

[Oklahoma City, United States](#)

[JOB POST](#)

[Download PDF](#)

[Download PDF](#)

## Related Articles

- [\*\*See more letters to the editor\*\*](#)

---

This article was downloaded by **calibre** from <https://www.nature.com/articles/d41586-021-01412-1>

# Work

- **How COVID-19 has stomped on scientists' travel plans** [ 21 May 2021]  
Career Feature • It could take years to reveal the true impact of closed borders, cancelled travel plans and vaccine delays.
- **How waste water is helping South Africa fight COVID-19**  
[ 24 May 2021]  
Technology Feature • Detecting the coronavirus in samples from treatment plants could give early warning of outbreaks and new variants.
- **'In software, the name of the game is innovation'** [ 24 May 2021]  
Where I Work • Nicolás Jodal codes software solutions for navigating pandemics and other obstacles.

- CAREER FEATURE
- 21 May 2021

# How COVID-19 has stomped on scientists' travel plans

It could take years to reveal the true impact of closed borders, cancelled travel plans and vaccine delays.

- [Chris Woolston](#) 0

1. Chris Woolston

1. Chris Woolston is a freelance journalist in Billings, Montana.

[View author publications](#)

You can also search for this author in [PubMed](#) [Google Scholar](#)





•

[Find a new job](#)



Many researchers' suitcases have remained empty now for more than a year.Credit: Shutterstock

In 'normal' times, Mike McCulloch has to scour the globe to find a person able and willing to join his laboratory. "My science is quite controversial, so I don't get many applications for posts," he says.

But these are not normal times. The COVID-19 pandemic has severely disrupted the mobility of scientists, as evidenced by McCulloch's recent job advertisement, posted in April on Twitter. Usually, McCulloch needs to look high and low for people able and willing to help him with his controversial work at the University of Plymouth, UK. His aim is to harness relativity to pull rockets through space without the need for backwards thrust — an approach with its fair share of detractors. But pandemic-related border restrictions meant that he needed to limit his search to the United Kingdom. Those restrictions have now eased a little, but McCulloch is unsure about what that means for his search. "It's quite important for me to have a wide range of countries to recruit from," he says.

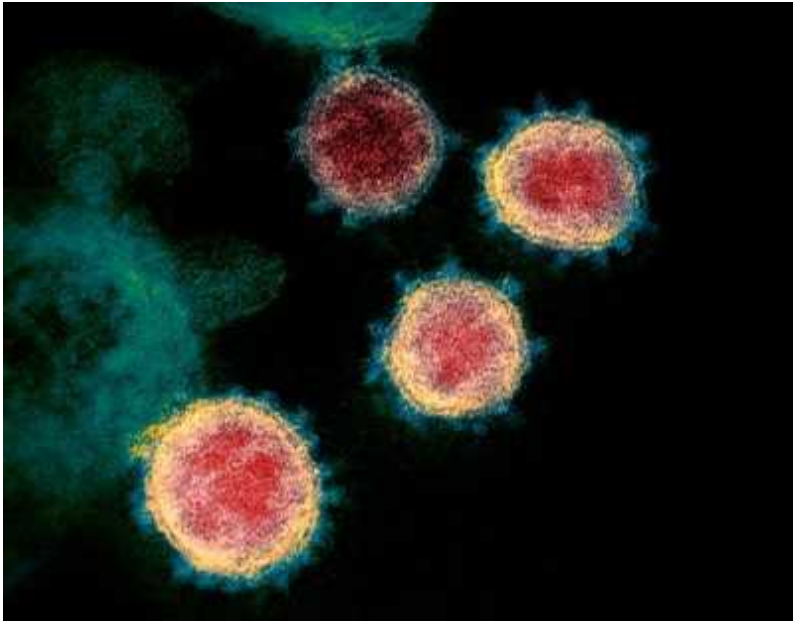
His last search for a postdoc turned up a single qualified and available researcher, who was from Spain. "I'll try to fill the post one way or another," he says. The United Kingdom's departure from the European Union is

widely expected to complicate research mobility, particularly if junior scientists in Europe foresee bureaucratic tangles associated with having to move, but McCulloch thinks pandemic-related restrictions will be a bigger problem.

More than a year after the first lockdowns and border closings, scientists around the world are still grappling with the pandemic's impacts on mobility. Researchers are navigating a world where the rules — and the challenges — are seemingly in constant flux. Whether they are stuck far from home, separated from team members or forced to rethink their approach to recruitment, they're trying to keep their science moving forwards (see 'Push on through').

## Uncertain future

Most scientists [managed to stay productive in the first year of the pandemic](#), but the relative lack of mobility for the global scientific enterprise will have long-lasting impacts that could transform research and collaboration, warns Giorgio Marinoni. Marinoni is the manager of higher education and internationalization at the International Association of Universities (IAU), a non-governmental organization based in Paris that promotes global cooperation in higher education. He worries that disruptions in travel could stifle the careers of junior scientists. "For a young researcher, mobility is part of the career," he says. "We might be heading for a future where there isn't such a global research community."



## [Coronavirus and COVID-19: Keep up to date](#)

The pandemic threatens to undo much progress towards scientific globalization, agrees IAU secretary-general Hillige van't Land. Researchers from economically disadvantaged countries will bear most of the brunt, she says. “There’s no way for them to travel, and they may not have a vaccine for a while depending on where they are from.” And that will not only limit their own opportunities, it will also deprive the system of their contributions and insights. “We could be seeing the beginning of a big tragedy. If they can’t come in today, they may never be able to come in. That is a very harmful thing for the future of research,” van’t Land says.

Mobility is tricky to quantify, and the full impacts are unlikely to be known for years, Marinoni says. The IAU is [conducting a survey](#) that will try to capture some of the consequences of lockdowns, border closings and travel restrictions. It hopes to release the results by October. But numbers — whether they track researcher movements, publications or impact factors — won’t tell the whole story, Marinoni says. “If you are focusing only on those indicators, you’re missing a lot of the picture of international collaboration,” he says.

Numbers wouldn’t, for instance, capture the dilemma that faced Anila Ajayan, an ecologist in Wuhan, China, the city widely considered to be the

starting point of the pandemic. Ajayan, who is from India, had been in Wuhan for only a couple of months for her postdoc at the Institute of Hydrobiology when the city went into lockdown in January 2020. Other countries were still accepting travellers from China, and many of Ajayan's international colleagues decided to head home while they still could. Ajayan opted to remain. She was worried that she might unwittingly carry the virus back with her, and she also feared that she might not be able to return to China if she left.

That concern turned out to be justified: China continues to bar almost all foreign travellers, including the thousands of PhD students and postdocs who left during the pandemic and are now unable to return. "Most of my friends decided to leave, and they couldn't get back," Ajayan says. She felt alone and far from home, but by June 2020, when travel restrictions were eased within China, she was able to resume her research, which requires an assistant to collect water samples from the upper stretches of the Yangtze River.



Anila Ajayan chose to stay in China.

Ajayan plans to return to India once she finishes her postdoc in July, but recognizes that she might have to wait until the surge of infections in her home country finally subsides. “I’m optimistic that the situation could be more under control as more people get vaccinated,” she says. If case rates are still high, she’s willing to spend a few more months living and working in Wuhan.

Whereas Ajayan could stay in place, some researchers were forced to cross borders, occasionally at great personal risk. Sergio Ramos, a Mexican plant ecologist at the University of Pittsburgh in Pennsylvania, left for Switzerland in March 2020 for what he thought would be a 10-day work visit. While he was there, the United States banned all non-US travellers from Europe, effectively stranding him from his postdoctoral position. He became determined to return to the United States. “I was feeling the pressure. I was certain I would lose my job if I didn’t go back.”

After three months of uncertainty, confusion and consultations with authorities, Ramos found a workaround. Mexico was accepting travellers from Europe, and the United States was accepting travellers from Mexico. He flew to Mexico City, intending to quarantine there for two weeks before flying to Pittsburgh. Unable to find a place to stay in Mexico City, he travelled nearly 900 kilometres to stay with his parents in the town of San Cristóbal de las Casas, where he quickly came down with COVID-19. “The virus was waiting for me,” he says.

It took him a month to fully recover, but Ramos finally made it back to Pittsburgh in mid-July, behind schedule yet determined to get back to work. He had to cancel one large-scale project, but was able to complete some experiments and submit a paper for publication. He has now applied for several postdoctoral positions in Europe, and hopes to leave for Switzerland by early June, if allowed — ideally with a position already secured. On 19 May, the EU said that by 24 May, it would unconditionally start to accept all travellers who are fully vaccinated by products approved by the European Medicines Agency; these include those manufactured by Pfizer–BioNTech, Moderna and Johnson & Johnson. Travellers will need to participate in Europe’s [Digital Green Certificate](#) programme.

## Uncertain path

Although some researchers are starting to regain their footing, others remain in limbo. In 2019, Elisabeth Schober, an anthropologist at the University of Oslo, landed a prestigious five-year ‘starting grant’ from the European Research Council to study the cultures of various shipping-port cities around the world. She hand-picked her team, but four of her five collaborators got locked out of the country when Norway closed its borders in January 2021. Instead of meeting in person to plan field trips to Busan in South Korea or Rotterdam in the Netherlands, the team meets occasionally on Zoom to keep the project ticking over. The Norwegian government is now allowing entry to foreign researchers on a case-by-case basis, and Schober has started investigating the application process. “The group is still scattered in various places, but we may be making some progress towards getting people together this summer,” she says.



Elisabeth Schober studies the dynamics of communities in port cities. Credit: Ian M. Cook

In theory, Schober says, she could catch a flight to Busan any day. (South Korea currently admits travellers who test negative for COVID-19.) But the pandemic has a way of ruining plans. If she left any time soon, she'd have to quarantine for two weeks when she arrived, an unpleasant prospect given that she would be travelling with her two young children. Besides, the very thing that she's supposed to study — the social life in the communities surrounding the port — has essentially vanished. "The clock is ticking on the contract," she says. "It feels like we're all flying blind here in terms of making decisions."

In Australia, says Nathan Kilah, a chemist at the University of Tasmania in Hobart, the pandemic has created an unusual dynamic. Some institutions are in financial crisis and have slashed scholarships; others have open positions that they can't fill, thanks to border closings and lockdowns. Much like McCulloch, Kilah is trying to fill a position — in his case, a spot for a PhD student — at a time when people from abroad can't enter the country. "I've advertised similar positions in the past and had up to 50 or more applicants from all around the world," he says. "In this case, I put in the specifier 'must be in Australia'." The funds, and the position, will vanish if he can't find the right person by the end of the year.

The pandemic is about to squelch the dreams of at least one hopeful young scientist. More than two years ago, Kilah offered a scholarship to a prospective PhD student from Pakistan. After many months of waiting, the student finally secured the necessary travel visa, but she hasn't been able to enter the country because of the closed border. The scholarship offer will expire on 1 June.

Australia is known for its strong international scientific enterprise. With 27% of its students from abroad, it has the world's highest proportion of international students, and nearly half (45%) of academics were born elsewhere. But Kilah says that the strict border controls that Australia has imposed to keep out the virus are harming the country's reputation as a prime destination for researchers. "Limiting our researcher talent weakens

our capacity and breadth of research, the scope for future collaboration and the reach of our science,” he says.

The global scientific enterprise will suffer if international researchers continue to be stuck in their own countries, van’t Land says. “Nobody will know what a person could have contributed if they had gone to that position,” she says. “It affects everybody.”

## Push on through

Scientists are finding ways to stay productive despite closed borders and cancelled plans. Here are some keys for moving forwards in a world that’s largely stuck in place.

**Think local.** Researchers who are unable to recruit from abroad or travel themselves will have to make the most of local resources. Instead of engaging in a normal global search for a new postdoc, physicist Mike McCulloch at the University of Plymouth, UK, started asking around to see whether there might be a candidate already on campus. That effort didn’t work out, however, so he’s now looking beyond campus.

**Buy some time, or at least some understanding.** With so many people affected by pandemic-related mobility issues, many individual supervisors, funding agencies and institutions are giving researchers a chance to work around any delays and disruptions. Sergio Ramos managed to keep his postdoctoral job at the University of Pittsburgh in Pennsylvania, despite having to spend longer than expected in Europe and then return through Mexico. This was largely because he was clearly doing everything he could to return home. “My principal investigators were very understanding,” he says.

Some institutions are taking extreme steps to accommodate researchers who have been stranded by the pandemic. For example, the Alexander von Humboldt Foundation, a government funding agency in Germany that brings researchers from around the world to the country, is allowing fellows to start their projects in their home country if they are unable to travel.

**Be patient.** Nobody knows when, but science will get moving again, says Hilligje van't Land, secretary-general of the International Association of Universities (IAU) in Paris. “It might take a few more years,” she says, and that’s assuming that countries and researchers can cooperate to make the most of vaccines and other control measures. Even then, she says, it probably won’t be a science as normal. “We will not build back, but we will build forward in a different way.”

**Stay connected.** Video conferences might be a poor substitute for face-to-face collaboration, but any connection is better than nothing. For researchers and institutions who never did have much money to travel abroad, the pandemic has somewhat evened the playing field. “We see researchers from Africa who are enthusiastic about the opportunities brought on by online collaboration,” says Giorgio Marinoni, manager of higher education and internationalization at the IAU. “On one hand, COVID-19 disrupts collaboration, but on the other, it opens up new possibilities.”

Nature **593**, 613-615 (2021)

doi: <https://doi.org/10.1038/d41586-021-01389-x>

## Jobs from Nature Careers

- - - [All jobs](#)
    - - [\*\*Postdoctoral Training Fellow - Kassiotis Lab\*\*](#)
        - [Francis Crick Institute](#)
        - [London, United Kingdom](#)
        - [JOB POST](#)
  - [\*\*Biological Safety Specialist\*\*](#)

[Francis Crick Institute](#)

[London, United Kingdom](#)

[JOB POST](#)

▪ [\*\*Post-doctoral Fellow - Autoimmune Pathogenesis\*\*](#)

[Oklahoma Medical Research Foundation \(OMRF\)](#)

[Oklahoma City, United States](#)

[JOB POST](#)

▪ [\*\*Research Technician / Research Assistant\*\*](#)

[Oklahoma Medical Research Foundation \(OMRF\)](#)

[Oklahoma City, United States](#)

[JOB POST](#)

[Download PDF](#)

[Download PDF](#)

## Related Articles



- ['It's like we're going back 30 years': how the coronavirus is gutting diversity in science](#)

-  **How to manage when your fieldwork is cancelled**
-  **Pandemic darkens postdocs' work and career hopes**

---

This article was downloaded by **calibre** from <https://www.nature.com/articles/d41586-021-01389-x>

| [Section menu](#) | [Main menu](#) |

- TECHNOLOGY FEATURE
- 24 May 2021

# How waste water is helping South Africa fight COVID-19

Detecting the coronavirus in samples from treatment plants could give early warning of outbreaks and new variants.

- [Heather Richardson](#) 0

1. Heather Richardson

1. Heather Richardson is a science writer based in Cape Town, South Africa.

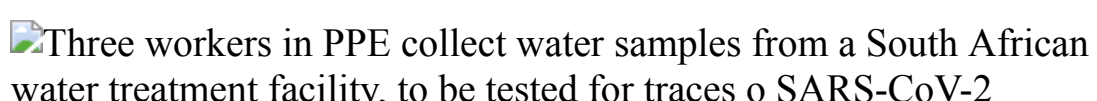
[View author publications](#)

You can also search for this author in [PubMed](#) [Google Scholar](#)





•



A team from the South African Medical Research Association samples the water at a sewage-treatment facility in Tshwane. Credit: Delwyn Verasamy/Mail & Guardian

Monday is sample-collection day in Cape Town, South Africa, and Aqeelah Benjamin is halfway through her shift. At the Green Point wastewater-treatment plant, under the Atlantic coast promenade, she fills a 500-millilitre bottle from a tap of untreated water. She wipes the bottle's exterior, cleans it with a spritz of ethanol and stores it on ice.

It's one of nine samples that Benjamin will collect today, each from a different facility. Later, she'll drop them off at the South African Medical Research Council (SAMRC) laboratory, where they will be tested for the presence of SARS-CoV-2, the virus that causes COVID-19. But that's just a fraction of the samples' potential — waste water contains a wealth of information about public health, and scientists are only just starting to tap into its potential.

Wastewater testing can provide an unbiased snapshot of community health: whatever access they have to the health-care system, everyone has to go to the toilet. And as the effluent makes its way to treatment facilities, researchers can test it to determine what pathogens might be present. For more than 40 years, researchers have used waste water to monitor the spread of poliovirus. Norovirus, influenza, hepatitis and measles viruses can also be found in waste water. Now, a growing number of countries are using waste water to monitor the spread of COVID-19. The memorably named COVIDPoops19 Dashboard, run by researchers at the University of California, Merced, lists more than 2,200 monitoring sites in 54 countries (see [go.nature.com/3fjfcjt](https://go.nature.com/3fjfcjt)).

South Africa is one of a handful of countries rolling out the technology nationwide. But the process isn't easy: researchers are struggling to overcome logistical hurdles and extend the techniques to the large part of the population that has no sewerage infrastructure.



## The myriad ways sewage surveillance is helping fight COVID around the world

The SAMRC runs a research programme across four of South Africa's nine provinces — the Western Cape, home of Cape Town; the rural Eastern Cape and Limpopo; and Gauteng, which includes South Africa's largest city, Johannesburg, and its administrative capital, Pretoria. After showing that it could detect SARS-CoV-2 in waste water in 5 treatment plants last June, the SAMRC extended the testing to another 19 plants to work out the logistics of scaling up the work.

The exercise highlighted problems specific to operating in South Africa. Difficulties collecting samples from remote sites can slow down the diagnostic process, for instance. And rolling electricity blackouts, known locally as 'load shedding', can hinder the operation of the equipment that samples waste water throughout the day. These machines, known as composite samplers, are also prone to theft. Considering this, and the cost of the samplers, South African researchers tend to use 'grab samples', such as Benjamin's. These samples are generally considered less representative than are those from composite samplers, because they represent just a single snapshot in time. But a study by the South African Water Research Commission (WRC) has found little difference in the effectiveness of the two approaches in detecting SARS-CoV-2 (see [go.nature.com/3v1mpm4](https://go.nature.com/3v1mpm4)).

On Monday afternoon, after Benjamin and two other collectors deliver their samples to the SAMRC lab in the northern Cape Town suburb of Parow, I meet Rabia Johnson, deputy director at the SAMRC's Biomedical Research and Innovation Platform. The lab specializes in molecular biology and cell-culture systems, and has been testing waste water for SARS-CoV-2 for nearly a year. "I think we've got the most comprehensive longitudinal database [in South Africa], from the first wave through the second wave," Johnson says.



Researchers process samples for testing at their lab in Tshwane.Credit: Delwyn Verasamy/Mail & Guardian

In the lab upstairs from Johnson's office, the researchers concentrate the samples in a centrifuge and then extract any viral RNA using a kit from the molecular-reagents company Qiagen in Hilden, Germany. The kit is optimized for extracting RNA from soil rather than water, but researchers at Yale University in New Haven, Connecticut, have shown that it is better at handling the unwanted organic materials found in wastewater than are conventional techniques ([J. Peccia et al. Preprint at medRxiv https://doi.org/gc9k; 2020](https://doi.org/gc9k)). The team then moves the extracted RNA to a 'clean' room to test for SARS-CoV-2 to avoid the risk of contamination. The researchers use a technique called real-time quantitative polymerase chain reaction (RT-qPCR) to quantify the amount of RNA that encodes the viral nucleocapsid protein. Other viral sequences are added in to assess performance. And positive controls are added for two key variants: 501Y.V2, first identified in South Africa, and B.1.1.7, detected in the United Kingdom. A fluorescent signal indicates that the nucleocapsid RNA is present.

Finally, Johnson cleans up the data and sends them to the SAMRC's Environment and Health Resource Unit. Researchers there upload the data to the SAMRC dashboard, a public resource launched in November 2020 that plots virus spread on a map (see [go.nature.com/3ukn74u](https://go.nature.com/3ukn74u)). Around 700 people per week access the service, according to Renée Street, a senior scientist at the unit.

## Early warning system

Because wastewater testing can capture the presence of the virus 7–14 days before the onset of symptoms, it can provide valuable early warning of localized outbreaks. Health officials can then make sure the necessary resources, equipment and personal protective equipment are available, says Johnson.



### How sewage could reveal true scale of coronavirus outbreak

But that's still theoretical. Wastewater data have not been used directly to inform decisions about control measures such as targeted lockdowns or resource allocation in South Africa, but they have been used alongside other sources of information, including case numbers and hospital admissions. "It's still very new science," says Street. "We're still working out what the different signals are, and at what signal level we would need to take action."

The ability of the technology to identify hotspots is governed by the service area of the treatment plant: the wider the spread, the harder it is to pinpoint small outbreaks, and at least one facility serves more than 850,000 people. But Cape Town epidemiologist Natacha Berkowitz, says that the goal is to “localize infection down to a small unit area, like a suburb”.

After the pandemic, the city plans to use waste water to regularly monitor for polio and other viruses. Although South Africa has been declared polio-free, missed vaccinations during the pandemic could result in an outbreak. “If we get a positive signal for polio, we’ll look at that specific drainage area, and perhaps do increased vaccinations or community education,” Berkowitz says.

## Remote areas

The advantage of wastewater testing is that it samples the population without requiring any action from individuals. It’s also cost-effective, because a single sample can be tested for multiple pathogens. And most labs can do the testing. “If you have a medical set-up for pathogen testing,” says Janet Mans, a virologist at the University of Pretoria, “you should be able to do this.”

But the technology also has downsides. It’s not easy to tie a signal to a specific location or group, for instance. Furthermore, it monitors only households that are connected to the sewerage system. And some 40% of the nation’s households do not have a flush toilet attached to the sewers, according to the 2011 census. Extending testing to these areas would capture much more of the population.



A centrifuge is used to concentrate the samples.Credit: Delwyn Verasamy/Mail & Guardian

In Pretoria, a private facility known as Waterlab is working with the WRC to expand testing to unsewered communities. The idea is to build a framework to start using samples from rivers and surface waters, says Gina Pocock, Waterlab's specialist consultant.

To monitor trends over time, samples are taken from sites that are consistently contaminated with waste water. That includes rivers downstream of unsewered, informal (or unplanned) settlements and surface run-off both of 'grey' water from bathing and sinks around standpipes and of 'black' water, which pools near latrines and contains faecal matter.

Such samples can be difficult to work with. Mans, who is working with Waterlab on ways to extract and test nucleic acids, says that environmental samples often contain compounds that can inhibit the amplification of nucleic acid by PCR, so addition of internal control sequences are a must. If the internal control is still inhibited after the sample has been diluted by one

part to ten, that sample is considered invalid, says Mans. A target can be considered negative only if the internal control amplifies at that dilution.

Equally difficult is the analysis, especially determining how many people the sample might represent. The researchers have to use overall trends in other parameters as proxies for the number of people. At Waterlab, Pocock says, researchers use bacterial density “to get an indication of the faecal load in the water”.

We don’t know “how many people flushed their toilet this morning”, Pocock says. “It’s not a definite science, where you can say this is our viral load and  $X$  amount of people in this community are sick. And with the rivers, even less so. So, we look at trends.”

## Pros and cons

Those trends should help in assessing the effectiveness of South Africa’s response to COVID-19.

Rolf Halden, director of the Biodesign Center for Environmental Health Engineering at Arizona State University in Tempe, has been testing waste water for nearly 20 years. Last year, he took part in a study to look at the feasibility of mass surveillance, testing the waste water of 36 million people in 100 US cities twice a week for 8 weeks for SARS-CoV-2. His goal is to scale that up to one billion people globally. He and his team found that it was possible to collect a lot of actionable information for very little investment, while still protecting people’s privacy.



## NatureTech hub

Although obviously enthusiastic about the technology's potential, Halden acknowledges its shortcomings. For instance, the temperature at the monitoring site matters, as does the distance that people live from it. A signal at a monitoring site could come from a single person close to the site, or from 10,000 people farther away, he explains.

There are also ethical and moral considerations as the technology becomes more powerful. Aggregated data on populations are generally considered safe from a privacy perspective, because individuals cannot be identified. However, as analytical techniques advance, it might become possible to identify human DNA, prompting concerns about who should have access to both the technology and the data ([D. Jacobs et al. IEEE Trans. Technol. Soc. https://doi.org/gc9m; 2021](https://doi.org/gc9m)). “The moral and ethical framework has to grow, ideally before the technology is applied,” Halden says.

Still, the potential benefits remain powerful motivators. Wastewater testing, Halden says, allows researchers to keep “a finger on the pulse of humanity”.

Nature **593**, 616-617 (2021)

doi: <https://doi.org/10.1038/d41586-021-01399-9>

## Jobs from Nature Careers

- - - [All jobs](#)
    - - [Postdoctoral Training Fellow - Kassiotis Lab](#)  
[Francis Crick Institute](#)  
[London, United Kingdom](#)  
[JOB POST](#)
      - [Biological Safety Specialist](#)  
[Francis Crick Institute](#)  
[London, United Kingdom](#)  
[JOB POST](#)
      - [Post-doctoral Fellow - Autoimmune Pathogenesis](#)  
[Oklahoma Medical Research Foundation \(OMRF\)](#)  
[Oklahoma City, United States](#)  
[JOB POST](#)
      - [Research Technician / Research Assistant](#)  
[Oklahoma Medical Research Foundation \(OMRF\)](#)  
[Oklahoma City, United States](#)

## JOB POST

[Download PDF](#)

[Download PDF](#)

## Related Articles



- [How sewage could reveal true scale of coronavirus outbreak](#)



- [The myriad ways sewage surveillance is helping fight COVID around the world](#)



- [Tracking COVID-19 with wastewater](#)



- [NatureTech hub](#)

---

This article was downloaded by **calibre** from <https://www.nature.com/articles/d41586-021-01399-9>

- WHERE I WORK
- 24 May 2021

# ‘In software, the name of the game is innovation’

Nicolás Jodal codes software solutions for navigating pandemics and other obstacles.

- [Kendall Powell](#)<sup>0</sup>

1. Kendall Powell

1. Kendall Powell is a freelance writer in Boulder, Colorado.

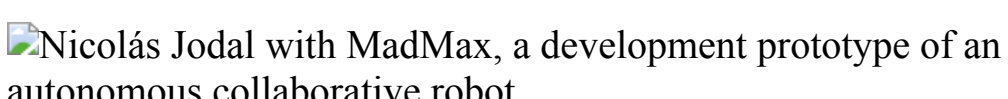
[View author publications](#)

You can also search for this author in [PubMed](#) [Google Scholar](#)





•



Nicolás Jodal is a systems engineer, co-founder and chief executive of GeneXus, and a director of the innovation accelerator ThalesLab in Montevideo, Uruguay. Credit: Pablo Albarenga for *Nature*

At GeneXus, we build software that builds software. A robot or artificial intelligence, not a human, writes the code for new apps. The company, which I co-founded in 1988, is also working on small autonomous vehicles for agrobusiness. The prototype in this picture — at our global headquarters

in Montevideo — which I helped to program, is named MadMax (after the 1979 film). It will work in a greenhouse, transporting lettuces after workers pick them.

This means solving a very big engineering problem — autonomous navigation. We humans can move easily from one place to another because of our sophisticated visual systems and our brain's complex mapping algorithms. But it is hard for a machine, which has neither, to answer the question: “Where am I?” Autonomous vehicles also have to avoid hitting obstacles, whether stationary or mobile, such as a running child.

In software, the name of the game is innovation. When the COVID-19 pandemic started, the Uruguayan government needed a digital relationship with every citizen — it was like a war situation. So a group of developers, including some from GeneXus, made the app Coronavirus UY in one week.

The app monitors symptoms, connects users to a doctor on a video call and sends out exposure alerts. This feature was a challenge because the government absolutely did not want to track people's positions. We solved that by using Bluetooth. Phones that are close to one another exchange some data. The app tracks these exchanges and sends an alert to a user's phone when it has spent more than 15 minutes within 3 metres of another phone whose user has tested positive for COVID-19.

I don't know where my drive to build things that didn't exist comes from. But once I have it, I cannot stop it. A painter told me that when he gets inspired, “there are no weekends”. The same thing happens to me.

Nature **593**, 620 (2021)

doi: <https://doi.org/10.1038/d41586-021-01400-5>

## **Jobs from Nature Careers**

- - - [All jobs](#)

o

- **Postdoctoral Training Fellow - Kassiotis Lab**

Francis Crick Institute

London, United Kingdom

JOB POST

- **Biological Safety Specialist**

Francis Crick Institute

London, United Kingdom

JOB POST

- **Post-doctoral Fellow - Autoimmune Pathogenesis**

Oklahoma Medical Research Foundation (OMRF)

Oklahoma City, United States

JOB POST

- **Research Technician / Research Assistant**

Oklahoma Medical Research Foundation (OMRF)

Oklahoma City, United States

JOB POST

Download PDF

Download PDF

## Related Articles

-  [Using robots to probe how people react to simple behaviours](#)
-  [Taking graphene out of the laboratory and into the real world](#)
-  [Engineering a dream work space](#)

---

This article was downloaded by **calibre** from <https://www.nature.com/articles/d41586-021-01400-5>

| [Section menu](#) | [Main menu](#) |

# Research

- **[Fibroblast cells reveal their ancestry](#)** [ 12 May 2021]  
News & Views • Cells called fibroblasts can boost health yet also drive disease. Cell-lineage analysis has unveiled the first comprehensive atlas of fibroblasts from various healthy and diseased tissues, a result that has major clinical implications.
- **[Nanocrystals form a superfluorescent lattice mimicking the atomic structure of perovskite materials](#)** [ 26 May 2021]  
News & Views • Nanocrystals with tailored shapes and compositions have been shown to form ‘superlattice’ arrays analogous to the ionic lattices of perovskite compounds. One such superlattice exhibits a phenomenon called superfluorescence.
- **[A mitochondrial gatekeeper that helps cells escape death by ferroptosis](#)** [ 12 May 2021]  
News & Views • Ferroptosis is a type of cell death driven by oxidative damage to lipid membranes. The discovery that organelles called mitochondria have an antioxidant system that counteracts ferroptosis might lead to new anticancer therapies.
- **[Trip frequency is key ingredient in new law of human travel](#)** [ 26 May 2021]  
News & Views • An analysis of mobile-phone tracking data has revealed a universal pattern that describes the interplay between the distances travelled by humans on trips and the frequency with which those trips are made.
- **[Evidence of hydrogen–helium immiscibility at Jupiter-interior conditions](#)** [ 26 May 2021]  
Article • Hydrogen and helium mixtures can be compressed to the extreme temperature and pressure conditions found in the interior of Jupiter and Saturn, and the immiscibility revealed supports models of Jupiter that invoke a layered interior.
- **[The universal visitation law of human mobility](#)** [ 26 May 2021]  
Article • Using large-scale mobility data from diverse cities around the globe, a simple and robust scaling law that captures the temporal and spatial range of population movement is revealed.
- **[Long-range nontopological edge currents in charge-neutral graphene](#)** [ 26 May 2021]  
Article • Nanoscale imaging of edge currents in charge-neutral graphene shows that charge accumulation can explain various exotic nonlocal transport measurements, bringing into

question some theories about their origins.

- **Perovskite-type superlattices from lead halide perovskite nanocubes** [ 26 May 2021]

Article • Through precise structural engineering, perovskite nanocrystals are co-assembled with other nanocrystal materials to form a range of binary and ternary perovskite-type superlattices that exhibit superfluorescence.

- **A 10 per cent increase in global land evapotranspiration from 2003 to 2019** [ 26 May 2021]

Article • Using a global mass-balance approach to calculate evapotranspiration, it is shown that global land evapotranspiration increased by 10% between 2003 and 2019, driven mainly by warming land temperatures.

- **Overriding water table control on managed peatland greenhouse gas emissions** [ 21 April 2021]

Article • Halving average drainage depths in agricultural peatlands could reduce greenhouse gas emissions by the equivalent of 1 per cent of all anthropogenic emissions.

- **Expanded diversity of Asgard archaea and their relationships with eukaryotes** [ 28 April 2021]

Article • Comparative analysis of 162 genomes of Asgard archaea results in six newly proposed phyla, including a deep branch that is provisionally named Wukongarchaeota, and sheds light on the evolutionary history of this clade.

- **Fast odour dynamics are encoded in the olfactory system and guide behaviour** [ 05 May 2021]

Article • Fast temporal dynamics of the olfactory environment can be perceived by mice and used to perform scene segmentation.

- **The spatial landscape of lung pathology during COVID-19 progression** [ 29 March 2021]

Article • Imaging mass cytometry of the human lung reveals the cellular composition and spatial architecture during COVID-19 and other acute injuries, enabling the characterization of lung pathophysiology from structural, immunological and clinical perspectives.

- **Response of the microbiome–gut–brain axis in Drosophila to amino acid deficit** [ 05 May 2021]

Article • In Drosophila, an amino acid deficit triggers the expression of the neuropeptide CNMamide in gut enterocytes, which promotes a compensatory appetite for essential over non-essential amino acids, and this process is modulated by the microbiome.

- **Cross-tissue organization of the fibroblast lineage** [ 12 May 2021]

Article • Single-cell and genetic tools are used to characterize the diversity of fibroblasts across healthy and perturbed tissues in mice and humans.

- **Mitochondrial TNAP controls thermogenesis by hydrolysis of phosphocreatine** [ 12 May 2021]

Article • Tissue nonspecific alkaline phosphatase (TNAP) within mitochondria hydrolyses phosphocreatine to initiate a futile cycle of creatine dephosphorylation and phosphorylation in thermogenic fat cells.

- **DHODH-mediated ferroptosis defence is a targetable vulnerability in cancer** [ 12 May 2021]

Article • DHO dehydrogenase regulates ferroptosis by preventing mitochondrial lipid peroxidation and its inhibition suppresses growth in tumours with low levels of GPX4.

- **Replication stress promotes cell elimination by extrusion**

[ 05 May 2021]

Article • A cell-cycle checkpoint triggers the extrusion of both nematode and mammalian cells experiencing replication stress.

- **Small-molecule inhibition of METTL3 as a strategy against myeloid leukaemia** [ 26 April 2021]

Article • Treatment with a specific inhibitor of the N6-methyladenosine methyltransferase METTL3 leads to reduced growth of cancer cells, indicating the potential of approaches targeting RNA-modifying enzymes for anticancer therapy.

- **Global miRNA dosage control of embryonic germ layer specification** [ 05 May 2021]

Article • The levels of microRNAs in mouse and human cells control lipid metabolism and germ cell specification during development.

- **Gasdermin D pore structure reveals preferential release of mature interleukin-1** [ 21 April 2021]

Article • A cryo-electron microscopy study of the gasdermin D pore reveals a model of pore assembly and a charge-based mechanism for the preferential release of mature cytokines.

- NEWS AND VIEWS
- 12 May 2021

# Fibroblast cells reveal their ancestry

Cells called fibroblasts can boost health yet also drive disease. Cell-lineage analysis has unveiled the first comprehensive atlas of fibroblasts from various healthy and diseased tissues, a result that has major clinical implications.

- [Christopher D. Buckley](#) 0

1. [Christopher D. Buckley](#)

1. Christopher D. Buckley is at the Kennedy Institute of Rheumatology, University of Oxford, Oxford OX3 7FY, UK, and at the Institute for Inflammation and Ageing, University of Birmingham, UK.

[View author publications](#)

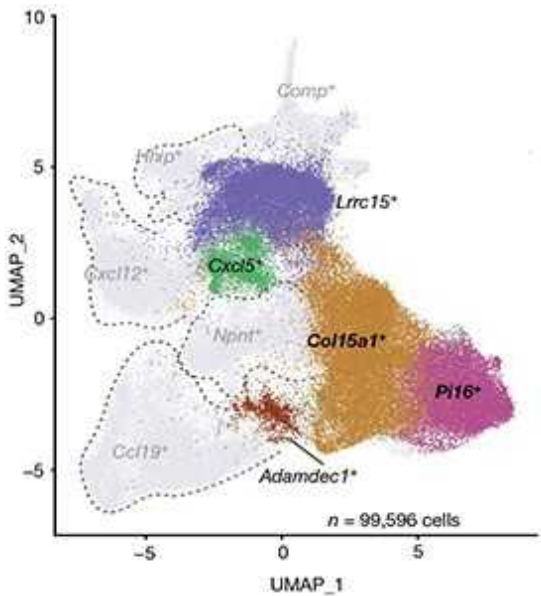
You can also search for this author in [PubMed](#) [Google Scholar](#)





•

Fibroblasts are cells that are easily identified by their distinctive spindle shape, a characteristic that delineates them from other structural cells of tissues, such as epithelial cells. They are a diverse group of cells with a multifaceted role in health and disease: they help to define tissue architecture by producing the extracellular-matrix material that surrounds cells, they aid the functioning and positioning of other cell types and, after injury, they promote healing or drive inflammation and scarring.



### [Read the paper: Cross-tissue organization of the fibroblast lineage](#)

Innovations in single-cell RNA-sequencing technology have provided evidence that fibroblasts consist of functionally distinct populations, which differ according to their tissue of origin and the disease with which they are associated<sup>1,2</sup>. Moreover, even in a single tissue, not all fibroblasts are the same. Discrete, non-overlapping subtypes drive different aspects of the many biological functions assigned to these cells<sup>3</sup>. [Writing in Nature](#), Buechler *et al.*<sup>4</sup> report a cross-tissue comparative atlas of fibroblast gene expression that reveals the general organizing principles of the fibroblast cellular lineage within and across organs. This work indicates the existence of universal, specialized and disease-specific subsets of fibroblast, and points to a shared ancestry for these three subtypes.

The family relationships between fibroblasts isolated either from the same or from different tissues has long been an enigma. One reason is that, until the advent of methods to profile RNA in single cells, it was hard to classify fibroblasts into distinct subtypes. All fibroblasts perform similar functions consistent with their lineage, such as making and modifying molecules of the extracellular matrix. Yet they can also execute specialized programs that are suited to the needs of the particular tissues in which they reside. For example, specialized fibroblasts support the development of haematopoietic (blood and immune) cells in the bone marrow. How fibroblasts achieve both general and specialized functions has been unclear.

Haematopoietic cells, such as macrophages of the immune system, solve the problem of being both generalists and specialists by adopting a shared, lineage-wide, core pattern of gene expression, which is then supplemented with tissue-specific gene expression driven by microenvironmental cues<sup>5–7</sup>. Macrophages are replenished from a cell type called a monocyte, which circulates in the blood and acts as a universal reservoir for the production of tissue macrophages. The question unanswered until now is whether fibroblasts follow this macrophage approach, or whether there is an alternative scenario for fibroblasts in a given tissue, in that a ‘universal’, pan-tissue fibroblast-precursor subset exists alongside a more mature, tissue-specific subset of these cells.

To address this question, Buechler and colleagues first took a bioinformatics approach to generate a cross-tissue atlas of gene expression in mouse fibroblasts, using single-cell RNA studies from data sets across 16 tissues. The authors thereby identified ten distinct clusters of gene-expression profiles, of which two (named the *Pi16* and *Col15a1* clusters) were found in certain cells across nearly all organs surveyed, suggesting that these clusters might represent the transcriptional profiles of universal, pan-tissue fibroblasts (Fig. 1). A more limited set of tissues had fibroblasts corresponding to the eight remaining clusters, raising the possibility that these are hallmarks of specialized fibroblasts, or particular fibroblast states, that are specific for certain tissues.

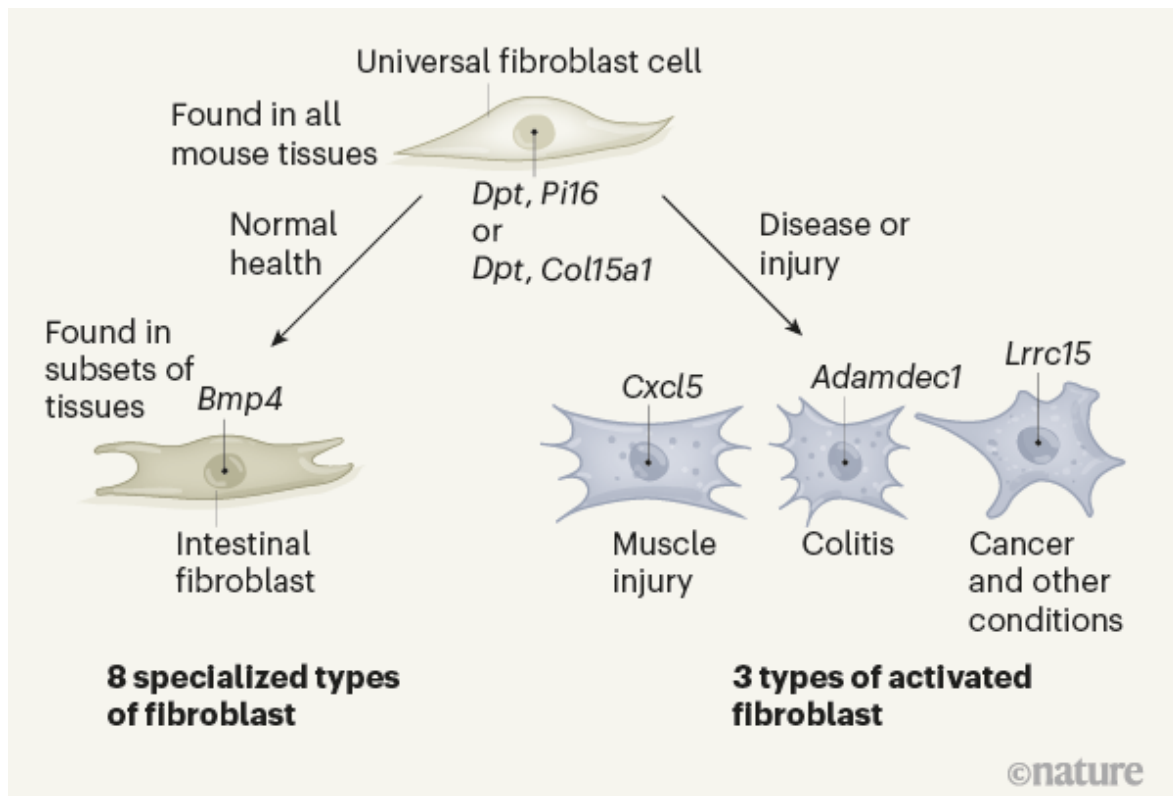
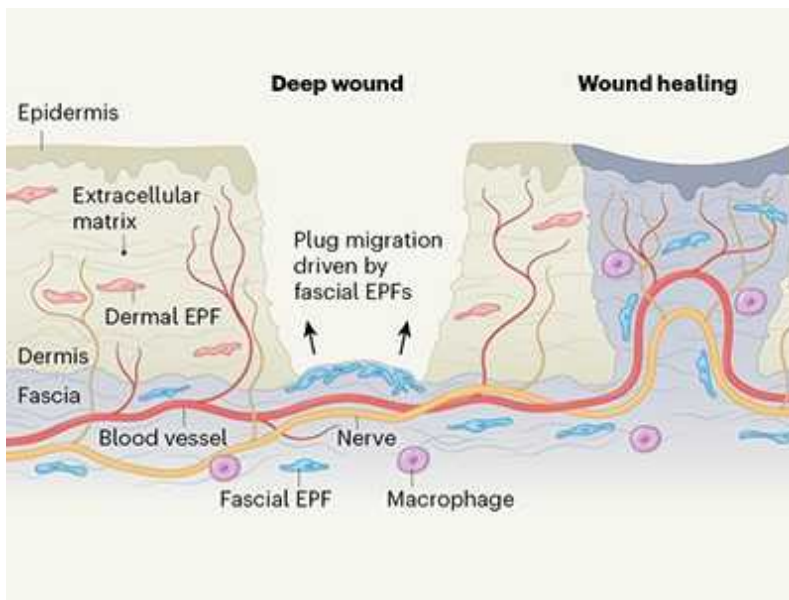


**Figure 1 | The organization of fibroblast cells across various organs.** Fibroblasts are structural cells that have key roles in the body. Buechler *et al.*<sup>4</sup> report their analysis of the relationship between fibroblasts found in various mouse organs. By analysing gene-expression data sets and using other approaches, the authors report the identification of two ‘universal’ types of fibroblast cell (that express either the genes *Dpt* and *Pi16* or the genes *Dpt* and *Col15a1*), which were found across the different tissues examined. The authors’ work indicates that these cells give rise to eight types of specialized fibroblast that are found only in certain normal tissues, such as intestinal fibroblasts that express the gene *Bmp4*. Buechler *et al.* report that the universal fibroblasts also give rise to three types of activated fibroblast in the context of disease or injury. Fibroblasts that express the gene *Cxcl5* are associated with muscle injury, fibroblasts associated with the gut disease colitis express the gene *Adamdec1*, and fibroblasts found in tumours and at sites of inflammation express the gene *Lrrc15*.

The ubiquity of the two *Pi16* and *Col15a1* clusters, which included high levels of expression of genes such as *Cd34* and *Ly6a* that are associated with stem-cell properties, combined with a bioinformatics technique that can infer

developmental relatedness by what is called trajectory analysis, led the authors to propose the following model: that universal and specialized fibroblasts exist side by side in normal, ‘steady state’ mouse tissues, and that these fibroblasts might be developmentally linked. The locations of fibroblasts expressing the *Col15a1* and *Pi16* clusters suggested that the *Col15a1* cells, which reside in the internal region of a tissue, might regulate the extracellular matrix, whereas the *Pi16* cells, which are found near blood vessels, might act as reservoir cells from which tissue fibroblasts originate.

To test this hunch, Buechler *et al.* set out to find cell-surface markers that could be used to identify *Pi16* and *Col15a1* fibroblasts. This work revealed a set of genes whose expression correlated inversely with fibroblast specialization and that was highly enriched in *Pi16* fibroblasts, and to a lesser extent in *Col15a1* fibroblasts. Of these genes, the authors focused on *Dpt* as a possible marker for *Pi16* and *Col15a1* universal fibroblasts.



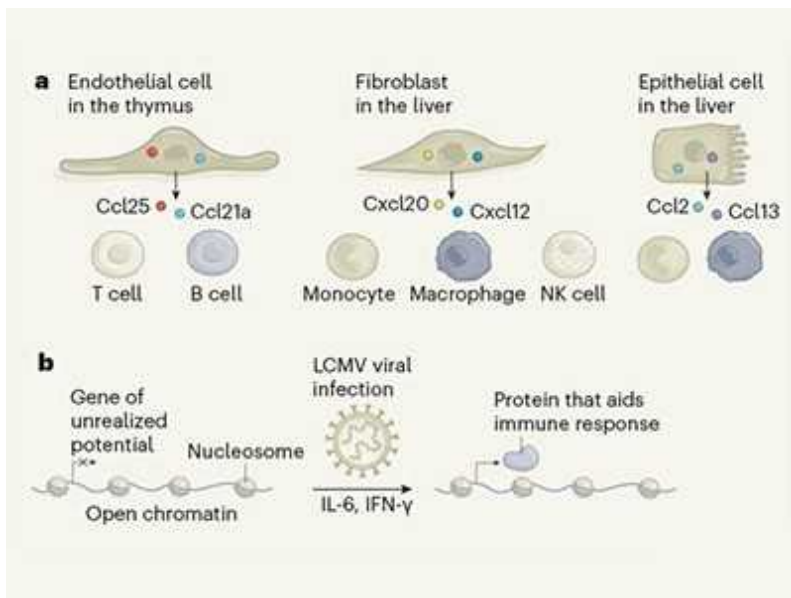
### Ready-made cellular plugs heal skin wounds

Buechler and colleagues engineered mice to express a fluorescent version of the protein encoded by *Dpt*. Genetic analysis and cell-tracking experiments that compared the progeny of universal fibroblasts and tissue-specific fibroblasts provided compelling experimental evidence supporting the bioinformatics data. The authors’ results point to the existence of a set of

two universal fibroblast populations from which all specialized fibroblasts originate, in a wide range of mouse tissues under physiological conditions.

The authors next investigated whether the fibroblast populations they had discovered changed when tissues were injured or were damaged in disease. They found that, in perturbed tissues, the *Pi16* and *Col15a1* fibroblasts seemed to be universally present and expressed high levels of *Dpt*, consistent with the idea that the *Pi16 Dpt* cell type serves as a reservoir cell. Excitingly, they identified three clusters of gene expression (marked by the genes *Cxcl5*, *Adamdec1* and *Lrrc15*, respectively) that seem to represent perturbation-specific, activated states of fibroblasts not observed in the steady state. Each of these fibroblast clusters was associated with certain organ-specific injuries. For example, the *Cxcl5* cluster was characteristic of muscle injury. Importantly, when *Dpt* reservoir cells in mice were genetically marked before a tumour was transplanted into the animals, they developed into *Lrrc15* cancer-associated fibroblasts, supporting the idea that the universal fibroblasts give rise to activated fibroblasts after injury and inflammation.

Finally, Buechler *et al.* investigated whether human tissue contains universal and activated fibroblast clusters, similar to those identified in mice. The authors investigated a range of tissues (such as pancreas and lung) and diseases (cancer, infection and inflammation). Their results, limited by the number of relevant data sets for human fibroblasts that are publicly available, suggest that, as in mice, an equivalent *Pi16* universal human fibroblast subset exists, as well as five activation subsets, or states, found in disease. Interestingly, although this work in humans confirmed aspects of the authors' results in mice, such as the findings relating to *Lrrc15* fibroblasts, Buechler *et al.* discovered some activated fibroblast subsets not observed in mice, such as those marked by expression of *COL3A1* (observed in COVID-19) or *CCL19* (associated with the gut disease colitis). Of note, *CCL19* and *COL3A1* clusters of gene expression in fibroblasts were found to be associated with disease in another study<sup>8</sup> that focused on common fibroblast subsets across four inflamed human tissues.



### An antiviral response beyond immune cells

Buechler and colleagues' landmark study has far-reaching implications. It establishes the key organizing principles of the fibroblast lineage in health and disease. Unlike macrophages, which, like fibroblasts, act as sentinel cells looking for signs of danger in tissues, the fibroblast lineage is compartmentalized into three major subtypes — universal and specialized (steady-state) subsets, as well as activated (perturbed state) subsets — all of which exist together in the same tissue. The concordance between certain fibroblasts in mice and in humans is particularly relevant, because it indicates that mechanistic studies in mice might have direct relevance for human disease. Moreover, this work provides a resource that will help to clarify nomenclature and boost the precision of identification of specific fibroblast subtypes across tissues. Such progress is urgently needed to standardize the fibroblast subsets that are currently used as cellular therapies to repair tissues in clinical studies.

As the authors acknowledge, more studies remain to be done. These investigations include defining the anatomical location of fibroblast subtypes, searching for the existence of other subtypes, particularly in human tissue, and trying to identify the cells (possibly structural or immune cells) that might promote the development and differentiation of different types of fibroblast. It is unclear why two universal fibroblast subtypes exist in mice, compared with the single universal haematopoietic progenitor cell.

But the authors speculate that having two universal subtypes might be a necessary division of labour for the fibroblast lineage in tissues.

Perhaps the most exciting implications of these findings lie in the clinical dividends that might result from the observation that non-overlapping disease-associated subsets of fibroblasts exist in specific tissues, and that these cells are distinct from other subtypes involved in healthy tissue repair and tissue specialization. If these disease-causing fibroblast subsets could be targeted without affecting the fibroblast subsets associated with health, it might be possible to treat certain inflammatory and malignant diseases in a more targeted and less immunosuppressive manner. Being able to target harmful fibroblasts while sparing beneficial ones and haematopoietic cells would revolutionize the treatment of many chronic diseases.

Nature **593**, 511-512 (2021)

doi: <https://doi.org/10.1038/d41586-021-01204-7>

## References

1. 1.

Koliaraki, V., Prados, A., Armaka, M. & Kollias, G. *Nature Immunol.* **21**, 974–982 (2020).

[PubMed](#) [Article](#) [Google Scholar](#)

2. 2.

Davidson, S. *et al.* *Nature Rev. Immunol.* <https://doi.org/10.1038/s41577-021-00540-z> (2021).

[Article](#) [Google Scholar](#)

3. 3.

Croft, A. P. *et al.* *Nature* **570**, 246–251 (2019).

[PubMed](#) [Article](#) [Google Scholar](#)

4. 4.

Buechler, M. B. *et al.* *Nature* **593**, 575–579 (2021).

[Article](#) [Google Scholar](#)

5. 5.

Gautier, E. L. *et al.* *Nature Immunol.* **13**, 1118–1128 (2012).

[PubMed](#) [Article](#) [Google Scholar](#)

6. 6.

Gosselin, D. *et al.* *Cell* **159**, 1327–1340 (2014).

[PubMed](#) [Article](#) [Google Scholar](#)

7. 7.

Lavin, Y. *et al.* *Cell* **159**, 1312–1326 (2014).

[PubMed](#) [Article](#) [Google Scholar](#)

8. 8.

Korsunsky, I. *et al.* Preprint at bioRxiv  
<https://doi.org/10.1101/2021.01.11.426253> (2021).

[Download references](#)

## Competing Interests

The author has founder's equity in Mestag Therapeutics, a company that aims to discover, develop and deliver impactful precision medicines through targeting disease-driving fibroblast subpopulations.

## Jobs from Nature Careers

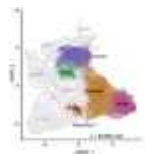
- - - [All jobs](#)
    - - [Postdoctoral Training Fellow - Kassiotis Lab](#)  
[Francis Crick Institute](#)  
[London, United Kingdom](#)  
[JOB POST](#)
      - [Biological Safety Specialist](#)  
[Francis Crick Institute](#)  
[London, United Kingdom](#)  
[JOB POST](#)
      - [Post-doctoral Fellow - Autoimmune Pathogenesis](#)  
[Oklahoma Medical Research Foundation \(OMRF\)](#)  
[Oklahoma City, United States](#)  
[JOB POST](#)
      - [Research Technician / Research Assistant](#)  
[Oklahoma Medical Research Foundation \(OMRF\)](#)  
[Oklahoma City, United States](#)

## JOB POST

[Download PDF](#)

[Download PDF](#)

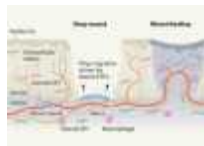
## Related Articles



- [Read the paper: Cross-tissue organization of the fibroblast lineage](#)



- [An antiviral response beyond immune cells](#)



- [Ready-made cellular plugs heal skin wounds](#)

- [See all News & Views](#)

---

This article was downloaded by **calibre** from <https://www.nature.com/articles/d41586-021-01204-7>

- NEWS AND VIEWS
- 26 May 2021

# Nanocrystals form a superfluorescent lattice mimicking the atomic structure of perovskite materials

Nanocrystals with tailored shapes and compositions have been shown to form ‘superlattice’ arrays analogous to the ionic lattices of perovskite compounds. One such superlattice exhibits a phenomenon called superfluorescence.

- [Gerd Bacher](#) 0

## 1. [Gerd Bacher](#)

1. Gerd Bacher is in the Department of Electronic Materials and Nanostructures, Faculty of Engineering, University of Duisburg-Essen, 47057 Duisburg, Germany.

[View author publications](#)

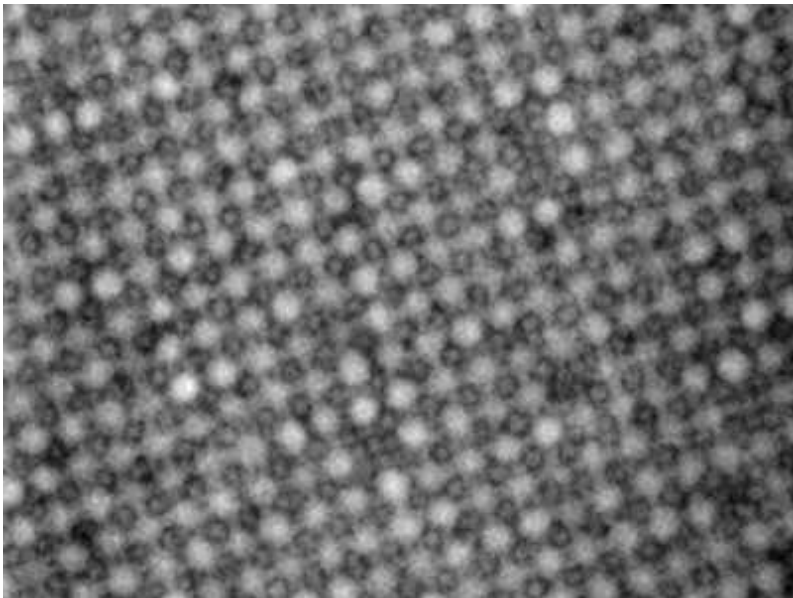
You can also search for this author in [PubMed](#) [Google Scholar](#)





•

Crystalline compounds known as perovskites are currently a hot topic of research. Composed of at least three different ionic species, these materials are renowned for their electrical and optical properties and have outstanding potential for use in solar cells<sup>1</sup> and optoelectronic devices<sup>2</sup>. Writing in *Nature*, Cherniukh *et al.*<sup>3</sup> report that when nanocubes of perovskites are combined with nanospheres of other materials, with or without a third type of nanocrystal, the various nanostructures obtained can arrange into a 3D ‘superlattice’ that has the same sort of arrangement as the ionic lattice in perovskites. Moreover, the nanocubes’ high degree of orientational order in the superlattice induces the phenomenon of superfluorescence, a collective emission of photon bursts that might have practical applications.



[Read the paper: Perovskite-type superlattices from lead halide perovskite nanocubes](#)

Methods for preparing nanocrystals of identical size and shape (monodisperse nanocrystals) were first reported<sup>4</sup> in 1993. A couple of years later, researchers began making superlattices consisting of monodisperse nanocrystals<sup>5</sup>. Since then, it has become possible to tailor a rich variety of nanocrystal shapes and sizes, and to control their interactions and environments, allowing an extensive range of nanocrystal superlattices to be made<sup>6</sup>. Such work is partly inspired by a desire to investigate the fundamental science that triggers the formation of artificial lattices from tiny crystals. But researchers are also spurred on by the fact that periodic arrangements of nanocrystals exhibit new or improved properties<sup>6,7</sup> — such as enhanced electron transport, catalytic activity, or light emission and absorption — compared with the properties of nanocrystals that aren't in superlattices.

Cherniukh and co-workers now show that artificial perovskite-like superlattices can be constructed by combining different types of nanocrystal. By mixing nanocubes of the perovskite  $\text{CsPbBr}_3$  (Cs, caesium; Pb, lead; Br, bromine) with spherical nanocrystals of iron(ii,iii) oxide ( $\text{Fe}_3\text{O}_4$ ; Fe, iron) or of  $\text{NdGdF}_4$  (Nd, neodymium; Gd, gadolinium; F, fluorine), they obtained binary superlattices. And by adding truncated-cuboid lead sulfide ( $\text{PbS}$ )

nanoparticles to the mix, they obtained ternary superlattices. The general formula of a perovskite is  $\text{ABO}_3$ , in which A and B represent positively charged ions and the three oxygens are negatively charged oxide ions. In Cherniukh and colleagues' ternary superlattices, the nanocubes adopt lattice positions equivalent to the sites of the oxide ions in a perovskite crystal lattice; the spherical nanocrystals occupy the A sites; and the PbS nanocrystals occupy the B sites (Fig. 1a).

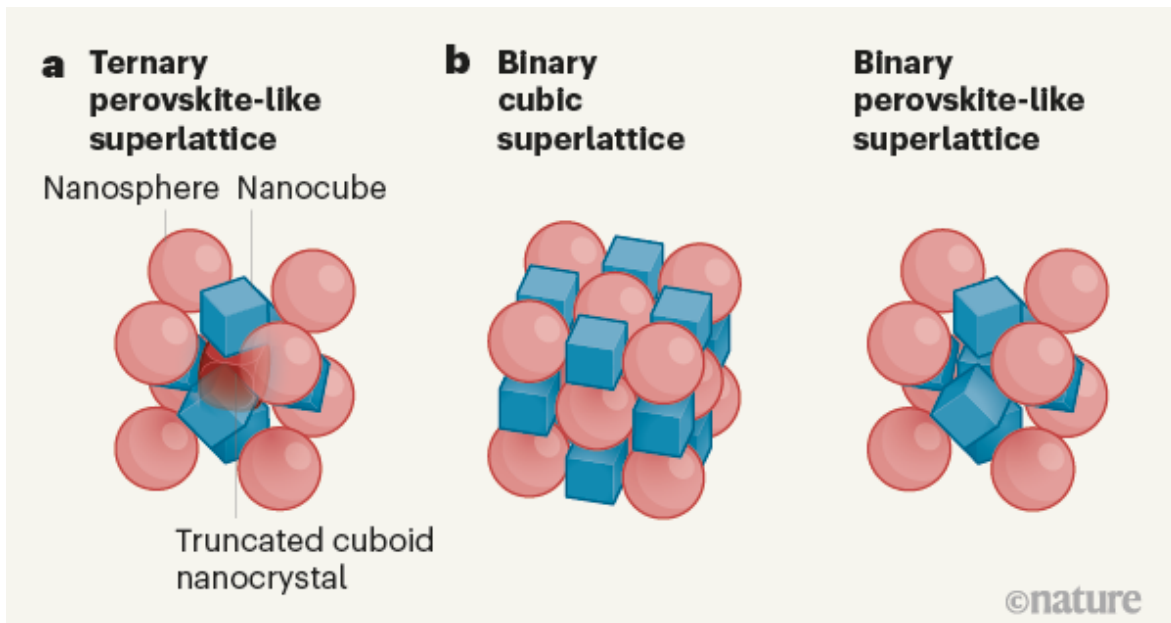
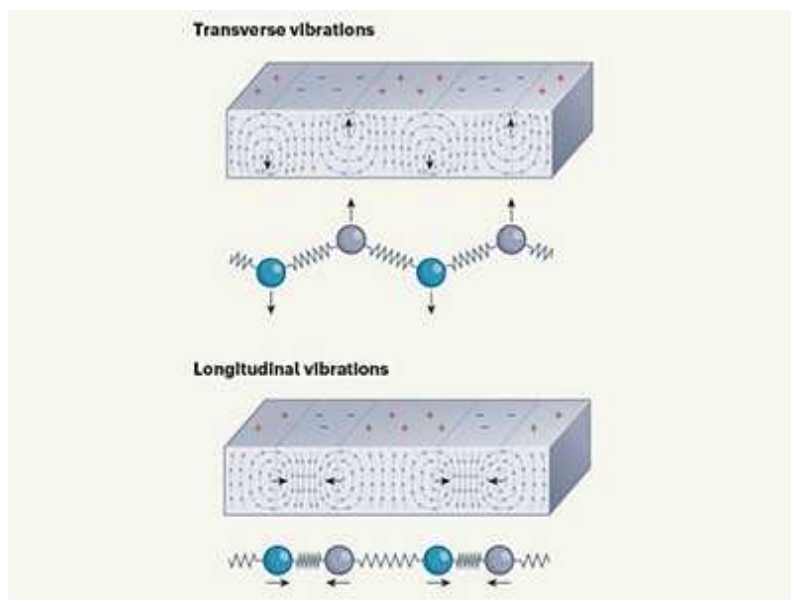


**Figure 1 | Perovskite-like superlattices of nanocrystals.** Perovskite compounds have the general formula  $\text{ABO}_3$ , in which A and B represent positively charged ions and the three oxygens are negatively charged oxide ions. **a**, Cherniukh *et al.*<sup>3</sup> report that combinations of spherical, cubic and truncated cuboid nanocrystals can form ordered arrangements analogous to the lattice structure of ionic perovskites. The spherical nanocrystals occupy the A sites; the nanocubes adopt the oxide sites; and the truncated cuboid nanocrystals occupy the B sites. Only the unit cell (the smallest repeating unit) of the lattice is shown here. **b**, The authors report that superlattices also form without the truncated cuboid nanocrystals. The lattice can be cubic, analogous to that found in crystals of sodium chloride, or an  $\text{ABO}_3$  arrangement, depending on the relative sizes and fractions of the two types of nanocrystal and the orientation of the nanocubes.

In ionic perovskite crystals, at least three ions with different radii are required to achieve the characteristic perovskite lattice. By contrast, Cherniukh *et al.* observed that perovskite-like superlattices can be achieved using only two types of nanocrystal. This is because the cuboid nanocrystals have a rotational degree of freedom. The cubic shape and surface deformability of these nanocrystals cause them to become locked in specific orientations in the superlattice.

The authors also found that, for systems composed of  $\text{CsPbBr}_3$  nanocubes and  $\text{Fe}_3\text{O}_4$  nanospheres, tiny changes in the relative sizes and fractions of the two types of nanocrystal can transform the resulting superlattice from a cubic arrangement, analogous to that found in crystals of sodium chloride, to an  $\text{ABO}_3$  arrangement (Fig. 1b). High-resolution transmission electron microscopy and electron diffraction studies of these binary superlattices showed that the orientations of the nanocubes are highly ordered. By contrast, the axes of the crystal lattices in the spherical nanoparticles have random orientations.



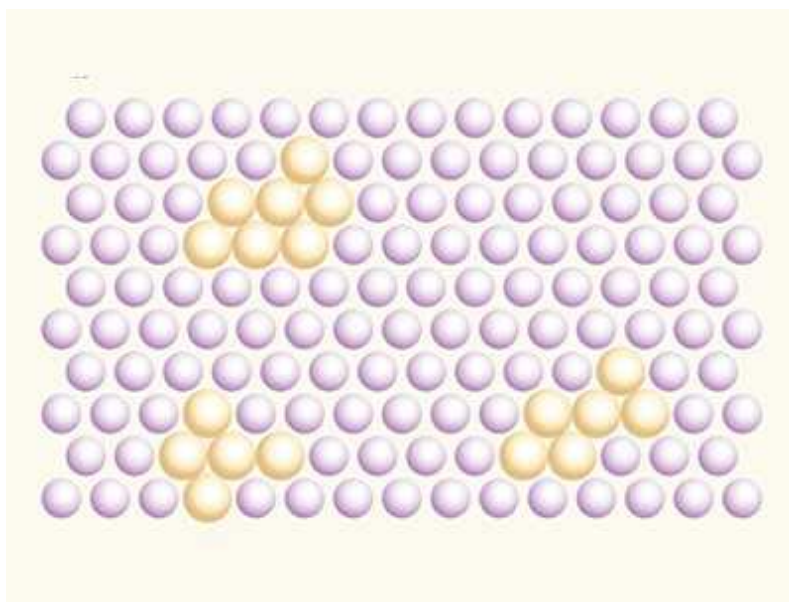
### Dynamics of polarization vortices revealed in a ferroelectric material

In a final piece of superlattice engineering, Cherniukh and co-workers carefully adjusted the relative sizes of the nanocrystals in the ternary system consisting of  $\text{CsPbBr}_3$  nanocubes,  $\text{Fe}_3\text{O}_4$  nanospheres and truncated  $\text{PbS}$

nanocubes. The authors observed that the nanocrystals in the superlattice could pack together to fill approximately 92% of the space available. Such a high packing density has not been observed in ionic perovskite crystals.

Cherniukh *et al.* found that, in a binary  $\text{ABO}_3$  superlattice consisting of  $\text{CsPbBr}_3$  nanocubes and spherical  $\text{NdGdF}_4$  nanocrystals, the high orientational order of the nanocubes, together with their large oscillator strength (a quantity that expresses the likelihood that the nanocubes will absorb or emit light in processes associated with electronic transitions), leads to an unusual radiation phenomenon known as superfluorescence. In this effect, laser excitation of the nanocubes causes a spontaneous macroscopic optical polarization that results in an intense burst of light from the nanocubes.

Superfluorescence has previously been observed in superlattices formed from  $\text{CsPbBr}_3$  nanocubes alone<sup>8</sup>. However, the flexibility with which the periodicity, packing density and orientation of the highly fluorescent  $\text{CsPbBr}_3$  nanocubes in Cherniukh and colleagues' superlattices can be tailored opens up fresh avenues of research into this phenomenon. The superfluorescence pulses were as short as 22 picoseconds (1 ps is  $10^{-12}$  seconds), which makes these superlattices attractive potential candidates for use as highly energy-efficient, ultrafast light emitters.



## Superlattice substitution

What is next for this field of research? It seems feasible that the family of superlattices will expand still further: Cherniukh *et al.* briefly report that they have also made binary superlattices that have a columnar structure, and others that have an arrangement analogous to the crystal structure of aluminium diboride (which consists of sheets of boron atoms interleaved by layers of aluminium atoms).

The findings could also aid the development of applications for superfluorescence — which has been observed in a wide variety of atomic, molecular and nanoscale systems<sup>9</sup>, but has not yet been used in a device. The ability to customize the 3D structures of superlattices might provide a way to tailor superfluorescence at will, and thereby enable its use, for example, as a quantum light source. This, in turn, might require further efforts to improve the 3D ordering of superlattices, and to increase the size of the materials that can be made in which the ordering is strictly maintained. Research might also be needed to stabilize the ordered structure when superlattices are incorporated into a device, probably by using linker molecules between the nanocrystals.

In the meantime, the new findings open the way for researchers to try out many combinations of nanocrystals that have various attributes — such as emissive, magnetic or insulating properties — as building blocks for superlattices. This could result in materials with multiple functionalities, all of which could be controlled by the spatial arrangement and distance between the nanocrystals.

Nature **593**, 513-514 (2021)

doi: <https://doi.org/10.1038/d41586-021-01331-1>

## References

1. 1.

Green, M. A., Ho-Baillie, A. & Snaith, H. J. *Nature Photon.* **8**, 506–514 (2014).

[Article](#) [Google Scholar](#)

2. 2.

Lin, K. *et al.* *Nature* **562**, 245–248 (2018).

[PubMed](#) [Article](#) [Google Scholar](#)

3. 3.

Cherniukh, I. *et al.* *Nature* **593**, 535–542 (2021).

[Article](#) [Google Scholar](#)

4. 4.

Murray, C. B., Norris, D. J. & Bawendi, M. G. *J. Am. Chem. Soc.* **115**, 8706–8715 (1993).

[Article](#) [Google Scholar](#)

5. 5.

Murray, C. B., Kagan, C. R. & Bawendi, M. G. *Science* **270**, 1335–1338 (1995).

[Article](#) [Google Scholar](#)

6. 6.

Boles, M. A., Engel, M. & Talapin, D. V. *Chem. Rev.* **116**, 11220–11289 (2016).

[PubMed](#) [Article](#) [Google Scholar](#)

7. 7.

Baek, W. *et al.* *Nature Mater.* **20**, 650–657 (2021).

[PubMed](#) [Article](#) [Google Scholar](#)

8. 8.

Rainò, G. *et al.* *Nature* **563**, 671–675 (2018).

[PubMed](#) [Article](#) [Google Scholar](#)

9. 9.

Cong, K. *et al.* *J. Opt. Soc. Am. B* **33**, C80–C101 (2016).

[Article](#) [Google Scholar](#)

[Download references](#)

## Competing Interests

The author declares no competing interests.

## [Jobs from Nature Careers](#)

- - - [All jobs](#)
    - - [\*\*Postdoctoral Training Fellow - Kassiotis Lab\*\*](#)  
[Francis Crick Institute](#)  
[London, United Kingdom](#)  
[JOB POST](#)
      - [\*\*Biological Safety Specialist\*\*](#)  
[Francis Crick Institute](#)  
[London, United Kingdom](#)

JOB POST

- **Post-doctoral Fellow - Autoimmune Pathogenesis**

Oklahoma Medical Research Foundation (OMRF)

Oklahoma City, United States

JOB POST

- **Research Technician / Research Assistant**

Oklahoma Medical Research Foundation (OMRF)

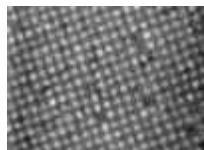
Oklahoma City, United States

JOB POST

Download PDF

Download PDF

## Related Articles



- **Read the paper: Perovskite-type superlattices from lead halide perovskite nanocubes**



- **Dynamics of polarization vortices revealed in a ferroelectric material**



- **Superlattice substitution**
- **See all News & Views**

---

This article was downloaded by **calibre** from <https://www.nature.com/articles/d41586-021-01331-1>

| [Section menu](#) | [Main menu](#) |

- NEWS AND VIEWS
- 12 May 2021

# A mitochondrial gatekeeper that helps cells escape death by ferroptosis

Ferroptosis is a type of cell death driven by oxidative damage to lipid membranes. The discovery that organelles called mitochondria have an antioxidant system that counteracts ferroptosis might lead to new anticancer therapies.

- [Javier Garcia-Bermudez](#)<sup>⑨</sup> &
- [Kıvanç Birsoy](#)<sup>⑩</sup>

1. Javier Garcia-Bermudez

1. Javier Garcia-Bermudez is at the Rockefeller University, New York, New York 10065, USA.

[View author publications](#)

You can also search for this author in [PubMed](#) [Google Scholar](#)

2. [Kıvanç Birsoy](#)

1. Kıvanç Birsoy is at the Rockefeller University, New York, New York 10065, USA.

[View author publications](#)

You can also search for this author in [PubMed](#) [Google Scholar](#)

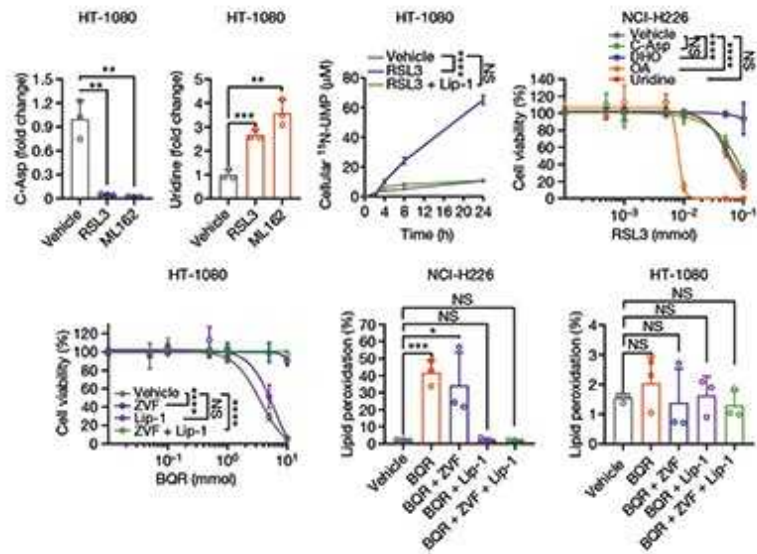




•

Mitochondria, the organelles that enable our cells to generate energy, are thought to have evolved from formerly free-living, oxygen-dependent microorganisms<sup>1</sup>. However, oxygen-dependent energy production using an organelle enclosed by lipid membranes comes at a cost. Such respiration often generates reactive oxygen species (ROS), which can damage cellular structures and compromise their function. For example, ROS react with membrane lipids in a process termed lipid peroxidation, and the resulting abnormal lipid peroxides ultimately trigger an iron-dependent form of regulated cell death called ferroptosis<sup>2</sup>. Cells use multiple protection and repair systems to combat the toxic effects of these modified membrane

lipids. [Writing in Nature](#), Mao *et al.*<sup>3</sup> report the discovery of a system that protects mitochondrial lipids from oxidative damage.



### [Read the paper: DHODH-mediated ferroptosis defence is a targetable vulnerability in cancer](#)

Mammalian cells rely on three main systems to repair lipid peroxides. The key proteins that underpin the three systems are, respectively, GPX4, FSP1 and DHFR<sup>2,4–6</sup>. Each of these antioxidant repair nodes also involves a metabolite molecule that exists in chemically reduced and oxidized states. Among these, ubiquinone (also known as coenzyme Q<sub>10</sub>) is a lipid that has functions in both mitochondrial membranes and the cell membrane. The reduced form of ubiquinone, termed ubiquinol, has antioxidant properties and can repair lipid peroxides.

Cells need to continuously replenish ubiquinol to retain this protective function for their membrane lipids. The enzyme FSP1 counteracts ferroptosis by generating ubiquinol from ubiquinone, but FSP1 activity is restricted to the cell membrane<sup>4,5</sup>. This finding raised the question of whether mitochondria exploit a similar mechanism to generate ubiquinol and thereby repair oxidative damage to mitochondrial membrane lipids.

Mao and colleagues hypothesized that a system mitigating lipid peroxidation also exists in mitochondria. Given the close relationship between cellular

metabolism and ferroptosis, the authors focused on metabolite molecules that are altered in cancer cells on lipid peroxidation. Surprisingly, they observed that peroxidation is associated with substantial changes in the abundance of metabolites in the pathway that synthesizes the pyrimidine bases that are a component of DNA and RNA. Building on this observation, the authors investigated the possibility that a component of this synthesis pathway is involved in preventing ferroptosis.

Most of the components of this pathway exist in the cytoplasm, but one enzyme, DHODH, is found in mitochondria. DHODH catalyses the conversion of the molecule dihydroorotate to orotate through an oxidation reaction that uses ubiquinone and thereby generates ubiquinol. Further experiments by Mao *et al.* revealed that DHODH protects cells against lipid peroxidation by regenerating ubiquinol, enabling ubiquinol-mediated repair of oxidative damage to mitochondrial lipids (Fig. 1). Supplementing cells with the end products of the pyrimidine-synthesis pathway did not affect lipid peroxidation, demonstrating that this anti-ferroptotic role of DHODH is independent of its function in pyrimidine synthesis.

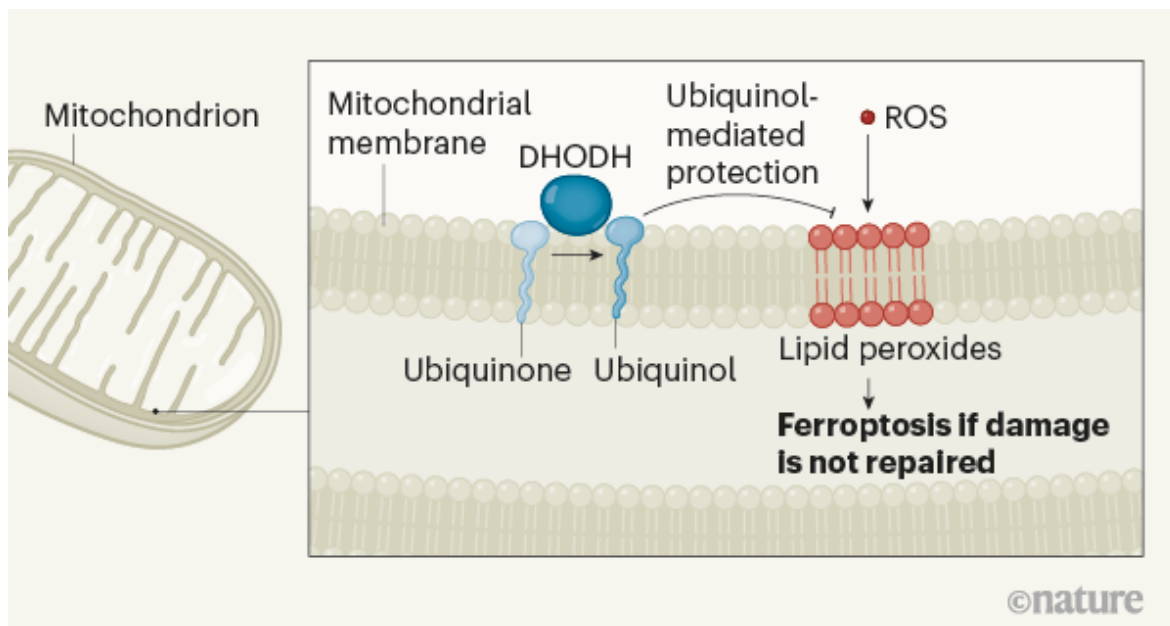
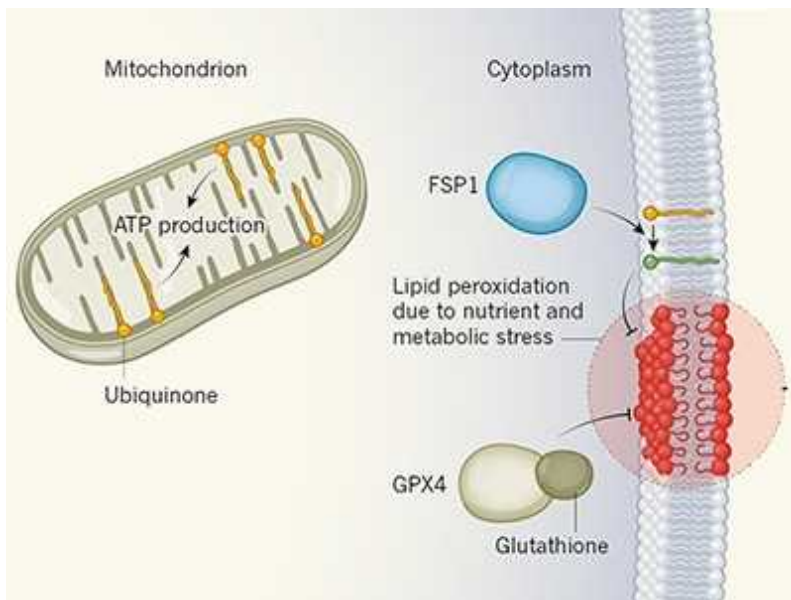


**Figure 1 | A system for repairing mitochondrial lipids.** Energy-generating processes in mitochondria produce reactive oxygen species (ROS), which can damage the organelle's membrane lipids through oxidation. This process forms toxic lipids, termed lipid peroxides, which can trigger a type of cell

death called ferroptosis. Mao *et al.*<sup>3</sup> report the identification of a system that protects mitochondrial organelles. The enzyme DHODH converts the molecule ubiquinone to ubiquinol, which helps to combat the effects of lipid peroxidation and protects cells from ferroptosis.

These findings establish DHODH-mediated regulation of ubiquinol production as an efficient system for the mitigation of lipid peroxidation exclusively in mitochondria, in a mechanism that has echoes of the FSP1 system. Interestingly, a version of the GPX4 protein is found in the mitochondria of some cells, and its level of expression varies in different types of cancer. This mitochondrially localized GPX4 is not essential for mouse survival<sup>7</sup>, indicating that it has a redundant role. By contrast, DHODH is ubiquitously expressed and has a role in cell proliferation owing to its function in nucleotide synthesis. Rapidly dividing cells, such as cancer cells, might therefore take advantage of this active pathway as a way to inhibit lipid peroxidation.

Indeed, Mao and colleagues found that if human tumour cells that expressed low levels of GPX4 were transplanted into mice treated with an inhibitor of DHODH, the resulting loss of DHODH function led to ferroptosis of the cells and impaired tumour growth. The effect was independent of DHODH's role in pyrimidine synthesis. It remains to be seen whether this mitochondrial ferroptosis-blocking antioxidant system contributes to the spread of cancer cells through metastasis<sup>8</sup> or to the tumour response to radiotherapy<sup>9</sup>. These are processes in which the induction of ferroptosis might help to thwart tumour progression. Potent DHODH inhibitors are being developed as anticancer agents, and are currently undergoing clinical trials. Perhaps they will be particularly effective in cancer cells that have low levels of expression of GPX4.



### A powerful cell-protection system prevents cell death by ferroptosis

Mao and colleagues' discovery of a system for the specific protection of mitochondrial membranes suggests that dedicated mechanisms to counteract lipid peroxidation might exist in other subcellular compartments. Interestingly, squalene, which is an intermediate molecule in the biosynthetic pathway that generates cholesterol, protects cancers called lymphomas from lipid peroxidation, and is found in high concentrations in lipid droplets<sup>10</sup>. However, it is unclear whether squalene's protective function is due to this specific localization to droplets.

Organelles such as the endoplasmic reticulum and peroxisomes also harbour ROS-generating reactions. Glutathione and tetrahydrobiopterin are redox-active molecules (which can alter the oxidation state of other molecules), and thus might offer alternative ways to combat lipid peroxidation in such cases. However, the precise mechanisms and components that could enable the transport of these molecules to organelles are poorly understood.

Advances in ways of assessing the molecular and protein compositions of organelles, through techniques such as metabolomics and proteomics, should provide insights into this fundamental issue, and improve our understanding of the role of antioxidants in tumour progression.

doi: <https://doi.org/10.1038/d41586-021-01203-8>

## References

1. 1.

Gray, M. W. *Mol. Biol. Cell* **28**, 1285–1287 (2017).

[PubMed](#) [Article](#) [Google Scholar](#)

2. 2.

Yang, W. S. *et al.* *Cell* **156**, 317–331 (2014).

[PubMed](#) [Article](#) [Google Scholar](#)

3. 3.

Mao, C. *et al.* *Nature* **593**, 586–590 (2021).

[Article](#) [Google Scholar](#)

4. 4.

Bersuker, K. *et al.* *Nature* **575**, 688–692 (2019).

[PubMed](#) [Article](#) [Google Scholar](#)

5. 5.

Doll, S. *et al.* *Nature* **575**, 693–698 (2019).

[PubMed](#) [Article](#) [Google Scholar](#)

6. 6.

Soula, M. *et al.* *Nature Chem. Biol.* **16**, 1351–1360 (2020).

[PubMed](#) [Article](#) [Google Scholar](#)

7. 7.

Schneider, M. *et al.* *FASEB J.* **23**, 3233–3242 (2009).

[PubMed](#) [Article](#) [Google Scholar](#)

8. 8.

Ubellacker, J. M. *et al.* *Nature* **585**, 113–118 (2020).

[PubMed](#) [Article](#) [Google Scholar](#)

9. 9.

Lang, X. *et al.* *Cancer Discov.* **9**, 1673–1685 (2019).

[PubMed](#) [Article](#) [Google Scholar](#)

10. 10.

Garcia-Bermudez, J. *et al.* *Nature* **567**, 118–122 (2019).

[PubMed](#) [Article](#) [Google Scholar](#)

[Download references](#)

## Competing Interests

The authors declare no competing interests.

## [Jobs from Nature Careers](#)

- - - [All jobs](#)
    - 
    - [Postdoctoral Training Fellow - Kassiotis Lab](#)

[Francis Crick Institute](#)

[London, United Kingdom](#)

[JOB POST](#)

▪ [Biological Safety Specialist](#)

[Francis Crick Institute](#)

[London, United Kingdom](#)

[JOB POST](#)

▪ [Post-doctoral Fellow - Autoimmune Pathogenesis](#)

[Oklahoma Medical Research Foundation \(OMRF\)](#)

[Oklahoma City, United States](#)

[JOB POST](#)

▪ [Research Technician / Research Assistant](#)

[Oklahoma Medical Research Foundation \(OMRF\)](#)

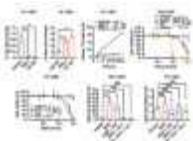
[Oklahoma City, United States](#)

[JOB POST](#)

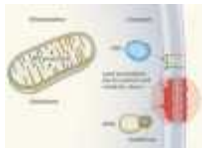
[Download PDF](#)

[Download PDF](#)

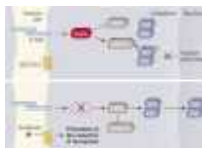
## **Related Articles**



- [Read the paper: DHODH-mediated ferroptosis defence is a targetable vulnerability in cancer](#)



- [A powerful cell-protection system prevents cell death by ferroptosis](#)



- [Cancer-cell death ironed out](#)

- [See all News & Views](#)

---

This article was downloaded by **calibre** from <https://www.nature.com/articles/d41586-021-01203-8>

- NEWS AND VIEWS
- 26 May 2021

# Trip frequency is key ingredient in new law of human travel

An analysis of mobile-phone tracking data has revealed a universal pattern that describes the interplay between the distances travelled by humans on trips and the frequency with which those trips are made.

- [Laura Alessandretti](#)<sup>0</sup> &
- [Sune Lehmann](#)<sup>1</sup>

1. Laura Alessandretti

1. Laura Alessandretti is in the Department of Applied Mathematics and Computer Science, Technical University of Denmark, Kongens Lyngby DK 2100, Denmark.

[View author publications](#)

You can also search for this author in [PubMed](#) [Google Scholar](#)

2. [Sune Lehmann](#)

1. Sune Lehmann is in the Department of Applied Mathematics and Computer Science, Technical University of Denmark, Kongens Lyngby DK 2100, Denmark, and at the Center for Social Data Science, University of Copenhagen, Denmark.

[View author publications](#)

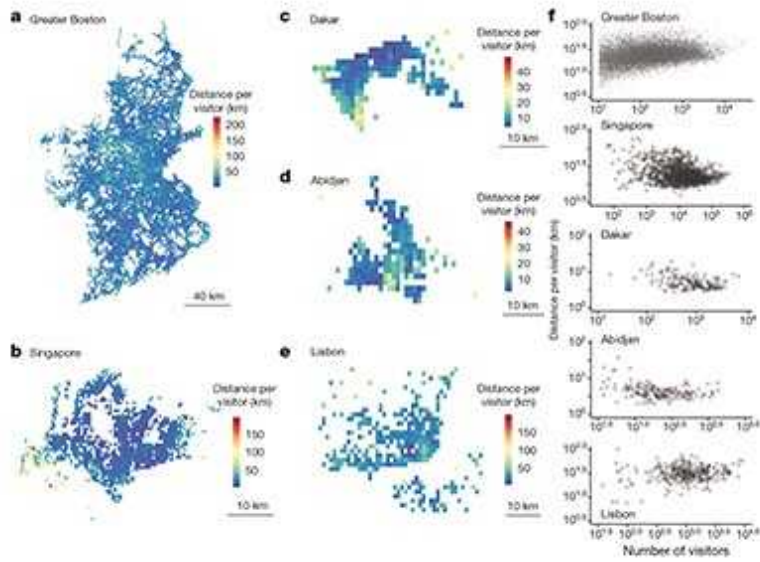
You can also search for this author in [PubMed](#) [Google Scholar](#)





•

As a scientist, you sometimes come across a finding that is clear and robust, revealing a pattern that was right in front of you all along — and which makes you want to kick yourself for not noticing it before. The universal visitation law of human mobility, [reported in \*Nature\*](#) by Schläpfer *et al.*<sup>1</sup>, is just such a finding. The authors uncover a pattern of human behaviour that connects travel distance to the frequency of trips.



## [Read the paper: The universal visitation law of human mobility](#)

Consider any two places. Can we predict how many people travel from one to the other, and vice versa, on the basis of the position and simple characteristics of the two locations? This question is at the core of a large body of literature whose origin dates back to the mid-nineteenth century. In 1885, the geographer Ernst Ravenstein showed empirically that two key elements explain the number of individuals who move between any two places<sup>2</sup>: the distance between the places, and the socio-economic properties of the origin and destination. The number of travellers tends to decrease with distance, for example, and more-populated places attract more travellers.

These key observations were later integrated into the gravity law of human mobility, which states that the number of travellers between two cities increases with a power of the cities' population sizes, and decreases with a power of the distance between them<sup>3</sup>. A refinement of the gravity law, known as the radiation model, proposes that the number of travellers does not depend directly on the distance between two cities, but rather on the number of places between the cities at which people would realistically stop<sup>4</sup>.

Research into human mobility has flourished in the past few years, as a result of data becoming available with increasingly fine spatial and temporal resolution<sup>5</sup>. This has allowed researchers to adjust the radiation and gravity

models, and a plethora of variations, to capture travel patterns on a range of timescales, including home relocation (residential mobility), airline travel, urban transportation and commuting. Schläpfer and colleagues now report a fundamental discovery in this highly active area of research. They have identified a key component that was missing from existing theoretical frameworks of human mobility: visitation frequency ( $f$ ), the number of trips that someone makes to a location per unit of time.

The authors made their discovery by reframing the challenge faced by modellers. Instead of focusing solely on distance and sociodemographic features, they asked a further question: ‘How many people living in any given place travel to any other place exactly  $n$  times in a period  $T$ ?’ This change in perspective is possible because mobility data for individuals are now available from mobile-phone tracking. By studying mobility traces extracted from phones at seven urban locations around the world, the authors uncovered a phenomenological law that answers their question: the number decreases with  $r^2$  (where  $r$  is the distance from someone’s home to a given location), and with  $f^2$ , where  $f = n/T$  (Fig. 1).

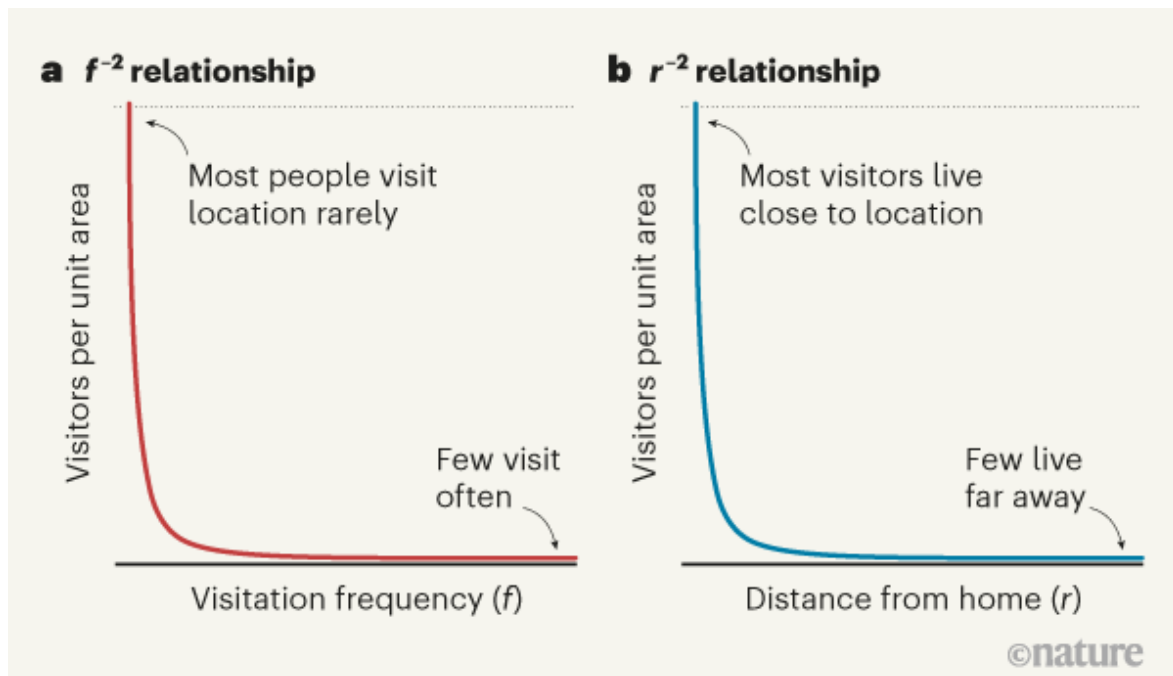
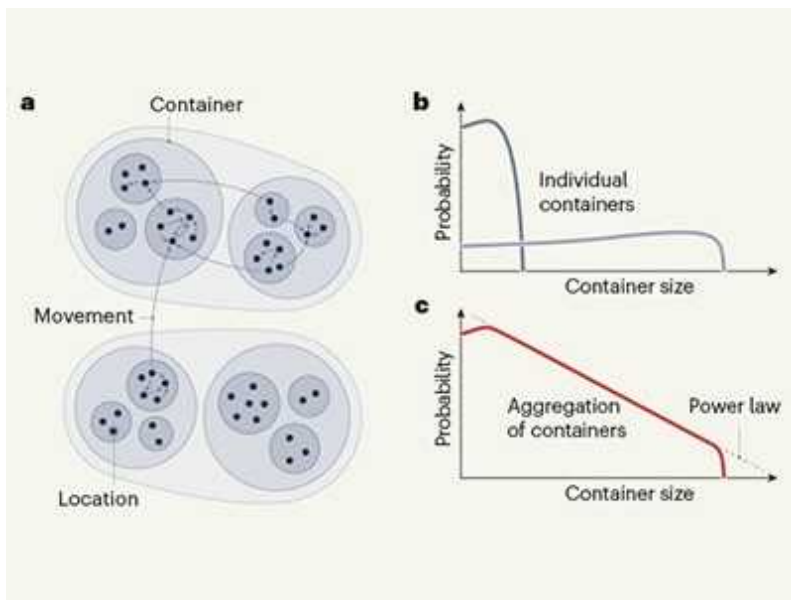


**Figure 1 | A universal law of human mobility.** Schläpfer *et al.*<sup>1</sup> analysed mobile-phone tracking data to determine the patterns of human journeys in several cities. **a**, The authors find that, for people who live at a specific

distance  $r_0$  from a particular location, the number of individuals per unit area who travel with a visitation frequency  $f$  to that location is inversely proportional to  $f^2$ . **b**, An inverse-square relationship is also observed for the distance from home,  $r$ , given a specific visitation frequency  $f_0$ . That is, for people who travel with a given frequency of trips  $f_0$  to a particular location, the number of individuals per unit area who travel a distance  $r$  from home is inversely proportional to  $r^2$ . The observed relationships hold for any choice of location,  $r_0$  and  $f_0$ . The graphs shown are illustrations of the observed relationships, and do not represent actual data.

Surprisingly, this law is valid for all the widely different urban systems considered in the study, and thus provides a general framework for describing and predicting mobility flows across timescales. Importantly, the model accommodates diverse mobility behaviours, from commuting to residential mobility, without requiring a change of parameters.

To understand how the observed pattern emerges robustly from the multitude of individual behaviours, Schläpfer *et al.* developed a model of the mobility of individuals that incorporates realistic and well-understood mechanisms, such as people's tendency to explore places that are popular with other visitors, and preferential return — an empirical phenomenon in which the number of visits received by a location is proportional to the number of visits previously received<sup>6</sup>. This model reproduces the collective patterns of mobility observed in the phone data. By linking the mobility of individuals to collective outcomes, the authors' work helps to narrow the gap between two streams of literature that have previously been broadly distinct<sup>5</sup>. The findings therefore pave the way for studies that could deepen our theoretical understanding of how individual and collective mobility patterns are connected.



### Hierarchies defined through human mobility

One unanswered question is whether the patterns of mobility observed in urban areas also apply outside cities. The geographies of rural areas are less centralized and contain fewer places of interest to visitors than do urban areas; these characteristics might result in travel patterns different from those observed by Schläpfer and colleagues. Another key question is whether mobility patterns are different for trips that are not anchored to people's homes.

In their modelling of travel patterns, the authors assume that people head straight home after visiting any location. But in the real world, geographical considerations and the need to minimize travel time tend to result in trips in specific recurring sequences. People often visit places in a certain order, for example going from work to the supermarket and gym, and then home. We therefore anticipate that models that capture the ordering of trips will be key to providing a truly comprehensive description of collective mobility flows across space and time, and even more accurate predictions of real-world behaviour. In the meantime, we expect the mobility patterns uncovered by Schläpfer *et al.* to be useful for a variety of purposes, from epidemic modelling to transportation planning and urban design.

doi: <https://doi.org/10.1038/d41586-021-01355-7>

## References

1. 1.

Schl  pfer, M. *et al.* *Nature* **593**, 522–527 (2021).

[Article](#) [Google Scholar](#)

2. 2.

Ravenstein, E. G. *J. Stat. Soc. Lond.* **48**, 167–235 (1885).

[Article](#) [Google Scholar](#)

3. 3.

Zipf, G. K. *Am. Sociol. Rev.* **11**, 677–686 (1946).

[Article](#) [Google Scholar](#)

4. 4.

Simini, F., Gonz  lez, M. C., Maritan, A. & Barab  si, A.-L. *Nature* **484**, 96–100 (2012).

[PubMed](#) [Article](#) [Google Scholar](#)

5. 5.

Barbosa, H. *et al.* *Phys. Rep.* **734**, 1–74 (2018).

[Article](#) [Google Scholar](#)

6. 6.

Song, C., Koren, T., Wang, P. & Barab  si, A.-L. *Nature Phys.* **6**, 818–823 (2010).

[Article](#) [Google Scholar](#)

[Download references](#)

## Competing Interests

The authors declare no competing interests.

## [Jobs from Nature Careers](#)

- - - [All jobs](#)
    - 
    - [\*\*Postdoctoral Training Fellow - Kassiotis Lab\*\*](#)
      - [Francis Crick Institute](#)
      - [London, United Kingdom](#)
      - [JOB POST](#)
    - [\*\*Biological Safety Specialist\*\*](#)
      - [Francis Crick Institute](#)
      - [London, United Kingdom](#)
      - [JOB POST](#)
    - [\*\*Post-doctoral Fellow - Autoimmune Pathogenesis\*\*](#)
      - [Oklahoma Medical Research Foundation \(OMRF\)](#)
      - [Oklahoma City, United States](#)

## JOB POST

### ▪ **Research Technician / Research Assistant**

Oklahoma Medical Research Foundation (OMRF)

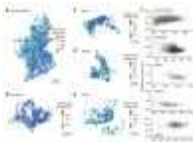
Oklahoma City, United States

## JOB POST

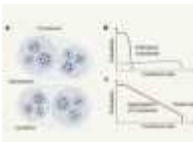
Download PDF

Download PDF

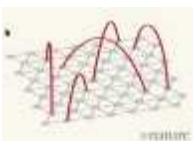
## Related Articles



- [Read the paper: The universal visitation law of human mobility](#)



- [Hierarchies defined through human mobility](#)



- [Twenty years of network science](#)

- [See all News & Views](#)

---

This article was downloaded by **calibre** from <https://www.nature.com/articles/d41586-021-01355-7>

- Article
- [Published: 26 May 2021](#)

# Evidence of hydrogen–helium immiscibility at Jupiter-interior conditions

- [S. Brygoo](#)<sup>1</sup>,
- [P. Loubeyre](#) [ORCID: orcid.org/0000-0002-1778-3510](#)<sup>1</sup>,
- [M. Millot](#) [ORCID: orcid.org/0000-0003-4414-3532](#)<sup>2</sup>,
- [J. R. Rygg](#)<sup>3</sup>,
- [P. M. Celliers](#)<sup>2</sup>,
- [J. H. Eggert](#)<sup>2</sup>,
- [R. Jeanloz](#) [ORCID: orcid.org/0000-0002-3519-7929](#)<sup>4</sup> &
- [G. W. Collins](#)<sup>3</sup>

[Nature](#) volume 593, pages 517–521 (2021) [Cite this article](#)

- 638 Accesses
- 119 Altmetric
- [Metrics details](#)

## Subjects

- [Astronomy and planetary science](#)
- [Condensed-matter physics](#)
- [Phase transitions and critical phenomena](#)

## Abstract

The phase behaviour of warm dense hydrogen–helium (H–He) mixtures affects our understanding of the evolution of Jupiter and Saturn and their interior structures<sup>1,2</sup>. For example, precipitation of He from a H–He atmosphere at about 1–10 megabar and a few thousand kelvin has been invoked to explain both the excess luminosity of Saturn<sup>1,3</sup>, and the depletion of He and neon (Ne) in Jupiter’s atmosphere as observed by the Galileo probe<sup>4,5</sup>. But despite its importance, H–He phase behaviour under relevant planetary conditions remains poorly constrained because it is challenging to determine computationally and because the extremes of temperature and pressure are difficult to reach experimentally. Here we report that appropriate temperatures and pressures can be reached through laser-driven shock compression of H<sub>2</sub>–He samples that have been pre-compressed in diamond-anvil cells. This allows us to probe the properties of H–He mixtures under Jovian interior conditions, revealing a region of immiscibility along the Hugoniot. A clear discontinuous change in sample reflectivity indicates that this region ends above 150 gigapascals at 10,200 kelvin and that a more subtle reflectivity change occurs above 93 gigapascals at 4,700 kelvin. Considering pressure–temperature profiles for Jupiter, these experimental immiscibility constraints for a near-protosolar mixture suggest that H–He phase separation affects a large fraction—we estimate about 15 per cent of the radius—of Jupiter’s interior. This finding provides microphysical support for Jupiter models that invoke a layered interior to explain Juno and Galileo spacecraft observations<sup>1,4,6,7,8</sup>.

## Access options

Subscribe to Journal

Get full journal access for 1 year

\$199.00

only \$3.90 per issue

[Subscribe](#)

All prices are NET prices.  
VAT will be added later in the checkout.  
Tax calculation will be finalised during checkout.

Rent or Buy article

Get time limited or full article access on ReadCube.

from \$8.99

[Rent or Buy](#)

All prices are NET prices.

### **Additional access options:**

- [Log in](#)
- [Access through your institution](#)
- [Learn about institutional subscriptions](#)

**Fig. 1: Experimental configuration used for laser-shock experiments on pre-compressed targets, and representative line-imaging pyrometer (SOP) and interferometric Doppler velocimeter (VISAR) data.**



**Fig. 2: Ratio of VISAR output at the shock front in the 11 mol% He in H mixture over that in quartz versus shock velocity through the H–He mixture.**



**Fig. 3: Reflectivity versus temperature along the Hugoniot for H–He mixtures with 11 mol% He (blue) and 33 mol% He (inset, green).**

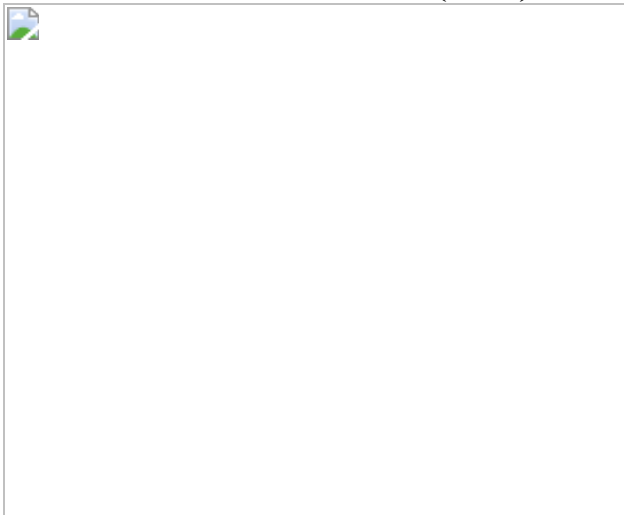
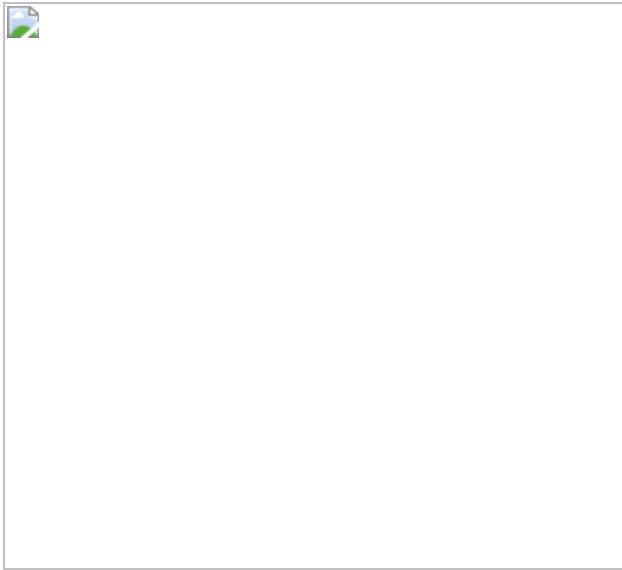


**Fig. 4: Phase diagram of a near protosolar H–He mixture and implications for Jupiter’s interior.**



## Data availability

The data that support the findings of this study are available in Extended Data Table 1, Extended Data Table 2 and in the [Supplementary Information](#). Upon request, the raw VISAR and SOP images could be transferred to anyone willing to redo the data analysis from the start.

## References

1. 1.

Stevenson, D. J. Jupiter's interior as revealed by Juno. *Annu. Rev. Earth Planet. Sci.* **48**, 465–489 (2020).

[ADS](#) [CAS](#) [Google Scholar](#)

2. 2.

Salpeter, E. On convection and gravitational layering in Jupiter and in stars of low mass. *Astrophys. J.* **181**, L83–L89 (1973).

[ADS](#) [CAS](#) [Google Scholar](#)

3. 3.

Fortney, J. J. & Hubbard, W. B. Phase separation in giant planets: inhomogeneous evolution of Saturn. *Icarus* **164**, 228–243 (2003).

[ADS](#) [CAS](#) [Google Scholar](#)

4. 4.

von Zahn, U. & Hunten, D. M. The helium mass fraction in Jupiter's atmosphere. *Science* **272**, 849–851 (1996).

[ADS](#) [Google Scholar](#)

5. 5.

Wilson, H. F. & Militzer, B. Sequestration of noble gases in giant planet interiors. *Phys. Rev. Lett.* **104**, 121101 (2010).

[ADS](#) [PubMed](#) [PubMed Central](#) [Google Scholar](#)

6. 6.

Wahl, S. M. et al. Comparing Jupiter interior structure models to Juno gravity measurements and the role of a dilute core. *Geophys. Res. Lett.* **44**, 4649–4659 (2017).

[ADS](#) [Google Scholar](#)

7. 7.

Debras, F. & Chabrier, G. New models of Jupiter in the context of Juno and Galileo. *Astrophys. J.* **872**, 100 (2019).

[ADS](#) [CAS](#) [Google Scholar](#)

8. 8.

Bolton, S. J. et al. Jupiter's interior and deep atmosphere: the initial pole-to-pole passes with the Juno spacecraft. *Science* **356**, 821–825 (2017).

[ADS](#) [CAS](#) [PubMed](#) [PubMed Central](#) [Google Scholar](#)

9. 9.

Guillot, T. & Gautier, D. Giant planets. In *Treatise on Geophysics* (eds Shubert, G. & Spohn, T.) 2nd edn, Vol. 10 (Elsevier, 2014).

10. 10.

Schöttler, M. & Redmer, R. *Ab initio* calculation of the miscibility diagram for hydrogen-helium mixtures. *Phys. Rev. Lett.* **120**, 115703 (2018).

[ADS](#) [Google Scholar](#)

11. 11.

Stevenson, D. J. & Salpeter, E. E. The phase diagram and transport properties for hydrogen-helium fluid planets. *Astrophys. J. Suppl. Ser.* **35**, 221–237 (1977).

[ADS](#) [CAS](#) [Google Scholar](#)

12. 12.

Vorberger, J., Tamblyn, I., Militzer, B. & Bonev, S.A. Hydrogen-helium mixtures in the interiors of giant planets. *Phys. Rev. B* **75**, 024206 (2007).

[ADS](#) [Google Scholar](#)

13. 13.

Lorenzen, W., Holst, B. & Redmer, R. Demixing of hydrogen and helium at megabar pressures. *Phys. Rev. Lett.* **102**, 115701 (2009).

[ADS](#) [Google Scholar](#)

14. 14.

Morales, M. A. et al. Phase separation in hydrogen-helium mixtures at Mbar pressures. *Proc. Natl Acad. Sci. USA* **106**, 1324–1329 (2009).

[ADS](#) [CAS](#) [Google Scholar](#)

15. 15.

Loubeyre, P., LeToullec, R. & Pinceaux, J. P. Binary phase diagrams of H<sub>2</sub>-He mixtures at high temperature and high pressure. *Phys. Rev. B* **36**, 3723–3730 (1987).

[ADS](#) [CAS](#) [Google Scholar](#)

16. 16.

Morales, M., Hamel, S., Casperson, K. & Schwegler, E. Hydrogen-helium demixing from first principles: from diamond anvil cells to planetary interiors. *Phys. Rev. B* **87**, 174105 (2013).

[ADS](#) [Google Scholar](#)

17. 17.

Militzer, B., Soubiran, F., Wahl, S. M. & Hubbard, W. Understanding Jupiter's interior. *J. Geophys. Res. Planets* **121**, 1552–1572 (2016).

[ADS](#) [Google Scholar](#)

18. 18.

Clay, R. C. III, Holzmann, M., Ceperley, D. & Morales, M. Benchmarking density functionals for hydrogen-helium mixtures with quantum Monte Carlo: energetics, pressures and forces. *Phys. Rev. B* **93**, 035121 (2016).

[ADS](#) [Google Scholar](#)

19. 19.

Loubeyre, P. et al. Coupling static and dynamic compressions: first measurements in dense hydrogen. *High Press. Res.* **24**, 25–31 (2004).

[ADS](#) [CAS](#) [Google Scholar](#)

20. 20.

Jeanloz, R. et al. Achieving high-density states through shock-wave loading of precompressed samples. *Proc. Natl Acad. Sci. USA* **104**, 9172–9177 (2007).

[ADS](#) [CAS](#) [PubMed](#) [PubMed Central](#) [Google Scholar](#)

21. 21.

Celliers, P. et al. Insulator-to-conducting transition in dense fluid helium. *Phys. Rev. Lett.* **104**, 184503 (2010).

[ADS](#) [CAS](#) [PubMed](#) [PubMed Central](#) [Google Scholar](#)

22. 22.

Loubeyre, P. et al. Extended data set for the equation of state of warm dense hydrogen isotopes. *Phys. Rev. B* **86**, 144115 (2012).

[ADS](#) [Google Scholar](#)

23. 23.

Knudson, M. & Desjarlais, M. P. Adiabatic release measurements in  $\alpha$ -quartz between 300 and 1200 GPa: characterization of  $\alpha$ -quartz as a shock standard in the multimegabar regime. *Phys. Rev. B* **88**, 184107 (2013).

[ADS](#) [Google Scholar](#)

24. 24.

Brygoo, S. et al. Analysis of laser shock experiments on precompressed samples using a quartz reference and application to warm dense hydrogen and helium. *J. Appl. Phys.* **118**, 195901 (2015).

[ADS](#) [Google Scholar](#)

25. 25.

Hamel, S., Morales, M. A. & Schwegler, E. Signature of helium segregation in hydrogen-helium mixtures. *Phys. Rev. B* **84**, 165110 (2011).

[ADS](#) [Google Scholar](#)

26. 26.

Soubiran, F., Mazevet, S., Winisdoerffer, C. & Chabrier, G. Optical signature of hydrogen–helium demixing at extreme density-temperature conditions. *Phys. Rev. B* **87**, 165114 (2013).

[ADS](#) [Google Scholar](#)

27. 27.

Soubiran, F. PhD thesis. Ecole Normale Supérieure de Lyon (2012).

28. 28.

Jiang, S. et al. A spectroscopic study of the insulator-metal transition in liquid hydrogen and deuterium. *Adv. Sci.* **7**, 1901668 (2020).

[CAS](#) [Google Scholar](#)

29. 29.

Militzer, B. & Hubbard, W. B. Ab initio equation of state for hydrogen-helium mixtures with recalibration of the giant-planet mass-radius relation. *Astrophys. J.* **774**, 148 (2013).

[ADS](#) [Google Scholar](#)

30. 30.

Soubiran, F. K., Mazevet, S., Winisdoerffer, C. & Chabrier, G. Helium gap in the warm dense matter regime and experimental reflectivity measurements. *Phys. Rev. B* **86**, 115102 (2012).

[ADS](#) [Google Scholar](#)

31. 31.

Püstow, R., Nettelmann, N., Lorenzen, W. & Redmer, R. H/He demixing and the cooling behavior of Saturn. *Icarus* **267**, 323–333 (2016).

[ADS](#) [Google Scholar](#)

32. 32.

Mankovich, C. R. & Fortney, J. J. Evidence for a dichotomy in the interior structures of Jupiter and Saturn from helium phase separation. *Astrophys. J.* **889**, 51 (2020).

[ADS](#) [CAS](#) [Google Scholar](#)

33. 33.

Schouten, J. A., de Kuijper, A. & Michels, J. P. Critical line of He-H<sub>2</sub> up to 2500 K and the influence of attraction on fluid-fluid separation. *Phys. Rev. B* **44**, 6630–6634 (1991).

[ADS](#) [CAS](#) [Google Scholar](#)

34. 34.

Knudson, M. D. et al. Direct observation of an abrupt insulator-to-metal transition in dense liquid deuterium. *Science* **348**, 1455–1460 (2015).

[ADS](#) [CAS](#) [Google Scholar](#)

35. 35.

Celliers, P. M. et al. Insulator-metal transition in dense fluid deuterium. *Science* **361**, 677–682 (2018).

[ADS](#) [CAS](#) [PubMed](#) [PubMed Central](#) [Google Scholar](#)

36. 36.

Nettelmann, N., Becker, A., Holst, B. & Redmer, R. Jupiter models with improved ab-initio hydrogen equation of state (H-REOS.2). *Astrophys. J.* **750**, 52 (2012).

[ADS](#) [Google Scholar](#)

37. 37.

Saumon, D., Chabrier, G. & Van Horn, H. M. An equation of state for low-mass stars and giant planets. *Astrophys. J.* **99**, 713 (1995).

[CAS](#) [Google Scholar](#)

38. 38.

Mao, H. K., Xu, J. & Bell, P. M. Calibration of the ruby gauge to 800 Kbar under quasi-hydrostatic conditions. *J. Geophys. Res. Solid Earth* **91**, 4673–4676 (1986).

[CAS](#) [Google Scholar](#)

39. 39.

Le Toullec, R. & Loubeyre, P. & Pinceaux, J. P. Refractive-index measurements of dense helium up to 16 GPa at T=298 K: analysis of its thermodynamic and electronic properties. *Phys. Rev. B* **40**, 2368–2378 (1989).

[ADS](#) [Google Scholar](#)

40. 40.

Mills, R. L., Liebenberg, D. H. & Bronson, J. C. Equation of state of fluid n-D<sub>2</sub> from P-V-T and ultrasonic velocity measurements. *J. Chem. Phys.* **68**, 2663–2668 (1978).

[ADS](#) [CAS](#) [Google Scholar](#)

41. 41.

Dewaele, A., Eggert, J., Loubeyre, P. & LeToullec, R. Measurement of refractive index and equation of state in dense He, H<sub>2</sub>, H<sub>2</sub>O, and Ne under high pressure in a diamond anvil cell. *Phys. Rev. B* **67**, 094112 (2003).

[ADS](#) [Google Scholar](#)

42. 42.

Celliers, P. M. et al. Line-imaging velocimeter for shock diagnostics at the OMEGA laser facility. *Rev. Sci. Instrum.* **75**, 4916–4929 (2004).

[ADS](#) [CAS](#) [Google Scholar](#)

43. 43.

Miller, J. E. et al. Streaked optical pyrometer system for laser-driven shock-wave experiments on OMEGA. *Rev. Sci. Instrum.* **78**, 034903 (2007).

[ADS](#) [CAS](#) [PubMed](#) [PubMed Central](#) [Google Scholar](#)

44. 44.

Caillabet L., Mazevert, S. & Loubeyre, P. Multiphase equation of state of hydrogen from ab-initio calculations in the range 0.2 to 5 g/cc up to 10 eV. *Phys. Rev. B* **83**, 094101 (2011).

[ADS](#) [Google Scholar](#)

45. 45.

Eggert, J. et al. Melting temperature of diamond at ultra-high pressure. *Nat. Phys.* **6**, 40–43 (2010).

[CAS](#) [Google Scholar](#)

46. 46.

Walsh, J. M. & Christian, R. H. Equation of state of metals from shock wave measurements. *Phys. Rev.* **97**, 1544–1556 (1955).

[ADS](#) [CAS](#) [Google Scholar](#)

[Download references](#)

## Acknowledgements

We gratefully acknowledge M. Milleroux and F. Occelli for help in the preparation of the pre-compressed targets. We thank F. Soubiran and S. Hamel for useful discussions and F. Soubiran for sharing unpublished data. We thank the OMEGA laser facility management, staff and support crew for excellent shots and diagnostic support with special thanks to C. Sorce, A. Sorce and J. Kendrick. The OMEGA Laser Facility shots were allocated under the NLUF programme. Part of this work was prepared by LLNL under contract number DE-AC52-07NA27344 with support from LLNL LDRD programme and the US Department of Energy Fusion Energy Sciences Program. This work was performed under the auspices of a cooperation agreement CEA/DAM and DOE/NNSA on fundamental sciences. Partial funding for G.W.C. and J.R.R. was provided by NSF Physics Frontier Center award PHY-2020249 and DOE NNSA award DE6NA 0003856.

## Author information

## Affiliations

1. Commissariat à l'Énergie Atomique, DAM/DIF, Bruyères-le-Châtel, France  
S. Brygoo & P. Loubeyre
2. Lawrence Livermore National Laboratory, Livermore, CA, USA  
M. Millot, P. M. Celliers & J. H. Eggert
3. University of Rochester, Department of Mechanical Engineering, Physics and Astronomy, and Laboratory for Laser Energetics, Rochester, NY, USA  
J. R. Rygg & G. W. Collins
4. University of California, Berkeley, CA, USA  
R. Jeanloz

## Authors

1. S. Brygoo  
[View author publications](#)  
You can also search for this author in [PubMed](#) [Google Scholar](#)

2. P. Loubeyre  
[View author publications](#)  
You can also search for this author in [PubMed](#) [Google Scholar](#)

3. M. Millot  
[View author publications](#)  
You can also search for this author in [PubMed](#) [Google Scholar](#)

4. J. R. Rygg

[View author publications](#)

You can also search for this author in [PubMed](#) [Google Scholar](#)

5. P. M. Celliers

[View author publications](#)

You can also search for this author in [PubMed](#) [Google Scholar](#)

6. J. H. Eggert

[View author publications](#)

You can also search for this author in [PubMed](#) [Google Scholar](#)

7. R. Jeanloz

[View author publications](#)

You can also search for this author in [PubMed](#) [Google Scholar](#)

8. G. W. Collins

[View author publications](#)

You can also search for this author in [PubMed](#) [Google Scholar](#)

## **Contributions**

R.J., G.W.C. and P.L. designed the project and R.J. was PI of the NLUF proposal. P.L. and S.B. prepared the diamond-anvil cell targets. S.B. and M.M. conducted the OMEGA shots. S.B. and P.L. analysed the data. M.M. and J.R.R. contributed to the data analysis. All authors discussed the results and wrote the manuscript.

## **Corresponding authors**

Correspondence to [S. Brygoo](#) or [P. Loubeyre](#).

## **Ethics declarations**

## Competing interests

The authors declare no competing interests.

## Additional information

**Peer review information** *Nature* thanks Tristan Guillot, William Nellis and the other, anonymous, reviewer(s) for their contribution to the peer review of this work.

**Publisher's note** Springer Nature remains neutral with regard to jurisdictional claims in published maps and institutional affiliations.

## Extended data figures and tables

### [Extended Data Fig. 1 Compression data for the 11 mol% He mixture pre-compressed to 4 GPa.](#)

Full and open circles indicate experimental data obtained using diamond and sapphire anvils, respectively, with error bars including both random and systematic uncertainties (red shading indicates the pressure range over which our reflectivity measurements indicate immiscibility. Yellow and grey lines show simulation results for a 8 mol% He mixture<sup>29</sup>, and the Rostock equation of state (REOS) linear mixing calculation for the 11 mol% He mixture, respectively<sup>36</sup>. The theoretical Hugoniot curves begin at the same initial density as the experimental data points.

### [Extended Data Fig. 2 Temperature \(dark blue, left scale\) and pressure \(black, right scale\) versus shock velocity for the 11 mol% He mixture.](#)

Orange and red triangles denote, respectively, the temperatures and pressures at the shock velocities for which the two discontinuities in sample optical properties are experimentally observed (Figs. 2 and 3); these correspond to the two red triangles determining the immiscibility boundary

in Fig. 4 (values and uncertainties are listed in the table below). Yellow and red dashed lines connect the corresponding two points on the immiscibility boundary, and are distinct from the lower-pressure trends (black and dark-blue solid lines are illustrative guides to the eye). The breaks in trends shown here for temperature and pressure as functions of shock velocity in the H–He sample,  $T(U_s)$  and  $P(U_s)$ , offer independent evidence (from SOP intensities and VISAR timing, respectively) for the discontinuities identified in Fig. 2 from VISAR intensities. Based on thermodynamic scaling<sup>46</sup>, and not evident at the present scale, the low-pressure trends are expected to have positive curvature,  $T'(U_s)$  and  $P'(U_s) > 0$ . The apparent temperatures obtained between shock velocities of  $23 \text{ km s}^{-1}$  and  $28 \text{ km s}^{-1}$  lie below the red dashed line, implying anomalous thermal (temperature, thermal energy, specific heat) and/or optical properties in the region of immiscibility. The two experimentally determined ( $P$ ,  $T$ ) points on the immiscibility boundary line obtained from the figure are given in the table (uncertainties in last digit(s) given in parentheses).

### Extended Data Fig. 3 Reflectivity of pure hydrogen versus temperature and density.

Circles are the experimental data, previously published for densities below 0.32 g per mole (see ref. <sup>24</sup>) and unpublished for higher densities. The colour of each point indicates the measured reflectivity at the shock front, with background colour filling giving the fitted reflectivity. The hydrogen density is estimated using the ab initio equation of state of ref. <sup>44</sup>, which is in good agreement with experiment<sup>24</sup>. The density–temperature paths of the two H–He Hugoniot curves measured here, for 11 mol% He at 4 GPa pre-compression and for 33 mol% He at 2 GPa pre-compression, are plotted as full and dashed black lines respectively. The error bars have been estimated by propagating the random and systematic uncertainties in the case of pure hydrogen as for the present H–He measurements, as explained in Methods.

### Extended Data Fig. 4 Saturated value of reflectivity along the Hugoniot of the pre-compressed H–He mixture, shown as a function of He concentration.

Squares give the experimental values, as indicated by horizontal dashed lines in Fig. 3: blue and green for the 11 and 33 mol% He mixtures, respectively. Black points are from the calculations of ref. 25. The error bars are estimated from those of the reflectivity at saturation in pure hydrogen and in the H–He mixture.

### Extended Data Fig. 5 Energy versus temperature along the H–He Hugoniot for 11 mol% He mixture pre-compressed to 4 GPa.

Full and open circles are experimental data for diamond and sapphire anvils, respectively (red shading indicates the pressure range over which our reflectivity measurements indicate immiscibility); the orange solid line is the Hugoniot calculated for an 8 mol% He mixture<sup>29</sup>. Experiment and calculation are expected to have similar slopes below 2 kK, in the homogeneous H<sub>2</sub>–He mixture, and above 12 kK in the homogeneous H–He mixture. The dashed line is a smooth curve connecting these two slopes. The deviation from this smooth curve is associated with dissociation of molecular hydrogen, according to the calculation. A similar bump is observed in the experiments, concomitant with the sudden rise in reflectivity and thus signalling the transition to an electronically conducting state. Error bars are estimated by propagating random and systematic uncertainties as described in Methods.

### Extended Data Fig. 6 Boundary for He ionization.

Blue shading indicates where a few per cent ionization of He first appears, based on experimental He reflectivity measurements<sup>21</sup>, subsequently analysed by Soubiran<sup>30</sup> in the framework of an intrinsic semiconductor model with a bandgap energy depending on density and temperature. The blue dashed line is drawn using this He gap model<sup>30</sup>, and the REoS table to estimate the He density<sup>36</sup>. The intrinsic ionization fraction of He depends exponentially on the ratio of gap energy to temperature,  $E_g/k_B T$ . He ionization is considered sufficient to perturb H–He miscibility properties when the temperature exceeds  $T = E_g/3k_B$ , upon entering the blue-shaded

domain. The present Hugoniot data (open circles) are far from this boundary. Jupiter's internal isentrope crosses into the He ionization domain only near its central maximum pressure, implying that no He ionization should take place inside the planet. Error bars are those of the data in Table 1.

**Extended Data Fig. 7 Relative contributions of random and systematic uncertainties illustrated by the pressure-versus-compression and reflectivity-versus-temperature data points.**

In both figures, the inset is a zoom of the data point indicated by the circle.

**Extended Data Fig. 8 Reflectivity versus shock velocity obtained from the decaying shock analysis for all experiments.**

**a**, The plot is constructed by adding the reflectivity evolutions obtained from the decaying shock analysis of the VISAR images of all experiments (see [Supplementary Information](#)). The 5 different colours identify the 5 different experiments highlighted here around the two reflectivity discontinuous changes. All other experiments are plotted in grey. The discrete more accurate data points obtained at the quartz/H–He sample interface are plotted as circles. A crossover transition is observed at about  $28.5 \text{ km s}^{-1}$  between the high-reflectivity to the low-reflectivity behaviours as the H–He mixture goes from the demixed to the mixed states. **b–f**, The sample photos and the VISAR images of selected experiments, all using sapphire anvils, are shown. The blue lines represent the propagation of the quartz edge disturbances that can perturb the measurements at late time (see [Methods](#)). Error bars are estimated by propagating random and systematic uncertainties as described in Methods.

**Extended Data Table 1 H–He Hugoniot data for 11 mol% He pre-compressed to 4 GPa**

[Full size table](#)

**Extended Data Table 2 H–He Hugoniot data for 33 mol% He pre-compressed to 2 GPa**

[Full size table](#)

# Supplementary information

## Supplementary Information

This file contains a Supplementary Table showing decaying shock analysis for all experiments and an overview figure of the reflectivity versus shock velocity obtained from the decaying shocks of all experiments.

## Rights and permissions

### Reprints and Permissions

## About this article



Check for  
updates

## Cite this article

Brygoo, S., Loubeyre, P., Millot, M. *et al.* Evidence of hydrogen–helium immiscibility at Jupiter-interior conditions. *Nature* **593**, 517–521 (2021). <https://doi.org/10.1038/s41586-021-03516-0>

### Download citation

- Received: 13 October 2015
- Accepted: 06 April 2021
- Published: 26 May 2021
- Issue Date: 27 May 2021
- DOI: <https://doi.org/10.1038/s41586-021-03516-0>

# Comments

By submitting a comment you agree to abide by our [Terms](#) and [Community Guidelines](#). If you find something abusive or that does not comply with our terms or guidelines please flag it as inappropriate.

[Access through your institution](#)

[Change institution](#)

[Buy or subscribe](#)

Advertisement

---

This article was downloaded by **calibre** from <https://www.nature.com/articles/s41586-021-03516-0>

| [Section menu](#) | [Main menu](#) |

- Article
- [Published: 26 May 2021](#)

# The universal visitation law of human mobility

- [Markus Schläpfer<sup>1,2,3</sup> na1](#),
- [Lei Dong](#) [ORCID: orcid.org/0000-0002-1615-5424<sup>1,4</sup> na1](#),
- [Kevin O'Keeffe<sup>1</sup> na1](#),
- [Paolo Santi](#) [ORCID: orcid.org/0000-0002-8942-8702<sup>1,5</sup>](#),
- [Michael Szell](#) [ORCID: orcid.org/0000-0003-3022-2483<sup>1,6,7</sup>](#),
- [Hadrien Salat](#) [ORCID: orcid.org/0000-0003-0958-9715<sup>3,8</sup>](#),
- [Samuel Anklesaria<sup>1</sup>](#),
- [Mohammad Vazifeh<sup>1</sup>](#),
- [Carlo Ratti<sup>1</sup> na2](#) &
- [Geoffrey B. West<sup>2</sup> na2](#)

[Nature](#) volume 593, pages 522–527 (2021) [Cite this article](#)

- 4517 Accesses
- 305 Altmetric
- [Metrics details](#)

## Subjects

- [Geography](#)
- [Statistical physics](#)

## Abstract

Human mobility impacts many aspects of a city, from its spatial structure<sup>1,2,3</sup> to its response to an epidemic<sup>4,5,6,7</sup>. It is also ultimately key to social interactions<sup>8</sup>, innovation<sup>9,10</sup> and productivity<sup>11</sup>. However, our quantitative understanding of the aggregate movements of individuals remains incomplete. Existing models—such as the gravity law<sup>12,13</sup> or the radiation model<sup>14</sup>—concentrate on the purely spatial dependence of mobility flows and do not capture the varying frequencies of recurrent visits to the same locations. Here we reveal a simple and robust scaling law that captures the temporal and spatial spectrum of population movement on the basis of large-scale mobility data from diverse cities around the globe. According to this law, the number of visitors to any location decreases as the inverse square of the product of their visiting frequency and travel distance. We further show that the spatio-temporal flows to different locations give rise to prominent spatial clusters with an area distribution that follows Zipf's law<sup>15</sup>. Finally, we build an individual mobility model based on exploration and preferential return to provide a mechanistic explanation for the discovered scaling law and the emerging spatial structure. Our findings corroborate long-standing conjectures in human geography (such as central place theory<sup>16</sup> and Weber's theory of emergent optimality<sup>10</sup>) and allow for predictions of recurrent flows, providing a basis for applications in urban planning, traffic engineering and the mitigation of epidemic diseases.

## Access options

Subscribe to Journal

Get full journal access for 1 year

\$199.00

only \$3.90 per issue

[Subscribe](#)

All prices are NET prices.

VAT will be added later in the checkout.

Tax calculation will be finalised during checkout.

Rent or Buy article

Get time limited or full article access on ReadCube.

from \$8.99

[Rent or Buy](#)

All prices are NET prices.

### **Additional access options:**

- [Log in](#)
- [Access through your institution](#)
- [Learn about institutional subscriptions](#)

**Fig. 1: The universal distance–frequency distribution of population flows.**

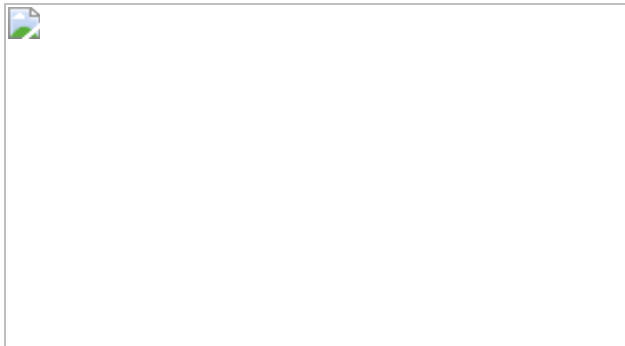


**Fig. 2: Constant effective travel distance per visitor.**

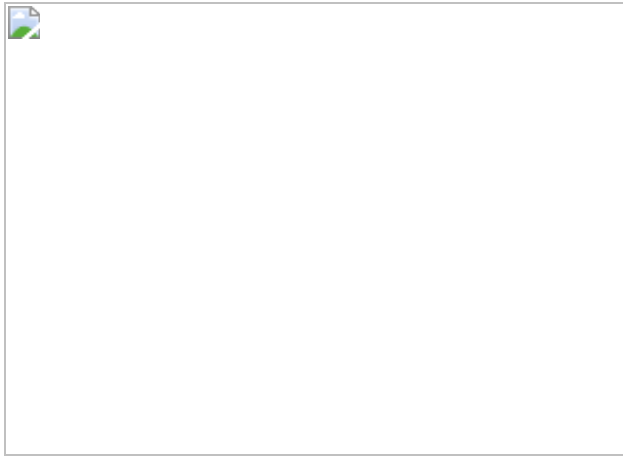


**Fig. 3: Spatial structure of the location-specific attractiveness.**

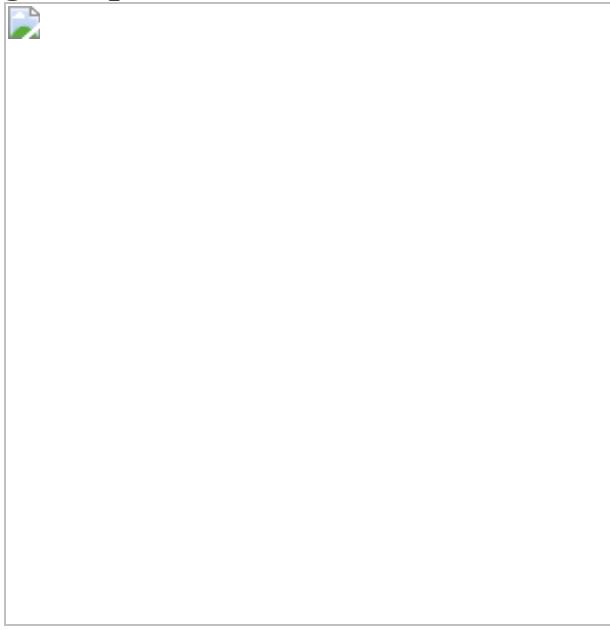
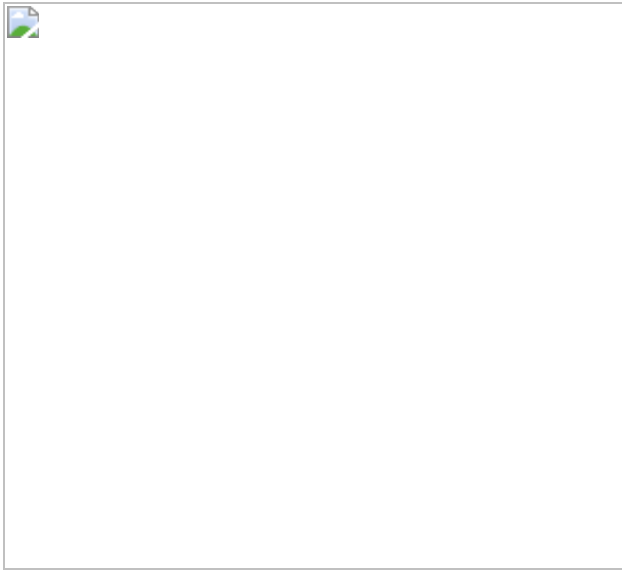


**Fig. 4: Microscopic model of spectral population flows.**



**Fig. 5: Predicting the flows between individual locations.**



## Data availability

Raw mobility data are not publicly available to preserve privacy. Grid-cell-level data to reproduce the findings of this study can be requested from the corresponding author.

## Code availability

The code to replicate this research can be requested from the corresponding author.

## References

1. 1.

Batty, M. *The New Science of Cities* (MIT Press, 2013).

2. 2.

Barthelemy, M. *The Structure and Dynamics of Cities* (Cambridge Univ. Press, 2016).

3. 3.

Louail, T. et al. Uncovering the spatial structure of mobility networks. *Nat. Commun.* **6**, 6007 (2015).

[ADS](#) [CAS](#) [Article](#) [Google Scholar](#)

4. 4.

Anderson, R. M. & May, R. M. *Infectious Diseases of Humans: Dynamics and Control* (Oxford Univ. Press, 1991).

5. 5.

Eubank, S. et al. Modelling disease outbreaks in realistic urban social networks. *Nature* **429**, 180–184 (2004).

[ADS](#) [CAS](#) [Article](#) [Google Scholar](#)

6. 6.

Wesolowski, A. et al. Quantifying the impact of human mobility on malaria. *Science* **338**, 267–270 (2012).

[ADS](#) [CAS](#) [Article](#) [Google Scholar](#)

7. 7.

Jia, J. S. et al. Population flow drives spatio-temporal distribution of COVID-19 in China. *Nature* **582**, 389–394 (2020).

[ADS](#) [CAS](#) [Article](#) [Google Scholar](#)

8. 8.

Bettencourt, L. M. A. The origins of scaling in cities. *Science* **340**, 1438–1441 (2013).

[ADS](#) [MathSciNet](#) [CAS](#) [Article](#) [Google Scholar](#)

9. 9.

Glaeser, E. L., Kallal, H. D., Scheinkman, J. A. & Shleifer, A. Growth in cities. *J. Polit. Econ.* **100**, 1126–1152 (1992).

[Article](#) [Google Scholar](#)

10. 10.

Fujita, M., Krugman, P. R. & Venables, A. J. *The Spatial Economy: Cities, Regions, and International Trade* (MIT Press, 1999).

11. 11.

Sveikauskas, L. The productivity of cities. *Q. J. Econ.* **89**, 393–413 (1975).

[Article](#) [Google Scholar](#)

12. 12.

Zipf, G. K. The P1P2/D hypothesis: on the intercity movement of persons. *Am. Sociol. Rev.* **11**, 677–686 (1946).

[Article](#) [Google Scholar](#)

13. 13.

Erlander, S. & Stewart, N. F. *The Gravity Model in Transportation Analysis: Theory and Extensions* (CRC Press, 1990).

14. 14.

Simini, F., González, M. C., Maritan, A. & Barabási, A.-L. A universal model for mobility and migration patterns. *Nature* **484**, 96–100 (2012).

[ADS](#) [CAS](#) [Article](#) [Google Scholar](#)

15. 15.

Zipf, G. K. *Human Behavior and the Principle of Least Effort* (Addison-Wesley, 1949).

16. 16.

Christaller, W. *Die zentralen Orte in Süddeutschland* (Gustav Fischer, 1933).

17. 17.

Pan, W., Ghoshal, G., Krumme, C., Cebrian, M. & Pentland, A. Urban characteristics attributable to density-driven tie formation. *Nat. Commun.* **4**, 1961 (2013).

[ADS](#) [Article](#) [Google Scholar](#)

18. 18.

Schlüpfner, M. et al. The scaling of human interactions with city size. *J. R. Soc. Interface* **11**, 20130789 (2014).

[Article](#) [Google Scholar](#)

19. 19.

Li, R. et al. Simple spatial scaling rules behind complex cities. *Nat. Commun.* **8**, 1841 (2017).

[ADS](#) [Article](#) [Google Scholar](#)

20. 20.

Anas, A., Arnott, R. & Small, K. A. Urban spatial structure. *J. Econ. Lit.* **36**, 1426–1464 (1998).

[Google Scholar](#)

21. 21.

Henderson, V. & Thisse, J.-F. *Handbook of Regional and Urban Economics: Cities and Geography* (Elsevier, 2004).

22. 22.

Ewing, R. & Hamidi, S. Compactness versus sprawl: a review of recent evidence from the United States. *J. Plann. Lit.* **30**, 413–432 (2015).

[Article](#) [Google Scholar](#)

23. 23.

Chang, S. et al. Mobility network models of COVID-19 explain inequities and inform reopening. *Nature* **589**, 82–87 (2021).

[ADS](#) [CAS](#) [Article](#) [Google Scholar](#)

24. 24.

Axhausen, K. W. & Gärling, T. Activity-based approaches to travel analysis: conceptual frameworks, models, and research problems. *Transp. Rev.* **12**, 323–341 (1992).

[Article](#) [Google Scholar](#)

25. 25.

Barbosa, H. et al. Human mobility: models and applications. *Phys. Rep.* **734**, 1–74 (2018).

[ADS](#) [MathSciNet](#) [Article](#) [Google Scholar](#)

26. 26.

Stouffer, S. A. Intervening opportunities: a theory relating mobility and distance. *Am. Sociol. Rev.* **5**, 845–867 (1940).

[Article](#) [Google Scholar](#)

27. 27.

Noulas, A., Scellato, S., Lambiotte, R., Pontil, M. & Mascolo, C. A tale of many cities: universal patterns in human urban mobility. *PLoS ONE* **7**, e37027 (2012); correction **7**, <https://doi.org/10.1371/annotation/ca85bf7a-7922-47d5-8bfb-bcdf25af8c72> (2012).

[ADS](#) [CAS](#) [Article](#) [PubMed](#) [PubMed Central](#) [Google Scholar](#)

28. 28.

Yan, X.-Y., Wang, W.-X., Gao, Z.-Y. & Lai, Y.-C. Universal model of individual and population mobility on diverse spatial scales. *Nat. Commun.* **8**, 1639 (2017).

[ADS](#) [Article](#) [Google Scholar](#)

29. 29.

Mazzoli, M. et al. Field theory for recurrent mobility. *Nat. Commun.* **10**, 3895 (2019).

[ADS](#) [Article](#) [Google Scholar](#)

30. 30.

Brockmann, D., Hufnagel, L. & Geisel, T. The scaling laws of human travel. *Nature* **439**, 462–465 (2006).

[ADS](#) [CAS](#) [Article](#) [Google Scholar](#)

31. 31.

Gonzalez, M. C., Hidalgo, C. A. & Barabási, A.-L. Understanding individual human mobility patterns. *Nature* **453**, 779–782 (2008); addendum **453**, 779–782 (2008).

[ADS](#) [CAS](#) [Article](#) [Google Scholar](#)

32. 32.

Song, C., Koren, T., Wang, P. & Barabási, A.-L. Modelling the scaling properties of human mobility. *Nat. Phys.* **6**, 818–823 (2010).

[CAS](#) [Article](#) [Google Scholar](#)

33. 33.

Alessandretti, L., Aslak, U. & Lehmann, S. The scales of human mobility. *Nature* **587**, 402–407 (2020).

[ADS](#) [Article](#) [Google Scholar](#)

34. 34.

Bertaud, A. *Order Without Design: How Markets Shape Cities* (MIT Press, 2018).

35. 35.

Louail, T. et al. From mobile phone data to the spatial structure of cities. *Sci. Rep.* **4**, 5276 (2014).

[CAS](#) [Article](#) [Google Scholar](#)

36. 36.

Zhong, C. et al. Revealing centrality in the spatial structure of cities from human activity patterns. *Urban Stud.* **54**, 437–455 (2017).

[Article](#) [Google Scholar](#)

37. 37.

Rozenfeld, H. D. et al. Laws of population growth. *Proc. Natl Acad. Sci. USA* **105**, 18702–18707 (2008).

[ADS](#) [CAS](#) [Article](#) [Google Scholar](#)

38. 38.

Cao, W., Dong, L., Wu, L. & Liu, Y. Quantifying urban areas with multi-source data based on percolation theory. *Remote Sens. Environ.* **241**, 111730 (2020).

[ADS](#) [Article](#) [Google Scholar](#)

39. 39.

Batty, M. The size, scale, and shape of cities. *Science* **319**, 769–771 (2008).

[ADS](#) [CAS](#) [Article](#) [Google Scholar](#)

40. 40.

Rozenfeld, H. D., Rybski, D., Gabaix, X. & Makse, H. A. The area and population of cities: new insights from a different perspective on cities. *Am. Econ. Rev.* **101**, 2205–2225 (2011).

[Article](#) [Google Scholar](#)

41. 41.

Pappalardo, L. et al. Returners and explorers dichotomy in human mobility. *Nat. Commun.* **6**, 8166 (2015).

[ADS](#) [Article](#) [Google Scholar](#)

42. 42.

Weber, A. & Friedrich, C. J. *Alfred Weber's Theory of the Location of Industries* (Univ. Chicago Press, 1929).

43. 43.

Kreps, D. M. *Game Theory and Economic Modelling* (Oxford Univ. Press, 1990).

44. 44.

Myerson, R. B. *Game Theory* (Harvard Univ. Press, 2013).

45. 45.

Blondel, V. D., Decuyper, A. & Krings, G. A survey of results on mobile phone datasets analysis. *EPJ Data Sci.* **4**, 10 (2015).

[Article](#) [Google Scholar](#)

46. 46.

Calabrese, F., Diao, M., Di Lorenzo, G., Ferreira, J. Jr & Ratti, C. Understanding individual mobility patterns from urban sensing data: a mobile phone trace example. *Transp. Res. Part C* **26**, 301–313 (2013).

[Article](#) [Google Scholar](#)

47. 47.

de Montjoye, Y.-A., Smoreda, Z., Trinquart, R., Ziemlicki, C. & Blondel, V. D. D4D-Senegal: the second mobile phone data for development challenge. Preprint at <https://arxiv.org/abs/1407.4885> (2014).

48. 48.

Blondel, V. D. et al. Data for development: the D4D challenge on mobile phone data. Preprint at <https://arxiv.org/abs/1210.0137> (2012).

49. 49.

Jiang, S. et al. The TimeGeo modeling framework for urban mobility without travel surveys. *Proc. Natl Acad. Sci. USA* **113**, E5370–E5378 (2016); correction **113**, E7137 (2016).

50. 50.

Song, C., Qu, Z., Blumm, N. & Barabási, A.-L. Limits of predictability in human mobility. *Science* **327**, 1018–1021 (2010).

[ADS](#) [MathSciNet](#) [CAS](#) [Article](#) [Google Scholar](#)

51. 51.

Wilson, A. G. The use of entropy maximising models in the theory of trip distribution, mode split and route split. *J. Transp. Econ. Policy* **3**, 108–126 (1969).

[Google Scholar](#)

52. 52.

Masucci, A. P., Serras, J., Johansson, A. & Batty, M. Gravity versus radiation models: on the importance of scale and heterogeneity in commuting flows. *Phys. Rev. E* **88**, 022812 (2013).

[ADS](#) [Article](#) [Google Scholar](#)

[Download references](#)

## Acknowledgements

We thank L. M. A. Bettencourt, R. Sinatra, P. Herthogs, G. Du, Y. Qin and Y. Liu for helpful discussions; W. Cao for assistance with performing the CCA analysis; and S. Grauwin for providing the MATLAB code for the radiation model. We acknowledge Airsage, ORANGE/SONATEL and Singtel for providing the data. This work was supported by the National Science Foundation (grant number PHY1838420), the AT&T Foundation, the MIT SMART programme, the MIT CCES programme, Audi Volkswagen, BBVA, Ericsson, Ferrovial, GE, the MIT Senseable City Lab Consortium, the John Templeton Foundation (grant number 15705), the Eugene and Clare Thaw Charitable Trust, Toby Shannan, the Charities Aid Foundation of Canada, the US Army Research Office Minerva Programme (grant number W911NF-12-1-0097), the Singapore National Research

Foundation (FI 370074016) and the National Natural Science Foundation of China (grant number 41801299).

## Author information

### Author notes

1. These authors contributed equally: Markus Schläpfer, Lei Dong, Kevin O’Keeffe
2. These authors jointly supervised this work: Carlo Ratti, Geoffrey B. West

### Affiliations

1. Senseable City Laboratory, Massachusetts Institute of Technology, Cambridge, MA, USA

Markus Schläpfer, Lei Dong, Kevin O’Keeffe, Paolo Santi, Michael Szell, Samuel Anklesaria, Mohammad Vazifeh & Carlo Ratti

2. Santa Fe Institute, Santa Fe, NM, USA

Markus Schläpfer & Geoffrey B. West

3. Future Cities Laboratory, Singapore-ETH Centre, ETH Zurich, Singapore, Singapore

Markus Schläpfer & Hadrien Salat

4. Institute of Remote Sensing and Geographical Information Systems, School of Earth and Space Sciences, Peking University, Beijing, China

Lei Dong

5. Istituto di Informatica e Telematica del CNR, Pisa, Italy

Paolo Santi

6. IT University of Copenhagen, Copenhagen, Denmark

Michael Szell

7. ISI Foundation, Turin, Italy

Michael Szell

8. Sociology and Economics of Networks and Services, Orange Labs,  
Châtillon, France

Hadrien Salat

## Authors

1. Markus Schläpfer

[View author publications](#)

You can also search for this author in [PubMed](#) [Google Scholar](#)

2. Lei Dong

[View author publications](#)

You can also search for this author in [PubMed](#) [Google Scholar](#)

3. Kevin O'Keeffe

[View author publications](#)

You can also search for this author in [PubMed](#) [Google Scholar](#)

4. Paolo Santi

[View author publications](#)

You can also search for this author in [PubMed](#) [Google Scholar](#)

5. Michael Szell

[View author publications](#)

You can also search for this author in [PubMed](#) [Google Scholar](#)

6. Hadrien Salat

[View author publications](#)

You can also search for this author in [PubMed](#) [Google Scholar](#)

7. Samuel Anklesaria

[View author publications](#)

You can also search for this author in [PubMed](#) [Google Scholar](#)

8. Mohammad Vazifeh

[View author publications](#)

You can also search for this author in [PubMed](#) [Google Scholar](#)

9. Carlo Ratti

[View author publications](#)

You can also search for this author in [PubMed](#) [Google Scholar](#)

10. Geoffrey B. West

[View author publications](#)

You can also search for this author in [PubMed](#) [Google Scholar](#)

## Contributions

G.B.W., C.R., M. Schläpfer, L.D., K.O. and P.S. designed the research. L.D., M. Schläpfer, K.O. and M.V. processed and analysed the data. G.B.W. and M. Schläpfer identified the data collapse to a single, universal curve. K.O., L.D., S.A. and P.S. developed the PEPR model. H.S., M. Schläpfer and G.B.W. developed the theoretical argument. M.V. and P.S. tested the Fermat–Toricelli–Weber metric. L.D., M. Schläpfer, K.O., M. Szell, P.S., G.B.W. and C.R. wrote the paper. C.R. and G.B.W. contributed equally as senior authors. All authors discussed the results and reviewed the manuscript.

## Corresponding author

Correspondence to [Lei Dong](#).

## Ethics declarations

### Competing interests

The authors declare no competing interests.

## Additional information

**Peer review information** *Nature* thanks Laura Alessandretti, Marc Barthelemy and the other, anonymous, reviewer(s) for their contribution to the peer review of this work.

**Publisher's note** Springer Nature remains neutral with regard to jurisdictional claims in published maps and institutional affiliations.

## Extended data figures and tables

### [Extended Data Fig. 1 The spatio-temporal structure of movement in cities.](#)

Panels show visitor influx maps for Greater Boston for different parameters  $(r, f)$ . The colour of each grid cell ( $500 \text{ m} \times 500 \text{ m}$ ) indicates the value of the spectral flow  $\rho$ . Remarkably, visitor influx maps for the same quantity  $v = rf$  are nearly identical, as is clear from viewing along the diagonals indicated by the coloured arrows in the figure. Hence, doubling the visitation frequency  $f$  (from top row to bottom row) results in the same quantitative decrease of the influx as doubling the travel distance  $r$  (from left column to right column).

### [Extended Data Fig. 2 Empirical power-law exponents of the distance–frequency distribution.](#)

**a**, Histogram of the exponents for all locations in the Greater Boston area. The values were determined using ordinary least squares minimization to a linear relation of the logarithmically transformed variables. The red line shows  $\eta = 2$ , consistent with our theoretical argument. **b**, Corresponding histogram of the  $R^2$  values.

**Extended Data Fig. 3 Universality of the scaling relation  $\rho \propto (rf)^{-2}$  across Greater Boston.**

The panels depict the data for individual locations (500 m  $\times$  500 m grid cells), ranked according to the total number of visitors from neighbouring cells. Shown are locations of rank 1–30 (from top left to bottom right). The geographic coordinates of each location (latitude and longitude of the centre point of the grid cell) are indicated. The straight lines denote the inverse square of  $rf$  (slope = −2), consistent with our theoretical argument.

**Extended Data Fig. 4 Universality of the scaling relation  $\rho \propto (rf)^{-2}$  across Portugal.**

The panels depict the data for individual locations (1 km  $\times$  1 km grid cells), ranked according to the total number of visitors from neighbouring cells. Shown are locations of rank 1–30 (from top left to bottom right). The geographic coordinates of each location (latitude and longitude of the centre point of the grid cell) are indicated. The straight lines denote the inverse square of  $rf$  (slope = −2), consistent with our theoretical argument.

**Extended Data Fig. 5 Universality of the scaling relation  $\rho \propto (rf)^{-2}$  across Dakar.**

The panels depict the data for individual locations (1 km  $\times$  1 km grid cells), ranked according to the total number of visitors from neighbouring cells. Shown are locations of rank 1–30 (from top left to bottom right). The geographic coordinates of each location (latitude and longitude of the centre point of the grid cell) are indicated. The straight lines denote the inverse square of  $rf$  (slope = −2), consistent with our theoretical argument.

## Extended Data Fig. 6 Universality of the scaling relation $\rho \propto (rf)^{-2}$ across Singapore.

The panels depict the data for individual locations (500 m × 500 m grid cells), ranked according to the total number of visitors from neighbouring cells. Shown are locations of rank 1–30 (from top left to bottom right). The geographic coordinates of each location (latitude and longitude of the centre point of the grid cell) are indicated. The straight lines denote the inverse square of  $rf$  (slope = −2), consistent with our theoretical argument.

## Extended Data Fig. 7 Simulation results of the EPR model.

**a, b**, Generated number of visits (**a**) and attractiveness values  $\mu_i$  (**b**). **c, d**, The EPR model generates the  $rf$  scaling of the population flows with a scaling exponent that is in remarkable agreement with the data. The generated visitor counts,  $N_i(r, f)$ , are shown in **c**, and the resulting  $rf$  scaling of the spectral flows,  $\rho_i(r, f)$ , is shown in **d**. The generated attractiveness values  $\mu_i$  are rather homogeneous and uniform across space, which is in contrast to the empirical data (**b**). Model parameters are taken from Song et al.<sup>32</sup> (Methods).

## Extended Data Fig. 8 Estimation of the magnitude of flows from population density $\rho_{\text{pop}}$ .

The schematic shows a zoom-in on the immediate vicinity of a destination location  $j$  (small values of  $r$ ), where it is reasonable to assume that  $\rho_{\text{pop}}(j) \approx \text{constant}$ . Hence, the local population density imposes an upper bound on the influx,  $\int \rho_j df \leq \rho_{\text{pop}}(j)$ . A simple boundary condition of the continuous model then dictates that the minimum visiting frequency of all individuals living directly on the boundary (each being assigned to a point at  $r = r_j$ ) assumes the minimum frequency with which the individuals living inside the attracting location return home,  $f_{\min} \approx f_{\text{home}}$ . The minimum distance  $r_{\min}$  for locations from which individuals visit with minimum frequency  $f_{\min} < f_{\text{home}}$  increases with decreasing value of  $f_{\min}$ .

## Extended Data Fig. 9 CPT and radius of attraction.

**a**, Schematics of CPT, showing the spatial arrangement of three tiers of centres (see Supplementary Information for details). This hierarchical arrangement of central places results in the most efficient transport network. **b–f**, Average travel distance per visit  $\langle r \rangle_f$  to perform activities with fixed visiting frequency  $f$  across all locations in Greater Boston (**b**), Singapore (**c**), Dakar (**d**), Abidjan (**e**) and Lisbon (**f**). We find a clear inverse relation,  $\langle r \rangle_f \propto 1/f$ . The quantity  $\langle r \rangle_f$  can be interpreted as the characteristic distance associated with the level of specialization of the functions provided by the locations.

## Extended Data Fig. 10 Fermat–Torricelli–Weber (FTW) efficiency of collective human movements.

**a**, The schematic shows how the FTW efficiency is computed (see Supplementary Information). The effective distance travelled by the visitors of a specific location (cell) can be minimized by moving it on the grid. The efficiency is  $(\Delta D)/D$ , which is the ratio between the reduction of the effective travel distance of all visitors when moving the cell from its actual location to the optimum FTW point ( $\Delta D$ ) and the actual effective travel distance of all visitors to that cell ( $D$ ). **b**, Density plots representing the number of cells with a given number of visits and FTW efficiency for the Greater Boston area (for the month of August 2009). The FTW efficiency is computed for each cell based on visits made by visitors who live at distances larger than a given threshold value  $r_{\text{thr}}$ . For  $r_{\text{thr}} = 0$  (top left), the density of locations is particularly high where the FTW efficiency is very high. As the number of visits is increased, the distribution becomes narrower and the FTW efficiency increases. This pattern is generally also valid for larger values of  $r_{\text{thr}}$  but becomes weaker.

## Supplementary information

### Supplementary Information

This file contains supplementary text, supplementary figures 1 – 28, supplementary equations 1 – 10 and supplementary references.

## Rights and permissions

### [Reprints and Permissions](#)

## About this article



Check for  
updates

## Cite this article

Schläpfer, M., Dong, L., O’Keeffe, K. *et al.* The universal visitation law of human mobility. *Nature* **593**, 522–527 (2021).  
<https://doi.org/10.1038/s41586-021-03480-9>

### [Download citation](#)

- Received: 30 May 2017
- Accepted: 22 March 2021
- Published: 26 May 2021
- Issue Date: 27 May 2021
- DOI: <https://doi.org/10.1038/s41586-021-03480-9>

## Comments

By submitting a comment you agree to abide by our [Terms](#) and [Community Guidelines](#). If you find something abusive or that does not comply with our terms or guidelines please flag it as inappropriate.

[Access through your institution](#)  
[Change institution](#)  
[Buy or subscribe](#)

## Associated Content

### [Trip frequency is key ingredient in new law of human travel](#)

- Laura Alessandretti
- Sune Lehmann

Nature News & Views 26 May 2021

Advertisement

---

This article was downloaded by **calibre** from <https://www.nature.com/articles/s41586-021-03480-9>

| [Section menu](#) | [Main menu](#) |

- Article
- [Published: 26 May 2021](#)

# Long-range nontopological edge currents in charge-neutral graphene

- [A. Aharon-Steinberg](#) ORCID: orcid.org/0000-0002-0024-6014<sup>1 na1</sup>,
- [A. Marguerite](#) ORCID: orcid.org/0000-0002-0916-6176<sup>1 na1</sup>,
- [D. J. Perello](#)<sup>2</sup>,
- [K. Bagani](#) ORCID: orcid.org/0000-0001-8136-0806<sup>1</sup>,
- [T. Holder](#) ORCID: orcid.org/0000-0003-1365-4276<sup>1</sup>,
- [Y. Myasoedov](#)<sup>1</sup>,
- [L. S. Levitov](#)<sup>3</sup>,
- [A. K. Geim](#)<sup>2</sup> &
- [E. Zeldov](#) ORCID: orcid.org/0000-0002-8200-4974<sup>1</sup>

[Nature](#) volume 593, pages 528–534 (2021) [Cite this article](#)

- 1316 Accesses
- 13 Altmetric
- [Metrics details](#)

## Subjects

- [Electronic properties and devices](#)
- [Electronic properties and materials](#)
- [Imaging techniques](#)
- [Quantum Hall](#)

- [Two-dimensional materials](#)

## Abstract

Van der Waals heterostructures display numerous unique electronic properties. Nonlocal measurements, wherein a voltage is measured at contacts placed far away from the expected classical flow of charge carriers, have been widely used in the search for novel transport mechanisms, including dissipationless spin and valley transport<sup>1,2,3,4,5,6,7,8,9</sup>, topological charge-neutral currents<sup>10,11,12</sup>, hydrodynamic flows<sup>13</sup> and helical edge modes<sup>14,15,16</sup>. Monolayer<sup>1,2,3,4,5,10,15,16,17,18,19</sup>, bilayer<sup>9,11,14,20</sup> and few-layer<sup>21</sup> graphene, transition-metal dichalcogenides<sup>6,7</sup> and moiré superlattices<sup>8,10,12</sup> have been found to display pronounced nonlocal effects. However, the origin of these effects is hotly debated<sup>3,11,17,22,23,24</sup>. Graphene, in particular, exhibits giant nonlocality at charge neutrality<sup>1,15,16,17,18,19</sup>, a striking behaviour that has attracted competing explanations. Using a superconducting quantum interference device on a tip (SQUID-on-tip) for nanoscale thermal and scanning gate imaging<sup>25</sup>, here we demonstrate that the commonly occurring charge accumulation at graphene edges<sup>23,26,27,28,29,30,31</sup> leads to giant nonlocality, producing narrow conductive channels that support long-range currents. Unexpectedly, although the edge conductance has little effect on the current flow in zero magnetic field, it leads to field-induced decoupling between edge and bulk transport at moderate fields. The resulting giant nonlocality at charge neutrality and away from it produces exotic flow patterns that are sensitive to edge disorder, in which charges can flow against the global electric field. The observed one-dimensional edge transport is generic and nontopological and is expected to support nonlocal transport in many electronic systems, offering insight into the numerous controversies and linking them to long-range guided electronic states at system edges.

## Access options

Subscribe to Journal

Get full journal access for 1 year

\$199.00

only \$3.90 per issue

[Subscribe](#)

All prices are NET prices.

VAT will be added later in the checkout.

Tax calculation will be finalised during checkout.

Rent or Buy article

Get time limited or full article access on ReadCube.

from \$8.99

[Rent or Buy](#)

All prices are NET prices.

### **Additional access options:**

- [Log in](#)
- [Access through your institution](#)
- [Learn about institutional subscriptions](#)

**Fig. 1: Nonlocal transport characteristics.**

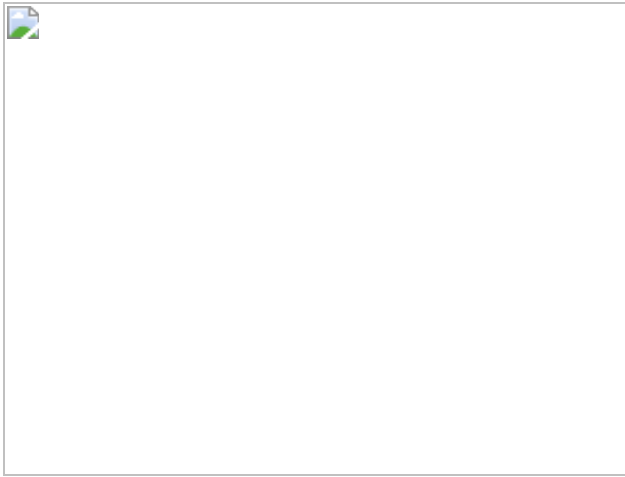


**Fig. 2: Scanning SOT thermal imaging of the graphene sample at 4.2 K.**

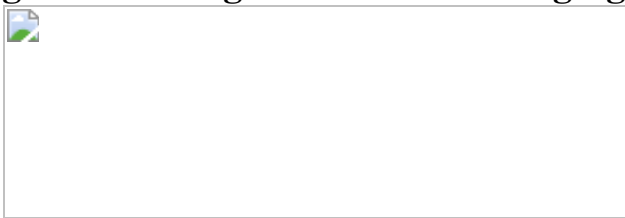


**Fig. 3: Scanning gate microscopy at  $B = 5$  T.**

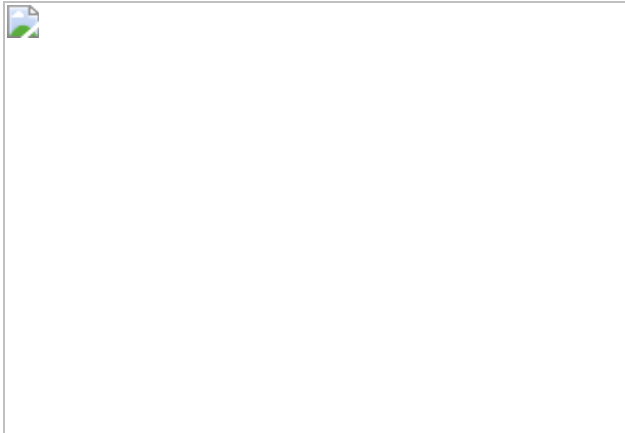
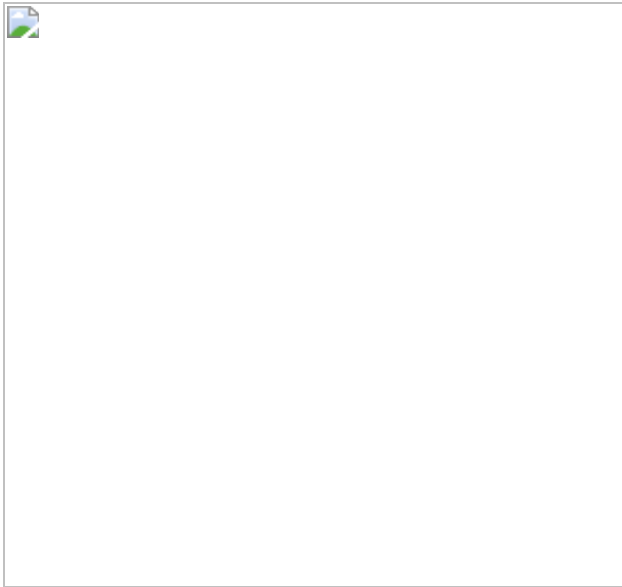


**Fig. 4: Numerical simulations of the nonlocal transport.**



## Data availability

The data that support the findings of this study are available from the corresponding authors on reasonable request.

## Code availability

The COMSOL simulation codes used in this study are available from the corresponding authors on reasonable request.

## References

1. 1.

Abanin, D. A. et al. Giant nonlocality near the Dirac point in graphene. *Science* **332**, 328–330 (2011).

[ADS](#) [CAS](#) [PubMed](#) [PubMed Central](#) [Google Scholar](#)

2. 2.

Balakrishnan, J., Kok Wai Koon, G., Jaiswal, M., Castro Neto, A. H. & Özyilmaz, B. Colossal enhancement of spin–orbit coupling in weakly hydrogenated graphene. *Nat. Phys.* **9**, 284–287 (2013).

[CAS](#) [Google Scholar](#)

3. 3.

Völk, T. et al. Absence of a giant spin Hall effect in plasma-hydrogenated graphene. *Phys. Rev. B* **99**, 085401 (2019).

[ADS](#) [Google Scholar](#)

4. 4.

Wei, P. et al. Strong interfacial exchange field in the graphene/EuS heterostructure. *Nat. Mater.* **15**, 711–716 (2016).

[ADS](#) [CAS](#) [PubMed](#) [PubMed Central](#) [Google Scholar](#)

5. 5.

Stepanov, P. et al. Long-distance spin transport through a graphene quantum Hall antiferromagnet. *Nat. Phys.* **14**, 907–911 (2018); correction **14**, 967 (2018).

[CAS](#) [Google Scholar](#)

6. 6.

Wu, Z. et al. Intrinsic valley Hall transport in atomically thin MoS<sub>2</sub>. *Nat. Commun.* **10**, 611 (2019).

[ADS](#) [CAS](#) [PubMed](#) [PubMed Central](#) [Google Scholar](#)

7. 7.

Hung, T. Y. T., Rustagi, A., Zhang, S., Upadhyaya, P. & Chen, Z. Experimental observation of coupled valley and spin Hall effect in p-

doped WSe<sub>2</sub> devices. *InfoMat* **2**, 968–974 (2020).

[CAS](#) [Google Scholar](#)

8. 8.

Sinha, S. et al. Bulk valley transport and Berry curvature spreading at the edge of flat bands. *Nat. Commun.* **11**, 5548 (2020).

[ADS](#) [CAS](#) [PubMed](#) [PubMed Central](#) [Google Scholar](#)

9. 9.

Tanaka, M. et al. Charge neutral current generation in a spontaneous quantum Hall antiferromagnet. *Phys. Rev. Lett.* **126**, 016801 (2021).

[ADS](#) [CAS](#) [PubMed](#) [PubMed Central](#) [Google Scholar](#)

10. 10.

Gorbachev, R. V. et al. Detecting topological currents in graphene superlattices. *Science* **346**, 448–451 (2014).

[ADS](#) [CAS](#) [PubMed](#) [PubMed Central](#) [Google Scholar](#)

11. 11.

Sui, M. et al. Gate-tunable topological valley transport in bilayer graphene. *Nat. Phys.* **11**, 1027–1031 (2015).

[CAS](#) [Google Scholar](#)

12. 12.

Ma, C. et al. Moiré band topology in twisted bilayer graphene. *Nano Lett.* **20**, 6076–6083 (2020).

[ADS](#) [CAS](#) [PubMed](#) [PubMed Central](#) [Google Scholar](#)

13. 13.

Bandurin, D. A. et al. Negative local resistance caused by viscous electron backflow in graphene. *Science* **351**, 1055–1058 (2016).

[ADS](#) [CAS](#) [PubMed](#) [PubMed Central](#) [Google Scholar](#)

14. 14.

Tiwari, P., Srivastav, S. K., Ray, S., Das, T. & Bid, A. Observation of time-reversal invariant helical edge modes in bilayer graphene/WSe<sub>2</sub> heterostructure. *ACS Nano* **15**, 916–922 (2021).

[CAS](#) [PubMed](#) [PubMed Central](#) [Google Scholar](#)

15. 15.

Li, Y. et al. Transition between canted antiferromagnetic and spin-polarized ferromagnetic quantum Hall states in graphene on a ferrimagnetic insulator. *Phys. Rev. B* **101**, 241405 (2020).

[ADS](#) [CAS](#) [Google Scholar](#)

16. 16.

Veyrat, L. et al. Helical quantum Hall phase in graphene on SrTiO<sub>3</sub>. *Science* **367**, 781–786 (2020).

[ADS](#) [CAS](#) [PubMed](#) [PubMed Central](#) [Google Scholar](#)

17. 17.

Ribeiro, M., Power, S. R., Roche, S., Hueso, L. E. & Casanova, F. Scale-invariant large nonlocality in polycrystalline graphene. *Nat. Commun.* **8**, 2198 (2017).

[ADS](#) [PubMed](#) [PubMed Central](#) [Google Scholar](#)

18. 18.

Wei, D. S. et al. Electrical generation and detection of spin waves in a quantum Hall ferromagnet. *Science* **362**, 229–233 (2018).

[ADS](#) [CAS](#) [PubMed](#) [PubMed Central](#) [Google Scholar](#)

19. 19.

Nachawaty, A. et al. Large nonlocality in macroscopic Hall bars made of epitaxial graphene. *Phys. Rev. B* **98**, 045403 (2018).

[ADS](#) [CAS](#) [Google Scholar](#)

20. 20.

Shimazaki, Y. et al. Generation and detection of pure valley current by electrically induced Berry curvature in bilayer graphene. *Nat. Phys.* **11**, 1032–1036 (2015).

[CAS](#) [Google Scholar](#)

21. 21.

Gopinadhan, K. et al. Extremely large magnetoresistance in few-layer graphene/boron–nitride heterostructures. *Nat. Commun.* **6**, 8337 (2015).

[ADS](#) [CAS](#) [PubMed](#) [PubMed Central](#) [Google Scholar](#)

22. 22.

Renard, J., Studer, M. & Folk, J. A. Origins of nonlocality near the neutrality point in graphene. *Phys. Rev. Lett.* **112**, 116601 (2014).

[ADS](#) [PubMed](#) [PubMed Central](#) [Google Scholar](#)

23. 23.

Marmolejo-Tejada, J. M. et al. Deciphering the origin of nonlocal resistance in multiterminal graphene on hexagonal-boron-nitride with

ab initio quantum transport: Fermi surface edge currents rather than Fermi sea topological valley currents. *J. Phys. Mater.* **1**, 015006 (2018).

[CAS](#) [Google Scholar](#)

24. 24.

Van Tuan, D. et al. Spin Hall effect and origins of nonlocal resistance in adatom-decorated graphene. *Phys. Rev. Lett.* **117**, 176602 (2016).

[ADS](#) [PubMed](#) [PubMed Central](#) [Google Scholar](#)

25. 25.

Halbertal, D. et al. Nanoscale thermal imaging of dissipation in quantum systems. *Nature* **539**, 407–410 (2016).

[ADS](#) [CAS](#) [PubMed](#) [PubMed Central](#) [Google Scholar](#)

26. 26.

Chae, J. et al. Enhanced carrier transport along edges of graphene devices. *Nano Lett.* **12**, 1839–1844 (2012).

[ADS](#) [CAS](#) [PubMed](#) [PubMed Central](#) [Google Scholar](#)

27. 27.

Allen, M. T. et al. Spatially resolved edge currents and guided-wave electronic states in graphene. *Nat. Phys.* **12**, 128–133 (2016).

[CAS](#) [Google Scholar](#)

28. 28.

Cui, Y.-T. et al. Unconventional correlation between quantum Hall transport quantization and bulk state filling in gated graphene devices. *Phys. Rev. Lett.* **117**, 186601 (2016).

[ADS](#) [PubMed](#) [PubMed Central](#) [Google Scholar](#)

29. 29.

Zhu, M. J. et al. Edge currents shunt the insulating bulk in gapped graphene. *Nat. Commun.* **8**, 14552 (2017).

[ADS](#) [CAS](#) [PubMed](#) [PubMed Central](#) [Google Scholar](#)

30. 30.

Marguerite, A. et al. Imaging work and dissipation in the quantum Hall state in graphene. *Nature* **575**, 628–633 (2019); correction **576**, E6 (2019).

[ADS](#) [CAS](#) [PubMed](#) [PubMed Central](#) [Google Scholar](#)

31. 31.

Dou, Z. et al. Imaging bulk and edge transport near the Dirac point in graphene moiré superlattices. *Nano Lett.* **18**, 2530–2537 (2018).

[ADS](#) [CAS](#) [PubMed](#) [PubMed Central](#) [Google Scholar](#)

32. 32.

Avsar, A. et al. Spintronics in graphene and other two-dimensional materials. *Rev. Mod. Phys.* **92**, 021003 (2020).

[ADS](#) [CAS](#) [Google Scholar](#)

33. 33.

Halbertal, D. et al. Imaging resonant dissipation from individual atomic defects in graphene. *Science* **358**, 1303–1306 (2017).

[ADS](#) [CAS](#) [PubMed](#) [PubMed Central](#) [Google Scholar](#)

34. 34.

Lensky, Y. D., Song, J. C. W., Samutpraphoot, P. & Levitov, L. S. Topological valley currents in gapped Dirac materials. *Phys. Rev. Lett.* **114**, 256601 (2015).

[ADS](#) [PubMed](#) [PubMed Central](#) [Google Scholar](#)

35. 35.

Zhang, X.-P., Huang, C. & Cazalilla, M. A. Valley Hall effect and nonlocal transport in strained graphene. *2D Mater.* **4**, 024007 (2017).

[Google Scholar](#)

36. 36.

Wang, Z., Liu, H., Jiang, H. & Xie, X. C. Numerical study of negative nonlocal resistance and backflow current in a ballistic graphene system. *Phys. Rev. B* **100**, 155423 (2019).

[ADS](#) [CAS](#) [Google Scholar](#)

37. 37.

Xie, H.-Y. & Levchenko, A. Negative viscosity and eddy flow of the imbalanced electron–hole liquid in graphene. *Phys. Rev. B* **99**, 045434 (2019).

[ADS](#) [CAS](#) [Google Scholar](#)

38. 38.

Danz S. & Narozhny, B. N. Vorticity of viscous electronic flow in graphene. *2D Mater.* **7**, 035001 (2020).

[CAS](#) [Google Scholar](#)

39. 39.

Danz, S., Titov, M. & Narozhny, B. N. Giant nonlocality in nearly compensated two-dimensional semimetals. *Phys. Rev. B* **102**, 081114 (2020).

[ADS](#) [CAS](#) [Google Scholar](#)

40. 40.

Young, A. F. et al. Tunable symmetry breaking and helical edge transport in a graphene quantum spin Hall state. *Nature* **505**, 528–532 (2014).

[ADS](#) [CAS](#) [PubMed](#) [PubMed Central](#) [Google Scholar](#)

41. 41.

Abanin, D. A. et al. Dissipative quantum Hall effect in graphene near the Dirac point. *Phys. Rev. Lett.* **98**, 196806 (2007).

[ADS](#) [PubMed](#) [PubMed Central](#) [Google Scholar](#)

42. 42.

McEuen, P. L. et al. New resistivity for high-mobility quantum Hall conductors. *Phys. Rev. Lett.* **64**, 2062–2065 (1990).

[ADS](#) [CAS](#) [PubMed](#) [PubMed Central](#) [Google Scholar](#)

43. 43.

Silvestrov, P. G. & Efetov, K. B. Charge accumulation at the boundaries of a graphene strip induced by a gate voltage: electrostatic approach. *Phys. Rev. B* **77**, 155436 (2008).

[ADS](#) [Google Scholar](#)

44. 44.

Akiho, T., Irie, H., Onomitsu, K. & Muraki, K. Counterflowing edge current and its equilibration in quantum Hall devices with sharp edge potential: roles of incompressible strips and contact configuration. *Phys. Rev. B* **99**, 121303 (2019).

[ADS](#) [CAS](#) [Google Scholar](#)

45. 45.

Finkler, A. et al. Self-aligned nanoscale SQUID on a tip. *Nano Lett.* **10**, 1046–1049 (2010).

[ADS](#) [CAS](#) [PubMed](#) [PubMed Central](#) [Google Scholar](#)

46. 46.

Finkler, A. et al. Scanning superconducting quantum interference device on a tip for magnetic imaging of nanoscale phenomena. *Rev. Sci. Instrum.* **83**, 073702 (2012).

[ADS](#) [CAS](#) [PubMed](#) [PubMed Central](#) [Google Scholar](#)

47. 47.

Vasyukov, D. et al. A scanning superconducting quantum interference device with single electron spin sensitivity. *Nat. Nanotechnol.* **8**, 639–644 (2013).

[ADS](#) [CAS](#) [PubMed](#) [PubMed Central](#) [Google Scholar](#)

48. 48.

Bagani, K. et al. Sputtered Mo<sub>66</sub>Re<sub>34</sub> SQUID-on-tip for high-field magnetic and thermal nanoimaging. *Phys. Rev. Appl.* **12**, 044062 (2019).

[ADS](#) [CAS](#) [Google Scholar](#)

49. 49.

Herbschleb, E. D. et al. Direct imaging of coherent quantum transport in graphene p–n–p junctions. *Phys. Rev. B* **92**, 125414 (2015).

[ADS](#) [Google Scholar](#)

50. 50.

Garcia, A. G. F., König, M., Goldhaber-Gordon, D. & Todd, K. Scanning gate microscopy of localized states in wide graphene constrictions. *Phys. Rev. B* **87**, 085446 (2013).

[ADS](#) [Google Scholar](#)

51. 51.

Pascher, N., Bischoff, D., Ihn, T. & Ensslin, K. Scanning gate microscopy on a graphene nanoribbon. *Appl. Phys. Lett.* **101**, 063101 (2012).

[ADS](#) [Google Scholar](#)

52. 52.

Kaverzin, A. A. & van Wees, B. J. Electron transport nonlocality in monolayer graphene modified with hydrogen silsesquioxane polymerization. *Phys. Rev. B* **91**, 165412 (2015).

[ADS](#) [Google Scholar](#)

53. 53.

Wang, Y., Cai, X., Reutt-Robey, J. & Fuhrer, M. S. Neutral-current Hall effects in disordered graphene. *Phys. Rev. B* **92**, 161411 (2015).

[ADS](#) [Google Scholar](#)

54. 54.

Mishchenko, A. et al. Nonlocal response and anamorphosis: the case of few-layer black phosphorus. *Nano Lett.* **15**, 6991–6995 (2015).

[ADS](#) [CAS](#) [PubMed](#) [PubMed Central](#) [Google Scholar](#)

55. 55.

Wu, Y.-F. et al. Magnetic proximity effect in graphene coupled to a BiFeO<sub>3</sub> nanoplate. *Phys. Rev. B* **95**, 195426 (2017).

[ADS](#) [Google Scholar](#)

56. 56.

Komatsu, K. et al. Observation of the quantum valley Hall state in ballistic graphene superlattices. *Sci. Adv.* **4**, eaaq0194 (2018).

[ADS](#) [PubMed](#) [PubMed Central](#) [Google Scholar](#)

57. 57.

Hong, S. J., Belke, C., Rode, J. C., Brechtken, B. & Haug, R. J. Helical-edge transport near  $v = 0$  of monolayer graphene. *Current Applied Physics* **27**, 25-30 (2021).

58. 58.

Endo, K. et al. Topological valley currents in bilayer graphene/hexagonal boron nitride superlattices. *Appl. Phys. Lett.* **114**, 243105 (2019).

[ADS](#) [Google Scholar](#)

59. 59.

Zhao, L. et al. Interference of chiral Andreev edge states. *Nat. Phys.* **16**, 862–867 (2020).

[CAS](#) [Google Scholar](#)

60. 60.

Afzal, A. M., Min, K. H., Ko, B. M. & Eom, J. Observation of giant spin-orbit interaction in graphene and heavy metal heterostructures. *RSC Advances* **9**, 31797–31805 (2019).

[ADS](#) [CAS](#) [Google Scholar](#)

61. 61.

Tang, C., Zhang, Z., Lai, S., Tan, Q. & Gao, W. Magnetic proximity effect in graphene/CrBr<sub>3</sub> van der Waals heterostructures. *Adv. Mater.* **32**, 1908498 (2020).

[CAS](#) [Google Scholar](#)

62. 62.

Ruzin, I. M. Hall transport in nonuniform two-dimensional conductors. *Phys. Rev. B* **47**, 15727–15734 (1993).

[ADS](#) [CAS](#) [Google Scholar](#)

63. 63.

Ruzin, I. M., Cooper, N. R. & Halperin, B. I. Nonuniversal behavior of finite quantum Hall systems as a result of weak macroscopic inhomogeneities. *Phys. Rev. B* **53**, 1558–1572 (1996).

[ADS](#) [CAS](#) [Google Scholar](#)

64. 64.

Ilan, R., Cooper, N. R. & Stern, A. Longitudinal resistance of a quantum Hall system with a density gradient. *Phys. Rev. B* **73**, 235333 (2006).

[ADS](#) [Google Scholar](#)

65. 65.

Shylau, A. A., Zozoulenko, I. V., Xu, H. & Heinzel, T. Generic suppression of conductance quantization of interacting electrons in graphene nanoribbons in a perpendicular magnetic field. *Phys. Rev. B* **82**, 121410 (2010).

[ADS](#) [Google Scholar](#)

66. 66.

Vera-Marun, I. J. et al. Quantum Hall transport as a probe of capacitance profile at graphene edges. *Appl. Phys. Lett.* **102**, 013106 (2013).

[ADS](#) [Google Scholar](#)

67. 67.

Moreau, N. et al. Upstream modes and antidots poison graphene quantum Hall effect. Preprint at <https://arxiv.org/abs/2010.12499> (2020).

68. 68.

Caridad, J. M. et al. Conductance quantization suppression in the quantum Hall regime. *Nat. Commun.* **9**, 659 (2018).

[ADS](#) [PubMed](#) [PubMed Central](#) [Google Scholar](#)

69. 69.

Seredinski, A. et al. Quantum Hall-based superconducting interference device. *Sci. Adv.* **5**, eaaw8693 (2019).

[ADS](#) [CAS](#) [PubMed](#) [PubMed Central](#) [Google Scholar](#)

70. 70.

Slizovskiy, S. & Fal'ko, V. I. Suppressed compressibility of quantum Hall effect edge states in epitaxial graphene on SiC. *Phys. Rev. B* **97**, 075404 (2018).

[ADS](#) [CAS](#) [Google Scholar](#)

71. 71.

Graf, D. et al. Spatially resolved Raman spectroscopy of single- and few-layer graphene. *Nano Lett.* **7**, 238–242 (2007).

[ADS](#) [CAS](#) [PubMed](#) [PubMed Central](#) [Google Scholar](#)

72. 72.

Shtanko, O. & Levitov, L. Robustness and universality of surface states in Dirac materials. *Proc. Natl Acad. Sci. USA* **115**, 5908–5913 (2018).

[ADS](#) [MathSciNet](#) [CAS](#) [PubMed](#) [PubMed Central](#) [MATH](#) [Google Scholar](#)

73. 73.

Abanin, D. A., Lee, P. A. & Levitov, L. S. Spin-filtered edge states and quantum Hall effect in graphene. *Phys. Rev. Lett.* **96**, 176803 (2006).

[ADS](#) [PubMed](#) [PubMed Central](#) [Google Scholar](#)

74. 74.

Kononov, A. et al. One-dimensional edge transport in few-layer WTe<sub>2</sub>. *Nano Lett.* **20**, 4228–4233 (2020).

[ADS](#) [CAS](#) [PubMed](#) [PubMed Central](#) [Google Scholar](#)

75. 75.

Vasko, F. T. & Zozoulenko, I. V. Conductivity of a graphene strip: width and gate-voltage dependencies. *Appl. Phys. Lett.* **97**, 092115 (2010).

[ADS](#) [Google Scholar](#)

76. 76.

Klusek, Z. et al. Local electronic edge states of graphene layer deposited on Ir(111) surface studied by STM/CITS. *Appl. Surf. Sci.* **252**, 1221–1227 (2005).

[ADS](#) [CAS](#) [Google Scholar](#)

77. 77.

Lee, E. J. H., Balasubramanian, K., Weitz, R. T., Burghard, M. & Kern, K. Contact and edge effects in graphene devices. *Nat. Nanotechnol.* **3**, 486–490 (2008).

[ADS](#) [CAS](#) [PubMed](#) [PubMed Central](#) [Google Scholar](#)

78. 78.

Venugopal, A. et al. Effective mobility of single-layer graphene transistors as a function of channel dimensions. *J. Appl. Phys.* **109**, 104511 (2011).

[ADS](#) [Google Scholar](#)

79. 79.

Li, J., Martin, I., Büttiker, M. & Morpurgo, A. F. Topological origin of subgap conductance in insulating bilayer graphene. *Nat. Phys.* **7**, 38–42 (2011).

[CAS](#) [Google Scholar](#)

80. 80.

Barraud, C. et al. Field effect in the quantum Hall regime of a high mobility graphene wire. *J. Appl. Phys.* **116**, 073705 (2014).

[ADS](#) [Google Scholar](#)

81. 81.

Yin, L.-J., Zhang, Y., Qiao, J.-B., Li, S.-Y. & He, L. Experimental observation of surface states and Landau levels bending in bilayer graphene. *Phys. Rev. B* **93**, 125422 (2016).

[ADS](#) [Google Scholar](#)

82. 82.

Woessner, A. et al. Near-field photocurrent nanoscopy on bare and encapsulated graphene. *Nat. Commun.* **7**, 10783 (2016).

[ADS](#) [CAS](#) [PubMed](#) [PubMed Central](#) [Google Scholar](#)

83. 83.

Amet, F. et al. Supercurrent in the quantum Hall regime. *Science* **352**, 966–969 (2016).

[ADS](#) [MathSciNet](#) [CAS](#) [PubMed](#) [PubMed Central](#) [MATH](#) [Google Scholar](#)

84. 84.

Kraft, R. et al. Tailoring supercurrent confinement in graphene bilayer weak links. *Nat. Commun.* **9**, 1722 (2018).

[ADS](#) [PubMed](#) [PubMed Central](#) [Google Scholar](#)

85. 85.

Draeles, A. W. et al. Investigation of supercurrent in the quantum Hall regime in graphene Josephson junctions. *J. Low Temp. Phys.* **191**, 288–

300 (2018).

[ADS](#) [CAS](#) [Google Scholar](#)

86. 86.

Alavirad, Y., Lee, J., Lin, Z.-X. & Sau, J. D. Chiral supercurrent through a quantum Hall weak link. *Phys. Rev. B* **98**, 214504 (2018).

[ADS](#) [CAS](#) [Google Scholar](#)

87. 87.

Wei, M. T. et al. Chiral quasiparticle tunneling between quantum Hall edges in proximity with a superconductor. *Phys. Rev. B* **100**, 121403 (2019).

[ADS](#) [CAS](#) [Google Scholar](#)

88. 88.

Tao, C. et al. Spatially resolving edge states of chiral graphene nanoribbons. *Nat. Phys.* **7**, 616–620 (2011).

[CAS](#) [Google Scholar](#)

89. 89.

Nichele, F. et al. Edge transport in the trivial phase of InAs/GaSb. *New J. Phys.* **18**, 083005 (2016).

[ADS](#) [Google Scholar](#)

90. 90.

Akhmerov, A. R. & Beenakker, C. W. J. Boundary conditions for Dirac fermions on a terminated honeycomb lattice. *Phys. Rev. B* **77**, 085423 (2008).

[ADS](#) [Google Scholar](#)

[Download references](#)

## Acknowledgements

We thank M. E. Huber for the SOT readout system, S. Grover for the data acquisition setup, and G. Zhang, I. V. Gornyi, Y. Gefen and A. Uri for discussions. This work was supported by the European Research Council (ERC) under the European Union’s Horizon 2020 Research and Innovation programme (grant nos 785971 and 786532), by the Israel Science Foundation (ISF) (grant nos 921/18 and 994/19), by the Sagol Weizmann–MIT Bridge Program, by the German–Israeli Foundation for Scientific Research and Development (GIF) grant no. I-1505-303.10/2019, and by Lloyd’s Register Foundation. E.Z. acknowledges the support of the Andre Deloro Prize for Scientific Research and Leona M. and Harry B. Helmsley Charitable Trust grant 2018PG-ISL006.

## Author information

### Author notes

1. These authors contributed equally: A. Aharon-Steinberg, A. Marguerite

## Affiliations

1. Department of Condensed Matter Physics, Weizmann Institute of Science, Rehovot, Israel

A. Aharon-Steinberg, A. Marguerite, K. Bagani, T. Holder, Y. Myasoedov & E. Zeldov

2. National Graphene Institute and School of Physics and Astronomy, The University of Manchester, Manchester, UK

D. J. Perello & A. K. Geim

3. Department of Physics, Massachusetts Institute of Technology,  
Cambridge, MA, USA

L. S. Levitov

## Authors

1. A. Aharon-Steinberg

[View author publications](#)

You can also search for this author in [PubMed](#) [Google Scholar](#)

2. A. Marguerite

[View author publications](#)

You can also search for this author in [PubMed](#) [Google Scholar](#)

3. D. J. Perello

[View author publications](#)

You can also search for this author in [PubMed](#) [Google Scholar](#)

4. K. Bagani

[View author publications](#)

You can also search for this author in [PubMed](#) [Google Scholar](#)

5. T. Holder

[View author publications](#)

You can also search for this author in [PubMed](#) [Google Scholar](#)

6. Y. Myasoedov

[View author publications](#)

You can also search for this author in [PubMed](#) [Google Scholar](#)

7. L. S. Levitov

[View author publications](#)

You can also search for this author in [PubMed](#) [Google Scholar](#)

8. A. K. Geim

[View author publications](#)

You can also search for this author in [PubMed](#) [Google Scholar](#)

9. E. Zeldov

[View author publications](#)

You can also search for this author in [PubMed](#) [Google Scholar](#)

## Contributions

A.A.-S., A.M. and E.Z. conceived the experiments. D.J.P. and A.K.G. provided the studied devices. A.M. and A.A.-S. carried out the measurements and data analysis. K.B. and Y.M. fabricated the SOTs and the tuning fork feedback. T.H., A.A.-S. and L.S.L. developed the analytic models. A.A.-S. performed the numerical simulations. A.A.-S., A.M., T.H., E.Z., L.S.L and A.K.G. wrote the manuscript with contributions from the rest of the authors.

## Corresponding author

Correspondence to [E. Zeldov](#).

## Ethics declarations

## Competing interests

The authors declare no competing interests.

## Additional information

**Peer review information** *Nature* thanks Boris Narozhny, Katja Nowack and the other, anonymous, reviewer(s) for their contribution to the peer

review of this work. Peer reviewer reports are available.

**Publisher's note** Springer Nature remains neutral with regard to jurisdictional claims in published maps and institutional affiliations.

## Extended data figures and tables

### Extended Data Fig. 1 Nonlocal transport measurements.

**a, b**, The two-probe resistance  $R_{2p}$  (right axis) and the nonlocal resistances  $R_{NL}$  and  $\langle R \rangle_{NL}$  (left axis) at  $B = 5$  T (**a**) and  $3$  T (**b**) for negative  $V_{bg}$  at  $T = 4.2$  K using an a.c. voltage bias  $V_0 = 9.0$  mV. The  $R_{NL}$  is normalized by  $R_{NL}(V_{bg} = 0)$  of  $220$  k $\Omega$  at  $5$  T (**a**) and  $106$  k $\Omega$  at  $3$  T (**b**). The  $\langle R \rangle_{NL}$  emphasizes the giant nonlocality at larger  $|V_{bg}|$  as compared to  $R_{NL}$  which drops much faster with  $|V_{bg}|$  due to the trivial drop in  $\rho_{xx}(V_{bg})$ . The  $R_{2p}$  shows quantization at quantum Hall plateaus as indicated by the dashed lines. **c**,  $\langle R \rangle_{NL}$  versus  $V_{bg}$  at  $B = 1, 1.2$ , and  $1.4$  T with dashed guide-to-the-eye envelope curves. **d**,  $\langle R \rangle_{NL}$  data with envelopes of  $1$  T and  $1.2$  T data normalized to that of  $1.4$  T illustrating that the nonlocal mechanism is described by a smooth and continuous envelope function.

### Extended Data Fig. 2 Scanning gate microscopy and simulations away from charge neutrality.

**a, b**, Simultaneous scanning gate imaging of  $\langle V \rangle_{NL}$  (**a**) and  $\langle R \rangle_{NL}$  (**b**) at  $B = 5$  T,  $V_{bg} = -1.4$  V and  $V_{tg} = 8$  V. The graphene device is biased with a voltage  $V_0 = 5.5$  mV and the SOT is scanned over a large fraction of the sample area in Fig. [1a](#). At this  $V_{bg}$  we estimate the decay length of the edge current to be  $\lambda \approx 9W$  (based on

Extended Data Fig. 3b and not taking into account the suppression of the edge currents by the edge disorder). Note the large suppression of  $\langle \{ \{ \mathbf{V} \} \} \rangle_{\{ \{ \mathbf{rm} \{ NL \} \} \}^{\{ \{ \mathbf{rm} \{ R \} \} \}}}$  by the tip along the top-right edge (blue) and a hardly visible suppression at few locations along the bottom-right edge (light red), in contrast to Fig. 3a, which shows a more symmetric suppression close to the CNP. c, d, Numerical simulations of  $\langle \{ \{ \mathbf{V} \} \} \rangle_{\{ \{ \mathbf{rm} \{ NL \} \} \}^{\{ \{ \mathbf{rm} \{ L \} \} \}}}$  (c) and  $\langle \{ \{ \mathbf{V} \} \} \rangle_{\{ \{ \mathbf{rm} \{ NL \} \} \}^{\{ \{ \mathbf{rm} \{ R \} \} \}}}$  (d) scanning gate signal for  $\lambda \approx 9W$  ( $\eta = 0.15$ ,  $V_{bg} = -1.4$  V, and  $v_{tg} = 2$ ) with disordered edge accumulation along the top-right edge (with the same disorder function  $f(x)$  as in Fig. 3l) and bottom-left edge, and uniform accumulation along the rest of the edges. The tip-induced suppression of  $\langle \{ \{ \mathbf{V} \} \} \rangle_{\{ \{ \mathbf{rm} \{ NL \} \} \}^{\{ \{ \mathbf{rm} \{ R \} \} \}}}$  is visible predominantly along the top-right edge (blue) and of  $\langle \{ \{ \mathbf{V} \} \} \rangle_{\{ \{ \mathbf{rm} \{ NL \} \} \}^{\{ \{ \mathbf{rm} \{ L \} \} \}}}$  along the bottom-left edge, consistent with experimental data in a, b.

### Extended Data Fig. 3 Edge accumulation ratio $\eta$ and nonlocal decay length $\lambda$ behaviour.

a, Plot of the calculated edge accumulation ratio  $\eta(V_{bg})$  for hole doping with  $P_e = 1.8 \times 10^8$  m<sup>-1</sup> and  $p_{dis} = 2.9 \times 10^{10}$  cm<sup>-2</sup> in the limit of  $w = 0$ . b, The corresponding nonlocal decay length  $\lambda$  given by equation (1) versus  $V_{bg}$  at  $B = 0, 1$  and  $5$  T. The dashed line shows  $\lambda/W = 1/\pi$  in the ohmic regime and the dotted line shows the distance to our nonlocal contacts  $x/W = 2.85$ . c, The corresponding calculated  $\langle \{ \{ \mathbf{V} \} \} \rangle_{\{ \{ \mathbf{rm} \{ NL \} \} \}^{\{ \{ \mathbf{rm} \{ bg \} \} \}}}$  (dashed) using  $\lambda(V_{bg})$  from b, along with the experimental  $\langle \{ \{ \mathbf{V} \} \} \rangle_{\{ \{ \mathbf{rm} \{ NL \} \} \}^{\{ \{ \mathbf{rm} \{ bg \} \} \}}}$  at  $B = 0, 1$  and  $5$  T from Fig. 1e. d, Calculated  $\lambda/W$  versus  $\eta$ , as in Fig. 1b but on a log-log scale using the 2D analytic expressions (blue) along with the 1D results (dotted red). The coloured region shows the span of  $\eta(V_{bg})$  in a. e, COMSOL numerical calculation of  $\eta = |2P_e/(p_b W)|$  versus  $V_{bg}$  with edge charge accumulation  $P_e$  arising due to combined effects of electrostatic gating of the graphene by the backgate potential  $V_{bg}$  and of the negatively charged impurities with line density  $N_{imp} = 0.18$  nm<sup>-1</sup> (blue) and  $1$  nm<sup>-1</sup>

(red) along the edges. A pronounced asymmetry is observed with a faster decay of  $\eta$  and of the corresponding nonlocality upon n bulk doping.  $\eta$  vanishes at a specific value of positive  $V_{bg}$  at which hole edge doping due to  $N_{imp}$  is compensated by electron edge doping due to electrostatic gating by  $V_{bg}$ . At larger  $V_{bg}$  both the edges and the bulk become n-doped (dashed curves). For the red and blue curves we have used  $p_{dis} = 0$ , which results in diverging  $\eta$  at the CNP due to vanishing of  $p_b$  at  $V_{bg} = 0$ . The green curve shows  $\eta(V_{bg})$  for the case of pure electrostatic gating ( $N_{imp} = 0$ ) with  $p_{dis} = 2.9 \times 10^{10} \text{ cm}^{-2}$ . In this case, the transport is local at the CNP with  $\eta = 0$  because  $P_e$  vanishes at  $V_{bg} = 0$ , whereas  $p_b = p_{dis}$  is finite.

#### Extended Data Fig. 4 Analytic solution of nonlocal transport in infinite strip with edge accumulation.

**a**, Schematic drawing of the sample consisting of a bulk strip of width  $W$  described by conductivity tensor  $\sigma$  and two edge strips of width  $w/2$  with conductivity  $\eta\sigma W/w$ . All the analytic solutions are derived in the limit  $w \rightarrow 0$ . **b**, Schematic drawing of the current flow at elevated field in presence of edge accumulation. The current flows from the source predominantly along the top-right edge in the  $\hat{x}$  direction (red) and gradually leaks into the bulk where it reverts its direction and flows in the  $-\hat{x}$  direction (green) to the left side of the sample. The current is then gradually absorbed by the bottom edge where it reverts its direction again and flows to the drain (blue). Note that the edge currents (red and blue) flow ‘downstream’ along the potential drop (red and blue arrows in **c**), whereas the  $x$  component of the bulk current,  $\langle I \rangle_{\rm bulk}, \hat{x}$ , flows against the potential drop (green arrow in **c**). **c**, Calculated normalized potentials  $\langle V \rangle_{\rm top}(x)$  (red) and  $\langle V \rangle_{\rm bot}(x)$  (blue) along the top and bottom edges and  $\langle V \rangle_{\rm bulk}(x, y=0)$  (green) for the case of  $\eta = 0.2$  and  $\theta = 26$  ( $\lambda = 2.4W$ ). **d**, The corresponding normalized currents  $\langle I \rangle_{\rm top}(x)$  (red),  $\langle I \rangle_{\rm bot}(x)$  (blue), and the  $x$  component of the bulk current integrated over the strip width,  $\langle I \rangle_{\rm bulk}, \hat{x}$ , (green) showing the flow pattern described schematically in **b**.

## Extended Data Fig. 5 Inversion of the Hall voltage owing to edge charge disorder.

Numerical simulations of the normalized potential  $\langle \{V\} \rangle$  (left column) and of the magnitude of the normalized current density  $\langle \{J\} \rangle$  (right column) at  $B = 5$  T and  $\lambda = 30W$  ( $\eta = 0.58$ ,  $V_{bg} = -0.2$  V). **a, b**, Uniform edge accumulation giving rise to strong nonlocal transport and positive Hall voltage  $V_H$  as defined in **a** (potential at the left contact is higher than at the right contact). **c, d**, The edge charge accumulation is suppressed to 10% of its original value ( $f(x) = 0.1$ ) at two points along the edge marked by the arrows. A major part of the edge current is diverted into the bulk (**d**) and the potential distribution is altered markedly (**c**) leading to inversion of the Hall voltage (the potential at the left contact is lower than at the right contact).

## Extended Data Fig. 6 Field-orientation-dependent nonlocal transport in presence of nonuniform edge accumulation.

Numerical simulations of the normalized potential  $\langle \{V\} \rangle$  (left column) and of the magnitude of the normalized current density  $\langle \{J\} \rangle$  (right column) at  $B = \pm 4$  T and  $\lambda = 2.54W$  ( $\eta = 0.05$ ,  $V_{bg} = -4$  V) for the case of charge edge accumulation being present only in the top-right and bottom-left quadrants of the sample indicated by the pink outlines in **b**. **a, b**,  $B = 4$  T and  $V_0$  applied to the top contact. Highly nonlocal transport is observed similar to the case presented in Fig. 4e, f with charge accumulation along the entire edges. **c, d**, Same as **a, b** but with  $V_0$  applied to the bottom contact. The polarities of the potentials and the currents are flipped but the spatial distributions remain the same. **e, f**,  $B = -4$  T and  $V_0$  applied to the top contact. The transport becomes local resembling the ohmic case in Fig. 4c, d in absence of edge accumulation. **g, h**, Same as **e, f** but with  $V_0$  applied to the bottom contact. The transport remains local with flipped current and potential polarities. This nonuniform edge accumulation exemplifies the strong field-orientation dependence of the nonlocal transport that can arise in presence of edge accumulation disorder.

## Extended Data Fig. 7 Nonlocal transport in presence of one-sided edge accumulation.

Numerical simulations of the normalized potential  $\langle \{V\} \rangle$  (left column) and of the magnitude of the normalized current density  $\langle \{J\} \rangle$  (right column) at  $B = \pm 4$  T and  $\lambda = 2.54W$  ( $\eta = 0.05$ ,  $V_{bg} = -4$  V) for the case of charge edge accumulation being present only in the right side of the sample indicated by the pink outline in **b**. Highly nonlocal transport is observed solely on the right side of the sample, while the left side of the sample exhibits local ohmic transport. **a, b**,  $B = 4$  T and  $V_0$  applied to the top contact. The current (**b**) emerges from the source (top) and flows clockwise along the top-right edge against the chiral (counterclockwise) direction. It then leaks to the bulk and flows to the left against the global potential drop (**a**). Since the left side of the sample has local behaviour, in contrast to Fig. 4e, f and Extended Data Fig. 6a, b, the bulk current is drained directly to the bottom contact without continuing its nonlocal flow to the left side. **c, d**, Same as **a, b** but with  $V_0$  applied to the bottom contact. The polarities of the potentials and the currents are flipped but the spatial distributions remain the same. The current emanates from the source (bottom) into the bulk, flows to the right against the potential, and is drained along the top-right edge. **e, f**,  $B = -4$  T and  $V_0$  applied to the top contact. The polarity of the potential distribution (**e**) flips relative to **a**, but the transport (**f**) remains local in the left side and nonlocal in the right side. The current (**f**) flows as in **d**, but along inverted trajectory. **g, h**, Same as **e, f** but with  $V_0$  applied to the bottom contact. The polarities of the potentials and the currents are flipped relative to **a, b**, but the spatial distributions remain the same. This one-sided edge accumulation case exemplifies how the two sides of the sample behave almost independently, with nonlocal transport properties of each side being determined by its edge accumulation and disorder.

## Supplementary information

### Supplementary Information

This file contains supplementary text, supplementary equations s1 – s27 and supplementary references.

## Peer Review File

### Supplementary Video 1 Thermal imaging of dissipation vs. $V_{bg}$ at $B = 0$ T.

Temperature maps  $T_{2f}$  of the central part of the sample acquired with the scanning Pb SOT at  $B = 0$  T and  $V_{tg} = 0$  V with  $V_{bg}$  varying from -6 V to 5 V with applied constant power  $V_0I_0 = 15$  nW. At large  $|V_{bg}|$  most of the dissipation occurs at the top and bottom contacts outside the imaging frame, while dissipation within the sample is limited mainly to the central region where the current is expected to flow. On approaching CNP the dissipation extends from the central region into the right and left arms with enhanced thermal signal along the edges.

### Supplementary Video 2 Thermal imaging of dissipation vs. $V_{bg}$ at $B = 5$ T and $V_{tg} = 0$ V.

Temperature maps  $T_{2f}$  of the full Hall bar structure acquired with the scanning MoRe SOT at  $B = 5$  T and  $V_{tg} = 0$  V with  $V_{bg}$  varying from -10 V to 10 V with applied constant power  $V_0I_0 = 15$  nW. At large  $|V_{bg}|$  the dissipation is observed in the central region while near CNP the thermal signal extends over the entire sample. At  $V_{bg}$  values corresponding to QH plateaus (e.g. -8, -2, 3, and 8 V) the dissipation in the sample is reduced with most of the dissipation occurring at the top and bottom contacts outside the imaging frame.

### Supplementary Video 3 Thermal imaging of dissipation vs. $V_{bg}$ at $B = 5$ T and $V_{tg} = 8$ V.

Temperature maps  $T_{2f}$  at  $B = 5$  T and  $V_{tg} = 8$  V with  $V_{bg}$  varying from -10 V to 10 V with applied constant power  $V_0 I_0 = 15$  nW. At large  $|V_{bg}|$  the dissipation is observed in the central region while near CNP the thermal signal extends over the entire sample similar to Supplementary Video 2, but with enhanced signal along the edges. The tip potential  $V_{tg}$  causes local depletion of the hole edge accumulation leading to diversion of the edge current into the bulk and to corresponding enhancement in dissipation as demonstrated by numerical simulations in Supplementary Video 9. The irregular pattern with enhanced thermal signal reveals the locations of suppressed edge charge accumulation along the edges.

### Supplementary Video 4 Scanning gate microscopy vs. $V_{bg}$ at $B = 5$ T.

A constant  $V_0 = 5.5$  mV is applied to contact 2 and  $\langle \langle \mathcal{V} \rangle \rangle_{NL}$ ,  $\langle \langle \mathcal{V} \rangle \rangle_3$  and  $R_{2p}$  are measured as a function of the tip position in the central part of the sample (dotted area in Fig. 1a) with  $V_{tg} = 8$  V at  $B = 5$  T upon varying  $V_{bg}$  from -10 V to 4 V. When the SOT is located above the sample edges the local depletion of the hole edge accumulation by the tip potential  $V_{tg}$  causes suppression in  $V_{NL}$  and enhancement of  $R_{2p}$  at  $V_{bg}$  values corresponding to large  $\mathcal{R}_{NL}$  in Fig. 1e.  $\langle \langle \mathcal{V} \rangle \rangle_3$  is enhanced along the top edge and suppressed along the bottom edge in contrast to Fig. 3b due to  $\langle \langle \mathcal{V} \rangle \rangle_0$  applied to contact 2 instead of contact 1. The signals fade away at  $V_{bg}$  values corresponding to QH plateaus.

### Supplementary Video 5 Scanning gate microscopy along the top edge of the sample vs. $V_{tg}$ and $V_{bg}$ at $B = 5$ T.

A constant  $V_0 = 3.8$  mV is applied to contact 1 and  $\langle \langle \mathcal{V} \rangle \rangle_{NL}$  is measured as a function of the tip position along the top-right edge of the sample marked by the yellow line in Fig. 3a vs.  $V_{tg}$  from -2 V to 8 V. Each frame corresponds to a different  $V_{bg}$  that varies from -10 V to 4 V. A

positive  $V_{tg}$  depletes the hole edge accumulation causing suppression of  $\langle \mathcal{V} \rangle_{NL}$ . This suppression is strongly position dependent due to edge accumulation disorder. Locations with weaker edge accumulation show a lower  $V_{tg}$  threshold for  $\langle \mathcal{V} \rangle_{NL}$  suppression. Negative  $V_{tg}$  causes additional hole accumulation along the edges which has no significant effect except at the weakest point of edge accumulation, which acts as a bottleneck for the edge current flow. At this point, a negative  $V_{tg}$  can “repair” the suppressed edge accumulation, thus enhancing  $V_{NL}$  as observed at few values of  $V_{bg}$ . The overall  $\langle \mathcal{V} \rangle_{NL}$  signal fades away at  $V_{bg}$  values corresponding to QH plateaus.

### Supplementary Video 6 Simulations of nonlocal potential and current distributions vs. $B$ with and without edge accumulation.

Numerical simulations of the normalized potential  $\langle \mathcal{V} \rangle$  (top) and of the magnitude of the normalized current density  $\langle \mathcal{J} \rangle$  (bottom) upon increasing  $B$  for  $\eta = 0$  (left column) and  $\eta = 0.1$  (right column). At low fields up to  $B \approx 0.2$  T the normalized potential and the current density distributions for  $\eta = 0$  and  $\eta = 0.1$  evolve very similarly. At higher fields in absence of edge accumulation (left) the transport remains ohmic and essentially field independent. A small edge accumulation ( $\eta = 0.1$ ), which has little effect at low fields, causes to a dramatic change in the potential and current distributions with increasing field (right). The potential becomes highly nonlocal and the spatial extent of the edge currents grows rapidly with field. At  $B = 5$  T the nontopological edge currents extend all the way from the source (top contact) to the drain (bottom contact). In regions of  $\langle \mathcal{V} \rangle > 1.2$  the red color is saturated for clarity.

### Supplementary Video 7 Simulations of nonlocal potential and current distributions vs. $V_{bg}$ at $B = 2$ T.

Numerical simulations of the normalized potential  $\langle \mathcal{V} \rangle$  (top) and of the magnitude of the normalized current density  $\langle \mathcal{J} \rangle$

(bottom) at  $B = 2$  T upon varying  $V_{bg}$  from  $-10$  V ( $\lambda = 0.57W$ ) to  $0$  V ( $\lambda = 13.72W$ ). At small  $\lambda$  the transport is similar to the ohmic regime. Upon increasing  $\lambda$  the current along the edges expands, and the bulk current rotates its direction from vertical to horizontal, while the electric field rotates from horizontal to vertical. When the enhanced edge current extends all the way from source (top) to drain (bottom) the magnitude of the bulk current drops sharply. In regions of  $\mathcal{J} > 1.2$  the red color is saturated for clarity.

### Supplementary Video 8 Numerical simulation of scanning gate microscopy at $B = 5$ T.

Numerical simulations of the normalized potential  $\mathcal{V}$  (top) and the normalized current density  $\mathcal{J}$  (bottom) at  $B = 5$  T and  $V_{bg} = -1$  V ( $\lambda = 11.9W$ ) upon scanning a positively biased tip (marked by a black circle) that causes local depletion of the hole carriers. When the tip resides in the bulk, the potential and the current are deformed only locally. When the tip is above the edge in the right-hand-side of the sample, the enhanced current flows along the edge from the source up to the tip position only, where it is diverted into the bulk with almost no current flowing along the rest of the edge. In the left-hand-side of the sample, the situation is opposite where the tip blocks the current from the source up to the tip position, whereas along the rest of the edge the current is gathered from the bulk into the edge and channeled towards the drain.

### Supplementary Video 9 Simulations of scanning gate microscopy in presence of edge disorder.

Numerical simulations of the normalized potential  $\mathcal{V}$  (top) and the normalized current density  $\mathcal{J}$  (bottom) where the edge accumulation is position dependent along the top-right edge giving rise to a non-uniform potential. When the tip resides in the bulk, the potential and the current are deformed only locally. When the tip scans above the disordered top edge the suppression of the edge current is strongly position dependent with largest suppression occurring at the points

of weakest edge charge accumulation. These types of simulations were used to produce Figs. 3j-l.

## Rights and permissions

### [Reprints and Permissions](#)

## About this article



Check for  
updates

## Cite this article

Aharon-Steinberg, A., Marguerite, A., Perello, D.J. *et al.* Long-range nontopological edge currents in charge-neutral graphene. *Nature* **593**, 528–534 (2021). <https://doi.org/10.1038/s41586-021-03501-7>

### [Download citation](#)

- Received: 11 September 2020
- Accepted: 26 March 2021
- Published: 26 May 2021
- Issue Date: 27 May 2021
- DOI: <https://doi.org/10.1038/s41586-021-03501-7>

## Comments

By submitting a comment you agree to abide by our [Terms](#) and [Community Guidelines](#). If you find something abusive or that does not comply with our terms or guidelines please flag it as inappropriate.

[Access through your institution](#)

[Change institution](#)

[Buy or subscribe](#)

## Advertisement

---

This article was downloaded by **calibre** from <https://www.nature.com/articles/s41586-021-03501-7>

| [Section menu](#) | [Main menu](#) |

- Article
- [Published: 26 May 2021](#)

# Perovskite-type superlattices from lead halide perovskite nanocubes

- [Ihor Cherniukh](#) ORCID: [orcid.org/0000-0001-7155-5095](https://orcid.org/0000-0001-7155-5095)<sup>1,2</sup>,
- [Gabriele Rainò](#) ORCID: [orcid.org/0000-0002-2395-4937](https://orcid.org/0000-0002-2395-4937)<sup>1,2</sup>,
- [Thilo Stöferle](#) ORCID: [orcid.org/0000-0003-0612-7195](https://orcid.org/0000-0003-0612-7195)<sup>3</sup>,
- [Max Burian](#) ORCID: [orcid.org/0000-0001-6728-6347](https://orcid.org/0000-0001-6728-6347)<sup>4</sup>,
- [Alex Travasset](#) ORCID: [orcid.org/0000-0001-7030-9570](https://orcid.org/0000-0001-7030-9570)<sup>5</sup>,
- [Denys Naumenko](#)<sup>6</sup>,
- [Heinz Amenitsch](#)<sup>6</sup>,
- [Rolf Erni](#) ORCID: [orcid.org/0000-0003-2391-5943](https://orcid.org/0000-0003-2391-5943)<sup>7</sup>,
- [Rainer F. Mahrt](#) ORCID: [orcid.org/0000-0002-9772-1490](https://orcid.org/0000-0002-9772-1490)<sup>3</sup>,
- [Maryna I. Bodnarchuk](#) ORCID: [orcid.org/0000-0001-6597-3266](https://orcid.org/0000-0001-6597-3266)<sup>1,2</sup> &
- [Maksym V. Kovalenko](#) ORCID: [orcid.org/0000-0002-6396-8938](https://orcid.org/0000-0002-6396-8938)<sup>1,2</sup>

[Nature](#) volume 593, pages 535–542 (2021) [Cite this article](#)

- 4148 Accesses
- 149 Altmetric
- [Metrics details](#)

## Subjects

- [Nanoparticles](#)
- [Quantum dots](#)
- [Self-assembly](#)

# Abstract

Atomically defined assemblies of dye molecules (such as H and J aggregates) have been of interest for more than 80 years because of the emergence of collective phenomena in their optical spectra<sup>1,2,3</sup>, their coherent long-range energy transport, their conceptual similarity to natural light-harvesting complexes<sup>4,5</sup>, and their potential use as light sources and in photovoltaics. Another way of creating versatile and controlled aggregates that exhibit collective phenomena involves the organization of colloidal semiconductor nanocrystals into long-range-ordered superlattices<sup>6</sup>. Caesium lead halide perovskite nanocrystals<sup>7,8,9</sup> are promising building blocks for such superlattices, owing to the high oscillator strength of bright triplet excitons<sup>10</sup>, slow dephasing (coherence times of up to 80 picoseconds) and minimal inhomogeneous broadening of emission lines<sup>11,12</sup>. So far, only single-component superlattices with simple cubic packing have been devised from these nanocrystals<sup>13</sup>. Here we present perovskite-type ( $\text{ABO}_3$ ) binary and ternary nanocrystal superlattices, created via the shape-directed co-assembly of steric-stabilized, highly luminescent cubic  $\text{CsPbBr}_3$  nanocrystals (which occupy the B and/or O lattice sites), spherical  $\text{Fe}_3\text{O}_4$  or  $\text{NaGdF}_4$  nanocrystals (A sites) and truncated-cuboid PbS nanocrystals (B sites). These  $\text{ABO}_3$  superlattices, as well as the binary  $\text{NaCl}$  and  $\text{AlB}_2$  superlattice structures that we demonstrate, exhibit a high degree of orientational ordering of the  $\text{CsPbBr}_3$  nanocubes. They also exhibit superfluorescence—a collective emission that results in a burst of photons with ultrafast radiative decay (22 picoseconds) that could be tailored for use in ultrabright (quantum) light sources. Our work paves the way for further exploration of complex, ordered and functionally useful perovskite mesostructures.

## Access options

Subscribe to Journal

Get full journal access for 1 year

\$199.00

only \$3.90 per issue

[Subscribe](#)

All prices are NET prices.

VAT will be added later in the checkout.

Tax calculation will be finalised during checkout.

Rent or Buy article

Get time limited or full article access on ReadCube.

from \$8.99

[Rent or Buy](#)

All prices are NET prices.

### **Additional access options:**

- [Log in](#)
- [Access through your institution](#)
- [Learn about institutional subscriptions](#)

**Fig. 1: Characterization of a binary  $\text{ABO}_3$ -type superlattice assembled from 8.6-nm  $\text{CsPbBr}_3$  and 19.5-nm  $\text{Fe}_3\text{O}_4$  nanocrystals ( $\gamma = 0.420$ ).**

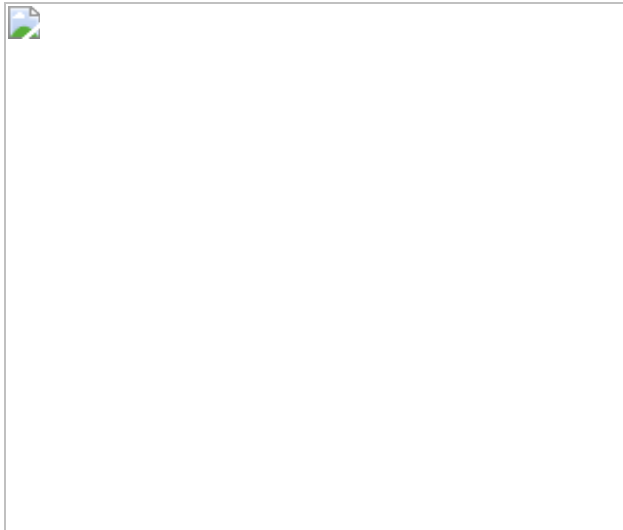


**Fig. 2: Structural characterization of a binary  $\text{ABO}_3$ -type superlattice.**

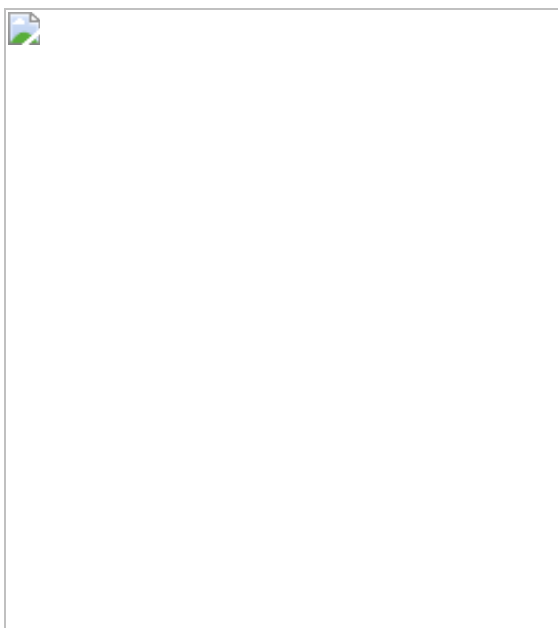


**Fig. 3: Characterization of a binary  $\text{NaCl}$ -type superlattice formed from 8.6-nm  $\text{CsPbBr}_3$  and 19.8-nm  $\text{Fe}_3\text{O}_4$  nanocrystals ( $\gamma = 0.414$ ).**

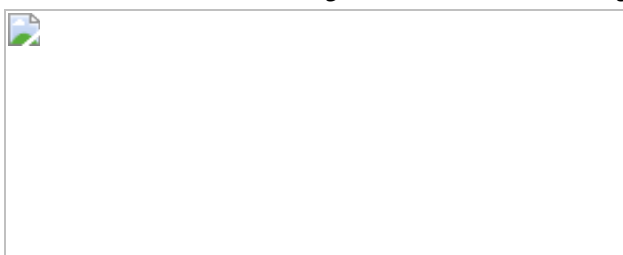


**Fig. 4: Characterization of a ternary  $\text{ABO}_3$ -type superlattice assembled from 8.6-nm  $\text{CsPbBr}_3$ , 10.7-nm  $\text{PbS}$  and 19.8-nm  $\text{Fe}_3\text{O}_4$  nanocrystals.**

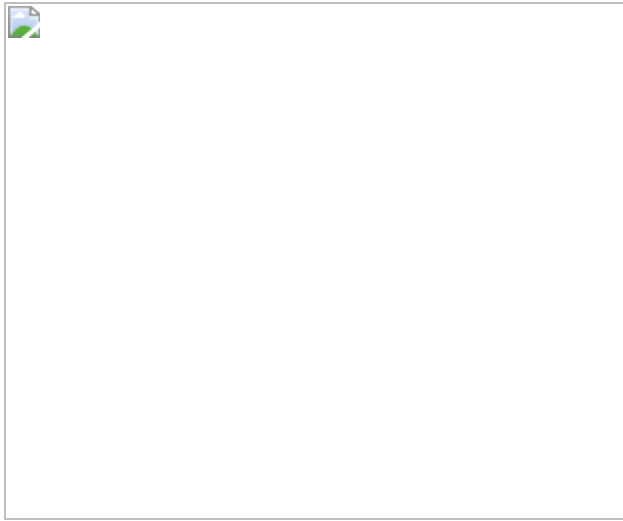
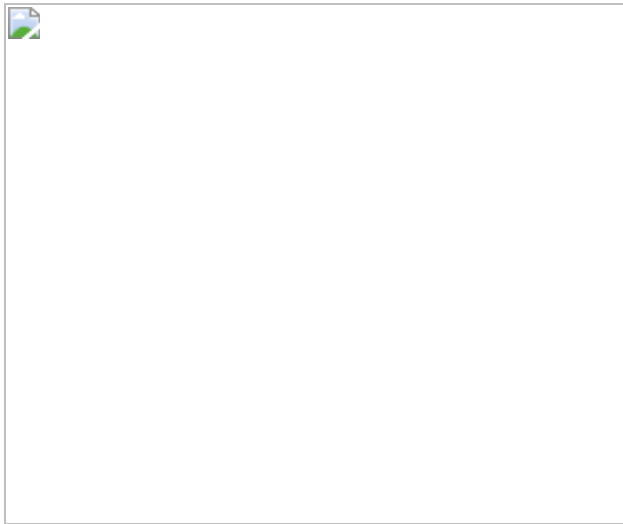


**Fig. 5: Superfluorescence from binary  $\text{ABO}_3$ -type superlattices assembled from 8.6-nm  $\text{CsPbBr}_3$  and 16.5-nm  $\text{NaGdF}_4$  nanocrystals.**



## Data availability

The data that support the findings of this study are available from the corresponding author on reasonable request.

## References

1. 1.

Spano, F. C. The spectral signatures of Frenkel polarons in H- and J-aggregates. *Acc. Chem. Res.* **43**, 429–439 (2010).

[CAS](#) [Google Scholar](#)

2. 2.

Scheibe, G. Über den mechanismus der sensibilisierung photochemischer reaktionen durch farbstoffe, insbesondere der assimilation. *Naturwissenschaften* **25**, 795 (1937).

[ADS](#) [CAS](#) [Google Scholar](#)

3. 3.

Franck, J. & Teller, E. Migration and photochemical action of excitation energy in crystals. *J. Chem. Phys.* **6**, 861–872 (1938).

[ADS](#) [CAS](#) [Google Scholar](#)

4. 4.

Haedler, A. T. et al. Long-range energy transport in single supramolecular nanofibres at room temperature. *Nature* **523**, 196–199 (2015).

[ADS](#) [CAS](#) [Google Scholar](#)

5. 5.

Brédas, J.-L., Sargent, E. H. & Scholes, G. D. Photovoltaic concepts inspired by coherence effects in photosynthetic systems. *Nat. Mater.* **16**, 35–44 (2017).

[ADS](#) [Google Scholar](#)

6. 6.

Boles, M. A., Engel, M. & Talapin, D. V. Self-assembly of colloidal nanocrystals: from intricate structures to functional materials. *Chem. Rev.* **116**, 11220–11289 (2016).

[CAS](#) [Google Scholar](#)

7. 7.

Protesescu, L. et al. Nanocrystals of cesium lead halide perovskites ( $\text{CsPbX}_3$ , X=Cl, Br, and I): novel optoelectronic materials showing bright emission with wide color gamut. *Nano Lett.* **15**, 3692–3696 (2015).

[ADS](#) [CAS](#) [PubMed](#) [PubMed Central](#) [Google Scholar](#)

8. 8.

Kovalenko, M. V., Protesescu, L. & Bodnarchuk, M. I. Properties and potential optoelectronic applications of lead halide perovskite nanocrystals. *Science* **358**, 745–750 (2017).

[ADS](#) [CAS](#) [Google Scholar](#)

9. 9.

Akkerman, Q. A., Rainò, G., Kovalenko, M. V. & Manna, L. Genesis, challenges and opportunities for colloidal lead halide perovskite nanocrystals. *Nat. Mater.* **17**, 394–405 (2018).

[ADS](#) [CAS](#) [Google Scholar](#)

10. 10.

Becker, M. A. et al. Bright triplet excitons in caesium lead halide perovskites. *Nature* **553**, 189–193 (2018).

[ADS](#) [CAS](#) [Google Scholar](#)

11. 11.

Becker, M. A. et al. Long exciton dephasing time and coherent phonon coupling in CsPbBr<sub>2</sub>Cl perovskite nanocrystals. *Nano Lett.* **18**, 7546–7551 (2018).

[ADS](#) [CAS](#) [PubMed](#) [PubMed Central](#) [Google Scholar](#)

12. 12.

Utzat, H. et al. Coherent single-photon emission from colloidal lead halide perovskite quantum dots. *Science* **363**, 1068–1072 (2019).

[ADS](#) [CAS](#) [PubMed](#) [PubMed Central](#) [Google Scholar](#)

13. 13.

Rainò, G. et al. Superfluorescence from lead halide perovskite quantum dot superlattices. *Nature* **563**, 671–675 (2018).

[ADS](#) [Google Scholar](#)

14. 14.

Skribanowitz, N., Herman, I. P., MacGillivray, J. C. & Feld, M. S. Observation of Dicke superradiance in optically pumped HF gas. *Phys. Rev. Lett.* **30**, 309–312 (1973).

[ADS](#) [Google Scholar](#)

15. 15.

Miyajima, K., Kagotani, Y., Saito, S., Ashida, M. & Itoh, T. Superfluorescent pulsed emission from biexcitons in an ensemble of semiconductor quantum dots. *J. Phys. Condens. Matter* **21**, 195802 (2009).

[ADS](#) [CAS](#) [PubMed](#) [PubMed Central](#) [Google Scholar](#)

16. 16.

Malcuit, M. S., Maki, J. J., Simkin, D. J. & Boyd, R. W. Transition from superfluorescence to amplified spontaneous emission. *Phys. Rev. Lett.* **59**, 1189–1192 (1987).

[ADS](#) [CAS](#) [PubMed](#) [PubMed Central](#) [Google Scholar](#)

17. 17.

Timothy Noe, G., II et al. Giant superfluorescent bursts from a semiconductor magneto-plasma. *Nat. Phys.* **8**, 219–224 (2012).

[Google Scholar](#)

18. 18.

Shevchenko, E. V., Talapin, D. V., Kotov, N. A., O'Brien, S. & Murray, C. B. Structural diversity in binary nanoparticle superlattices. *Nature* **439**, 55–59 (2006).

[ADS](#) [CAS](#) [Google Scholar](#)

19. 19.

Tan, R., Zhu, H., Cao, C. & Chen, O. Multi-component superstructures self-assembled from nanocrystal building blocks. *Nanoscale* **8**, 9944–9961 (2016).

[ADS](#) [CAS](#) [Google Scholar](#)

20. 20.

Nykypanchuk, D., Maye, M. M., van der Lelie, D. & Gang, O. DNA-guided crystallization of colloidal nanoparticles. *Nature* **451**, 549–552 (2008).

[ADS](#) [CAS](#) [Google Scholar](#)

21. 21.

Laramy, C. R., O'Brien, M. N. & Mirkin, C. A. Crystal engineering with DNA. *Nat. Rev. Mater.* **4**, 201–224 (2019).

[ADS](#) [CAS](#) [Google Scholar](#)

22. 22.

Murray, C. B., Kagan, C. R. & Bawendi, M. G. Self-organization of CdSe nanocrystallites into three-dimensional quantum dot superlattices. *Science* **270**, 1335–1338 (1995).

[ADS](#) [CAS](#) [Google Scholar](#)

23. 23.

Kang, Y., Ye, X. & Murray, C. B. Size- and shape-selective synthesis of metal nanocrystals and nanowires using CO as a reducing agent. *Angew. Chem. Int. Ed.* **49**, 6156–6159 (2010).

[CAS](#) [Google Scholar](#)

24. 24.

Kovalenko, M. V. & Bodnarchuk, M. I. Lead halide perovskite nanocrystals: from discovery to self-assembly and applications. *Chimia* **71**, 461–470 (2017).

[CAS](#) [Google Scholar](#)

25. 25.

Nagaoka, Y. et al. Nanocube superlattices of cesium lead bromide perovskites and pressure-induced phase transformations at atomic and mesoscale levels. *Adv. Mater.* **29**, 1606666 (2017).

[Google Scholar](#)

26. 26.

van der Burgt, J. S. et al. Cuboidal supraparticles self-assembled from cubic  $\text{CsPbBr}_3$  perovskite nanocrystals. *J. Phys. Chem. C* **122**, 15706–15712 (2018).

[Google Scholar](#)

27. 27.

Baranov, D., Toso, S., Imran, M. & Manna, L. Investigation into the photoluminescence red shift in cesium lead bromide nanocrystal superlattices. *J. Phys. Chem. Lett.* **10**, 655–660 (2019).

[CAS](#) [PubMed](#) [PubMed Central](#) [Google Scholar](#)

28. 28.

Chen, Z. & O'Brien, S. Structure direction of II–VI semiconductor quantum dot binary nanoparticle superlattices by tuning radius ratio. *ACS Nano* **2**, 1219–1229 (2008).

[CAS](#) [Google Scholar](#)

29. 29.

Coropceanu, I., Boles, M. A. & Talapin, D. V. Systematic mapping of binary nanocrystal superlattices: the role of topology in phase selection. *J. Am. Chem. Soc.* **141**, 5728–5740 (2019).

[CAS](#) [Google Scholar](#)

30. 30.

Bodnarchuk, M. I. et al. Rationalizing and controlling the surface structure and electronic passivation of cesium lead halide nanocrystals. *ACS Energy Lett.* **4**, 63–74 (2019).

[CAS](#) [Google Scholar](#)

31. 31.

Jishkariani, D. et al. Nanocrystal core size and shape substitutional doping and underlying crystalline order in nanocrystal superlattices. *ACS Nano* **13**, 5712–5719 (2019).

[CAS](#) [Google Scholar](#)

32. 32.

Dong, Y. et al. Precise control of quantum confinement in cesium lead halide perovskite quantum dots via thermodynamic equilibrium. *Nano Lett.* **18**, 3716–3722 (2018).

[ADS](#) [CAS](#) [Google Scholar](#)

33. 33.

Landman, U. & Luedtke, W. D. Small is different: energetic, structural, thermal, and mechanical properties of passivated nanocluster assemblies. *Faraday Discuss.* **125**, 1–22 (2004).

[ADS](#) [CAS](#) [Google Scholar](#)

34. 34.

Travesset, A. Topological structure prediction in binary nanoparticle superlattices. *Soft Matter* **13**, 147–157 (2017).

[ADS](#) [CAS](#) [Google Scholar](#)

35. 35.

Travesset, A. Soft skyrmions, spontaneous valence and selection rules in nanoparticle superlattices. *ACS Nano* **11**, 5375–5382 (2017).

[CAS](#) [Google Scholar](#)

36. 36.

Evers, W. H. et al. Entropy-driven formation of binary semiconductor-nanocrystal superlattices. *Nano Lett.* **10**, 4235–4241 (2010).

[ADS](#) [CAS](#) [Google Scholar](#)

37. 37.

Boles, M. A. & Talapin, D. V. Many-body effects in nanocrystal superlattices: departure from sphere packing explains stability of binary phases. *J. Am. Chem. Soc.* **137**, 4494–4502 (2015).

[CAS](#) [Google Scholar](#)

38. 38.

Dang, N. V., Dang, N. T., Ho, T. A., Tran, N. & Phan, T. L. Electronic structure and magnetic properties of  $\text{BaTi}_{1-x}\text{Mn}_x\text{O}_3$ . *Curr. Appl. Phys.* **18**, 150–154 (2018).

[ADS](#) [Google Scholar](#)

39. 39.

Shi, C.-Y., Hao, Y.-M. & Hu, Z.-B. Structural and magnetic properties of single perovskite  $\text{Ca}(\text{Ti}_{1/2}\text{Mn}_{1/2})\text{O}_3$ . *J. Magn. Magn. Mater.* **323**, 1973–1976 (2011).

[ADS](#) [CAS](#) [Google Scholar](#)

40. 40.

Vieten, J. et al. Materials design of perovskite solid solutions for thermochemical applications. *Energy Environ. Sci.* **12**, 1369–1384 (2019).

[CAS](#) [Google Scholar](#)

41. 41.

Evers, W. H., Friedrich, H., Filion, L., Dijkstra, M. & Vanmaekelbergh, D. Observation of a ternary nanocrystal superlattice and its structural characterization by electron tomography. *Angew. Chem. Int. Ed.* **48**, 9655–9657 (2009).

[CAS](#) [Google Scholar](#)

42. 42.

Dong, A., Ye, X., Chen, J. & Murray, C. B. Two-dimensional binary and ternary nanocrystal superlattices: the case of monolayers and bilayers. *Nano Lett.* **11**, 1804–1809 (2011).

[ADS](#) [CAS](#) [Google Scholar](#)

43. 43.

Paik, T., Diroll, B. T., Kagan, C. R. & Murray, C. B. Binary and ternary superlattices self-assembled from colloidal nanodisks and nanorods. *J. Am. Chem. Soc.* **137**, 6662–6669 (2015).

[CAS](#) [Google Scholar](#)

44. 44.

Scheiber, G. Über die Veränderlichkeit der Absorptionsspektren in Lösungen und die Nebenvalenzen als ihre Ursache. *Angew. Chem.* **50**, 212–219 (1937).

[Google Scholar](#)

45. 45.

Jelle, E. E. Spectral absorption and fluorescence of dyes in the molecular state. *Nature* **138**, 1009–1010 (1936).

[ADS](#) [CAS](#) [Google Scholar](#)

46. 46.

Bonifacio, R. & Lugiato, L. A. Cooperative radiation processes in two-level systems: superfluorescence. *Phys. Rev. A* **11**, 1507–1521 (1975).

[ADS](#) [Google Scholar](#)

47. 47.

Baumann, K., Guerlin, C., Brennecke, F. & Esslinger, T. Dicke quantum phase transition with a superfluid gas in an optical cavity. *Nature* **464**, 1301–1306 (2010).

[ADS](#) [CAS](#) [Google Scholar](#)

48. 48.

Strack, P. & Sachdev, S. Dicke quantum spin glass of atoms and photons. *Phys. Rev. Lett.* **107**, 277202 (2011).

[Google Scholar](#)

49. 49.

Muñoz, C. S. et al. Emitters of N-photon bundles. *Nat. Photon.* **8**, 550–555 (2014).

[ADS](#) [Google Scholar](#)

50. 50.

Wang, H. et al. Boson sampling with 20 input photons and a 60-mode interferometer in a  $10^{14}$ -dimensional Hilbert space. *Phys. Rev. Lett.* **123**, 250503 (2019).

[ADS](#) [CAS](#) [Google Scholar](#)

51. 51.

Tenne, R. et al. Super-resolution enhancement by quantum image scanning microscopy. *Nat. Photon.* **13**, 116–122 (2019).

[ADS](#) [CAS](#) [Google Scholar](#)

52. 52.

Park, J. et al. Ultra-large-scale syntheses of monodisperse nanocrystals. *Nat. Mater.* **3**, 891–895 (2004).

[ADS](#) [CAS](#) [Google Scholar](#)

53. 53.

Paik, T., Ko, D. K., Gordon, T. R., Doan-Nguyen, V. & Murray, C. B. Studies of liquid crystalline self-assembly of  $\text{GdF}_3$  nanoplates by in-plane, out-of-plane SAXS. *ACS Nano* **5**, 8322–8330 (2011).

[CAS](#) [Google Scholar](#)

54. 54.

Ibáñez, M. et al. Electron doping in bottom-up engineered thermoelectric nanomaterials through HCl-mediated ligand displacement. *J. Am. Chem. Soc.* **137**, 4046–4049 (2015).

[Google Scholar](#)

55. 55.

Amenitsch, H., Bernstorff, S. & Laggner, P. High-flux beamline for small-angle X-ray scattering at ELETTRA. *Rev. Sci. Instrum.* **66**, 1624–1626 (1995).

[ADS](#) [CAS](#) [Google Scholar](#)

56. 56.

Ilavsky, J. Nika: software for two-dimensional data reduction. *J. Appl. Crystallogr.* **45**, 324–328 (2012).

[CAS](#) [Google Scholar](#)

57. 57.

Jiang, Z. GIXSGUI: a MATLAB toolbox for grazing-incidence X-ray scattering data visualization and reduction, and indexing of buried three-dimensional periodic nanostructured films. *J. Appl. Crystallogr.* **48**, 917–926 (2015).

[CAS](#) [Google Scholar](#)

[Download references](#)

## Acknowledgements

This work was primarily supported by the European Union through Horizon 2020 Research and Innovation Programme (ERC CoG Grant, grant agreement number 819740, project SCALE-HALO) and, in part, by the Swiss National Science Foundation (grant number 200021\_192308, project Q-Light). We acknowledge the funding received from EU-H2020 under grant agreement number 654360 supporting the Transnational Access Activity within the framework NFFA-Europe to the TUG's ELETTRA SAXS beamline of CERIC-ERIC. A.T. acknowledges the funding received from the National Science Foundation (USA) DMR-CMMT 1606336. We thank Y. Shynkarenko for assistance with high-resolution SEM imaging.

## Author information

### Affiliations

1. Department of Chemistry and Applied Biosciences, Institute of Inorganic Chemistry, ETH Zürich, Zürich, Switzerland  
Ihor Cherniukh, Gabriele Rainò, Maryna I. Bodnarchuk & Maksym V. Kovalenko
2. Laboratory of Thin Films and Photovoltaics, Empa – Swiss Federal Laboratories for Materials Science and Technology, Dübendorf, Switzerland

Ihor Cherniukh, Gabriele Rainò, Maryna I. Bodnarchuk & Maksym V. Kovalenko

3. IBM Research Europe — Zurich, Rüschlikon, Switzerland

Thilo Stöferle & Rainer F. Mahrt

4. Swiss Light Source, Paul Scherrer Institut, Villigen, Switzerland

Max Burian

5. Department of Physics and Astronomy, Iowa State University and Ames Lab, Ames, IA, USA

Alex Travasset

6. Institute of Inorganic Chemistry, Graz University of Technology, Graz, Austria

Denys Naumenko & Heinz Amenitsch

7. Electron Microscopy Center, Empa – Swiss Federal Laboratories for Materials Science and Technology, Dübendorf, Switzerland

Rolf Erni

## Authors

1. Ihor Cherniukh

[View author publications](#)

You can also search for this author in [PubMed](#) [Google Scholar](#)

2. Gabriele Rainò

[View author publications](#)

You can also search for this author in [PubMed](#) [Google Scholar](#)

3. Thilo Stöferle

[View author publications](#)

You can also search for this author in [PubMed](#) [Google Scholar](#)

4. Max Burian

[View author publications](#)

You can also search for this author in [PubMed](#) [Google Scholar](#)

5. Alex Travesset

[View author publications](#)

You can also search for this author in [PubMed](#) [Google Scholar](#)

6. Denys Naumenko

[View author publications](#)

You can also search for this author in [PubMed](#) [Google Scholar](#)

7. Heinz Amenitsch

[View author publications](#)

You can also search for this author in [PubMed](#) [Google Scholar](#)

8. Rolf Erni

[View author publications](#)

You can also search for this author in [PubMed](#) [Google Scholar](#)

9. Rainer F. Mahrt

[View author publications](#)

You can also search for this author in [PubMed](#) [Google Scholar](#)

10. Maryna I. Bodnarchuk

[View author publications](#)

You can also search for this author in [PubMed](#) [Google Scholar](#)

11. Maksym V. Kovalenko  
[View author publications](#)

You can also search for this author in [PubMed](#) [Google Scholar](#)

## Contributions

M.V.K., M.I.B. and G.R. conceived and supervised the project. I.C. performed the synthesis and self-assembly experiments. I.C. and R.E. characterized the materials by electron microscopy. M.B., D.N. and H.A. characterized the materials by GISAXS. G.R., R.F.M. and T.S. carried out optical measurements. A.T. provided theoretical guidance and contributed to packing density analysis. I.C. and M.V.K. wrote the manuscript, with input from all authors.

## Corresponding author

Correspondence to [Maksym V. Kovalenko](#).

## Ethics declarations

## Competing interests

The authors declare no competing interests.

## Additional information

**Peer review information** *Nature* thanks Gerd Bacher and the other, anonymous, reviewer(s) for their contribution to the peer review of this work.

**Publisher's note** Springer Nature remains neutral with regard to jurisdictional claims in published maps and institutional affiliations.

## Extended data figures and tables

**Extended Data Fig. 1 Structural characterization of a binary  $\text{ABO}_3$ -type superlattice (SL) of 8.6-nm  $\text{CsPbBr}_3$  and 14.5-nm  $\text{Fe}_3\text{O}_4$  nanocrystals ( $\gamma = 0.541$ ).**

**a**, Low-magnification TEM image showing the large size of superlattice domains and homogeneous coverage over the carbon-coated TEM grid. **b**, TEM image of the area indicated by the box in **a**; upper inset is a higher-magnification TEM image; bottom inset is a small-angle ED pattern from a single superlattice domain in  $[001]_{\text{SL}}$  projection. **c**, HAADF-STEM image of a  $[001]_{\text{SL}}$ -oriented domain. **d**, EDX elemental maps of a  $[001]_{\text{SL}}$ -oriented domain for Fe (grey, K line) and Pb (blue, L line). **e**, EDX line scans along the arrow in **d**. **f**, 2D GISAXS pattern showing long-range order. The superlattice reflections can be indexed using a tetragonal ( $P4/mmm$ ) lattice: white markers correspond to the theoretical diffraction peak positions of a unit cell with  $a = b = 20.5$  nm and  $c = 19.0$  nm (red markers show the corresponding diffraction set for transmission channels, while white markers are for reflection channels;  $L$  defines the out-of-plane diffraction order).

**Extended Data Fig. 2 Binary  $\text{ABO}_3$ -type superlattice assembled from 8.6-nm  $\text{CsPbBr}_3$  and 16.5-nm  $\text{NaGdF}_4$  nanocrystals ( $\gamma = 0.486$ ).**

**a, b**, TEM images at different magnification of a superlattice domain deposited on a carbon-coated TEM grid; inset in **b** is a HAADF-STEM image. **c**, ED pattern from an area in **b**. ED reflections from  $\text{CsPbBr}_3$  confirm the  $\text{ABO}_3$  structure of the superlattice. **d, e**, SEM images at different magnification showing large-area coverage of the silicon substrate by binary superlattice domains; inset in **e** is a higher-magnification SEM image. **f**, Tilted SEM image revealing the thickness of the superlattice domain. The photoluminescence quantum yield of binary  $\text{ABO}_3$ -type superlattices assembled from 8.6-nm  $\text{CsPbBr}_3$  and 16.5-nm  $\text{NaGdF}_4$  nanocrystals on sapphire substrates is about 50%, and rises above 70% after cooling with liquid nitrogen.

### Extended Data Fig. 3 Binary AlB<sub>2</sub>-type superlattices.

**a**, AlB<sub>2</sub> unit cell, along with crystallographic models of [001]- and [120]-oriented AlB<sub>2</sub> lattices. Fe<sub>3</sub>O<sub>4</sub> is shown as grey spheres and CsPbBr<sub>3</sub> as blue cubes. **b–d**, 5.3-nm CsPbBr<sub>3</sub> nanocrystals combined with 12.5-nm Fe<sub>3</sub>O<sub>4</sub> nanocrystals ( $\gamma = 0.353$ ). **e, f**, 8.6-nm CsPbBr<sub>3</sub> nanocrystals combined with 19.8-nm Fe<sub>3</sub>O<sub>4</sub> nanocrystals ( $\gamma = 0.414$ ). **b**, TEM image of a superlattice domain in the [001]<sub>SL</sub> orientation. **c–f**, TEM images (**c, e**) of superlattice domains in the [120]<sub>SL</sub> orientation, along with the corresponding ED patterns (**d, f**). The inset in **c** shows a HAADF-STEM image. The presence of orthogonal reflections from the (110) and (111) lattice planes of CsPbBr<sub>3</sub> indicates alignment of nanocubes in the superlattice such that the [111] and [110] crystallographic directions of CsPbBr<sub>3</sub> orient along [001]<sub>SL</sub> and [100]<sub>SL</sub>, respectively.

### Extended Data Fig. 4 Ternary ABO<sub>3</sub>-type superlattice domains assembled from 8.6-nm CsPbBr<sub>3</sub>, 10.7-nm PbS and 19.8-nm Fe<sub>3</sub>O<sub>4</sub> nanocrystals.

**a–d**, [112]<sub>SL</sub> crystallographic orientation. **e, f**, [111]<sub>SL</sub> crystallographic orientation. **g, h**, [110]<sub>SL</sub> crystallographic orientation. **a, e, g**, HAADF-STEM images; insets show higher-magnification images. **b–d**, TEM image (**b**) of the [112]<sub>SL</sub>-oriented domain, along with the corresponding small-angle ED (**c**) and ED (**d**) patterns; the colour of diffraction arcs matches the nanocrystal orientations sketched as an inset in **d** (electron beam is normal to the plane of view). **f, h**, HAADF-STEM images and corresponding EDX-STEM maps for Fe (grey, K line), S (red, K line), Pb (blue, L line), Cs (green, L line) and Br (yellow, K line).

### Extended Data Fig. 5 HAADF-STEM tilting series of a ternary ABO<sub>3</sub>-type superlattice of 8.6-nm CsPbBr<sub>3</sub>, 10.7-nm PbS and 19.8-nm Fe<sub>3</sub>O<sub>4</sub> nanocrystals.

**a**, Tilting around the  $[010]_{\text{SL}}$  axis. **b**, Tilting around the  $[110]_{\text{SL}}$  axis. The HAADF-STEM images at different tilting angles match well with the corresponding projections of the  $\text{CaTiO}_3$  structure.

**Extended Data Fig. 6 Transition from a binary  $\text{ABO}_3$  superlattice of 8.6-nm  $\text{CsPbBr}_3$  and 19.8-nm  $\text{Fe}_3\text{O}_4$  nanocrystals to a ternary  $\text{ABO}_3$  superlattice of 8.6-nm  $\text{CsPbBr}_3$  and 25.1-nm  $\text{Fe}_3\text{O}_4$  nanocrystals on incorporation of 10.7–11.7-nm truncated-cuboid  $\text{PbS}$  nanocrystals.**

**a, b**, TEM image (**a**) and corresponding ED pattern (**b**) of a single binary  $[001]_{\text{SL}}$ -oriented domain assembled from 8.6-nm  $\text{CsPbBr}_3$  and 19.8-nm  $\text{Fe}_3\text{O}_4$  nanocrystals. Inset in **a**, model of the binary  $\text{ABO}_3$  lattice. **c, d**, TEM image (**c**) and corresponding ED pattern (**d**) of a single ternary  $[001]_{\text{SL}}$ -oriented domain assembled from 8.6-nm  $\text{CsPbBr}_3$ , 10.7-nm  $\text{PbS}$  and 19.8-nm  $\text{Fe}_3\text{O}_4$  nanocrystals. Inset in **c**, model of the ternary  $\text{ABO}_3$  structure, showing the formation of a solid solution by substitution of  $\text{CsPbBr}_3$  nanocrystals on the B site of the lattice by  $\text{PbS}$  nanocrystals. The number ratio of  $\text{PbS}$  to  $\text{CsPbBr}_3$  nanocrystals in the mixture is too small to form an exclusively ternary superlattice. As a result,  $\text{CsPbBr}_3$  and  $\text{PbS}$  nanocrystals are both present on B sites, as is evident from ED patterns. In the ED pattern of the partially ternary lattice, the intensity of the  $(110)$  reflection ‘1d’, which originates from only the centre  $\text{CsPbBr}_3$ , is weakened compared to reflection ‘1b’ in the ED pattern of the binary superlattice, because the number of perovskite nanocrystals on B sites is reduced. By contrast, the intensity of the  $(220)$  reflection ‘2d’, which originates from  $\text{CsPbBr}_3$  and  $\text{PbS}$  nanocrystals located on B sites, is enhanced compared to reflection ‘2b’ in the ED pattern of the binary superlattice, because the scattering from  $\text{PbS}$  nanocrystals, which contributes to this peak, is stronger than from the  $\text{CsPbBr}_3$  lattice. As the degree of substitution increases,  $(111)$ ,  $(200)$  and  $(220)$  ED reflections for  $\text{CsPbBr}_3$  and  $\text{PbS}$  nanocrystals add up (because of similar lattice parameters) and give rise to higher intensity, whereas the  $(100)$  and  $(110)$  reflections, to which  $\text{PbS}$  nanocrystals do not contribute

owing to their  $Fm\bar{3}m$  symmetry, eventually vanish (Fig. 4d, Supplementary Fig. 5q,t). e, TEM and HAADF-STEM (bottom inset) images of a single ternary [001]<sub>SL</sub>-oriented  $\text{ABO}_3$  domain assembled from 8.6-nm  $\text{CsPbBr}_3$ , 11.7-nm PbS and 25.1-nm  $\text{Fe}_3\text{O}_4$  nanocrystals. f, Respective ED and small-angle ED (inset) patterns. Upper inset in e, model of the ternary  $\text{ABO}_3$  lattice. 25.1-nm  $\text{Fe}_3\text{O}_4$  nanocrystals are too large to form a binary  $\text{ABO}_3$ -type superlattice. However, the addition of 11.7-nm truncated-cuboid PbS nanocrystals makes the ternary  $\text{ABO}_3$ -type superlattice stable.

### Extended Data Fig. 7 Ternary $\text{ABO}_3$ -type superlattice domains assembled from 8.6-nm $\text{CsPbBr}_3$ , 11.7-nm PbS and 21.5-nm $\text{Fe}_3\text{O}_4$ nanocrystals.

a, b, TEM image (a) of a single superlattice domain in the [001]<sub>SL</sub> orientation and the corresponding small-angle ED (a, inset) and ED (b) patterns. c, Low-magnification and high-magnification (inset) HAADF-STEM images of [001]<sub>SL</sub>-oriented domains. d, e, HAADF-STEM images of [101]<sub>SL</sub>-oriented (d) and [112]<sub>SL</sub>-oriented (e) domains.

### Extended Data Fig. 8 TEM images of columnar binary superlattices assembled from 5.3-nm $\text{CsPbBr}_3$ cubes and $\text{LaF}_3$ nanodisks.

a, AB(I)-type superlattice of 16.6-nm  $\text{LaF}_3$  nanocrystals. b,  $\text{AB}_2(\text{I})$ -type superlattice of 26.5-nm  $\text{LaF}_3$  nanocrystals. c,  $\text{AB}_x$ -type superlattice of 12.5-nm  $\text{LaF}_3$  nanocrystals. d, AB(II)-type superlattice of 9.2-nm  $\text{LaF}_3$  nanocrystals. e,  $\text{AB}_2(\text{II})$ -type superlattice of 12.5-nm  $\text{LaF}_3$  nanocrystals. f,  $\text{AB}_6$ -type superlattice of 21.0-nm  $\text{LaF}_3$  nanocrystals. Structural models of the superlattices are presented as insets. Six different columnar structures are observed, as a result of adjusting the cube-to-disk size and number ratios. None of these structures had previously been reported for disk–sphere systems and nor observed by us, highlighting the crucial role of the

cubic shape for the formation of these structures (owing to a much higher resulting packing density compared to disk–sphere systems). However, the yield and the lateral extent of the superlattice grains are considerably smaller than those of  $\text{ABO}_3$ - and  $\text{NaCl}$ -type superlattices and require further optimization.

**Extended Data Fig. 9 Luminescence spectroscopy of  $\text{ABO}_3$ -type binary superlattices made from 8.6-nm  $\text{CsPbBr}_3$  and 16.5-nm  $\text{NaGdF}_4$  nanocrystals on a carbon-coated Cu grid.**

**a**, Photoluminescence (PL) spectrum, which, similarly to Fig. 5, is composed of two bands (coupled and uncoupled nanocrystals). **b**, Photoluminescence intensity for the uncoupled (blue circles) and coupled (red circles) nanocrystal bands, on a logarithmic scale. Fits to the data (red solid lines) reveal sublinear behaviour, with fitted power-law exponents  $m \approx 0.4\text{--}0.5$ . These exponents differ from those when using  $\text{Si}_3\text{N}_4$  as a substrate, indicative of non-radiative processes at higher fluences and much enhanced superlattice–substrate interaction in the case of a conductive carbon film. **c**, Streak camera images obtained with an excitation fluence of  $175 \mu\text{J cm}^{-2}$ . In contrast to the results reported in the main text for  $\text{ABO}_3$ -type superlattices on  $\text{Si}_3\text{N}_4$ -membranes, no evidence of drastic shortening or time oscillations was found. Furthermore, a pronounced dynamic redshift characterizes the initial decay, which could be related to thermal effects (rapid cooling after heating through the excitation pulse). This is in stark contrast with typical superfluorescence spectral dynamics<sup>13</sup> (Fig. 5), which exhibits a dynamic blueshift versus time<sup>13</sup>. **d**, Spectrally integrated time-resolved emission intensity traces for two excitation fluences ( $8 \mu\text{J cm}^{-2}$ , black;  $175 \mu\text{J cm}^{-2}$ , red). Although a slight shortening of the decay is clearly observed, this is probably due to a non-radiative process, presumably energy transfer to the substrate, given the sublinear fluence dependence observed in **b** and the reduction of the fluorescence lifetime of uncoupled nanocrystals from 350 ps to about 100 ps even at low fluences. Carbon-coated grids might introduce absorbing states, which strongly influence the exciton dynamics and the onset of superfluorescence emission. This pronounced substrate effect is unsurprising given that

superlattices are morphologically two-dimensional, being at most 10 unit cells in thickness.

### **Extended Data Fig. 10 Emission properties of different binary superlattices of 8.6-nm perovskite nanocrystals.**

**a, b, d, e, g, h**, Fluence-dependent photoluminescence (**a, d, g**) and time-resolved photoluminescence traces (**b, e, h**) for NaCl-type superlattices with 18.6-nm NaGdF<sub>4</sub> nanocrystals (**a, b**), ABO<sub>3</sub>-type superlattices with 15.2 nm NaGdF<sub>4</sub> nanocrystals (**d, e**) and ABO<sub>3</sub>-type superlattices with 19.5-nm NaGdF<sub>4</sub> nanocrystals (**g, h**). **c, f, i**, Corresponding typical streak camera images obtained at high fluences. See Supplementary Note 4 for a discussion of the results.

## **Supplementary information**

### **Supplementary Information**

This file contains Supplementary Notes 1-4, Supplementary Tables 1, 2, Supplementary Figures 1-14 and Supplementary References. It includes additional data and discussion on calculation of packing densities of SL structures, relationship between lattice planes and facets in CsPbBr<sub>3</sub> nanocubes, GISAXS characterization of SLs, superfluorescence in various binary SLs, TEM characterization of SLs.

### **Supplementary Video 1**

Tomographic reconstruction of binary ABO<sub>3</sub>-type SL. ABO<sub>3</sub>-type binary SL domain comprising 8.6 nm CsPbBr<sub>3</sub> nanocubes and 19.5 nm NaGdF<sub>4</sub> spherical NCs reconstructed from electron tomography. The orientation of B- and O-site cubes is resolvable.

## **Rights and permissions**

## [Reprints and Permissions](#)

## About this article



Check for  
updates

## Cite this article

Cherniukh, I., Rainò, G., Stöferle, T. *et al.* Perovskite-type superlattices from lead halide perovskite nanocubes. *Nature* **593**, 535–542 (2021).  
<https://doi.org/10.1038/s41586-021-03492-5>

## [Download citation](#)

- Received: 24 October 2020
- Accepted: 25 March 2021
- Published: 26 May 2021
- Issue Date: 27 May 2021
- DOI: <https://doi.org/10.1038/s41586-021-03492-5>

## Comments

By submitting a comment you agree to abide by our [Terms](#) and [Community Guidelines](#). If you find something abusive or that does not comply with our terms or guidelines please flag it as inappropriate.

[Access through your institution](#)

[Change institution](#)

[Buy or subscribe](#)

# Associated Content

## [Nanocrystals form a superfluorescent lattice mimicking the atomic structure of perovskite materials](#)

- Gerd Bacher

Nature News & Views 26 May 2021

Advertisement

---

This article was downloaded by **calibre** from <https://www.nature.com/articles/s41586-021-03492-5>

| [Section menu](#) | [Main menu](#) |

- Article
- [Published: 26 May 2021](#)

# A 10 per cent increase in global land evapotranspiration from 2003 to 2019

- [Madeleine Pascolini-Campbell](#) ORCID: [orcid.org/0000-0002-6449-0841<sup>1</sup>](https://orcid.org/0000-0002-6449-0841),
- [John T. Reager](#) ORCID: [orcid.org/0000-0001-7575-2520<sup>1</sup>](https://orcid.org/0000-0001-7575-2520),
- [Hrishikesh A. Chandanpurkar](#) ORCID: [orcid.org/0000-0002-7573-8056<sup>1</sup>](https://orcid.org/0000-0002-7573-8056) &
- [Matthew Rodell](#) ORCID: [orcid.org/0000-0003-0106-7437<sup>2</sup>](https://orcid.org/0000-0003-0106-7437)

[Nature](#) volume 593, pages 543–547 (2021) [Cite this article](#)

- 1854 Accesses
- 213 Altmetric
- [Metrics details](#)

## Subjects

- [Climate change](#)
- [Climate sciences](#)
- [Hydrology](#)

## Abstract

Accurate quantification of global land evapotranspiration is necessary for understanding variability in the global water cycle, which is expected to intensify under climate change<sup>1,2,3</sup>. Current global evapotranspiration products are derived from a variety of sources, including models<sup>4,5</sup>, remote sensing<sup>6,7</sup> and in situ observations<sup>8,9,10</sup>. However, existing approaches contain extensive uncertainties; for example, relating to model structure or the upscaling of observations to a global level<sup>11</sup>. As a result, variability and trends in global evapotranspiration remain unclear<sup>12</sup>. Here we show that global land evapotranspiration increased by  $10 \pm 2$  per cent between 2003 and 2019, and that land precipitation is increasingly partitioned into evapotranspiration rather than runoff. Our results are based on an independent water-balance ensemble time series of global land evapotranspiration and the corresponding uncertainty distribution, using data from the Gravity Recovery and Climate Experiment (GRACE) and GRACE-Follow On (GRACE-FO) satellites<sup>13</sup>. Variability in global land evapotranspiration is positively correlated with El Niño–Southern Oscillation. The main driver of the trend, however, is increasing land temperature. Our findings provide an observational constraint on global land evapotranspiration, and are consistent with the hypothesis that global evapotranspiration should increase in a warming climate.

## Access options

Subscribe to Journal

Get full journal access for 1 year

\$199.00

only \$3.90 per issue

[Subscribe](#)

All prices are NET prices.

VAT will be added later in the checkout.

Tax calculation will be finalised during checkout.

Rent or Buy article

Get time limited or full article access on ReadCube.

from \$8.99

[Rent or Buy](#)

All prices are NET prices.

### **Additional access options:**

- [Log in](#)
- [Access through your institution](#)
- [Learn about institutional subscriptions](#)

**Fig. 1: Water-balance seasonal cycles.**

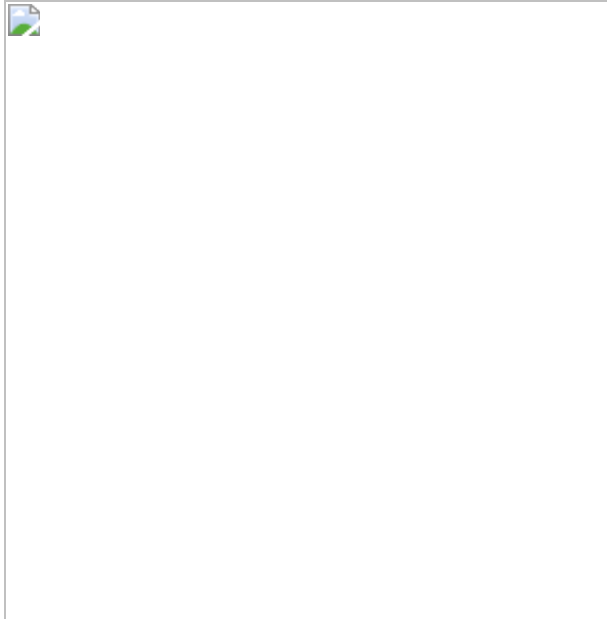


**Fig. 2: Comparison of ET with other products.**

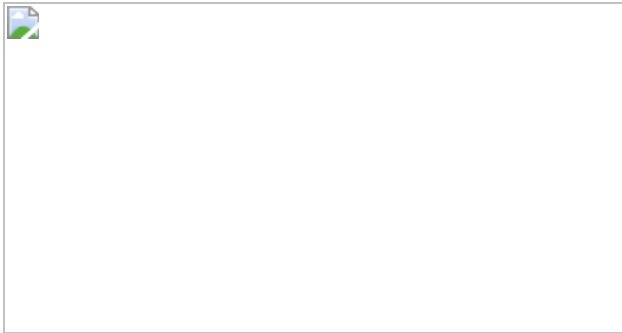


**Fig. 3: Trends in the water balance.**



## Data availability

The data that support the findings of this study have been added to the Zenodo repository and can be accessed at <https://doi.org/10.5281/zenodo.4601596>. [Source data](#) are provided with this paper.

## Code availability

The code that produced the findings of this study is available from the corresponding author upon reasonable request.

## References

1. 1.

Held, I. M. & Soden, B. J. Robust responses of the hydrological cycle to global warming. *J. Clim.* **19**, 5686–5699 (2006).

[ADS](#) [Google Scholar](#)

2. 2.

Greve, P. et al. Global assessment of trends in wetting and drying over land. *Nat. Geosci.* **7**, 716–721 (2014); corrigendum **7**, 848 (2014).

[ADS](#) [CAS](#) [Google Scholar](#)

3. 3.

Huntington, T. G. Evidence for intensification of the global water cycle: review and synthesis. *J. Hydrol.* **319**, 83–95 (2006).

[ADS](#) [Google Scholar](#)

4. 4.

Mueller, B. et al. Evaluation of global observations-based evapotranspiration datasets and IPCC AR4 simulations. *Geophys. Res. Lett.* **38**, L06402 (2011).

[ADS](#) [Google Scholar](#)

5. 5.

Haddeland, I. et al. Multi-model estimate of the global terrestrial water balance: setup and first results. *J. Hydrometeorol.* **12**, 869–884 (2011).

[ADS](#) [Google Scholar](#)

6. 6.

Mu, Q., Heinsch, F. A., Zhao, M. & Running, S. W. Development of a global evapotranspiration algorithm based on MODIS and global meteorology data. *Remote Sens. Environ.* **111**, 519–536 (2007).

[ADS](#) [Google Scholar](#)

7. 7.

Rodell, M. et al. The observed state of the water cycle in the early twenty-first century. *J. Clim.* **28**, 8289–8318 (2015).

[ADS](#) [Google Scholar](#)

8. 8.

Fisher, J. B., Tu, K. P. & Baldocchi, D. D. Global estimates of the land–atmosphere water flux based on monthly AVHRR and ISLSCP-II data, validated at 16 FLUXNET sites. *Remote Sens. Environ.* **112**, 901–919 (2008).

[ADS](#) [Google Scholar](#)

9. 9.

Jung, M. et al. The FLUXCOM ensemble of global land-atmosphere energy fluxes. *Sci. Data* **6**, 74 (2019).

[PubMed](#) [PubMed Central](#) [Google Scholar](#)

10. 10.

Hobeichi, S., Abramowitz, G., Evans, J. & Ukkola, A. Derived Optimal Linear Combination Evapotranspiration (DOLCE): a global gridded synthesis ET estimate. *Hydrol. Earth Syst. Sci.* **22**, 1317–1336 (2018).

[ADS](#) [Google Scholar](#)

11. 11.

Baldocchi, D. Assessing the eddy covariance technique for evaluating carbon dioxide exchange rates of ecosystems: past, present and future. *Glob. Change Biol.* **9**, 479–492 (2003).

[ADS](#) [Google Scholar](#)

12. 12.

Fisher, J. B. et al. The future of evapotranspiration: global requirements for ecosystem functioning, carbon and climate feedbacks, agricultural management, and water resources. *Water Resour. Res.* **53**, 2618–2626 (2017).

[ADS](#) [Google Scholar](#)

13. 13.

Tapley, B. D., Bettadpur, S., Ries, J. C., Thompson, P. F. & Watkins, M. M. GRACE measurements of mass variability in the Earth system. *Science* **305**, 503–505 (2004).

[ADS](#) [CAS](#) [PubMed](#) [PubMed Central](#) [Google Scholar](#)

14. 14.

Trenberth, K., Smith, L., Qian, T., Dai, A. & Fasullo, J. Estimates of the global water budget and its annual cycle using observational and model data. *J. Hydrometeorol.* **8**, 758–769 (2007).

[ADS](#) [Google Scholar](#)

15. 15.

Mu, Q., Zhao, M. & Running, S. W. Improvements to a MODIS global terrestrial evapotranspiration algorithm. *Remote Sens. Environ.* **115**, 1781–1800 (2011).

[ADS](#) [Google Scholar](#)

16. 16.

Anderson, M. C., Allen, R. G., Morse, A. & Kustas, W. P. Use of Landsat thermal imagery in monitoring evapotranspiration and managing water resources. *Remote Sens. Environ.* **122**, 50–65 (2012).

[ADS](#) [Google Scholar](#)

17. 17.

Allan, R. et al. Advances in understanding large-scale responses of the water cycle to climate change. *Ann. NY Acad. Sci.* **1472**, 49–75 (2020).

[ADS](#) [PubMed](#) [PubMed Central](#) [Google Scholar](#)

18. 18.

Milly, P. C. & Dunne, K. A. Potential evapotranspiration and continental drying. *Nat. Clim. Change* **6**, 946–949 (2016).

[ADS](#) [Google Scholar](#)

19. 19.

Jung, M. et al. Recent decline in the global land evapotranspiration trend due to limited moisture supply. *Nature* **467**, 951–954 (2010).

[ADS](#) [CAS](#) [PubMed](#) [PubMed Central](#) [Google Scholar](#)

20. 20.

Miralles, D. G. et al. El Niño–La Niña cycle and recent trends in continental evaporation. *Nat. Clim. Change* **4**, 122–126 (2014).

[ADS](#) [Google Scholar](#)

21. 21.

Dong, B. & Dai, A. The uncertainties and causes of the recent changes in global evapotranspiration from 1982 to 2010. *Clim. Dyn.* **49**, 279–296 (2017); correction **53**, 3707–3708 (2019).

[Google Scholar](#)

22. 22.

Zhang, K. et al. Vegetation greening and climate change promote multidecadal rises of global land evapotranspiration. *Sci. Rep.* **5**, 15956 (2015).

[ADS](#) [CAS](#) [PubMed](#) [PubMed Central](#) [Google Scholar](#)

23. 23.

Douville, H., Ribes, A., Decharme, B., Alkama, R. & Sheffield, J. Anthropogenic influence on multidecadal changes in reconstructed global evapotranspiration. *Nat. Clim. Change* **3**, 59–62 (2013).

[ADS](#) [Google Scholar](#)

24. 24.

Swann, A. L. & Koven, C. D. A direct estimate of the seasonal cycle of evapotranspiration over the Amazon Basin. *J. Hydrometeorol.* **18**, 2173–2185 (2017).

[ADS](#) [Google Scholar](#)

25. 25.

Pascolini-Campbell, M. A., Reager, J. T. & Fisher, J. B. GRACE-based mass conservation as a validation target for basin-scale evapotranspiration in the contiguous United States. *Water Resour. Res.* **56**, e2019WR026594 (2020).

[ADS](#) [Google Scholar](#)

26. 26.

Li, X. et al. Evapotranspiration estimation for Tibetan Plateau headwaters using conjoint terrestrial and atmospheric water balances and multisource remote sensing. *Wat. Resour. Res.* **55**, 8608–8630 (2019).

[ADS](#) [Google Scholar](#)

27. 27.

Ramillien, G. et al. Time variations of the regional evapotranspiration rate from Gravity Recovery and Climate Experiment (GRACE) satellite gravimetry. *Wat. Resour. Res.* **42**, W10403 (2006).

[ADS](#) [Google Scholar](#)

28. 28.

Rodell, M. et al. Basin scale estimates of evapotranspiration using GRACE and other observations. *Geophys. Res. Lett.* **31**, L20504 (2004).

[ADS](#) [Google Scholar](#)

29. 29.

Billah, M. M. et al. A methodology for evaluating evapotranspiration estimates at the watershed-scale using GRACE. *J. Hydrol.* **523**, 574–586 (2015).

[ADS](#) [Google Scholar](#)

30. 30.

Rodell, M., McWilliams, E. B., Famiglietti, J. S., Beaudoin, H. K. & Nigro, J. Estimating evapotranspiration using an observation based terrestrial water budget. *Hydrol. Process.* **25**, 4082–4092 (2011).

[ADS](#) [Google Scholar](#)

31. 31.

Liu, W. et al. A worldwide evaluation of basin-scale evapotranspiration estimates against the water balance method. *J. Hydrol.* **538**, 82–95 (2016).

[ADS](#) [Google Scholar](#)

32. 32.

Dai, A., Qian, T., Trenberth, K. E. & Milliman, J. D. Changes in continental freshwater discharge from 1948 to 2004. *J. Clim.* **22**, 2773–2792 (2009).

[ADS](#) [Google Scholar](#)

33. 33.

Chandanpurkar, H. A., Reager, J. T., Famiglietti, J. S. & Syed, T. H. Satellite- and reanalysis-based mass balance estimates of global continental discharge (1993–2015). *J. Clim.* **30**, 8481–8495 (2017).

[ADS](#) [Google Scholar](#)

34. 34.

Syed, T. H., Famiglietti, J. S., Chambers, D. P., Willis, J. K. & Hilburn, K. Satellite-based global-ocean mass balance estimates of interannual variability and emerging trends in continental freshwater discharge. *Proc. Natl Acad. Sci. USA* **107**, 17916–17921 (2010).

[ADS](#) [CAS](#) [Google Scholar](#)

35. 35.

Ropelewski, C. F. & Halpert, M. S. North American precipitation and temperature patterns associated with the El Niño/Southern Oscillation

(ENSO). *Mon. Weath. Rev.* **114**, 2352–2362 (1986).

[ADS](#) [Google Scholar](#)

36. 36.

Ropelewski, C. F. & Halpert, M. S. Precipitation patterns associated with the high index phase of the Southern Oscillation. *J. Clim.* **2**, 268–284 (1989).

[ADS](#) [Google Scholar](#)

37. 37.

Trenberth, K. E., Fasullo, J. T. & Kiehl, J. Earth's global energy budget. *Bull. Am. Meteorol. Soc.* **90**, 311–324 (2009).

[ADS](#) [Google Scholar](#)

38. 38.

Landerer, F. W. et al. Extending the global mass change data record: GRACE Follow-On instrument and science data performance. *Geophys. Res. Lett.* **47**, e2020GL088306 (2020).

[ADS](#) [Google Scholar](#)

39. 39.

Scanlon, B. R. et al. Global models underestimate large decadal declining and rising water storage trends relative to GRACE satellite data. *Proc. Natl Acad. Sci. USA* **115**, E1080–E1089 (2018).

[CAS](#) [PubMed](#) [PubMed Central](#) [Google Scholar](#)

40. 40.

Wiese, D. N., Landerer, F. W. & Watkins, M. M. Quantifying and reducing leakage errors in the JPL RL05M GRACE mascon solution.

*Water Resour. Res.* **52**, 7490–7502 (2016).

[ADS](#) [Google Scholar](#)

41. 41.

Landerer, F. W., Dickey, J. O. & Guntner, A. Terrestrial water budget of the Eurasian pan-Arctic from GRACE satellite measurements during 2003–2009. *J. Geophys. Res. D* **115**, D23115 (2010).

[ADS](#) [Google Scholar](#)

42. 42.

Long, D., Longuevergne, L. & Scanlon, B. R. Uncertainty in evapotranspiration from land surface modeling, remote sensing, and GRACE satellites. *Water Resour. Res.* **50**, 1131–1151 (2014).

[ADS](#) [Google Scholar](#)

43. 43.

Adler, R. F. et al. The Global Precipitation Climatology Project (GPCP) monthly analysis (new version 2.3) and a review of 2017 global precipitation. *Atmosphere* **9**, 138 (2018).

[ADS](#) [PubMed](#) [PubMed Central](#) [Google Scholar](#)

44. 44.

Kalnay, E. et al. The NCEP/NCAR 40-Year Reanalysis Project. *Bull. Am. Meteorol. Soc.* **77**, 437–472 (1996).

[ADS](#) [Google Scholar](#)

45. 45.

Gelaro, R. et al. The Modern-Era Retrospective Analysis for Research and Applications, Version 2 (MERRA-2). *J. Clim.* **30**, 5419–5454

(2017).

[ADS](#) [PubMed](#) [PubMed Central](#) [Google Scholar](#)

46. 46.

Hersbach, H. et al. The ERA5 global reanalysis. *Q. J. R. Meteorol. Soc.* **146**, 1999–2049 (2020).

[ADS](#) [Google Scholar](#)

47. 47.

Suzuki, T. et al. A dataset of continental river discharge based on JRA-55 for use in a global ocean circulation model. *J. Oceanogr.* **74**, 421–429 (2018).

[Google Scholar](#)

48. 48.

Huffman, G. J. et al. The global precipitation climatology project (GPCP) combined precipitation dataset. *Bull. Am. Meteorol. Soc.* **78**, 5–20 (1997).

[ADS](#) [Google Scholar](#)

49. 49.

Xie, P. P. & Arkin, P. A. Global precipitation: a 17-year monthly analysis based on gauge observations, satellite estimates, and numerical model outputs. *Bull. Am. Meteorol. Soc.* **78**, 2539–2558 (1997).

[ADS](#) [Google Scholar](#)

50. 50.

Jin, X. & Weller, R. A. *Multidecade Global Flux Datasets from the Objectively Analyzed Air–Sea Fluxes (OAFlux) Project: Latent and Sensible Heat Fluxes, Ocean Evaporation, and Related Surface Meteorological Variables* OAFlux Project Technical Report OA-2008-01 (OAFlux Project, 2008).

51. 51.

Good, S. A., Martin, M. J. & Rayner, N. A. EN4: quality controlled ocean temperature and salinity profiles and monthly objective analyses with uncertainty estimates. *J. Geophys. Res. Oceans* **118**, 6704–6716 (2013).

[ADS](#) [Google Scholar](#)

52. 52.

Rodell, M. et al. The Global Land Data Assimilation System. *Bull. Am. Meteorol. Soc.* **85**, 381–394 (2004).

[ADS](#) [Google Scholar](#)

53. 53.

Huang, B. et al. Extended Reconstructed Sea Surface Temperature version 4 (ERSST.v4). Part I: upgrades and intercomparisons. *J. Clim.* **28**, 911–930 (2015).

[ADS](#) [Google Scholar](#)

54. 54.

Lenssen, N. J. et al. Improvements in the GISTEMP uncertainty model. *J. Geophys. Res. D* **124**, 6307–6326 (2019).

[ADS](#) [Google Scholar](#)

55. 55.

Gehne, M., Hamill, T. M., Kiladis, G. N. & Trenberth, K. E. Comparison of global precipitation estimates across a range of temporal and spatial scales. *J. Clim.* **29**, 7773–7795 (2016).

[ADS](#) [Google Scholar](#)

56. 56.

Jolliffe, I. T. Uncertainty and inference for verification measures. *Weather Forecast.* **22**, 637–650 (2007).

[ADS](#) [Google Scholar](#)

57. 57.

Bamber, J. et al. Land ice freshwater budget of the Arctic and North Atlantic oceans: 1. Data, methods, and results. *J. Geophys. Res. Oceans* **123**, 1827–1837 (2018).

[ADS](#) [CAS](#) [PubMed](#) [PubMed Central](#) [Google Scholar](#)

58. 58.

Rye, C. D. et al. Rapid sea-level rise along the Antarctic margins in response to increased glacial discharge. *Nat. Geosci.* **7**, 732–735 (2014).

[ADS](#) [CAS](#) [Google Scholar](#)

59. 59.

Depoorter, M. A. et al. Calving fluxes and basal melt rates of Antarctic ice shelves. *Nature* **502**, 89–92 (2013); corrigendum **502**, 580 (2013).

[ADS](#) [CAS](#) [PubMed](#) [PubMed Central](#) [Google Scholar](#)

[Download references](#)

# Acknowledgements

The research was carried out at the Jet Propulsion Laboratory, California Institute of Technology, under a contract with the National Aeronautics and Space Administration. Government sponsorship acknowledged. This work was supported by funding from NASA's GRACE-FO Science Team, Principal Investigator J.T.R. We thank A. Bloom for sharing code used to produce the confidence interval plots.

# Author information

## Affiliations

1. NASA Jet Propulsion Laboratory, California Institute of Technology, Pasadena, CA, USA

Madeleine Pascolini-Campbell, John T. Reager & Hrishikesh A. Chandanpurkar

2. NASA Goddard Space Flight Center, Greenbelt, MD, USA

Matthew Rodell

## Authors

1. Madeleine Pascolini-Campbell  
[View author publications](#)

You can also search for this author in [PubMed](#) [Google Scholar](#)

2. John T. Reager  
[View author publications](#)

You can also search for this author in [PubMed](#) [Google Scholar](#)

3. Hrishikesh A. Chandanpurkar  
[View author publications](#)

You can also search for this author in [PubMed](#) [Google Scholar](#)

4. Matthew Rodell

[View author publications](#)

You can also search for this author in [PubMed](#) [Google Scholar](#)

## Contributions

M.P.-C. conceived, and carried out the research, led the data analysis and wrote the manuscript. J.T.R. conceived the research, designed the analysis and provided comments on the manuscript. H.A.C. produced the global discharge dataset and also provided input on the analysis. M.R. provided comments on the manuscript.

## Corresponding author

Correspondence to [Madeleine Pascolini-Campbell](#).

## Ethics declarations

## Competing interests

The authors declare no competing interests.

## Additional information

**Peer review information** *Nature* thanks Di Long, Bart Nijssen and the other, anonymous, reviewer(s) for their contribution to the peer review of this work.

**Publisher's note** Springer Nature remains neutral with regard to jurisdictional claims in published maps and institutional affiliations.

## Extended data figures and tables

## Extended Data Fig. 1 Input water cycle timeseries.

**a–c**, The raw time series for global land precipitation (GPCPv2.3, MERRA-2, NOAA–NCEP and ERA-5) (**a**), discharge (JRA-55, and ocean mass-balance estimates EN4–OAFlux–GPCP, EN4–OAFlux–CMAP, EN4–ERA5, EN4–MERRA2) (**b**) and change in total water storage ( $dS/dt$ ) from GRACE/GRACE-FO using three different methods to compute the derivative (backward difference with three-month smoothing, centred finite difference and backward difference) (**c**). [Source data](#)

## Extended Data Fig. 2 Error budget of water-balance components.

**a, b**, Monthly error time series for precipitation (**a**) and discharge (**b**) calculated as the standard deviation of input data sets. **c**, Error in  $dS/dt$  calculated from the formal GRACE JPL RL06 mascon error product, and propagated into derivative. Monthly time series of errors plotted for 2003 to 2019 in units of  $\text{mm yr}^{-1}$ . [Source data](#)

## Extended Data Fig. 3 Ratios of water-balance components.

**a–c**, Ratios between components of the water balance for  $ET/Q$  (**a**),  $ET/Pr$  (**b**) and  $Q/Pr$  (**c**). In each case, the ratios are calculated using the time series with the seasonal cycle removed and 15-month smoothing applied. The ensemble mean for each variable (ET, Pr and  $Q$ ) is used. [Source data](#)

## Extended Data Fig. 4 Water-balance relationship with ENSO.

Left: correlation with ERSST version 4 SST against ET (**a**), Pr (**c**),  $Q$  (**e**) and  $dS/dt$  (**g**). Right: time series of MEI index against ET (**b**), Pr (**d**),  $Q$  (**f**) and  $dS/dt$  (**h**). For each panel, the SST and water-balance variable have the seasonal cycle removed and a 15-month moving average filter applied. The  $r$  value of the correlation between the MEI and water-cycle variable are shown in top left corner (right panels). Stippling on the maps (left panels) indicates that the value of the Pearson correlation between the SST and the water-balance variable (ET, Pr,  $Q$  and  $dS/dt$ ) at that grid point is significant

( $\alpha = 0.05$  level). Maps created using MATLAB with the M\_Map package (online at <https://www.eoas.ubc.ca/~rich/map.html>). [Source data](#)

### Extended Data Fig. 5 Effect of ENSO and temperature.

**a**, Multiple linear regression of global surface temperature (yellow line) and MEI (red line) onto ET (blue line). **b–d**, Multiple regression of MEI (red line) onto Pr (**b**),  $Q$  (**c**) and  $dS/dt$  (**d**). In each, the input times series data has been filtered using a 15-month moving average. The amount of variability explained is indicated by  $R^2$  (top left corner of panels). [Source data](#)

### Extended Data Fig. 6 Effect of removing natural climate variability and temperature on ET.

**a**, ET anomaly time series (solid blue line) and linear trend (dashed blue line), and ET anomaly time series minus the multiple regression model of MEI onto ET (solid red lines) and trend (dashed red line). **b**, Same as **a**, but for multiple regression model of surface temperature. The value of the trends in  $\text{mm yr}^{-1}$  are indicated in the top left. [Source data](#)

### Extended Data Fig. 7 Influence of ENSO on ET products.

Left: correlation with ERSST version 4 SST against different ET products: ET (**a**), MOD16A2GF (**c**), FLUXCOM (**e**), PT-JPL (**g**) and GLDAS2.2 (**i**). Right: time series of MEI index against ET (**b**), MOD16A2GF (**d**), FLUXCOM (**f**), PT-JPL (**h**) and GLDAS2.2 (**j**). For each panel, the SST and water-balance variable have the seasonal cycle removed and a 15-month moving average filter applied. The  $r$  value of the correlation between MEI and ET shown in top left corner (right panels) ( $r$  values surrounded by  $()$  are not significant at the  $\alpha = 0.05$  level). Stippling on the maps (left panels) indicates that the value of the correlation at that grid point is significant ( $\alpha = 0.05$  level). Maps created using MATLAB with the M\_Map package (online at <https://www.eoas.ubc.ca/~rich/map.html>). [Source data](#)

### Extended Data Fig. 8 Contribution of ice sheets to ET.

**a–c**, Seasonal cycle for ET, Pr,  $Q$  and  $dS/dt$  calculated without Greenland + Antarctica (**a**), without Antarctica (**b**) and with all global land (ET from this study) (**c**). The shading is the standard deviation among the bias-corrected seasonal cycle of the ET ensemble (red shading), and input datasets used for Pr (four datasets, blue shading),  $Q$  (five datasets, black shading) and  $dS/dt$  (three methods to calculate derivative from JPL RL06 GRACE TWS, teal shading). **d–f**, Ensemble of ET compared with other ET products for ET calculated without Greenland + Antarctica (**d**), without Antarctica (**e**) and with all global land (ET from this study) (**f**). The shading represents the confidence intervals for the ensemble of ET (range shown in the colour bar). [Source data](#)

#### Extended Data Table 1 ET long-term mean and trends

[Full size table](#)

#### Extended Data Table 2 ET seasonal cycle and trends

[Full size table](#)

## Source data

[Source Data Fig. 1](#)

[Source Data Fig. 2](#)

[Source Data Fig. 3](#)

[Source Data Extended Data Fig. 1](#)

[Source Data Extended Data Fig. 2](#)

[Source Data Extended Data Fig. 3](#)

[Source Data Extended Data Fig. 4](#)

[Source Data Extended Data Fig. 5](#)

[\*\*Source Data Extended Data Fig. 6\*\*](#)

[\*\*Source Data Extended Data Fig. 7\*\*](#)

[\*\*Source Data Extended Data Fig. 8\*\*](#)

## Rights and permissions

[Reprints and Permissions](#)

## About this article



Check for  
updates

## Cite this article

Pascolini-Campbell, M., Reager, J.T., Chandanpurkar, H.A. *et al.* A 10 per cent increase in global land evapotranspiration from 2003 to 2019. *Nature* **593**, 543–547 (2021). <https://doi.org/10.1038/s41586-021-03503-5>

[Download citation](#)

- Received: 06 October 2020
- Accepted: 26 March 2021
- Published: 26 May 2021
- Issue Date: 27 May 2021
- DOI: <https://doi.org/10.1038/s41586-021-03503-5>

## Comments

By submitting a comment you agree to abide by our [Terms](#) and [Community Guidelines](#). If you find something abusive or that does not comply with our terms or guidelines please flag it as inappropriate.

[Access through your institution](#)

[Change institution](#)

[Buy or subscribe](#)

Advertisement

---

This article was downloaded by **calibre** from <https://www.nature.com/articles/s41586-021-03503-5>

| [Section menu](#) | [Main menu](#) |

- Article
- [Published: 21 April 2021](#)

# Overriding water table control on managed peatland greenhouse gas emissions

- [C. D. Evans](#) [ORCID: orcid.org/0000-0002-7052-354X](#)<sup>1,2</sup>,
- [M. Peacock](#) [ORCID: orcid.org/0000-0002-3086-2854](#)<sup>2</sup>,
- [A. J. Baird](#) [ORCID: orcid.org/0000-0001-8198-3229](#)<sup>3</sup>,
- [R. R. E. Artz](#) [ORCID: orcid.org/0000-0002-8462-6558](#)<sup>4</sup>,
- [A. Burden](#) [ORCID: orcid.org/0000-0002-7694-1638](#)<sup>1</sup>,
- [N. Callaghan](#)<sup>1</sup>,
- [P. J. Chapman](#) [ORCID: orcid.org/0000-0003-0438-6855](#)<sup>3</sup>,
- [H. M. Cooper](#) [ORCID: orcid.org/0000-0002-1382-3407](#)<sup>5</sup>,
- [M. Coyle](#)<sup>4,6</sup>,
- [E. Craig](#) [ORCID: orcid.org/0000-0001-8036-2930](#)<sup>1,7</sup>,
- [A. Cumming](#) [ORCID: orcid.org/0000-0001-5704-9006](#)<sup>5</sup>,
- [S. Dixon](#) [ORCID: orcid.org/0000-0002-6801-6098](#)<sup>8</sup>,
- [V. Gauci](#)<sup>9</sup>,
- [R. P. Grayson](#) [ORCID: orcid.org/0000-0003-3637-3987](#)<sup>3</sup>,
- [C. Helfter](#) [ORCID: orcid.org/0000-0001-5773-4652](#)<sup>6</sup>,
- [C. M. Heppell](#) [ORCID: orcid.org/0000-0001-6028-1359](#)<sup>10</sup>,
- [J. Holden](#) [ORCID: orcid.org/0000-0002-1108-4831](#)<sup>3</sup>,
- [D. L. Jones](#) [ORCID: orcid.org/0000-0002-1482-4209](#)<sup>7,11,12</sup>,
- [J. Kaduk](#) [ORCID: orcid.org/0000-0003-4051-3081](#)<sup>13</sup>,
- [P. Levy](#) [ORCID: orcid.org/0000-0002-8505-1901](#)<sup>6</sup>,
- [R. Matthews](#)<sup>14</sup>,
- [N. P. McNamara](#)<sup>15</sup>,
- [T. Misselbrook](#) [ORCID: orcid.org/0000-0002-4594-3606](#)<sup>14</sup>,

- [S. Oakley](#) [ORCID: orcid.org/0000-0002-5757-7420<sup>15</sup>](#),
- [S. E. Page<sup>13</sup>](#),
- [M. Rayment<sup>7</sup>](#),
- [L. M. Ridley](#) [ORCID: orcid.org/0000-0001-5060-5823<sup>7</sup>](#),
- [K. M. Stanley](#) [ORCID: orcid.org/0000-0003-3388-0932<sup>16</sup>](#),
- [J. L. Williamson](#) [ORCID: orcid.org/0000-0001-8216-5885<sup>1</sup>](#),
- [F. Worrall<sup>8</sup>](#) &
- [R. Morrison](#) [ORCID: orcid.org/0000-0002-1847-3127<sup>5</sup>](#)

[Nature](#) volume **593**, pages 548–552 (2021) [Cite this article](#)

- 4339 Accesses
- 1 Citations
- 174 Altmetric
- [Metrics details](#)

## Subjects

- [Carbon cycle](#)
- [Climate-change mitigation](#)
- [Environmental impact](#)
- [Hydrology](#)

## Abstract

Global peatlands store more carbon than is naturally present in the atmosphere<sup>1,2</sup>. However, many peatlands are under pressure from drainage-based agriculture, plantation development and fire, with the equivalent of around 3 per cent of all anthropogenic greenhouse gases emitted from drained peatland<sup>3,4,5</sup>. Efforts to curb such emissions are intensifying through the conservation of undrained peatlands and re-wetting of drained systems<sup>6</sup>. Here we report eddy covariance data for carbon dioxide from 16 locations and static chamber measurements for methane from 41 locations

in the UK and Ireland. We combine these with published data from sites across all major peatland biomes. We find that the mean annual effective water table depth ( $WTD_e$ ; that is, the average depth of the aerated peat layer) overrides all other ecosystem- and management-related controls on greenhouse gas fluxes. We estimate that every 10 centimetres of reduction in  $WTD_e$  could reduce the net warming impact of  $CO_2$  and  $CH_4$  emissions (100-year global warming potentials) by the equivalent of at least 3 tonnes of  $CO_2$  per hectare per year, until  $WTD_e$  is less than 30 centimetres. Raising water levels further would continue to have a net cooling effect until  $WTD_e$  is within 10 centimetres of the surface. Our results suggest that greenhouse gas emissions from peatlands drained for agriculture could be greatly reduced without necessarily halting their productive use. Halving  $WTD_e$  in all drained agricultural peatlands, for example, could reduce emissions by the equivalent of over 1 per cent of global anthropogenic emissions.

## Access options

Subscribe to Journal

Get full journal access for 1 year

\$199.00

only \$3.90 per issue

[Subscribe](#)

All prices are NET prices.

VAT will be added later in the checkout.

Tax calculation will be finalised during checkout.

Rent or Buy article

Get time limited or full article access on ReadCube.

from \$8.99

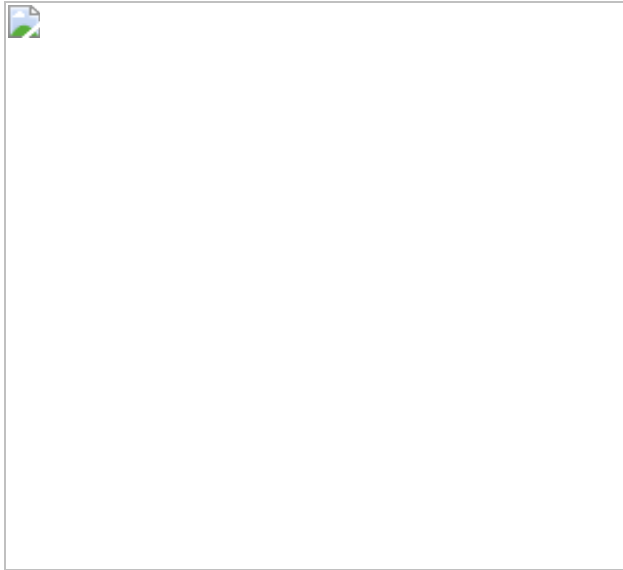
## Rent or Buy

All prices are NET prices.

## **Additional access options:**

- [Log in](#)
- [Access through your institution](#)
- [Learn about institutional subscriptions](#)

**Fig. 1: Annual mean values of carbon dioxide and methane flux versus mean water table depth.**



## **Data availability**

The UK eddy covariance data set used in the study is available from the UK Environmental Information Data Centre (EIDC), with the identifier: <https://doi.org/10.5285/b8c9fd3d-f9ea-4fd8-9557-9022884f711d>. Summary and literature-derived data are included in Extended Data Tables [1–3](#).

## **References**

1. 1.

Yu, Z. C. Northern peatland carbon stocks and dynamics: a review. *Biogeosciences* **9**, 4071–4085 (2012).

[CAS](#) [ADS](#) [Google Scholar](#)

2. 2.

Dargie, G. C. et al. Age, extent and carbon storage of the central Congo Basin peatland complex. *Nature* **542**, 86–90 (2017).

[CAS](#) [PubMed](#) [ADS](#) [Google Scholar](#)

3. 3.

Smith, P. et al. in *Climate Change 2014: Mitigation of Climate Change* (eds Edenhofer, O. et al.) Ch. 11 (2014).

4. 4.

Leifeld, J. & Menichetti, L. The underappreciated potential of peatlands in global climate change mitigation strategies. *Nat. Commun.* **9**, 1071 (2018).

[CAS](#) [PubMed](#) [PubMed Central](#) [ADS](#) [Google Scholar](#)

5. 5.

Le Quéré, C. et al. Global Carbon Budget 2017. *Earth Syst. Sci. Data* **10**, 405–448 (2018).

[ADS](#) [Google Scholar](#)

6. 6.

*Towards Climate-responsible Peatlands Management*. Mitigation of Climate Change in Agriculture Series 9 (FAO, 2014).

7. 7.

Byrne, K. A. et al. *EU Peatlands: Current Carbon Stocks and Trace Gas Fluxes*. Report 4/2004 to Concerted action: Synthesis of the European Greenhouse Gas Budget (Geosphere-Biosphere Centre, Univ. Lund, 2004).

8. 8.

Wijedasa, L. et al. Carbon emissions from South-East Asian peatlands will increase despite emission-reduction schemes. *Glob. Change Biol.* **24**, 4598–4613 (2018).

[ADS](#) [Google Scholar](#)

9. 9.

Hutchinson, J. N. Record of peat wastage in the East-Anglian fenlands at Holme Post, 1848–1978 AD. *J. Ecol.* **68**, 229–249 (1980).

[Google Scholar](#)

10. 10.

Hooijer, A. et al. Subsidence and carbon loss in drained tropical peatlands. *Biogeosciences* **9**, 1053–1071 (2012).

[CAS](#) [ADS](#) [Google Scholar](#)

11. 11.

Turetsky, M. R. et al. Global vulnerability of peatlands to fire and carbon loss. *Nat. Geosci.* **8**, 11–14 (2015).

[CAS](#) [ADS](#) [Google Scholar](#)

12. 12.

Evans, C. D. et al. Rates and spatial variability of peat subsidence in Acacia plantation and forest landscapes in Sumatra, Indonesia. *Geoderma* **338**, 410–421 (2019).

[ADS](#) [Google Scholar](#)

13. 13.

Carlson, K. M. et al. Greenhouse gas emissions intensity of global croplands. *Nat. Clim. Change* **7**, 62–68 (2016).

[Google Scholar](#)

14. 14.

IPCC Task Force on National Greenhouse Gas Inventories. *2013 Supplement to the 2006 IPCC Guidelines for National Greenhouse Gas Inventories: Wetlands*. (IPCC, 2014).

15. 15.

Tiemeyer, B. et al. High emissions of greenhouse gases from grasslands on peat and other organic soils. *Glob. Change Biol.* **22**, 4134–4149 (2016).

[ADS](#) [Google Scholar](#)

16. 16.

Couwenberg, J. et al. Assessing greenhouse gas emissions from peatlands using vegetation as a proxy. *Hydrobiologia* **674**, 67–89 (2011).

[CAS](#) [Google Scholar](#)

17. 17.

Dias, A. T. C. et al. Plant species composition can be used as a proxy to predict methane emissions in peatland ecosystems after landuse changes. *Ecosystems* **13**, 526–538 (2010).

[CAS](#) [Google Scholar](#)

18. 18.

Pohl, M. et al. Dynamic C and N stocks—key factors controlling the C gas exchange of maize in heterogeneous peatland. *Biogeosciences* **12**, 2737–2752 (2015).

[ADS](#) [Google Scholar](#)

19. 19.

Joosten, H., Tapiro-Biström, M.-L. & Tol, S. *Peatlands—Guidance for Climate Change Mitigation, Conservation, Rehabilitation and Sustainable Use*. Mitigation of Climate Change in Agriculture Series 5 (FAO, 2012).

20. 20.

Cooper, M. et al. Infilled ditches are hotspots of landscape methane flux following peatland restoration. *Ecosystems (N. Y.)* **17**, 1227–1241 (2014).

[CAS](#) [Google Scholar](#)

21. 21.

Turetsky, M. R. et al. A synthesis of methane emissions from 71 northern, temperate, and subtropical wetlands. *Glob. Change Biol.* **20**, 2183–2197 (2014).

[ADS](#) [Google Scholar](#)

22. 22.

Frolking, S., Roulet, N. & Fuglestvedt, J. How northern peatlands influence the Earth's radiative budget: sustained methane emission versus sustained carbon sequestration. *J. Geophys. Res.* **111**, G01008 (2006).

[ADS](#) [Google Scholar](#)

23. 23.

Evans, C. et al. *Implementation of an Emission Inventory for UK Peatlands*. (Centre for Ecology and Hydrology, Bangor, 2017).

24. 24.

Brown, P. et al. *UK Greenhouse Gas Inventory, 1990 to 2017: Annual Report for Submission under the Framework Convention on Climate Change*. (Ricardo Energy & Environment, 2019).

25. 25.

IPCC. *2006 IPCC Guidelines for National Greenhouse Gas Inventories* (IGES, 2006).

26. 26.

Food and Agriculture Organisation of the United Nations. FAOSTAT. [www.fao.org/faostat/en/#data](http://www.fao.org/faostat/en/#data) (accessed 5 May 2019).

27. 27.

Evans, C. D., Renou-Wilson, F. & Strack, M. The role of waterborne carbon in the greenhouse gas balance of drained and re-wetted peatlands. *Aquat. Sci.* **78**, 573–590 (2016).

[CAS](#) [Google Scholar](#)

28. 28.

Granath, G., Moore, P. A., Lukenbach, M. C. & Waddington, J. M. Mitigating wildfire carbon loss in managed northern peatlands through restoration. *Sci. Rep.* **6**, 28498 (2016).

[CAS](#) [PubMed](#) [PubMed Central](#) [ADS](#) [Google Scholar](#)

29. 29.

Paustian, K. et al. Climate-smart soils. *Nature* **532**, 49–57 (2016).

[CAS](#) [PubMed](#) [ADS](#) [Google Scholar](#)

30. 30.

Ferré, M. Sustainable management of cultivated peatlands in Switzerland: insights, challenges, and opportunities. *Land Use Policy* **87**, 104019 (2019).

[ADS](#) [Google Scholar](#)

31. 31.

Günther, A. et al. Prompt rewetting of drained peatlands reduces climate warming despite methane emissions. *Nat. Commun.* **11**, 1644 (2020).

[PubMed](#) [PubMed Central](#) [ADS](#) [Google Scholar](#)

32. 32.

Evans, C. D. et al. *Lowland Peatland Systems in England and Wales – Evaluating Greenhouse Gas Fluxes and Carbon Balances*. Final report to Defra on Project SP1210 (Centre for Ecology and Hydrology, 2016).

33. 33.

Levy, P. E. & Gray, A. Greenhouse gas balance of a semi-natural peatbog in northern Scotland. *Environ. Res. Lett.* **10**, 094019 (2015).

[ADS](#) [Google Scholar](#)

34. 34.

Helfter, C. et al. Drivers of long-term variability in CO<sub>2</sub> net ecosystem exchange in a temperate peatland. *Biogeosciences* **12**, 1799–1811 (2015).

[ADS](#) [Google Scholar](#)

35. 35.

Peacock, M. et al. The full carbon balance of a rewetted cropland fen and a conservation-managed fen. *Agric. Ecosyst. Environ.* **269**, 1–12 (2019).

[Google Scholar](#)

36. 36.

Hambley, G. et al. Net ecosystem exchange from two formerly afforested peatlands undergoing restoration in the Flow Country of northern Scotland. *Mires Peat* **23**, 05 (2019).

[Google Scholar](#)

37. 37.

McVeigh, P., Sottocornola, M., Foley, N., Leahy, P. & Keily, G. Meteorological and functional response partitioning to explain interannual variability of CO<sub>2</sub> exchange at an Irish Atlantic blanket bog. *Agric. For. Meteorol.* **194**, 8–19 (2014).

[ADS](#) [Google Scholar](#)

38. 38.

Papale, D. et al. Towards a standardized processing of net ecosystem exchange measured with eddy covariance technique: algorithms and uncertainty estimation. *Biogeosciences* **3**, 571–583 (2006).

[CAS](#) [ADS](#) [Google Scholar](#)

39. 39.

Foken, T. et al. in *Handbook of Micrometeorology*, 181–208 (Kluwer Academic, 2004)

40. 40.

Kormann, R. & Meixner, F. X. An analytical footprint model for non-neutral stratification. *Boundary-Layer Meteorol.* **99**, 207–224 (2001).

[ADS](#) [Google Scholar](#)

41. 41.

Reichstein, M. et al. On the separation of net ecosystem exchange into assimilation and ecosystem respiration: review and improved algorithm. *Glob. Change Biol.* **11**, 1424–1439 (2005).

[ADS](#) [Google Scholar](#)

42. 42.

Reichstein, M., Moffat, M. A., Wutzler, T. & Sickel, K. REddyProc: Data processing and plotting utilities of (half-)hourly eddy-covariance measurements. (2016); <https://rdrr.io/rforge/REddyProc/>.

43. 43.

Finkelstein, P. L. & Sims, P. F. Sampling error in eddy correlation flux measurements. *J. Geophys. Res.* **106**, 3503–3509 (2001).

[CAS](#) [ADS](#) [Google Scholar](#)

44. 44.

Wang, M. et al. Can abandoned peatland pasture sequester more carbon dioxide from the atmosphere than an adjacent pristine bog in Newfoundland, Canada? *Agric. For. Meteorol.* **248**, 91–108 (2018).

[ADS](#) [Google Scholar](#)

45. 45.

Roulet, N. T. et al. Contemporary carbon balance and late Holocene carbon accumulation in a northern peatland. *Glob. Change Biol.* **13**, 397–411 (2007).

[ADS](#) [Google Scholar](#)

46. 46.

Nugent, K. A., Strachan, I. B., Strack, M., Roulet, N. T. & Rochefort, L. Multi-year net ecosystem carbon balance of a restored peatland reveals a return to carbon sink. *Glob. Change Biol.* **24**, 5751–5768 (2018).

[Google Scholar](#)

47. 47.

Lund, M., Lindroth, A., Christensen, T. R. & Ström, L. Annual CO<sub>2</sub> balance of a temperate bog. *Tellus B* **59**, 804–811 (2007).

[ADS](#) [Google Scholar](#)

48. 48.

Ratcliffe, J. L., Campbell, D. I., Clarkson, B. R., Wall, A. M. & Schipper, L. A. Water table fluctuations control CO<sub>2</sub> exchange in wet and dry bogs through different mechanisms. *Sci. Total Environ.* **655**, 1037–1046 (2019).

[CAS](#) [PubMed](#) [ADS](#) [Google Scholar](#)

49. 49.

Lee, S.-C. et al. Annual greenhouse gas budget for a bog ecosystem undergoing restoration by rewetting. *Biogeosciences* **14**, 2799–2814 (2017).

[CAS](#) [ADS](#) [Google Scholar](#)

50. 50.

D' Acunha, B., Morillas, L., Black, T. A., Christen, A. & Johnson, M. S. Net ecosystem carbon balance of a peat bog undergoing restoration: integrating CO<sub>2</sub> and CH<sub>4</sub> fluxes from eddy covariance and aquatic evasion with DOC drainage fluxes. *J. Geophys. Res. Biogeosci.* **124**, 884–901 (2019).

[Google Scholar](#)

51. 51.

Strachan, I. B., Pelletier, L. & Bonneville, M. C. Inter-annual variability in water table depth controls net ecosystem carbon dioxide exchange in a boreal bog. *Biogeochemistry* **127**, 99–111 (2016).

[CAS](#) [Google Scholar](#)

52. 52.

Humphreys, E. R., Charron, C., Brown, M. & Jones, R. Two bogs in the Canadian Hudson Bay Lowlands and a temperate bog reveal similar annual net ecosystem exchange of CO<sub>2</sub>. *Arct. Antarct. Alp. Res.* **46**, 103–113 (2014).

[Google Scholar](#)

53. 53.

Holl, D., Pancotto, V., Heger, A., Camargo, S. J. & Kutzbach, L. Cushion bogs are stronger carbon dioxide net sinks than moss-dominated bogs as revealed by eddy covariance measurements on Tierra del Fuego, Argentina. *Biogeosciences* **16**, 3397–3423 (2019).

[CAS](#) [ADS](#) [Google Scholar](#)

54. 54.

Hao, Y. B. et al. Predominance of precipitation and temperature controls on ecosystem CO<sub>2</sub> exchange in Zoige alpine wetlands of Southwest China. *Wetlands* **31**, 413–422 (2011).

[Google Scholar](#)

55. 55.

Helbig, M. et al. Direct and indirect climate change effects on carbon dioxide fluxes in a thawing boreal forest–wetland landscape. *Glob. Change Biol.* **23**, 3231–3248 (2017).

[ADS](#) [Google Scholar](#)

56. 56.

Helbig, M., Quinton, W. L. & Sonnentag, O. Warmer spring conditions increase annual methane emissions from a boreal peat landscape with sporadic permafrost. *Environ. Res. Lett.* **12**, 115009 (2017).

[ADS](#) [Google Scholar](#)

57. 57.

Hommeltenberg, J. et al. Ecosystem scale methane fluxes in a natural temperate bog-pine forest in southern Germany. *Agric. For. Meteorol.* **198–199**, 273–284 (2014).

[ADS](#) [Google Scholar](#)

58. 58.

Drollinger, S., Maier, A. & Glatzel, S. Interannual and seasonal variability in carbon dioxide and methane fluxes of a pine peat bog in the Eastern Alps, Austria. *Agric. For. Meteorol.* **275**, 69–78 (2019).

[ADS](#) [Google Scholar](#)

59. 59.

Olefeldt, D. et al. Net carbon accumulation of a high-latitude permafrost palsa mire similar to permafrost-free peatlands. *Geophys. Res. Lett.* **39**, L03501 (2012).

[ADS](#) [Google Scholar](#)

60. 60.

Nilsson, M. et al. Contemporary carbon accumulation in a boreal oligotrophic minerogenic mire—a significant sink after accounting for all C-fluxes. *Glob. Change Biol.* **14**, 2317–2332 (2008).

[ADS](#) [Google Scholar](#)

61. 61.

Pullens, J. W. M., Sottocornola, M., Kiely, G., Toscano, P. & Gianelle, D. Carbon fluxes of an alpine peatland in Northern Italy. *Agric. Forest Meteorol.* **220**, 69–82 (2016).

[ADS](#) [Google Scholar](#)

62. 62.

Olson, D. M., Griffis, T. J., Noormets, A., Kolka, R. & Chen, J. Interannual, seasonal, and retrospective analysis of the methane and carbon dioxide budgets of a temperate peatland. *J. Geophys. Res. Biogeosci.* **118**, 226–238 (2013).

[CAS](#) [Google Scholar](#)

63. 63.

Liu, L. et al. Contemporary, modern and ancient carbon fluxes in the Zoige peatlands on the Qinghai-Tibetan Plateau. *Geoderma* **352**, 138–149 (2019).

[CAS](#) [ADS](#) [Google Scholar](#)

64. 64.

Yu, X., Song, C., Sun, L., Wang, X. & Tan, W. Towards an improved utilization of eddy covariance data: growing season CO<sub>2</sub> exchange from a permafrost peatland in the Great Hing'an Mountains, Northeast China. *Ecol. Indic.* **115**, 106427 (2020).

[CAS](#) [Google Scholar](#)

65. 65.

Miao, Y. et al. Growing season methane emission from a boreal peatland in the continuous permafrost zone of Northeast China: effects of active layer depth and vegetation. *Biogeosciences* **9**, 4455–4464 (2012).

[CAS](#) [ADS](#) [Google Scholar](#)

66. 66.

Sonnentag, O., Van Der Kamp, G., Barr, A. G. & Chen, J. M. On the relationship between water table depth and water vapor and carbon dioxide fluxes in a minerotrophic fen. *Glob. Change Biol.* **16**, 1762–1776 (2010).

[ADS](#) [Google Scholar](#)

67. 67.

Aurela, M. et al. Carbon dioxide exchange on a northern boreal fen. *Boreal Environ. Res.* **14**, 699–710 (2009).

[CAS](#) [Google Scholar](#)

68. 68.

Aurela, M. et al. Carbon dioxide and energy flux measurements in four northern-boreal ecosystems at Pallas. *Boreal Environ. Res.* **20**, 455–473 (2015).

[Google Scholar](#)

69. 69.

Aurela, M. et al. CO<sub>2</sub> exchange of a sedge fen in southern Finland—the impact of a drought period. *Tellus B* **59**, 826–837 (2007).

[ADS](#) [Google Scholar](#)

70. 70.

Aurela, M., Laurila, T. & Tuovinen, J. P. The timing of snow melt controls the annual CO<sub>2</sub> balance in a subarctic fen. *Geophys. Res. Lett.* **31**, L16119 (2004).

[ADS](#) [Google Scholar](#)

71. 71.

Schulze, E. D., Prokuschkin, A., Arneth, A., Knorre, N. & Vaganov, E. A. Net ecosystem productivity and peat accumulation in a Siberian Aapa mire. *Tellus B* **54**, 531–536 (2002).

[ADS](#) [Google Scholar](#)

72. 72.

Friborg, T., Soegaard, H., Christensen, T. R., Lloyd, C. R. & Panikov, N. S. Siberian wetlands: where a sink is a source. *Geophys. Res. Lett.* **30**, 2129 (2003).

[ADS](#) [Google Scholar](#)

73. 73.

Flanagan, L. B. & Syed, K. H. Stimulation of both photosynthesis and respiration in response to warmer and drier conditions in a boreal peatland ecosystem. *Glob. Change Biol.* **17**, 2271–2287 (2011).

[ADS](#) [Google Scholar](#)

74. 74.

Adkinson, A.C., Syed, K.H. & Flanagan, L.B. Contrasting responses of growing season ecosystem CO<sub>2</sub> exchange to variation in temperature and water table depth in two peatlands in northern Alberta, Canada. *J. Geophys. Res. Biogeosci.* **116**, G01004 (2011).

[ADS](#) [Google Scholar](#)

75. 75.

Joiner, D. W., Lafleur, P. M., McCaughey, J. H. & Bartlett, P. A. Interannual variability in carbon dioxide exchanges at a boreal wetland in the BOREAS northern study area. *J. Geophys. Res. Atmos.* **104**, 27663–27672 (1999).

[CAS](#) [ADS](#) [Google Scholar](#)

76. 76.

Bubier, J., Moore, T., Savage, K. & Crill, P. A comparison of methane flux in a boreal landscape between a dry and a wet year. *Global Biogeochem. Cycles* **19**, GB1023 (2005).

[ADS](#) [Google Scholar](#)

77. 77.

Aslan-Sungur, G., Lee, X., Evrendilek, F. & Karakaya, N. Large interannual variability in net ecosystem carbon dioxide exchange of a disturbed temperate peatland. *Sci. Total Environ.* **554–555**, 192–202 (2016).

[PubMed](#) [ADS](#) [Google Scholar](#)

78. 78.

Schrier-Uijl, A. P. et al. Agricultural peatlands: towards a greenhouse gas sink-a synthesis of a Dutch landscape study. *Biogeosciences* **11**, 4559–4576 (2014).

[ADS](#) [Google Scholar](#)

79. 79.

Hadden, D. & Grelle, A. The impact of cultivation on CO<sub>2</sub> and CH<sub>4</sub> fluxes over organic soils in Sweden. *Agric. For. Meteorol.* **243**, 1–8 (2017).

[ADS](#) [Google Scholar](#)

80. 80.

Valdés-Barrera, A. et al. Effects of disturbance on the carbon dioxide balance of an anthropogenic peatland in northern Patagonia. *Wetlands Ecol. Manage.* **27**, 635–650 (2019).

[Google Scholar](#)

81. 81.

Langeveld, C. A. et al. Emissions of CO<sub>2</sub>, CH<sub>4</sub> and N<sub>2</sub>O from pasture on drained peat soils in the Netherlands. *Eur. J. Agron.* **7**, 35–42 (1997).

[CAS](#) [Google Scholar](#)

82. 82.

Hatala, J. A. et al. Greenhouse gas (CO<sub>2</sub>, CH<sub>4</sub>, H<sub>2</sub>O) fluxes from drained and flooded agricultural peatlands in the Sacramento–San Joaquin Delta. *Agric. Ecosyst. Environ.* **150**, 1–18 (2012).

[CAS](#) [Google Scholar](#)

83. 83.

Knox, S. H. et al. Agricultural peatland restoration: effects of land-use change on greenhouse gas ( $\text{CO}_2$  and  $\text{CH}_4$ ) fluxes in the Sacramento–San Joaquin Delta. *Glob. Change Biol.* **21**, 750–765 (2015).

[ADS](#) [Google Scholar](#)

84. 84.

Campbell, D. I., Wall, A. M., Nieveen, J. P. & Schipper, L. A. Variations in  $\text{CO}_2$  exchange for dairy farms with year-round rotational grazing on drained peatlands. *Agric. Ecosyst. Environ.* **202**, 68–78 (2015).

[Google Scholar](#)

85. 85.

Fleischer, E., Khashimov, I., Hözel, N. & Klemm, O. Carbon exchange fluxes over peatlands in Western Siberia: possible feedback between land-use change and climate change. *Sci. Total Environ.* **545–546**, 424–433 (2016).

[PubMed](#) [ADS](#) [Google Scholar](#)

86. 86.

Lohila, A., Aurela, M., Tuovinen, J. P. & Laurila, T. Annual  $\text{CO}_2$  exchange of a peat field growing spring barley or perennial forage grass. *J. Geophys. Res. Atmos.* **109**, D18116 (2004).

[ADS](#) [Google Scholar](#)

87. 87.

Regina, K., Pihlatie, M., Esala, M. & Alakukku, L. Methane fluxes on boreal arable soils. *Agric. Ecosyst. Environ.* **119**, 346–352 (2007).

[CAS](#) [Google Scholar](#)

88. 88.

Rankin, T., Strachan, I. B. & Strack, M. Carbon dioxide and methane exchange at a post-extraction, unrestored peatland. *Ecol. Eng.* **122**, 241–251 (2018).

[Google Scholar](#)

89. 89.

Hendriks, D. M. D., Van Huissteden, J., Dolman, A. J. & Van der Molen, M. K. The full greenhouse gas balance of an abandoned peat meadow. *Biogeosciences* **4**, 411–424 (2007).

[CAS](#) [ADS](#) [Google Scholar](#)

90. 90.

Shurpali, N. J. et al. Cultivation of a perennial grass for bioenergy on a boreal organic soil—carbon sink or source? *Glob. Change Biol. Bioenergy* **1**, 35–50 (2009).

[CAS](#) [Google Scholar](#)

91. 91.

Gong, J. et al. Climatic sensitivity of the CO<sub>2</sub> flux in a cutaway boreal peatland cultivated with a perennial bioenergy crop (*Phalaris arundinaceae*, L.): beyond diplotelmic modeling. *Agric. For. Meteorol.* **198–199**, 232–249 (2014).

[ADS](#) [Google Scholar](#)

92. 92.

Nieveen, J. P., Jacobs, C. M. & Jacobs, A. F. Diurnal and seasonal variation of carbon dioxide exchange from a former true raised bog.

*Glob. Change Biol.* **4**, 823–833 (1998).

[ADS](#) [Google Scholar](#)

93. 93.

Rigney, C. et al. Greenhouse gas emissions from two rewetted peatlands previously managed for forestry. *Mires Peat* **21**, 24 (2018).

[Google Scholar](#)

94. 94.

Kiew, F. et al. CO<sub>2</sub> balance of a secondary tropical peat swamp forest in Sarawak, Malaysia. *Agric. For. Meteorol.* **248**, 494–501 (2018).

[ADS](#) [Google Scholar](#)

95. 95.

Hirano, T. et al. Effects of disturbances on the carbon balance of tropical peat swamp forests. *Glob. Change Biol.* **18**, 3410–3422 (2012).

[ADS](#) [Google Scholar](#)

96. 96.

Griffis, T. J. et al. Hydrometeorological sensitivities of net ecosystem carbon dioxide and methane exchange of an Amazonian palm swamp peatland. *Agric. For. Meteorol.* **295**, 108167 (2020).

[ADS](#) [Google Scholar](#)

97. 97.

Brown, E. L. *Greenhouse Gas Flux Response to Restoration Management in UK Lowland Peatlands*. PhD thesis, Bangor Univ. (2017).

98. 98.

Denmead, O. T. Approaches to measuring fluxes of methane and nitrous oxide between landscapes and the atmosphere. *Plant Soil* **309**, 5–24 (2008).

[CAS](#) [Google Scholar](#)

99. 99.

Baird, A. J., Holden, J. & Chapman, P. *A Literature Review of Evidence on Emissions of Methane in Peatlands*. Defra Project SP0574 (Univ. Leeds, 2009).

100. 100.

Green, S. M. & Baird, A. J. Using ‘snapshot’ measurements of CH<sub>4</sub> fluxes from an ombrotrophic peatland to estimate annual budgets: interpolation versus modelling. *Mires Peat* **19**, 9 (2017).

[Google Scholar](#)

101. 101.

Green, S. M. & Baird, A. J. A mesocosm study of the role of the sedge *Eriophorum angustifolium* in the efflux of methane—including that due to episodic ebullition—from peatlands. *Plant Soil* **351**, 207–218 (2012).

[CAS](#) [Google Scholar](#)

102. 102.

Stanley, K. M., Heppell, C. M., Belyea, L. R., Baird, A. J. & Field, R. H. The importance of CH<sub>4</sub> ebullition in floodplain fens. *J. Geophys. Res. Biogeosci.* **124**, 1750–1763 (2019).

[CAS](#) [Google Scholar](#)

103. 103.

Yamulki, S., Peace, A. & Morison, J. I. L. Soil CO<sub>2</sub>, CH<sub>4</sub> and N<sub>2</sub>O fluxes from an afforested lowland raised peatbog in Scotland: implications for drainage and restoration. *Biogeosciences* **10**, 1051–1065 (2013).

[ADS](#) [Google Scholar](#)

104. 104.

Gauci, V., Dise, N. & Fowler, D. Controls on suppression of methane flux from a peat bog subjected to simulated acid rain sulfate deposition. *Glob. Biogeochem. Cycles* **16**, 4-1–4-12 (2002).

[ADS](#) [Google Scholar](#)

105. 105.

Laine, A., Wilson, D., Kiely, G. & Byrne, K. A. Methane flux dynamics in an Irish lowland blanket bog. *Plant Soil* **299**, 181–193 (2007).

[CAS](#) [Google Scholar](#)

106. 106.

Drewer, J. et al. Comparison of greenhouse gas fluxes and nitrogen budgets from an ombotrophic bog in Scotland and a minerotrophic sedge fen in Finland. *Eur. J. Soil Sci.* **61**, 640–650 (2010).

[CAS](#) [Google Scholar](#)

107. 107.

Renou-Wilson, F., Müller, C., Moser, G. & Wilson, D. To graze or not to graze? Four years greenhouse gas balances and vegetation composition from a drained and a rewetted organic soil under grassland. *Agric. Ecosyst. Environ.* **222**, 156–170 (2016).

[Google Scholar](#)

108. 108.

Wilson, D. et al. Rewetting of cutaway peatlands: are we re-creating hot spots of methane emissions? *Restor. Ecol.* **17**, 796–806 (2009).

[Google Scholar](#)

109. 109.

Wilson, D. et al. Multiyear greenhouse gas balances at a rewetted temperate peatland. *Glob. Change Biol.* **22**, 4080–4095 (2016).

[ADS](#) [Google Scholar](#)

110. 110.

Levy, P. E. et al. Methane emissions from soils: synthesis and analysis of a large UK data set. *Glob. Change Biol.* **18**, 1657–1669 (2012).

[ADS](#) [Google Scholar](#)

111. 111.

Myhre, G. et al. in *Climate Change 2013: The Physical Science Basis* (eds. Stocker, T. F. et al.) 659–684 (IPCC, Cambridge Univ. Press, 2013).

112. 112.

<https://unfccc.int/process-and-meetings/transparency-and-reporting/methods-for-climate-change-transparency/common-metrics>  
(accessed 1 February 2021).

113. 113.

Sterner, E. O. & Johansson, D. J. A. The effect of climate–carbon cycle feedbacks on emission metrics. *Environ. Res. Lett.* **12**, 034019

(2017).

[ADS](#) [Google Scholar](#)

114. 114.

Gasser, T. et al. Accounting for the climate–carbon feedback in emission metrics. *Earth Syst. Dyn.* **8**, 235–253 (2017).

[ADS](#) [Google Scholar](#)

115. 115.

Neubauer, S. C. & Megonigal, J. P. Moving beyond global warming potentials to quantify the climatic role of ecosystems. *Ecosystems* **18**, 1000–1013 (2015).

[Google Scholar](#)

116. 116.

Tiemeyer, B. et al. A new methodology for organic soils in national greenhouse gas inventories: data synthesis, derivation and application. *Ecol. Indic.* **109**, 105838 (2020).

[CAS](#) [Google Scholar](#)

117. 117.

Fick, S. E. & Hijmans, R. J. WorldClim 2: new 1-km spatial resolution climate surfaces for global land areas. *Int. J. Climatol.* **37**, 4302–4315 (2017).

[Google Scholar](#)

[Download references](#)

## Acknowledgements

This study was supported by the UK Department for Environment, Food and Rural Affairs (projects SP1210 and SP1218), with additional data provided from projects funded by the UK Natural Environment Research Council (SEFLOS, NE/P0140971/1 and UKSCAPE, NE/R016429/1), Scottish Government and Natural Resources Wales (NRW). UK flux sites were hosted by a range of organizations including G's Fresh, the National Trust, NRW and the Balmoral Estate. We thank all those responsible for collecting the published data used in the study, in particular M. Strack, D. Holl, H. Keck and C. Deshmukh for providing additional data and information on individual studies, L. Menichetti for sharing peat mapping data and L. Barber at the University of Leicester for preparing the site maps.

## Author information

### Affiliations

1. UK Centre for Ecology and Hydrology, Bangor, UK  
C. D. Evans, A. Burden, N. Callaghan, E. Craig & J. L. Williamson
2. Department of Aquatic Sciences and Assessment, Swedish University of Agricultural Sciences, Uppsala, Sweden  
C. D. Evans & M. Peacock
3. School of Geography, University of Leeds, Leeds, UK  
A. J. Baird, P. J. Chapman, R. P. Grayson & J. Holden
4. The James Hutton Institute, Aberdeen, UK  
R. R. E. Artz & M. Coyle
5. UK Centre for Ecology and Hydrology, Wallingford, UK  
H. M. Cooper, A. Cumming & R. Morrison

6. UK Centre for Ecology and Hydrology, Penicuik, UK  
M. Coyle, C. Helfter & P. Levy
7. School of Natural Sciences, Bangor University, Bangor, UK  
E. Craig, D. L. Jones, M. Rayment & L. M. Ridley
8. Department of Earth Sciences, Durham University, Durham, UK  
S. Dixon & F. Worrall
9. School of Geography, Earth and Environmental Sciences, University of Birmingham, Birmingham, UK  
V. Gauci
10. School of Geography, Queen Mary University of London, London, UK  
C. M. Heppell
11. SoilsWest, Centre for Sustainable Farming Systems, Food Futures Institute, Murdoch University, Murdoch, Western Australia, Australia  
D. L. Jones
12. UWA School of Agriculture and Environment, University of Western Australia, Perth, Western Australia, Australia  
D. L. Jones
13. School of Geography, Geology and the Environment, University of Leicester, Leicester, UK  
J. Kaduk & S. E. Page
14. Rothamsted Research, North Wyke, Okehampton, UK  
R. Matthews & T. Misselbrook

15. UK Centre for Ecology and Hydrology, Lancaster, UK

N. P. McNamara & S. Oakley

16. Institut für Atmosphäre und Umwelt, Goethe Universität Frankfurt,  
Frankfurt am Main, Germany

K. M. Stanley

## Authors

1. C. D. Evans

[View author publications](#)

You can also search for this author in [PubMed](#) [Google Scholar](#)

2. M. Peacock

[View author publications](#)

You can also search for this author in [PubMed](#) [Google Scholar](#)

3. A. J. Baird

[View author publications](#)

You can also search for this author in [PubMed](#) [Google Scholar](#)

4. R. R. E. Artz

[View author publications](#)

You can also search for this author in [PubMed](#) [Google Scholar](#)

5. A. Burden

[View author publications](#)

You can also search for this author in [PubMed](#) [Google Scholar](#)

6. N. Callaghan

[View author publications](#)

You can also search for this author in [PubMed](#) [Google Scholar](#)

7. P. J. Chapman

[View author publications](#)

You can also search for this author in [PubMed](#) [Google Scholar](#)

8. H. M. Cooper

[View author publications](#)

You can also search for this author in [PubMed](#) [Google Scholar](#)

9. M. Coyle

[View author publications](#)

You can also search for this author in [PubMed](#) [Google Scholar](#)

10. E. Craig

[View author publications](#)

You can also search for this author in [PubMed](#) [Google Scholar](#)

11. A. Cumming

[View author publications](#)

You can also search for this author in [PubMed](#) [Google Scholar](#)

12. S. Dixon

[View author publications](#)

You can also search for this author in [PubMed](#) [Google Scholar](#)

13. V. Gauci

[View author publications](#)

You can also search for this author in [PubMed](#) [Google Scholar](#)

14. R. P. Grayson

[View author publications](#)

You can also search for this author in [PubMed](#) [Google Scholar](#)

15. C. Helfter

[View author publications](#)

You can also search for this author in [PubMed](#) [Google Scholar](#)

16. C. M. Heppell

[View author publications](#)

You can also search for this author in [PubMed](#) [Google Scholar](#)

17. J. Holden

[View author publications](#)

You can also search for this author in [PubMed](#) [Google Scholar](#)

18. D. L. Jones

[View author publications](#)

You can also search for this author in [PubMed](#) [Google Scholar](#)

19. J. Kaduk

[View author publications](#)

You can also search for this author in [PubMed](#) [Google Scholar](#)

20. P. Levy

[View author publications](#)

You can also search for this author in [PubMed](#) [Google Scholar](#)

21. R. Matthews

[View author publications](#)

You can also search for this author in [PubMed](#) [Google Scholar](#)

22. N. P. McNamara

[View author publications](#)

You can also search for this author in [PubMed](#) [Google Scholar](#)

23. T. Misselbrook

[View author publications](#)

You can also search for this author in [PubMed](#) [Google Scholar](#)

24. S. Oakley

[View author publications](#)

You can also search for this author in [PubMed](#) [Google Scholar](#)

25. S. E. Page

[View author publications](#)

You can also search for this author in [PubMed](#) [Google Scholar](#)

26. M. Rayment

[View author publications](#)

You can also search for this author in [PubMed](#) [Google Scholar](#)

27. L. M. Ridley

[View author publications](#)

You can also search for this author in [PubMed](#) [Google Scholar](#)

28. K. M. Stanley

[View author publications](#)

You can also search for this author in [PubMed](#) [Google Scholar](#)

29. J. L. Williamson

[View author publications](#)

You can also search for this author in [PubMed](#) [Google Scholar](#)

30. F. Worrall

[View author publications](#)

You can also search for this author in [PubMed](#) [Google Scholar](#)

31. R. Morrison

[View author publications](#)

You can also search for this author in [PubMed](#) [Google Scholar](#)

## Contributions

C.D.E. conceived and led the study, undertook the global upscaling and drafted the paper. R.M. coordinated eddy covariance measurements and led the analysis of eddy covariance data. M.P. and S.E.P. supported the global flux data synthesis. P.L. undertook additional statistical analysis. A.J.B. designed and oversaw the chamber flux CH<sub>4</sub> measurement programme.

J.H., R.P.G. and A.J.B. were responsible for the hydrological measurement programme. F.W. was responsible for site surveys. M.P., R.R.E.A., P.J.C., N.C., M.C., E.C., A.C., S.D., V.G., C.H., C.M.H., D.L.J., J.K., P.L., R.M., N.P.M., T.M., S.O., M.R., L.M.R., K.M.S., R.M. and F.W. were responsible for the management, operation and processing of data for one or more of the flux measurement sites. A.B., R.M., J.L.W. and H.M.C. were responsible for central data management and processing. All authors contributed to data analysis and interpretation, and commented on the draft manuscript.

## Corresponding author

Correspondence to [C. D. Evans](#).

## Ethics declarations

## Competing interests

A number of the authors are on peatland advisory boards for the UK government, devolved governments and agencies, and for other public, private and charitable sector organizations. C.D.E. and S.E.P. are on the International Peatland Expert Working Group of Asia Pacific Resources

International Ltd. S.E.P. is on the International Advisory Panel on Peatland Research for the Malaysian Palm Oil Board. J.H. is on the science advisory board for MS Amlin. None of the authors receive direct remuneration for any advisory roles undertaken or have any financial or non-financial interests in organizations that may be affected by the results of this study.

## Additional information

**Peer review information** *Nature* thanks Dennis Baldocchi, Torben Christensen and Maria Strack for their contribution to the peer review of this work.

**Publisher's note** Springer Nature remains neutral with regard to jurisdictional claims in published maps and institutional affiliations.

## Extended data figures and tables

### [Extended Data Fig. 1 Location and land-cover class of UK and Irish CO<sub>2</sub> flux-tower sites analysed.](#)

Sites are overlaid on the global peat map of Leifeld and Menichetti<sup>4</sup>. For detailed site information, see Extended Data Table 1.

### [Extended Data Fig. 2 Cumulative measured NEE and NEP \(harvested sites only\) for UK eddy covariance sites.](#)

Positive values indicate net CO<sub>2</sub> emission to the atmosphere, negative values indicate net CO<sub>2</sub> uptake. Years with missing data at Anglesey 2 and Tadham Moor were assigned the average long-term NEP value for the site for presentational purposes only; these years were not used in the calculations.

### [Extended Data Fig. 3 Location and land-cover type of all study sites included in global CO<sub>2</sub> flux data synthesis.](#)

Sites are overlaid on the peat map of Leifeld and Menichetti<sup>4</sup>. For detailed site information, see Extended Data Table [2](#).

### [Extended Data Fig. 4 Observed relationship between mean CH<sub>4</sub> flux and WTD<sub>e</sub> for British and Irish sites.](#)

Results are compared with previous relationships derived from independent data in the United Kingdom (Levy et al.<sup>110</sup>), Continental Europe (Couwenberg et al.<sup>16</sup>), and North America and Fennoscandia (Turetsky et al.<sup>21</sup>).

### [Extended Data Fig. 5 Comparison of predicted and observed NEP versus WTD<sub>e</sub> for tropical peatlands.](#)

Filled red circles show observations from six tropical peatland flux towers. Dashed line shows a linear regression fitted to these data points ( $\text{NEP} = 0.1887 \text{ WTD}_e - 3.19$ ,  $R^2 = 0.79$ ,  $P = 0.017$ ). Solid line shows relationship derived from high-latitude regression (equation (2)), scaled for tropical peatlands based on IPCC Tier 1 emission factors (see [Methods](#)).

#### **Extended Data Table 1 Locations and characteristics of UK and Ireland study sites**

[Full size table](#)

#### **Extended Data Table 2 Locations and characteristics of global CO<sub>2</sub> flux synthesis sites**

[Full size table](#)

#### **Extended Data Table 3 Locations and characteristics of UK and Irish sites used in CH<sub>4</sub> flux synthesis**

[Full size table](#)

#### **Extended Data Table 4 Area and emissions estimates for global peatlands under drained cropland and grassland**

[Full size table](#)

#### **Extended Data Table 5 Disaggregated global emissions of CO<sub>2</sub> and CH<sub>4</sub> from drained cropland and grassland. a, CO<sub>2</sub>; b, CH<sub>4</sub>. Emissions are based on application of our empirical relationships to the global peat**

area estimates of Leifeld and Menichetti<sup>4</sup> (Extended Data Table 4) and used to derive Table 1. Scenarios and calculations are as described in the Methods

[Full size table](#)

## Rights and permissions

[Reprints and Permissions](#)

## About this article



Check for  
updates

## Cite this article

Evans, C.D., Peacock, M., Baird, A.J. *et al.* Overriding water table control on managed peatland greenhouse gas emissions. *Nature* **593**, 548–552 (2021). <https://doi.org/10.1038/s41586-021-03523-1>

[Download citation](#)

- Received: 06 November 2020
- Accepted: 08 April 2021
- Published: 21 April 2021
- Issue Date: 27 May 2021
- DOI: <https://doi.org/10.1038/s41586-021-03523-1>

## Further reading

- **Peatland subsidence enhances cultivated lowland flood risk**

- Lauri Ikkala
- , Anna-Kaisa Ronkanen
- , Olli Utriainen
- , Bjørn Kløve
- & Hannu Marttila

*Soil and Tillage Research* (2021)

## Comments

By submitting a comment you agree to abide by our [Terms](#) and [Community Guidelines](#). If you find something abusive or that does not comply with our terms or guidelines please flag it as inappropriate.

[Access through your institution](#)

[Change institution](#)

[Buy or subscribe](#)

Advertisement

---

This article was downloaded by **calibre** from <https://www.nature.com/articles/s41586-021-03523-1>

| [Section menu](#) | [Main menu](#) |

- Article
- [Published: 28 April 2021](#)

# Expanded diversity of Asgard archaea and their relationships with eukaryotes

- [Yang Liu](#) ORCID: [orcid.org/0000-0002-1109-0756](#)<sup>1</sup> na1,
- [Kira S. Makarova](#) ORCID: [orcid.org/0000-0002-8174-2844](#)<sup>2</sup> na1,
- [Wen-Cong Huang](#) ORCID: [orcid.org/0000-0002-1328-4087](#)<sup>1</sup> na1,
- [Yuri I. Wolf](#) ORCID: [orcid.org/0000-0002-0247-8708](#)<sup>2</sup>,
- [Anastasia N. Nikolskaya](#)<sup>2</sup>,
- [Xinxu Zhang](#) ORCID: [orcid.org/0000-0002-4299-2795](#)<sup>1</sup>,
- [Mingwei Cai](#) ORCID: [orcid.org/0000-0002-2757-6742](#)<sup>1</sup>,
- [Cui-Jing Zhang](#) ORCID: [orcid.org/0000-0003-0904-5531](#)<sup>1</sup>,
- [Wei Xu](#) ORCID: [orcid.org/0000-0003-0213-8823](#)<sup>3</sup>,
- [Zhuhua Luo](#) ORCID: [orcid.org/0000-0002-7553-8628](#)<sup>3</sup>,
- [Lei Cheng](#) ORCID: [orcid.org/0000-0003-1178-8190](#)<sup>4</sup>,
- [Eugene V. Koonin](#) ORCID: [orcid.org/0000-0003-3943-8299](#)<sup>2</sup> &
- [Meng Li](#) ORCID: [orcid.org/0000-0001-8675-0758](#)<sup>1</sup>

*Nature* volume 593, pages 553–557 (2021) [Cite this article](#)

- 7476 Accesses
- 315 Altmetric
- [Metrics details](#)

## Subjects

- [Archaea](#)
- [Metagenomics](#)
- [Molecular evolution](#)
- [Phylogenetics](#)

## Abstract

Asgard is a recently discovered superphylum of archaea that appears to include the closest archaeal relatives of eukaryotes<sup>1,2,3,4,5</sup>. Debate continues as to whether the archaeal ancestor of eukaryotes belongs within the Asgard superphylum or whether this ancestor is a sister group to all other archaea (that is, a two-domain versus a three-domain tree of life)<sup>6,7,8</sup>. Here we present a comparative analysis of 162 complete or nearly complete genomes of Asgard archaea, including 75 metagenome-assembled genomes that—to our knowledge—have not previously been reported. Our results substantially expand the phylogenetic diversity of Asgard and lead us to propose six additional phyla that include a deep branch that we have provisionally named Wukongarchaeota. Our phylogenomic analysis does not resolve unequivocally the evolutionary relationship between eukaryotes and Asgard archaea, but instead—depending on the choice of species and conserved genes used to build the phylogeny—supports either the origin of eukaryotes from within Asgard (as a sister group to the expanded Heimdallarchaeota–Wukongarchaeota branch) or a deeper branch for the eukaryote ancestor within archaea. Our comprehensive protein domain analysis using the 162 Asgard genomes results in a major expansion of the set of eukaryotic signature proteins. The Asgard eukaryotic signature proteins show variable phyletic distributions and domain architectures, which is suggestive of dynamic evolution through horizontal gene transfer, gene loss, gene duplication and domain shuffling. The phylogenomics of the Asgard archaea points to the accumulation of the components of the mobile archaeal ‘eukaryome’ in the archaeal ancestor of eukaryotes (within or outside Asgard) through extensive horizontal gene transfer.

## Access options

Subscribe to Journal

Get full journal access for 1 year

\$199.00

only \$3.90 per issue

[Subscribe](#)

All prices are NET prices.

VAT will be added later in the checkout.

Tax calculation will be finalised during checkout.

Rent or Buy article

Get time limited or full article access on ReadCube.

from \$8.99

[Rent or Buy](#)

All prices are NET prices.

### **Additional access options:**

- [Log in](#)
- [Access through your institution](#)
- [Learn about institutional subscriptions](#)

**Fig. 1: Phylogenetic analysis of Asgard archaea and their relationships with eukaryotes.**

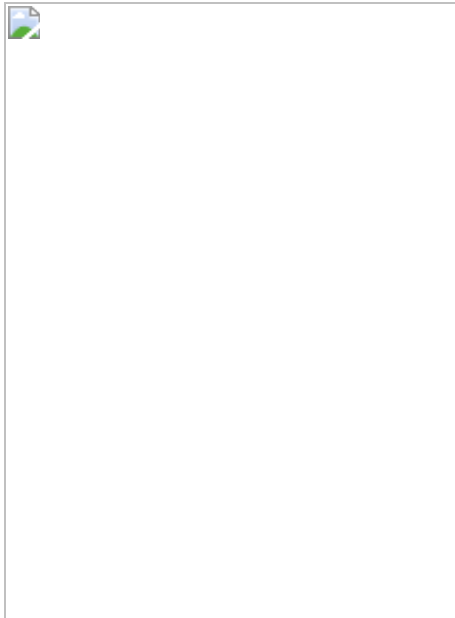


**Fig. 2: Domain architectures of selected ESPs in Asgard archaea.**

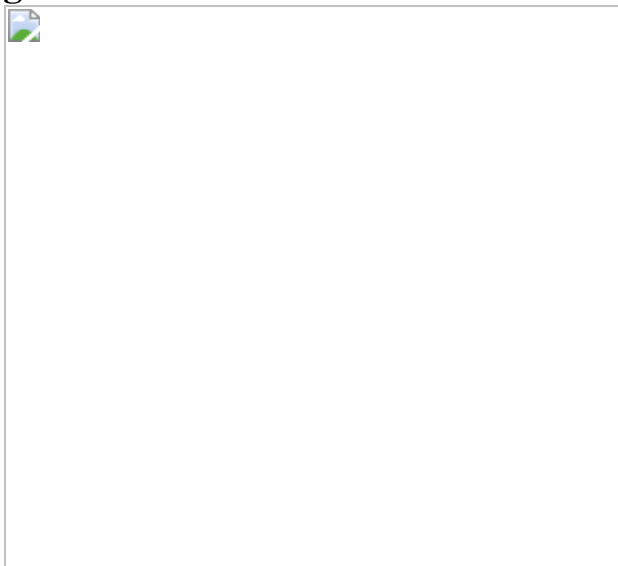
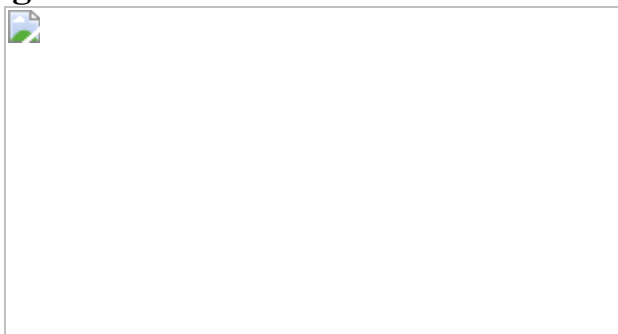


**Fig. 3: Reconstruction and evolution of key metabolic processes in Asgard archaea.**



## Data availability

Asgard archaea genomes generated in this study have been deposited in the eLibrary of Microbial Systematics and Genomics (<https://www.biosino.org/elmsg/index>) and are also available from the NCBI under BioProject identifier [PRJNA680430](#). Publicly available genomes were retrieved from NCBI GenBank, MG-RAST and the figshare repository. The accession numbers of the newly generated and the public genomes are available in Supplementary Table 1. Supplementary data file 1 comprises the complete Asgard COG data archive (supplementary\_data\_file\_1.tgz), and supplementary data file 2 contains the phylogenetic trees and alignments archive (supplementary\_data\_file\_2.tgz); these files are available without restriction from <https://doi.org/10.5281/zenodo.4624280> or [https://ftp.ncbi.nih.gov/pub/wolf/\\_suppl/asgard20/](https://ftp.ncbi.nih.gov/pub/wolf/_suppl/asgard20/). Any other relevant data are available from the corresponding authors upon reasonable request.

## References

1. 1.  
Spang, A. et al. Complex archaea that bridge the gap between prokaryotes and eukaryotes. *Nature* **521**, 173–179 (2015).  
[CAS](#) [PubMed](#) [PubMed Central](#) [ADS](#) [Google Scholar](#)
2. 2.  
Zaremba-Niedzwiedzka, K. et al. Asgard archaea illuminate the origin of eukaryotic cellular complexity. *Nature* **541**, 353–358 (2017).  
[CAS](#) [PubMed](#) [ADS](#) [Google Scholar](#)
3. 3.  
MacLeod, F., Kindler, G. S., Wong, H. L., Chen, R. & Burns, B. P. Asgard archaea: diversity, function, and evolutionary implications in a

range of microbiomes. *AIMS Microbiol.* **5**, 48–61 (2019).

[CAS](#) [PubMed](#) [PubMed Central](#) [Google Scholar](#)

4. 4.

Cai, M. et al. Diverse Asgard archaea including the novel phylum Gerdarchaeota participate in organic matter degradation. *Sci. China Life Sci.* **63**, 886–897 (2020).

[CAS](#) [PubMed](#) [Google Scholar](#)

5. 5.

Williams, T. A., Cox, C. J., Foster, P. G., Szöllősi, G. J. & Embley, T. M. Phylogenomics provides robust support for a two-domains tree of life. *Nat. Ecol. Evol.* **4**, 138–147 (2020).

[PubMed](#) [Google Scholar](#)

6. 6.

Williams, T. A., Foster, P. G., Cox, C. J. & Embley, T. M. An archaeal origin of eukaryotes supports only two primary domains of life. *Nature* **504**, 231–236 (2013).

[CAS](#) [PubMed](#) [ADS](#) [Google Scholar](#)

7. 7.

Cox, C. J., Foster, P. G., Hirt, R. P., Harris, S. R. & Embley, T. M. The archaeabacterial origin of eukaryotes. *Proc. Natl Acad. Sci. USA* **105**, 20356–20361 (2008).

[CAS](#) [PubMed](#) [ADS](#) [Google Scholar](#)

8. 8.

Yutin, N., Makarova, K. S., Mekhedov, S. L., Wolf, Y. I. & Koonin, E. V. The deep archaeal roots of eukaryotes. *Mol. Biol. Evol.* **25**, 1619–1630 (2008).

[CAS](#) [PubMed](#) [PubMed Central](#) [Google Scholar](#)

9. 9.

Da Cunha, V., Gaia, M., Gadelle, D., Nasir, A. & Forterre, P. Lokiarchaea are close relatives of Euryarchaeota, not bridging the gap between prokaryotes and eukaryotes. *PLoS Genet.* **13**, e1006810 (2017).

[PubMed](#) [PubMed Central](#) [Google Scholar](#)

10. 10.

Da Cunha, V., Gaia, M., Nasir, A. & Forterre, P. Asgard archaea do not close the debate about the universal tree of life topology. *PLoS Genet.* **14**, e1007215 (2018).

[PubMed](#) [PubMed Central](#) [Google Scholar](#)

11. 11.

Spang, A. et al. Asgard archaea are the closest prokaryotic relatives of eukaryotes. *PLoS Genet.* **14**, e1007080 (2018).

[PubMed](#) [PubMed Central](#) [Google Scholar](#)

12. 12.

Forterre, P. The universal tree of life: an update. *Front. Microbiol.* **6**, 717 (2015).

[PubMed](#) [PubMed Central](#) [Google Scholar](#)

13. 13.

Lombard, J., López-García, P. & Moreira, D. The early evolution of lipid membranes and the three domains of life. *Nat. Rev. Microbiol.* **10**, 507–515 (2012).

[CAS](#) [PubMed](#) [Google Scholar](#)

14. 14.

Akıl, C. & Robinson, R. C. Genomes of Asgard archaea encode profilins that regulate actin. *Nature* **562**, 439–443 (2018).

[PubMed](#) [ADS](#) [Google Scholar](#)

15. 15.

Akıl, C. et al. Insights into the evolution of regulated actin dynamics via characterization of primitive gelsolin/cofilin proteins from Asgard archaea. *Proc. Natl Acad. Sci. USA* **117**, 19904–19913 (2020).

[PubMed](#) [Google Scholar](#)

16. 16.

Lu, Z. et al. Coevolution of eukaryote-like Vps4 and ESCRT-III subunits in the Asgard archaea. *mBio* **11**, e00417-20 (2020).

[PubMed](#) [PubMed Central](#) [Google Scholar](#)

17. 17.

Imachi, H. et al. Isolation of an archaeon at the prokaryote–eukaryote interface. *Nature* **577**, 519–525 (2020).

[CAS](#) [PubMed](#) [PubMed Central](#) [ADS](#) [Google Scholar](#)

18. 18.

Zhang, J.-W. et al. Newly discovered Asgard archaea Hermodarchaeota potentially degrade alkanes and aromatics via

alkyl/benzyl-succinate synthase and benzoyl-CoA pathway. *ISME J.* <https://doi.org/10.1038/s41396-020-00890-x> (2021).

19. 19.

Ciccarelli, F. D. et al. Toward automatic reconstruction of a highly resolved tree of life. *Science* **311**, 1283–1287 (2006).

[CAS](#) [PubMed](#) [ADS](#) [Google Scholar](#)

20. 20.

Rinke, C. et al. Insights into the phylogeny and coding potential of microbial dark matter. *Nature* **499**, 431–437 (2013).

[CAS](#) [PubMed](#) [ADS](#) [Google Scholar](#)

21. 21.

Nayfach, S. et al. A genomic catalog of Earth's microbiomes. *Nat. Biotechnol.* **39**, 499–509 (2021).

22. 22.

Balasingam, N., Brandon, H. E., Ross, J. A., Wieden, H.-J. & Thakor, N. Cellular roles of the human Obg-like ATPase 1 (hOLA1) and its YchF homologs. *Biochem. Cell Biol.* **98**, 1–11 (2020).

[CAS](#) [PubMed](#) [Google Scholar](#)

23. 23.

Rinke, C. et al. Resolving widespread incomplete and uneven archaeal classifications based on a rank-normalized genome-based taxonomy. Preprint at <https://doi.org/10.1101/2020.03.01.972265> (2020).

24. 24.

Eme, L., Spang, A., Lombard, J., Stairs, C. W. & Ettema, T. J. G. Archaea and the origin of eukaryotes. *Nat. Rev. Microbiol.* **15**, 711–723 (2017).

[CAS](#) [PubMed](#) [Google Scholar](#)

25. 25.

Klinger, C. M., Spang, A., Dacks, J. B. & Ettema, T. J. G. Tracing the archaeal origins of eukaryotic membrane-trafficking system building blocks. *Mol. Biol. Evol.* **33**, 1528–1541 (2016).

[CAS](#) [PubMed](#) [Google Scholar](#)

26. 26.

Puigbò, P., Lobkovsky, A. E., Kristensen, D. M., Wolf, Y. I. & Koonin, E. V. Genomes in turmoil: quantification of genome dynamics in prokaryote supergenomes. *BMC Biol.* **12**, 66 (2014).

[PubMed](#) [PubMed Central](#) [Google Scholar](#)

27. 27.

Christ, L., Raiborg, C., Wenzel, E. M., Campsteijn, C. & Stenmark, H. Cellular functions and molecular mechanisms of the ESCRT membrane-scission machinery. *Trends Biochem. Sci.* **42**, 42–56 (2017).

[CAS](#) [PubMed](#) [Google Scholar](#)

28. 28.

Su, M.-Y., Fromm, S. A., Zoncu, R. & Hurley, J. H. Structure of the C9orf72 ARF GAP complex that is haploinsufficient in ALS and FTD. *Nature* **585**, 251–255 (2020).

[CAS](#) [PubMed](#) [PubMed Central](#) [Google Scholar](#)

29. 29.

de Martín Garrido, N. & Aylett, C. H. S. Nutrient signaling and lysosome positioning crosstalk through a multifunctional protein, folliculin. *Front. Cell Dev. Biol.* **8**, 108 (2020).

[PubMed](#) [PubMed Central](#) [Google Scholar](#)

30. 30.

Shen, K. et al. Architecture of the human GATOR1 and GATOR1–Rag GTPases complexes. *Nature* **556**, 64–69 (2018).

[CAS](#) [PubMed](#) [PubMed Central](#) [ADS](#) [Google Scholar](#)

31. 31.

López-García, P. & Moreira, D. The syntrophy hypothesis for the origin of eukaryotes revisited. *Nat. Microbiol.* **5**, 655–667 (2020).

[PubMed](#) [Google Scholar](#)

32. 32.

Martin, W. & Müller, M. The hydrogen hypothesis for the first eukaryote. *Nature* **392**, 37–41 (1998).

[CAS](#) [PubMed](#) [ADS](#) [Google Scholar](#)

33. 33.

Moreira, D. & López-García, P. Symbiosis between methanogenic archaea and  $\delta$ -proteobacteria as the origin of eukaryotes: the syntrophic hypothesis. *J. Mol. Evol.* **47**, 517–530 (1998).

[CAS](#) [PubMed](#) [ADS](#) [Google Scholar](#)

34. 34.

López-García, P. & Moreira, D. Cultured Asgard archaea shed light on eukaryogenesis. *Cell* **181**, 232–235 (2020).

[PubMed](#) [Google Scholar](#)

35. 35.

Spang, A. et al. Proposal of the reverse flow model for the origin of the eukaryotic cell based on comparative analyses of Asgard archaeal metabolism. *Nat. Microbiol.* **4**, 1138–1148 (2019).

[CAS](#) [PubMed](#) [Google Scholar](#)

36. 36.

Koonin, E. V. & Yutin, N. The dispersed archaeal eukaryome and the complex archaeal ancestor of eukaryotes. *Cold Spring Harb. Perspect. Biol.* **6**, a016188 (2014).

[PubMed](#) [PubMed Central](#) [Google Scholar](#)

37. 37.

Liu, Y. et al. Comparative genomic inference suggests mixotrophic lifestyle for Thorarchaeota. *ISME J.* **12**, 1021–1031 (2018).

[CAS](#) [PubMed](#) [PubMed Central](#) [Google Scholar](#)

38. 38.

Cheng, L. et al. Isolation and characterization of *Methanoculleus receptaculi* sp. nov. from Shengli oil field, China. *FEMS Microbiol. Lett.* **285**, 65–71 (2008).

[CAS](#) [PubMed](#) [Google Scholar](#)

39. 39.

Peng, J., Lü, Z., Rui, J. & Lu, Y. Dynamics of the methanogenic archaeal community during plant residue decomposition in an anoxic rice field soil. *Appl. Environ. Microbiol.* **74**, 2894–2901 (2008).

[CAS](#) [PubMed](#) [PubMed Central](#) [Google Scholar](#)

40. 40.

Uritskiy, G. V., DiRuggiero, J. & Taylor, J. MetaWRAP—a flexible pipeline for genome-resolved metagenomic data analysis. *Microbiome* **6**, 158 (2018).

[PubMed](#) [PubMed Central](#) [Google Scholar](#)

41. 41.

Li, D., Liu, C. M., Luo, R., Sadakane, K. & Lam, T. W. MEGAHIT: an ultra-fast single-node solution for large and complex metagenomics assembly via succinct de Bruijn graph. *Bioinformatics* **31**, 1674–1676 (2015).

[CAS](#) [Google Scholar](#)

42. 42.

Langmead, B. & Salzberg, S. L. Fast gapped-read alignment with Bowtie 2. *Nat. Methods* **9**, 357–359 (2012).

[CAS](#) [PubMed](#) [PubMed Central](#) [Google Scholar](#)

43. 43.

Kang, D. D. et al. MetaBAT 2: an adaptive binning algorithm for robust and efficient genome reconstruction from metagenome assemblies. *PeerJ* **7**, e7359 (2019).

[PubMed](#) [PubMed Central](#) [Google Scholar](#)

44. 44.

Sieber, C. M. K. et al. Recovery of genomes from metagenomes via a dereplication, aggregation and scoring strategy. *Nat. Microbiol.* **3**, 836–843 (2018).

[CAS](#) [PubMed](#) [PubMed Central](#) [Google Scholar](#)

45. 45.

Peng, Y., Leung, H. C. M., Yiu, S. M. & Chin, F. Y. L. IDBA-UD: a de novo assembler for single-cell and metagenomic sequencing data with highly uneven depth. *Bioinformatics* **28**, 1420–1428 (2012).

[CAS](#) [PubMed](#) [PubMed Central](#) [Google Scholar](#)

46. 46.

Bolger, A. M., Lohse, M. & Usadel, B. Trimmomatic: a flexible trimmer for Illumina sequence data. *Bioinformatics* **30**, 2114–2120 (2014).

[CAS](#) [PubMed](#) [PubMed Central](#) [Google Scholar](#)

47. 47.

Nurk, S., Meleshko, D., Korobeynikov, A. & Pevzner, P. A. metaSPAdes: a new versatile metagenomic assembler. *Genome Res.* **27**, 824–834 (2017).

[CAS](#) [PubMed](#) [PubMed Central](#) [Google Scholar](#)

48. 48.

Parks, D. H., Imelfort, M., Skennerton, C. T., Hugenholtz, P. & Tyson, G. W. CheckM: assessing the quality of microbial genomes recovered from isolates, single cells, and metagenomes. *Genome Res.* **25**, 1043–1055 (2015).

[CAS](#) [PubMed](#) [PubMed Central](#) [Google Scholar](#)

49. 49.

Hyatt, D. et al. Prodigal: prokaryotic gene recognition and translation initiation site identification. *BMC Bioinformatics* **11**, 119 (2010).

[PubMed](#) [PubMed Central](#) [Google Scholar](#)

50. 50.

Seemann, T. Prokka: rapid prokaryotic genome annotation. *Bioinformatics* **30**, 2068–2069 (2014).

[CAS](#) [PubMed](#) [PubMed Central](#) [Google Scholar](#)

51. 51.

Chan, P. P. & Lowe, T. M. tRNAscan-SE: searching for tRNA genes in genomic sequences. *Methods Mol. Biol.* **1962**, 1–14 (2019).

[CAS](#) [PubMed](#) [PubMed Central](#) [Google Scholar](#)

52. 52.

Schäffer, A. A. et al. Improving the accuracy of PSI-BLAST protein database searches with composition-based statistics and other refinements. *Nucleic Acids Res.* **29**, 2994–3005 (2001).

[PubMed](#) [PubMed Central](#) [Google Scholar](#)

53. 53.

Steinegger, M. & Söding, J. MMseqs2 enables sensitive protein sequence searching for the analysis of massive data sets. *Nat. Biotechnol.* **35**, 1026–1028 (2017).

[CAS](#) [PubMed](#) [Google Scholar](#)

54. 54.

Edgar, R. C. MUSCLE: a multiple sequence alignment method with reduced time and space complexity. *BMC Bioinformatics* **5**, 113 (2004).

[PubMed](#) [PubMed Central](#) [Google Scholar](#)

55. 55.

Söding, J. Protein homology detection by HMM–HMM comparison. *Bioinformatics* **21**, 951–960 (2005).

[PubMed](#) [Google Scholar](#)

56. 56.

Price, M. N., Dehal, P. S. & Arkin, A. P. FastTree 2—approximately maximum-likelihood trees for large alignments. *PLoS ONE* **5**, e9490 (2010).

[PubMed](#) [PubMed Central](#) [ADS](#) [Google Scholar](#)

57. 57.

Rice, P., Longden, I. & Bleasby, A. EMBOSS: the European Molecular Biology Open Software Suite. *Trends Genet.* **16**, 276–277 (2000).

[CAS](#) [PubMed](#) [Google Scholar](#)

58. 58.

Katoh, K. & Standley, D. M. MAFFT multiple sequence alignment software version 7: improvements in performance and usability. *Mol. Biol. Evol.* **30**, 772–780 (2013).

[CAS](#) [PubMed](#) [PubMed Central](#) [Google Scholar](#)

59. 59.

Nguyen, L.-T., Schmidt, H. A., von Haeseler, A. & Minh, B. Q. IQ-TREE: a fast and effective stochastic algorithm for estimating maximum-likelihood phylogenies. *Mol. Biol. Evol.* **32**, 268–274 (2015).

[CAS](#) [PubMed](#) [Google Scholar](#)

60. 60.

Larsson, A. AliView: a fast and lightweight alignment viewer and editor for large datasets. *Bioinformatics* **30**, 3276–3278 (2014).

[CAS](#) [PubMed](#) [PubMed Central](#) [Google Scholar](#)

61. 61.

Esterman, E. S., Wolf, Y. I., Kogay, R., Koonin, E. V. & Zhaxybayeva, O. Evolution of DNA packaging in gene transfer agents. *Virus Evol.* **7**, veab015 (2021).

[PubMed](#) [PubMed Central](#) [Google Scholar](#)

62. 62.

Puigbò, P., Wolf, Y. I. & Koonin, E. V. Search for a ‘Tree of Life’ in the thicket of the phylogenetic forest. *J. Biol.* **8**, 59 (2009).

[PubMed](#) [PubMed Central](#) [Google Scholar](#)

63. 63.

R Core Team. *R: A Language and Environment for Statistical Computing* (R Foundation for Statistical Computing, 2019).

64. 64.

Zimmermann, L. et al. A completely reimplemented MPI bioinformatics toolkit with a new HHpred server at its core. *J. Mol. Biol.* **430**, 2237–2243 (2018).

[CAS](#) [PubMed](#) [Google Scholar](#)

65. 65.

Yang, M., Derbyshire, M. K., Yamashita, R. A. & Marchler-Bauer, A. NCBI’s conserved domain database and tools for protein domain

analysis. *Curr. Protoc. Bioinformatics* **69**, e90 (2020).

[CAS](#) [PubMed](#) [PubMed Central](#) [Google Scholar](#)

66. 66.

Søndergaard, D., Pedersen, C. N. S. & Greening, C. HydDB: a web tool for hydrogenase classification and analysis. *Sci. Rep.* **6**, 34212 (2016).

[PubMed](#) [PubMed Central](#) [ADS](#) [Google Scholar](#)

67. 67.

Criscuolo, A. & Gribaldo, S. BMGE (block mapping and gathering with entropy): a new software for selection of phylogenetic informative regions from multiple sequence alignments. *BMC Evol. Biol.* **10**, 210 (2010).

[PubMed](#) [PubMed Central](#) [Google Scholar](#)

68. 68.

Swofford, D. L. & Maddison, W. P. Reconstructing ancestral character states under Wagner parsimony. *Math. Biosci.* **87**, 199–229 (1987).

[MathSciNet](#) [MATH](#) [Google Scholar](#)

[Download references](#)

## Acknowledgements

We thank P. Forterre and T. Williams for critical reading of the manuscript and helpful suggestions; J. Chen, H. Li, P. Du and D. Zou for support with sampling and preliminary analysis of Changjiang estuary sediments; Z. Zhou and J.-D. Gu for support with sampling and preliminary analysis of Mai Po Nature Reserve sediments; S. Zheng and F. Liu for support with sampling and preliminary analysis of Rongcheng Swan Lake Nature

Reserve sediments; and the crew and scientific team of RV *Xiangyanghong* 09, the pilots and the supporting team of *Jiaolong* manned submersible in the 37th Dayang Cruise for the sampling. M.L., Y.L., X.Z., W.X., Z.L. and L.C. are supported by National Natural Science Foundation of China (grant no. 91851105, 31970105, 92051102, 31700430, 91951102, 41776170 and 92051108), the Innovation Team Project of Universities in Guangdong Province (no. 2020KCXTD023), the Shenzhen Science and Technology Program (grant no. JCYJ20200109105010363 and JCYJ20190808152403587), the Scientific Research Foundation of Third Institute of Oceanography, MNR (2019022), the China Ocean Mineral Resources R&D Association (COMRA) Program (DY135-B2-09) and the National Key Basic Research Program of China ('973'-Program, 2015CB755903). K.S.M., Y.I.W., A.N. and E.V.K. are supported by the Intramural Research Program of the National Institutes of Health of the USA (National Library of Medicine).

## Author information

### Author notes

1. These authors contributed equally: Yang Liu, Kira S. Makarova, Wen-Cong Huang

## Affiliations

1. Shenzhen Key Laboratory of Marine Microbiome Engineering, Institute for Advanced Study, Shenzhen University, Shenzhen, P. R. China

Yang Liu, Wen-Cong Huang, Xinxu Zhang, Mingwei Cai, Cui-Jing Zhang & Meng Li

2. National Center for Biotechnology Information, National Library of Medicine, National Institutes of Health, Bethesda, MD, USA

Kira S. Makarova, Yuri I. Wolf, Anastasia N. Nikolskaya & Eugene V. Koonin

3. Key Laboratory of Marine Biogenetic Resources, Third Institute of Oceanography, Ministry of Natural Resources, Xiamen, P. R. China

Wei Xu & Zhuhua Luo

4. Key Laboratory of Development and Application of Rural Renewable Energy, Biogas Institute of Ministry of Agriculture, Chengdu, P. R. China

Lei Cheng

## Authors

1. Yang Liu

[View author publications](#)

You can also search for this author in [PubMed](#) [Google Scholar](#)

2. Kira S. Makarova

[View author publications](#)

You can also search for this author in [PubMed](#) [Google Scholar](#)

3. Wen-Cong Huang

[View author publications](#)

You can also search for this author in [PubMed](#) [Google Scholar](#)

4. Yuri I. Wolf

[View author publications](#)

You can also search for this author in [PubMed](#) [Google Scholar](#)

5. Anastasia N. Nikolskaya

[View author publications](#)

You can also search for this author in [PubMed](#) [Google Scholar](#)

6. Xinxu Zhang

[View author publications](#)

You can also search for this author in [PubMed](#) [Google Scholar](#)

7. Mingwei Cai

[View author publications](#)

You can also search for this author in [PubMed](#) [Google Scholar](#)

8. Cui-Jing Zhang

[View author publications](#)

You can also search for this author in [PubMed](#) [Google Scholar](#)

9. Wei Xu

[View author publications](#)

You can also search for this author in [PubMed](#) [Google Scholar](#)

10. Zhuhua Luo

[View author publications](#)

You can also search for this author in [PubMed](#) [Google Scholar](#)

11. Lei Cheng

[View author publications](#)

You can also search for this author in [PubMed](#) [Google Scholar](#)

12. Eugene V. Koonin

[View author publications](#)

You can also search for this author in [PubMed](#) [Google Scholar](#)

13. Meng Li

[View author publications](#)

You can also search for this author in [PubMed](#) [Google Scholar](#)

## Contributions

M.L., E.V.K., K.S.M. and Y.L. initiated the study; Y.L., W.-C.H., M.C., C.-J.Z., W.X., Z.L. and L.C. participated in sample collections; Y.L., X.Z., M.C., C.-J.Z., W.X., Z.L. and L.C. performed metagenomic assembly and binning analysis. Y.L. performed metabolism analysis; K.S.M., A.N.N. and Y.I.W. performed comparative genomic analysis; Y.L., K.S.M., Y.I.W. and W.-C.H. performed phylogenetic analysis; K.S.M. and Y.I.W. constructed Asgard COGs; K.S.M., Y.I.W., Y.L., M.L. and E.V.K. analysed the data; Y.L., K.S.M., W.-C.H., X.Z., M.C., C.-J.Z., W.X., Z.L., L.C., E.V.K. and M.L. wrote the manuscript that was read, edited and approved by all authors.

## Corresponding authors

Correspondence to [Eugene V. Koonin](#) or [Meng Li](#).

## Ethics declarations

## Competing interests

The authors declare no competing interests.

## Additional information

**Peer review information** *Nature* thanks the anonymous reviewer(s) for their contribution to the peer review of this work.

**Publisher's note** Springer Nature remains neutral with regard to jurisdictional claims in published maps and institutional affiliations.

## Extended data figures and tables

[Extended Data Fig. 1 Global distribution of the Asgard genomes analysed in this Article.](#)

The world map was generated using R package rnaturalearth v.0.1.0., in R v.3.6.3<sup>63</sup>. The pie chart shows the proportion of Asgard genomes that were found in a given biotope. The numbers of these genomes per biotope are as follows: coastal sediment, 94; freshwater sediment, 15; hot spring, 1; hydrothermal vent, 13; hypersaline lake sediment, 1; marine sediment 26; marine water, 26; petroleum seep (marine), 6; and petroleum field, 1. Boldface in the map indicates the sampling locations.

### **Extended Data Fig. 2 Completeness and contamination for 75 Asgard MAGs.**

These MAGs were assessed using CheckM v.1.0.12. **a**, Distribution of completeness and contamination for 75 Asgard MAGs assessed by CheckM v.1.0.12. **b, c**, Distribution of depth coverage (**b**) and N50 statistics (**c**) for Asgard MAGs reconstructed in this Article. The numbers in parentheses indicate the number of Asgard genomes recovered from a given sampling location. In cases in which fewer than three samples were recovered, these are presented as individual points. Thick black bar, median; upper and lower bounds of the box plot, first and third quartile, respectively; upper and lower whiskers, largest and smallest values less than  $1.5 \times$  interquartile range, respectively; black points, values greater than  $1.5 \times$  interquartile range. Data for this plot are given in Supplementary Table 1.

### **Extended Data Fig. 3 Gene commonality plot for Asgard archaea and the TACK superphylum.**

Gene commonality plot showing the number of Asgard COGs (log scale) (*y* axis) that include the given fraction of analysed genomes (*x* axis). The Asgard plot is compared with the TACK superphylum plot on the basis of the assignment of TACK genomes to archaeal COGs.

### **Extended Data Fig. 4 Comparison of the mean amino acid identity of Asgard and TACK superphyla.**

In this figure, -archaeota is omitted from the phylum names. Sample sizes of less than three are presented as individual points. **a**, Shared amino acid

identity across Asgard and TACK lineages. Comparison of representative genomes from all Asgard and TACK lineages analysed in this Article (excluding the six putative phyla proposed in this Article), which characterizes the distribution of amino acid identities that is typical of a phylum. **b–m**, Amino acid identity comparisons between Thorarchaeota (**b**), Hermodarchaeota (**c**), Odinarchaeota (**d**), Baldrarchaeota (**e**), Lokiarchaeota (**f**), Helarchaeota (**g**), Borrarchaeota (**h**), Heimdallarchaeota (**i**), Kariarchaeota (**j**), Gerdarchaeota (**k**), Hodarchaeota (**l**) and Wukongarchaeota (**m**) and other Asgard and TACK lineages. Thick black bar, median; upper and lower bounds of the box plot, first and third quartile respectively; upper and lower whiskers, largest and smallest values less than  $1.5 \times$  interquartile range, respectively; black points, values greater than  $1.5 \times$  interquartile range; number in the parentheses, number of genomes in the lineage. Data for this plot are given in Supplementary Table 2.

### Extended Data Fig. 5 Comparison of the 16S rRNA gene sequence identity of Asgard and TACK lineages.

In this figure, -archaeota is omitted from the phylum names. Sample sizes of less than three are presented as individual points. **a**, 16S rRNA gene sequence identity across Asgard and TACK lineages. Comparison of 16S RNA gene sequences from representative genomes of all Asgard and TACK lineages analysed in this Article (excluding the six putative phyla proposed in this Article), which characterizes the distribution of 16S rRNA sequence that is typical of a phylum. **b–k**, Comparison of 16S rRNA gene sequence identity between Thorarchaeota (**b**), Hermodarchaeota (**c**), Odinarchaeota (**d**), Lokiarchaeota (**e**), Helarchaeota (**f**), Heimdallarchaeota (**g**), Kariarchaeota (**h**), Gerdarchaeota (**i**), Hodarchaeota (**j**) and Wukongarchaeota (**k**) and other Asgard and TACK lineages. Thick black bar, median; upper and lower bounds of the box plot, first and third quartile respectively; upper and lower whiskers, largest and smallest values less than  $1.5 \times$  interquartile range, respectively; black points, values greater than  $1.5 \times$  interquartile range; number in the parentheses, number of genomes in the lineage. Data for this plot are given in Supplementary Table 3.

## Extended Data Fig. 6 Classification of Asgard archaea by the phyletic patterns and the core gene set of Asgard archaea.

**a**, Classical multidimensional scaling analysis of binary presence–absence phyletic patterns for 13,939 Asgard COGs that are represented in at least two genomes (Methods). **b**, Functional breakdown of Asgard core genes (378 Asgard COGs) compared with TACK-superphylum core genes (489 archaeal COGs). Values were normalized as described in the Methods. Functional classes of genes: J, translation, ribosomal structure and biogenesis; K, transcription; L, replication, recombination and repair; D, cell cycle control, cell division and chromosome partitioning; V, defence mechanisms; T, signal transduction mechanisms; M, biogenesis of the cell wall, membrane or envelope; N, cell motility; U, intracellular trafficking, secretion and vesicular transport; O, posttranslational modification, protein turnover and chaperones; X, mobilome (prophages, plasmids and transposons); C, energy production and conversion; G, carbohydrate transport and metabolism; E, amino acid transport and metabolism; F, nucleotide transport and metabolism; H, coenzyme transport and metabolism; I, lipid transport and metabolism; P, inorganic ion transport and metabolism; Q, secondary metabolites biosynthesis, transport and catabolism; R, general function prediction only; S, function unknown. **c**, Presence–absence of orthologues of Asgard core genes in other archaea, bacteria and eukaryotes.

## Extended Data Fig. 7 Phylogenetic trees.

**a**, Phylogenetic tree of bacteria, archaea and eukaryotes (inferred with IQ-tree using the LG + R10 model) that was constructed from the concatenated alignments of the protein sequences of 30 universally conserved genes (Methods). The tree shows the relationships between the major clades. **b**, Phylogenetic tree of COG0012 (ribosome-binding ATPase YchF) the tree was reconstructed using IQ-tree with LG + R10 evolutionary model (selected by IQ-tree ModelFinder as the best fit). **zc**, Phylogenetic tree of COG0201 (preprotein translocase subunit SecY). The tree was reconstructed using IQ-tree with LG + F + R10 evolutionary model (selected by IQ-tree ModelFinder as the best fit). **d**, Phylogenetic tree of the reduced set of bacteria, archaea and eukaryotes (excluding the genomes of

derived parasites), constructed from concatenated alignments of the protein sequences of 29 universal markers (excluding COG0012) using IQ-tree with LG + R10 evolutionary model (selected by IQ-tree ModelFinder as the best fit). The tree shows the relationships between the major clades. **e**, Phylogenetic analysis of the evolutionary relationship between archaea and eukaryotes, excluding the Asgard superphylum. The tree was reconstructed from a concatenated alignment of the 29 universal markers (excluding COG0012) using IQ-tree with LG + R10 evolutionary model (selected by IQ-tree ModelFinder as the best fit).

### **Extended Data Fig. 8 Phyletic patterns of ESPs in Asgard genomes.**

All 505 Asgard COGs that correspond to ESP are grouped by distance between binary presence–absence phyletic patterns. For a given pair of Asgard COGs A and B that are present in the set of genomes  $\{G_A\}$  and  $\{G_B\}$ , respectively, we calculate the similarity between the patterns as  $S_{A,B} = |\{G_A\} \times \{G_B\}| / |\{G_A\} + \{G_B\}|$ , and the distance between the patterns as  $D_{A,B} = -\ln(S_{A,B})$ . A dendrogram was reconstructed using the unweighted-pair group method with arithmetic mean, from the distance matrix  $D$ ; the order of leaves in the tree determines the order of Asgard COGs in the figure. Top, patterns are shown schematically by pale blue lines, in which the respective Asgard COG is present and mapped to the 12 major Asgard lineages (as shown by the coloured bar above). The Asgard COGs that correspond to the most highly conserved ESP protein families are shown within the red rectangle. Bottom, plot of the number of Asgard COGs that correspond to ESPs in each of 76 genomes is shown. Complete data are provided in Supplementary Table 7. The colour code for the plot is the same as for the bar graph.

### **Extended Data Fig. 9 Metabolic features of Asgard archaea.**

Schematic of the presence and absence of selected metabolic features in all phyla and putative phyla of Asgard archaea.

## Extended Data Fig. 10 Phylogenetic analysis of [NiFe] hydrogenases in Asgard archaea.

**a**, Phylogenetic analysis of group-4 [NiFe] hydrogenases in Asgard archaea. The unrooted maximum-likelihood phylogenetic tree was built from an alignment of 425 sequences that included 110 sequences of Asgard archaea, with 308 amino acid positions. **b**, Phylogenetic analysis of group-3 [NiFe] hydrogenases in Asgard archaea. The unrooted maximum-likelihood phylogenetic tree was built from an alignment of 813 sequences that included 335 sequences of Asgard archaea, with 331 amino acid positions. **c**, Phylogenetic analysis of group-1 [NiFe] hydrogenases in the Asgard archaea. The unrooted maximum-likelihood phylogenetic tree was built from an alignment of 541 sequences that included 2 sequences of Wukongarchaeota, with 376 amino acid positions.

## **Supplementary information**

### Supplementary Information

This file contains (1) Description of new taxa; (2) Clusters of orthologous genes of Asgard archaea; (3) The core gene set of Asgard archaea; (4) Phylogenomic analysis of the Asgard superphylum and Asgard-eukaryote evolutionary relationship; (5) Eukaryotic Signature Proteins in Asgard archaea; and (6) Reconstruction of metabolic pathways in Asgard archaea.

### Reporting Summary

### Supplementary Table 1

Genome information, proposed taxonomy and isolation data.

### Supplementary Table 2

Mean amino-acid identity values (%) among 66 TACK genomes and 184 Asgard genomes (162 high quality and 22 low-quality).

## **Supplementary Table 3**

The 16S rRNA gene sequence identity (%) among TACK and Asgard lineages. Identity was calculated using sequences longer than 1,300 bps.

## **Supplementary Table 4**

Species and phylogenetic markers used for the tree of life reconstruction.

## **Supplementary Table 5**

Data for phylogenetic trees: methods, markers, bootstrap data and comments. The trees in the Newick format and the underlying alignments are provided in the additional data file 2.

## **Supplementary Table 6**

The core asCOGs list.

## **Supplementary Table 7**

Eukaryotic signature proteins in Asgard archaea.

## **Supplementary Table 8**

The presence-absence of metabolic enzymes in Asgard archaea.

## **Rights and permissions**

[Reprints and Permissions](#)

## **About this article**



Check for  
updates

## Cite this article

Liu, Y., Makarova, K.S., Huang, WC. *et al.* Expanded diversity of Asgard archaea and their relationships with eukaryotes. *Nature* **593**, 553–557 (2021). <https://doi.org/10.1038/s41586-021-03494-3>

### [Download citation](#)

- Received: 15 November 2020
- Accepted: 26 March 2021
- Published: 28 April 2021
- Issue Date: 27 May 2021
- DOI: <https://doi.org/10.1038/s41586-021-03494-3>

## Comments

By submitting a comment you agree to abide by our [Terms](#) and [Community Guidelines](#). If you find something abusive or that does not comply with our terms or guidelines please flag it as inappropriate.

[Access through your institution](#)

[Change institution](#)

[Buy or subscribe](#)

Advertisement

| [Section menu](#) | [Main menu](#) |

- Article
- [Published: 05 May 2021](#)

# Fast odour dynamics are encoded in the olfactory system and guide behaviour

- [Tobias Ackels](#) [ORCID: orcid.org/0000-0002-4964-1162](#)<sup>1,2 na1</sup>,
- [Andrew Erskine](#)<sup>1,2 na1</sup>,
- [Debanjan Dasgupta](#)<sup>1,2 na1</sup>,
- [Alina Cristina Marin](#)<sup>1</sup>,
- [Tom P. A. Warner](#)<sup>1</sup>,
- [Sina Tootoonian](#)<sup>1,2</sup>,
- [Izumi Fukunaga](#) [ORCID: orcid.org/0000-0003-1860-5377](#)<sup>1</sup>,
- [Julia J. Harris](#)<sup>1,2</sup> &
- [Andreas T. Schaefer](#) [ORCID: orcid.org/0000-0002-4677-8788](#)<sup>1,2</sup>

[Nature](#) volume 593, pages 558–563 (2021) [Cite this article](#)

- 5019 Accesses
- 192 Altmetric
- [Metrics details](#)

## Subjects

- [Olfactory bulb](#)
- [Sensory processing](#)

This article has been [updated](#)

## Abstract

Odours are transported in turbulent plumes, which result in rapid concentration fluctuations<sup>1,2</sup> that contain rich information about the olfactory scenery, such as the composition and location of an odour source<sup>2,3,4</sup>. However, it is unclear whether the mammalian olfactory system can use the underlying temporal structure to extract information about the environment. Here we show that ten-millisecond odour pulse patterns produce distinct responses in olfactory receptor neurons. In operant conditioning experiments, mice discriminated temporal correlations of rapidly fluctuating odours at frequencies of up to 40 Hz. In imaging and electrophysiological recordings, such correlation information could be readily extracted from the activity of mitral and tufted cells—the output neurons of the olfactory bulb. Furthermore, temporal correlation of odour concentrations<sup>5</sup> reliably predicted whether odorants emerged from the same or different sources in naturalistic environments with complex airflow. Experiments in which mice were trained on such tasks and probed using synthetic correlated stimuli at different frequencies suggest that mice can use the temporal structure of odours to extract information about space. Thus, the mammalian olfactory system has access to unexpectedly fast temporal features in odour stimuli. This endows animals with the capacity to overcome key behavioural challenges such as odour source separation<sup>5</sup>, figure–ground segregation<sup>6</sup> and odour localization<sup>7</sup> by extracting information about space from temporal odour dynamics.

## Access options

Subscribe to Journal

Get full journal access for 1 year

\$199.00

only \$3.90 per issue

[Subscribe](#)

All prices are NET prices.

VAT will be added later in the checkout.

Tax calculation will be finalised during checkout.

Rent or Buy article

Get time limited or full article access on ReadCube.

from \$8.99

[Rent or Buy](#)

All prices are NET prices.

### **Additional access options:**

- [Log in](#)
- [Access through your institution](#)
- [Learn about institutional subscriptions](#)

**Fig. 1: Sub-sniff detection of odour signals in olfactory bulb inputs.**

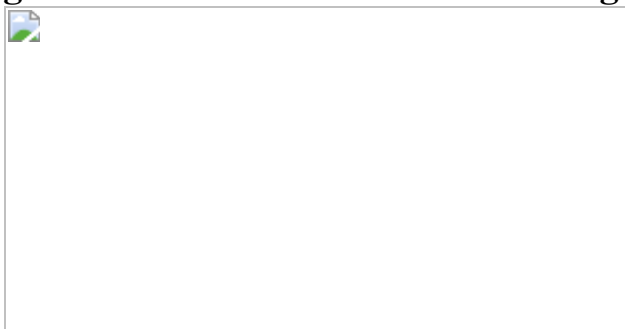


**Fig. 2: Mice can discriminate odour correlation structure at frequencies up to 40 Hz.**

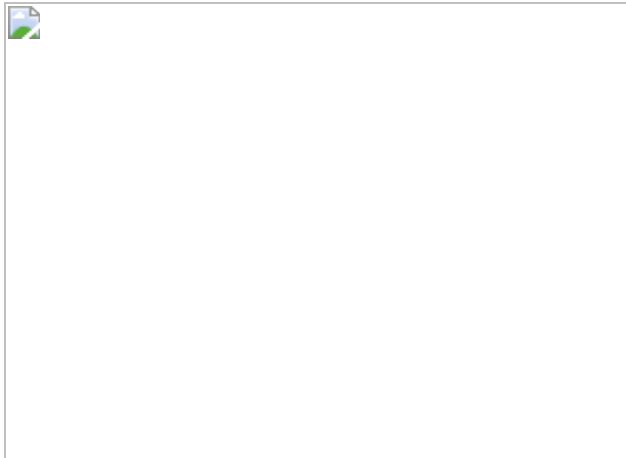


**Fig. 3: Odour correlation structure is encoded by OB output neurons.**

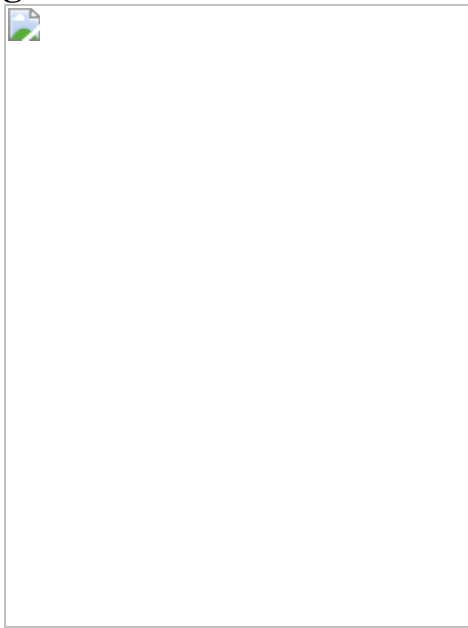
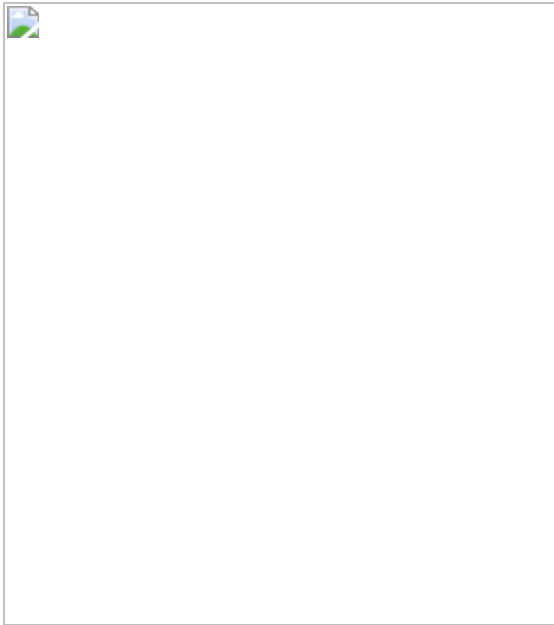


**Fig. 4: Source separation using correlations of odour concentration fluctuations.**



## Data availability

Data related to the OSN model (Extended Data Fig. 1) are available at <https://github.com/stootoon/crick-osn-model-release>. Data related to the glomerular classifier analysis (Extended Data Fig. 6) are available at <https://github.com/stootoon/crick-osn-decoding-release>. The remaining data that support the findings of this study will be made available by the authors upon request.

## Code availability

All custom Python scripts to generate pulses (PyPulse, PulseBoy) are available at <https://github.com/RoboDoig> and <https://github.com/warnerwarner>. Code for controlling AutonoMouse is available at [https://figshare.com/articles/AutonoMouse\\_Code/7616090](https://figshare.com/articles/AutonoMouse_Code/7616090). Code related to the OSN model is available at <https://github.com/stootoon/crick-osn-model-release>. Code related to the glomerular classifier analysis is available at <https://github.com/stootoon/crick-osn-decoding-release>.

## Change history

- **12 May 2021**

This Article was amended to correct the linking to Supplementary Videos 1 and 2.

## References

1. 1.

Fackrell, J. & Robins, A. Concentration fluctuations and fluxes in plumes from point sources in a turbulent boundary layer. *J. Fluid Mech.* **117**, 1–26 (1982).

[CAS](#) [ADS](#) [Google Scholar](#)

2. 2.

Mylne, K. R. & Mason, P. J. Concentration fluctuation measurements in a dispersing plume at a range of up to 1000 m. *Q. J. R. Meteorol. Soc.* **117**, 177–206 (1991).

[ADS](#) [Google Scholar](#)

3. 3.

Schmuker, M., Bahr, V. & Huerta, R. Exploiting plume structure to decode gas source distance using metal-oxide gas sensors. *Sens. Actuators B Chem.* **235**, 636–646 (2016).

[CAS](#) [Google Scholar](#)

4. 4.

Murlis, J., Elkington, J. S. & Carde, R. T. Odor plumes and how insects use them. *Annu. Rev. Entomol.* **37**, 505–532 (1992).

[Google Scholar](#)

5. 5.

Hopfield, J. J. Olfactory computation and object perception. *Proc. Natl Acad. Sci. USA* **88**, 6462–6466 (1991).

[CAS](#) [PubMed](#) [ADS](#) [Google Scholar](#)

6. 6.

Rokni, D., Hemmeler, V., Kapoor, V. & Murthy, V. N. An olfactory cocktail party: figure-ground segregation of odorants in rodents. *Nat. Neurosci.* **17**, 1225–1232 (2014).

[CAS](#) [PubMed](#) [PubMed Central](#) [Google Scholar](#)

7. 7.

Vergassola, M., Villermaux, E. & Shraiman, B. I. ‘Infotaxis’ as a strategy for searching without gradients. *Nature* **445**, 406–409 (2007).

[CAS](#) [PubMed](#) [ADS](#) [Google Scholar](#)

8. 8.

Celani, A., Villermaux, E. & Vergassola, M. Odor landscapes in turbulent environments. *Phys. Rev. X* **4**, 041015 (2014).

[Google Scholar](#)

9. 9.

Crimaldi, J. P. & Koseff, J. R. High-resolution measurements of the spatial and temporal scalar structure of a turbulent plume. *Exp. Fluids* **31**, 90–102 (2001).

[Google Scholar](#)

10. 10.

Moore, P. A. & Atema, J. Spatial information in the three-dimensional fine structure of an aquatic odor plume. *Biol. Bull.* **181**, 408–418 (1991).

[CAS](#) [PubMed](#) [Google Scholar](#)

11. 11.

Mafra-Neto, A. & Cardé, R. T. Fine-scale structure of pheromone plumes modulates upwind orientation of flying moths. *Nature* **369**, 142–144 (1994).

[CAS](#) [ADS](#) [Google Scholar](#)

12. 12.

Vickers, N. J. Mechanisms of animal navigation in odor plumes. *Biol. Bull.* **198**, 203–212 (2000).

[CAS](#) [PubMed](#) [Google Scholar](#)

13. 13.

Riffell, J. A. et al. Flower discrimination by pollinators in a dynamic chemical environment. *Science* **344**, 1515–1518 (2014).

[CAS](#) [PubMed](#) [ADS](#) [Google Scholar](#)

14. 14.

Szyszka, P., Stierle, J. S., Biergans, S. & Galizia, C. G. The speed of smell: odor-object segregation within milliseconds. *PLoS ONE* **7**, e36096 (2012).

[CAS](#) [PubMed](#) [PubMed Central](#) [ADS](#) [Google Scholar](#)

15. 15.

Szyszka, P., Gerkin, R. C., Galizia, C. G. & Smith, B. H. High-speed odor transduction and pulse tracking by insect olfactory receptor neurons. *Proc. Natl Acad. Sci. USA* **111**, 16925–16930 (2014).

[CAS](#) [PubMed](#) [ADS](#) [Google Scholar](#)

16. 16.

Kepecs, A., Uchida, N. & Mainen, Z. F. The sniff as a unit of olfactory processing. *Chem. Senses* **31**, 167–179 (2006).

[PubMed](#) [Google Scholar](#)

17. 17.

Shusterman, R., Smear, M. C., Koulakov, A. A. & Rinberg, D. Precise olfactory responses tile the sniff cycle. *Nat. Neurosci.* **14**, 1039–1044 (2011).

[CAS](#) [PubMed](#) [Google Scholar](#)

18. 18.

Cury, K. M. & Uchida, N. Robust odor coding via inhalation-coupled transient activity in the mammalian olfactory bulb. *Neuron* **68**, 570–585 (2010).

[CAS](#) [PubMed](#) [Google Scholar](#)

19. 19.

Burton, S. D. Inhibitory circuits of the mammalian main olfactory bulb. *J. Neurophysiol.* **118**, 2034–2051 (2017).

[CAS](#) [PubMed](#) [PubMed Central](#) [Google Scholar](#)

20. 20.

Duchamp-Viret, P., Chaput, M. A. & Duchamp, A. Odor response properties of rat olfactory receptor neurons. *Science* **284**, 2171–2174 (1999).

[CAS](#) [PubMed](#) [Google Scholar](#)

21. 21.

Munger, S. D., Leinders-Zufall, T. & Zufall, F. Subsystem organization of the mammalian sense of smell. *Annu. Rev. Physiol.* **71**, 115–140 (2009).

[CAS](#) [PubMed](#) [Google Scholar](#)

22. 22.

Bressel, O. C., Khan, M. & Mombaerts, P. Linear correlation between the number of olfactory sensory neurons expressing a given mouse odorant receptor gene and the total volume of the corresponding glomeruli in the olfactory bulb. *J. Comp. Neurol.* **524**, 199–209 (2016).

[CAS](#) [PubMed](#) [Google Scholar](#)

23. 23.

Carr, C. E. & Amagai, S. Processing of temporal information in the brain. *Adv. Psychol.* **115**, 27–52 (1996).

[Google Scholar](#)

24. 24.

Erskine, A., Bus, T., Herb, J. T. & Schaefer, A. T. AutonoMouse: high throughput automated operant conditioning shows progressive behavioural impairment with graded olfactory bulb lesions. *PLoS ONE* **14**, e0211571 (2019).

[PubMed](#) [PubMed Central](#) [Google Scholar](#)

25. 25.

Brown, J. L. Visual sensitivity. *Annu. Rev. Psychol.* **24**, 151–186 (1973).

[CAS](#) [PubMed](#) [Google Scholar](#)

26. 26.

Westheimer, G. & McKee, S. P. Perception of temporal order in adjacent visual stimuli. *Vision Res.* **17**, 887–892 (1977).

[CAS](#) [PubMed](#) [Google Scholar](#)

27. 27.

Smear, M., Shusterman, R., O'Connor, R., Bozza, T. & Rinberg, D. Perception of sniff phase in mouse olfaction. *Nature* **479**, 397–400 (2011).

[CAS](#) [PubMed](#) [ADS](#) [Google Scholar](#)

28. 28.

Rebello, M. R. et al. Perception of odors linked to precise timing in the olfactory system. *PLoS Biol.* **12**, e1002021 (2014).

[PubMed](#) [PubMed Central](#) [Google Scholar](#)

29. 29.

Li, A., Gire, D. H., Bozza, T. & Restrepo, D. Precise detection of direct glomerular input duration by the olfactory bulb. *J. Neurosci.* **34**, 16058–16064 (2014).

[CAS](#) [PubMed](#) [PubMed Central](#) [Google Scholar](#)

30. 30.

Geffen, M. N., Broome, B. M., Laurent, G. & Meister, M. Neural encoding of rapidly fluctuating odors. *Neuron* **61**, 570–586 (2009).

[CAS](#) [PubMed](#) [Google Scholar](#)

31. 31.

Rajan, R., Clement, J. P. & Bhalla, U. S. Rats smell in stereo. *Science* **311**, 666–670 (2006).

[CAS](#) [PubMed](#) [ADS](#) [Google Scholar](#)

32. 32.

Catania, K. C. Stereo and serial sniffing guide navigation to an odour source in a mammal. *Nat. Commun.* **4**, 1441 (2013).

[PubMed](#) [ADS](#) [Google Scholar](#)

33. 33.

Baker, T., Fadamiro, H. & Cosse, A. Moth uses fine tuning for odour resolution. *Nature* **393**, 530 (1998).

[CAS](#) [ADS](#) [Google Scholar](#)

34. 34.

Stierle, J. S., Galizia, C. G. & Szyszka, P. Millisecond stimulus onset-asynchrony enhances information about components in an odor mixture. *J. Neurosci.* **33**, 6060–6069 (2013).

[CAS](#) [PubMed](#) [PubMed Central](#) [Google Scholar](#)

35. 35.

Abeles, M. Time is precious. *Science* **304**, 523–524 (2004).

[CAS](#) [PubMed](#) [Google Scholar](#)

36. 36.

Padmanabhan, K. & Urban, N. N. Intrinsic biophysical diversity decorrelates neuronal firing while increasing information content. *Nat. Neurosci.* **13**, 1276–1282 (2010).

[CAS](#) [PubMed](#) [PubMed Central](#) [Google Scholar](#)

37. 37.

Park, I. M., Bobkov, Y. V., Ache, B. W. & Príncipe, J. C. Intermittency coding in the primary olfactory system: a neural substrate for olfactory scene analysis. *J. Neurosci.* **34**, 941–952 (2014).

[CAS](#) [PubMed](#) [PubMed Central](#) [Google Scholar](#)

38. 38.

Fukunaga, I., Herb, J. T., Kollo, M., Boyden, E. S. & Schaefer, A. T. Independent control of gamma and theta activity by distinct interneuron networks in the olfactory bulb. *Nat. Neurosci.* **17**, 1208–1216 (2014).

[CAS](#) [PubMed](#) [PubMed Central](#) [Google Scholar](#)

39. 39.

Ishii, T., Hirota, J. & Mombaerts, P. Combinatorial coexpression of neural and immune multigene families in mouse vomeronasal sensory neurons. *Curr. Biol.* **13**, 394–400 (2003).

[CAS](#) [PubMed](#) [Google Scholar](#)

40. 40.

Haddad, R. et al. Olfactory cortical neurons read out a relative time code in the olfactory bulb. *Nat. Neurosci.* **16**, 949–957 (2013).

[CAS](#) [PubMed](#) [PubMed Central](#) [Google Scholar](#)

41. 41.

Madisen, L. et al. Transgenic mice for intersectional targeting of neural sensors and effectors with high specificity and performance. *Neuron* **85**, 942–958 (2015).

[CAS](#) [PubMed](#) [PubMed Central](#) [Google Scholar](#)

42. 42.

Raiser, G., Galizia, C. G. & Szyszka, P. A high-bandwidth dual-channel olfactory stimulator for studying temporal sensitivity of olfactory processing. *Chem. Senses* **42**, 141–151 (2017).

[CAS](#) [PubMed](#) [Google Scholar](#)

43. 43.

Abraham, N. M. et al. Maintaining accuracy at the expense of speed: stimulus similarity defines odor discrimination time in mice. *Neuron* **44**, 865–876 (2004).

[CAS](#) [PubMed](#) [Google Scholar](#)

44. 44.

Wadhwa, N., Rubinstein, M., Durand, F. & Freeman, W. T. Phase-based video motion processing. *ACM Trans. Graph.* **32**, 1–10 (2013).

[MATH](#) [Google Scholar](#)

45. 45.

Lopes, G. et al. Bonsai: an event-based framework for processing and controlling data streams. *Front. Neuroinform.* **9**, 7 (2015).

[PubMed](#) [PubMed Central](#) [Google Scholar](#)

46. 46.

Ghatpande, A. S. & Reisert, J. Olfactory receptor neuron responses coding for rapid odour sampling. *J. Physiol. (Lond.)* **589**, 2261–2273 (2011).

[CAS](#) [Google Scholar](#)

47. 47.

Pachitariu, M. et al. Suite2p: beyond 10,000 neurons with standard two-photon microscopy. Preprint at <https://doi.org/10.1101/061507> (2016).

48. 48.

Pachitariu, M., Steinmetz, N., Kadir, S., Carandini, M. & Harris, K. D. Kilosort: realtime spike-sorting for extracellular electrophysiology with hundreds of channels. *bioRxiv* 061481 (2016) doi:..

49. 49.

Jordan, R., Fukunaga, I., Kollo, M. & Schaefer, A. T. Active sampling state dynamically enhances olfactory bulb odor representation. *Neuron* **98**, 1214–1228.e5 (2018).

[CAS](#) [PubMed](#) [PubMed Central](#) [Google Scholar](#)

50. 50.

Margrie, T. W., Brecht, M. & Sakmann, B. In vivo, low-resistance, whole-cell recordings from neurons in the anaesthetized and awake mammalian brain. *Pflugers Arch.* **444**, 491–498 (2002).

[CAS](#) [PubMed](#) [Google Scholar](#)

51. 51.

Abraham, N. M. et al. Synaptic inhibition in the olfactory bulb accelerates odor discrimination in mice. *Neuron* **65**, 399–411 (2010).

[CAS](#) [PubMed](#) [PubMed Central](#) [Google Scholar](#)

[Download references](#)

## Acknowledgements

We thank the animal facilities at the National Institute for Medical Research and the Francis Crick Institute for animal care and technical assistance, the mechanical and electronic workshops in MPI Heidelberg (N. Neef, K. Schmidt, M. Lukat, R. Roedel, C. Kieser) and London (A. Ling, A. Hurst, M. Stopps) for support during development and construction, the Aurora Scientific team for suggestions for adapting the miniPID, T. Margrie for discussion, V. Murthy for discussions and suggestions on the OSN imaging experiments, and A. Fleischmann, K. Franks, F. Guillemot, M. Hausser, F. Iacaruso, R. Jordan, J. Kohl, T. Mrsic-Flogel, V. Pachnis, A. Silver, and P. Znamenskiy for comments on earlier versions of the manuscript. We thank the members of the Odor2Action NeuroNex network, in particular J. Victor, J. Crimaldi, B. Smith, M. Schmucker, and J. Verhagen for discussions. This work was supported by the Francis Crick Institute which receives its core funding from Cancer Research UK (FC001153), the UK Medical Research Council (FC001153), and the Wellcome Trust (FC001153); by the UK Medical Research Council (grant reference MC\_UP\_1202/5); a Wellcome Trust Investigator grant to A.T.S. (110174/Z/15/Z), a BIF doctoral fellowship to A.C.M., and a DFG postdoctoral fellowship to T.A.

## Author information

### Author notes

1. These authors contributed equally: Tobias Ackels, Andrew Erskine, Debanjan Dasgupta

## Affiliations

1. Sensory Circuits and Neurotechnology Laboratory, The Francis Crick Institute, London, UK

Tobias Ackels, Andrew Erskine, Debanjan Dasgupta, Alina Cristina Marin, Tom P. A. Warner, Sina Tootoonian, Izumi Fukunaga, Julia J. Harris & Andreas T. Schaefer

2. Department of Neuroscience, Physiology & Pharmacology, University College London, London, UK

Tobias Ackels, Andrew Erskine, Debanjan Dasgupta, Sina Tootoonian, Julia J. Harris & Andreas T. Schaefer

## Authors

1. Tobias Ackels

[View author publications](#)

You can also search for this author in [PubMed](#) [Google Scholar](#)

2. Andrew Erskine

[View author publications](#)

You can also search for this author in [PubMed](#) [Google Scholar](#)

3. Debanjan Dasgupta

[View author publications](#)

You can also search for this author in [PubMed](#) [Google Scholar](#)

4. Alina Cristina Marin

[View author publications](#)

You can also search for this author in [PubMed](#) [Google Scholar](#)

5. Tom P. A. Warner

[View author publications](#)

You can also search for this author in [PubMed](#) [Google Scholar](#)

6. Sina Tootoonian

[View author publications](#)

You can also search for this author in [PubMed](#) [Google Scholar](#)

7. Izumi Fukunaga

[View author publications](#)

You can also search for this author in [PubMed](#) [Google Scholar](#)

8. Julia J. Harris

[View author publications](#)

You can also search for this author in [PubMed](#) [Google Scholar](#)

9. Andreas T. Schaefer

[View author publications](#)

You can also search for this author in [PubMed](#) [Google Scholar](#)

## Contributions

A.T.S. conceived the project; T.A., A.E., D.D. and A.T.S. designed experiments with input from A.C.M., T.P.A.W., J.J.H., and S.T.; T.A. (in vivo imaging, plume measurements), A.E. (plume measurements, frequency and correlation behaviour), D.D. (plume measurements, whole-cell recordings), A.C.M. (source separation behaviour), T.P.A.W. (unit recordings), S.T. (analysis for OSN imaging) and J.J.H. (source separation behaviour) performed experiments and analysed data; I.F. contributed tools and to experimental design; S.T. performed simulations; and T.A., A.E. and A.T.S. wrote the manuscript with input from all authors.

## Corresponding author

Correspondence to [Andreas T. Schaefer](#).

## Ethics declarations

## Competing interests

The authors declare no competing interests.

## Additional information

**Peer review information** *Nature* thanks Venkatesh Murthy and Diego Restrepo for their contribution to the peer review of this work. Peer reviewer reports are available.

**Publisher's note** Springer Nature remains neutral with regard to jurisdictional claims in published maps and institutional affiliations.

## Extended data figures and tables

### [Extended Data Fig. 1 Distinguishing fast odour stimuli with slow OSNs.](#)

**a**, Membrane voltage relative to baseline of a single model OSN in response to a 10-ms odour pulse. Black traces are individual trials; red trace is average over 20 trials. OSN spike threshold has been set high enough to prevent spiking to illustrate the subthreshold voltage time course. **b**, Membrane voltages (grey traces) of ten OSNs from a population of 5,000 in response to a paired odour pulse with pulse width 10 ms and PPI of 25 ms. The voltage time course for one example OSN is in black. Several OSNs reach the OSN spike threshold (dashed red line) and are temporarily reset to the refractory voltage of  $-1$ . The population average membrane voltage (red) reveals membrane charging in response to odour stimulation and the subsequent discharging and refractory period. **c**, Raster showing the spike times (dots) of the full population from **b** and the corresponding mean firing rate (trace) estimated in 1-ms bins. **d**, Mean firing rates computed over 20 trials in response to paired odour pulses of width 10 ms and PPIs of 10 ms (green) and 25 ms (black). **e**, Model calcium signals are produced by squaring the instantaneous mean firing rate and filtering the result with a calcium imaging kernel. **f**, Model calcium responses to the paired odour stimulus with a PPI of 10 ms (green) and 25 ms (black). Thin traces are single trials, thick traces are averages over 15 trials. **g**, Schematic of the OSN model. Variables in dashed bounding boxes are changed for each

glomerulus ([Methods](#)). **h**, Linear classifier analysis over an increasing subset size of glomeruli (1–100; plotted is mean  $\pm$  s.d., 256 repeats for random subsets of  $n$  glomeruli generating 256 unshuffled and 256 shuffled accuracies).

## [Extended Data Fig. 2 Sub-sniff odour information in the olfactory bulb input layer.](#)

**a**, GCaMP6f fluorescence recorded in OB glomeruli in an anaesthetized *OMP-cre: Ai95(RCL-GCaMP6f)-D* mouse (maximum projection of 8,200 frames, glomerulus marked with red asterisk corresponds to first example trace shown in **b**). Scale bar, 50  $\mu\text{m}$ . **b**, Example calcium traces in response to 10 and 25 ms PPI odour stimuli (mean of 50 trials  $\pm$  s.e.m.). Bottom, example respiration traces.  $P$  values derived from unpaired two-sided  $t$ -tests comparing responses of individual trials integrated over 2-s windows to paired odour pulse stimulation. **c**, Classifier accuracy over an increasing number of glomeruli when a linear classifier was trained on several response windows (colour-coded; black, shuffle control) to PPI 10 versus 25 ms stimuli (mean  $\pm$  s.d. of up to 93 glomeruli from 4 individual animals; 500 repetitions). **d<sub>i</sub>**, Classifier accuracy when trained on all glomeruli in response to PPI 10 versus 25 ms stimuli recorded in anaesthetized animals ( $n = 93$  glomeruli, mean  $\pm$  s.d. from 4 individual animals) with a sliding window of different durations (colour-coded; black, shuffle control; 100 repetitions) starting at 2 s before odour onset (left) and time period between –0.5 and 0.5 s from odour onset shown at higher magnification (right). **d<sub>ii</sub>**, Same as **d<sub>i</sub>** for awake animals ( $n = 100$  glomeruli, mean  $\pm$  s.d. from 5 individual animals). **e**, **f**, Odour (**e**) and flow (**f**) signals integrated over 2 s for PPI 10 ms and PPI 25 ms stimuli (10 repeats each; odour,  $P = 0.1841$ ; flow,  $P = 0.1786$ ; unpaired two-sided  $t$ -test). **g**, Correlation coefficients of glomerular calcium responses to PPI 10 versus 25 ms in anaesthetized ( $n = 93$  glomeruli from 4 individual animals) and awake ( $n = 100$  glomeruli from 5 individual animals) mice ( $P = 0.3187$ , unpaired two-sided  $t$ -test, measured as in Fig. [1](#) from *OMP-Cre: Ai95(RCL-GCaMP6f)-D* mice). Violin plots show the median as a black dot and the first and third quartiles by the bounds of the black bar. **h<sub>i</sub>**, Example respiration traces recorded using a flow sensor from awake mice. Inhalation goes in the upwards

direction, exhalation downwards. **h<sub>ii</sub>**, Average instantaneous sniff frequency from one example animal plotted as a function of time ( $n = 24$  trials, mean  $\pm$  s.e.m.). The odour stimulus consisted of two 10-ms odour pulses either 10 or 25 ms apart (Fig. 1c). **h<sub>iii</sub>**, Distribution of sniff intervals during a 2-s window before (grey) and a 5-s window after (blue) odour stimulus onset ( $P = 1.02 \times 10^{-189}$ , two-sample Kolmogorov–Smirnov test). **h<sub>iv–vi</sub>**, Same as top row but for the anaesthetized condition ( $P = 0.3952$ , two-sample Kolmogorov–Smirnov test). **i**, Mean odour signal for PPI 10 and 25 ms for 10 increasing concentration steps defined by modulating valve pulse duty ([Methods](#) and Supplementary Fig. 1). There were no significant differences in odour concentration between both stimuli (unpaired two-sided *t*-tests). **j**, Modelled response integrals to PPI 10 versus 25 ms stimulations over a tenfold concentration range pooled over all 20 trials and 100 glomeruli ([Methods](#)). Box plots show median and extend from the 25th to 75th percentiles, whiskers extend to the 5th and 95th percentiles. **k<sub>i</sub>**, Confusion matrix of SVM-based classification results of modelled glomerular signals in response to a range of ten odour concentrations ranked and colour-coded ( $n = 100$  glomeruli). **k<sub>ii</sub>**, Shuffle control with labels assigned randomly. **k<sub>iii</sub>**, Confusion matrix showing the ranked and colour-coded results of glomerular responses independently classified for 10 ms versus 25 ms PPI and across the range of ten odour concentrations. **k<sub>iv</sub>**, shuffle control for **k<sub>iii</sub>** with labels assigned randomly. **l**, As in **j** but with 2-s response integrals derived from  $\text{Ca}^{2+}$  imaging data (10 repeats for each concentration). **m**, As in **k** for  $\text{Ca}^{2+}$  imaging data ( $n = 57$  glomeruli, from 2 individual animals, 10 repeats for each concentration). Note that 10 ms PPI could be reliably distinguished from 25 ms PPI with only few instances where a response to, for example, a 10 ms PPI stimulus was misclassified as 25 ms or vice versa (compare light red quadrants to light green quadrants). **n**, Shifting the position of 10 ms PPI within a single inhalation. PPI 10 ms at position 1 (**n<sub>i</sub>**) or at position 2 (**n<sub>ii</sub>**) of three 10-ms odour pulses. Odour pulses as recorded with a PID shown in red, valve commands are shown in dark grey. Light grey area shows additional compensatory blank valve command to keep the flow profile indistinguishable between stimuli. **n<sub>iii</sub>**, Total odour concentration was independent of the pulse profile (10 repeats,  $P = 0.57$ , unpaired two-sided *t*-test). **o**, The 10 ms PPI at both position 1 (**o<sub>i</sub>**)

and position 2 ( $\mathbf{o}_{ii}$ ) are presented during the inhalation phase (respiration shown in black, inhalation upwards, exhalation downwards). **p**, Example calcium traces in response to 10 ms PPI at position 1 (black) and position 2 (red), shown is the mean of 10 trials  $\pm$  s.e.m. *P* values derived from unpaired *t*-tests comparing 2 s integrated responses of individual trials to odour pulses. **q**, Classifier accuracy over increasing number of glomeruli when a linear classifier was trained on the 2-s response to PPI 10 ms at position 1 versus position 2 (mean  $\pm$  s.d. of up to 57 glomeruli, from 2 individual animals, 500 repetitions; blue: PPI 10 ms at position 1 versus position 2; black: shuffle control). For box plots, boxes indicate 25th–75th percentiles, thick line is median, whiskers are most extreme data points not considered outliers ([Methods](#)).

### **Extended Data Fig. 3 Frequency discrimination experiments.**

**a**, Frequency discrimination stimuli are produced by alternating presentation of two odours to generate a desired odour change frequency. During odour delivery, valves are not held open but rather are randomly opened and closed over time to produce slight variation in odour amplitude for each pulse. This means that odour concentration cannot be used as a cue to learn the task and odour switching frequency is the primary stimulus signal. Furthermore, valve clicking is randomized to minimize any acoustic cues. **b**, Replacing one odour channel with blank, un-odourized air and recording the frequency stimuli with a PID reveals that the desired odour pulse frequency is being produced. **c**, Mice readily learn to discriminate 2 versus 20 Hz pulse frequency stimuli in a go/no-go task. Replacing the odours with blank channels results in chance-level performance (no odour), which recovers when odours are replaced (recovery), showing that mice were probably discriminating the odour switching frequency rather than any extraneous cues such as valve noise. The order of odour presentation in the stimuli had no effect on behaviour as when it was shifted (phase switch) no decrease in performance was observed. Additionally, performance was dependent on the alternation between different odours, as when the experiment was repeated with the same odours in each channel (equal odours) performance was at chance level. **d**, To determine the perceptual limit of frequency discrimination, the floor frequency used in the task over successive experiments was increased such that the difference in frequency

between the stimuli progressively narrowed. Overall performance decreased as the difference in frequency grew smaller, reaching near-chance level with a frequency difference of 10 Hz (10 versus 20 Hz). Switching back to the original discrimination (2 versus 20 Hz) recovered performance quickly, showing that the drop in discrimination ability was truly due to the frequency difference rather than general deterioration of performance over time. **e<sub>i</sub>**, Example uncorrelated stimuli. Combinations of odour 1 (red) and odour 2 (blue) valves are opened with temporal offsets and randomized pulse timing resulting in a correlation of 0 ([Methods](#)). Blank (black) valves are used to keep total airflow constant throughout the stimulus. **e<sub>ii</sub>**, Higher magnification of the area shaded in grey. **f**, Animals show similar average accuracy as shown in Fig. [2k](#) when probed to discriminate correlated from uncorrelated odour pulses at 10 Hz ( $n = 19$  mice, mean  $\pm$  s.e.m. of average accuracy =  $0.6506 \pm 0.0016$ ; after scrambling stimulus identity:  $0.4997 \pm 0.0032$ ;  $P = 0.0175$ , unpaired two-sided  $t$ -test). **g**, Animals show similar average accuracy when discriminating the correlation structure of a different odour pair (acetophenone versus cineol) at 10 Hz ( $n = 19$  mice, mean  $\pm$  s.e.m. of average accuracy =  $0.6558 \pm 0.0026$ ; after scrambling stimulus identity:  $0.5165 \pm 0.0048$ ;  $P = 0.0129$ , unpaired two-sided  $t$ -test). Grey dots mark average performance of individual animals. Boxes in **f**, **g** indicate 25th–75th percentiles, thick line is median, whiskers are most extreme data points not considered outliers ([Methods](#)).

## [Extended Data Fig. 4 AutonoMouse stimulus and experimental design.](#)

**a**, Detailed schematic of stimulus production; odour presentation (odour 1: blue, odour 2: red) is always offset by clean air (mineral oil: grey) valves at the same flow levels, to ensure that total flow during the stimulus is constant. **b**, Schematic of the use of valve subsets to produce the desired stimulus.  $t_1$  and  $t_2$  represent valve openings at the corresponding time points shown in **a**. **c<sub>1</sub>** (left) and **c<sub>2</sub>** (middle) represent two possible configurations that could be used to produce the same resulting stimulus at the two time points. Opacity in the colours represents total concentration contribution to the resulting stimulus at the time point. For example, to produce the dual odour pulse at  $t_1$ , configuration **c<sub>1</sub>** can be used where odour 1 (blue) is

delivered from one valve and odour 2 (red) from another valve. During  $t_2$  two valves contribute clean air. Alternatively, configuration  $c_2$  can be used in which during  $t_1$  odour 1 (blue) is generated by 50% opening of two valves, with odour 2 (red) produced by 70%–30% opening of two other valves. Right, scramble control: valve maps (represented by arrow colour) are maintained compared to the training condition but odour vial positions are scrambled resulting in odour stimuli that are uninformative about reward association while maintaining any non-odour cue such as putative sound or flow contributions. **c**, Predicted accuracy for animals in the case that they use solely olfactory temporal correlations (black) and in the case that they use extraneous non-olfactory cues or non-intended olfactory cues (for example, contaminations, clicking noises) (violet). Note that when switching stimulus preparations to a new set of valves (as in Fig. 2*i* and *i*–*k*), such non-intended cues would not provide any information about stimulus–reward association, so accuracy would transiently drop back to chance. **d<sub>i</sub>**, Average flow recordings (mean ± s.d.) of 2 Hz correlated (black,  $n = 75$ ) and anti-correlated (red,  $n = 70$ ) trials taken from the AutonoMouse odour port. **d<sub>ii</sub>**, Fourier transform of the flow plots from **d<sub>i</sub>**, showing the power of the signal over a range of 1 kHz. **d<sub>iii</sub>**, An expanded view over the range of 10 Hz indicated by the dotted box in **d<sub>ii</sub>**. **d<sub>iv</sub>**, Mean accuracy of a series of linear classifiers trained on an increasing window of the integrated signal starting from 1 s before trial shown in **d<sub>i</sub>**. Classifiers were tested on two withheld trials, one correlated and one anti-correlated, and repeated 100 times. **e**, As in **d** but for 40 Hz trials ( $n = 69$  correlated and  $n = 72$  anti-correlated). **f<sub>i</sub>**, Average audio recording trace (mean ± s.d.) of 2 Hz stimuli using a microphone placed in close proximity to the AutonoMouse odour port. **f<sub>ii</sub>**, **f<sub>iii</sub>**, Fourier transforms of the audio signal from **f<sub>i</sub>**. Note, although there are notable peaks at specific frequencies, these are present in both correlated and anti-correlated trials. **f<sub>iv</sub>**, Accuracy of a series of linear classifiers as shown in **d** but using the modulus of the audio signal. **g**, As in **f** but for 40 Hz trials. Note, whereas the sound profile and the Fourier transforms are different between 2 and 40 Hz, there is no difference detectable between correlated and anti-correlated trials. **h**, Example traces of odour signal (ethyl butyrate, isoamyl acetate, PID recorded) during correlated (top) and anti-correlated trials (middle). Simulated maximum

accuracy based on differences in mean odour signal (bottom). Simulated accuracy was calculated as the fraction of trials correctly identified as correlated or anti-correlated based on a decision threshold set at some level between the minimum and maximum mean signal. Simulated accuracy was calculated for multiple decision thresholds, increasing the decision threshold from minimum odour signal to maximum odour signal in steps of 1/5,000th of the range between minimum and maximum. **i**, Detailed schematic of correlated (top left) and anti-correlated (top right) stimulus production before (middle) and after (bottom) switching valves. For the switch control, a set of previously unused odour valves is introduced to rule out potential bias towards a specific valve combination when performing the odour correlation discrimination task. **j**, Trial map of five representative animals during 2 Hz (**j<sub>i</sub>**) and 12 Hz (**j<sub>ii</sub>**) correlation discrimination tasks before and after the introduction of control valves ( $n = 12$  trials before and 12 trials after new valve introduction, which is indicated by black vertical dotted line. Each row corresponds to an animal, each column represents a trial. Light green: hit, dark green: correct rejection, light red: false alarm, dark red: miss. **k<sub>i</sub>**, Boxplots of mean accuracy for animals ( $n = 5$  mice) pre- and post-control for 2 Hz (left) and 12 Hz (right). Box indicates 25th–75th percentiles, thick line is median, whiskers are most extreme data points not considered outliers; [Methods](#).  $P$  values derived from unpaired *t*-tests. **k<sub>ii</sub>**, Summary histograms of performance change for all animals during all ‘valve switch’ control tests ([Methods](#)), indicating that discrimination accuracy was based on intended olfactory cues. The five animals with the best performance before the valve switch or bottle change (and thus the largest potential to drop in performance) were analysed. **l**, Discrimination accuracy ( $n = 33$  animals, mean  $\pm$  s.e.m.) for rewarded S+ (left) and unrewarded S- (right) trials when odours were presented using standard training valve configurations (black) and scrambled valve identity (red), data from Fig. [2k](#). Note that frequencies above 40 Hz were presented predominantly in the last block of the training schedule and reduced licking in the control group (decreased S+ performance and increased S- performance) might be due to decreased motivation at that point.

## [Extended Data Fig. 5 Respiration recordings, stimulus onset model and reaction time for correlation discrimination](#)

## experiments.

**a**, An overhead camera was used to image a head-fixed mouse during a sequence of odour presentations. Simultaneously, a flow sensor was placed close to one nostril to monitor respiration to establish the validity of motion imaging-based respiration recording. Phase-based motion amplification was used to magnify motion on the animal's flank to capture body movements associated with respiration. Right, example of simultaneous respiration measurement with motion imaging (red) and flow sensor (black; [Methods](#) and Supplementary Video 2). **b**, Three further example trials with respiration rate extracted from motion imaging (red) and simultaneous flow sensor recording (black). Below, instantaneous sniff frequencies calculated from either sensor were tightly correlated. **c**, Correlation between respiration traces extracted from motion imaging and respiration captured by flow sensor ( $n = 26$  trials, 10 s duration each). Violin plot shows the median as a black dot and the first and third quartiles by the bounds of the black bar. **d**, **e**, Probability distributions of inter-sniff intervals for odour presentations (isoamyl acetate versus ethyl butyrate, 2 Hz and 20 Hz) for freely moving animals in AutonoMouse before stimulus onset (**d**) and during 2 s odour stimulation (**e**;  $n = 605$  sniffs for 2 Hz and  $n = 668$  sniffs for 20 Hz, two-sample Kolmogorov–Smirnov test). **f**, Heat map of accuracy difference between a model in which animals rely on onset information only ([Methods](#)) and actual animal accuracies across a range of sniff frequencies and inhalation fractions ( $n = 10$  mice). No matter the assumed sniff frequency and inhalation frequency, the ‘onset model’ deviates substantially from the accuracy measured in the behavioural experiments (**h**, **i**). **g**, Difference between a model in which animals use the entire stimulus structure ([Methods](#)) and actual behavioural accuracies across different stimulus sampling times ( $n = 10$  repeats, mean  $\pm$  s.d.). The ‘whole stimulus’ model accurately describes animal behaviour, indicating that mice do not base a decision about the correlation structure of a stimulus predominantly on the onset. Note the different scales in **f** and **g**. **h**, Schematic of experimental stimuli in which the first stimulus pulse was disrupted when presented on probe trials. Top, normal stimulus design; bottom, ‘onset disrupt’ stimuli, in which the first pulse in a correlated stimulus is disrupted to be anti-correlated; and vice versa for an anti-correlated stimulus. **i**, Animals were trained on standard (non-probe)

correlation discrimination stimuli ( $f = 10$  Hz) but onset disrupt (probe) stimuli were presented randomly on probe trials with a 1/10 probability. Accuracy was only slightly degraded on probe trials (mean  $\pm$  s.d. of accuracy for non-probe trials  $75.8 \pm 4.4\%$ ; for probe trials  $67.8 \pm 6.1\%$ ;  $P = 0.001$ , paired two-sided  $t$ -test,  $n = 9$  mice) but did not drop below chance ( $P = 7.3 \times 10^{-6}$ , paired  $t$ -test). Notably, accuracy on probe trials was consistent with whole-structure prediction ( $70.3 \pm 3.5\%$ ,  $P = 0.13$ , paired  $t$ -test of comparison to probe trials) and differed significantly from the accuracy of onset-only prediction ( $41.6 \pm 1.5\%$ ;  $P = 1.02 \times 10^{-6}$ , paired  $t$ -test of comparison to probe trials). **j**, Mean reaction time (time from stimulus onset to first lick in S+ trials) plotted as a function of stimulus pulse frequency for the three animals with the best (left) and the worst (right) global accuracy (mean accuracy across all trials). Better-performing animals tend to increase their reaction time as stimulus pulse frequency increases. **k**, Scatter plot of mean accuracy versus mean reaction time for each animal and stimulus pulse frequency condition (averaged over blocks of 100 trials). Points are colour-coded according to stimulus pulse frequency. Accuracy was significantly positively correlated with reaction time, suggesting that mice that sampled a greater portion of the stimulus made more accurate decisions about its correlation structure (Pearson correlation coefficient  $R = 0.49$ ,  $P < 1.1 \times 10^{-112}$ ). **l**, Accuracy (mean  $\pm$  s.e.m.) is plotted as in Fig. 2k, but only trial blocks with reaction times above or below a certain threshold (colour code) are included in the analysis. Where only longer reaction times are considered, global performance is higher than the case in which only shorter reaction times are included, again suggesting that longer stimulus sampling improves discrimination of odour correlation structure across all stimulus pulse frequencies.

### **Extended Data Fig. 6 OSN imaging in response to correlated versus anti-correlated odour stimulation.**

**a<sub>i</sub>**, Four example fields of view (FOVs) recorded from the dorsal olfactory bulb of individual mice. **a<sub>ii</sub>**, Number of individual glomeruli per FOV in all experimental mice ( $n = 15$ ). The number of individually delineated glomeruli ranges from 20 to 36 with an average of 28 glomeruli per FOV.

Labelled data points (1–4) correspond to FOVs shown in **a**. Scale bars, 50  $\mu$ m. Centre line is median, the edges of the box are the 25th and 75th percentiles, and the whiskers extend to the most extreme data points not considered as outliers; [Methods](#). **b**, Example glomerulus response from *OMP-Cre: Ai95(RCL-GCaMP6f)-D* mice to presentation of individual odours plotted pairwise (AB, CD, EF; mean  $\pm$  s.e.m. of 6 trials). Stimulation period (1 s) is indicated by vertical bar (blue, green and yellow). Bottom, typical example respiration trace. *P* values derived from unpaired two-sided *t*-tests comparing 2-s integrated responses between paired odours. **c**, Averaged calcium transients from all glomeruli ( $n = 145$  from 5 individual animals) in response to individual odours, plotted as colour maps sorted by response magnitude. **d**, Difference between glomerulus responses to individual odours plotted pairwise as colour maps. Glomeruli are sorted by average magnitude of response difference. **e**, Example glomerulus response to presentation of correlated versus anti-correlated odour pairs fluctuating at 2 Hz (mean  $\pm$  s.e.m. of 12 trials). Bottom, typical example respiration trace. *P* values derived from unpaired two-sided *t*-tests comparing 2-s integrated responses of individual trials to correlated and anti-correlated odour stimulation. **f**, Difference between glomerulus responses to 2 Hz correlated and anti-correlated odours as colour maps, sorted as in **d**. **g**, **h**, As in **e**, **f** but for 20 Hz correlated versus anti-correlated stimuli. Example glomerulus from **b**, **e**, **g** indicated with an asterisk in colour maps in **c**, **d**, **f**, **h**. **i**, Left, *P* values derived from comparing trials of the summed 2-s response to correlated versus anti-correlated odour stimulation at 2 Hz (unpaired two-sided *t*-tests) for three odour pairs (colour-coded) as a function of glomerulus selectivity to individual odours ( $n = 145$  glomeruli). Selectivity is calculated as the difference between the absolute response to single odours scaled by the summed absolute response. A threshold is set at 0.5 to define glomeruli as low- or high-selective. Dot size represents magnitude of the summed response. Middle, comparison of *P* values between low- and high-selective glomeruli ( $P < 0.05$ , unpaired two-sided *t*-test). Violin plots show the median as a white dot and the first and third quartiles by the bounds of the grey bar. Right, cumulative distribution function of *P* values for low- and high-selective glomeruli ( $P < 0.01$  for all pairwise comparisons, two-sample Kolmogorov–Smirnov test). **j**, As in **i** but for 20 Hz ( $n = 145$  glomeruli). **k**, Top, mean  $\pm$  s.d. of classifier accuracy over 100 repetitions when trained on

all responsive glomeruli ( $n = 145$  available, from 5 individual animals, [Methods](#)) to discriminate 2 Hz correlated versus anti-correlated stimuli, trained separately for each of the three odour pairs and within sliding windows of different widths (colours);  $x$ -coordinates indicate latest extent of each window. Bottom, same as top row but with labels shuffled as control. **I**, As in **k** for 20 Hz correlated versus anti-correlated odours. Some data points in **k**, **I** are absent because not all time points had responsive ROIs for every window size ([Methods](#)).

### **Extended Data Fig. 7 Odour correlation structure is encoded in dendrites of olfactory bulb output neurons.**

**a**, GCaMP6f fluorescence from mitral and tufted cells and their dendrites recorded in the dorsal portion of the olfactory bulb of a *Tbet-cre; Ai95(RCL-GCaMP6f)-D* mouse (maximum projection of 8,000 frames). Dendritic ROIs are superimposed in colour. Four dendritic segments (1–4) are shown in higher magnification; scale bars, 20  $\mu\text{m}$ . **b**, Four example calcium traces extracted from dendritic segments shown in **a** that show differential response kinetics to correlated (black) and anti-correlated (red) stimulation (mean  $\pm$  s.e.m. of 24 trials,  $f = 20$  Hz). In total, 24% of dendritic segments showed significantly different integral responses (0–5 s after odour onset,  $P < 0.01$ , unpaired two-sided  $t$ -test; 121/514) to the two stimuli. **c**, Average calcium transients as colour maps for correlated (left) and anti-correlated stimuli (middle) and the difference between the two (right) of all analysed dendritic segments ( $n = 514$ , from 6 individual animals). **d**, Classifier accuracy over an increasing number of dendritic ROIs trained on several response windows (colour-coded) to discriminate correlated versus anti-correlated stimuli at 20 Hz ( $n = \text{up to } 514$ , mean  $\pm$  s.d. from 6 individual animals, black: shuffle control). **e**, Method of aligning calcium traces to first inhalation after odour stimulus onset. **e<sub>i</sub>**, Representative respiration traces recorded using a flow sensor placed in front of the nostril contralateral to the imaging window. The first inhalation peaks were detected and the time ( $\Delta t$ ) to the first inhalation after odour onset was calculated for each trial individually. **e<sub>ii</sub>**, Representative calcium transients in response to a single odour presentation (here: 20 Hz correlated). **e<sub>iii</sub>**, Transients are shifted according to  $\Delta t$ . **e<sub>iv</sub>**, Individual

calcium transients (faint colours, 24 trials) in response to 20 Hz correlated odour presentations with the average calcium signal (thick traces) superimposed. Top, before aligning to first inhalation after odour onset; bottom, after alignment. Blue bar represents the odour presentation phase (approximate for the aligned data). **f**, Distribution of odour response integrals from all recorded ROIs ( $n = 514$ ) for correlated (grey) and anti-correlated (red) stimulation. Box indicates 25th–75th percentiles, thick line is median, whiskers are most extreme data points not considered outliers; [Methods](#). **g**, Histogram of the difference between correlated and anti-correlated odour responses. Box plot as in **f**. **h**, Comparison of correlated and anti-correlated odour responses of all dendritic ROIs ( $f = 20$  Hz,  $n = 514$  dendrites). **i**, Classifier accuracy when trained on all dendritic ROIs recorded with a sliding window of different durations starting 2 s before odour onset (colour-coded; black, shuffle control;  $n = 514$  from 6 individual animals; mean  $\pm$  s.d., 100 repetitions). **j–m**, As in **f–i** but for projection neuron somata ( $f = 20$  Hz,  $n = 680$  cells; Fig. [3](#)).

### [Extended Data Fig. 8 Projection neuron unit recordings in response to correlated versus anti-correlated stimulation and short odour pulse combinations.](#)

**a**, Data from unit recordings as in Fig. [3h–k](#). Average waveforms across all channels of two isolated units shown in **b<sub>i,ii</sub>**. Each waveform represents the average waveform for the unit on a specific channel. Red waveform indicates the channel with the largest average waveform for the unit. Scale bars, 100  $\mu$ V (vertically) and 1 ms (horizontally). **b**, Additional example single unit odour responses to correlated (black) and anti-correlated (red) stimuli shown as raster plots (top) and PSTHs (mean  $\pm$  s.e.m. of 64 trials for each condition) of spike times before (second from top) and after baseline subtraction (second from bottom), and the differential PSTHs for correlated and anti-correlated stimuli (bottom, blue). Average spike waveforms shown as insets in **b<sub>i,ii</sub>**. Duration of odour presentation (2 s) is indicated in light blue.  $P$  values derived from a two-sided Mann–Whitney  $U$  test comparing the spike time distributions of correlated and anti-correlated trials during the 4 s after odour onset. **c**, Average baseline firing rate for all units ( $n = 97$  from 6 individual animals). Baseline firing rates were calculated from 4 s to

0 s before odour onset for each of the 1,312 trials presented during all recordings. Violin plot shows the median as a black dot and the first and third quartiles by the bounds of the black bar. **d<sub>i</sub>**, Classifier accuracy when trained on all baseline-subtracted units in response to 20 Hz correlated versus anti-correlated stimulation ( $n = 97$  units, mean  $\pm$  s.d. from 6 individual animals) with a sliding window of different durations (colour-coded; black, shuffle control; 100 repetitions) starting at 2 s before odour onset. Time along the  $x$ -axis represents the end time of the window. **d<sub>ii</sub>**, Time period between  $-0.5$  and  $0.5$  s from odour onset shown at higher magnification ( $n = 97$  units, mean  $\pm$  s.d. from 6 individual animals). **e**, To take the entire temporal structure of responses into account we performed a PCA on the temporal evolution of the firing rate responses ([Methods](#)). Shown here is the accuracy for linear SVM classifiers (mean  $\pm$  s.d.) trained on increasing numbers of PCs. Classifiers were trained on all but two trials (one correlated, one anti-correlated). Training and testing were repeated 1,000 times. The colour code represents the same window sizes as in **d**. **f**, The first (**f<sub>i</sub>**), second (**f<sub>ii</sub>**), and third (**f<sub>iii</sub>**) PCs found from PCA for different rolling window sizes (colour code as in **d**). In the second and third PCs, the windows have been split as to better compare the similarities in PCs for different window sizes. **g**, Average classifier accuracy of a set of classifiers trained on the PC weights of increasing number of units. Classifiers were trained on all but two trials (one correlated, one anti-correlated). The number of PCs used for each window was selected by the peak accuracies in **e** (colour-coded;  $n =$  up to 97 units from 6 individual animals; mean  $\pm$  s.d. of 1,000 classifier repetitions). **h**, Schematic of odour pulse stimulus timings in relation to the respiration cycle. Three combinations were presented, with each trial 120 ms in length. For example, 11000 (top) consisted of a 40-ms odour pulse (light blue) followed by 80 ms of blank odourless air (grey). All trials were triggered at the onset of inhalation. **i**, PSTHs from four example units (**i<sub>i</sub>-iv**) showing their average firing rate before, during, and after odour presentation (light blue vertical bar). Responses are to either 11000 trial (black) or 10100 odour presentation (red). The instantaneous firing rate was calculated by summing the number of detected spikes in 10-ms windows and multiplying the value by 100 to get Hz. **j**, Accuracy of linear classifiers as a function of the number of units available for training or testing (mean  $\pm$  s.d. of  $n =$  up to 145 units from 8

individual anaesthetized animals). Each classifier was trained on the summed spike count of the available units in a window of 500 ms starting at odour onset. The classifiers were trained on all but two trials (one 11000 and one 10100 trial) and the number of repeats between animals varied between 11 and 30. To account for this and to minimize the variability of the training set, trial number was bootstrapped to 1,000 repeats. This was achieved by randomly selecting a repetition for each unit independently. The test set was isolated from the responses before bootstrapping and thus was not seen by the classifier until it was tested on it. Each classification was repeated 500 times with a different selection of units, and a different test set. The shuffled control (black) was accomplished by shuffling the training labels during each iteration of the classifier without shuffling test labels. **k**, As in **j** but classifying all three odour pulse combinations shown in **h**. **l**, Confusion matrix showing the fractions that each trial type was classified as ( $n = 145$  units from 8 individual animals). True labels are shown on the  $x$ -axis and labels predicted by the classifier on the  $y$ -axis. Accuracies correspond to maximum unit count shown in **c**, **d**. The classifiers can readily separate between trials containing a single 40-ms odour pulse. Accuracy is lower when distinguishing between an intermission of 20 or 40 ms but remains above chance (chance = 0.33).

### Extended Data Fig. 9 Whole-cell recordings of projection neurons in response to correlated versus anti-correlated odour stimulation.

**a**, Schematic of the whole-cell patch-clamp recording approach. **b**, **c**, Distributions of input resistance (**b**) and recording depth (**c**) as measured from all recorded projection neurons ( $n = 31$ ). **d**, Left, example recordings from single cells with consecutive presentations of correlated (black) and anti-correlated (red) odour stimulus at 2 Hz. Duration of odour presentation (2 s) is indicated in light blue. Right, baseline-subtracted and spike-clipped subthreshold voltage response from a single cell to odour 1 (green) and odour 2 (blue) for 2 Hz. **e**, As in **d** but for 20 Hz odour stimulation. **f**, Voltage response from three example cells for correlated (black) and anti-correlated (red) odour stimuli for 2 Hz (top) and 20 Hz (bottom). The cell shown in **f** corresponds to the cell shown in **d**, **e**. The grey overlaid traces

correspond to the arithmetic sum estimated from the response to individual odours. Bottom, linear prediction histogram calculated by thresholding the arithmetic sum of the subthreshold responses to the individual odours. Differences here suggest that correlation can be calculated at the single-cell level if the two individual odours engage overlapping OSN populations.  $P$  values are derived from a paired two-sided  $t$ -test of the membrane potential and the firing rate in the first 500 ms after odour onset. **g, h**, Average change in voltage ( $\mathbf{g}_i$ ) and in instantaneous spike frequency ( $\mathbf{g}_{ii}$ ) in the first 500 ms after odour onset from baseline membrane potential for 2 Hz (**g**) and 20 Hz (**h**) correlated versus anti-correlated odour presentation. Each marker corresponds to a single cell; error bars represent s.e.m. Data points in black represent cells where  $P < 0.05$  between correlated and anti-correlated conditions.  $P$  values are derived from a paired  $t$ -test of the membrane potential and the firing rate in the first 500 ms after odour onset. Indicators **i**, **ii** and **iii** represent cells shown in **f**. **i**, Pie charts depicting the proportions of cells showing significant difference as described above (blue) in subthreshold membrane potential (left) and spike frequency (right) for all 2 Hz (top) and 20 Hz (bottom) cells.  $P$  values are derived from a paired  $t$ -test of the membrane potential and the firing rate in the first 500 ms after odour onset.

### **Extended Data Fig. 10 Odour plume generation and additional analysis of source separation experiments.**

**a**, Power spectrum of all recorded odour plumes (mean  $\pm$  s.d. of log power,  $n = 132$  plumes). **b**, Cross-correlation of all recordings at different lateral separation distances. **c**, Correlation coefficients over all recordings for odours from the same source and for odour sources separated by 50 cm in a controlled laboratory environment with complex airflow (indoors; ethyl valerate (EV) versus tripropylamine (TPA);  $n = 25$  for same source,  $n = 27$  for sources separated by 50 cm;  $P < 0.0001$ , unpaired two-sided  $t$ -test). Box indicates 25th–75th percentiles, thick line is median, whiskers are most extreme data points not considered outliers; [Methods](#). **d**, As in Fig. [4b](#) (for  $\alpha$ -terpinene and ethyl butyrate) but for radial distances to the PID of 20 cm and 60 cm ( $P < 0.0001$ , unpaired two-sided  $t$ -test). **e**, As in **d** but measured outdoors ( $n = 7$  for same source, 10 for sources separated by 50 cm;  $P < 0.001$ , unpaired  $t$ -test; indoors versus outdoors, one source:  $P = 0.0060$ ,

$s = 50$  cm:  $P = 0.0632$ , unpaired two-sided  $t$ -test). **f**, Example plume structures originating from the same source or separated sources as recorded with a PID (blue) and replayed with the multi-channel high bandwidth odour delivery device (orange). **g**, Correlation coefficients over all recordings of replayed plumes for one source ( $n = 53$  plumes) and for sources separated by 50 cm from each other ( $n = 74$  plumes;  $P = 2.27 \times 10^{-41}$ , unpaired two-sided  $t$ -test). **h**, Odour signals integrated over 2 s for all recordings of replayed plumes for one source ( $n = 53$  plumes) and for sources separated by 50 cm ( $n = 74$  plumes;  $P = 0.75$ , unpaired two-sided  $t$ -test). **i**, Odour plume signals integrated over 2 s for rewarded and unrewarded trials ( $n = 150$  trials each; odour 1:  $P = 0.4739$ , odour 2:  $P = 0.0923$ , unpaired two-sided  $t$ -test). **j**, Overlaid power spectra (mean  $\pm$  s.d. of log power) of all plumes ( $n = 127$  plumes) recorded in complex, natural airflow conditions (blue) and replayed plumes (orange). **k**, Schematic of plume reproduction. First, a 2-s window is selected from the PID recording, starting around the middle of the trace and such that odour is present during the first 500 ms. Second, the trace is normalized between 0 and 1. Third, the trace is converted into a series of binary opening and closing commands directly related to the value of the normalized signal. A value of 1 translates to a continuous opening, and a value of 0 translates to continuously closed. This series of commands is relayed to an odour valve and an inverted version of the commands is relayed to a mineral oil valve to generate a compensatory airflow. The resulting output resembles the original plume, as measured with a PID, and there is constant airflow throughout the trial, as measured with a flow meter. The same procedure is then applied to the accompanying odour, to create both plumes needed for each trial. **l**, Group learning curves (mean  $\pm$  s.d.) for the two groups of animals trained on the virtual source separation task, but on different sets of valves. Group 1 ( $n = 6$  mice, blue) were trained on the task from the start, whereas group 2 ( $n = 6$  mice, cyan) were first exposed to a scrambled version of the task and were later transferred to the same plumes as group 1. This served as a control that the cue required for learning is indeed olfactory information contained in the odour plumes. For the third stage of learning, the plumes were refined to ensure odour was always present in the first 500 ms of the trial and performance stabilized for the two groups. Mice progressed through these learning stages as a group, based on time elapsed from the beginning of training. Therefore, some mice performed more trials

than others. The last trial performed by a mouse in each phase is represented by a colour-coded circle above the plot. Accuracy is calculated over a 100-trial sliding window. **m**, Rejection fraction (fraction of trials the mouse abstained from licking) calculated for each plume pair plotted in relation to the correlation between the two odour traces in that plume pair. Animals are trained to lick (expected low rejection fraction) for source-separated trials (low correlation) and abstain from licking (high rejection fraction) for one-source trials (high correlation). **n**, Difference in lick rates in response to source-separation training trials ( $n = 9$  mice, mean  $\pm$  s.d.), calculated for each mouse as lick rate (licks per 100 ms) in response to S+ trials minus the lick rate in response to S- trials, normalized to averaged lick rate for all trials across the corresponding time period. **o**, Reaction times for each mouse, calculated as the time point when the difference in lick rate for each mouse crossed a threshold (mean + 3 s.d. over the baseline, defined as the first 200 ms of the trace, when odour was not present). Box indicates 25th–75th percentiles, thick line is median, whiskers are most extreme data points not considered outliers; [Methods](#). **p**, Trial map of all animals during virtual source separation tasks before and after introduction of control valves similar to Extended Data Fig. 4 ( $n = 40$  trials before and 40 trials after new valve introduction, which is indicated by black vertical line). Each row corresponds to an animal, each column represents a trial. Light green, hit; dark green, correct rejection; light red, false alarm; dark red, miss. **q**, Mean performance of animals ( $n = 11$  mice) that reached performance criterion during training during before and after control. **r**, Discrimination accuracy split by stimulus valence (green, S+; black, S-) for odour correlation fluctuation frequencies 2, 20 and 40 Hz (Fig. 4e;  $n = 9$  mice, data are mean  $\pm$  s.d., unpaired two-sided *t*-test). **s**, Group performance for the square pulse probe trials at different frequencies, in animals trained on the source separation task (blue dots,  $n = 9$  mice, data are mean  $\pm$  s.d.), compared to group performance where animals were trained on correlated and anti-correlated square pulse trains (from Fig. 2k, black line and s.e.m. band,  $n = 33$  mice; 2 Hz:  $P = 0.0018$ , 20 Hz:  $P = 0.19$ , 40 Hz:  $P = 0.94$ , unpaired two-sided *t*-test). Violin plots in **g–i** show the median as a black dot and the first and third quartiles by the bounds of the black bar.

## Supplementary information

## Supplementary Tables

This file contains Supplementary Table 1: Parameters of the olfactory sensory neuron population model; and Supplementary Table 2: Parameters of the olfactory sensory neuron population model that were varied.

## Reporting Summary

### Supplementary Figure 1

Characterization of odorants presented with a high-speed odour delivery device. **a**, Calculated signal fidelities for seven different odours (colours, see legend in **b**) pulsed for 2 s over a frequency range of 2 to 100 Hz at 50% pulse duty ( $n = 5$  repeats for each condition, mean  $\pm$  SEM). **b**, Amount of released odour ( $n = 5$  repeats for each condition, mean  $\pm$  SEM). Odours are: AA (isoamyl acetate), ACP (acetophenone), AT ( $\alpha$ -Terpinene), CN (cineol), EB (ethyl butyrate), Hex (2-hexanone), PEA (phenylethyl alcohol). **c**, Left: Schematic of the pulse-width modulation (PWM) method. For any period of odour release, maximum final concentration is achieved by keeping the valve open for the entire time (top). The amount of odour released can be reduced by cycling the valve at a high frequency (here 500 Hz) with a different level of PWM (middle and bottom panel). Right: Odours were released over a 2 s period with different PWM duties at 500 Hz ( $n = 5$  repeats for each condition, mean  $\pm$  SEM). The resulting amount of released odour is normalised to the maximum release (PWM = 1). **d**, Average PID signal of single 100 ms pulses (pulse indicated in blue) for seven different odours ( $n = 60$  pulses for each odour, mean  $\pm$  SEM). **e**, Summary table: delay (time from start of the odour pulse to 5% of maximum signal amplitude), rise (time from 5% to 95% of maximum signal amplitude), decay (time for the signal to decay back to 5% of maximum amplitude after the end of the odour pulse). **f**, Effect of tubing length attached to the valve manifold on signal fidelity at different pulse frequencies pulsed for 2 s at 50% pulse duty (ethyl butyrate).

### Supplementary Figure 2

Dual-energy fast photoionisation detection (defPID). **a**, Schematic of the dual-energy fast photoionisation detection method. Two odours are recorded simultaneously by two PIDs with different ionizing energies (different wavelength UV light sources). The odours are chosen such that one odour (odour 2 (ethyl butyrate), 9.5 eV) has an ionization energy greater than the low energy PID bulb, but less than the high energy PID bulb, thus only being detectable by the high energy PID. The other odour (odour 1 ( $\alpha$ -Terpinene), 7.9 eV) is chosen such that its ionization energy is lower than both PID bulbs (detectable by both PIDs, see also **e**). **b**, Method of decomposing odour signals. Top panel: high energy PID signal (grey: recorded signal, blue: calculated signal due to odour 1, red: calculated signal due to odour 2). Bottom panel: low energy PID signal (green: recorded signal, red: calculated signal due to odour 2; the entire signal is due to odour 1). **c**, Single data points of the PID signal evoked by  $\alpha$ -Terpinene in the two PIDs. The slope of the linear fit serves as a scaling factor to map the low energy PID to the high energy PID signal. **d**, Histogram of R-squared values of all dual-PID  $\alpha$ -Terpinene recordings to define the scaling factor ( $n = 59$  recordings). **e**, Summary of signal combinations for defPID recordings. The scaling factor for the PID<sub>low</sub> signal is determined by the slope in **c**. **f**, Schematic of outdoors odour plume recording setup. PIDs and odour delivery system were used to record for multiple trials at different lateral distances (s) between odours held in ceramic crucibles. Data was collected on a day with low wind (~8-12 mph, equivalent to ~3-5 m/s, recorded with a 2-axis ultrasonic wind sensor at the height of the PID inlet. Outdoor experiments were performed on a ~6 m x 10 m wooden patio structure surrounded by trees. There was >300 cm of unobstructed space on an artificial grass mat in front of the PIDs to capture air movements. **g**, Indoor setup: A digitally controlled fan was placed at a distance of 325 cm facing the PID inlet. An exhaust line was situated behind the PID inlet to ensure the direction of air from the fan towards the PID inlet. During a recording, the fan was set to maximum speed such that it pushed approximately 552 cf/min (cubic feet per minute, ~260 l/s) of air towards the PID inlet. A 25x25x25 cm Thermocool box was placed 200 cm downwind of the fan acting as an obstacle to air movement, promoting complex air movement patterns at the PID location. The pump at the PID was set to ~0.02 l/s suction speed, unlikely to perturb overall airflow dynamics substantially.

## Supplementary Video 1

Automated operant conditioning system (“AutonoMouse”) equipped with high speed odour delivery device.

## Supplementary Video 2

Comparison between original video-based respiration recording and phase-based motion amplification (red trace) in head-fixed condition on the animal’s flank to capture body movements associated with respiration. Simultaneously, respiration was recorded with a flow sensor placed in front of one nostril (black trace). Odour stimulus highlighted with blue bar.

## Peer Review File

## Rights and permissions

### Reprints and Permissions

## About this article



## Cite this article

Ackels, T., Erskine, A., Dasgupta, D. *et al.* Fast odour dynamics are encoded in the olfactory system and guide behaviour. *Nature* **593**, 558–563 (2021). <https://doi.org/10.1038/s41586-021-03514-2>

### Download citation

- Received: 10 July 2020

- Accepted: 23 March 2021
- Published: 05 May 2021
- Issue Date: 27 May 2021
- DOI: <https://doi.org/10.1038/s41586-021-03514-2>

## Comments

By submitting a comment you agree to abide by our [Terms](#) and [Community Guidelines](#). If you find something abusive or that does not comply with our terms or guidelines please flag it as inappropriate.

[Access through your institution](#)

[Change institution](#)

[Buy or subscribe](#)

Advertisement

---

This article was downloaded by **calibre** from <https://www.nature.com/articles/s41586-021-03514-2>

| [Section menu](#) | [Main menu](#) |

The spatial landscape of lung pathology during COVID-19 progression

[Download PDF](#)

- Article
- [Published: 29 March 2021](#)

# The spatial landscape of lung pathology during COVID-19 progression

- [André F. Rendeiro](#) ORCID: [orcid.org/0000-0001-9362-5373](#)<sup>1,2 na1</sup>,
- [Hiranmayi Ravichandran](#)<sup>2,3,4 na1</sup>,
- [Yaron Bram](#)<sup>5</sup>,
- [Vasuretha Chandar](#)<sup>5</sup>,
- [Junbum Kim](#) ORCID: [orcid.org/0000-0001-7344-1593](#)<sup>1</sup>,
- [Cem Meydan](#) ORCID: [orcid.org/0000-0002-0663-6216](#)<sup>1,4</sup>,
- [Jiwoon Park](#) ORCID: [orcid.org/0000-0003-0045-1429](#)<sup>4</sup>,
- [Jonathan Fook](#)<sup>1,4</sup>,
- [Tyler Hether](#)<sup>6</sup>,
- [Sarah Warren](#)<sup>6</sup>,
- [Youngmi Kim](#)<sup>6</sup>,
- [Jason Reeves](#)<sup>6</sup>,
- [Steven Salvatore](#)<sup>7</sup>,
- [Christopher E. Mason](#) ORCID: [orcid.org/0000-0002-1850-1642](#)<sup>1,3,4,8</sup>,
- [Eric C. Swanson](#) ORCID: [orcid.org/0000-0001-8454-1207](#)<sup>9</sup>,
- [Alain C. Borczuk](#) <sup>7 na2</sup>,
- [Olivier Elemento](#) <sup>1,2,3,4 na2</sup> &
- [Robert E. Schwartz](#) ORCID: [orcid.org/0000-0002-5417-5995](#)<sup>4,5 na2</sup>

[Nature](#) volume 593, pages 564–569 (2021) [Cite this article](#)

- 34k Accesses
- 2 Citations
- 494 Altmetric
- [Metrics details](#)

## Subjects

- [Infection](#)
- [SARS-CoV-2](#)
- [Viral infection](#)

## Abstract

Recent studies have provided insights into the pathology of and immune response to COVID-19<sup>1,2,3,4,5,6,7,8</sup>. However, a thorough investigation of the interplay between infected cells and the immune system at sites of infection has been lacking. Here we use high-parameter imaging mass cytometry<sup>9</sup> that targets the expression of 36 proteins to investigate the cellular composition and spatial architecture of acute lung injury in humans (including injuries derived from SARS-CoV-2 infection) at single-cell resolution. These spatially resolved single-cell data unravel the disordered structure of the infected and injured lung, alongside the distribution of extensive immune infiltration. Neutrophil and macrophage infiltration are hallmarks of bacterial pneumonia and COVID-19, respectively. We provide evidence that SARS-CoV-2 infects predominantly alveolar epithelial cells and induces a localized hyperinflammatory cell state that is associated with lung damage. We leverage the temporal range of fatal outcomes of COVID-19 in relation to the onset of symptoms, which reveals increased macrophage extravasation and increased numbers of mesenchymal cells and fibroblasts concomitant with increased proximity between these cell types as the disease progresses—possibly as a result of attempts to repair the damaged lung tissue. Our data enable us to develop a biologically interpretable landscape of lung pathology from a structural, immunological and clinical standpoint. We use this landscape to characterize the pathophysiology of the human lung from its macroscopic presentation to the single-cell level, which provides an important basis for understanding COVID-19 and lung pathology in general.

[Download PDF](#)

## Main

SARS-CoV-2 is the coronavirus that causes COVID-19, which has become a global pandemic: as of February 2021, over 100 million people have been infected and there have been more than 2 million fatalities<sup>10,11</sup>. A growing body of evidence indicates that the severity of COVID-19 is driven by an inflammatory syndrome caused by hyperactivation of the immune system<sup>8,12</sup> in an attempt to clear the virus. Persistent inflammation can result in damage to lung tissue<sup>13</sup>, the exudation of pulmonary-oedema fluid that leads to dyspnoea, and acute respiratory distress syndrome

(ARDS)<sup>14,15</sup>. Immune profiling in peripheral blood<sup>1,2,3,5,7,16</sup> or bronchoalveolar lavage fluid<sup>17</sup> have revealed major changes in the immune system; excessive neutrophil activation<sup>18</sup>, lymphopenia<sup>3</sup> and aberrant responses of the adaptive immune system<sup>2</sup> are among the most prominent changes. However, thorough analysis of infected tissue and the immune system in a spatial context has only recently been started<sup>4,19,20,21</sup> and is currently lacking for most infected organs, including the lung. Although most patients with severe COVID-19 develop ARDS, administering routine clinical supportive care as for other ARDS does not entirely aid in patient recovery. The degree to which SARS-CoV-2 infection and the immune response to COVID-19 resemble or differ from other insults in the lung is therefore unclear. To elucidate the cellular composition, spatial context and interplay between immune and structural cell types during SARS-CoV-2 infection in the lung, we performed imaging mass cytometry (IMC) in post-mortem lung tissue from patients with COVID-19 or with other lung infections that cause ARDS, and in otherwise-healthy individuals.

## Pathophysiology of lungs in patients with COVID-19

We investigated a cohort of 23 patients that included individuals who died with ARDS after influenza ( $n = 2$ ) or bacterial infection ( $n = 4$ ), with acute bacterial pneumonia ( $n = 3$ ) or with COVID-19 respiratory distress syndrome ( $n = 10$ ), as well as individuals who died without lung disease ( $n = 4$ ) and from whom post-mortem lung tissue was available (Fig. 1a, Extended Data Fig. 1a,b, Supplementary Table 1). To better understand and capture anatomical manifestations of the progression of lung disease, we divided patients with COVID-19 into those with ‘early’ and ‘late’ disease, depending on whether death occurred before or after 30 days from the start of respiratory symptoms, respectively (Supplementary Table 1). To comprehensively investigate the cellular environment and spatial organization of the lung, we designed a metal-labelled antibody panel for IMC that was composed of 36 biomarkers, and used it to generate 237 highly multiplexed images at 1- $\mu\text{m}$  resolution: in total, we profiled 332 mm<sup>2</sup> of tissue and identified 664,006 single cells across all specimens. IMC leverages laser ablation based on inductively coupled plasma mass spectrometry of lanthanide-metal-tagged antibodies from tissues for the quantitative detection of epitope abundance in a spatially resolved manner (Fig. 1a, Supplementary Table 2). Our panel included phenotypic markers of endothelial, epithelial, mesenchymal and immune cells, functional markers (activation, inflammation and cell death), and an antibody specific to the spike (S) protein of SARS-CoV-2. We used the IMC data to quantify the histopathology of the lung under infection (Methods), as we observed that the post-mortem lungs showed a considerable increase in weight across all pathologies (Fig. 1b). Consistent with the gain of weight during infection, the lacunar space of infected lungs was significantly reduced from 41.1% in the healthy lung to median ranges of 28.72% and 15.3% in the lungs of individuals with influenza and late

COVID-19, respectively (Fig. 1c, e); the most pronounced change was seen in the alveolar epithelium (Extended Data Fig. 1c, d). As collagen deposition is a known mediator of both normal and dysregulated tissue repair during recovery from infection<sup>22</sup>, we quantified the extent and intensity of collagen deposition into a fibrosis score that was inspired by the Ashcroft score<sup>23</sup> (Methods). The fibrosis score was significantly higher for lung pathologies than for the healthy lung, especially for the two COVID-19 groups (Fig. 1d, f, Extended Data Fig. 1e–g). We constructed a spatially resolved single-cell atlas to understand the cellular composition of the lung during various insults (Methods). We projected the 664,006 single cells from all disease groups into a two-dimensional space (Fig. 1g, Extended Data Fig. 1h) and clustered them on the basis of their phenotype (Fig. 1h, Extended Data Fig. 2a), which resulted in a single-cell phenotypic atlas for the human lung. We identified 36 clusters, which we organized into 17 metaclusters on the basis of predominant markers, overall phenotypes and proximity to lung structures (Fig. 1h, Extended Data Fig. 2a). This atlas was dominated by abundant structural cell types, including KRT8<sup>+</sup>KRT18<sup>+</sup> alveolar epithelial cells,  $\alpha$ -smooth muscle actin<sup>+</sup> ( $\alpha$ SMA) cells that line the vasculature and immune cells such as CD15<sup>+</sup>CD11b<sup>+</sup> polymorphonuclear neutrophils and CD68<sup>+</sup> macrophages (Extended Data Fig. 2c). Although the broad compartments of lung structural cells and immune cells did not show large changes in absolute numbers between the patient groups, the specific internal composition of the structural cells of the lung and the immune system differed extensively (Extended Data Fig. 2d). We observed increased immune infiltration in the lungs of patients with COVID-19 as compared to the healthy lung, but to a degree that was comparable with other lung infections (Extended Data Fig. 2d). Within the specific immune components, we observed a prominent increase in infiltration of myeloid cells in the lungs of patients with COVID-19 (as compared with the healthy lung), but to a lesser extent than was seen in the lungs of patients with bacterial pneumonia (Fig. 1i, Extended Data Fig. 3a, b). We performed a more detailed examination of the phenotypic diversity of myeloid cells in respect to their location in the lung (Extended Data Fig. 3c–e), which revealed that CD14<sup>+</sup>CD16<sup>+</sup>CD206<sup>+</sup>CD163<sup>+</sup>CD123<sup>+</sup> interstitial macrophages—which were probably recruited from peripheral blood—displayed the greatest increase in the lungs of patients with COVID-19 (particularly in the late COVID-19 group) as compared with the healthy lung (Fig. 1j), and the highest expression of IL-1 $\beta$  in monocytes in the lungs of patients in the early COVID-19 group (Extended Data Fig. 3d). Although neutrophil levels are similar between the lungs of patients in the early COVID-19 group and healthy lungs, they are present in significantly lower absolute numbers in late COVID-19 (Fig. 1j, Extended Data Fig. 3a, b); this is in stark contrast to the lungs of individuals with bacterial pneumonia, which contain the highest numbers of neutrophils across all disease groups. Populations of macrophages were particularly increased in the lungs of patients with COVID-19, as compared to all other disease states (Fig. 1j, Extended Data Fig. 3a, b). We also observed that CD8<sup>+</sup> T cells were significantly increased in lungs of individuals with ARDS not associated with

COVID-19, but depleted in bacterial pneumonia, in comparison with the healthy lung (Extended Data Fig. 3a, b). To further functionally characterize the immune system in healthy lungs and the lungs of individuals with COVID-19, we performed IMC with an immune panel of 39 markers on a subset of samples (2 healthy lungs and 4 lungs from patients with COVID-19) (Extended Data Fig. 4). In comparison with healthy lungs, we observed increased levels of the alarmin calprotectin (S100A9) across several cell types in the lungs of individuals with COVID-19—most prominently, in macrophages and neutrophils, but also in alveolar epithelial cells (Extended Data Fig. 4d–f). Alveolar epithelial cells also expressed increased levels of HLA-DR in COVID-19. Beyond the immune compartment, we observed a shift in the stromal compartment of the lung in COVID-19, with a significant reduction in absolute numbers of endothelial cells and an increase in mesenchymal cells and fibroblasts in lungs of patients in the late COVID-19 group (Fig. 1k, Extended Data Fig. 3a, b). The increase in fibroblast abundance with COVID-19 is consistent with the increased fibrosis score that we observed in the lungs of patients with COVID-19 (Fig. 1d, Extended Data Fig. 5a). To orthogonally validate our findings, we performed immunohistochemical staining of lung tissue from the same donors for two markers and found excellent agreement between the relative frequency of cells that were positive for the markers in IMC and immunohistochemistry (Fig. 1l, Extended Data Fig. 5b–h), as well in the ability to estimate the size of the lacunar space of lungs in the various disease states (Extended Data Fig. 5i–k). We also observed good agreement between the changes in cell-type composition between disease groups using targeted spatial transcriptomics<sup>24</sup>, both for matched samples in the same cohort (Fig. 1m, Extended Data Fig. 6a–d) and samples in an independent study<sup>25</sup> (Fig. 1m, Extended Data Fig. 6e–h).

**Fig. 1: Structural and immunological disorder of lung infection.**

---

 **figure1**

---

**a**, Composition of lung-infection cohort, and schematic procedure to acquire highly multiplexed spatially resolved data with IMC from post-mortem lung samples. **b**, Total lung weight per disease group measured at autopsy.  $n = 16$  biologically independent samples. **c**, Lacunar space for each acquired IMC image as a percentage of image area. **d**, Fibrosis score for each acquired IMC image. **e**, Representative images illustrating the lacunar and parenchymal structure of healthy lungs, and lungs from patients with ARDS or COVID-19. **f**, Collagen in images from healthy lungs and lungs from patients with ARDS or COVID-19 and the associated fibrosis score. Images with lowest and highest fibrosis scores are depicted. **g**, Uniform manifold approximation and projection (UMAP) of all cells, and the metacluster of each cell. Centroids are shown as squares. **h**, Mean intensity of each marker in each metacluster. Histogram indicates metacluster abundance. Heat maps on left indicate relative proximity to lung structures or abundance per disease group. AT2, alveolar type 2 cells; KRT8/8, KRT8 and KRT18; NK, natural killer. **i**, Spatial distribution of immune cells in healthy lungs and lungs from a patient with COVID-19. **j**, Left, abundance of neutrophils (top) and macrophages (bottom) in each disease group. Right, macrophages divided into alveolar (top) and interstitial (bottom) subsets. **k**, Abundance of mesenchymal cells (left) and fibroblasts (right) in each disease group. **l**, Amount of change (effect size) pairwise between all disease groups ( $n = 15$ ) in MPO (left) and CD163 (right) markers between IMC ( $x$  axis) and immunohistochemistry (IHC) ( $y$  axis). **m**, Amount of

change between late and early COVID-19 groups, pairwise for each cell type ( $n = 24$ ), as estimated by IMC ( $x$  axis) and targeted spatial transcriptomics ( $y$  axis) for the same (left) and independent (right) cohorts. For **c**, **d**, **j**, **l**, **m**, **n**,  $n = 237$  images from 27 biologically independent samples. \*\* $P < 0.01$ ; \* $P < 0.05$ , two-sided Mann–Whitney  $U$  test, pairwise between groups, Benjamini–Hochberg false-discovery rate (FDR) adjustment. In **o**, **p**,  $r$ , Pearson correlation coefficient;  $P$ , two-sided  $P$  value; shade indicates 95th confidence interval. Scale bars, 100  $\mu\text{m}$  (**e**, **f**, **k**). Box plots show interquartile range (25th to 75th percentiles) with centre line as the median (50th percentile).

[Full size image](#)

## Tissue damage by widespread inflammation

Our phenotypic single-cell atlas of the lung contains clusters that are defined by cell-identity markers and markers of cell state across all of the diseases that we evaluated. We developed an unsupervised classification of cells according to the abundance of each marker as a complementary approach (Extended Data Fig. [7a](#)), and observed a high concordance with the phenotypic clusters (Extended Data Fig. [7b](#)). Using this approach, we observed a high specificity of our SARS-CoV-2 S antibody to tissue samples from patients with COVID-19 (Fig. [2a](#), Extended Data Fig. [7c](#)). Among all cell types, alveolar epithelial cells displayed the highest rate of SARS-CoV-2 S positivity (Fig. [2b](#)). These alveolar epithelial cells were also highly positive for the phosphorylated signal transducer and activator of transcription 3 (pSTAT3), the receptor tyrosine kinase and proto-oncogene KIT and contained increased levels of interleukin 6 (IL-6), arginase 1, the apoptosis marker cleaved caspase 3 (CASP3) and the assembled complement membrane attack complex C5b–C9 (Fig. [2c](#), [d](#)). Given that S<sup>−</sup> alveolar epithelial cells in the same regions showed no increase in the levels of functional markers, this probably indicates viral-specific alterations of the cellular state. Increased IL-6 and pSTAT3 levels were also seen in the lungs of individuals with influenza and pneumonia as compared with healthy lung, but were not seen in ARDS that was not associated with COVID-19 (Extended Data Fig. [7d](#)). However, high levels of cleaved CASP3 and C5b–C9 were exclusive to S<sup>+</sup> alveolar epithelial cells from individuals with COVID-19, and indicate the initiation of apoptosis and complement-mediated host immune defence, respectively, which led to increased damage to the alveolar lining. Although the alveolar epithelium was the predominant cell type that was positive for S, we also found that a mean of 7.8% and 2.7% of macrophages and neutrophils, respectively, were positive for S across all images of lungs of patients with COVID-19; some regions were up to 38.6% and 43.6% S<sup>+</sup>, respectively (Extended Data Fig. [7e](#), [f](#)). Consistent with our observations in S<sup>+</sup> epithelial cells, both macrophages and neutrophils exhibited higher levels of cleaved CASP3, pSTAT3 and IL-6 but—unlike the alveolar epithelial cells—these cells

showed no positive staining for C5b–C9 (Extended Data Fig. [7g–j](#)). However, KIT was specifically upregulated in macrophages and not in neutrophils (Extended Data Fig. [7g, h](#)). This non-epithelial cell marker profile phenotype seen in S<sup>+</sup> cells was also seen in other cell types, albeit at a much lower frequency (Extended Data Fig. [7k](#)). We also observed high heterogeneity in the localization of S<sup>+</sup> cells, often within the same 1-mm<sup>2</sup> tissue region (Fig. [2e](#)). Although we observed interactions between S<sup>+</sup> epithelial cells and immune and nonimmune cells (Fig. [2e](#) top right), other S<sup>+</sup> cells did not interact with these cells at all or seemed to be encapsulated in structures that precluded interactions with other cell types (Fig. [2e](#) bottom right). To generate a quantitative map of cellular interactions, we quantified proximal interactions between and within cell types for each image and generated disease-specific interaction maps (Extended Data Fig. [8a–c](#), Methods). Comparing interactions between the healthy lung and lungs from patients with COVID-19, we observed increased interactions between neutrophils and macrophages and decreased interactions within macrophages; in late COVID-19, the intra-cell-type interactions in macrophages, fibroblasts and CD4<sup>+</sup> T cells decreased further, and were accompanied by an increase in interactions between macrophages and fibroblasts or dendritic cells (Fig. [2f, g](#)). When spatially contextualizing these interactions, we observed that macrophages preferentially interacted with fibroblasts in the alveolar walls, which suggests a contribution to fibrosis and the thickening of the alveolar wall in late COVID-19 (Fig. [2h](#)). As epithelial cells as a whole did not show any particular change in interactions in the lungs of patients with COVID-19 as compared with healthy lung, we investigated whether S<sup>+</sup> epithelial cells differed in cellular interactions to their S<sup>-</sup> counterparts in the lungs of patients with COVID-19 (Extended Data Fig. [8d–i](#)). Across all cell types, there was a trend for S<sup>+</sup> cells to have reduced cellular interactions (Extended Data Fig. [8d–f](#)). S<sup>+</sup> alveolar epithelial cells in particular lacked interactions with other cell types, as compared with S<sup>-</sup> cells (Extended Data Fig. [8g–i](#)). We observed progressively more cells with markers of cell death (particularly macrophages and neutrophils with cleaved CASP3) (Fig. [2i](#)), whereas epithelial and endothelial cells preferentially had C5b–C9 (Fig. [2j, k](#))—which probably indicates alveolar damage. Using spatial transcriptomics data, we observed that pathways of inflammatory response (such as interferon and interleukin signalling) were increased in the lungs of patients with COVID-19 as compared with healthy lung—particularly in the alveolar and airway compartments in early COVID-19 (Extended Data Fig. [9a–e](#)). However, pathways related to angiogenesis, myogenesis and the epithelial-to-mesenchymal transition were increased in the lungs of individuals with COVID-19 as compared with healthy lungs, which increased progressively in late COVID-19 (Extended Data Fig. [9b](#)). In accordance with the IMC data, we also observed that coagulation, complement activation and apoptosis pathways were upregulated in alveolar areas and in blood vessels in late COVID-19 (Extended Data Fig. [9c](#)). This suggests that, after an early period of disease that is dominated by inflammatory responses to SARS-CoV-2, late

COVID-19 in the lung may be driven by pathogen-independent mechanisms that are a consequence of an immune response with an aberrant resolution.

**Fig. 2: Cellular tropism of SARS-CoV-2 infection.**

 figure2



**a**, Absolute abundance of S<sup>+</sup> cells for lungs of patients without COVID-19 (grey) or with COVID-19 (red). **b**, Distribution of S<sup>+</sup> cells across metaclusters in COVID-19. Inset displays intensity of KRT8/18 and S<sup>+</sup> for single cells from non-COVID-19 (left) and COVID-19 (right) groups. **c**, Phenotype of alveolar epithelial cells in COVID-19, depending on levels of S. **d**, Intensity of differential markers between cells dependent on S levels. **e**, Distribution of S signal in a spatial context. Structural, cell-type-specific and functional markers are displayed alone or in combination. For the green channel in the images in the rightmost column, the S channel was multiplied with KRT8/18 or CD68 to highlight T cells that are positive for both markers. Scale bar, 200 μm (main panels), 50 μm (magnified images on right (unless otherwise indicated)). **f, g**, Differential interactions in healthy lung and lungs of patients with COVID-19 (**f**) or between early and late COVID-19 (**g**). **h**, Fibroblasts and macrophages from early and late COVID-19. Scale bars, 200 μm. **i, j**, Proportion of

cleaved CASP3<sup>+</sup> macrophages (left) or neutrophils (right) (**i**), and C5b–C9<sup>+</sup> epithelial (left) or endothelial (right) cells (**j**), for each disease group. **k**, Deposition of C5b–C9 in epithelial cells in healthy lung and lungs from patients with COVID-19. Scale bars, 100 µm. In **a**, **i**, **j**,  $n = 237$  images from 27 biologically independent samples; \*\* $P < 0.01$ ; \* $P < 0.05$ , two-sided Mann–Whitney  $U$  test, pairwise between groups, Benjamini–Hochberg FDR adjustment. In **f**, **g**,  $P$  values are from two-sided Mann–Whitney  $U$  test with Benjamini–Hochberg FDR adjustment. Box plots show interquartile range (25th–75th percentiles); centre line is median (50th percentile).

[Full size image](#)

## An interpretable landscape of lung pathology

Building on the cell types we identified, their functional status and their interactions, we sought to define a landscape of lung pathology from the data to form an unbiased view of the multicellular architecture of lung tissue during infection (Fig. 3a, Extended Data Fig. 9f–j, Methods; available at <http://covid-imc.eipm-research.org/>). The major axes of this landscape, which is based on a principal component analysis, demonstrate the distribution of samples and the major drivers of the establishment of the landscape. This confers biological interpretability to the landscape, as the underlying cellular composition at each given point is readily identifiable. Although the landscape was determined in an unsupervised manner (without knowledge of sample groups), it largely recapitulates the disease ontogeny of the samples: it is dominated by the difference between samples of healthy lung and lungs of patients with COVID-19 who succumbed after prolonged disease (Fig. 3a). This is exemplified by the abundance of immune cell types such as macrophages or neutrophils (which are most abundant in the lungs of patients with COVID-19 or pneumonia, respectively), but also by collagen deposition in lungs from patients with COVID-19 (Fig. 3b). We largely recapitulated the structure of this landscape when using complementary methods (Extended Data Fig. 9h–j). To add a layer of clinical interpretability to the landscape, we performed an association analysis between its axes and known demographic, clinical and pathological factors of patients with lung infections (Fig. 3c, Extended Data Fig. 10a–d, Methods). We observed strong associations primarily between clinical factors and the first principal component (Extended Data Fig. 10a): specifically, a significant positive association between the distribution of samples in the first principal component axis with the presence of alveolar type 2 cells with fibroblasts, organizing pneumonia, the number of days that elapsed since beginning of symptoms, hospitalization and intubation, and lung weight at death (Fig. 3c, Extended Data Fig. 10a). We also observed a significant association between a reduction in white blood cell counts and the major axis associated with disease progression (principal component 1) (Fig. 3c, Extended Data Fig. 10a). The values of clinical factors overlaid with their respective images in the landscape confer a convenient way of interpreting

the associations, effectively rendering a landscape annotated with clinical information both biologically (Fig. 3a) and clinically interpretable (Fig. 3d, Extended Data Fig. 10e). To develop the clinical interpretation of the landscape, we further related the associated clinical, demographic and pathological variables by how similar they are in explaining the IMC data (Fig. 3e, Extended Data Fig. 10b). We found that variables were organized into three large blocks: (1) high C-reactive protein and white blood cell count at presentation, as well as pathology characterized by acute inflammation of the alveolar wall; (2) high values of IL-6, erythrocyte sedimentation rate and D-dimer at presentation, comorbidities such as obesity and hypertension, lung pathology characterized by microthrombi and chronic alveolar inflammation with macrophages, and haemorrhagic stroke as the cause of death; and (3) prolonged disease and associated interventions such as intubation and treatment, with pathology characterized by squamous hyperplasia, large thrombi, organizing pneumonia and alveolar type-2 cells associated with fibroblasts. These groups probably represent a progressive range of pathology that is associated with extremely acute disease that results in early death (1) to a chronic manifestation of prolonged disease (3). Beyond these dominant clusters, we found that demographic and behavioural variables (such as age, gender or smoking) did not strongly associate with the larger groups, which suggests they have little influence in the pathology of lethal disease associated with SARS-CoV-2 lung infection. The similarity between variables in the IMC data differs considerably from that obtained from simple co-occurrence of the variables (Extended Data Fig. 10c,d), which provides evidence for the added value of high-content multiplexed imaging of lung tissue in infectious disease.

**Fig. 3: A data-driven and clinically annotated landscape of lung pathology.**

---

 **figure3**

---

**a**, Principal component analysis (PCA) of all IMC images. Points represent images, and are coloured by disease group. Arrows are vectors for each cell cluster, and indicate the area in which each cell type is most abundant. **b**, Microanatomy and immune content of the disease groups. Scale bar, 100  $\mu\text{m}$ . **c**, Volcano plot showing strength of association between clinical parameters and principal component (PC)1, and significance. WBC, white blood cell. **d**, Projections of white blood cell count (measured at admission) (top left), days of disease (top right), lung weight (bottom left) and alveolar type-2 cells with fibroblasts (bottom right) onto the two-dimensional PCA space. **e**, Similarity of landscape of IMC data. Pairwise correlation of demographic, clinical and pathological variables in the association with the principal components. Matrix rows and columns are the same. Highlighted groups of variables reflect hierarchically clustered groups of variables explaining the IMC data. In **c–e**, an asterisk indicates that the clinical parameter was measured at admission.

[Full size image](#)

## Discussion

Our spatially resolved single-cell analyses of post-mortem lung tissue from patients with COVID-19 or other lung infections provides a comprehensive examination of the

response of the human lung to infection, from the macroscopic to the single-cell level. Across all diseases, we observed a significant reduction in alveolar lacunar space, increased immune infiltration and cell death by apoptosis, as compared with healthy lungs. We also noted that neutrophil infiltration—although it is increased in the lungs of patients with ARDS or early COVID-19 compared with normal lung—is a hallmark of bacterial pneumonia, and that a high degree of inflammation, infiltration of interstitial macrophages, complement activation and fibrosis is particular to the lungs of individuals with late COVID-19. Our analysis agrees with recent reports that indicate that the type of pathophysiological response to SARS-CoV-2 infection may not be entirely different from ARDS that is unrelated to COVID-19<sup>14</sup>, but contradicts reports that suggest that the hyperinflammatory phenotype (as assessed by cytokine levels in peripheral blood) is not specific to COVID-19<sup>15</sup>. Our observation that S<sup>+</sup> alveolar epithelial cells do not differentially interact with cells of the immune system (despite extensive immune infiltration in the lung) potentially highlights the lack of an ‘on-target’ immunological response, and the high amount of complement activation in lung tissue from patients with COVID-19 probably results in indiscriminate ‘off-target’ tissue damage—exacerbating COVID-19 and continuing the cycle of inflammation. The increased presence of IL-1 $\beta$ <sup>+</sup> monocytes in the lungs of patients with early COVID-19 suggests a mechanism for neutrophil recruitment to the lung. Neutrophil recruitment was highest in the lungs of patients with bacterial pneumonia (the only group that we studied with an active disease of bacterial pathogen origin). The differential pathogen recognition between viral and bacterial infection in the lung could explain the differences in chemokine secretion in the ensuing immune response. However, despite sharing a viral pathogenic origin with influenza, COVID-19 (specifically the expansion of mesenchymal cells and fibroblasts, particularly in late COVID-19) probably reflects a response to the extensive tissue damage from complement activation. Despite this, the high mortality rate of COVID-19 is at odds with productive recovery from tissue damage and healing, which suggests the need for further investigation into complement-activation-induced damage to the lung, additional immunological factors (such as neutrophil extracellular traps) and microthrombi formation<sup>19</sup>. This raises the possibility that early immunological interventions that suppress excessive complement activation could have a therapeutic benefit. Our biologically interpretable and clinically annotated landscape of lung pathology provides a framework for a data-driven, spatially aware understanding of lung pathology, and will be an important resource for the study of COVID-19 and other lung infections.

## Methods

### Data reporting

No statistical methods were used to predetermine sample size. Image acquisition, segmentation, quantification and clustering were blinded to patient identifiers and clinical metadata.

## **Human studies**

Tissue samples were provided by the Weill Cornell Medicine Department of Pathology. The Tissue Procurement Facility operates under Institutional Review Board (IRB) approved protocol and follows guidelines set by Health Insurance Portability and Accountability Act. Experiments using samples from human subjects were conducted in accordance with local regulations and with the approval of the IRB at the Weill Cornell Medicine. The autopsy samples were collected under protocol 20-04021814. Autopsy consent was obtained from the families of the patients.

## **Tissue section preparation**

Lung tissues were fixed via 10% neutral buffered formalin inflation, sectioned and fixed for 24 h before processing and embedding into paraffin blocks. Freshly cut 5- $\mu\text{m}$  sections were mounted onto charged slides.

## **Antibody panel design and validation**

We designed an antibody panel to capture different immune and stromal compartments of the lung. Antibody clones were extensively validated through immunofluorescence and chromogenic staining and verified by a pathologist. Once the clone was approved, 100  $\mu\text{g}$  of purified antibody in BSA and azide free format was procured and conjugated using the MaxPar X8 multimetal labelling kit (Fluidigm) as per the manufacturer's protocol. To confirm the antibody binding specificity after conjugation and to identify the optimal dilution for each custom conjugated antibody, sections from healthy lung, and bacterial pneumonia, non-COVID-19 ARDS and SARS-CoV-2-infected lung were stained. These sections were then imaged on Fluidigm Hyperion Imaging System and visualized using MCD Viewer for an expected staining pattern and optimal dilution that presented with good signal-to-noise ratio for each channel. For channels with visible spillover into the neighbouring channels, a higher dilution factor was adopted when staining the cohort tissues.

## **IMC**

On the basis of the clinical and pathological characteristics and quality of the preserved tissues, suitable representative fresh cut 4- $\mu\text{m}$ -thick FFPE sections were acquired from the Department of Pathology of Weill Cornell Medicine for IMC staining. The tissues were stored at 4 °C for a day before staining. Slides were first

incubated for 1 h at 60 °C on a slide warmer followed by dewaxing in fresh CitriSolv (Decon Labs) twice for 10 min, rehydrated in descending series of 100%, 95%, 80% and 75% ethanol for 5 min each. After 5 min of MilliQ water wash, the slides were treated with antigen retrieval solution (Tris-EDTA pH 9.2) for 30 min at 96 °C. Slides were cooled to room temperature, washed twice in TBS and blocked for 1.5 h in SuperBlock Solution (ThermoFischer), followed by overnight incubation at 4 °C with the prepared antibody cocktail containing all 36 metal-labelled antibodies (Supplementary Table 2). The next day, slides were washed twice in 0.2% Triton X-100 in PBS and twice in TBS. DNA staining was performed using Intercalator-Iridium in PBS solution for 30 min in a humid chamber at room temperature. Slides were washed with MilliQ water and air-dried before ablation.

The instrument was calibrated using a tuning slide to optimize the sensitivity of the detection range. Haematoxylin and eosin-stained slides were used to guide the selection of regions of interest (ROIs) containing alveolar parenchyma, airways and thrombotic vessels to obtain regions that were representative of the whole range of lung pathology. All ablations were performed with a laser frequency of 200 Hz. Tuning was performed intermittently to ensure the signal detection integrity was within the detectable range. A total of 240 image stacks were ablated. The raw MCD files were exported for further downstream processing.

## IHC

Automated IHC on a Leica Bond III instrument was performed on 5-μm tissue sections using antibodies for myeloperoxidase (clone 59A5, Leica ready to use antibody, without antigen retrieval) and CD163 (clone MRQ-26, Leica ready to use antibody, antigen retrieval 20 min, high pH) using 3,3' diaminobenzidine chromogen. For each slide, a grid (5 × 5 grid, 0.4-cm × 0.4-cm boxes) was placed on the section and 5 alveolar, 2 vascular and 2 airway regions were randomly selected using random number-generated  $x,y$  coordinates and that ROI (using a 20× objective) was photographed.

## Targeted spatial transcriptomics using GeoMx

In brief, selected cases of lung injury associated with COVID-19 (4 patients with early COVID-19 and 4 patients with late COVID-19), bacterial pneumonia (2) and healthy lung (3) from the IMC cohort were evaluated using the GeoMx<sup>24</sup> COVID-19 Immune Response Atlas with approximately 1,850 RNA targets. Spatial transcriptomics analysis included up to 24 ROIs per tissue. Alveolar, airway and vascular compartments were analysed.

For GeoMx DSP slide preparation, we followed the GeoMx DSP slide preparation user manual (MAN-10087-04). In brief, tissue slides were baked in a drying oven at 60 °C for 1 h and then loaded to Leica Biosystems BOND RX FFPE for deparaffinization and rehydration. After the target retrieval step, tissues were treated with proteinase K solution to expose RNA targets followed by fixation with 10% NBF. After all tissue pretreatments were done, tissue slides were unloaded from the Leica Biosystems BOND RX and incubated overnight with RNA probe mix (COVID-19 Immune Response Atlas; a pool of *in situ* hybridization probes with UV photocleavable oligonucleotide barcodes). The next day, tissues were washed and stained with tissue visualization markers: CD68-647 at 1:400 (Novus Bio, NBP2-34736AF647), CD45-594 at 1:10 (NanoString Technologies), panCK-532 at 1:20 (NanoString Technologies) and/or SYTO 13 at 1:10 (Thermo Scientific S7575).

For GeoMx DSP sample collections, we followed the GeoMx DSP instrument user manual (MAN-10088-03). In brief, tissue slides were loaded on the GeoMx DSP instrument and then scanned to visualize whole-tissue images. For each tissue sample, a board-certified pathologist selected 24 total ROIs from 3 types of functional tissue: vascular zone, large airway and alveoli zone. Each ROI was subdivided into compartments on the basis of fluorescent cell-specific markers, and serial UV illumination of each compartment was used to sequentially collect the probe barcodes from the different cell types.

Each GeoMx DSP sample plus nontemplate controls (NTCs) was uniquely indexed using the i5 × i7 dual-indexing system of Illumina. Four µl of a GeoMx DSP sample was used in a PCR reaction with 1 µM of i5 primer, 1 µM i7 primer and 1× NSTG PCR Master Mix. Thermocycler conditions were 37 °C for 30 min, 50 °C for 10 min, 95 °C for 3 min, 18 cycles of 95 °C for 15 s, 65 °C for 60 s, 68 °C for 30 s, and final extension of 68 °C for 5 min. PCR reactions were purified with two rounds of AMPure XP beads (Beckman Coulter) at 1.2× bead-to-sample ratio. Libraries were paired-end sequenced (2 × 75) on a NextSeq550 generating up to 400 million aligned reads in total.

Processing and filtering of the raw next-generation sequencing data was performed on the DNA sample libraries that were sequenced, producing about 1.3 billion reads. NextSeq-derived FASTQ files for each sample were compiled for each compartment using the bcl2fastq program of Illumina, and then demultiplexed and converted to digital count conversion (DCC) files using the GeoMx DnD pipeline (v.1) of Nanostring. These DCC files were then converted to an expression count matrix using a custom Python script. A minimum of 10,000 reads were required for each non-NTC sample (2 compartments removed). Probes were checked for outlier status by implementing a global Grubb's outlier test with alpha set to 0.01. The counts for all remaining probes for a given target were then collapsed into a single metric by taking the geometric mean of probe counts. A count of 1 was added to any probe that yielded

0 counts before the geometric mean was taken. For each sample, an RNA-probe-pool-specific negative probe normalization factor was generated on the basis of the geometric mean of negative probes in each pool. To ensure good data quality, we calculated the 75th percentile of the gene counts (that is, geometric mean across all non-outlier probes for a given gene) for each ROI, and normalized to the geometric mean of the 75th percentile across all ROIs to give the upper quartile (Q3) normalization factors for each ROI. The distribution of these Q3 normalization factors were then checked for outliers defined as any ROI greater than two s.d. from the mean log<sub>2</sub>-transformed Q3 normalization factor. This criterion removed 15 ROIs that fell below the range and 1 ROI that fell above the range.

## Preprocessing IMC data

IMC data were preprocessed as previously described<sup>26</sup> with some modifications. In brief, image data were extracted from MCD files acquired with the Fluidigm Hyperion instrument. Hot pixels were removed using a fixed threshold, the image was amplified two times, Gaussian smoothing was applied and, from each image, a square 500-pixel crop was saved as a HDF5 file for image segmentation. Segmentation of cells in the image was performed with ilastik<sup>27</sup> (version 1.3.3) by manually labelling pixels as belonging to one of three classes: nuclei (the area marked by signal in the DNA and histone H3 channels), cytoplasm (the area immediately surrounding the nuclei and overlapping with signal in cytoplasmic channels) and background (pixels with low signal across all channels). Ilastik uses the labelled pixels to train a random forest classifier using features derived from the image and its derivatives. Features used were the Laplacian of the Gaussian, Gaussian gradient magnitude, difference of Gaussians, structure tensor eigenvalues and the Hessian of Gaussian eigenvalues, each of which had Gaussian kernels of widths from 0.3 to 10 (37 features in total). The outputs of prediction are class probabilities for each pixel, which were used to segment the image using CellProfiler<sup>28</sup> (version 3.1.8) with the IdentifyPrimaryObjects module. This was followed by the IdentifySecondaryObjects module, in which the identified nuclei are used to seed an expansion of the cell area to the area with the sum of the nuclear and cytoplasmatic probability map, and finally gaps in the identified cells are filled.

We assessed the quality of each acquired channel by computing a set of metrics for each channel across all images: the mean and squared coefficient of variation of each channel in the whole image and, in the area with cells, a difference between those values in the cells and the whole image (foreground versus background signal), an estimate of noise variance<sup>29</sup>, a robust wavelet-based estimator of Gaussian noise s.d.<sup>29,30</sup>, the fractal dimension (Minkowski–Bouligand approximation using the box counting method) and lacunarity of the image<sup>31</sup>. Across all 240 ablated images three were discarded based on these metrics and visual inspection.

## Computing lacunarity and fibrosis score

To identify lacunae in the images, we used the mean of all channels in each image stack after performing histogram equalization per channel (`skimage.exposure.equalize_hist`). Images were thresholded with Otsu's method (`skimage.filters.threshold_otsu`), successively dilated and closed (`ski.morphology.binary_dilation/ski.morphology.closing`) with a disk of 5- $\mu\text{m}$  diameter to remove objects without holes and—for the objects with holes—objects within the hole were removed on the negative image (`scipy.ndimage.binary_fill_holes`) and only objects with area larger than 625 pixels ( $25^2$ ) were kept (`skimage.morphology.remove_small_objects`). To provide biological context for the single-cell clusters we identified, we further classified each of the lacuna of healthy lungs into one of three classes: blood vessels (arteries and veins), airways and alveoli. Vessels showed a very thin lining of endothelial cells, followed by a thick layer of smooth muscle cells that are  $\alpha$ -SMA $^+$ ; the airway epithelium is lined by KRT8 $^+$ KRT18 $^+$  cells; and alveoli are covered in alveolar epithelial cells that have various degrees of CD31, vimentin, KRT8 and KRT18. On the basis of this, we developed a semisupervised strategy for lacuna classification that had two stages: first each of the lacuna objects was dilated by a 15-pixel disk and the mean intensity of the channels above was quantified only in the dilated area, and these values were Z-score-transformed per image. We used these values in three ways, in which each provided a vote towards a lacuna being one of the three classes: absolute intensity, Z-score-transformed intensity, ratio of  $\alpha$ -SMA to KRT8 and KRT18. For each, a set of rules was enforced in which lacunae with higher values in  $\alpha$ -SMA and low in KRT8 and KRT18 were labelled as vessels, and those with higher KRT8 and KRT18 were labelled as airways; the remaining lacunae were labelled as alveoli. Essentially, absolute and relative intensity of the markers determine the class, and the ratio of the two is the tiebreaker in case of disagreement. In a second phase, the suggested labels were reviewed by an expert and overruled if needed. In general, we found that the rules above were accurate with only a systematic bias to underclassify vessels (hence the need for supervision).

To develop a score for fibrosis, we were inspired by the Ashcroft score<sup>23</sup> in which the fraction of fibrotic tissue that occupies each image is translated into a score in a Likert scale. We quantified the fraction of the image occupied by collagen type I as thresholded by the Otsu method (`skimage.filters.threshold_otsu`), but in addition quantified the density of collagen per area unit by using the spectral counts given by the IMC data. The final score is the mean of a Z-score of the fraction covered by collagen and a Z-score of its intensity.

## Cell-type identification

To identify cell types in an unsupervised fashion, we first quantified the intensity of each channel in each segmented cell that did not overlap image borders. In addition, for each cell we computed the morphological features ‘area’, ‘perimeter’, ‘major\_axis\_length’, ‘eccentricity’ and ‘solidity’ (`skimage.measure.regionprops_table`). Values were Z-scored per image and cells with area values above  $-1.5$ , solidity above  $-1$  and eccentricity below  $1$  were kept. In addition, we calculated the sum of  $\log(1 + x)$  signals in the IMC channels and kept cells with values between  $2$  and  $7$ . We used Scanpy<sup>[32](#)</sup> (version 1.6.0) to perform a PCA, compute a neighbour graph on the PCA latent space, compute a UMAP<sup>[10](#)</sup> embedding (`umap` package, version 0.4.6) and cluster the cells with the Leiden algorithm<sup>[33](#)</sup> with resolution  $1.0$  (`leidenalg` package, version 0.8.1). Each cluster was manually labelled with a broad ontogeny and the channels that were most abundant in each cluster. These broad labels formed the basis of the metaclusters used to aggregate clusters on the basis of cell type and regardless of cellular state. Clusters without enrichment for any particular marker were not aggregated.

To obtain an easy way to quantify the fraction of cells positive for a given marker, we used univariate Gaussian mixture models using scikit-learn<sup>[34](#)</sup> (version 0.23.0). For each channel, we performed model selection with models with two to six mixtures, selected the model on the basis of the Davies–Bouldin index<sup>[35](#)</sup> and labelled a cell as positive for a given channel if its value was in the top mixture (in cases in which the selected model had only two mixtures) or the top two mixtures (if the selected model had more).

The analysis of the immune-centric IMC panel was performed in the same manner as the larger dataset, with the exception that the thresholds for cell filtering based on area, DNA intercalator intensity and solidity were performed automatically with Gaussian mixture models as described in the previous paragraph. Differential marker abundance was tested with a two-sided Wald test between healthy lung samples and samples from patients with COVID-19, and adjusted for multiple comparisons with the Benjamini–Hochberg FDR.

## Quantification of cellular interactions

To quantify the degree and importance of intra- and inter-cell-type interactions, we started by constructing a region adjacency graph representing the interactions between cells, in which the edges are weighted by the Euclidean distances between cells, using scikit-image<sup>[36](#)</sup> (version 0.17.2). A pairwise adjacency matrix between cell clusters was computed using networkx<sup>[37](#)</sup> (version 2.5). To get a degree of confidence on cellular interactions given the cell type abundance in each image, we permuted the cell cluster assignments 1,000 times and computed the difference between the log-normalized frequency of cell-type interactions in the real data versus the permuted (interaction

scores). For visualization, we generated chord plots by aggregating the interaction scores of the images from each disease group or subgroups by the fraction of images with an interaction score was higher than 1. To discover differential interactions specific to a subgroup, we tested whether the distribution of interaction scores between disease groups or subgroups for each pairwise cell-type combination was different as described in ‘Analysis of IHC data’.

## Analysis of IHC data

IHC images were segmented with Stardist<sup>38</sup> (version 0.6.1) with the 2D\_versatile\_he pretrained model and normalization to the unit space after capping the intensity to the 3rd and 98th percentiles. The image was decomposed into a haematoxylin and diaminobenzidine intensity channels using a preset colour space for the stains from the scikit-image package<sup>36</sup> (skimage.colour.hdx\_from\_rgb) and the intensity of each nuclei in both channels was calculated by a mean reduction. As the H-DAB and IHC signal in general does not linearly reflect the molecular stoichiometry of chemical reactions, we discretized the signal into positive and negative fractions per image by using Gaussian mixture models with model selection in the same way as for the IMC data. Cells were declared positive for a stain if they belonged to the group with highest signal.

For the quantification of image lacunarity in IHC data we first normalized illumination in YCrCb colour space by applying a Gaussian blur with 5 pixels of s.d. per  $300 \times 300$  size image and subtracting this background from the brightness channel (Y or luma). Images were converted back to RGB colour space and the inverted mean of the channels was segmented using the Otsu method. The lacunarity of the image is the fraction of the image covered in background. This was performed only for MPO-stained images within the alveolar space and not with airways or vessels.

## Analysis of targeted spatial transcriptomics data using GeoMx

To transform the gene set space into a cell-type space that would be compatible with the cell types identified in the IMC dataset, we performed single-sample gene set enrichment analysis (ssGSEA) using GSEAPY (version 0.10.2). For each ROI, gene set signatures used were from the molecular signatures database (MSigDB, version 7.2); in particular, the cell-type signature gene sets (group C8) were used. ssGSEA enrichment values were Z-scored, and signatures containing the keywords ‘Epithelial’, ‘Mesenchym’, ‘Fibroblast’, ‘Smooth\_muscle’, ‘Club’, ‘CD4\_T’, ‘CD8\_T’, ‘NK\_cell’, ‘Macrophage’, ‘Monocyte’, ‘Neutrophil’, ‘B\_cell’, ‘Mast’ and ‘Dendritic’ were grouped and averaged, generating an enrichment score for each ROI in each cell type. If a group was composed of less than three signatures it was discarded. For the pathway-based functional analysis of lung tissue, ssGSEA was performed on the

Hallmark group of gene set signatures from MSigDB (group H) without further aggregation.

## PCA of lung pathology and association with clinical parameters

To create the unsupervised landscape of lung pathology, we used PCA on a matrix of cell counts per cell cluster (features) and per image (observations), after previous normalization by total, scaling and centring, using the Scanpy implementation. The feature loadings were plotted on the same dimensions as the observations by scaling them by a constant factor of 20. The correlation coefficient between each principal component and the continuous clinical variables was used as a relative measure of direction and strength of association. However, the significance of association was assessed by permuting the clinical variables  $10^6$  times and using the mean and s.d. of the correlation coefficients from the permuted data as location and scale parameters, respectively, of a normal distribution, from which the  $2 \times \text{CDF}(|x|)$  was calculated as a two-tailed empirical  $P$  value. All principal components and clinical factors were permuted and the empirical  $P$  values were adjusted with the Benjamini–Hochberg FDR method. We used the signed empirical, FDR-corrected  $P$  values as an effectively regularized measure of association between principal components and clinical factors. To project the clinical parameters into the PCA space, we fit Gaussian kernel density estimator functions to the distribution of the images in the first principal components, in one case without and another with the numeric values of the clinical variables as weights. The difference in predicted densities in the two-dimensional space between the weighted and unweighted kernels was used as a visual aid to identify regions in the latent space with relatively higher or lower fraction of samples with that clinical parameter.

## Statistics and reproducibility

Unless otherwise stated in the figure legends, statistical testing was performed pairwise between groups with a two-sided Mann–Whitney  $U$  test, and adjusted for multiple comparisons with the Benjamini–Hochberg FDR method using pingouin<sup>39</sup> (version 0.3.7). Estimated values of central tendency, effect sizes and  $P$  values are provided in Supplementary Tables 3, 4. In the box plots in all figures, the box is the interquartile range (25th to 75th percentiles) and the centre line is the median (50th percentile). Experiments were not repeated independently, owing to the use of unique autopsy material.

The following software versions were used: Python, version 3.8.2; numpy<sup>40</sup>, version 1.18.5; scipy<sup>41</sup>, version 1.4.1; scikit-image<sup>36</sup>, version 0.17.2; networkx<sup>37</sup>, version 2.5; Scanpy, version 1.6.0; pingouin<sup>39</sup>, version 0.3.7; CellProfiler<sup>28</sup>, version 3.1.8; and Stardist<sup>38</sup>, version 0.6.1.

## Reporting summary

Further information on research design is available in the [Nature Research Reporting Summary](#) linked to this paper.

## Data availability

IMC data are available at <https://doi.org/10.5281/zenodo.4110560>, <https://doi.org/10.5281/zenodo.4139442> and <https://doi.org/10.5281/zenodo.4637034>.

IHC data are available at <https://doi.org/10.5281/zenodo.4633905>. Targeted spatial transcriptomics data are available at <https://doi.org/10.5281/zenodo.4635285>. Any other relevant data are available from the corresponding author upon reasonable request.

## Code availability

The source code for data preprocessing and analysis is available at <https://github.com/ElementoLab/covid-imc> and <https://github.com/ElementoLab/covid-imc-viz>.

## References

1. 1.

Laing, A. G. et al. A dynamic COVID-19 immune signature includes associations with poor prognosis. *Nat. Med.* **26**, 1623–1635 (2020).

[CAS](#) [Article](#) [Google Scholar](#)

2. 2.

Lucas, C. et al. Longitudinal analyses reveal immunological misfiring in severe COVID-19. *Nature* **584**, 463–469 (2020).

[CAS](#) [Article](#) [Google Scholar](#)

3. 3.

Mathew, D. et al. Deep immune profiling of COVID-19 patients reveals distinct immunotypes with therapeutic implications. *Science* **369**, eabc8511 (2020).

[CAS](#) [Article](#) [Google Scholar](#)

4. 4.

Nienhold, R. et al. Two distinct immunopathological profiles in autopsy lungs of COVID-19. *Nat. Commun.* **11**, 5086 (2020).

[CAS](#) [Article](#) [ADS](#) [Google Scholar](#)

5. 5.

Wang, W. et al. High-dimensional immune profiling by mass cytometry revealed immunosuppression and dysfunction of immunity in COVID-19 patients. *Cell. Mol. Immunol.* **17**, 650–652 (2020).

[CAS](#) [Article](#) [Google Scholar](#)

6. 6.

Unterman, A. et al. Single-cell omics reveals dyssynchrony of the innate and adaptive immune system in progressive COVID-19. Preprint at <https://doi.org/10.1101/2020.07.16.20153437> (2020).

7. 7.

Takahashi, T. et al. Sex differences in immune responses that underlie COVID-19 disease outcomes. *Nature* **588**, 315–320 (2020).

[CAS](#) [Article](#) [ADS](#) [Google Scholar](#)

8. 8.

Hadjadj, J. et al. Impaired type I interferon activity and inflammatory responses in severe COVID-19 patients. *Science* **369**, 718–724 (2020).

[CAS](#) [Article](#) [ADS](#) [Google Scholar](#)

9. 9.

Giesen, C. et al. Highly multiplexed imaging of tumor tissues with subcellular resolution by mass cytometry. *Nat. Methods* **11**, 417–422 (2014).

[CAS](#) [Article](#) [Google Scholar](#)

10. 10.

McInnes, L., Healy, J., Saul, N. & Großberger, L. UMAP: uniform manifold approximation and projection. *J. Open Source Softw.* **3**, 861 (2018).

[Article](#) [Google Scholar](#)

11. 11.

Dong, E., Du, H. & Gardner, L. An interactive web-based dashboard to track COVID-19 in real time. *Lancet Infect. Dis.* **20**, 533–534 (2020).

[CAS](#) [Article](#) [Google Scholar](#)

12. 12.

Manson, J. J. et al. COVID-19-associated hyperinflammation and escalation of patient care: a retrospective longitudinal cohort study. *Lancet Rheumatol* **2**, e594–e602 (2020).

[Article](#) [Google Scholar](#)

13. 13.

Tay, M. Z., Poh, C. M., Rénia, L., MacAry, P. A. & Ng, L. F. P. The trinity of COVID-19: immunity, inflammation and intervention. *Nat. Rev. Immunol.* **20**, 363–374 (2020).

[CAS](#) [Article](#) [Google Scholar](#)

14. 14.

Grasselli, G. et al. Pathophysiology of COVID-19-associated acute respiratory distress syndrome: a multicentre prospective observational study. *Lancet Respir. Med.* **8**, 1201–1208 (2020).

[CAS](#) [Article](#) [Google Scholar](#)

15. 15.

Sinha, P. et al. Prevalence of phenotypes of acute respiratory distress syndrome in critically ill patients with COVID-19: a prospective observational study. *Lancet Respir. Med.* **8**, 1209–1218 (2020).

[CAS](#) [Article](#) [Google Scholar](#)

16. 16.

Arunachalam, P. S. et al. Systems biological assessment of immunity to mild versus severe COVID-19 infection in humans. *Science* **369**, 1210–1220 (2020).

[CAS](#) [Article](#) [ADS](#) [Google Scholar](#)

17. 17.

Liao, M. et al. Single-cell landscape of bronchoalveolar immune cells in patients with COVID-19. *Nat. Med.* **26**, 842–844 (2020).

[CAS](#) [Article](#) [Google Scholar](#)

18. 18.

Reyes, L. et al. A type I IFN, prothrombotic hyperinflammatory neutrophil signature is distinct for COVID-19 ARDS. Preprint at <https://doi.org/10.1101/2020.09.15.20195305> (2020).

19. 19.

Bradley, B. T. et al. Histopathology and ultrastructural findings of fatal COVID-19 infections in Washington State: a case series. *Lancet* **396**, 320–332 (2020).

[CAS](#) [Article](#) [Google Scholar](#)

20. 20.

Bengsch, B. et al. Deep spatial profiling of COVID19 brains reveals neuroinflammation by compartmentalized local immune cell interactions and targets for intervention. Preprint at <https://doi.org/10.21203/rs.3.rs-63687/v1> (2020).

21. 21.

Tian, S. et al. Pathological study of the 2019 novel coronavirus disease (COVID-19) through postmortem core biopsies. *Mod. Pathol.* **33**, 1007–1014 (2020).

[CAS](#) [Article](#) [Google Scholar](#)

22. 22.

Duffield, J. S., Luper, M., Thannickal, V. J. & Wynn, T. A. Host responses in tissue repair and fibrosis. *Annu. Rev. Pathol.* **8**, 241–276 (2013).

[CAS Article](#) [Google Scholar](#)

23. 23.

Ashcroft, T., Simpson, J. M. & Timbrell, V. Simple method of estimating severity of pulmonary fibrosis on a numerical scale. *J. Clin. Pathol.* **41**, 467–470 (1988).

[CAS Article](#) [Google Scholar](#)

24. 24.

Merritt, C. R. et al. Multiplex digital spatial profiling of proteins and RNA in fixed tissue. *Nat. Biotechnol.* **38**, 586–599 (2020).

[CAS Article](#) [ADS](#) [Google Scholar](#)

25. 25.

Desai, N. et al. Temporal and spatial heterogeneity of host response to SARS-CoV-2 pulmonary infection. *Nat. Commun.* **11**, 6319 (2020).

[CAS Article](#) [ADS](#) [Google Scholar](#)

26. 26.

Jackson, H. W. et al. The single-cell pathology landscape of breast cancer. *Nature* **578**, 615–620 (2020).

[CAS Article](#) [ADS](#) [Google Scholar](#)

27. 27.

Berg, S. et al. ilastik: interactive machine learning for (bio)image analysis. *Nat. Methods* **16**, 1226–1232 (2019).

[CAS Article](#) [Google Scholar](#)

28. 28.

McQuin, C. et al. CellProfiler 3.0: next-generation image processing for biology. *PLoS Biol.* **16**, e2005970 (2018).

[Article](#) [Google Scholar](#)

29. 29.

Immerkær, J. Fast noise variance estimation. *Comput. Vis. Image Underst.* **64**, 300–302 (1996).

[Article](#) [Google Scholar](#)

30. 30.

Donoho, D. L. & Johnstone, I. M. Ideal spatial adaptation by wavelet shrinkage. *Biometrika* **81**, 425–455 (1994).

[MathSciNet](#) [Article](#) [Google Scholar](#)

31. 31.

Kit, O. & Lüdeke, M. Automated detection of slum area change in Hyderabad, India using multitemporal satellite imagery. *ISPRS J. Photogramm. Remote Sens.* **83**, 130–137 (2013).

[Article](#) [ADS](#) [Google Scholar](#)

32. 32.

Wolf, F. A., Angerer, P. & Theis, F. J. SCANPY: large-scale single-cell gene expression data analysis. *Genome Biol.* **19**, 15 (2018).

[Article](#) [Google Scholar](#)

33. 33.

Traag, V. A., Waltman, L. & van Eck, N. J. From Louvain to Leiden: guaranteeing well-connected communities. *Sci. Rep.* **9**, 5233 (2019).

[CAS](#) [Article](#) [ADS](#) [Google Scholar](#)

34. 34.

Pedregosa, F. & Varoquaux, G. Scikit-learn: machine learning in Python. *J. Mach. Learn. Res.* **12**, 2825–2830 (2011).

[MathSciNet](#) [MATH](#) [Google Scholar](#)

35. 35.

Davies, D. L. & Bouldin, D. W. A cluster separation measure. *IEEE Trans. Pattern Anal. Mach. Intell. PAMI* **1**, 224–227 (1979).

[CAS](#) [Article](#) [Google Scholar](#)

36. 36.

van der Walt, S. et al. scikit-image: image processing in Python. *PeerJ* **2**, e453 (2014).

[Article](#) [Google Scholar](#)

37. 37.

Hagberg, A. A., Schult, D. A. & Swart, P. J. Exploring network structure, dynamics, and function using NetworkX. In *Proc. 7th Python in Science Conference (SciPy2008)* (eds Varoquaux, G. et al.) 11–15 (2008).

38. 38.

Schmidt, U., Weigert, M., Broaddus, C. & Myers, G. in *Medical Image Computing and Computer Assisted Intervention – MICCAI 2018* (eds Frangi, A. F. et al.) 265–273 (Springer, 2018).

39. 39.

Vallat, R. Pingouin: statistics in Python. *J. Open Source Softw.* **3**, 1026 (2018).

[Article](#) [ADS](#) [Google Scholar](#)

40. 40.

Harris, C. R. et al. Array programming with NumPy. *Nature* **585**, 357–362 (2020).

[CAS](#) [Article](#) [ADS](#) [Google Scholar](#)

41. 41.

Virtanen, P. et al. SciPy 1.0: fundamental algorithms for scientific computing in Python. *Nat. Methods* **17**, 261–272 (2020).

[CAS](#) [Article](#) [Google Scholar](#)

[Download references](#)

## Acknowledgements

We thank the patients and their families for their contributions to our study. We apologize to colleagues whose work we could not cite owing to editorial constraints. This work was partially supported by the WorldQuant Initiative for Quantitative Prediction. A.F.R. is supported by a NCI T32CA203702 grant. O.E. is supported by Volastra, Janssen and Eli Lilly research grants, NIH grants UL1TR002384 and R01CA194547, and Leukemia and Lymphoma Society SCOR 7012-16, SCOR 7021-20 and SCOR 180078-02 grants. R.E.S. is supported by NIH grants NCI R01CA234614, NIAID 2R01AI107301, NIDDK R01DK121072 and 1RO3DK117252. R.E.S. is supported as Irma Hirschl Trust Research Award Scholar. We thank the Englander Institute of Precision Medicine Mass Cytometry Core facility for processing, labelling and acquiring samples for IMC imaging, and the translational research laboratory (Department of Pathology, Weill Cornell Medicine) for histology and IHC support. We thank Zenodo for storing the raw data associated with this Article with a higher usage quota.

## Author information

### Author notes

1. These authors contributed equally: André F. Rendeiro, Hiranmayi Ravichandran
2. These authors jointly supervised this work: Alain C. Borczuk, Olivier Elemento, Robert E. Schwartz

### Affiliations

1. Institute for Computational Biomedicine, Weill Cornell Medicine, New York, NY, USA  
André F. Rendeiro, Junbum Kim, Cem Meydan, Jonathan Foox, Christopher E. Mason & Olivier Elemento
2. Caryle and Israel Englander Institute for Precision Medicine, Weill Cornell Medicine, New York, NY, USA  
André F. Rendeiro, Hiranmayi Ravichandran & Olivier Elemento

3. WorldQuant Initiative for Quantitative Prediction, Weill Cornell Medicine, New York, NY, USA

Hiranmayi Ravichandran, Christopher E. Mason & Olivier Elemento

4. Department of Physiology, Biophysics and Systems Biology, Weill Cornell Medicine, New York, NY, USA

Hiranmayi Ravichandran, Cem Meydan, Jiwoon Park, Jonathan Foox, Christopher E. Mason, Olivier Elemento & Robert E. Schwartz

5. Division of Gastroenterology and Hepatology, Department of Medicine, Weill Cornell Medicine, New York, NY, USA

Yaron Bram, Vasuretha Chandar & Robert E. Schwartz

6. NanoString Technologies, Inc, Seattle, WA, USA

Tyler Hether, Sarah Warren, Youngmi Kim & Jason Reeves

7. Department of Pathology and Laboratory Medicine, Weill Cornell Medicine, New York, NY, USA

Steven Salvatore & Alain C. Borczuk

8. New York Genome Center, New York, NY, USA

Christopher E. Mason

9. Fluidigm Inc., Markham, Ontario, Canada

Eric C. Swanson

## Authors

1. André F. Rendeiro

[View author publications](#)

You can also search for this author in [PubMed](#) [Google Scholar](#)

2. Hiranmayi Ravichandran

[View author publications](#)

You can also search for this author in [PubMed](#) [Google Scholar](#)

3. Yaron Bram

[View author publications](#)

You can also search for this author in [PubMed](#) [Google Scholar](#)

4. Vasuretha Chandar

[View author publications](#)

You can also search for this author in [PubMed](#) [Google Scholar](#)

5. Junbum Kim

[View author publications](#)

You can also search for this author in [PubMed](#) [Google Scholar](#)

6. Cem Meydan

[View author publications](#)

You can also search for this author in [PubMed](#) [Google Scholar](#)

7. Jiwoon Park

[View author publications](#)

You can also search for this author in [PubMed](#) [Google Scholar](#)

8. Jonathan Foox

[View author publications](#)

You can also search for this author in [PubMed](#) [Google Scholar](#)

9. Tyler Hether

[View author publications](#)

You can also search for this author in [PubMed](#) [Google Scholar](#)

10. Sarah Warren

[View author publications](#)

You can also search for this author in [PubMed](#) [Google Scholar](#)

11. Youngmi Kim

[View author publications](#)

You can also search for this author in [PubMed](#) [Google Scholar](#)

12. Jason Reeves

[View author publications](#)

You can also search for this author in [PubMed](#) [Google Scholar](#)

13. Steven Salvatore

[View author publications](#)

You can also search for this author in [PubMed](#) [Google Scholar](#)

14. Christopher E. Mason

[View author publications](#)

You can also search for this author in [PubMed](#) [Google Scholar](#)

15. Eric C. Swanson

[View author publications](#)

You can also search for this author in [PubMed](#) [Google Scholar](#)

16. Alain C. Borczuk

[View author publications](#)

You can also search for this author in [PubMed](#) [Google Scholar](#)

17. Olivier Elemento

[View author publications](#)

You can also search for this author in [PubMed](#) [Google Scholar](#)

18. Robert E. Schwartz

[View author publications](#)

You can also search for this author in [PubMed](#) [Google Scholar](#)

## Contributions

A.F.R., H.R., O.E., A.C.B. and R.E.S. planned the study; A.C.B., Y.B., V.C., R.E.S. and S.S. provided and evaluated samples and clinical data; H.R. and E.C.S. performed IMC; T.H., S.W., Y.K. and J.R. performed the digital spatial transcriptomics with contributions from C.M., J.P., J.F. and C.E.M. A.F.R. performed analysis of the data, with contributions from J.K.; O.E., and R.E.S. supervised the research. A.F.R., H.R., O.E., A.C.B. and R.E.S. wrote the manuscript with contributions from all authors.

## Corresponding authors

Correspondence to [Alain C. Borczuk](#) or [Olivier Elemento](#) or [Robert E. Schwartz](#).

## Ethics declarations

### Competing interests

O.E. is scientific advisor and equity holder in Freenome, Owkin, Volastra Therapeutics and OneThree Biotech. R.E.S. is on the scientific advisory board of Miromatrix Inc and is a consultant and speaker for Alnylam Inc. C.E.M. is a cofounder of Biotia and Onegevity Health. E.C.S. is an employee of Fluidigm. T.H., S.W., Y. K. and J.R. are employees of Nanostring Inc. The remaining authors declare no competing financial interests.

## Additional information

**Peer review information** *Nature* thanks John Alcorn, Ross Levine and the other, anonymous, reviewer(s) for their contribution to the peer review of this work. Peer reviewer reports are available.

**Publisher's note** Springer Nature remains neutral with regard to jurisdictional claims in published maps and institutional affiliations.

## Extended data figures and tables

### [Extended Data Fig. 1 Macroscopic pathology of the SARS-CoV-2-infected lung.](#)

**a**, Heat map depicting the values of each individual for all clinical and demographic variables. Grey colour indicates missing or non-applicable values. **b**, Time of death relative to start of symptoms in patients with COVID-19. **c, d**, Percentage of lacunar space attributed to vessel (**c**) or epithelial (**d**) space per image, grouped by disease. **e**, Collagen type I in images of healthy lungs or lungs from patients with lung pathology, and the associated fibrosis score. Images with the lowest, median and highest fibrosis scores are depicted. **f**, Percentage of image covered in collagen type I for each image, grouped by disease group. **g**, Mean intensity of collagen type I in lung IMC images, grouped by disease group. **h**, UMAP projection of all single cells, in which cells are coloured by the intensity of each channel. In **c, d, f, g**, \*\* $P < 0.01$ ; \* $P < 0.05$ , two-

sided Mann–Whitney *U*-test, pairwise between groups, Benjamini–Hochberg FDR adjustment.

**Extended Data Fig. 2 Clustering analysis and quantification of structural cell types across disease types.**

**a**, Hierarchically clustered heat map of discovered clusters (rows) and the mean intensity of each channel (columns) for each. The histogram on the left represents the absolute abundance of each cluster across all images. The dot plot represents the relative abundance of each cluster in each disease group. **b**, Classification of lung lacunae. Representative images of healthy lung with the mean of all channels, and channels that are important for discerning between vessels, airways and alveoli. The rightmost column represents the final classification of lacunae into each of the three classes of structures. **c**, Representative spatial context of three metaclusters (rows). Left column, spatial distribution of the predominant marker for each metacluster; right column, segmented cells coloured by the metacluster to which they were assigned. **d**, Global abundance of structural and immune cells. Absolute (top panels) and relative (bottom panels) abundance of groups of cells, depending on disease group.

\*\* $P < 0.01$ ; \* $P < 0.05$ , two-sided Mann–Whitney *U*-test, pairwise between groups, Benjamini–Hochberg FDR adjustment.

**Extended Data Fig. 3 Analysis of cellular phenotypes reveals alterations in the myeloid and epithelial compartments.**

**a, b**, Absolute abundance of metaclusters (**a**) or clusters (**b**) per image, grouped by disease group. **c–e**, Diversity of myeloid cells in the lung. **c**, UMAP representation of myeloid cells and the prominent markers associated with them. **d**, Phenotypic markers, spatial context and abundance in disease groups for each of the six myeloid clusters. **e**, Abundance of each myeloid cluster in the disease groups. Each point represents the abundance of that cluster in a given ROI. In **a, b, e**, \*\* $P < 0.01$ ; \* $P < 0.05$ , two-sided Mann–Whitney *U*-test, pairwise between groups, Benjamini–Hochberg FDR adjustment.

**Extended Data Fig. 4 Immune cell analysis using an orthogonal probe set.**

**a**, Schematic of IMC panel, and its application to healthy lung tissue samples and lung tissue samples from patients with COVID-19. **b**, UMAP representation of single cells, coloured by the intensity of the marker for cell-type-defining markers and functional markers. **c**, Expression of markers for each single cell grouped by the cell type. **d**, Differential expression of functional markers between lungs of patients with COVID-

19 and healthy lung for each cell type. **e**, Expression range represented as violin plots for the selected cell types from **b**, between lungs of patients with COVID-19 and healthy lung.  $**P < 0.01$  two-sided Wald test, Benjamini–Hochberg FDR adjustment. **f**, Representative images of S100A9 and CD15 marker expression in healthy lung and lungs of patients with COVID-19. Scale bars, 100  $\mu\text{m}$ .

## **Extended Data Fig. 5 Validation of IMC findings with IHC.**

**a**, Relationship between fibrosis score and fibroblast metacluster abundance, visualized as a scatter plot. **b**, **c**, IHC for two markers across all disease groups. Haematoxylin–diaminobenzidine staining of CD163 (**b**) or MPO (**c**) in tissue from healthy and diseased lung, matching the patients in the IMC cohort. Scale bars, 200  $\mu\text{m}$ . **d**, Analysis of IHC data. Example images demonstrating the process of colour decomposition that underlies the separation of the haematoxylin (nuclei) and diaminobenzidine (CD163 or MPO) (H-DAB) in lung tissues. Scale bars, 400  $\mu\text{m}$  (long bars), 50  $\mu\text{m}$  (short bars). **e**, Example images demonstrating the process of nuclei segmentation. Left column, original images in RGB space; middle column, resulting segmentation in which each nucleus has a random colour and the background is black; and right column, borders of segmented nuclei in red overlain on the original image. Scale bars, 200  $\mu\text{m}$ . **f**, Example image section, demonstrating the process of quantification of the diaminobenzidine stain. Top, original image in RGB space; second panel, nuclei segmentation; third panel, numeric value of the DAB stain for each nucleus; and bottom, histogram of nuclei intensity in DAB stain, modelled as a Gaussian mixture with two components used to discretize nuclei into negative or positive for DAB on the basis of a threshold that best separates the two mixtures. Scale bars, 50  $\mu\text{m}$ . **g**, Percentage of cells within an image that are positive for the respective DAB stain in IHC (left column) or positive for the respective marker in IMC data (right column). **h**, Comparison of the estimated effect sizes of change between disease groups estimated from IMC (*x* axis) or IHC (*y* axis) data for the two stains. The Pearson correlation coefficient and its significance are indicated. **i**, Analysis of lacunae with IHC data. Representative images of the amount of lacuna space in IHC data for healthy lungs and lungs of patients with late COVID-19. For each image, the original image and the segmented background space is shown along with a value denoting the amount of lacuna space for the image (fraction of the image without cells that represents the alveolar or capillary space). Scale bars, 200  $\mu\text{m}$ . **j**, Quantification of lacuna space across MPO images in IHC.  $**P < 0.01$ ;  $*P < 0.05$ , two-sided Mann–Whitney *U*-test, pairwise between groups, Benjamini–Hochberg FDR adjustment. **k**, Comparison of the estimated effect sizes of change in the amount of lacuna space between disease groups, estimated from IMC (*x* axis) or IHC (*y*-axis) data. For **a**, **h**, **k**, **r**, Pearson coefficient; *P*, its two-tailed *P* value.

## Extended Data Fig. 6 Profiling of lung tissue with targeted spatial transcriptomics using GeoMx.

**a**, Experimental design of GeoMx dataset. **b**, Representation of the procedure of choosing a ROI within the lung tissue to capture with GeoMx. **c**, Enrichment of cell-type-specific gene set signatures for various cell types that match the IMC data, across disease groups. **d**, Comparison of the estimated changes in cell-type abundance with IMC (*x* axis) and gene set signatures in GeoMx (*y* axis). **e**, Viral load, dependent on the time of death relative to the onset of COVID-19 symptoms in an independent cohort. COVID-19 samples were categorized into ‘early’ or ‘late’ death depending on whether death occurred before or after 15 days after the onset of symptoms, respectively. **f**, Schematic of the cohort of patients for whom GeoMx data are available (in total, 5 patients and 231 ROIs). **g**, Estimated fractions of cell-type composition, using the CYBERSORT program, between early and late COVID-19 from the original publication<sup>25</sup>. **h**, Comparison of the estimated changes in cell-type abundance with IMC (*x* axis) and GeoMx (*y* axis) between late and early COVID-19. In **d**, **h**, *r*, Pearson coefficient, *P*, its two tailed *P* value; shaded area indicates 95th confidence interval. In **c**, **g**, \*\**P* < 0.01; \**P* < 0.05, two-sided Mann–Whitney *U*-test, pairwise between groups, Benjamini–Hochberg FDR adjustment.

## Extended Data Fig. 7 Functional state of myeloid cells across disease cohorts.

**a**, Percentage of cells positive for each IMC channel, as classified by univariate Gaussian mixture models per disease group. **b**, Percentage of channel-positive cells for each metacluster. Values represent a column-wise Z-score. **c**, Absolute (top) and relative (bottom) frequency of SARS-CoV-2 S<sup>+</sup> cells per disease group. **d**, Proportional abundance of SARS-CoV-2 S<sup>+</sup>, IL-6<sup>+</sup> and pSTAT3<sup>+</sup> cells across disease groups. **e**, Proportional amount of SARS-CoV-2 S<sup>+</sup> cells grouped by metacluster and disease group. **f**, Proportional frequencies of cells positive for SARS-CoV-2 S<sup>+</sup> cells by metacluster and disease group. **g**, **h**, Heat map of single macrophages or neutrophils (**g**) (columns) and functional markers (**h**) (rows) with cells grouped by SARS-CoV-2 S positivity. **i**, **j**, Intensity of IMC channels per single cell, depending on SARS-CoV-2 S positivity for macrophages (**i**) and neutrophils (**j**). **k**, Mean channel intensity for all metaclusters dependent on SARS-CoV-2 S positivity. In **c**, **d**, **f**, \*\**P* < 0.01; \**P* < 0.05, two-sided Mann–Whitney *U*-test, pairwise between groups, Benjamini–Hochberg FDR adjustment.

## Extended Data Fig. 8 Mapping cellular interactions between SARS-CoV2-infected and non-infected compartments.

**a**, Example description of the derivation of a region adjacency graph for a given lung IMC image. Left, DNA channel that marks nuclei; middle, identified metaclusters; and right, region adjacency graph represented as edges between adjacent cells. Scale bar, 100  $\mu\text{m}$ . **b**, Observed values of pairwise cluster interactions over the expected values for the same cellular interactions for the image in **a**. **c**, Pairwise interactions between metaclusters, aggregated by the mean value across images depending on the disease group. **d–f**, Pairwise cellular interactions between metaclusters, depending on SARS-CoV-2 S positivity in uninfected cells (**d**), between SARS-CoV-2 S<sup>+</sup> and S<sup>-</sup> cells (**e**) and between infected cells (**f**). **g–i**, Statistical testing of differential interactions of infected cells and other cell types, and uninfected cells and other cell types, depending on SARS-CoV-2 S positivity of the second cell type. **g**, Both SARS-CoV-2 S<sup>-</sup> and S<sup>+</sup> cells. **h**, Only SARS-CoV-2 S<sup>+</sup> cells. **i**, Only SARS-CoV-2 S<sup>-</sup> cells. The rows display a volcano plot in which the *x* axis displays the difference in interaction between SARS-CoV-2 S<sup>+</sup> and S<sup>-</sup> cells and the *y* axis displays the  $-\log_{10}$ -transformed Mann–Whitney *U*-test, FDR-adjusted *P* value.

### [Extended Data Fig. 9 Pathway enrichment analysis in spatial transcriptomics and IMC datasets.](#)

**a**, Enrichment scores for hallmark pathways in MsigDB across all ROIs in the GeoMx dataset. **b–e**, Enrichment score of selected pathways from **a**, across disease groups but dependent on the location within the lung from which they were obtained. \*\**P* < 0.01; \**P* < 0.05, two-sided Mann–Whitney *U*-test, pairwise between groups, Benjamini–Hochberg FDR adjustment. **f**, **g**, Pairwise Pearson correlation of cell-type abundances between IMC samples (**f**) or disease groups (**g**). **h–j**, UMAP (**h**), diffusion map (**i**) or PCA (**j**) projection of IMC images, coloured by disease group, subgroup or sample identifier.

### [Extended Data Fig. 10 Association analysis between known demographic, clinical and pathological factors of patients with lung infections.](#)

**a**, Correlation coefficients (left) or FDR-adjusted *P* values (middle) and signed p-values (right), demonstrating the association between demographic, pathological and clinical factors, and principal components. **b**, Pairwise correlation of demographic, pathological and clinical factors across all principal components. Matrix was clustered using average linking and the Pearson correlation as the distance metric. Values used were signed FDR-adjusted *P* values. **c**, Pairwise correlation of demographic, pathological and clinical factors across samples (co-occurrence). Matrix was clustered using average linking and the Pearson correlation as the distance metric. **d**, As in **b**, **c**; the top triangular matrix is from **b** and the bottom is from **c**. The order of the rows and

columns is the same as in **b. e**, Projection of clinical factors onto the pathology landscape. Kernel density estimation for various clinical and demographic factors weighted by the factor values, unweighted or their difference.

## Supplementary information

### Reporting Summary

### Supplementary Table 1

Detailed clinical annotations and demographic characteristics for patients included in the study representing different disease groups (ARDS post -viral influenza (n=2), ARDS post bacterial infection (n=4), bacterial pneumonia (n=3) and COVID-19 ARDS (n=10)) and control group (normal lung (n=4)).

### Supplementary Table 2

List of metal-tagged antibodies used in imaging mass cytometry. Panel 1 (“Lung\_COVID-19”) includes 36 markers characterizing immune cell phenotypes and functional markers related with COVID-19 such as IL-6, IL-1beta, cKIT, pSTAT3 and viral infection component S protein. Panel 2 (Immune activation) includes 38 markers characterizing immune cell activation states.

### Supplementary Table 3

Statistical testing of difference in abundance for clusters and meta-clusters between disease groups. A two tailed Mann-Whitney U-test was performed and p-values were adjusted with the Benjamini-Hochberg False Discovery Rate method. The uncorrected p-value is in the “p-unc” column, the corrected p-value in the “p-cor” column, and a measure of effect size is given in the “hedges” column, which indicates a Hedge’s  $g$  value.

### Supplementary Table 4

Statistical testing of difference in fraction of cells positive in functional markers for clusters and meta-clusters between disease groups. A two tailed Mann-Whitney U-test was performed and p-values were adjusted with the Benjamini-Hochberg False Discovery Rate method. The uncorrected p-value is in the “p-unc” column, the corrected p-value in the “p-cor” column, and a measure of effect size is given in the “hedges” column, which indicates a Hedge’s  $g$  value.

## Peer Review File

## Rights and permissions

### Reprints and Permissions

## About this article



## Cite this article

Rendeiro, A.F., Ravichandran, H., Bram, Y. *et al.* The spatial landscape of lung pathology during COVID-19 progression. *Nature* **593**, 564–569 (2021).  
<https://doi.org/10.1038/s41586-021-03475-6>

### Download citation

- Received: 25 October 2020
- Accepted: 19 March 2021
- Published: 29 March 2021
- Issue Date: 27 May 2021
- DOI: <https://doi.org/10.1038/s41586-021-03475-6>

## Further reading

- [Targeting the Complement Cascade in the Pathophysiology of COVID-19 Disease](#)
  - Nicole Ng
  - & Charles A. Powell

*Journal of Clinical Medicine* (2021)

- **A molecular single-cell lung atlas of lethal COVID-19**

- Johannes C. Melms
- , Jana Biermann
- , Huachao Huang
- , Yiping Wang
- , Ajay Nair
- , Somnath Tagore
- , Igor Katsyv
- , André F. Rendeiro
- , Amit Dipak Amin
- , Denis Schapiro
- , Chris J. Frangieh
- , Adrienne M. Luoma
- , Aveline Filliol
- , Yinshan Fang
- , Hiranmayi Ravichandran
- , Mariano G. Clausi
- , George A. Alba
- , Meri Rogava
- , Sean W. Chen
- , Patricia Ho
- , Daniel T. Montoro
- , Adam E. Kornberg
- , Arnold S. Han
- , Mathieu F. Bakhoum
- , Niroshana Anandasabapathy
- , Mayte Suárez-Fariñas
- , Samuel F. Bakhoum
- , Yaron Bram
- , Alain Borczuk
- , Xinzheng V. Guo
- , Jay H. Lefkowitch
- , Charles Marboe
- , Stephen M. Lagana
- , Armando Del Portillo
- , Emmanuel Zorn
- , Glen S. Markowitz
- , Robert F. Schwabe
- , Robert E. Schwartz
- , Olivier Elemento
- , Anjali Saqi

- , Hanina Hibshoosh
- , Jianwen Que
- & Benjamin Izar

*Nature* (2021)

## Comments

By submitting a comment you agree to abide by our [Terms](#) and [Community Guidelines](#). If you find something abusive or that does not comply with our terms or guidelines please flag it as inappropriate.

[Download PDF](#)

Advertisement

---

This article was downloaded by **calibre** from <https://www.nature.com/articles/s41586-021-03475-6>

| [Section menu](#) | [Main menu](#) |

- Article
- [Published: 05 May 2021](#)

# Response of the microbiome–gut–brain axis in *Drosophila* to amino acid deficit

- [Boram Kim](#) [ORCID: orcid.org/0000-0002-4786-6675](#)<sup>1,2</sup> nal,
- [Makoto I. Kanai](#)<sup>3</sup> nal,
- [Yangkyun Oh](#)<sup>3</sup>,
- [Minsoo Kyung](#)<sup>1</sup>,
- [Eun-Kyoung Kim](#)<sup>1</sup>,
- [In-Hwan Jang](#)<sup>1</sup>,
- [Ji-Hoon Lee](#)<sup>1</sup>,
- [Sang-Gyu Kim](#) [ORCID: orcid.org/0000-0003-2574-3233](#)<sup>2</sup>,
- [Greg S. B. Suh](#) [ORCID: orcid.org/0000-0003-4381-658X](#)<sup>2,3,4</sup> &
- [Won-Jae Lee](#) [ORCID: orcid.org/0000-0002-1438-8005](#)<sup>1</sup>

[Nature](#) volume 593, pages 570–574 (2021) [Cite this article](#)

- 8633 Accesses
- 121 Altmetric
- [Metrics details](#)

## Subjects

- [Feeding behaviour](#)
- [Metabolism](#)

# Abstract

A balanced intake of macronutrients—protein, carbohydrate and fat—is essential for the well-being of organisms. An adequate calorific intake but with insufficient protein consumption can lead to several ailments, including kwashiorkor<sup>1</sup>. Taste receptors (T1R1–T1R3)<sup>2</sup> can detect amino acids in the environment, and cellular sensors (Gcn2 and Tor)<sup>3</sup> monitor the levels of amino acids in the cell. When deprived of dietary protein, animals select a food source that contains a greater proportion of protein or essential amino acids (EAAs)<sup>4</sup>. This suggests that food selection is geared towards achieving the target amount of a particular macronutrient with assistance of the EAA-specific hunger-driven response, which is poorly understood. Here we show in *Drosophila* that a microbiome–gut–brain axis detects a deficit of EAAs and stimulates a compensatory appetite for EAAs. We found that the neuropeptide CNMamide (CNMa)<sup>5</sup> was highly induced in enterocytes of the anterior midgut during protein deprivation. Silencing of the CNMa–CNMa receptor axis blocked the EAA-specific hunger-driven response in deprived flies. Furthermore, gnotobiotic flies bearing an EAA-producing symbiotic microbiome exhibited a reduced appetite for EAAs. By contrast, gnotobiotic flies with a mutant microbiome that did not produce leucine or other EAAs showed higher expression of *CNMa* and a greater compensatory appetite for EAAs. We propose that gut enterocytes sense the levels of diet- and microbiome-derived EAAs and communicate the EAA-deprived condition to the brain through CNMa.

## Access options

Subscribe to Journal

Get full journal access for 1 year

\$199.00

only \$3.90 per issue

[Subscribe](#)

All prices are NET prices.  
VAT will be added later in the checkout.  
Tax calculation will be finalised during checkout.

Rent or Buy article

Get time limited or full article access on ReadCube.

from \$8.99

[Rent or Buy](#)

All prices are NET prices.

### **Additional access options:**

- [Log in](#)
- [Access through your institution](#)
- [Learn about institutional subscriptions](#)

**Fig. 1: Amino acid deprivation promotes the compensatory EAA appetite independently of taste and stimulates *CNMa* expression in the gut.**

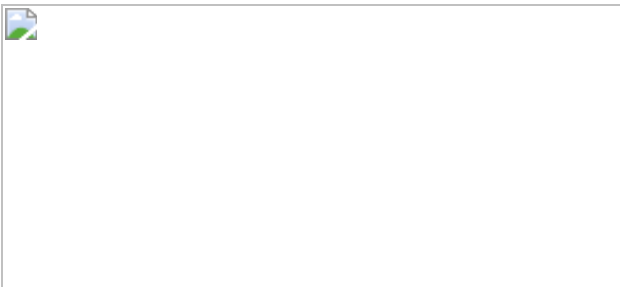


**Fig. 2: Intestinal *CNMa* and neuronal *CNMaR* comprising the gut–brain axis promote the compensatory EAA appetite.**

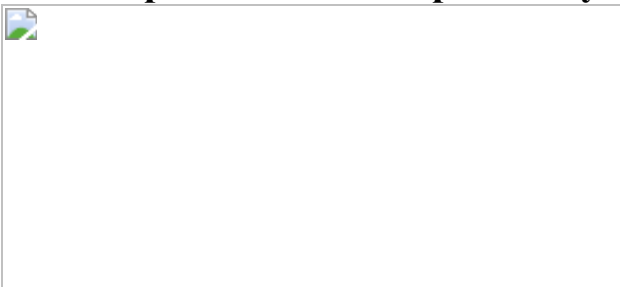


**Fig. 3: The gut microbiome regulates the compensatory EAA appetite.**



## Data availability

The original data for the immunoblotting are shown in Supplementary Fig. 1. All other raw data are available from corresponding authors on request. [Source data](#) are provided with this paper.

## References

1. 1.

Müller, O. & Krawinkel, M. Malnutrition and health in developing countries. *CMAJ* **173**, 279–286 (2005).

[PubMed](#) [PubMed Central](#) [Google Scholar](#)

2. 2.

Nelson, G. et al. An amino-acid taste receptor. *Nature* **416**, 199–202 (2002).

[CAS](#) [PubMed](#) [ADS](#) [Google Scholar](#)

3. 3.

Efeyan, A., Comb, W. C. & Sabatini, D. M. Nutrient-sensing mechanisms and pathways. *Nature* **517**, 302–310 (2015).

[CAS](#) [PubMed](#) [PubMed Central](#) [ADS](#) [Google Scholar](#)

4. 4.

Simpson, S. J., Le Couteur, D. G. & Raubenheimer, D. Putting the balance back in diet. *Cell* **161**, 18–23 (2015).

[CAS](#) [PubMed](#) [Google Scholar](#)

5. 5.

Jung, S.-H. et al. Identification of a novel insect neuropeptide, CNMa and its receptor. *FEBS Lett.* **588**, 2037–2041 (2014).

[CAS](#) [PubMed](#) [Google Scholar](#)

6. 6.

Ganguly, A. et al. A molecular and cellular context-dependent role for Ir76b in detection of amino acid taste. *Cell Rep.* **18**, 737–750 (2017).

[CAS](#) [PubMed](#) [PubMed Central](#) [Google Scholar](#)

7. 7.

Croset, V., Schleyer, M., Arguello, J. R., Gerber, B. & Benton, R. A molecular and neuronal basis for amino acid sensing in the *Drosophila* larva. *Sci. Rep.* **6**, 34871 (2016).

[CAS](#) [PubMed](#) [PubMed Central](#) [ADS](#) [Google Scholar](#)

8. 8.

Nottebohm, E. et al. The gene *poxn* controls different steps of the formation of chemosensory organs in *Drosophila*. *Neuron* **12**, 25–34 (1994).

[CAS](#) [PubMed](#) [Google Scholar](#)

9. 9.

Dus, M. et al. Nutrient sensor in the brain directs the action of the brain–gut axis in *Drosophila*. *Neuron* **87**, 139–151 (2015).

[CAS](#) [PubMed](#) [PubMed Central](#) [Google Scholar](#)

10. 10.

Yang, Z. et al. A post-ingestive amino acid sensor promotes food consumption in *Drosophila*. *Cell Res.* **28**, 1013–1025 (2018).

[CAS](#) [PubMed](#) [PubMed Central](#) [Google Scholar](#)

11. 11.

Buchon, N. et al. Morphological and molecular characterization of adult midgut compartmentalization in *Drosophila*. *Cell Rep.* **3**, 1725–1738 (2013).

[CAS](#) [PubMed](#) [Google Scholar](#)

12. 12.

Masuyama, K., Zhang, Y., Rao, Y. & Wang, J. W. Mapping neural circuits with activity-dependent nuclear import of a transcription factor. *J. Neurogenet.* **26**, 89–102 (2012).

[CAS](#) [PubMed](#) [PubMed Central](#) [Google Scholar](#)

13. 13.

Gallinetti, J., Harputlugil, E. & Mitchell, J. R. Amino acid sensing in dietary-restriction-mediated longevity: roles of signal-transducing kinases GCN2 and TOR. *Biochem. J.* **449**, 1–10 (2013).

[CAS](#) [PubMed](#) [PubMed Central](#) [Google Scholar](#)

14. 14.

Dong, J., Qiu, H., Garcia-Barrio, M., Anderson, J. & Hinnebusch, A. G. Uncharged tRNA activates GCN2 by displacing the protein kinase moiety from a bipartite tRNA-binding domain. *Mol. Cell* **6**, 269–279 (2000).

[CAS](#) [PubMed](#) [Google Scholar](#)

15. 15.

Wolfson, R. L. & Sabatini, D. M. The dawn of the age of amino acid sensors for the mTORC1 pathway. *Cell Metab.* **26**, 301–309 (2017).

[CAS](#) [PubMed](#) [PubMed Central](#) [Google Scholar](#)

16. 16.

Ye, J. et al. The GCN2-ATF4 pathway is critical for tumour cell survival and proliferation in response to nutrient deprivation. *EMBO J.* **29**, 2082–2096 (2010).

[CAS](#) [PubMed](#) [PubMed Central](#) [Google Scholar](#)

17. 17.

Rocznak-Ferguson, A. et al. The transcription factor TFEB links mTORC1 signaling to transcriptional control of lysosome homeostasis. *Sci. Signal.* **5**, ra42 (2012).

[PubMed](#) [PubMed Central](#) [Google Scholar](#)

18. 18.

Bouché, V. et al. *Drosophila* Mitf regulates the V-ATPase and the lysosomal-autophagic pathway. *Autophagy* **12**, 484–498 (2016).

[PubMed](#) [PubMed Central](#) [Google Scholar](#)

19. 19.

Leitão-Gonçalves, R. et al. Commensal bacteria and essential amino acids control food choice behavior and reproduction. *PLoS Biol.* **15**, e2000862 (2017).

[PubMed](#) [PubMed Central](#) [Google Scholar](#)

20. 20.

Shin, S. C. et al. *Drosophila* microbiome modulates host developmental and metabolic homeostasis via insulin signaling. *Science* **334**, 670–674 (2011).

[CAS](#) [PubMed](#) [ADS](#) [Google Scholar](#)

21. 21.

Erkosar, B., Storelli, G., Defaye, A. & Leulier, F. Host-intestinal microbiota mutualism: “learning on the fly”. *Cell Host Microbe* **13**, 8–14 (2013).

[CAS](#) [PubMed](#) [Google Scholar](#)

22. 22.

Sun, J. et al. *Drosophila* FIT is a protein-specific satiety hormone essential for feeding control. *Nat. Commun.* **8**, 14161 (2017).

[CAS](#) [PubMed](#) [PubMed Central](#) [ADS](#) [Google Scholar](#)

23. 23.

Liu, Q. et al. Branch-specific plasticity of a bifunctional dopamine circuit encodes protein hunger. *Science* **356**, 534–539 (2017).

[CAS](#) [PubMed](#) [PubMed Central](#) [ADS](#) [Google Scholar](#)

24. 24.

Bjordal, M., Arquier, N., Kniazeff, J., Pin, J. P. & Léopold, P. Sensing of amino acids in a dopaminergic circuitry promotes rejection of an incomplete diet in *Drosophila*. *Cell* **156**, 510–521 (2014).

[CAS](#) [PubMed](#) [Google Scholar](#)

25. 25.

Hao, S. et al. Uncharged tRNA and sensing of amino acid deficiency in mammalian piriform cortex. *Science* **307**, 1776–1778 (2005).

[CAS](#) [PubMed](#) [ADS](#) [Google Scholar](#)

26. 26.

Gribble, F. M. & Reimann, F. Enteroendocrine cells: chemosensors in the intestinal epithelium. *Annu. Rev. Physiol.* **78**, 277–299 (2016).

[CAS](#) [PubMed](#) [Google Scholar](#)

27. 27.

Gribble, F. M. & Reimann, F. Function and mechanisms of enteroendocrine cells and gut hormones in metabolism. *Nat. Rev. Endocrinol.* **15**, 226–237 (2019).

[CAS](#) [PubMed](#) [Google Scholar](#)

28. 28.

Marianes, A. & Spradling, A. C. Physiological and stem cell compartmentalization within the *Drosophila* midgut. *eLife* **2**, e00886

(2013).

[PubMed](#) [PubMed Central](#) [Google Scholar](#)

29. 29.

Lemaitre, B. & Miguel-Aliaga, I. The digestive tract of *Drosophila melanogaster*. *Annu. Rev. Genet.* **47**, 377–404 (2013).

[CAS](#) [PubMed](#) [Google Scholar](#)

30. 30.

Kiela, P. R. & Ghishan, F. K. Physiology of intestinal absorption and secretion. *Best Pract. Res. Clin. Gastroenterol.* **30**, 145–159 (2016).

[CAS](#) [PubMed](#) [PubMed Central](#) [Google Scholar](#)

31. 31.

Redhai, S. et al. An intestinal zinc sensor regulates food intake and developmental growth. *Nature* **580**, 263–268 (2020).

[CAS](#) [PubMed](#) [ADS](#) [Google Scholar](#)

32. 32.

Hill, C. M., Berthoud, H.-R., Münzberg, H. & Morrison, C. D. Homeostatic sensing of dietary protein restriction: a case for FGF21. *Front. Neuroendocrinol.* **51**, 125–131 (2018).

[PubMed](#) [PubMed Central](#) [Google Scholar](#)

33. 33.

Fisher, F. M. & Maratos-Flier, E. Understanding the physiology of FGF21. *Annu. Rev. Physiol.* **78**, 223–241 (2016).

[CAS](#) [PubMed](#) [Google Scholar](#)

34. 34.

De Sousa-Coelho, A. L., Marrero, P. F. & Haro, D. Activating transcription factor 4-dependent induction of FGF21 during amino acid deprivation. *Biochem. J.* **443**, 165–171 (2012).

[PubMed](#) [Google Scholar](#)

35. 35.

Zhang, Y. et al. TFEB-dependent induction of thermogenesis by the hepatocyte SLC2A inhibitor trehalose. *Autophagy* **14**, 1959–1975 (2018).

[CAS](#) [PubMed](#) [PubMed Central](#) [Google Scholar](#)

36. 36.

Fon Tacer, K. et al. Research resource: comprehensive expression atlas of the fibroblast growth factor system in adult mouse. *Mol. Endocrinol.* **24**, 2050–2064 (2010).

[PubMed](#) [PubMed Central](#) [Google Scholar](#)

37. 37.

Arrese, E. L. & Soulages, J. L. Insect fat body: energy, metabolism, and regulation. *Annu. Rev. Entomol.* **55**, 207–225 (2010).

[CAS](#) [PubMed](#) [PubMed Central](#) [Google Scholar](#)

38. 38.

Hadjieconomou, D. et al. Enteric neurons increase maternal food intake during reproduction. *Nature* **587**, 455–459 (2020).

[CAS](#) [PubMed](#) [PubMed Central](#) [ADS](#) [Google Scholar](#)

39. 39.

Wang, P., Jia, Y., Liu, T., Jan, Y. N. & Zhang, W. Visceral mechano-sensing neurons control drosophila feeding by using Piezo as a sensor. *Neuron* **108**, 640–650 (2020).

[CAS](#) [PubMed](#) [Google Scholar](#)

40. 40.

Semba, R. D. et al. Child stunting is associated with low circulating essential amino acids. *EBioMedicine* **6**, 246–252 (2016).

[PubMed](#) [PubMed Central](#) [Google Scholar](#)

41. 41.

Simpson, S. J. & Raubenheimer, D. Obesity: the protein leverage hypothesis. *Obes. Rev.* **6**, 133–142 (2005).

[CAS](#) [PubMed](#) [Google Scholar](#)

42. 42.

Venken, K. J. T. et al. MiMIC: a highly versatile transposon insertion resource for engineering *Drosophila melanogaster* genes. *Nat. Methods* **8**, 737–743 (2011).

[CAS](#) [PubMed](#) [PubMed Central](#) [Google Scholar](#)

43. 43.

Kondo, S. & Ueda, R. Highly improved gene targeting by germline-specific Cas9 expression in *Drosophila*. *Genetics* **195**, 715–721 (2013).

[CAS](#) [PubMed](#) [PubMed Central](#) [Google Scholar](#)

44. 44.

Dus, M., Ai, M. & Suh, G. S. B. Taste-independent nutrient selection is mediated by a brain-specific  $\text{Na}^+$ /solute co-transporter in *Drosophila*. *Nat. Neurosci.* **16**, 526–528 (2013).

[CAS](#) [PubMed](#) [PubMed Central](#) [Google Scholar](#)

45. 45.

Ryu, J.-H. et al. Innate immune homeostasis by the homeobox gene *Caudal* and commensal-gut mutualism in *Drosophila*. *Science* **319**, 777–782 (2008).

[CAS](#) [PubMed](#) [ADS](#) [Google Scholar](#)

46. 46.

Tasanapak, K., Masud-Tippayasak, U., Matsushita, K., Yongmanitchai, W. & Theeragool, G. Influence of *Acetobacter pasteurianus* SKU1108 *aspS* gene expression on *Escherichia coli* morphology. *J. Microbiol.* **51**, 783–790 (2013).

[CAS](#) [PubMed](#) [Google Scholar](#)

47. 47.

Katzen, F., Becker, A., Ielmini, M. V., Oddo, C. G. & Ielpi, L. New mobilizable vectors suitable for gene replacement in gram-negative bacteria and their use in mapping of the 3' end of the *Xanthomonas campestris* pv. *campestris* *gum* operon. *Appl. Environ. Microbiol.* **65**, 278–282 (1999).

[CAS](#) [PubMed](#) [PubMed Central](#) [Google Scholar](#)

48. 48.

Altschul, S. F., Gish, W., Miller, W., Myers, E. W. & Lipman, D. J. Basic local alignment search tool. *J. Mol. Biol.* **215**, 403–410 (1990).

[CAS](#) [PubMed](#) [Google Scholar](#)

[Download references](#)

## Acknowledgements

We thank the W.-J.L. and G.S.B.S. laboratory members for discussion and critical reading of the manuscript, and we thank the KAIST Biocore center (operator: J. Kim). This work is supported by grants from the Samsung Science and Technology Foundation (project number: SSTF-BA-1802-11) and the National Research Foundation of Korea (NRF-2020R1A2C2009865); by NIH R01 grants (R01DK116294 and R01DK106636, which have been transferred to H. Don Ryoo at New York University) to G.S.B.S; and by grants from National Creative Research Initiative programs of the National Research Foundation of South Korea (2015R1A3A2033475) and the Samsung Science and Technology Foundation (project number: SSTF-BA-1401-15) to W.-J.L. B.K. is supported by the National Research Foundation of South Korea (NRF-2020R1I1A1A01072255).

## Author information

### Author notes

1. These authors contributed equally: Boram Kim, Makoto I. Kanai

## Affiliations

1. National Creative Research Initiative Center for Hologenomics and School of Biological Sciences, Seoul National University, Seoul, Republic of Korea

Boram Kim, Minsoo Kyung, Eun-Kyoung Kim, In-Hwan Jang, Ji-Hoon Lee & Won-Jae Lee

2. Department of Biological Sciences, Korea Advanced Institute of Science and Technology, Daejeon, Republic of Korea

Boram Kim, Sang-Gyu Kim & Greg S. B. Suh

3. Skirball Institute of Biomolecular Medicine, Department of Cell Biology, New York University Grossman School of Medicine, New York, NY, USA

Makoto I. Kanai, Yangkyun Oh & Greg S. B. Suh

4. KAIST Institute, Korea Advanced Institute of Science and Technology, Daejeon, Republic of Korea

Greg S. B. Suh

## Authors

1. Boram Kim

[View author publications](#)

You can also search for this author in [PubMed](#) [Google Scholar](#)

2. Makoto I. Kanai

[View author publications](#)

You can also search for this author in [PubMed](#) [Google Scholar](#)

3. Yangkyun Oh

[View author publications](#)

You can also search for this author in [PubMed](#) [Google Scholar](#)

4. Minsoo Kyung

[View author publications](#)

You can also search for this author in [PubMed](#) [Google Scholar](#)

5. Eun-Kyoung Kim

[View author publications](#)

You can also search for this author in [PubMed](#) [Google Scholar](#)

6. In-Hwan Jang

[View author publications](#)

You can also search for this author in [PubMed](#) [Google Scholar](#)

7. Ji-Hoon Lee

[View author publications](#)

You can also search for this author in [PubMed](#) [Google Scholar](#)

8. Sang-Gyu Kim

[View author publications](#)

You can also search for this author in [PubMed](#) [Google Scholar](#)

9. Greg S. B. Suh

[View author publications](#)

You can also search for this author in [PubMed](#) [Google Scholar](#)

10. Won-Jae Lee

[View author publications](#)

You can also search for this author in [PubMed](#) [Google Scholar](#)

## Contributions

B.K. and M.I.K. conceived, designed, performed and analysed the experiments. Y.O., M.K., E.-K.K., I.-H.J., J.-H.L. and S.-G.K. performed the experiments. G.S.B.S. and W.-J.L. conceived and supervised the project and designed and analysed the experiments. G.S.B.S., W.-J.L. and B.K. wrote the manuscript.

## Corresponding authors

Correspondence to [Greg S. B. Suh](#) or [Won-Jae Lee](#).

## Ethics declarations

## Competing interests

The authors declare no competing interests.

## Additional information

**Peer review information** *Nature* thanks Catherine Schretter and the other, anonymous, reviewer(s) for their contribution to the peer review of this work. Peer reviewer reports are available.

**Publisher's note** Springer Nature remains neutral with regard to jurisdictional claims in published maps and institutional affiliations.

## Extended data figures and tables

### [Extended Data Fig. 1 Compensatory appetite for EAAs in amino-acid-deprived male flies, virgin female flies, \*poxn\*-mutant flies and mated female flies in which \*Ir76b\*<sup>+</sup> neurons or \*Dh44\*<sup>+</sup> neurons were inactivated.](#)

**a–c**, Two-choice preferences of wild-type *w<sup>1118</sup>* mated female (**a**), male (**b**) and virgin female (**c**) flies that had been fed (–) or had been deprived of amino acids for the indicated durations (5, 24, 48 and 72 h). Flies were given a choice between: l-EAA + l-NEAA + d-glucose and d-EAA + d-NEAA + d-glucose (**a**) or l-EAA + d-glucose and d-EAA + d-glucose (**b, c**). **d**, Food preferences of *w<sup>1118</sup>* mated female flies fed with diets containing different amounts of dietary yeast were given a choice between l-EAA + d-glucose and d-EAA + d-glucose. **e**, Food preferences of flies in which *Ir76b*<sup>+</sup> neurons had been inactivated by expressing tetanus toxin (TNT) (*Ir76b-LexA>LexAop-TNT* flies) were fed (–) or were deprived of amino acids for 48 h before the two-choice assay: l-EAA + d-glucose versus d-EAA + d-glucose. Flies carrying *Ir76b-LexA* alone or *LexAop-TNT* alone were used as controls. **f**, Two-choice preferences of control *w<sup>1118</sup>* and *poxn*<sup>–/–</sup> flies that had been deprived of amino acids for 48 h. **g**, Two-choice

preferences of flies carrying *Dh44-Gal4* and *UAS-Kir2.1* that had been fed (–) or had been deprived of amino acids for 48 h. Flies carrying *Dh44-Gal4* alone or *UAS-Kir2.1* alone were used as controls. Inactivation of  $\text{Dh}44^+$  neurons was achieved by expressing inwardly rectifying potassium channels (Kir2.1) in  $\text{Dh}44^+$  neurons. Data are mean  $\pm$  s.e.m. *P* values are indicated; unpaired two-tailed *t*-test in **a**; one-way ANOVA with Tukey's post-hoc test in **b–g**. *n* is experimental trials. Sample sizes and statistical analyses are shown in Supplementary Table 1. [Source data](#)

### Extended Data Fig. 2 Amino acid deprivation enhances the expression of *CNMa* in enterocytes, but not in intestinal stem cells, enteroblasts or enteroendocrine cells.

**a**, Normalized *CNMa* mRNA expression levels measured by qPCR in flies that were fed isocaloric diets containing varying amounts of dietary yeast for 5–6 days (*n* = 5). **b**, **c**, *CNMa* promoter activity in the gut of *CNMa-GAL4>UAS-GFP* flies that were fed an isocaloric diet containing 2% (low-amino-acid diet) versus 10% (high-amino-acid diet) of yeast for 7 days. Representative confocal images of the whole gut (**b**) and quantifications of the GFP fluorescence in the R2 segment of the anterior midgut (**c**) are shown. **d**, Representative confocal images showing enterocytes in the anterior R2 midgut that express *CNMa*. Intestinal stem cells (ISCs) and enteroblasts (EBs) were respectively marked by  $\beta$ -galactose ( $\beta$ -gal) staining of the gut in flies carrying *Delta-lacZ* (red), *CNMa-Gal4* and *UAS-GFP* (green) (top left), and in flies bearing *Su(H)-lacZ* (red), *CNMa-Gal4* and *UAS-GFP* (green) (top middle). Enteroendocrine cells (EEs) are labelled by anti-prospero antibody staining (red) (top right), whereas enterocytes (ECs) are identified on the basis of their large polyploid nuclei as revealed by DAPI staining (blue). In all cases, *CNMa* expression was visualized by GFP (green). A schematic representation of different intestinal cell types is shown. **e**, **f**, Representative confocal images of enterocytes in the R2 (**e**) and R4 (**f**) midgut regions of a fly carrying *NP1-Gal4* (enterocyte-specific driver) and *UAS-CD8-GFP* co-labelled with anti-GFP (green) and anti-*CNMa* (red) antibodies. Nuclei are stained with DAPI (blue). Scale bars, 200  $\mu\text{m}$  (**b**); 50  $\mu\text{m}$  (**c**); 10  $\mu\text{m}$  (**d–f**). Single-plane images are shown. Representative images are selected from at least 20 independent samples

collected in each experiment. Data are mean  $\pm$  s.e.m.  $P$  values are indicated; one-way ANOVA with Tukey's post-hoc test in **a**; unpaired two-tailed  $t$ -test in **c**. Sample sizes and statistical analyses are shown in Supplementary Table 1. [Source data](#)

**Extended Data Fig. 3 Amino acid deprivation has no effect on *CNMa* expression in the fat body or the brain, whereas EAA deprivation but not NEAA deprivation influences *CNMa* expression in the gut.**

**a, b**, Representative confocal images (left), the relative signal intensity of native GFP fluorescence (middle) and the numbers of GFP-positive cells (right) in the fat body (**a**) and the brain (**b**; insets show the dorsal region) in flies carrying *CNMa-Gal4* and *UAS-GFP* (green) that were fed a high-amino-acid versus a low-amino-acid diet. Nuclei in the fat body counterstained with DAPI (**a**, left), and the brain stained with anti-GFP antibody (green) and the neuropil marker nc82 (magenta) (**b**, left) are shown. The numbers of GFP-positive cells are as follows:  $41.00 \pm 7.28$  (high amino acids) and  $41.54 \pm 8.16$  (low amino acids) in the fat body;  $3.96 \pm 1.48$  (high amino acids) and  $3.29 \pm 1.33$  (low amino acids) in the brain. Scale bars,  $50 \mu\text{m}$  (**a, b**);  $10 \mu\text{m}$  (**b**, inset). **c, d**, EAA deprivation, but not NEAA deprivation, induced *CNMa* expression (**c**) and possibly mobilized intracellular calcium (**d**). Quantifications of GFP fluorescence in the R2 region of the anterior midgut in *CNMa-GAL4>UAS-GFP* flies (**c**) or *CNMa-GAL4>CaLexA* flies (**d**) that were fed with an EAA-deficient versus a NEAA-deficient diet for two days. **e, f**, Deficiency of a single EAA in a diet induced *CNMa* expression (**e**) and possibly mobilized intracellular calcium (**f**). Quantifications of GFP fluorescence in the R2 region in *CNMa-GAL4>UAS-GFP* flies (**e**) or *CNMa-GAL4>CaLexA* flies (**f**) that were fed with a holidic diet lacking a single EAA for three days. Data are mean  $\pm$  s.e.m.  $P$  values are indicated; unpaired two-tailed  $t$ -test in **a, b**; one-way ANOVA with Tukey's post-hoc test in **c–f**. Sample sizes and statistical analyses are shown in Supplementary Table 1. [Source data](#)

**Extended Data Fig. 4 Molecular characterization of *CNMa* and *CNMaR* knockout lines.**

**a, b**, The genomic loci of *CNMa* (**a**) and *CNMaR* (**b**) before and after the deletions were generated. The open reading frames and the cleavage sites used by gRNAs are indicated by yellow boxes and arrowheads, respectively. The gRNA-matching sequences are denoted in bold. Deleted regions were confirmed by sequencing of the genomic DNA; 20 base pairs (AGGAAGGAAGGCGATGGATT) and 2 base pairs (AC) were inserted in the deletion region of *CNMa* and *CNMaR* loci, respectively. **c**, The PCR analyses confirmed the lack of *CNMa* and *CNMaR* transcripts in *CNMa*<sup>−/−</sup> and *CNMaR*<sup>−/−</sup> flies, respectively. Representative images were selected from three independent samples collected in each experiment. [Source data](#)

**Extended Data Fig. 5 The activities of Tor and Gcn2 signalling pathways modulated by EAA deprivation regulate *CNMa* expression in the gut, but have no effect on *CNMa* expression in the brain or fat body.**

**a**, Two-choice behavioural preferences of amino-acid-deprived flies in which *UAS-CNMa*<sup>RNAi</sup> had been expressed specifically in the enterocytes (*NP1-Gal4*), fat body (*Cg-Gal4*) or neurons (*Nsyb-Gal4*). Flies carrying tissue-specific GAL4 alone were used as controls. **b, c**, Western blot analysis of phosphorylated eIF2α (p-eIF2α) and phosphorylated ribosomal protein S6K (p-S6K) in whole-gut lysates collected from mated female flies (around 5–6-days old) that were deprived of EAA (−EAA) for 48 h (**b**). The intensity of each band corresponding to phosphorylated eIF2α and S6K was quantified using the ImageJ automated digitizing program (NIH) (**c**). Results from three independent experiments were normalized against those in control flies, the average of which is arbitrarily set as 1. **d**, Quantifications of GFP fluorescence in the R2 region of the anterior midgut of *CNMa-Gal4>UAS-GFP* flies (control) or control flies carrying either *UAS-mRFP*, *UAS-ninaB*<sup>RNAi</sup>, *UAS-Gcn2*<sup>RNAi</sup>, *UAS-Atf4*<sup>RNAi</sup>, *UAS-Tor*<sup>WT</sup> or *UAS-Mitf*<sup>RNAi</sup>. **e, f**, Levels of *CNMa* expression in the brain or fat body of flies carrying *CNMa-Gal4* and *UAS-GFP* that also harboured either *UAS-Tor*<sup>WT</sup> or *UAS-Gcn2*<sup>RNAi</sup>. GFP signal intensities in the fat body (**e**) or brain (**f**) were measured by the native GFP fluorescence. Data are mean ± s.e.m. *P* values are indicated; unpaired two-tailed *t*-test in **a, c**; one-way ANOVA

with Tukey's post-hoc test in **d–f**. Sample sizes and statistical analyses are shown in Supplementary Table 1. [Source data](#)

### **Extended Data Fig. 6 Enhancement of the *CNMa* promoter activity by co-expression of *Atf4* and *Mitf*.**

The 5'-flanking region (−1573/+1) of the *CNMa* gene was used to generate a *pGL3-CNMa* reporter plasmid. *Drosophila* S2 cells were transfected with the *pGL3-CNMa* reporter plasmid with *pPac-Atf4* (*Atf4*), *pPac-Mitf* (*Mitf*) or both (*Atf4* + *Mitf*). Luciferase activities were measured at 48 h after transfection. The luciferase activity of the *pGL3-CNMa* reporter co-transfected with an empty pPac vector was arbitrarily set to 1. The relative luciferase activities are shown as the mean ± s.e.m. from three independent experiments. *P* values are indicated (one-way ANOVA with Tukey's post-hoc test). Statistical analyses are shown in Supplementary Table 1. [Source data](#)

### **Extended Data Fig. 7 *CNMaR*-expressing neurons are located in the anterior midgut and the brain and are not overlapped with *Ir76b*<sup>+</sup> neurons, and some respond to amino acid deprivation.**

**a, b**, Representative confocal images of the anterior midgut of an adult fly carrying *CNMaR-Gal4* and *UAS-CD8-GFP* that were co-labelled with anti-GFP antibody (green) and DAPI (blue) (**a**), and the brain of an adult fly carrying *Ir76b-Gal4>UAS-CD8-GFP* and *CNMaR-LexA>LexAop-tdT**Tomato*, probed with anti-GFP (green) and anti-DsRed (red) antibodies, illustrate two populations of neuronal processes: one from *Ir76b*<sup>+</sup> taste sensory neurons and another from *CNMaR*<sup>+</sup> central nervous system (CNS) neurons (**b**). **c**, Measurements of calcium mobilization by CaLexA reporter (green) in mated female flies carrying *CNMaR-Gal4>UAS-CaLexA* (flies of around 2 days old maintained for 5 days on a high-amino-acid diet containing 10% dietary yeast) that were subjected to amino acid deprivation by transferring half of the flies to an agar medium containing 100mM d-glucose only for 48 h (right, protein deprivation) or that continued on the high-amino-acid diet (left, no deprivation). Arrowheads denote the

enhancement of GFP intensity in the ellipsoid body (right). Scale bars, 200  $\mu\text{m}$  (**a**); 50  $\mu\text{m}$  (**b, c**). Z-stacked projection images are shown. Representative images were selected from at least five independent samples collected in each experiment. [Source data](#)

**Extended Data Fig. 8 Commensal bacteria influence CNMa expression in the gut, but not in the fat body or brain.**

**a**, Quantifications of GFP fluorescence in the R2 region of the gut of conventionally reared and GF female flies carrying *CNMa-Gal4>UAS-GFP* fed on 10% or 15% dietary yeast. **b, c**, The level of *CNMa* expression in the fat body (**b**) or the brain (**c**) of flies bearing *CNMa-Gal4* and *UAS-GFP* that had been reared in 10% dietary yeast were quantified using the GFP signal intensity measured by its native GFP fluorescence. **d**, Quantifications of GFP fluorescence in the R2 region of GF flies that had been mono-associated with *A. pomorum* or *L. plantarum* WJL. Data are mean  $\pm$  s.e.m. *P* values are indicated; one-way ANOVA with Tukey's post-hoc test in **a, d**; unpaired two-tailed *t*-test in **b, c**. Sample sizes and statistical analyses are shown in Supplementary Table 1. [Source data](#)

**Extended Data Fig. 9 Acetobacter colonization results in a significant increase in the amino acid absorption of the host and the suppression of the l-EAA preference through CNMaR-expressing neurons.**

**a**, Levels of ingested deuterium-labelled amino acids (l-leucine-5,5,5-d<sub>3</sub>, l-phenyl-d<sub>5</sub>-alanine-2,3,3-d<sub>3</sub> or l-glutamic acid-2,3,3,4,4-d<sub>5</sub>) in the haemolymph of GF control flies (−) fed on 5% sucrose alone and in the haemolymph of treated GF flies (+) fed on 5% sucrose containing deuterium-labelled amino acids (*n* = 3). **b**, Two-choice preferences of GF flies or GF flies that had been mono-associated with *A. pomorum* in which CNMaR<sup>+</sup> neurons were conditionally activated by the heat-inducible TrpA1 at 30 °C. Note that a significantly higher bacterial load (approximately 10 times higher number of colony-forming units) of intestinal *A. pomorum* was found in flies maintained at 30 °C than in flies maintained at 22 °C in which control experiments were conducted (data not shown). GF-Aceto, GF flies

mono-associated with *A. pomorum*; GF-Lacto, GF flies mono-associated with *L. plantarum* WJL. Data are mean  $\pm$  s.e.m. *P* values are indicated; one-way ANOVA with Tukey's post-hoc test in **a**, **b**. Sample sizes and statistical analyses are shown in Supplementary Table 1. [Source data](#)

## **Extended Data Fig. 10 CNMa expression and l-EAA preference are regulated by the microbiome and Tor signalling in the gut.**

**a**, Quantifications of GFP fluorescence in the R2 region of the gut of GF flies carrying *CNMa-Gal4>UAS-GFP* that had been mono-associated with *Acetobacter* that has a mutation in the *proC* gene (*Aceto<sup>ΔproC</sup>*) or the *leuB* gene (*Aceto<sup>ΔleuB</sup>*). Complementation of the *Aceto<sup>ΔleuB</sup>* strain was achieved by re-introducing the *leuB* gene to generate *Aceto<sup>ΔleuB\_leuB</sup>*. Dietary complementation of *Aceto<sup>ΔleuB</sup>* was achieved by adding 10 mM leucine to the diet. **b**, **c**, Representative confocal images (left) and quantifications of GFP fluorescence (right) in the R2 region of the gut (**b**) and two-choice preferences (**c**) of GF flies that had been mono-associated with *Acetobacter* that has a mutation in *ilvA* (*Aceto<sup>ΔilvA</sup>*). Dietary complementation of *Aceto<sup>ΔilvA</sup>* was achieved by adding 10 mM isoleucine to the diet. GF flies carrying *CNMa-Gal4>UAS-GFP* and GF *w<sup>1118</sup>* flies were used in **b** and **c**, respectively. **d**, Quantifications of GFP fluorescence in the R2 region of the gut of GF flies carrying *CNMa-Gal4>UAS-GFP* that had been mono-associated with an engineered strain of *L. plantarum* WJL that is capable of producing BCAAs (*Lacto<sup>BCAA</sup>*). Dietary complementation of *L. plantarum* WJL (*Lacto<sup>WT</sup>*) was achieved by adding 10 mM of leucine, isoleucine and valine to the diet (*Lacto<sup>WT</sup>* + BCAA). **e**, Representative confocal images (left) and quantifications of the GFP signal (right) in the anterior R2 midgut region of *Aceto<sup>ΔleuB</sup>* mono-associated GF flies carrying *CNMa-Gal4* and *UAS-GFP* (GF<sup>control</sup>), and flies carrying *CNMa-Gal4*, *UAS-GFP* and *UAS-Tor<sup>WT</sup>* (GF<sup>Tor-WT</sup>) on 10% dietary yeast, measured by the native GFP fluorescence. **f**, Two-choice preferences of *Aceto<sup>ΔleuB</sup>* mono-associated flies carrying enterocyte-specific *NPI-Gal4* (control), and flies carrying *NPI-Gal4* and *UAS-Tor<sup>WT</sup>* ( $n = 20$ ). Nuclei were stained with DAPI. Scale bars, 50  $\mu$ m (**b**, **e**). Data are mean  $\pm$  s.e.m. *P* values are indicated; one-way ANOVA with Tukey's post-hoc test in **a–d**; unpaired two-tailed *t*-test in **e**, **f**.

Sample sizes and statistical analyses are shown in Supplementary Table 1.  
[Source data](#)

## Supplementary information

### [Supplementary Figure 1](#)

Uncropped images of Western blot (related to Extended Data Figure 5b).

### [Reporting Summary](#)

### [Supplementary Tables](#)

This file contains Supplementary Tables 1-4. Supplementary Table 1 contains detailed descriptions of the experimental conditions, sample sizes, and statistical analyses that were used in this study. Supplementary Table 2 contains food sources for two choice assay that were used in this study. Supplementary Table 3 contains real-time qPCR primer sequences that were used in this study (related to Figure 1d and Extended Data Figure 2a). Supplementary Table 4 contains PCR primer sequences that were used in this study (related to Extended Data Figure 4c).

### [Peer Review File](#)

## Source data

### [Source Data Fig. 1](#)

### [Source Data Fig. 2](#)

### [Source Data Fig. 3](#)

### [Source Data Extended Data Fig. 1](#)

### [Source Data Extended Data Fig. 2](#)

[\*\*Source Data Extended Data Fig. 3\*\*](#)

[\*\*Source Data Extended Data Fig. 4\*\*](#)

[\*\*Source Data Extended Data Fig. 5\*\*](#)

[\*\*Source Data Extended Data Fig. 6\*\*](#)

[\*\*Source Data Extended Data Fig. 7\*\*](#)

[\*\*Source Data Extended Data Fig. 8\*\*](#)

[\*\*Source Data Extended Data Fig. 9\*\*](#)

[\*\*Source Data Extended Data Fig. 10\*\*](#)

## Rights and permissions

[Reprints and Permissions](#)

## About this article



Check for  
updates

## Cite this article

Kim, B., Kanai, M.I., Oh, Y. *et al.* Response of the microbiome–gut–brain axis in *Drosophila* to amino acid deficit. *Nature* **593**, 570–574 (2021).  
<https://doi.org/10.1038/s41586-021-03522-2>

[Download citation](#)

- Received: 24 March 2020
- Accepted: 08 April 2021
- Published: 05 May 2021
- Issue Date: 27 May 2021
- DOI: <https://doi.org/10.1038/s41586-021-03522-2>

## Comments

By submitting a comment you agree to abide by our [Terms](#) and [Community Guidelines](#). If you find something abusive or that does not comply with our terms or guidelines please flag it as inappropriate.

[Access through your institution](#)

[Change institution](#)

[Buy or subscribe](#)

Advertisement

---

This article was downloaded by **calibre** from <https://www.nature.com/articles/s41586-021-03522-2>

| [Section menu](#) | [Main menu](#) |

Cross-tissue organization of the fibroblast lineage

[Download PDF](#)

- Article
- [Published: 12 May 2021](#)

# Cross-tissue organization of the fibroblast lineage

- [Matthew B. Buechler<sup>1</sup>](#) na1,
- [Rachana N. Pradhan<sup>1</sup>](#) na1,
- [Akshay T. Krishnamurty](#) [ORCID: orcid.org/0000-0001-5382-1417<sup>1</sup>](#),
- [Christian Cox<sup>1</sup>](#),
- [Aslihan Karabacak Calviello<sup>1</sup>](#),
- [Amber W. Wang<sup>1</sup>](#),
- [Yeqing Angela Yang<sup>1</sup>](#),
- [Lucinda Tam<sup>1</sup>](#),
- [Roger Caothien<sup>1</sup>](#),
- [Merone Roose-Girma<sup>1</sup>](#),
- [Zora Modrusan<sup>1</sup>](#),
- [Joseph R. Aron<sup>1</sup>](#),
- [Richard Bourgon](#) [ORCID: orcid.org/0000-0002-5890-4374<sup>1</sup>](#),
- [Sören Müller](#) [ORCID: orcid.org/0000-0001-9490-5270<sup>1</sup>](#) &
- [Shannon J. Turley](#) [ORCID: orcid.org/0000-0002-0444-3031<sup>1</sup>](#)

[Nature](#) volume **593**, pages 575–579 (2021) [Cite this article](#)

- 16k Accesses
- 2 Citations
- 120 Altmetric
- [Metrics details](#)

## Subjects

- [Computational biology and bioinformatics](#)

- [Immunology](#)

## Abstract

Fibroblasts are non-haematopoietic structural cells that define the architecture of organs, support the homeostasis of tissue-resident cells and have key roles in fibrosis, cancer, autoimmunity and wound healing<sup>1</sup>. Recent studies have described fibroblast heterogeneity within individual tissues<sup>1</sup>. However, the field lacks a characterization of fibroblasts at single-cell resolution across tissues in healthy and diseased organs. Here we constructed fibroblast atlases by integrating single-cell transcriptomic data from about 230,000 fibroblasts across 17 tissues, 50 datasets, 11 disease states and 2 species. Mouse fibroblast atlases and a *Dpt*<sup>IRESCreERT2</sup> knock-in mouse identified two universal fibroblast transcriptional subtypes across tissues. Our analysis suggests that these cells can serve as a reservoir that can yield specialized fibroblasts across a broad range of steady-state tissues and activated fibroblasts in disease. Comparison to an atlas of human fibroblasts from perturbed states showed that fibroblast transcriptional states are conserved between mice and humans, including universal fibroblasts and activated phenotypes associated with pathogenicity in human cancer, fibrosis, arthritis and inflammation. In summary, a cross-species and pan-tissue approach to transcriptomics at single-cell resolution has identified key organizing principles of the fibroblast lineage in health and disease.

[Download PDF](#)

## Main

Fibroblasts populate all tissues, delineate the topography of organs by producing and remodelling extracellular matrix proteins (ECMs)<sup>2</sup> and support other tissue-resident cell types<sup>1,3</sup>. Fibroblasts perform functions associated with their lineage and specialized programs suited to the needs of specific tissue contexts to maintain organ homeostasis. Macrophages achieve generalized function and specialization via a lineage-wide core transcriptomic signature and tissue-specific programming driven by microenvironmental cues<sup>4,5,6</sup>. It is unclear how fibroblasts execute functions both common to their lineage and required by their organ of residence.

Technologies such as single-cell RNA-sequencing (scRNA-seq) have revealed intra-tissue fibroblast heterogeneity<sup>1</sup>. Elucidating the inter-tissue population structure of fibroblasts has clinical relevance, as subtypes of fibroblasts drive disease in arthritis<sup>7,8,9</sup>, cancer<sup>10,11,12</sup> and fibrotic indications such as idiopathic pulmonary fibrosis (IPF)<sup>2</sup>. Emerging paradigms<sup>7,10,13,14</sup> suggest that discrete fibroblast subtypes within tissues govern distinct aspects of tissue homeostasis and disease. Understanding

whether fibroblast phenotypes across indications are context-specific or more broadly conserved may inform therapeutic approaches. We hypothesized that fibroblast heterogeneity was promoted by tissue type in the steady-state and disease context during perturbation.

## Fibroblasts in steady-state mouse tissues

To investigate this hypothesis, we first performed bulk RNA-seq and assay for transposase-accessible chromatin with sequencing (ATAC-seq) on fluorescence-activated cell sorting (FACS)-sorted fibroblasts from multiple mouse tissues<sup>15</sup>. These data identified regions of open chromatin and transcriptional networks driven by tissue type, similar to recent reports<sup>15,16</sup> (Extended Data Figs. 1, 2, Supplementary Tables 1, 2). However, bulk sequencing cannot discriminate gene signatures that represent a single, homogeneous cell population from those that reflect the average of heterogeneous populations. To resolve this issue, we collected mouse scRNA-seq datasets enriched for non-haematopoietic cells from our laboratory and from public repositories. We removed non-fibroblast cells and corrected for cross-laboratory batch effects to produce a fibroblast-specific single-cell atlas composed of 28 datasets across 16 unperturbed tissues ( $n = 120,583$  cells; Fig. 1a, b, Extended Data Fig. 3a–c, Supplementary Table 3). An interactive data browser for the atlases is publicly available (see ‘Data availability’). Notably, our bulk RNA-seq and single-cell data were highly concordant, which indicates that our single-cell analytical approach did not introduce technical bias (Extended Data Fig. 3d).

**Fig. 1: Steady-state mouse fibroblast atlas.**

---

 **figure1**

**a**, Twenty-eight datasets for steady-state fibroblast atlas from 16 mouse tissues. **b**, Uniform manifold approximation and projection (UMAP) embedding of 120,583 single cells in the steady-state atlas. Ten clusters identified through graph-based clustering are indicated by colour. **c**, Heat map of the relative average expression of the most strongly enriched genes for each cluster ( $\log(\text{fold change})$ ) of one cluster versus all others,  $z$ -score by row) with key genes, functional annotation and tissue distributions listed. MSC, mesenchymal lineage cell; OLC, osteolineage cell. **d**, Pseudotime(s) visualized using principal curves representing trajectories of fibroblast differentiation across steady-state atlas with  $Pi16^+$  cluster set as root.

[Full size image](#)

In the steady-state atlas, ten clusters were identified on the basis of differential gene expression (Fig. 1b, c). The exact number of clusters in analyses of this type is data-driven but still somewhat subjective; some clusters were well-separated from others, while in other instances it is likely that an expression continuum, with intermediate states, exists. We identified more than 200 differentially expressed genes (DEGs) for each cluster and annotated clusters according to the dominant cluster-specific gene: *Pi16*<sup>+</sup>, *Col15a1*<sup>+</sup>, *Ccl19*<sup>+</sup>, *Coch*<sup>+</sup>, *Comp*<sup>+</sup>, *Cxcl12*<sup>+</sup>, *Fbln1*<sup>+</sup>, *Bmp4*<sup>+</sup>, *Npnt*<sup>+</sup> and *Hhip*<sup>+</sup> (Supplementary Table 4, Extended Data Fig. 3e). Known fibroblast-associated genes showed distinct expression across the clusters, confirming heterogeneity within the fibroblast lineage (Extended Data Fig. 3f). We were able to use tissue-distribution patterns and hallmark genes to ascribe functional identities to most clusters, including *Ccl19*<sup>+</sup> fibroblastic reticular cells (FRCs)<sup>3</sup>, *Coch*<sup>+</sup> red pulp fibroblasts<sup>17</sup>, *Cxcl12*<sup>+</sup> mesenchymal stromal cells and osteolineage cells<sup>18</sup>, *Fbln1*<sup>+</sup> and *Bmp4*<sup>+</sup> intestinal fibroblasts<sup>19</sup>, *Comp*<sup>+</sup> fibroblasts<sup>20</sup>, *Npnt*<sup>+</sup> alveolar fibroblasts and *Hhip*<sup>+</sup> peribronchial fibroblasts<sup>21</sup> (Fig. 1c, Extended Data Figs. 3g, 4a–p). The specialization of these clusters was reflected in differential enrichment of gene expression in core signalling pathways, including NFκB and TNF in the *Ccl19*<sup>+</sup> cluster and WNT signalling in the *Fbln1*<sup>+</sup> and *Bmp4*<sup>+</sup> clusters<sup>19</sup> (Extended Data Fig. 3h).

Notably, nearly all tissues contributed to the *Pi16*<sup>+</sup> and *Col15a1*<sup>+</sup> clusters, which suggests that these clusters are universal (Fig. 1c, Extended Data Fig. 3g). Genes that defined these two clusters differentiated fibroblasts from mesothelial cells in bulk RNA-seq data (Extended Data Fig. 4r–t). DEGs in the *Pi16*<sup>+</sup> cluster (*Pi16*, *Dpp4* and *Ly6c1*) suggested an identity similar to adventitial stromal cells<sup>22</sup>, which are found in vascular niches and can produce ECMs and acquire gene expression profiles consistent with specialized fibroblasts<sup>23,24</sup>. The *Col15a1*<sup>+</sup> cluster exhibited an association with the basement membrane, evidenced by expression of *Col4a1*, *Hspg2* and *Col15a1* (Extended Data Fig. 3i, Supplementary Table 4). The ubiquity of the universal *Pi16*<sup>+</sup> and *Col15a1*<sup>+</sup> subtypes across tissues and the elevated level of stemness-associated genes (*Cd34* and *Ly6a* (which encodes SCA1), Extended Data Fig. 3j), led us to investigate the potential for a developmental relationship among clusters. Slingshot lineage inference identified trajectories that emerged from the *Pi16*<sup>+</sup> cluster, passed through the *Col15a1*<sup>+</sup> cluster, and ended at specialized clusters (Fig. 1d).

Collectively, our analysis showed that in steady-state mouse tissues, universal (*Pi16*<sup>+</sup> and *Col15a1*<sup>+</sup>) and specialized fibroblast subtypes exist, and that these may be developmentally linked. The roles of universal fibroblasts include ECM secretion, with *Col15a1*<sup>+</sup> universal fibroblasts exhibiting the capacity to secrete basement

membrane proteins and the *Pi16*<sup>+</sup> subtype potentially serving as a resource cell that can develop into specialized fibroblasts.

## ***Dpt IRESCreERT2* mouse validates scRNA-seq**

To validate our scRNA-seq analysis, we used the surface markers SCA1 and LY6C (encoded by *Ly6c1*) to distinguish *Pi16*<sup>+</sup> (LY6C<sup>+</sup>SCA1<sup>+</sup>) and *Col15a1*<sup>+</sup> (LY6C<sup>-</sup>SCA1<sup>+</sup>) universal fibroblasts from specialized fibroblasts (LY6C<sup>-</sup>SCA1<sup>-</sup>; Extended Data Figs. 5a, 6a). Flow cytometry revealed that PDGFR $\alpha$ <sup>+</sup> fibroblasts could be sorted into these three groups across 11 tissues (Extended Data Fig. 6b,c). This approach confirmed the existence of bona fide universal and specialized phenotypes: expression of *Pi16* was enriched in LY6C<sup>+</sup>SCA1<sup>+</sup> fibroblasts, whereas markers of more specialized fibroblasts such as *Ccl19* (lymph node) and *Npnt* (lung) were enriched in LY6C<sup>-</sup> fibroblasts. Expression of dermatopontin (*Dpt*) was inversely correlated with specialization (Extended Data Fig. 6d,e). *Dpt* was diffusely expressed across the steady-state fibroblast atlas but was significantly enriched in *Pi16*<sup>+</sup> and *Col15a1*<sup>+</sup> universal fibroblasts, with highest expression in the *Pi16*<sup>+</sup> cluster. The intestine-specific *Fbln1*<sup>+</sup> cluster also showed *Dpt* expression at a level similar to the *Col15a1*<sup>+</sup> cluster (Extended Data Fig. 6e, Supplementary Table 4). Expression of *Dpt* and *Pi16* RNA in lung and small intestine was assayed histologically using RNAscope. *Dpt*<sup>+</sup>*Pi16*<sup>+</sup> cells were enriched near vascular structures in both tissues, as expected<sup>22</sup>. *Dpt*<sup>+</sup>*Pi16*<sup>-</sup> cells were observed in the lung parenchyma, in alignment with our predicted distribution of *Col15a1*<sup>+</sup> cells, and at the base of the villi in the small intestine, consistent with a lack of functional specialization<sup>19</sup> (Extended Data Fig. 6f).

We generated a genetically modified mouse model for tracking *Dpt*-expressing cells to test whether *Dpt* preferentially marked universal fibroblasts. An IresCreERT2 cassette, which requires the oestrogen receptor modulator tamoxifen for activity, was inserted downstream of the stop codon in exon 4 of *Dpt*. We crossed this strain with the *Rosa26LSLYFP* mouse line. The resulting *Dpt*<sup>IresCreERT2</sup>*Rosa26LSLYFP* mouse irreversibly marks *Dpt*<sup>IresCreERT2</sup>-positive cells and their progeny with yellow fluorescent protein (YFP) after tamoxifen administration (Extended Data Fig. 6g).

*Dpt*<sup>IresCreERT2</sup>*Rosa26LSLYFP* mice were given tamoxifen in their chow for 14 days. In the 11 tissues examined, PDGFR $\alpha$ <sup>+</sup> fibroblasts robustly expressed YFP (Fig. 2a, Extended Data Fig. 6h). Recombination efficiency varied across tissues: lymph nodes exhibited the lowest proportion of YFP<sup>+</sup> fibroblasts ( $28.7 \pm 5.5\%$  (mean  $\pm$  s.e.m.)) whereas the heart exhibited the highest ( $83.7 \pm 3.1\%$ ; Fig. 2b). Other cell types expressed little or no YFP (Extended Data Fig. 6i,j). FACS-sorted YFP-positive fibroblasts (sorted 14 days after *Dpt*<sup>IresCreERT2</sup> recombination) expressed higher levels

of *Pi16* and *Coll5a1* and lower levels of *Ccl19* and *Npnt* in the lymph node and lung, respectively, than YFP-negative fibroblasts. This suggests that *Dpt*-expressing cells are transcriptionally distinct from lymph node FRCs and lung alveolar fibroblasts (Extended Data Fig. [6k](#)). YFP<sup>+</sup> and YFP<sup>-</sup> fibroblasts expressed equivalent levels of *Csf1*, suggesting that both *Dpt*<sup>+</sup> and *Dpt*<sup>-</sup> fibroblasts are involved in macrophage homeostasis<sup>[25](#)</sup> (Extended Data Fig. [6l](#)).

**Fig. 2: *Dpt*<sup>IRESCreERT2</sup> marks universal fibroblasts.**

---

 **figure2**

**a**, Representative gating for YFP (*Dpt*) in pancreatic fibroblasts (live, EpCAM<sup>-</sup>CD45<sup>-</sup>CD31<sup>-</sup>PDPN<sup>+</sup>PDGFR $\alpha$ <sup>+</sup>). Red, *Dpt*<sup>IRESCreERT2ki/ki</sup>*Rosa26*<sup>LSLYFPwt/loxP</sup>; grey, *Dpt*<sup>IRESCreERT2wt/wt</sup>*Rosa26*<sup>LSLYFPwt/loxP</sup> mouse. Horizontal bar denotes the percentage of positive cells. **b**, Quantification of YFP<sup>+</sup> (*Dpt*<sup>+</sup>) cells. Frequency (blue

dots with mean, top  $x$ -axis) and cell number per milligram tissue (red boxplots, bottom  $x$ -axis). Percentage YFP $^+$  determined by subtracting fluorescence in  $Dpt^{IRES CreERT2ki/ki} Rosa26^{LSLYFPwt/loxP}$  mice from fluorescence in  $Dpt^{IRES CreERT2wt/wt} Rosa26^{LSLYFPwt/loxP}$  mice. **c**, YFP expression in LY6C $^+$ SCA1 $^+$ , LY6C $^-$ SCA1 $^+$  and SCA1 $^-$  fibroblasts from the lymph node in  $Ccl19^{YFP}$  mice. **d**, YFP expression in LY6C $^+$ SCA1 $^+$ , LY6C $^-$ SCA1 $^+$  and SCA1 $^-$  fibroblasts from lymph node in  $Grem1^{CreERT2wt/ki} Rosa26^{LSLYFPwt/loxP}$  mice treated with tamoxifen via intraperitoneal injection for 5 consecutive days, assayed on days 14–16 after first injection. Bars in **c**, **d** represent mean. **e**, YFP expression in LY6C $^+$ SCA1 $^+$ , LY6C $^-$ SCA1 $^+$  and SCA1 $^-$  fibroblasts from lymph node, omentum, lung, inguinal adipose, pancreas and skin (flank) in  $Dpt^{IRES CreERT2ki/ki} Rosa26^{LSLYFPwt/loxP}$  animals. Mean  $\pm$  s.e.m.  $n = 4$  (**b**) or 3 (**c–e**) or representative of 4 (**a**) biologically independent experiments with 4 (**b**), 7 (**c**), 10 (**d**) or 3 (**e**) mice. In **b**, centre lines in boxplots show median; box spans interquartile range, whiskers denote 10th–90th percentile. Each dot represents one mouse; mice received tamoxifen chow for 14 days and were analysed on days 14–16 (**b–d**). Subcut., subcutaneous adipose.

[Source data](#)

[Full size image](#)

The distinction between universal and specialized fibroblasts was also observed at the protein level via YFP expression in  $Ccl19^{YFP}$  (ref. [26](#)) and  $Gremlin1^{CreERT2} Rosa26^{LSLYFP}$  mice [27](#). Here, the fraction of YFP-expressing cells (denoting an FRC phenotype) increased from LY6C $^+$ SCA1 $^+$  ( $Pi16^+$ ) fibroblasts to LY6C $^-$ SCA1 $^+$  ( $Col15a1^+$ ) fibroblasts and further to SCA1 $^-$  (specialized) fibroblasts (Fig. [2c, d](#), Extended Data Fig. [5b, c](#)). YFP expression in  $Dpt^{Ires CreERT2}, Rosa26^{LSLYFP}$  mice showed the opposite trend in lymph node, lung, and other tissues (Fig. [2e](#), Extended Data Fig. [5d](#)). This evidence suggested that *Dpt* expression encompassed both of the universal fibroblast subtypes identified by scRNA-seq; therefore, we refer to these as  $Dpt^+Pi16^+$  and  $Dpt^+Col15a1^+$  universal fibroblasts.

## Fibroblasts in perturbed mouse tissues

We next investigated how fibroblasts are affected by infection, injury, cancer, fibrosis, metabolic changes and arthritis (Fig. [3a](#)). We integrated 17 publicly available scRNA-seq datasets across 13 tissues to generate a perturbed-state fibroblast atlas ( $n = 99,596$  cells; Fig. [3b, c](#), Extended Data Fig. [7a–c](#), Supplementary Table [3](#)). This approach showed ten clusters:  $Pi16^+$ ,  $Col15a1^+$ ,  $Ccl19^+$ ,  $Cxcl12^+$ ,  $Comp^+$ ,  $Npnt^+$ ,  $Hhip^+$ ,  $Adamdec1^+$ ,  $Cxcl5^+$  and  $Lrrc15^+$  (Fig. [3b, c](#), Extended Data Fig. [7d](#), Supplementary Table [5](#)). Clusters in the perturbed-state atlas displayed heterogeneous expression of

common fibroblast-associated genes (Extended Data Fig. 7e). In nearly all perturbed tissues and for all types of inflammation, some fibroblasts occupied the universal *Pi16*<sup>+</sup> and *Col15a1*<sup>+</sup> clusters, and these clusters expressed the highest levels of *Dpt* (Extended Data Figs. 7f, 8a–o, 1). The *Cxcl12*<sup>+</sup>, *Ccl19*<sup>+</sup>, *Comp*<sup>+</sup>, *Npnt*<sup>+</sup>, and *Hhip*<sup>+</sup> clusters were similar to the analogous steady-state clusters with respect to gene expression and tissue distribution (Fig. 3b,c, Extended Data Fig. 7g). Conversely, the *Cxcl5*<sup>+</sup>, *Adamdec1*<sup>+</sup> and *Lrrc15*<sup>+</sup> clusters appeared to represent perturbation-specific, activated fibroblast states that were not observed in the steady-state atlas.

**Fig. 3: Perturbed-state mouse fibroblast atlas.**

---

 **figure3**

**a**, Seventeen datasets for perturbed atlas from 13 perturbed mouse tissues. **b**, UMAP embedding of 99,596 cells in the perturbed-state atlas. Ten clusters identified through graph-based clustering are indicated by colour. Coloured clusters are universal (bold) or perturbation-specific; grey clusters have steady-state analogues. **c**, Heat map of the relative average expression of the most strongly enriched genes for each cluster (log(fold change) of one cluster versus all others, *z*-score by row). **d**, Representative

flow cytometry plots showing frequency of YFP<sup>+</sup> cells in LRRC15<sup>+</sup> fibroblasts from KPR3070 subcutaneous tumour at day 21 post-inoculation in *Dpt*<sup>iRESCreERT2ki/ki</sup>*Rosa26*<sup>LSLYFPwt/loxP</sup> mouse (representative of two biologically independent experiments).

[Full size image](#)

Fibroblasts from early muscle injury contributed the majority of cells to the *Cxcl5*<sup>+</sup> cluster and expressed chemokine genes such as *Ccl2* and *Ccl7* (Fig. 3c, Extended Data Fig. 8j,p). Analysis of co-regulated genes suggested that this cluster was driven by PI3K, TNF and NFκB signalling (Extended Data Fig. 8v). Cells in the *Adamdec1*<sup>+</sup> cluster were from colitis and showed upregulation of *Illi* and *Grem1* (Extended Data Figs. 7f, 8e,q). Gene expression in these cells was associated with MAPK signalling (Extended Data Fig. 8v). We subjected mice to DSS-induced colitis and found increased expression of *Grem1* in lesions as compared to healthy areas of the colon by RNAscope, validating the colitis-specific expression of *Grem1* in the mouse perturbed-state atlas (Extended Data Fig. 8w). The *Lrrc15*<sup>+</sup> cluster was composed of cells from arthritis, skin wound, fibrosis and small and large pancreatic ductal adenocarcinoma (PDAC; Extended Data Figs. 7f, 8a–o). This cluster showed high expression of *Cthrc1*, *Acta2*, *Postn* and *Adam12*, and of collagens, which suggests that these cells represented myofibroblasts (Extended Data Fig. 8p–u). The increase in collagens and TGFβ signalling is consistent with previous reports<sup>10</sup> (Extended Data Fig. 8v).

In perturbed tissues, universal *Dpt*<sup>+</sup>*Pi16*<sup>+</sup> fibroblasts maintained the highest expression of stemness-associated genes (Extended Data Fig. 8x). Lineage inference identified trajectories from *Dpt*<sup>+</sup>*Pi16*<sup>+</sup> through *Dpt*<sup>+</sup>*Col15a1*<sup>+</sup> and then on to perturbation-specific, activated *Cxcl5*<sup>+</sup> and *Lrrc15*<sup>+</sup> clusters or the *Adamdec1*<sup>+</sup> cluster (Extended Data Fig. 8y). We tested whether universal fibroblasts give rise to LRRC15<sup>+</sup> myofibroblasts using a subcutaneous tumour model in the *Dpt*<sup>iresCreERT2</sup>; *Rosa26*<sup>LSLYFP</sup> mouse. We found that 52 ± 7% of LRRC15<sup>+</sup> myofibroblasts were YFP<sup>+</sup> in *Dpt*<sup>iresCreERT2ki/ki</sup> mice (Fig. 3d, Extended Data Fig. 8z–b). This indicates that *Dpt*-expressing cells marked before tumour implantation can differentiate into LRRC15<sup>+</sup> myofibroblasts.

## Single-cell RNA-seq of human fibroblasts

We hypothesized that mice may exhibit some parity to humans in terms of steady- and perturbed-state fibroblast subtypes. We performed scRNA-seq on tumour and normal adjacent tissue (NAT) samples from three patients with pancreatic cancer and identified two subsets of fibroblasts ( $n = 21,262$  cells; Extended Data Fig. 9a–c,

Supplementary Tables 6, 7). Clusters c3 and c8 were annotated as cancer-associated fibroblasts (CAFs) and normal fibroblasts, respectively. Twelve of the 20 most upregulated genes in c8 were significantly upregulated in mouse steady-state *Dpt<sup>+</sup>Pi16<sup>+</sup>* (*DPT*, *IGFBP5*, *IGFBP6*, *C3*, *APOD*) or *Dpt<sup>+</sup>Col15a1<sup>+</sup>* (*CXCL12*, *SMOC2*, *C7*, *FBLN5*, *MFAP4*, *LUM*, *FMO2*) clusters (Supplementary Tables 4, 7). These 20 upregulated genes defined our human universal fibroblast expression module. To test whether c8 represented universal fibroblasts in humans, we inferred the abundance of these cells across tissues from the GTEx database ( $n = 5,961$  samples, Extended Data Fig. 9d, e). We found strong ( $r > 0.5$ ) co-expression of universal module genes in 12 human tissues, including normal pancreas (Extended Data Fig. 9f, g). At the single-cell level, the human universal module was observed in c8 pancreas and human adipose tissue (Extended Data Fig. 9h, i). We next scored samples from 122 patients with pancreatic cancer<sup>28</sup> for the human universal module as well as a human fibroblast activation program (20 most enriched genes in c3 versus c8; Extended Data Fig. 10a). There was a strong negative correlation between the universal and activated gene programs ( $r = -0.54$ ), which suggests that activation in human fibroblasts may be associated with loss of universal fibroblast gene expression (Extended Data Fig. 10b), reminiscent of the lineage relationship we observed in mice.

We investigated whether the transcriptional fibroblast subtypes we observed in humans had mouse orthologues and observed that the human c3 signature was enriched in the mouse *Lrrc15<sup>+</sup>* myofibroblast cluster (Extended Data Fig. 10c). This was not restricted to pancreatic cancer<sup>14</sup>: fibroblast signatures from human rheumatoid arthritis (RA)<sup>7,9</sup>, interstitial lung diseases<sup>29</sup>, IPF<sup>30</sup> and ulcerative colitis<sup>31</sup> also showed localized gene expression in the mouse *Lrrc15<sup>+</sup>* myofibroblast cluster (Extended Data Fig. 10c, Supplementary Table 8). We found evidence of universal fibroblasts in samples from patients with interstitial lung disease<sup>29</sup> and ulcerative colitis<sup>31</sup> (Extended Data Fig. 10d). Cells described as inflammatory fibroblasts across human samples and indications predominantly aligned with the universal clusters of the mouse perturbed-state atlas<sup>7,9,11</sup> (Extended Data Fig. 10e). We also observed that mouse IL-1<sup>+</sup> CAFs<sup>10</sup> localized to universal clusters in the mouse perturbed-state atlas (Extended Data Fig. 10f), suggesting that cells described as inflammatory fibroblasts may represent universal fibroblasts that have not undergone sufficient transcriptional change to constitute a new cell state.

Last, we composed a human perturbed-state fibroblast atlas by integrating c3 PDAC CAFs, colon fibroblasts from patients with colitis and lung fibroblasts from individuals with non-small cell lung cancer (NSCLC), IPF or COVID-19 (Fig. 4a). This human perturbed-state atlas ( $n = 10,355$  cells) exhibited six clusters (Fig. 4b, c, Supplementary Table 9). We observed expected clusters, including *NPNT<sup>+</sup>* alveolar fibroblasts<sup>21</sup> derived from individuals with lung disease, *ADAMDEC1<sup>+</sup>* and *CCL19<sup>+</sup>*<sup>31</sup> clusters primarily from colitis samples, and a *PII6<sup>+</sup>* cluster, in which the human

universal signature was most enriched (Fig. 4b, c, Extended Data Fig. 10g). We observed two myofibroblast clusters defined by *LRRC15*<sup>+</sup> and *COL3A1*<sup>+</sup> expression. *LRRC15*<sup>+</sup> myofibroblasts were enriched in cells from individuals with pancreatic and lung cancer, whereas the *COL3A1*<sup>+</sup> cluster was enriched in cells from patients with COVID-19 (Fig. 4d). Both myofibroblast subsets expressed high levels of collagens and ECM-modifying genes, including *CTHRC1* (Extended Data Fig. 10h, i). The human perturbed-state atlas validated aspects of the mouse perturbed-state atlas, including *LRRC15*<sup>+</sup> myofibroblasts and *ADAMDEC1*<sup>+</sup> fibroblasts, but also suggested that indication-specific stimuli or signal duration may drive additional myofibroblast populations in humans that were not seen in our mouse atlas.

**Fig. 4: Perturbed-state human fibroblast atlas.**

---

 **figure4**

**a**, Datasets for perturbation atlas from three perturbed human tissues. **b**, UMAP embedding of 10,355 cells in the perturbed-state human fibroblast atlas. Six clusters identified through graph-based clustering are indicated by colour. **c**, Heat map of relative average expression of the most strongly enriched genes for each cluster ( $\log(\text{fold change})$ ) of one cluster versus all others,  $z$ -score by row). **d**, Relative abundance of each disease in UMAP clusters.

[Full size image](#)

## Discussion

Fibroblasts have emerged as nexus cells that define the architecture of tissues, augment the function and positioning of other cell types, and have key roles in many diseases. We initially hypothesized that fibroblasts accomplish these diverse tasks through tissue-specific transcriptional programming. While our initial hypothesis was supported by bulk sequencing modalities, scRNA-seq across mouse tissues and perturbations led to a different conclusion—that the fibroblast lineage was compartmentalized into universal and specialized (steady-state) or activated (perturbed-state) subtypes. It is possible that fibroblast subsets may exhibit additional imprinting by their tissue of residence. Our scRNA-seq observations were supported experimentally by the *Dpt<sup>IresCreERT2</sup>* knock-in mouse. Our data suggest a paradigm in which *Dpt<sup>+</sup>* universal fibroblasts give rise to distinct subsets of fibroblasts across tissues, enabling this cell lineage to give rise to phenotypes that can execute the myriad functions ascribed to fibroblasts in the steady-state and in disease. In this paradigm, diverse tissues harbour *Dpt<sup>+</sup>* universal fibroblasts that can differentiate into activated fibroblasts during inflammation and, we speculate, into specialized fibroblasts during development. In this way, *Dpt<sup>+</sup>* universal fibroblasts operate as resource cells, providing functional plasticity to the fibroblast lineage.

Our data suggest concordance between fibroblast phenotypes in mice and humans. We confirmed that a subset of fibroblasts in human tissues has transcriptional similarities to mouse universal fibroblasts. Examination of human datasets representing an array of diseases identified mouse fibroblast orthologues, suggesting that our mouse perturbed-state atlas provides a basis for understanding fibroblast subtypes in human disease states. However, we observed a unique myofibroblast population that was enriched in patients with COVID-19, relative to the other human indications we analysed, which suggests that important inter-species or perturbation-specific differences may exist as well.

Our approach to understanding fibroblasts across tissues has identified both broad similarities and essential differences. Exposing the contours of fibroblast gene expression across tissues and activation states may help to clarify fibroblast subtyping and nomenclature. Open questions still remain about the spatial dynamics among fibroblast subtypes, the existence of other subtypes not captured in these datasets, and the structural or immune cells that promote specialization in the steady-state or activation during inflammation. It remains unclear why two universal *Dpt<sup>+</sup>* fibroblast subtypes exist, though we speculate that this may represent a necessary division of labour within the lineage. Overall, the organizing principles described here may enable a deeper understanding of the development, evolution and behaviour of universal, specialized and activated fibroblasts, which may in turn yield dividends for human medicine.

## Methods

## Mice

Wild-type mice were obtained from Jackson Laboratory (JAX; colony 00064) and maintained at Genentech. *Ccl19<sup>YFP</sup>* (ref. 32), *Grem1<sup>CreERT2</sup>* (ref. 27) and *Rosa26<sup>LSLYFP</sup>* mice were bred at Genentech. *Dpt<sup>IresCreERT2</sup>* mice were designed, generated and bred at Genentech. Male and female mice aged 6–12 weeks were used for all studies. For tamoxifen-induced cre expression, mice were injected with 2 mg tamoxifen (Sigma, cat. T5648) diluted in sunflower seed oil (Sigma, cat. 88921) for 5 consecutive days intraperitoneally or were fed chow containing tamoxifen (Envigo, cat. TD.130859). All experiments were performed under protocols approved by the Institutional Animal Care and Use Committee at Genentech. Other genotypes listed in Supplementary Table 3 were not bred in our facility but used in the integrated single-cell RNA-seq fibroblast atlases. No statistical methods were used to predetermine sample size. The experiments were not randomized and the investigators were not blinded to allocation during experiments and outcome assessment.

## Mouse tissue digestion and stromal cell isolation or identification by FACS

Tissues were isolated and fibroblasts and mesothelial cells were isolated as previously described<sup>15</sup>. In brief, tissues were obtained and minced, aside from the LN, omentum (neither minced) and bone (decapped, marrow removed and crushed). To isolate flank skin, hair was shaved, adipose tissue was removed and tissue was minced. Next, tissues were placed in a 15-ml conical tube with 5 ml digestion medium (RPMI + 2% FBS with 100 mg/ml Dispase (Life Tech., cat. 17105041), 100–200 mg/ml collagenase P (Roche, cat. 11249002001), and 50 mg/ml DNase I (Roche, cat. 10104159001)) and agitated. Tubes were placed in a 37 °C water bath for 15 min, and 5-ml fractions were removed and filtered (70 µm) into RPMI supplemented with 2% FCS (VWR) three times. For skin fibroblast scRNA-seq, skin was minced and digested in the enzymatic cocktail described above for 60 min. We used 200mg/ml collagenase P to isolate cells from dense tissues such as the spleen, liver, inguinal adipose, brown adipose and pancreas. After a single-cell suspension was obtained, the cells were layered on top of a 26% optiprep (Sigma, cat. D1556; diluted in phosphate buffered saline (PBS)) gradient in 15-ml conical tubes and spun at 1,500g for 15 min with slow acceleration and the brake off. Cells in suspension were isolated with a transfer pipette. After digestion, the preparations were incubated with Ack for 2–5 min to remove red blood cells.

Cells were labelled with the following monoclonal antibodies purchased from eBioscience, BioLegend, or BD Biosciences at 1:200 for 20–30 min, unless otherwise noted. Prior to cell surface staining with the following fluorescently labelled antibodies, cells were blocked with Fc block (2.4G2; 1:500–1:1,000, cat #553142).

Surface staining for experiments was performed as below, unless otherwise noted: CD45 (30-F11, cat. 564279), EPCAM (G8.8, cat. 118216), CD31 (390, cat. 612802 or 102524), PDGFR $\alpha$  (AP5, cat. 135906), PDPN (8.1.1; 1:800, cat. 127410), LY6C (HK1.4; 1:200, cat. 45-5932-82), SCA1 (D7; 1:200, cat. 108131), CD24 (M1/69; 1:200, cat. 612832) or LRRC15<sup>10</sup> (1:200, in-house). Live cells were identified by washing after Fc block and incubation with Fixable Viability Dye Violet (Invitrogen, cat. L34955, 1:1,000) before surface staining or incubation with calcein blue (Invitrogen, cat. C1429, 1:1,000) after surface staining. Data were acquired on a Fortessa, Symphony or LSRII (BD Biosciences) and analysed using FlowJo (Tree Star, v9.9.6) or cells were sorted on a Fusion or Aria (BD Biosciences). Data were presented using Prism (Graphpad, v9).

## qPCR, RNA extraction and cDNA synthesis

For each qPCR experiment, organs from 3–5 mice were pooled, digested and sorted by FACS. Total RNA was extracted from FACS-sorted cells using a QIAcube HT with the RNeasy Plus Mini Kit (QIAGEN, cat. 74134). cDNA were synthesized using the High Capacity cDNA Reverse Transcription Kit (Applied Biosystems, cat. 4368814) with an RNase Inhibitor (Applied Biosystems, cat. N8080119). Each cDNA sample was diluted 1:200–1:300 in RNase-free water before use in qPCR. qPCR was conducted using TaqMan Gene Expression Assay Probes for the genes *Pi16* (Mm00470084\_m1), *Col15a1* (Mm00456551\_m1), *Dpt* (Mm01273496\_m1), *Nppt* (Mm00473794\_m1), *Ccl19* (Mm00839967\_g1), *Csf1* (Mm00432686\_m1) and *Gapdh* (Mm99999915\_g1). Each TaqMan probe was diluted 1:10 in TaqMan Fast Advanced Master Mix (ThermoFisher, cat. 4444557) to create a TaqMan probe working solution. All qPCR reactions were carried out in a MicroAmp optical 384-well reaction plate. qPCR was performed using the QuantStudio 5 (Applied Biosystems) under the following cycling conditions: 1 cycle of 50 °C for 2 min and 95 °C for 10 min, followed by 40 cycles of 95 °C for 15 s and 60 °C for 1 min. The relative expression values were determined by: 1) subtracting the average  $C_t$  value of the gene of interest (GOI) from *Gapdh* (*Gapdh* – GOI) for each sample and 2) raising 2 to the power of (*Gapdh* – GOI). Data were presented using Prism (Graphpad, v9). Data points were called non-detectable if  $C_t$  values were over 36 or if replicates had a standard deviation greater than 1.

## Mouse scRNA-seq and cell hashing

Cells hashtagged with unique barcoded antibodies (Biolegend) were processed using Chromium Single Cell Gene Expression 3' v3 Library and Gel Bead Kit following the manufacturer's instructions (10X Genomics, Cat. PN-1000075). Cells were counted and checked for viability using Vi-CELL XR cell counter (Beckman Coulter), and then injected into microfluidic chips to form Gel Beads-in-Emulsion (GEMs) in the

10X Chromium instrument. Reverse transcription (RT) was performed on the GEMs, and RT products were purified and amplified. DNA from antibody-derived tags (ADTs) was separated from cDNA based on size selection using SPRIselect beads (Beckman Coulter, cat. B23318). Expression libraries and ADT libraries were generated and profiled using the Bioanalyzer High Sensitivity DNA kit (Agilent Technologies, cat. 5067-4626) and quantified with Kapa Library Quantification Kit (Roche, cat. 07960255001). Illumina HiSeq and NovaSeq (Illumina) were used to sequence the libraries.

## Tissue processing for histology

The small intestine or colon was removed, flushed with 10% neutral buffered formalin, and then cut into 1-inch-long strips from the duodenum, jejunum, ileum, and colon. The lung was removed and flushed with 10% neutral buffered formalin to inflate the tissue. A suture was then tied to the trachea to ensure the tissue stayed inflated while fixing in 10% neutral buffered formalin for 24 h. After fixation, the samples were transferred to 70% ethanol for 24 h and then processed for paraffin embedding. Once embedded, the blocks were trimmed on a Leica RM-2245 microtome until the centre of tissue was reached. Five-micrometre-thick sections were then collected for downstream analysis.

## RNAscope in situ hybridization

In situ hybridization (ISH) was performed using reagents and protocols from Advanced Cell Diagnostics (ACD). After sectioning, the slides were allowed to dry for 24 h before baking in an oven at 60 °C for 1 h. Sections were then rehydrated in two washes of xylene for 5 min each followed by two washes in 100% ethanol for 1 min each. After rehydration, endogenous peroxidase activity was quenched with hydrogen peroxide before the sections were boiled in antigen retrieval buffer (ACD, cat. 322500) for 15 min. After antigen retrieval, the sections were digested with proteinase (ACD, cat. 322330) for 25 min at 40 °C. After digestion, slides were washed twice for 1 min with ISH wash buffer (ACD, cat. 310091) then hybridized with probes of interest (*Grem1*-C1, cat. 314741; *Dpt*-C1 probe, 451311; *Pi16*-C1 and C2 probe; 451311 (C1) and 451318 (C2)) for 2 h at 40 °C. After hybridization, amplification steps were completed according to the ACD protocol. After the final amplification incubation, signal was detected with HRP-conjugated DAB (ACD, cat. 322360 and 322500), counterstained with haematoxylin for 30 s, then baked in an oven at 60 °C for 15 min before mounting with non-aqueous mounting medium.

## DSS-induced colitis

We added 3% (w/w) colitis-grade DSS (MP Biosciences, cat. 9011-18-1) to the drinking water for 7 days and then euthanized the animals and processed tissues for histology. The water was weighed daily to determine the average water consumption per cage. Mouse bodyweights were recorded daily and mice that lost 20% or more of their body weights were euthanized following IACUC standards

## Generation of *Dpt* *IresCreERT2* knock-in mouse

Homologous recombination and mouse embryonic stem (ES) cell technology<sup>33,34,35</sup> were used to generate a genetically modified mouse strain with a *Dpt*<sup>*IresCreERT2*</sup> knock-in. A gene-targeting vector was constructed with a 1,928-bp 5' arm of homology corresponding to GRCm38/mm10 chr1: 164,821,309–164,823,236 and a 1,810-bp arm of 3' homology corresponding to chr1: 164,823,237–164,825,046. IRES-CREERT2-SV40-FRT-pgk-neo-FRT was inserted immediately after the STOP codon (TAG) of exon 4. The final vector was confirmed by DNA sequencing, linearized and used to target C2 (C57BL/6N) ES cells using standard methods (G418 positive and ganciclovir negative selection)<sup>36</sup>.

C57BL/6N C2 ES cells<sup>37</sup> were electroporated with 20 µg linearized targeting vector DNA and cultured under drug selection essentially as described<sup>38</sup>. Positive clones were identified using long-range PCR followed by sequence confirmation. Correctly targeted ES cells were subjected to karyotyping. Euploid gene-targeted ES cell clones were treated with Adeno-FLP to remove PGK neomycin, ES cell clones were tested to identify clones with no copies of the PGK neomycin cassette, and the correct sequence of the targeted allele was verified. The presence of the Y chromosome was verified before microinjection into albino BALB/c embryos. Germline transmission was obtained after crossing the resulting chimaeras with C57BL/6N females. Genomic DNA from pups born was screened by long-range PCR to verify the desired gene targeted structure before mouse colony expansion. For genotyping, the following primers were used: 5'-CGCCAGTGGAAAGTTCA -3', 5'-TATAGGAACCTCGCTCGC -3' and 5'-GTGCTGTGCAAAGGAAG-3' amplified 329-bp wild-type and 278-bp knock-in DNA fragments.

## Tumour inoculation

Age-matched 6–10-week-old *Dpt*<sup>*IresCreERT2wt/wt*</sup> *Rosa26*<sup>LSLYFP</sup> and *Dpt*<sup>*IresCreERT2ki/ki*</sup> *Rosa26*<sup>LSLYFP</sup> mice received tamoxifen injections for 5 days, rested for 13–14 days and were inoculated subcutaneously in the right unilateral flank with  $1 \times 10^5$  KPR3070 tumour cells suspended in Hanks's buffered saline solution and phenol-red-free Matrigel (Corning, cat. 356237). Tumours were removed 21 days after implantation.

## **Human patient information**

Pancreatic cancer sample collection was approved by the Ethics Committee of Beijing Cancer Hospital. All patients in this study provided written informed consent.

## **Human tissue digestion and stromal cell isolation**

Samples were obtained and sequenced by Analytical Biosciences. Single cells were dissociated from tumour and adjacent non-cancer tissues as described previously<sup>39</sup>. In brief, tumours and adjacent non-cancer tissues were cut into approximately 1–2-mm<sup>3</sup> pieces in RPMI-1640 medium (Gibco) and enzymatically digested with gentleMACS (Miltenyi) for 60 min on a rotor at 37 °C, according to the manufacturer’s instructions. The dissociated cells were subsequently passed through a 100-µm SmartStrainer and centrifuged at 400g for 5 min. After the supernatant was removed, the pelleted cells were suspended in red blood cell lysis buffer (TIANDZ) and incubated on ice for 1–2 min to lyse red blood cells. After being washed twice with 1 × PBS (Gibco), the cell pellets were re-suspended in sorting buffer (PBS supplemented with 1% fetal bovine serum (FBS, Gibco)).

Single-cell suspensions were stained with antibodies against CD45 and 7AAD for FACS sorting, performed on a BD Aria SORP instrument. Based on FACS analysis, single cells were sorted into 1.5-ml tubes (Eppendorf) and counted manually under the microscope. The concentration of single cell suspensions was adjusted to 500–1,200 cells per µl. Cells were loaded at between 7,000 and 15,000 cells per chip position using the 10X Chromium Single cell 5' Library, Gel Bead & Multiplex Kit and Chip Kit (10X Genomics, V1.0 barcoding chemistry) according to the manufacturer’s instructions. All the subsequent steps were performed following the standard manufacturer’s protocols. Purified libraries were analysed using an Illumina Hiseq X Ten sequencer with 150-bp paired-end reads.

## **Mouse bulk RNA-seq analysis**

For ex vivo bulk RNA-seq, cells were isolated and stained as described above. Each tissue was represented by 2–3 individual replicates that were each derived by pooling tissues from 3–5 mice and FACS sorting cells directly into Trizol (Invitrogen, cat. 15596026). In some cases, lysed cells from at least three independent experiments were pooled for one replicate. In total, RNA was generated from an average of  $35,195 \pm 7,357$

(mean  $\pm$  s.e.m.) fibroblasts and  $17,318 \pm 7,618$  mesothelial cells. RNA was isolated as described<sup>40</sup> or at Expression Analysis, Inc.

Paired-end RNA-seq libraries were constructed from at least 747 pg of RNA using the SMART-Seq v4 ULTRA Low Input RNA Kit for Sequencing (Takara, cat. 634891) and NexteraXT kits (Illumina, cats. FC-131-1096 and FC-131-2001) for Low Input RNA Kits. Libraries were then sequenced on an Illumina HiSeq yielding, on average, 35 million read pairs ( $2 \times 50$  bp) per sample. Reads were aligned to the GENCODE basic mouse transcriptome index (M14) and transcript levels quantified using salmon with parameters --type quasi -k 25. Subsequently, counts were transformed into gene-level counts in R using the tximport package (<https://bioconductor.org/packages/release/bioc/html/ttximport.html>) package. Differential expression analysis taking batches into account was carried out on the gene by sample count matrix with DESeq2<sup>41</sup>, using a design of  $\sim 0 +$  condition + batch having a coefficient for each level of condition. For principal component analysis (PCA), log-transformed normalized counts (lengthScaledTPM) were batch corrected using Combat<sup>42</sup> and PCA was performed in the space of variable genes (coefficient of variation  $>0.3$ ). Gene set enrichment analysis (GSEA) using the fgsea method<sup>43</sup> was performed on genes ranked by their principal component 1 loadings using the top 20 marker genes for *Pi16*<sup>+</sup> and *Col15a1*<sup>+</sup> clusters from the steady-state fibroblast atlas.

## Mouse bulk ATAC-seq analysis

For ex vivo bulk ATAC-seq, cells were isolated and stained as described above. Each tissue was represented by 2–4 individual replicates that were each derived by pooling tissues from 3–5 mice and FACS-sorting fibroblasts. On average, 28,455 cells ( $\pm 5,325$  (s.e.m.)) were sorted per tissue. These cells were then frozen in Gibco Recovery Cell Culture Freezing Medium (ThermoFisher, cat. 12648010). The cells were then thawed in a 37 °C water bath, pelleted, washed with cold PBS, and fragmented as previously described<sup>44</sup>, with some modifications<sup>45</sup>. In brief, cell pellets were resuspended in lysis buffer, pelleted, and fragmented using the enzyme and buffer provided in the Nextera Library Prep Kit (Illumina,

cat. FC-121-1031). Tagmented DNA was then purified using the MinElute PCR purification kit (Qiagen, cat. 28004), amplified with 10 cycles of PCR, and purified using Agencourt AMPure SPRI beads (Beckman Coulter, cat. A63882). The resulting material was quantified using the KAPA Library Quantification Kit for Illumina platforms (Roche, 07960255001), and sequenced with PE42 sequencing on the NextSeq 500 sequencer (Illumina), with 42-bp paired-end reads. Library preparation and sequencing was performed by ActiveMotif, Inc.

Reads were aligned to the GRCm38/mm10 build of the mouse genome using GSnap<sup>46</sup> with parameters -M 2 -n 10 -B 2 -i 1 --pairmax-dna = 1000 --terminal-threshold = 1000 --gmap-mode = none --clip-overlap. Read pairs that aligned concordantly and uniquely to a single genomic location were retained for downstream analysis. PCR duplicates were removed using Picard MarkDuplicates (<http://broadinstitute.github.io/picard/>). Library depth-corrected coverage bigwig files were obtained to visualize the regions of interest.

## OCR identification

Open chromatin regions (OCRs) were identified as peaks on individual replicates and pooled samples combining the replicates of a given tissue using MACS2<sup>47</sup>, with parameters macs2 callpeak -f BAM --call-summits --nomodel-shift -95 --extsize 199 --keep-dup all -p 0.1 --call-summits (these choices of the shift and extsize parameters correct for the +5/-4 bp transposase insertion offset). The irreproducible discovery rate (IDR) pipeline<sup>48</sup> was used to assess peak concordance between the individual replicates of a given tissue, and these IDR estimates were subsequently appended to the associated pooled peaks. Robust peaks per tissue were defined as pooled peaks that overlapped at least 50% of a peak from at least two individual replicates and that passed an IDR threshold of 0.1. All robust peaks across all tissues were first centred on their summits (summit  $\pm$  199 bp) and then those that overlapped mitochondrial and noncanonical chromosomes were removed. Finally, all remaining peaks were merged to obtain the final set of all accessible regions ( $n = 207,803$ ). Per sample, reads that overlapped each region in the atlas were counted using the bedtools command multiBamCov<sup>49</sup>. To find tissue-specific OCRs, differential

accessibility analysis was conducted on the count matrix using DESeq2<sup>41</sup>, where the accessibility (that is, overlapping read count) of a given region in each tissue was compared against the count for that region in all other tissues. In this setting, the tissue-specific OCRs were defined according to the following criteria:  $\log_2(\text{fold change}) \geq 2$ , adjusted  $P$  value  $\leq 0.01$ . In addition, for each tissue a nondifferential/insignificant OCR set was defined according to:  $-0.585 \leq \log_2(\text{fold change}) \leq 0.585$ ,  $q$  value  $> 0.05$ .

## Motif enrichment analysis

For motif enrichment analysis, for each tissue-specific OCR set, an equally sized matched background set was selected on the basis of region length and GC content from among the nondifferential/insignificant OCRs, using MatchIt<sup>50</sup>. AME<sup>51</sup> from the MEME suite was used with default settings to assess the enrichment of a set of 321 position weight matrices (PWMs) from Homer (<http://homer.ucsd.edu/homer/>) in the tissue-specific OCR sets versus the background sets. Specifically, Fisher's exact test was used to compare the number of matches to a given PWM in the specific set versus the background set, and to assess statistical significance. Enriched PWMs were reported based on an adjusted  $P$  value threshold of 0.05.

## ATAC-seq and RNA-seq concordance

To compute the correlation of  $\log_2(\text{fold changes})$  inferred from the ATAC-seq and RNA-seq differential analyses, the ATAC-seq final atlas peaks were assigned to the gene with the closest transcription start site (TSS), using Gencode mouse M14 annotations and a distance threshold of 50 kb. Following the assignment, genes and atlas peaks with absolute  $\log_2(\text{fold change}) \geq 1$  and  $q$  value  $\leq 0.05$  in a given tissue were used in the correlation calculation.

An additional analysis to infer concordance between ATAC-seq and RNA-seq datasets was the BETA<sup>52</sup> analysis, which takes a set of peaks (tissue-specific OCRs from ATAC-seq) and differential gene expression results from RNA-seq. In short, BETA calculates a regulatory potential score based on the number of peaks in a fixed window (100 kb by default) around each

gene TSS and ranks the genes on the basis of this score. For each top gene set based on that rank, it calculates the percentage of the total up- and downregulated genes, as well as unregulated background genes, to provide *P* values for the overall up- or downregulation potential of the whole peak set. BETA was used with parameters -k BSF -g mm10 -n basic --df 0.1, for all pairwise tissue combinations, so for both matching and non-matching tissues.

## Mouse scRNA-seq meta-analysis

The steady-state fibroblast atlas was composed of 28 datasets<sup>10,18,19,20,21,31,53,54,55,56,57,58,59,60,61,62,63,64,65,66,67,68,69,70</sup> and the perturbed-state fibroblast atlas was composed of 17 datasets<sup>10,18,21,31,53,54,55,56,57,58,61,69,70,71</sup>. Integrated fibroblast atlases at steady and perturbed states were generated and analysed using the following steps: (1) processing and filtering individual scRNA-seq datasets from healthy and diseased tissues; (2) integrating healthy and diseased datasets separately to generate steady- and perturbed-state atlases; (3) clustering and annotation; and (4) trajectory inference. The aforementioned steps are described in detail in the following sections.

### (1) Processing and filtering individual scRNA-seq datasets

Single cell transcriptomics datasets, enriched in non-haematopoietic cells, generated using 10X Genomics and available as processed CellRanger files, were collected from public repositories and in-house lab datasets (Supplementary Table 3). For public datasets where processed files were not made available, we analysed raw data using cellranger count (CellRanger 2.1.0, 10X Genomics) using a custom reference package based on mouse reference genome GRCm38. A total of 32 scRNA-seq datasets representing multiple tissues and perturbations were analysed individually. In order to ensure comparability, for every individual dataset, we retained genes found in the Ensembl mouse (GRCm38) gene model, followed by implementing the Seurat single-cell analysis pipeline (version 3.9.9.9010)<sup>72,73</sup> in R (version 4.0.0). Specifically, for each dataset we filtered low quality cells with <500 measured genes and a high percentage

of mitochondrial contamination ( $>\sim 5\text{--}20\%$ , depending on the dataset). After filtering, data in each cell were normalized to  $\log(\text{CPM}/100+1)$ , the 2,000 most variable genes were identified, and the expression levels of these genes were scaled before performing PCA in variable gene space. Next, 20 principal components were used for graph-based clustering (resolution = 0.1) and UMAP dimensionality reduction was computed. All steps were performed using functions implemented in the Seurat package (NormalizeData, FindVariableFeatures, ScaleData, RunPCA, FindNeighbours, FindClusters, RunUMAP) with default parameters, except where mentioned. Cell clusters marked by the canonical marker gene for immune cells, *Ptprc* (*Cd45*), were discarded. All individual datasets devoid of  $\text{Cd45}^+$  cells were then used for integration to create two main atlases: (1) a steady-state fibroblast atlas comprising data from healthy tissues; and (2) a perturbed-state fibroblast atlas comprising data from diseased and inflamed tissues.

## (2) Dataset integration for steady- and perturbed-state atlases

Before dataset integration, we imported the aforementioned filtered, non-processed Seurat objects (not scaled) of healthy and diseased datasets, and determined a common gene space by retaining only those genes that were measured across all datasets (21,087 genes). Next, individual healthy and diseased Seurat objects were merged separately into two different steady- and perturbed-state objects, respectively. Each of these merged objects was normalized (function NormalizeData, method = ‘LogNormalize’, scale.factor = 10,000), and scaled to regress out the stress gene signature (computed using Seurat’s AddModuleScore) of subpopulations affected by tissue dissociation methods<sup>74</sup> before we performed PCA for the most variable genes. These processed, merged objects were next used for batch effect correction and integration using Harmony<sup>75</sup> (version 1.0). We adjusted the diversity clustering penalty parameter, theta, to 1. We then provided the top 20 harmony dimensions as an input for UMAP and visualized the first two UMAP dimensions at a clustering resolution of 0.1 for the  $\text{Cd45}^-$  atlases. Next, we identified distinct cell types using canonical marker genes such as *Sparc*, *Col3a1*, *Dcn* (fibroblasts), *Epcam* (epithelial cells), *Alb* (hepatocytes), *Pecam1* (endothelial cells), *Msln* (mesothelial

cells), *Rgs5* (mural cells: pericytes), *Myh11* (mural cells: smooth muscle cells), *Top2a* and *Mki67* (proliferating cells), and *Cd24a* (remnant immune cell populations) (Extended Data Figs. 3a–c, 7a–c). The computational pipeline for integration was iterated twice to generate the fibroblast atlases.

Specifically, at each of the following steps non-relevant or unwanted cell types were filtered followed by recalculation of the variable gene space, batch-effect correction and clustering to generate fibroblast-specific atlas for steady- and perturbed state: (1) a *Cd45<sup>-</sup>* steady- and perturbed-state atlas comprising 180,922 and 182,609 cells, respectively, and (2) a fibroblast-specific steady- and perturbed-state atlas comprising 120,697 and 99,596 cells, respectively, after selecting for *Dpt<sup>+</sup>Pdgfra<sup>+</sup>* fibroblast clusters from *Cd45<sup>-</sup>* atlases and discarding other stromal cells including endothelial and mesothelial cells, pericytes, smooth muscle cells and clusters with <1,000 cells.

### **(3) Clustering and annotation of steady- and perturbed-state fibroblast atlases**

Each fibroblast atlas was constructed from its *Cd45<sup>-</sup>* counterpart, in which the top 40 harmony dimensions were provided as an input for UMAP and visualized at a clustering resolution of 0.2. Differential gene expression was computed using the Seurat function FindAllMarkers using a Wilcoxon rank sum test and corrected for multiple testing using the Bonferroni method.

Gene expression scores were computed using Seurat's AddModuleScore function, visualized using VlnPlot or DotPlot. To determine markers for specialized or activated clusters relative to universal fibroblasts we used the Seurat function FindMarkers with default parameters. Next, we scored bulk tissue-specific signatures in the steady-state atlas, computed average scores per tissue signature across tissues represented in the steady-state atlas and visualized them using the ComplexHeatmap function Heatmap. We implemented the ClusterMap<sup>76</sup> algorithm using default parameters to identify matching steady- and perturbed-state clusters. ClusterMap compares clusters among two or more datasets via hierarchical clustering based on the binary expression patterns of marker genes. Next, similarity scores of matched clusters are determined from the clustering results.

To infer the activity of signalling pathways that govern different fibroblastic cells at steady state and after perturbation, we implemented the Bioconductor package PROGENy (1.10.0)<sup>77</sup>. For both fibroblast atlases, we implemented the same strategy. First, we down-sampled each atlas using the Seurat function subset with parameters ‘WhichCells(object, downsample, seed = 1)’ followed by implementing the function progeny with default parameters ‘scale = TRUE, organism = “Mouse”, top = 100, perm = 1, return.assay = TRUE’. We then summarized the progeny scores by cell population and visualized them as a heatmap using the function pheatmap.

#### (4) Pseudotime reconstruction and trajectory inference

Single-cell pseudotime trajectories for both steady and perturbed state maps were computed using the algorithm slingshot (version 1.6.1), which enables computation of lineage structures in a low-dimensional space<sup>78</sup>.

Specifically, slingshot was implemented in the analysis pipeline after dimensionality reduction and clustering of the integrated object. Each fibroblast object was first downsampled before trajectory inference. Pre-computed cell embeddings and clusters from the Seurat pipeline served as an input to the function slingshot (reducedDim = ‘UMAP’, clusterlabels = object\$ RNA\_snn\_res.0.2, start.clus = “Pi16”, extend = ‘n’, stretch = 0). The start cluster was chosen using prior biological knowledge and the expression of genes such as *Cd34* and *Ly6a*, known markers of progenitor-like cells. The wrapper function slingshot then performed lineage inference by treating clusters as nodes and constructing a minimum spanning tree (MST) between the nodes. Next, lineages or trajectories were defined by ordering clusters via tracing paths through the MST. Finally, individual pseudotime(s) were visualized using principal curves on the full fibroblast object.

### Human scRNA-seq meta-analysis

A human perturbed-state fibroblast atlas was constructed using scRNA-seq datasets generated with the 10X technology, from disease indications such as PDAC, idiopathic pulmonary fibrosis(IPF)<sup>29</sup>, COVID-19<sup>79</sup> and

ulcerative colitis<sup>31</sup> or SMART-seq2 technology in non-small cell lung carcinoma (NSCLC)<sup>80</sup>. Individual datasets were processed according to the description provided in ‘(1) Processing and filtering individual scRNA-seq datasets’, with the exception that LUM<sup>+</sup> fibroblasts were retained per dataset before final integration. Specifically, for COVID-19 we used data from individuals who had died from severe COVID-19-associated pneumonia. Next, we down-sampled the COVID-19 dataset to 2,500 cells, in order to mitigate the effects of over-representation of a dataset due to high cell number contribution. We then aggregated all the datasets, chose a common gene space (~17,000) and implemented the same pipeline as described in the section ‘(2) Dataset integration for steady- and perturbed-state atlases’. We adjusted the diversity clustering penalty parameter, theta, to 1, provided the top 30 harmony dimensions as an input for UMAP, and visualized the first two UMAP dimensions at a clustering resolution of 0.2. Differential gene expression analyses and visualization of markers were performed using Seurat functions described above. Note, in this meta-analysis we used datasets generated using 10X and SMART-seq2 technologies across a common cell type, fibroblasts. This is because a benchmarking study demonstrated the superior performance of Harmony batch-effect correction using single-cell data generated on different platforms for an identical cell type<sup>81</sup>.

## Bioinformatics data processing of human data

For the human pancreatic cancer single-cell data generated in our laboratory, raw sequencing data were transformed into FASTQ format with CellRanger’s (v2.1) mkfastq command, mapped to the human genome (GRCh38), and quantified with CellRanger count using default parameters. Quantified UMI count matrices from each patient were merged in R and analysed with the Seurat package (v 3.1.4). First, cells with <500 measured genes, or <2,700 UMIs, or >10% mitochondrial counts were removed from the dataset. In the resulting filtered dataset, data in each cell were normalized to  $\log(\text{CPM}/100 + 1)$ , the 2,000 most variable genes were identified, and the expression levels of these genes were scaled before PCA in the space of the most variable genes. Subsequently, 30 principal components were used for graph-based clustering (resolution = 0.1) and UMAP dimensionality reduction. All steps were performed with the

methods implemented in the Seurat package (NormalizeData, FindVariableFeatures, ScaleData, RunPCA, FindNeighbours, FindClusters, RunUMAP) and default parameters, except for parameters mentioned above. Markers for each cluster were identified using the FindAllMarkers function, limiting the maximum number of cells per cluster to 1,000 for runtime improvement. Genes that were differentially expressed between clusters 3 and 8 were detected using the FindMarkers function and default parameters. To map human expression signatures onto the mouse perturbed state map, human gene symbols were translated to their mouse orthologues and an enrichment score for the gene signature was calculated using Seurat's AddModuleScore function. Gene sets were identified within referenced papers (Supplementary Table 8).

Pseudo-bulk samples for co-expression analysis were generated from the human single-cell dataset using the following strategy: we randomly sampled 10% of cells from the pancreatic cancer single-cell dataset and pooled their reads into a bulk profile, which was subsequently normalized to  $\log_2(\text{CPM})$ . Using this strategy, we generated 100 bulk RNA-seq profiles with known proportions of cells from individual single-cell clusters. This allowed us to compare the expression of individual cluster 8 marker genes across pseudo-bulk samples both pairwise between genes and to the known cell type proportion of cluster 8 in the pseudo-bulks. Next, we generated similar bulk samples, but this time excluding cells from cluster 8 in the sampling process. On these samples we again calculated gene-by-gene correlation coefficients for C8 marker genes and compared the distributions of pairwise correlation coefficients to the distributions in the pseudo-bulk containing cells from cluster 8.

GTEX bulk RNA-seq data for normal tissues were obtained as batch-corrected, log-normalized counts from the UCSC Xenabrowser<sup>82</sup>. Pairwise correlations were visualized with the corrplot (<https://cran.r-project.org/web/packages/corrplot/>) package. For cross-tissue correlation analyses, only tissues with a median *DPT* expression  $>7.5$  were considered. In this analysis, the top 20 marker genes for cluster 8 of the single-cell dataset ordered by log(fold change), which were found in fewer than 15% of other cells, were used. For deconvolution of microdissected PDAC stromal samples, raw expression counts per sample ( $n = 122$ ) were

downloaded from GEO (GSE93326). Data were normalized to  $\log_2(\text{CPM} + 1)$ . Scores for cluster 8- and cluster 3-derived expression signatures (described above) in these bulk samples were calculated based on the average expression of the 20 most upregulated genes from the respective single-cell cluster (ordered by  $\log(\text{fold change})$ ), only genes expressed in at most 30% of other cells were considered).

## Pseudo-bulk analytical strategy

We first generated 100 pseudo-bulk RNA-seq profiles from our single-cell dataset with varying numbers of cells from individual single-cell clusters (Extended Data Fig. 9d, top). We observed that the expression of marker genes for fibroblast cluster 8 co-varied depending on the number of cells from cluster 8 in the bulks. As a consequence, their expression profiles were strongly correlated, but only if cells from cluster 8 were added to the pseudo-bulk. Leaving cells from cluster 8 out resulted in an extensive drop in gene-wise correlations to close to 0. Therefore, co-expression of a single-cell-derived marker gene set can be used to infer the presence or absence of a particular cell population in bulk RNA-seq.

## Projection of human gene sets onto mouse perturbed-state atlas

Gene expression signatures from human scRNA-seq datasets (Supplementary Table 7) corresponding to different fibroblast types were scored on the perturbed state atlas using the Seurat function AddModuleScore. The density of cells with the highest activation score (top 25th percentile for all clusters except in the Comp cluster (where we visualized the top 5th percentile)) was visualized using the function LSD::Heatscatter.

## Reporting summary

Further information on research design is available in the [Nature Research Reporting Summary](#) linked to this paper.

## Data availability

Raw and processed RNA-seq, ATAC-seq and mouse healthy skin scRNA-seq datasets are available from the ArrayExpress repository under the accession numbers [E-MTAB-10324](#), [E-MTAB-10316](#) and [E-MTAB-10315](#), respectively. Supplementary Table 3 lists the studies used to generate the *Cd45<sup>-</sup>* maps and fibroblast atlases. These integrated scRNA-seq objects used for analysis are provided in an online resource that can be accessed at <https://fibroXplorer.com>. Human pancreatic cancer single-cell data are available in the EGA database under accession EGAD00001005365. [Source data](#) are provided with this paper.

## Code availability

No new algorithms were developed for this manuscript. All code generated for analysis is available from the authors upon request.

## References

1. 1.

Koliaraki, V., Prados, A., Armaka, M. & Kollias, G. The mesenchymal context in inflammation, immunity and cancer. *Nat. Immunol.* **21**, 974–982 (2020).

[CAS](#) [Google Scholar](#)

2. 2.

Hinz, B. & Lagares, D. Evasion of apoptosis by myofibroblasts: a hallmark of fibrotic diseases. *Nat. Rev. Rheumatol.* **16**, 11–31 (2020).

[CAS](#) [Google Scholar](#)

3. 3.

Buechler, M. B. & Turley, S. J. A short field guide to fibroblast function in immunity. *Semin. Immunol.* **35**, 48–58 (2018).

[CAS](#) [Google Scholar](#)

4. 4.

Gautier, E. L. et al. Gene-expression profiles and transcriptional regulatory pathways that underlie the identity and diversity of mouse tissue macrophages. *Nat. Immunol.* **13**, 1118–1128 (2012).

[CAS](#) [PubMed](#) [PubMed Central](#) [Google Scholar](#)

5. 5.

Gosselin, D. et al. Environment drives selection and function of enhancers controlling tissue-specific macrophage identities. *Cell* **159**, 1327–1340 (2014).

[CAS](#) [PubMed](#) [PubMed Central](#) [Google Scholar](#)

6. 6.

Lavin, Y. et al. Tissue-resident macrophage enhancer landscapes are shaped by the local microenvironment. *Cell* **159**, 1312–1326 (2014).

[CAS](#) [PubMed](#) [PubMed Central](#) [Google Scholar](#)

7. 7.

Croft, A. P. et al. Distinct fibroblast subsets drive inflammation and damage in arthritis. *Nature* **570**, 246–251 (2019).

[ADS](#) [CAS](#) [PubMed](#) [PubMed Central](#) [Google Scholar](#)

8. 8.

Wei, K. et al. Notch signalling drives synovial fibroblast identity and arthritis pathology. *Nature* **582**, 259–264 (2020).

[ADS](#) [CAS](#) [PubMed](#) [PubMed Central](#) [Google Scholar](#)

9. 9.

Zhang, F. et al. Defining inflammatory cell states in rheumatoid arthritis joint synovial tissues by integrating single-cell transcriptomics and mass cytometry. *Nat. Immunol.* **20**, 928–942 (2019).

[PubMed](#) [PubMed Central](#) [Google Scholar](#)

10. 10.

Dominguez, C. X. et al. Single-cell RNA sequencing reveals stromal evolution into LRRC15+ myofibroblasts as a determinant of patient response to cancer immunotherapy. *Cancer Discov.* **10**, 232–253 (2020).

[CAS](#) [Google Scholar](#)

11. 11.

Elyada, E. et al. Cross-species single-cell analysis of pancreatic ductal adenocarcinoma reveals antigen-presenting cancer-associated fibroblasts. *Cancer Discov.* **9**, 1102–1123 (2019).

[CAS](#) [PubMed](#) [PubMed Central](#) [Google Scholar](#)

12. 12.

Lambrechts, D. et al. Phenotype molding of stromal cells in the lung tumor microenvironment. *Nat. Med.* **24**, 1277–1289 (2018).

[CAS](#) [Google Scholar](#)

13. 13.

Öhlund, D. et al. Distinct populations of inflammatory fibroblasts and myofibroblasts in pancreatic cancer. *J. Exp. Med.* **214**, 579–596 (2017).

[PubMed](#) [PubMed Central](#) [Google Scholar](#)

14. 14.

Rinkevich, Y. et al. Identification and isolation of a dermal lineage with intrinsic fibrogenic potential. *Science* **348**, aaa2151 (2015).

[PubMed](#) [PubMed Central](#) [Google Scholar](#)

15. 15.

Buechler, M. B. et al. A stromal niche defined by expression of the transcription factor WT1 mediates programming and homeostasis of cavity-resident macrophages. *Immunity* **51**, 119–130.e5 (2019).

[CAS](#) [PubMed](#) [PubMed Central](#) [Google Scholar](#)

16. 16.

Krausgruber, T. et al. Structural cells are key regulators of organ-specific immune responses. *Nature* **583**, 296–302 (2020).

[ADS](#) [CAS](#) [PubMed](#) [PubMed Central](#) [Google Scholar](#)

17. 17.

Bellomo, A. et al. Reticular fibroblasts expressing the transcription factor WT1 define a stromal niche that maintains and replenishes splenic red pulp macrophages. *Immunity* **53**, 127–142.e7 (2020).

[CAS](#) [Google Scholar](#)

18. 18.

Baryawno, N. et al. A cellular taxonomy of the bone marrow stroma in homeostasis and leukemia. *Cell* **177**, 1915–1932.e16 (2019).

[CAS](#) [PubMed](#) [PubMed Central](#) [Google Scholar](#)

19. 19.

McCarthy, N. et al. Distinct mesenchymal cell populations generate the essential intestinal BMP signaling gradient. *Cell Stem Cell* **26**, 391–402.e5 (2020).

[CAS](#) [PubMed](#) [PubMed Central](#) [Google Scholar](#)

20. 20.

Wirka, R. C. et al. Atheroprotective roles of smooth muscle cell phenotypic modulation and the TCF21 disease gene as revealed by single-cell analysis. *Nat. Med.* **25**, 1280–1289 (2019).

[CAS](#) [PubMed](#) [PubMed Central](#) [Google Scholar](#)

21. 21.

Tsukui, T. et al. Collagen-producing lung cell atlas identifies multiple subsets with distinct localization and relevance to fibrosis. *Nat. Commun.* **11**, 1920 (2020).

[ADS](#) [CAS](#) [PubMed](#) [PubMed Central](#) [Google Scholar](#)

22. 22.

Dahlgren, M. W. & Molofsky, A. B. Adventitial cuffs: regional hubs for tissue immunity. *Trends Immunol.* **40**, 877–887 (2019).

[CAS](#) [PubMed](#) [PubMed Central](#) [Google Scholar](#)

23. 23.

Sitnik, K. M. et al. Context-dependent development of lymphoid stroma from adult CD34<sup>+</sup> adventitial progenitors. *Cell Rep.* **14**, 2375–2388 (2016).

[CAS](#) [Google Scholar](#)

24. 24.

Merrick, D. et al. Identification of a mesenchymal progenitor cell hierarchy in adipose tissue. *Science* **364**, eaav2501 (2019).

[CAS](#) [PubMed](#) [PubMed Central](#) [Google Scholar](#)

25. 25.

Zhou, X. et al. Circuit design features of a stable two-cell system. *Cell* **172**, 744–757.e17 (2018).

[CAS](#) [PubMed](#) [PubMed Central](#) [Google Scholar](#)

26. 26.

Chai, Q. et al. Maturation of lymph node fibroblastic reticular cells from myofibroblastic precursors is critical for antiviral immunity. *Immunity* **38**, 1013–1024 (2013).

[CAS](#) [PubMed](#) [PubMed Central](#) [Google Scholar](#)

27. 27.

Kapoor et al.

28. 28.

Maurer, C. et al. Experimental microdissection enables functional harmonisation of pancreatic cancer subtypes. *Gut* **68**, 1034–1043 (2019).

[CAS](#) [PubMed](#) [PubMed Central](#) [Google Scholar](#)

29. 29.

Habermann, A. C. et al. Single-cell RNA sequencing reveals profibrotic roles of distinct epithelial and mesenchymal lineages in pulmonary fibrosis. *Sci. Adv.* **6**, eaba1972 (2020).

[ADS](#) [CAS](#) [PubMed](#) [PubMed Central](#) [Google Scholar](#)

30. 30.

Emblom-Callahan, M. C. et al. Genomic phenotype of non-cultured pulmonary fibroblasts in idiopathic pulmonary fibrosis. *Genomics* **96**, 134–145 (2010).

[CAS](#) [Google Scholar](#)

31. 31.

Kinchen, J. et al. Structural remodeling of the human colonic mesenchyme in inflammatory bowel disease. *Cell* **175**, 372–386.e17 (2018).

[CAS](#) [PubMed](#) [PubMed Central](#) [Google Scholar](#)

32. 32.

Cremasco, V. et al. B cell homeostasis and follicle confines are governed by fibroblastic reticular cells. *Nat. Immunol.* **15**, 973–981 (2014).

[CAS](#) [PubMed](#) [PubMed Central](#) [Google Scholar](#)

33. 33.

Kuehn, M. R., Bradley, A., Robertson, E. J. & Evans, M. J. A potential animal model for Lesch-Nyhan syndrome through introduction of HPRT mutations into mice. *Nature* **326**, 295–298 (1987).

[ADS](#) [CAS](#) [Google Scholar](#)

34. 34.

Smithies, O., Gregg, R. G., Boggs, S. S., Koralewski, M. A. & Kucherlapati, R. S. Insertion of DNA sequences into the human chromosomal  $\beta$ -globin locus by homologous recombination. *Nature* **317**, 230–234 (1985).

[ADS](#) [CAS](#) [Google Scholar](#)

35. 35.

Thomas, K. R., Folger, K. R. & Capecchi, M. R. High frequency targeting of genes to specific sites in the mammalian genome. *Cell* **44**, 419–428 (1986).

[CAS](#) [PubMed](#) [PubMed Central](#) [Google Scholar](#)

36. 36.

Newman, R. J., Roose-Girma, M. & Warming, S. Efficient conditional knockout targeting vector construction using co-selection BAC recombineering (CoSBR). *Nucleic Acids Res.* **43**, e124 (2015).

[PubMed](#) [PubMed Central](#) [Google Scholar](#)

37. 37.

Gertsenstein, M. et al. Efficient generation of germ line transmitting chimeras from C57BL/6N ES cells by aggregation with outbred host embryos. *PLoS ONE* **5**, e11260 (2010).

[ADS](#) [PubMed](#) [PubMed Central](#) [Google Scholar](#)

38. 38.

Hughes, E. D. & Saunders, T. L. *Advanced Protocols for Animal Transgenesis, An ISTT Manual* 291–325 (Springer, 2011).

39. 39.

Zhang, L. et al. Single-cell analyses inform mechanisms of myeloid-targeted therapies in colon cancer. *Cell* **181**, 442–459.e29 (2020).

[CAS](#) [PubMed](#) [PubMed Central](#) [Google Scholar](#)

40. 40.

Painter, M. W. et al. Transcriptomes of the B and T lineages compared by multiplatform microarray profiling. *J. Immunol.* **186**, 3047–3057 (2011).

[CAS](#) [PubMed](#) [PubMed Central](#) [Google Scholar](#)

41. 41.

Love, M. I., Huber, W. & Anders, S. Moderated estimation of fold change and dispersion for RNA-seq data with DESeq2. *Genome Biol.* **15**, 550 (2014).

[PubMed](#) [PubMed Central](#) [Google Scholar](#)

42. 42.

Johnson, W. E., Li, C. & Rabinovic, A. Adjusting batch effects in microarray expression data using empirical Bayes methods. *Biostatistics* **8**, 118–127 (2007).

[PubMed](#) [PubMed Central](#) [MATH](#) [Google Scholar](#)

43. 43.

Korotkevich, G., Sukhov, V. & Sergushichev, A. Fast gene set enrichment analysis. Preprint at <https://doi.org/10.1101/060012> (2021).

44. 44.

Buenrostro, J. D., Giresi, P. G., Zaba, L. C., Chang, H. Y. & Greenleaf, W. J. Transposition of native chromatin for fast and sensitive epigenomic profiling of open chromatin, DNA-binding proteins and nucleosome position. *Nat. Methods* **10**, 1213–1218 (2013).

[CAS](#) [PubMed](#) [PubMed Central](#) [Google Scholar](#)

45. 45.

Corces, M. R. et al. An improved ATAC-seq protocol reduces background and enables interrogation of frozen tissues. *Nat. Methods* **14**, 959–962 (2017).

[CAS](#) [PubMed](#) [PubMed Central](#) [Google Scholar](#)

46. 46.

Wu, T. D. & Nacu, S. Fast and SNP-tolerant detection of complex variants and splicing in short reads. *Bioinformatics* **26**, 873–881 (2010).

[CAS](#) [PubMed](#) [PubMed Central](#) [Google Scholar](#)

47. 47.

Zhang, Y. et al. Model-based analysis of ChIP-seq (MACS). *Genome Biol.* **9**, R137 (2008).

[PubMed](#) [PubMed Central](#) [Google Scholar](#)

48. 48.

Li, Q., Brown, J. B., Huang, H. & Bickel, P. J. Measuring reproducibility of high-throughput experiments. *Ann. Appl. Stat.* **5**, 1752–1779 (2011).

[MathSciNet](#) [MATH](#) [Google Scholar](#)

49. 49.

Quinlan, A. R. & Hall, I. M. BEDTools: a flexible suite of utilities for comparing genomic features. *Bioinformatics* **26**, 841–842 (2010).

[CAS](#) [PubMed](#) [PubMed Central](#) [Google Scholar](#)

50. 50.

Ho, D. E., Imai, K., King, G. & Stuart, E. A. MatchIt: nonparametric preprocessing for parametric causal inference. *J. Stat. Softw.* **42**, 1–28 (2011).

[Google Scholar](#)

51. 51.

McLeay, R. C. & Bailey, T. L. Motif enrichment analysis: a unified framework and an evaluation on ChIP data. *BMC Bioinformatics* **11**, 165 (2010).

[PubMed](#) [PubMed Central](#) [Google Scholar](#)

52. 52.

Wang, S. et al. Target analysis by integration of transcriptome and ChIP-seq data with BETA. *Nat. Protoc.* **8**, 2502–2515 (2013).

[CAS](#) [PubMed](#) [PubMed Central](#) [Google Scholar](#)

53. 53.

Soliman, H. et al. Pathogenic potential of Hic1-expressing cardiac stromal progenitors. *Cell Stem Cell* **26**, 205–220.e8 (2020).

[CAS](#) [Google Scholar](#)

54. 54.

Dobie, R. et al. Single-cell transcriptomics uncovers zonation of function in the mesenchyme during liver fibrosis. *Cell Rep.* **29**, 1832–1847.e8 (2019).

[CAS](#) [PubMed](#) [PubMed Central](#) [Google Scholar](#)

55. 55.

Xiong, X. et al. Landscape of intercellular crosstalk in healthy and NASH liver revealed by single-cell secretome gene analysis. *Mol. Cell* **75**, 644–660.e5 (2019).

[CAS](#) [PubMed](#) [PubMed Central](#) [Google Scholar](#)

56. 56.

Dahlgren, M. W. et al. Adventitial stromal cells define group 2 innate lymphoid cell tissue niches. *Immunity* **50**, 707–722.e6 (2019).

[CAS](#) [PubMed](#) [PubMed Central](#) [Google Scholar](#)

57. 57.

Peyser, R. et al. Defining the activated fibroblast population in lung fibrosis using single-cell sequencing. *Am. J. Respir. Cell Mol. Biol.* **61**, 74–85 (2019).

[CAS](#) [Google Scholar](#)

58. 58.

Xie, T. et al. Single-cell deconvolution of fibroblast heterogeneity in mouse pulmonary fibrosis. *Cell Rep.* **22**, 3625–3640 (2018).

[CAS](#) [PubMed](#) [PubMed Central](#) [Google Scholar](#)

59. 59.

Koga, S. et al. Peripheral PDGFR $\alpha^+$  gp38 $^+$  mesenchymal cells support the differentiation of fetal liver–derived ILC2. *J. Exp. Med.* **278**, jem.20172310-23 (2018).

[Google Scholar](#)

60. 60.

Dell'Orso, S. et al. Single cell analysis of adult mouse skeletal muscle stem cells in homeostatic and regenerative conditions. *Development* **146**, dev181743 (2019).

[PubMed](#) [PubMed Central](#) [Google Scholar](#)

61. 61.

Scott, R. W., Arostegui, M., Schweitzer, R., Rossi, F. M. V. & Underhill, T. M. Hic1 defines quiescent mesenchymal progenitor subpopulations with distinct functions and fates in skeletal muscle regeneration. *Cell Stem Cell* **25**, 797–813.e9 (2019).

[CAS](#) [PubMed](#) [PubMed Central](#) [Google Scholar](#)

62. 62.

Buechler, M. B. & Turley, S. J. Neutrophils follow stromal omens to limit peritoneal inflammation. *Immunity* **52**, 578–580 (2020).

[CAS](#) [Google Scholar](#)

63. 63.

Davidson, S. et al. Single-cell RNA sequencing reveals a dynamic stromal niche that supports tumor growth. *Cell Rep.* **31**, 107628 (2020).

[CAS](#) [PubMed](#) [PubMed Central](#) [Google Scholar](#)

64. 64.

Cheng, H.-W. et al. Origin and differentiation trajectories of fibroblastic reticular cells in the splenic white pulp. *Nat. Commun.* **10**, 1739 (2019).

[ADS](#) [PubMed](#) [PubMed Central](#) [Google Scholar](#)

65. 65.

Burl, R. B. et al. Deconstructing adipogenesis induced by  $\beta$ 3-adrenergic receptor activation with single-cell expression profiling. *Cell Metab.* **28**, 300–309.e4 (2018).

[CAS](#) [PubMed](#) [PubMed Central](#) [Google Scholar](#)

66. 66.

Schwalie, P. C. et al. A stromal cell population that inhibits adipogenesis in mammalian fat depots. *Nature* **559**, 103–108 (2018).

[ADS](#) [CAS](#) [Google Scholar](#)

67. 67.

Micheli, A. J. D. et al. Single-cell transcriptomics identify extensive heterogeneity in the cellular composition of mouse achilles tendons. Preprint at <https://doi.org/10.1101/801266> (2020).

68. 68.

Hepler, C. et al. Identification of functionally distinct fibro-inflammatory and adipogenic stromal subpopulations in visceral adipose tissue of adult mice. *eLife* **7**, 771 (2018).

[Google Scholar](#)

69. 69.

Boyd, D. F. et al. Exuberant fibroblast activity compromises lung function via ADAMTS4. *Nature* **587**, 466–471 (2020).

[ADS](#) [PubMed](#) [PubMed Central](#) [Google Scholar](#)

70. 70.

Perez-Shibayama, C. et al. Type I interferon signaling in fibroblastic reticular cells prevents exhaustive activation of antiviral CD8<sup>+</sup> T cells. *Sci. Immunol.* **5**, eabb7066 (2020).

[CAS](#) [Google Scholar](#)

71. 71.

Guerrero-Juarez, C. F. et al. Single-cell analysis reveals fibroblast heterogeneity and myeloid-derived adipocyte progenitors in murine skin wounds. *Nat. Commun.* **10**, 650 (2019).

[ADS](#) [CAS](#) [PubMed](#) [PubMed Central](#) [Google Scholar](#)

72. 72.

Butler, A., Hoffman, P., Smibert, P., Papalexis, E. & Satija, R. Integrating single-cell transcriptomic data across different conditions, technologies, and species. *Nat. Biotechnol.* **36**, 411–420 (2018).

[CAS](#) [PubMed](#) [PubMed Central](#) [Google Scholar](#)

73. 73.

Stuart, T. et al. Comprehensive integration of single-cell data. *Cell* **177**, 1888–1902.e21 (2019).

[CAS](#) [PubMed](#) [PubMed Central](#) [Google Scholar](#)

74. 74.

van den Brink, S. C. et al. Single-cell sequencing reveals dissociation-induced gene expression in tissue subpopulations. *Nat. Methods* **14**, 935–936 (2017).

[PubMed](#) [PubMed Central](#) [Google Scholar](#)

75. 75.

Korsunsky, I. et al. Fast, sensitive and accurate integration of single-cell data with Harmony. *Nat. Methods* **16**, 1289–1296 (2019).

[CAS](#) [PubMed](#) [PubMed Central](#) [Google Scholar](#)

76. 76.

Gao, X., Hu, D., Gogol, M. & Li, H. ClusterMap: compare multiple single cell RNA-seq datasets across different experimental conditions. *Bioinformatics* **35**, 3038–3045 (2019).

[CAS](#) [Google Scholar](#)

77. 77.

Schubert, M. et al. Perturbation-response genes reveal signaling footprints in cancer gene expression. *Nat. Commun.* **9**, 20 (2018).

[ADS](#) [PubMed](#) [PubMed Central](#) [Google Scholar](#)

78. 78.

Street, K. et al. Slingshot: cell lineage and pseudotime inference for single-cell transcriptomics. *BMC Genomics* **19**, 477 (2018).

[PubMed](#) [PubMed Central](#) [Google Scholar](#)

79. 79.

Bharat, A. et al. Lung transplantation for patients with severe COVID-19. *Sci. Transl. Med.* **12**, eabe4282 (2020).

[CAS](#) [PubMed](#) [PubMed Central](#) [Google Scholar](#)

80. 80.

Maynard, A. et al. Therapy-induced evolution of human lung cancer revealed by single-cell RNA sequencing. *Cell* **182**, 1232–1251.e22 (2020).

[CAS](#) [PubMed](#) [PubMed Central](#) [Google Scholar](#)

81. 81.

Tran, H. T. N. et al. A benchmark of batch-effect correction methods for single-cell RNA sequencing data. *Genome Biol.* **21**, 12 (2020).

[CAS](#) [PubMed](#) [PubMed Central](#) [Google Scholar](#)

82. 82.

Goldman, M. J. et al. Visualizing and interpreting cancer genomics data via the Xena platform. *Nat. Biotechnol.* **38**, 675–678 (2020).

[CAS](#) [PubMed](#) [PubMed Central](#) [Google Scholar](#)

[Download references](#)

## Acknowledgements

We thank members of the Turley laboratory and individuals in the bioinformatics department for discussions; C. Dominguez for experimental assistance; S. Lianoglou, Y. Senbabaoglu and N. Lounsbury for bioinformatics assistance; facility staff at Genentech for vivarium maintenance and core facility assistance; and Turley laboratory members and A. Berkley for their careful review of this manuscript. This work was supported by Genentech.

## Author information

### Author notes

1. These authors contributed equally: Matthew B. Buechler, Rachana N. Pradhan

## Affiliations

### 1. Genentech, South San Francisco, CA, USA

Matthew B. Buechler, Rachana N. Pradhan, Akshay T. Krishnamurty, Christian Cox, Aslihan Karabacak Calviello, Amber W. Wang, Yeqing Angela Yang, Lucinda Tam, Roger Caothien, Merone Roose-Girma, Zora Modrusan, Joseph R. Arron, Richard Bourgon, Sören Müller & Shannon. J. Turley

## Authors

### 1. Matthew B. Buechler

[View author publications](#)

You can also search for this author in [PubMed](#) [Google Scholar](#)

### 2. Rachana N. Pradhan

[View author publications](#)

You can also search for this author in [PubMed](#) [Google Scholar](#)

### 3. Akshay T. Krishnamurty

[View author publications](#)

You can also search for this author in [PubMed](#) [Google Scholar](#)

### 4. Christian Cox

[View author publications](#)

You can also search for this author in [PubMed](#) [Google Scholar](#)

### 5. Aslihan Karabacak Calviello

[View author publications](#)

You can also search for this author in [PubMed](#) [Google Scholar](#)

### 6. Amber W. Wang

[View author publications](#)

You can also search for this author in [PubMed](#) [Google Scholar](#)

7. Yeqing Angela Yang

[View author publications](#)

You can also search for this author in [PubMed](#) [Google Scholar](#)

8. Lucinda Tam

[View author publications](#)

You can also search for this author in [PubMed](#) [Google Scholar](#)

9. Roger Caothien

[View author publications](#)

You can also search for this author in [PubMed](#) [Google Scholar](#)

10. Merone Roose-Girma

[View author publications](#)

You can also search for this author in [PubMed](#) [Google Scholar](#)

11. Zora Modrusan

[View author publications](#)

You can also search for this author in [PubMed](#) [Google Scholar](#)

12. Joseph R. Arron

[View author publications](#)

You can also search for this author in [PubMed](#) [Google Scholar](#)

13. Richard Bourgon

[View author publications](#)

You can also search for this author in [PubMed](#) [Google Scholar](#)

14. Sören Müller

[View author publications](#)

You can also search for this author in [PubMed](#) [Google Scholar](#)

15. Shannon. J. Turley

[View author publications](#)

You can also search for this author in [PubMed](#) [Google Scholar](#)

## Contributions

Conceptualization: M.B.B., R.N.P., S.M., R.B. and S.J.T. Methodology: M.B.B., R.N.P., S.M., R.B. and S.J.T. Software, formal analysis and data curation: R.N.P., S.M., M.B.B. and A.K.C. Investigation: M.B.B., R.N.P., A.T.K., C.C., A.W.W., Y.A.Y., L.T., R.C. and A.K.C. Writing: M.B.B., R.N.P., S.M., R.B. and S.J.T. Visualization: M.B.B., R.N.P., A.T.K., C.C., S.M. Supervision: M.R.-G., Z.M., J.R.A., S.M., R.B. and S.J.T.

## Corresponding authors

Correspondence to [Richard Bourgon](#) or [Sören Müller](#) or [Shannon. J. Turley](#).

## Ethics declarations

## Competing interests

All authors except for R.B. are employees of Genentech. R.B. is an employee of Freenome.

## Additional information

**Peer review information** *Nature* thanks Christopher Buckley, Neil Henderson and the other, anonymous, reviewer(s) for their contribution to the peer review of this work.

**Publisher's note** Springer Nature remains neutral with regard to jurisdictional claims in published maps and institutional affiliations.

## Extended data figures and tables

### Extended Data Fig. 1 Mouse fibroblast bulk RNA-seq and ATAC-seq.

**a**, Diagram of tissues isolated for bulk RNA-seq and ATAC-seq (adipose tissue (brown, subcutaneous, epididymal), bone, liver, lung, lymph node, mesentery, omentum and pancreas) and experimental scheme. **b**, Correlation plot of bulk RNA sequencing samples based on top 1,000 most differentially expressed genes. **c**, Fraction of ATAC-seq reads identified as PCR duplicates, mitochondrial DNA, or unique non-duplicate non-mitochondrial DNA based on genomic mapping. **d**, Fragment lengths of ATAC-seq samples. **e**, Number of called peaks across ATAC-seq samples. Atlas describes the universe of all peaks. **f**, Distribution of ATAC-seq peaks across genomic regions. **g**, Aggregate signal around the TSS. SLN\_2 samples shown, representative of all other samples. **h**, Heatmap of pairwise correlation coefficients of ATAC-seq samples. Ing, subcutaneous adipose; Epi, epididymal adipose; Panc, pancreas; Om, omentum; SLN, lymph node.

### Extended Data Fig. 2 Bulk gene expression and open chromatin.

**a**, Heat map depicting enriched genes per tissue by bulk RNA-seq. Adjusted  $P \leq 0.05$ ,  $\log_2(\text{fold change}) \geq 2$  (DESeq2, two-sided). Row  $z$ -scored. Top, bar plot depicting number of signature genes per tissue. **b**, Heat map depicting regions of open chromatin per tissue by bulk ATAC-seq. Adjusted  $P \leq 0.01$ ,  $\log_2(\text{fold change}) \geq 2$  (DESeq2, two-sided). Row  $z$ -scored. Top, bar plot depicting number of open chromatin regions per tissue. **c**, Correlation (top) and BETA analysis (bottom) of bulk RNA-seq and ATAC-seq samples. **d**, BETA analysis of SLN evaluating enriched gene expression compared to enriched SLN OCRs. These data are representative of the rest of the dataset. **e**, Number of transcription factor binding motifs in signature OCRs per tissue. **f**, Statistical inference of

transcription factor motif enrichment in fibroblasts. Bar colours denote RNA expression of transcription factor. Subcut., subcutaneous adipose; LN, lymph node.

### **Extended Data Fig. 3 Steady-state fibroblast and *Cd45*<sup>-</sup> atlases.**

**a**, UMAP embedding of 180,922 single cells in steady-state *Cd45*<sup>-</sup> atlas. Fourteen clusters identified through graph-based clustering are indicated by colour. **b**, Relative abundance of each tissue in steady-state *Cd45*<sup>-</sup> UMAP clusters. The sizes of bubbles indicate the contributions of cells from each tissue to a cluster, and grey bubbles indicate lack of contribution (number of cells <0.02% of tissue) of that tissue to the corresponding cluster. Graph to be read column-wise. **c**, Fibroblast- and other lineage-associated genes (in grey) in steady-state *Cd45*<sup>-</sup> atlas. The sizes of circles denote the percentages of cells from each cluster, and colour encodes the average expression across all cells within a cluster. The colour scale shows the expression level based on row z-score. **d**, Average bulk tissue-specific fibroblast gene signature scores across tissues represented in the steady-state atlas. Mean-centred values shown. **e**, Expression of cluster hallmark genes in steady-state fibroblast atlas. The sizes of circles denote the percentages of cells from each cluster, and colour encodes the average expression across all cells within a cluster. The colour scale shows the expression level based on row z-score. **f**, Expression of fibroblast- and other lineage-associated genes (in grey). Circle sizes denote percentages of cells from each cluster, and colour encodes average expression across all cells within cluster. Colour scale shows expression level (z-score by row). **g**, Relative abundance of each tissue in steady-state fibroblast UMAP clusters. The sizes of bubbles indicate the contributions of cells from each tissue to a cluster, and grey bubbles indicate lack of contribution (number of cells <0.02% of tissue) of that tissue to the corresponding cluster. Graph to be read column-wise. **h**, Expression of pathway-responsive genes in perturbed-state atlas clusters as assessed by PROGEN(y) analysis (z-scored per row). **i**, Volcano plot comparing genes enriched in *Pi16*<sup>+</sup> cluster (left; blue) to *Col15a1*<sup>+</sup> cluster (right; red). Select genes are labelled. Dots labelled in red or blue were determined as having a  $\log_2$ (fold change) of greater than 1 or less than -1 and an adjusted *P* value less than or equal to 0.05 (Bonferroni

correction). **j**, Expression of *Ly6a* and *Cd34* in steady-state clusters. Wilcoxon's rank sum test  $P < 0.05$ .

### Extended Data Fig. 4 Bulk sequencing validates single-cell atlas.

**a–p**, UMAPs highlighting distribution of cells from individual tissues in the steady-state fibroblast atlas. **q**, PCA of FACS-sorted bulk RNA-seq of fibroblasts and mesothelial cells, calculated for the 1,000 genes with the highest interquartile range. Circles represent fibroblasts and triangles are mesothelial cells. Each colour denotes a different tissue. **r**, Heatmap depicting top 20 *Pi16*<sup>+</sup> (fibroblast) and *Col15a1*<sup>+</sup> genes from steady-state fibroblast atlas in bulk RNA-seq data. Rows are z-scored. **s**, Gene enrichment analysis of top genes ( $\log(\text{fold change}) > 0.5$ ) from *Pi16*<sup>+</sup> cluster and *Col15a1*<sup>+</sup> cluster in loadings of PC1, which discriminates between mesothelial cells and fibroblasts (test: FGSEA, Benjamini–Hochberg correction). **t**, ATAC–seq traces of select genes from *Pi16*<sup>+</sup> and *Col15a1*<sup>+</sup> clusters genes, *Ptprc* (encoding CD45) and *Hprt* at  $\pm 2$  kb of the TSS.

### Extended Data Fig. 5 Supplementary FACS gating.

**a**, Representative FACS gating of live EpCAM<sup>−</sup>CD45<sup>−</sup>CD31<sup>−</sup>PDPN<sup>+</sup>PDGFR $\alpha$ <sup>+</sup> fibroblasts in Figs. 2, 3, Extended Data Figs. 8, 9. **b, c**, Representative FACS gating on LY6C<sup>+</sup>SCA1<sup>+</sup> (red), LY6C<sup>+</sup>SCA1<sup>−</sup> (blue) and LY6C<sup>−</sup>SCA1<sup>−</sup> (green) PDGFR $\alpha$ <sup>+</sup> cells (as gated in Extended Data Fig. 7a) in lymph node of *Ccl19YFP* mice (**b**) and lymph node of *Grem1creERT2Rosa26LSLYFP* mice (**c**). *Grem1creERT2Rosa26LSLYFP* mice received tamoxifen via intraperitoneal injection for five consecutive days and were analysed on days 14–16 after first injection. **d**, Representative FACS gating on LY6C<sup>+</sup>SCA1<sup>+</sup> (red), LY6C<sup>+</sup>SCA1<sup>−</sup> (blue) and LY6C<sup>−</sup>SCA1<sup>−</sup> (green) PDGFR $\alpha$ <sup>+</sup> cells (as gated in Extended Data Fig. 7a) in tissues from *DptIRESCreERT2Rosa26LSLYFP* mice. Mice received tamoxifen chow for 14 days and were analysed on days 14–16.  $n =$  representative of 3 or more biologically independent experiments.

## Extended Data Fig. 6 Dpt<sup>IRESCreERT2</sup> marks universal fibroblasts.

**a**, Expression of *Ly6c* and *Ly6a* in the mouse steady-state fibroblast atlas. **b**, Representative gating for LY6C<sup>+</sup>SCA1<sup>+</sup>, LY6C<sup>-</sup>SCA1<sup>+</sup> and SCA1<sup>-</sup> fibroblasts across indicated tissues. **c**, Quantification of LY6C<sup>+</sup>SCA1<sup>+</sup>, LY6C<sup>-</sup>SCA1<sup>+</sup> and SCA1<sup>-</sup> fibroblasts across indicated tissues. Frequency (top), cell number per mg of tissue (bottom). **d**, Abundance of *Pi16*, *Ccl19*, *Npnt*, and *Dpt* transcripts in LY6C<sup>+</sup>SCA1<sup>+</sup>, LY6C<sup>-</sup>SCA1<sup>+</sup> and SCA1<sup>-</sup> fibroblasts from lymph node (black) and lung (red). **e**, Expression of *Pi16*, *Ccl19*, *Npnt* and *Dpt* in mouse steady-state fibroblast atlas. **f**, RNAscope for *Dpt* (blue) and *Pi16* (red) on lung (left) and small intestine (right). Scale bar, 50 µm. **g**, Schematic of generation of *Dpt*<sup>IRESCreERT2</sup>*Rosa26*<sup>LSLYFP</sup> mouse. YFP expression is achieved in *Dpt*-expressing cells following cre-mediated excision of a loxP-flanked transcriptional stop sequence. **h**, Representative gating for YFP (*Dpt*) in fibroblasts (live, EpCAM<sup>-</sup>CD45<sup>-</sup>CD31<sup>-</sup>PDPN<sup>+</sup>PDGFR $\alpha$ <sup>+</sup>) across indicated tissues. Red, shaded histogram is *Dpt*<sup>IRESCreERT2ki/ki</sup>*Rosa26*<sup>LSLYFPwt/loxP</sup> and black is *Dpt*<sup>IRESCreERT2wt/wt</sup>*Rosa26*<sup>LSLYFPwt/loxP</sup>. **i**, Representative gating for YFP (*Dpt*) in CD45<sup>+</sup> cells (live, EpCAM<sup>-</sup>CD45<sup>+</sup>), EpCAM<sup>+</sup> cells (live, EpCAM<sup>+</sup>), and endothelial cells (live, EpCAM<sup>-</sup>CD45<sup>-</sup>CD31<sup>+</sup>) from the pancreas. Red line is *Dpt*<sup>IRESCreERT2ki/ki</sup>*Rosa26*<sup>LSLYFPwt/loxP</sup> and grey, shaded histogram is *Dpt*<sup>IRESCreERT2wt/wt</sup>*Rosa26*<sup>LSLYFPwt/loxP</sup>. **j**, Quantification of YFP<sup>+</sup> cells in *Dpt*<sup>IRESCreERT2ki/ki</sup>*Rosa26*<sup>LSLYFPwt/loxP</sup> animals in indicated cell types across tissues. Percentage YFP<sup>+</sup> was determined by subtracting fluorescence in *Dpt*<sup>IRESCreERT2ki/ki</sup>*Rosa26*<sup>LSLYFPwt/loxP</sup> animals from *Dpt*<sup>IRESCreERT2wt/wt</sup>*Rosa26*<sup>LSLYFPwt/loxP</sup> animals. **k**, Abundance of *Pi16*, *Ccl19*, *Npnt*, and *Dpt* transcripts in FACS-sorted YFP<sup>+</sup> and YFP<sup>-</sup> cells from *Dpt*<sup>IRESCreERT2ki/ki</sup>*Rosa26*<sup>LSLYFPwt/loxP</sup> and *Dpt*<sup>IRESCreERT2wt/wt</sup>*Rosa26*<sup>LSLYFPwt/loxP</sup> animals 14–16 days after tamoxifen chow, in lymph node (top) and lung (bottom). **l**, Abundance of *Csf1* transcripts in FACS-sorted YFP<sup>+</sup> and YFP<sup>-</sup> cells from *Dpt*<sup>IRESCreERT2ki/ki</sup>*Rosa26*<sup>LSLYFPwt/loxP</sup> and *Dpt*<sup>IRESCreERT2wt/wt</sup>*Rosa26*<sup>LSLYFPwt/loxP</sup> animals 14–16 days after tamoxifen chow in lymph node and lung. *n* = 3 (**c**, **d**, **k**, **l**) or representative of 3 or

more biologically independent experiments (**b**, **f**, **h**, **i**). Dot represents each mouse with bar at mean (**c**, **j**), plots show minimum and maximum (whiskers) and median (centre line). (**d**, **k**, **l**). Mice received tamoxifen chow for 14 days and were analysed on days 14–16. [Source data](#)

## Extended Data Fig. 7 Perturbed-state fibroblast and *Cd45*<sup>−</sup> atlases.

**a**, UMAP embedding of 182,609 cells in perturbed-state *Cd45*<sup>−</sup> atlas. Twelve clusters identified through graph-based clustering are indicated by colour. **b**, Relative abundance of each tissue in perturbed-state *Cd45*<sup>−</sup> UMAP clusters. The sizes of bubbles indicate the contributions of cells from each tissue to a cluster, and grey bubbles indicate lack of contribution (number of cells <0.02% of tissue) of that tissue to the corresponding cluster. Graph to be read column-wise. **c**, Fibroblast- and other lineage-associated genes (in grey) in *Cd45*<sup>−</sup> perturbed-state map. The sizes of circles denote the percentages of cells from each cluster, and colour encodes the average expression across all cells within a cluster. The colour scale shows the expression level based on row z-score. **d**, Expression of cluster hallmark genes in perturbed-state fibroblast atlas. The sizes of circles denote the percentages of cells from each cluster, and colour encodes the average expression across all cells within a cluster. The colour scale shows the expression level based on row z-score. **e**, Fibroblast- and other lineage-associated genes (in grey) in mouse perturbed-state fibroblast atlas. Circle sizes denote percentages of cells from each cluster; colour encodes average expression across all cells within cluster. Colour scale shows expression level (z-score by row). **f**, Relative abundance of each tissue in perturbed-state fibroblast UMAP clusters. The sizes of bubbles indicate the contributions of cells from each tissue to a cluster, and grey bubbles indicate lack of contribution (number of cells <0.02% of tissue) of that tissue to the corresponding cluster. Graph to be read column-wise. Clusters with analogues in steady state are depicted in grey, irrespective of the tissue contribution. **g**, Dendrogram representation of the hierarchical clustering of steady-state (blue) and perturbed-state (red) cluster marker genes. Similarity scores are indicated at the bottom of matching clusters from steady-state and perturbed-state tissues.

## Extended Data Fig. 8 Validation of perturbed-state atlas.

**a–o**, UMAP representations of the distribution of fibroblasts across tissues and perturbations. **p–u**, Heat maps showing average relative gene expression in *Pi16*<sup>+</sup>, *Col15a1*<sup>+</sup>, *Adamdec1*<sup>+</sup>, *Cxcl5*<sup>+</sup>, and *Lrrc15*<sup>+</sup> clusters (*z*-scored per row) in the following categories. **p**, Cytokines and chemokines. **q**, Wnt-associated genes. **r**, ECM-associated genes. **s**, Collagens and laminins. **t**, Matrix metalloproteases and cathepsins. **u**, Receptors and surface molecules. **v**, Expression of pathway-responsive genes in perturbed-state atlas clusters as assessed by PROGEN(y) analysis (*z*-scored per row). **w**, RNAscope for *Dpt* (blue) and *Grem1* (red) in non-lesional colon (top) and lesional colon (bottom) on day 7 after induction of DSS colitis. Data are representative of three experiments. Scale bars, 50 μm (top) and 250 μm (bottom). **x**, *Ly6a* and *Cd34* expression in perturbed-state clusters. Wilcoxon's rank sum test,  $P < 0.05$ . **y**, Pseudotime(s) visualized using principal curves representing trajectories of fibroblast differentiation across perturbed-state fibroblast object. Blue lines show trajectory to activated clusters, grey lines show trajectory to clusters with a steady-state analogue. *Pi16*<sup>+</sup> cluster set as root. **z**, Representative FACS strategy for subcutaneous tumour experiments. **a'**, Representative flow cytometry plots showing frequency of YFP<sup>+</sup> cells in LRRC15<sup>+</sup> fibroblasts from KPR3070 subcutaneous tumour at day 21 post-inoculation in *Dpt*<sup>IRESCreERT2wt/wt</sup>*Rosa26*<sup>LSLYFPwt/loxP</sup> animals. **b'**, Quantification of FACS data (Fig. 3d, Extended Data Fig. 8z, a'). Data are from **b'** or representative of 2 (**z–a'**) or 3 (**w**) experiments. Each dot represents one mouse (**b'**).  $n = 2$  (**b'**) or representative of 2 (**z–a'**) or 3 (**w**) biologically independent experiments. [Source data](#)

## Extended Data Fig. 9 Human universal fibroblasts.

**a**, Top, UMAP embeddings of human pancreatic cancer tumour and normal adjacent tissue ( $n = 21,626$  cells). Bottom, percentage of cells in each cluster coming from tumour or NAT. **b**, UMAP as in **a**, coloured by expression of indicated genes. **c**, Relative average expression of top 10 marker genes (sorted by log(fold change)) for each cluster in the pancreatic cancer single-cell dataset. Two representative genes highlighted per cluster.

DEGs across clusters. **d**, Top, expression level of indicated marker genes (colour, *y*-axis) across 100 pseudo-bulk samples (*x*-axis) generated from human pancreatic cancer scRNA-seq data. The known percentage of cells from cluster 8 in each pseudo-bulk is shown by the dotted blue line. Bottom, boxplots representing the distributions of pairwise correlation coefficients of the top 20 marker genes for cluster 8 in pseudo-bulk samples containing (left) and not containing cells from cluster 8 (right). **e**, Boxplots summarizing *DPT* expression distributions across tissues from the GTEx portal. Tissues with mean above horizontal black line were included in correlation analysis (**f**).  $n = 7,851$  biologically independent samples. **f**, Co-expression as in **d**, results from the gene-by-gene correlation matrices are summarized as boxplots for each individual tissue from GTEx.  $n = 5,957$  biologically independent samples. **g**, Gene-by-gene correlation matrix of pairwise correlations in 205 normal pancreas bulk RNA-seq samples from GTEx. Blue indicates *Pi16<sup>+</sup>* cluster signature gene, red indicates *Col15a1<sup>+</sup>* signature gene. **h**, Human universal fibroblast score projected onto human pancreatic cancer samples. **i**, Human universal fibroblast score projected onto human subcutaneous adipose. **d–f**, Box and whisker plots show minimum and maximum (whiskers), interquartile range (box) and median (centre line).

## Extended Data Fig. 10 Perturbed-state human fibroblasts.

**a**, Volcano plot visualizing log(fold change) (*x*-axis) and adjusted *P* value (*y*-axis) comparing fibroblasts from cluster 3 in Extended Data Fig. 9a compared to fibroblasts from cluster 8 (Wilcoxon's rank sum test). **b**, Scatterplot visualizing the scores for a NAT (cluster 3) fibroblast expression gene set (*y*-axis) compared to scores for a CAF (cluster 8) expression gene set (*x*-axis) in 122 bulk RNA-seq samples of microdissected PDAC tissue. Each dot represents a sample, the regression line is given in blue. Error band, 95% confidence interval. **c–f**, UMAP representation of cells from the mouse perturbed-state atlas, each cell coloured by their score for gene sets corresponding to the following. **c**, *Lrrc15<sup>+</sup>* myofibroblasts from human pancreatic cancer (cluster 3 CAF, ‘MyCAF’<sup>11</sup>), rheumatoid arthritis (‘Human RA F2’<sup>7</sup>), lung disease (‘Myofibroblast’<sup>29</sup>), IPF<sup>30</sup> and ulcerative colitis (‘S2’<sup>31</sup>). **d**, Universal fibroblasts from human pancreatic cancer

(cluster 8 NAT), lung disease ('PLIN2<sup>+</sup> fibroblast'<sup>29</sup>) and ulcerative colitis ('S1'<sup>31</sup>). **e**, Inflammatory fibroblasts from pancreatic cancer ('iCAF'<sup>11</sup>) and rheumatoid arthritis ('Human RA F5'<sup>7</sup>). **f**, UMAP of IL-1 CAF cells derived from ref. <sup>10</sup>, projected onto perturbed-state fibroblast atlas. **g**, Expression of human universal fibroblast module across human perturbed-state atlas clusters. **h**, Abundance of *LRRC15* and *CTHRC1* expression in human perturbed-state atlas. **i**, Heat maps showing average relative gene expression in human perturbed-state atlas (z-scored by row).

## Supplementary information

### Reporting Summary

### Supplementary Table 1

Tissue-specific fibroblast and mesothelial cell genes by bulk RNAseq (related to Extended Data Fig. 2).

### Supplementary Table 2

Tissue-specific OCRs and TFs by bulk ATACseq (related to Extended Data Fig. 2).

### Supplementary Table 3

Tissue contributions to single cell RNAseq objects used in analyses of steady state and perturbed state murine tissues (related to Figs 1 and 3).

### Supplementary Table 4

DEGs for steady-state mouse fibroblast atlas (related to Fig. 1).

### Supplementary Table 5

DEGs for mouse perturbed-state fibroblast atlas (related to Fig. 3).

## **Supplementary Table 6**

Patient information (related to Fig. 4 and Extended Data Figs 11 and 12).

## **Supplementary Table 7**

DEGs for human pancreatic cancer samples (related to Fig. 4 and Extended Data Figs 11 and 12).

## **Supplementary Table 8**

Human gene sets projected onto mouse perturbed-state fibroblast atlas (related to Extended Data Fig. 12).

## **Supplementary Table 9**

DEGs for human perturbed-state atlas (related to Fig. 4).

## **Source data**

### **Source Data Fig. 2**

### **Source Data Extended Data Fig. 6**

### **Source Data Extended Data Fig. 8**

## **Rights and permissions**

### **Reprints and Permissions**

## **About this article**



Check for  
updates

## Cite this article

Buechler, M.B., Pradhan, R.N., Krishnamurty, A.T. *et al.* Cross-tissue organization of the fibroblast lineage. *Nature* **593**, 575–579 (2021). <https://doi.org/10.1038/s41586-021-03549-5>

### [Download citation](#)

- Received: 22 September 2020
- Accepted: 13 April 2021
- Published: 12 May 2021
- Issue Date: 27 May 2021
- DOI: <https://doi.org/10.1038/s41586-021-03549-5>

## Further reading

- [\*\*Fibroblast-macrophage reciprocal interactions in health, fibrosis, and cancer\*\*](#)
  - Matthew B. Buechler
  - , Wenxian Fu
  - & Shannon J. Turley
- [\*\*Fibroblast cells reveal their ancestry\*\*](#)
  - Christopher D. Buckley

*Nature* (2021)

## Comments

By submitting a comment you agree to abide by our [Terms](#) and [Community Guidelines](#). If you find something abusive or that does not comply with our terms or guidelines please flag it as inappropriate.

[Download PDF](#)

## Associated Content

Collection

[\*\*Stromal–immune cell interactions\*\*](#)

[\*\*Fibroblast cells reveal their ancestry\*\*](#)

- Christopher D. Buckley

Nature News & Views 12 May 2021

Advertisement

---

This article was downloaded by **calibre** from <https://www.nature.com/articles/s41586-021-03549-5>

- Article
- [Published: 12 May 2021](#)

# Mitochondrial TNAP controls thermogenesis by hydrolysis of phosphocreatine

- [Yizhi Sun](#) ORCID: [orcid.org/0000-0001-5911-1117<sup>1,2</sup>](https://orcid.org/0000-0001-5911-1117),
- [Janane F. Rahbani](#) ORCID: [orcid.org/0000-0003-4598-4683<sup>3,4</sup>](https://orcid.org/0000-0003-4598-4683),
- [Mark P. Jedrychowski<sup>1,2</sup>](#),
- [Christopher L. Riley<sup>1,2</sup>](#),
- [Sara Vidoni<sup>1,2</sup>](#),
- [Dina Bogoslavski<sup>1</sup>](#),
- [Bo Hu](#) ORCID: [orcid.org/0000-0002-5599-6875<sup>1,2</sup>](https://orcid.org/0000-0002-5599-6875),
- [Phillip A. Dumesic<sup>1,2</sup>](#),
- [Xing Zeng<sup>1,2</sup>](#),
- [Alex B. Wang](#) ORCID: [orcid.org/0000-0001-8678-5205<sup>1,2</sup>](https://orcid.org/0000-0001-8678-5205),
- [Nelson H. Knudsen<sup>1,2</sup>](#),
- [Caroline R. Kim<sup>1</sup>](#),
- [Anthony Marasciullo<sup>1</sup>](#),
- [José L. Millán<sup>5</sup>](#),
- [Edward T. Chouchani](#) ORCID: [orcid.org/0000-0002-9776-8790<sup>1,2</sup>](https://orcid.org/0000-0002-9776-8790),
- [Lawrence Kazak](#) ORCID: [orcid.org/0000-0002-7591-2544<sup>3,4</sup>](https://orcid.org/0000-0002-7591-2544) &
- [Bruce M. Spiegelman](#) ORCID: [orcid.org/0000-0002-7658-4802<sup>1,2</sup>](https://orcid.org/0000-0002-7658-4802)

[Nature](#) volume 593, pages 580–585 (2021) [Cite this article](#)

- 3559 Accesses
- 1 Citations

- 47 Altmetric
- [Metrics details](#)

## Subjects

- [Cellular imaging](#)
- [Fat metabolism](#)
- [Hydrolases](#)

## Abstract

Adaptive thermogenesis has attracted much attention because of its ability to increase systemic energy expenditure and to counter obesity and diabetes<sup>1,2,3</sup>. Recent data have indicated that thermogenic fat cells use creatine to stimulate futile substrate cycling, dissipating chemical energy as heat<sup>4,5</sup>. This model was based on the super-stoichiometric relationship between the amount of creatine added to mitochondria and the quantity of oxygen consumed. Here we provide direct evidence for the molecular basis of this futile creatine cycling activity in mice. Thermogenic fat cells have robust phosphocreatine phosphatase activity, which is attributed to tissue-nonspecific alkaline phosphatase (TNAP). TNAP hydrolyses phosphocreatine to initiate a futile cycle of creatine dephosphorylation and phosphorylation. Unlike in other cells, TNAP in thermogenic fat cells is localized to the mitochondria, where futile creatine cycling occurs. TNAP expression is powerfully induced when mice are exposed to cold conditions, and its inhibition in isolated mitochondria leads to a loss of futile creatine cycling. In addition, genetic ablation of TNAP in adipocytes reduces whole-body energy expenditure and leads to rapid-onset obesity in mice, with no change in movement or feeding behaviour. These data illustrate the critical role of TNAP as a phosphocreatine phosphatase in the futile creatine cycle.

## Access options

Subscribe to Journal

Get full journal access for 1 year

\$199.00

only \$3.90 per issue

[Subscribe](#)

All prices are NET prices.

VAT will be added later in the checkout.

Tax calculation will be finalised during checkout.

Rent or Buy article

Get time limited or full article access on ReadCube.

from \$8.99

[Rent or Buy](#)

All prices are NET prices.

### **Additional access options:**

- [Log in](#)
- [Access through your institution](#)
- [Learn about institutional subscriptions](#)

**Fig. 1: Isolation and identification of TNAP as a cold-inducible PCr phosphatase from mitochondria of thermogenic fat.**

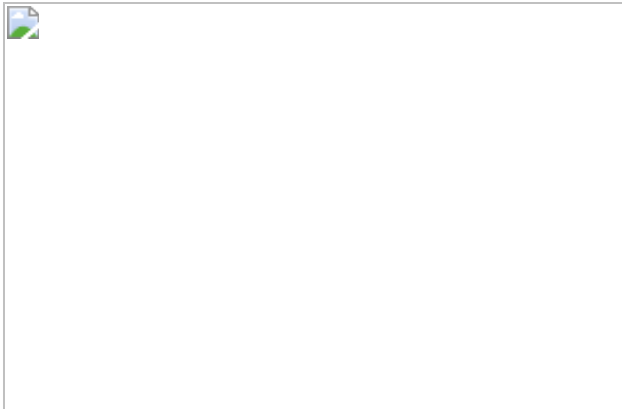


**Fig. 2: TNAP targets mitochondria in brown adipocytes.**

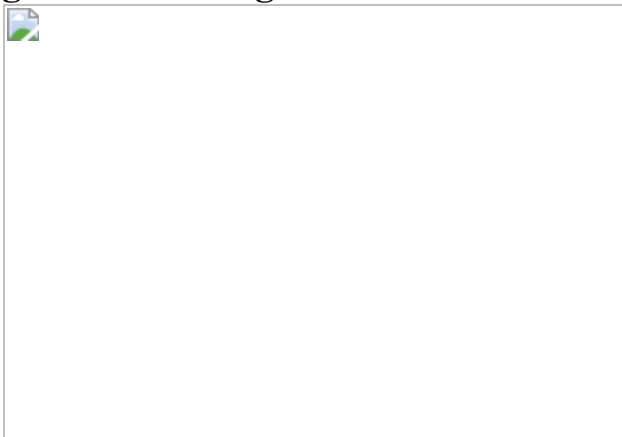


**Fig. 3: Ablation of TNAP activity abolishes the FCC by hydrolysis of phosphocreatine.**

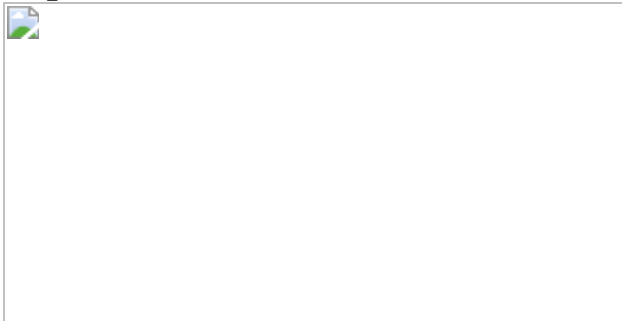
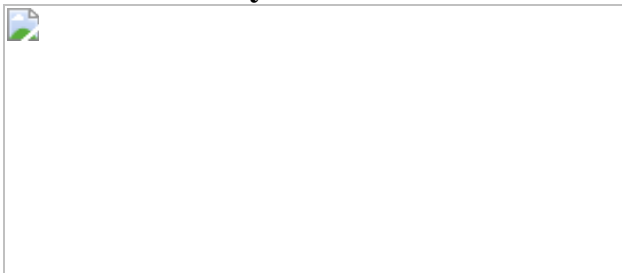


**Fig. 4: Ablation of TNAP in fat represses adaptive thermogenesis and stimulates obesity.**



## Data availability

The mass spectrometry proteomics data have been deposited to the ProteomeXchange Consortium via the PRIDE partner repository (<https://www.ebi.ac.uk/pride/>) with the dataset identifier PXD025032. The published adipocyte-specific ribosomal profiling dataset can be downloaded at <https://ars.els-cdn.com/content/image/1-s2.0-S1550413118301839-mmc2.xlsx>. Full scans for all western blots are provided in the Supplementary Information. All other data are available from the corresponding author on reasonable request. [Source data](#) are provided with this paper.

## References

1. 1.

Rosen, E. D. & Spiegelman, B. M. What we talk about when we talk about fat. *Cell* **156**, 20–44 (2014).

[CAS](#) [PubMed](#) [PubMed Central](#) [Google Scholar](#)

2. 2.

Harms, M. & Seale, P. Brown and beige fat: development, function and therapeutic potential. *Nat. Med.* **19**, 1252–1263 (2013).

[CAS](#) [PubMed](#) [Google Scholar](#)

3. 3.

Carobbio, S., Guénantin, A. C., Samuelson, I., Bahri, M. & Vidal-Puig, A. Brown and beige fat: from molecules to physiology and pathophysiology. *Biochim. Biophys. Acta Mol. Cell Biol. Lipids* **1864**, 37–50 (2019).

[CAS](#) [PubMed](#) [Google Scholar](#)

4. 4.

Chouchani, E. T., Kazak, L. & Spiegelman, B. M. New advances in adaptive thermogenesis: UCP1 and beyond. *Cell Metab.* **29**, 27–37 (2019).

[CAS](#) [PubMed](#) [Google Scholar](#)

5. 5.

Kazak, L. et al. A creatine-driven substrate cycle enhances energy expenditure and thermogenesis in beige fat. *Cell* **163**, 643–655 (2015).

[CAS](#) [PubMed](#) [PubMed Central](#) [Google Scholar](#)

6. 6.

Cypess, A. M. et al. Anatomical localization, gene expression profiling and functional characterization of adult human neck brown fat. *Nat. Med.* **19**, 635–639 (2013).

[CAS](#) [PubMed](#) [PubMed Central](#) [Google Scholar](#)

7. 7.

Cypess, A. M. et al. Activation of human brown adipose tissue by a  $\beta$ 3-adrenergic receptor agonist. *Cell Metab.* **21**, 33–38 (2015).

[CAS](#) [PubMed](#) [PubMed Central](#) [Google Scholar](#)

8. 8.

Leitner, B. P. et al. Mapping of human brown adipose tissue in lean and obese young men. *Proc. Natl Acad. Sci. USA* **114**, 8649–8654 (2017).

[CAS](#) [PubMed](#) [Google Scholar](#)

9. 9.

Bachman, E. S. et al.  $\beta$ AR signaling required for diet-induced thermogenesis and obesity resistance. *Science* **297**, 843–845 (2002).

[CAS](#) [PubMed](#) [ADS](#) [Google Scholar](#)

10. 10.

Zeng, X. et al. Innervation of thermogenic adipose tissue via a calsyntenin 3 $\beta$ -S100b axis. *Nature* **569**, 229–235 (2019).

[PubMed](#) [PubMed Central](#) [ADS](#) [Google Scholar](#)

11. 11.

Enerbäck, S. et al. Mice lacking mitochondrial uncoupling protein are cold-sensitive but not obese. *Nature* **387**, 90–94 (1997).

[PubMed](#) [ADS](#) [Google Scholar](#)

12. 12.

Hofmann, W. E., Liu, X., Bearden, C. M., Harper, M. E. & Kozak, L. P. Effects of genetic background on thermoregulation and fatty acid-induced uncoupling of mitochondria in UCP1-deficient mice. *J. Biol. Chem.* **276**, 12460–12465 (2001).

[CAS](#) [PubMed](#) [Google Scholar](#)

13. 13.

Kazak, L. et al. UCP1 deficiency causes brown fat respiratory chain depletion and sensitizes mitochondria to calcium overload-induced dysfunction. *Proc. Natl Acad. Sci. USA* **114**, 7981–7986 (2017).

[CAS](#) [PubMed](#) [Google Scholar](#)

14. 14.

Ikeda, K. et al. UCP1-independent signaling involving SERCA2b-mediated calcium cycling regulates beige fat thermogenesis and systemic glucose homeostasis. *Nat. Med.* **23**, 1454–1465 (2017).

[CAS](#) [PubMed](#) [PubMed Central](#) [Google Scholar](#)

15. 15.

Long, J. Z. et al. The secreted enzyme PM20D1 regulates lipidated amino acid uncouplers of mitochondria. *Cell* **166**, 424–435 (2016).

[CAS](#) [PubMed](#) [PubMed Central](#) [Google Scholar](#)

16. 16.

Kazak, L. et al. Genetic depletion of adipocyte creatine metabolism inhibits diet-induced thermogenesis and drives obesity. *Cell Metab.* **26**, 660–671.e3 (2017).

[CAS](#) [PubMed](#) [PubMed Central](#) [Google Scholar](#)

17. 17.

Kazak, L. et al. Ablation of adipocyte creatine transport impairs thermogenesis and causes diet-induced obesity. *Nat. Metab.* **1**, 360–370 (2019).

[CAS](#) [PubMed](#) [PubMed Central](#) [Google Scholar](#)

18. 18.

Rahbani, J. F. et al. Creatine kinase B controls futile creatine cycling in thermogenic fat. *Nature* **590**, 480–485 (2021).

[CAS](#) [PubMed](#) [ADS](#) [Google Scholar](#)

19. 19.

Müller, S. et al. Proteomic analysis of human brown adipose tissue reveals utilization of coupled and uncoupled energy expenditure pathways. *Sci. Rep.* **6**, 30030 (2016).

[PubMed](#) [PubMed Central](#) [ADS](#) [Google Scholar](#)

20. 20.

Svensson, P. A. et al. Gene expression in human brown adipose tissue. *Int. J. Mol. Med.* **27**, 227–232 (2011).

[CAS](#) [PubMed](#) [Google Scholar](#)

21. 21.

Bessman, S. P. & Carpenter, C. L. The creatine–creatine phosphate energy shuttle. *Annu. Rev. Biochem.* **54**, 831–862 (1985).

[CAS](#) [PubMed](#) [Google Scholar](#)

22. 22.

Pinkerton, A. B. et al. Discovery of 5-((5-chloro-2-methoxyphenyl)sulfonamido)nicotinamide (SBI-425), a potent and orally bioavailable tissue-nonspecific alkaline phosphatase (TNAP) inhibitor. *Bioorg. Med. Chem. Lett.* **28**, 31–34 (2018).

[CAS](#) [PubMed](#) [Google Scholar](#)

23. 23.

Roh, H. C. et al. Warming induces significant reprogramming of beige, but not brown, adipocyte cellular identity. *Cell Metab.* **27**, 1121–1137.e5 (2018).

[CAS](#) [PubMed](#) [PubMed Central](#) [Google Scholar](#)

24. 24.

Buchet, R., Millán, J. L. & Magne, D. Multisystemic functions of alkaline phosphatases. *Methods Mol. Biol.* **1053**, 27–51 (2013).

[CAS](#) [PubMed](#) [Google Scholar](#)

25. 25.

Hessle, L. et al. Tissue-nonspecific alkaline phosphatase and plasma cell membrane glycoprotein-1 are central antagonistic regulators of bone mineralization. *Proc. Natl Acad. Sci. USA* **99**, 9445–9449 (2002).

[CAS](#) [PubMed](#) [ADS](#) [Google Scholar](#)

26. 26.

Anderson, H. C. et al. Impaired calcification around matrix vesicles of growth plate and bone in alkaline phosphatase-deficient mice. *Am. J. Pathol.* **164**, 841–847 (2004).

[CAS](#) [PubMed](#) [PubMed Central](#) [Google Scholar](#)

27. 27.

Lam, S. S. et al. Directed evolution of APEX2 for electron microscopy and proximity labeling. *Nat. Methods* **12**, 51–54 (2015).

[CAS](#) [PubMed](#) [ADS](#) [Google Scholar](#)

28. 28.

Rhee, H. W. et al. Proteomic mapping of mitochondria in living cells via spatially restricted enzymatic tagging. *Science* **339**, 1328–1331 (2013).

[CAS](#) [PubMed](#) [PubMed Central](#) [ADS](#) [Google Scholar](#)

29. 29.

Kiffer-Moreira, T. et al. Catalytic signature of a heat-stable, chimeric human alkaline phosphatase with therapeutic potential. *PLoS ONE* **9**, e89374 (2014).

[PubMed](#) [PubMed Central](#) [ADS](#) [Google Scholar](#)

30. 30.

Chen, W. W., Freinkman, E., Wang, T., Birsoy, K. & Sabatini, D. M. Absolute quantification of matrix metabolites reveals the dynamics of mitochondrial metabolism. *Cell* **166**, 1324–1337.e11 (2016).

[CAS](#) [PubMed](#) [PubMed Central](#) [Google Scholar](#)

31. 31.

Chen, W. W., Freinkman, E. & Sabatini, D. M. Rapid immunopurification of mitochondria for metabolite profiling and absolute quantification of matrix metabolites. *Nat. Protoc.* **12**, 2215–2231 (2017).

[PubMed](#) [PubMed Central](#) [Google Scholar](#)

32. 32.

Haarhaus, M., Brandenburg, V., Kalantar-Zadeh, K., Stenvinkel, P. & Magnusson, P. Alkaline phosphatase: a novel treatment target for cardiovascular disease in CKD. *Nat. Rev. Nephrol.* **13**, 429–442 (2017).

[CAS](#) [PubMed](#) [Google Scholar](#)

33. 33.

Liu, X. et al. Paradoxical resistance to diet-induced obesity in UCP1-deficient mice. *J. Clin. Invest.* **111**, 399–407 (2003).

[CAS](#) [PubMed](#) [PubMed Central](#) [Google Scholar](#)

34. 34.

Feldmann, H. M., Golozoubova, V., Cannon, B. & Nedergaard, J. UCP1 ablation induces obesity and abolishes diet-induced thermogenesis in mice exempt from thermal stress by living at thermoneutrality. *Cell Metab.* **9**, 203–209 (2009).

[CAS](#) [PubMed](#) [Google Scholar](#)

35. 35.

Vendelin, M., Lemba, M. & Saks, V. A. Analysis of functional coupling: mitochondrial creatine kinase and adenine nucleotide translocase. *Biophys. J.* **87**, 696–713 (2004).

[CAS](#) [PubMed](#) [PubMed Central](#) [ADS](#) [Google Scholar](#)

36. 36.

Shulman, G. I., Ladenson, P. W., Wolfe, M. H., Ridgway, E. C. & Wolfe, R. R. Substrate cycling between gluconeogenesis and glycolysis in euthyroid, hypothyroid, and hyperthyroid man. *J. Clin. Invest.* **76**, 757–764 (1985).

[CAS](#) [PubMed](#) [PubMed Central](#) [Google Scholar](#)

37. 37.

Wolfe, R. R., Herndon, D. N., Jahoor, F., Miyoshi, H. & Wolfe, M. Effect of severe burn injury on substrate cycling by glucose and fatty acids. *N. Engl. J. Med.* **317**, 403–408 (1987).

[CAS](#) [PubMed](#) [Google Scholar](#)

38. 38.

Clark, M. G. et al. Accelerated substrate cycling of fructose-6-phosphate in the muscle of malignant hyperthermic pigs. *Nature* **245**, 99–101 (1973).

[CAS](#) [PubMed](#) [ADS](#) [Google Scholar](#)

39. 39.

Newsholme, E. A. & Crabtree, B. Substrate cycles in metabolic regulation and in heat generation. *Biochem. Soc. Symp.* 61–109 (1976).

40. 40.

Klein, S. & Wolfe, R. R. Whole-body lipolysis and triglyceride-fatty acid cycling in cachectic patients with esophageal cancer. *J. Clin. Invest.* **86**, 1403–1408 (1990).

[CAS](#) [PubMed](#) [PubMed Central](#) [Google Scholar](#)

41. 41.

Love, M. I., Huber, W. & Anders, S. Moderated estimation of fold change and dispersion for RNA-seq data with DESeq2. *Genome Biol.* **15**, 550 (2014).

[PubMed](#) [PubMed Central](#) [Google Scholar](#)

42. 42.

Klein, J. et al.  $\beta_3$ -adrenergic stimulation differentially inhibits insulin signaling and decreases insulin-induced glucose uptake in brown adipocytes. *J. Biol. Chem.* **274**, 34795–34802 (1999).

[CAS](#) [PubMed](#) [Google Scholar](#)

43. 43.

Wu, J. et al. Beige adipocytes are a distinct type of thermogenic fat cell in mouse and human. *Cell* **150**, 366–376 (2012).

[CAS](#) [PubMed](#) [PubMed Central](#) [Google Scholar](#)

44. 44.

Sharabi, K. et al. Selective chemical inhibition of PGC-1 $\alpha$  gluconeogenic activity ameliorates type 2 diabetes. *Cell* **169**, 148–160.e15 (2017).

[CAS](#) [PubMed](#) [PubMed Central](#) [Google Scholar](#)

45. 45.

Springer, M. L., Rando, T. A. & Blau, H. M. Gene delivery to muscle. *Curr. Protoc. Hum. Genet.* **31**, 13.4.1–13.4.19 (2002).

[Google Scholar](#)

46. 46.

Allan, C. et al. OMERO: flexible, model-driven data management for experimental biology. *Nat. Methods* **9**, 245–253 (2012).

[CAS](#) [PubMed](#) [PubMed Central](#) [Google Scholar](#)

47. 47.

Schindelin, J. et al. Fiji: an open-source platform for biological-image analysis. *Nat. Methods* **9**, 676–682 (2012).

[CAS](#) [Google Scholar](#)

48. 48.

Yuan, M., Breitkopf, S. B., Yang, X. & Asara, J. M. A positive/negative ion-switching, targeted mass spectrometry-based metabolomics platform for bodily fluids, cells, and fresh and fixed tissue. *Nat. Protoc.* **7**, 872–881 (2012).

[CAS](#) [PubMed](#) [PubMed Central](#) [Google Scholar](#)

49. 49.

Foster, B. L. et al. Conditional *Alpl* ablation phenocopies dental defects of hypophosphatasia. *J. Dent. Res.* **96**, 81–91 (2017).

[CAS](#) [PubMed](#) [Google Scholar](#)

50. 50.

Gettins, P., Metzler, M. & Coleman, J. E. Alkaline phosphatase.  $^{31}\text{P}$  NMR probes of the mechanism. *J. Biol. Chem.* **260**, 2875–2883 (1985).

[CAS](#) [PubMed](#) [Google Scholar](#)

51. 51.

Subramanian, A. et al. Gene set enrichment analysis: a knowledge-based approach for interpreting genome-wide expression profiles. *Proc. Natl Acad. Sci. USA* **102**, 15545–15550 (2005).

[CAS](#) [PubMed](#) [PubMed Central](#) [ADS](#) [Google Scholar](#)

52. 52.

Mootha, V. K. et al. PGC-1 $\alpha$ -responsive genes involved in oxidative phosphorylation are coordinately downregulated in human diabetes. *Nat. Genet.* **34**, 267–273 (2003).

[CAS](#) [Google Scholar](#)

[Download references](#)

## Acknowledgements

We thank C. J. Rosen for sharing the *Alpl*<sup>f/f</sup> mouse strain with permission of J.L.M.; R. Garrity for help with CLAMS studies; the NMR Core jointly operated by Harvard Medical School and Dana-Farber Cancer Institute for help with NMR data acquisition; Nikon Imaging Center at Harvard Medical School for help with fluorescence imaging studies; the EM Core at Harvard

Medical School for APEX2/EM imaging studies; and the Mass Spectrometry Facility at Beth Israel Deaconess Medical Center for targeted metabolomics studies. Y.S. and C.L.R. are supported by the American Heart Association postdoctoral fellowship. J.F.R. is supported by the Charlotte and Leo Karassik Fellowship. B.H. was a Cancer Research Institute/Leonard Kahn Foundation Fellow. P.A.D. is supported by a Damon Runyon Cancer Research Foundation Fellowship. This study was supported by NIDCR grant DE12889 to J.L.M., NIH grant DK 123095 to E.T.C., Canadian Institutes of Health Research (CIHR) grant PJT-159529 to L.K. and JPB Foundation 6293803 and NIH grant DK123228 to B.M.S.

## Author information

### Affiliations

1. Department of Cancer Biology, Dana-Farber Cancer Institute, Boston, MA, USA

Yizhi Sun, Mark P. Jedrychowski, Christopher L. Riley, Sara Vidoni, Dina Bogoslavski, Bo Hu, Phillip A. Dumesic, Xing Zeng, Alex B. Wang, Nelson H. Knudsen, Caroline R. Kim, Anthony Marasciullo, Edward T. Chouchani & Bruce M. Spiegelman

2. Department of Cell Biology, Harvard Medical School, Boston, MA, USA

Yizhi Sun, Mark P. Jedrychowski, Christopher L. Riley, Sara Vidoni, Bo Hu, Phillip A. Dumesic, Xing Zeng, Alex B. Wang, Nelson H. Knudsen, Edward T. Chouchani & Bruce M. Spiegelman

3. Goodman Cancer Research Centre, McGill University, Montreal, Quebec, Canada

Janane F. Rahbani & Lawrence Kazak

4. Department of Biochemistry, McGill University, Montreal, Quebec, Canada

Janane F. Rahbani & Lawrence Kazak

5. Sanford Children's Health Research Center, Sanford Burnham Prebys Medical Discovery Institute, La Jolla, CA, USA

José L. Millán

Authors

1. Yizhi Sun

[View author publications](#)

You can also search for this author in [PubMed](#) [Google Scholar](#)

2. Janane F. Rahbani

[View author publications](#)

You can also search for this author in [PubMed](#) [Google Scholar](#)

3. Mark P. Jedrychowski

[View author publications](#)

You can also search for this author in [PubMed](#) [Google Scholar](#)

4. Christopher L. Riley

[View author publications](#)

You can also search for this author in [PubMed](#) [Google Scholar](#)

5. Sara Vidoni

[View author publications](#)

You can also search for this author in [PubMed](#) [Google Scholar](#)

6. Dina Bogoslavski

[View author publications](#)

You can also search for this author in [PubMed](#) [Google Scholar](#)

7. Bo Hu

[View author publications](#)

You can also search for this author in [PubMed](#) [Google Scholar](#)

8. Phillip A. Dumesic

[View author publications](#)

You can also search for this author in [PubMed](#) [Google Scholar](#)

9. Xing Zeng

[View author publications](#)

You can also search for this author in [PubMed](#) [Google Scholar](#)

10. Alex B. Wang

[View author publications](#)

You can also search for this author in [PubMed](#) [Google Scholar](#)

11. Nelson H. Knudsen

[View author publications](#)

You can also search for this author in [PubMed](#) [Google Scholar](#)

12. Caroline R. Kim

[View author publications](#)

You can also search for this author in [PubMed](#) [Google Scholar](#)

13. Anthony Marasciullo

[View author publications](#)

You can also search for this author in [PubMed](#) [Google Scholar](#)

14. José L. Millán

[View author publications](#)

You can also search for this author in [PubMed](#) [Google Scholar](#)

15. Edward T. Chouchani

[View author publications](#)

You can also search for this author in [PubMed](#) [Google Scholar](#)

16. Lawrence Kazak

[View author publications](#)

You can also search for this author in [PubMed](#) [Google Scholar](#)

17. Bruce M. Spiegelman

[View author publications](#)

You can also search for this author in [PubMed](#) [Google Scholar](#)

## Contributions

Y.S. and B.M.S. conceived the study and designed the experiments. Y.S. performed experiments and analysed the data. Y.S. and J.F.R. performed cellular and mitochondrial respiration experiments and analysed the data. M.P.J. performed mass spectrometry analysis. C.L.R. and S.V. helped with fluorescence imaging studies. S.V. assisted with protease protection assays. D.B. assisted with all experiments. B.H. assisted with animal experiments. C.L.R., S.V., P.A.D., X.Z., A.B.W. and N.H.K. helped with animal and/or cellular experiments and data analyses. C.R.K. assisted with CLAMS studies. A.M. assisted with activity measurements and animal experiments. J.L.M. contributed essential genetic and pharmacological reagents and discussed data. L.K. and E.T.C. contributed to experimental discussions. Y.S. and B.M.S. wrote the manuscript with comments from all authors. All authors provided input and reviewed the manuscript.

## Corresponding author

Correspondence to [Bruce M. Spiegelman](#).

## Ethics declarations

## Competing interests

The authors declare no competing interests.

## Additional information

**Peer review information** *Nature* thanks the anonymous reviewers for their contribution to the peer review of this work.

**Publisher's note** Springer Nature remains neutral with regard to jurisdictional claims in published maps and institutional affiliations.

## Extended data figures and tables

### Extended Data Fig. 1 PCr phosphatase activities of thermogenic fat and TNAP.

**a**, PCr phosphatase activities of total mitochondrial protein extracts from different tissues of cold-acclimated mice. Mitochondrial protein extract was prepared from tissues excised from 10 mice for BAT or 20 mice for iWAT. Each reaction contains 10 mM of PCr and 0.4 mg ml<sup>-1</sup> of mitochondrial protein extract, except the buffer control. Data are presented as the estimated parameters ± uncertainties. Uncertainties are represented by the standard errors of nonlinear regression that fits a straight-line model to the initial linear phase of PCr hydrolysis kinetics measured by <sup>31</sup>P NMR over 11 time points for BAT and iWAT and 6 time points for the buffer control (shown in Source Data). **b**, Ion-exchange chromatography of the active fraction of SEC. The PCr phosphatase activity of each fraction was measured by enzyme-coupled assay. The activity of the most active fraction was also verified by <sup>31</sup>P NMR. Red and blue bars denote the fractions used for isobaric labelling (TMT) and quantitative mass spectrometric analysis. **c**, Western-blot analysis of the active SEC fraction prepared from cold-acclimated mice (cold), compared with the equivalent fraction prepared from room-temperature housed mice (RT). **d**, PCr phosphatase activities of total mitochondrial protein extracts from BAT of cold-acclimated mice

treated with vehicle or SBI-425 (10  $\mu$ M), measured by  $^{31}\text{P}$  NMR.  $n = 2$  technical replicates per group. Data are presented as mean  $\pm$  s.e.m. **e**, Stacked traces of  $^{31}\text{P}$  NMR spectra recorded at indicated time points, demonstrating the kinetics of PCr hydrolysis catalysed by recombinant TNAP. The minor peak marked with an asterisk on top is from glycerol-3-phosphate, a side-product of the phospho-transferase activity of TNAP<sup>50</sup>, that transfers the phosphoryl-group from PCr to glycerol present in the reaction buffer. **f**, Michaelis constant ( $K_m$ ) curves of hydrolysis of PCr (left) and PP<sub>i</sub> (right) catalysed by recombinant TNAP. Activities were measured by the enzyme-coupled assay;  $n = 2$  technical replicates. Data are presented as mean  $\pm$  s.e.m. **g**, Comparison of the Michaelis–Menten parameters extrapolated from **f**. Data are presented as the estimated parameters  $\pm$  uncertainties. Uncertainties are represented by standard errors derived from the nonlinear regression fit of Michaelis–Menten model to the data in **f**. [Source data](#)

### **Extended Data Fig. 2 Mitochondrial localization of ectopically expressed TNAP in non-thermogenic fat cell types.**

Confocal fluorescence microscopic images showing subcellular localization of ectopically expressed TNAP in different cell types. PTEC, kidney proximal tubule epithelial cells. The insets show a magnified view of the area outlined by the dotted box. Anti-TNAP and anti-HSP60 were used to visualize TNAP and mitochondria, respectively. Scale bars, 10  $\mu\text{m}$ .

### **Extended Data Fig. 3 Mitochondrial localization of endogenous TNAP in BAT and non-thermogenic fat cells.**

**a**, Confocal fluorescence images showing subcellular localization of endogenous TNAP in brown adipocytes (top and middle panels) and hepatocytes (bottom panels). Primary brown preadipocytes were prepared from *Alpl*<sup>f/f</sup> mice, transduced with either AdGFP (WT) or AdCre (*Alpl* KO) on day 4 of differentiation, and fixed for imaging on day 8. Arrows denote selected peri-nuclear areas of TNAP signal that co-localize with mitochondria signal. Antibodies for TNAP (red) and HSP60 (green) were used to visualize TNAP and mitochondria. Scale bar, 5  $\mu\text{m}$ . **b**, Pearson’s

correlation coefficient (PCC) analysis showing the extent of co-localization of TNAP with mitochondria in indicated cell types;  $n = 10$  cells per group; data are presented as mean  $\pm$  s.e.m.; statistical significance was calculated by one-way ANOVA with Bonferroni's multiple comparisons test. **c**, Western-blot analysis on TNAP in wild-type versus knockout cells. Vinculin (VCL) blot was used as a sample preparation control. **d**, Confocal fluorescence microscopic images showing subcellular localization of endogenous TNAP in different cell types. Anti-TNAP and anti-HSP60 were used to visualize TNAP and mitochondria, respectively. Scale bars, 5  $\mu\text{m}$ . **e**, Western-blot analysis on TNAP and mitochondrial markers in mitochondrial preparations from BAT of cold-acclimated, wild-type vs adipo-*Alpl* knockout mice. Blots were processed in parallel with samples derived from the same experiment. **f**, Western-blot analysis of the insoluble fraction of mitochondria extract treated with phosphatidylinositol-specific phospholipase-C (PI-PLC), followed by ultracentrifugation, showing that PLC treatment releases TNAP from membranes. P, pellet; S, supernatant. Mitochondrial preparation was fragmented by sonication before treatment. Blots were processed in parallel with samples derived from the same experiment. [Source data](#)

#### **Extended Data Fig. 4 Proximity-based fluorescent labelling by TNAP–APEX2 and trypsin protection assay on mitochondria from BAT.**

**a**, Confocal fluorescence microscopic images of immortalized brown adipocytes showing co-localization of the GFP signal from 3XHA-EGFP-OMP25 construct (mGFP, channel: 488 nm) with different mitochondria markers. Endogenous antibodies, OxPhos (upper red, channel: 561 nm) and HSP60 (lower red, channel: 640 nm), were used to visualize mitochondria. The insets show a magnified region of the image outlined by the dotted box. Scale bars, 5  $\mu\text{m}$ . **b**, Illustration of how APEX2 reports subcellular localization of TNAP by its peroxidase activity. X indicates either Alexa Fluor 647-conjugated tyramide (for confocal microscopy) or 3,3'-diaminobenzidine (for TEM studies). **c**, Confocal fluorescence analysis of immortalized brown adipocytes (top) and hepatocytes (bottom) ectopically expressing a TNAP–APEX2 construct. Cells were fixed and treated with

Alexa Fluor 647–tyramide/H<sub>2</sub>O<sub>2</sub> for proximity-based fluorescent labelling facilitated by the peroxidase activity of APEX2. Stably expressed 3XHA-EGFP-OMP25 was used as mitochondria reporter. Scale bars, 10 μm. **d**, Western blot analysis of the protease protection assay on mitochondria derived from BAT of cold-acclimated mice. TOMM20, GPD2 (glycerol-3-phosphate dehydrogenase), Cyt C (cytochrome *c*) and CS (citrate synthase) are shown as markers of outer mitochondrial membrane (OMM), intermembrane space (IMS) and mitochondrial matrix. Blots were processed in parallel with samples derived from the same experiment. **e**, Relative protein abundances in trypsin-digested mitochondria derived from band intensities of intact protein quantified from **d**; *n* = 2 technical replicates. Data are presented as mean ± s.e.m. [Source data](#)

### **Extended Data Fig. 5 Effect of *Alpl* silencing on cellular respiration.**

**a**, Quantitative PCR with reverse transcription (qRT–PCR) of differentiated primary brown preadipocytes treated with shLacZ or shAlpl; *n* = 3 biologically independent samples per group. **b**, Western-blot analysis on TNAP in cells treated with shLacZ or shAlpl. Vinculin (VCL) blot was used as a sample processing control. **c**, Effect of *Alpl* knockdown (adenoviral shAlpl) on the oxygen consumption rate (OCR) of primary brown adipocytes. Treatments to initiate different respiration states are as follows: stimulated, noradrenaline; uncoupled, oligomycin; maximum, carbonyl cyanide *m*-chlorophenyl hydrazone; *n* = 11 biologically independent samples for the shLacZ group and 18 biologically independent samples for the shAlpl group. Data are presented as mean ± s.e.m. Statistical significance was calculated by unpaired Student’s two-sided *t*-test. [Source data](#)

### **Extended Data Fig. 6 Effect of TNAP inhibition on the futile creatine cycle.**

**a**, Effect of SBI-425 treatment (10 μM) on the OCR of beige fat-derived mitochondria from wild-type vs adipo-*Alpl* knockout mice in the presence of 0.01 mM creatine and 0.1 mM ADP (limiting ADP) or 1 mM ADP

(saturating ADP), as measured by a Seahorse XF24 Extracellular Flux Analyzer;  $n = 7$  independent measurements per group. **b**, Effect of SBI-425 treatment (10  $\mu$ M) on OCR of beige fat-derived mitochondria in the presence of 0.1 mM ADP (limiting ADP) or 1 mM ADP (saturating ADP), but in the absence of creatine, as measured by a Seahorse XF24 Extracellular Flux Analyzer;  $n = 6$  independent measurements per group. Data are presented as mean  $\pm$  s.e.m. Statistical significance was calculated by either two-way ANOVA with Bonferroni's multiple comparisons test (**a**) or unpaired Student's two-sided *t*-test (**b**). [Source data](#)

### [Extended Data Fig. 7 Rapid mitochondria purification enriched mitochondrial metabolites and proteins.](#)

**a**, Relative abundances of citric acid cycle intermediates in mitochondria vs whole-cell metabolomics;  $n = 6$  biologically independent samples. Data are presented as mean  $\pm$  s.e.m. **b**, Western-blot analysis on mitochondrial markers in immunoprecipitated mitochondria for metabolomics study. Blots were processed in parallel with samples derived from the same experiment.  
[Source data](#)

### [Extended Data Fig. 8 Movement and food intake of mice upon SBI-425 treatment.](#)

**a, b**, Cumulative movement and food intake of wild-type mice (**a**) and adipo-*Alpl* knockout mice (**b**) for 24 h after treatment of SBI-425 versus vehicle;  $n = 10$  mice for wild-type and 4 mice for adipo-*Alpl* knockout. Data are presented as mean  $\pm$  s.e.m. Statistical significance was calculated using an unpaired Student's two-sided *t*-test. [Source data](#)

### [Extended Data Fig. 9 Energy expenditure and movement of wild-type and adipo-\*Alpl\* knockout mice on a HFD.](#)

**a**, Indirect calorimetric measurements taken for wild-type and adipo-*Alpl* knockout mice that had been on a HFD for 4 weeks at 22 °C;  $n = 7$  mice for wild-type and 6 mice for adipo-*Alpl* knockout; the grey area indicates the dark period. **b**, Averaged respiration rates over 24 h as measured in **a**;  $n = 7$

mice for wild-type and 6 mice for adipo-*Alpl* knockout. **c**, Cumulative movement of mice over 24 h;  $n = 7$  mice for wild-type and 6 mice for adipo-*Alpl* knockout. Data are presented as mean  $\pm$  s.e.m. Statistical significance was calculated by either two-way ANOVA (**a**) or unpaired Student's two-sided *t*-test (**b, c**). [Source data](#)

## Extended Data Fig. 10 Compensatory thermogenesis in adipo-*Alpl* knockout mice.

**a**, Indirect calorimetric measurement taken for wild-type and adipo-*Alpl* knockout mice kept in metabolic cages at 22 °C, showing stimulation of respiration by CL 316,243 administration (1.0 mg kg<sup>-1</sup>). Arrow denotes the time point of drug administration;  $n = 12$  mice for wild-type and 9 mice for adipo-*Alpl* knockout; all mice were pre-treated with CL 316,243 (1.0 mg kg<sup>-1</sup> day<sup>-1</sup>) for 5 days. **b**, Western-blot analysis of BAT and iWAT from wild-type or adipo-*Alpl* knockout mice pre-treated with CL 316,243 (1.0 mg kg<sup>-1</sup> day<sup>-1</sup>) for 5 days. **c, d**, Gene set enrichment plot of quantitative mass spectrometric analyses of BAT (**c**) and iWAT (**d**) from wild-type or adipo-*Alpl* knockout mice treated with CL 316,243 (1.0 mg kg<sup>-1</sup> day<sup>-1</sup>) for 5 days;  $n = 4$  mice for wild-type and 6 mice for adipo-*Alpl* knockout.

Enrichment analysis was performed with GSEA 4.1.0<sup>51,52</sup>. The hallmark gene sets were surveyed, and oxidative phosphorylation is the top hit for both BAT and iWAT. Family-wise error rate *P* value was presented for statistical significance (number of permutations, 1,000); NES, normalized enrichment score (enrichment statistics, 'classic'). **e, f**, qRT-PCR of BAT (**e**) and iWAT (**f**) from wild-type and adipo-*Alpl* knockout mice treated with CL 316,243 (1.0 mg kg<sup>-1</sup> day<sup>-1</sup>) for 5 days;  $n = 4$  mice for wild-type and 6 mice for adipo-*Alpl* knockout. Data are presented as mean  $\pm$  s.e.m. Statistical significance was calculated by either two-way ANOVA (**a**) or unpaired Student's two-sided *t*-test (**e, f**). [Source data](#)

## Supplementary information

### Supplementary Figure 1

This file contains the uncropped images of western blots represented in Extended Data Figure 1c, 3c, 3e-f, 4d, 5b, 7b, and 10b. Red boxes indicate regions displayed in the final figures.

## **Reporting Summary**

## **Supplementary Table 1**

This file contains the mitochondrial metabolomics data of brown adipocytes treated with vehicle vs SBI-425 (10  $\mu$ M) for 1 hour.

## **Supplementary Table 2**

This file contains the proteomics data of BAT and iWAT from WT vs Adipo-*Alpl* KO mice housed at room-temperature and pre-treated with CL 316,243 (1.0 mg/kg/day) for 5 days.

## **Source data**

### **Source Data Fig. 1**

### **Source Data Fig. 3**

### **Source Data Fig. 4**

### **Source Data Extended Data Fig. 1**

### **Source Data Extended Data Fig. 3**

### **Source Data Extended Data Fig. 4**

### **Source Data Extended Data Fig. 5**

### **Source Data Extended Data Fig. 6**

[Source Data Extended Data Fig. 7](#)

[Source Data Extended Data Fig. 8](#)

[Source Data Extended Data Fig. 9](#)

[Source Data Extended Data Fig. 10](#)

## Rights and permissions

[Reprints and Permissions](#)

## About this article



Check for  
updates

## Cite this article

Sun, Y., Rahbani, J.F., Jedrychowski, M.P. *et al.* Mitochondrial TNAP controls thermogenesis by hydrolysis of phosphocreatine. *Nature* **593**, 580–585 (2021). <https://doi.org/10.1038/s41586-021-03533-z>

[Download citation](#)

- Received: 31 August 2020
- Accepted: 11 April 2021
- Published: 12 May 2021
- Issue Date: 27 May 2021
- DOI: <https://doi.org/10.1038/s41586-021-03533-z>

## Further reading

- [Unravelling the molecular basis of futile creatine cycling](#)
  - Claire Greenhill

*Nature Reviews Endocrinology* (2021)

## Comments

By submitting a comment you agree to abide by our [Terms](#) and [Community Guidelines](#). If you find something abusive or that does not comply with our terms or guidelines please flag it as inappropriate.

[Access through your institution](#)  
[Change institution](#)  
[Buy or subscribe](#)

## Associated Content

### [Unravelling the molecular basis of futile creatine cycling](#)

- Claire Greenhill

Nature Reviews Endocrinology Research Highlight 21 May 2021

Advertisement

---

This article was downloaded by **calibre** from <https://www.nature.com/articles/s41586-021-03533-z>

- Article
- [Published: 12 May 2021](#)

# DHODH-mediated ferroptosis defence is a targetable vulnerability in cancer

- [Chao Mao](#) ORCID: orcid.org/0000-0002-8685-8539<sup>1</sup>,
- [Xiaoguang Liu](#) ORCID: orcid.org/0000-0001-6977-5128<sup>1</sup>,
- [Yilei Zhang](#) ORCID: orcid.org/0000-0003-1407-0301<sup>1</sup>,
- [Guang Lei](#) ORCID: orcid.org/0000-0002-3282-0666<sup>1</sup>,
- [Yuelong Yan](#) ORCID: orcid.org/0000-0001-8495-6445<sup>1</sup>,
- [Hyemin Lee](#)<sup>1</sup>,
- [Pranavi Koppula](#) ORCID: orcid.org/0000-0002-7567-1891<sup>1,2</sup>,
- [Shiqi Wu](#)<sup>1</sup>,
- [Li Zhuang](#)<sup>1</sup>,
- [Bingliang Fang](#)<sup>3</sup>,
- [Masha V. Poyurovsky](#)<sup>4</sup>,
- [Kellen Olszewski](#) ORCID: orcid.org/0000-0001-9691-0831<sup>4</sup> &
- [Boyi Gan](#) ORCID: orcid.org/0000-0001-8884-6040<sup>1,2</sup>

*Nature* volume 593, pages 586–590 (2021) [Cite this article](#)

- 13k Accesses
- 1 Citations
- 146 Altmetric
- [Metrics details](#)

## Subjects

- [Cancer metabolism](#)
- [Cancer therapy](#)
- [Cell death](#)

## Abstract

Ferroptosis, a form of regulated cell death that is induced by excessive lipid peroxidation, is a key tumour suppression mechanism<sup>1,2,3,4</sup>. Glutathione peroxidase 4 (GPX4)<sup>5,6</sup> and ferroptosis suppressor protein 1 (FSP1)<sup>7,8</sup> constitute two major ferroptosis defence systems. Here we show that treatment of cancer cells with GPX4 inhibitors results in acute depletion of *N*-carbamoyl-l-aspartate, a pyrimidine biosynthesis intermediate, with concomitant accumulation of uridine. Supplementation with dihydroorotate or orotate—the substrate and product of dihydroorotate dehydrogenase (DHODH)—attenuates or potentiates ferroptosis induced by inhibition of GPX4, respectively, and these effects are particularly pronounced in cancer cells with low expression of GPX4 (GPX4<sup>low</sup>). Inactivation of DHODH induces extensive mitochondrial lipid peroxidation and ferroptosis in GPX4<sup>low</sup> cancer cells, and synergizes with ferroptosis inducers to induce these effects in GPX4<sup>high</sup> cancer cells. Mechanistically, DHODH operates in parallel to mitochondrial GPX4 (but independently of cytosolic GPX4 or FSP1) to inhibit ferroptosis in the mitochondrial inner membrane by reducing ubiquinone to ubiquinol (a radical-trapping antioxidant with anti-ferroptosis activity). The DHODH inhibitor brequinar selectively suppresses GPX4<sup>low</sup> tumour growth by inducing ferroptosis, whereas combined treatment with brequinar and sulfasalazine, an FDA-approved drug with ferroptosis-inducing activity, synergistically induces ferroptosis and suppresses GPX4<sup>high</sup> tumour growth. Our results identify a DHODH-mediated ferroptosis defence mechanism in mitochondria and suggest a therapeutic strategy of targeting ferroptosis in cancer treatment.

## Access options

[Subscribe to Journal](#)

Get full journal access for 1 year

\$199.00

only \$3.90 per issue

[Subscribe](#)

All prices are NET prices.

VAT will be added later in the checkout.

Tax calculation will be finalised during checkout.

Rent or Buy article

Get time limited or full article access on ReadCube.

from \$8.99

[Rent or Buy](#)

All prices are NET prices.

### **Additional access options:**

- [Log in](#)
- [Access through your institution](#)
- [Learn about institutional subscriptions](#)

**Fig. 1: Metabolomics link DHODH to ferroptosis.**

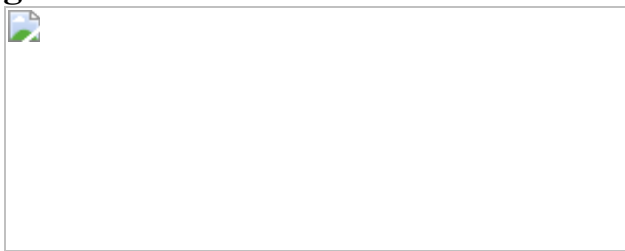


**Fig. 2: DHODH deletion promotes ferroptosis.**

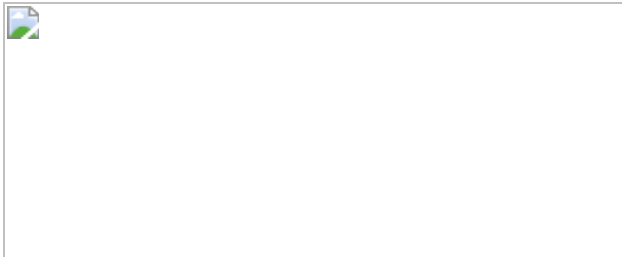


**Fig. 3: DHODH suppresses mitochondrial lipid peroxidation.**

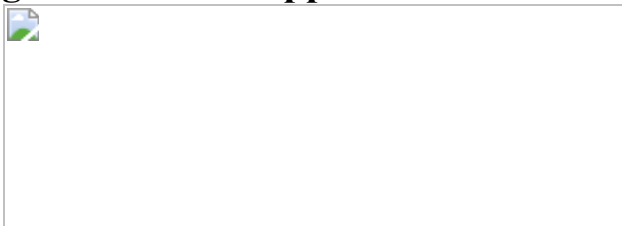
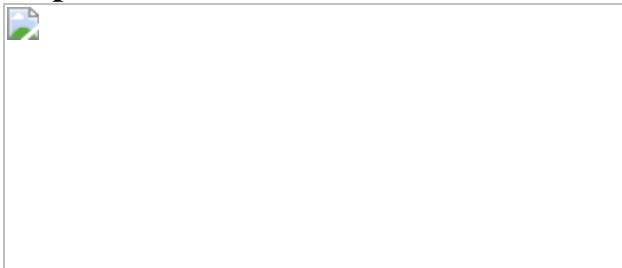


**Fig. 4: Inhibition of DHODH suppresses tumour growth by inducing ferroptosis.**



## Data availability

All data that support the conclusions in this manuscript are available from the corresponding author upon reasonable request. The source data of immunoblots are provided. The raw data used for generating Figs. 1–4 and Extended Data Figs. 1–9 are included in the Source Data. [Source data](#) are provided with this paper.

## References

1. 1.

Dixon, S. J. et al. Ferroptosis: an iron-dependent form of nonapoptotic cell death. *Cell* **149**, 1060–1072 (2012).

[CAS](#) [PubMed](#) [PubMed Central](#) [Google Scholar](#)

2. 2.

Stockwell, B. R. et al. Ferroptosis: a regulated cell death nexus linking metabolism, redox biology, and disease. *Cell* **171**, 273–285 (2017).

[CAS](#) [PubMed](#) [PubMed Central](#) [Google Scholar](#)

3. 3.

Jiang, L. et al. Ferroptosis as a p53-mediated activity during tumour suppression. *Nature* **520**, 57–62 (2015).

[ADS](#) [CAS](#) [PubMed](#) [PubMed Central](#) [Google Scholar](#)

4. 4.

Zhang, Y. et al. BAP1 links metabolic regulation of ferroptosis to tumour suppression. *Nat. Cell Biol.* **20**, 1181–1192 (2018).

[CAS](#) [PubMed](#) [PubMed Central](#) [Google Scholar](#)

5. 5.

Yang, W. S. et al. Regulation of ferroptotic cancer cell death by GPX4. *Cell* **156**, 317–331 (2014).

[CAS](#) [PubMed](#) [PubMed Central](#) [Google Scholar](#)

6. 6.

Friedmann Angeli, J. P. et al. Inactivation of the ferroptosis regulator Gpx4 triggers acute renal failure in mice. *Nat. Cell Biol.* **16**, 1180–1191 (2014).

[CAS](#) [Google Scholar](#)

7. 7.

Bersuker, K. et al. The CoQ oxidoreductase FSP1 acts parallel to GPX4 to inhibit ferroptosis. *Nature* **575**, 688–692 (2019).

[ADS](#) [CAS](#) [PubMed](#) [PubMed Central](#) [Google Scholar](#)

8. 8.

Doll, S. et al. FSP1 is a glutathione-independent ferroptosis suppressor. *Nature* **575**, 693–698 (2019).

[ADS](#) [CAS](#) [Google Scholar](#)

9. 9.

Koppula, P., Zhuang, L. & Gan, B. Cystine transporter SLC7A11/xCT in cancer: ferroptosis, nutrient dependency, and cancer therapy. *Protein Cell* <https://doi.org/10.1007/s13238-020-00789-5> (2020).

10. 10.

Doll, S. et al. ACSL4 dictates ferroptosis sensitivity by shaping cellular lipid composition. *Nat. Chem. Biol.* **13**, 91–98 (2017).

[CAS](#) [Google Scholar](#)

11. 11.

Basu, A. et al. An interactive resource to identify cancer genetic and lineage dependencies targeted by small molecules. *Cell* **154**, 1151–1161 (2013).

[CAS](#) [PubMed](#) [PubMed Central](#) [Google Scholar](#)

12. 12.

Vasan, K., Werner, M. & Chandel, N. S. Mitochondrial metabolism as a target for cancer therapy. *Cell Metab.* **32**, 341–352 (2020).

[CAS](#) [Google Scholar](#)

13. 13.

Arai, M. et al. Import into mitochondria of phospholipid hydroperoxide glutathione peroxidase requires a leader sequence. *Biochem. Biophys. Res. Commun.* **227**, 433–439 (1996).

[CAS](#) [Google Scholar](#)

14. 14.

Trnka, J., Blaikie, F. H., Smith, R. A. & Murphy, M. P. A mitochondria-targeted nitroxide is reduced to its hydroxylamine by ubiquinol in mitochondria. *Free Radic. Biol. Med.* **44**, 1406–1419 (2008).

[CAS](#) [Google Scholar](#)

15. 15.

Prime, T. A. et al. A ratiometric fluorescent probe for assessing mitochondrial phospholipid peroxidation within living cells. *Free Radic. Biol. Med.* **53**, 544–553 (2012).

[CAS](#) [Google Scholar](#)

16. 16.

Shimada, K. et al. Global survey of cell death mechanisms reveals metabolic regulation of ferroptosis. *Nat. Chem. Biol.* **12**, 497–503 (2016).

[CAS](#) [PubMed](#) [PubMed Central](#) [Google Scholar](#)

17. 17.

Hakkaart, G. A., Dassa, E. P., Jacobs, H. T. & Rustin, P. Allotopic expression of a mitochondrial alternative oxidase confers cyanide resistance to human cell respiration. *EMBO Rep.* **7**, 341–345 (2006).

[CAS](#) [Google Scholar](#)

18. 18.

Peters, G. J. et al. In vivo inhibition of the pyrimidine de novo enzyme dihydroorotic acid dehydrogenase by brequinar sodium (DUP-785; NSC 368390) in mice and patients. *Cancer Res.* **50**, 4644–4649 (1990).

[CAS](#) [Google Scholar](#)

19. 19.

Natale, R. et al. Multicenter phase II trial of brequinar sodium in patients with advanced melanoma. *Ann. Oncol.* **3**, 659–660 (1992).

[CAS](#) [Google Scholar](#)

20. 20.

Urba, S. et al. Multicenter phase II trial of brequinar sodium in patients with advanced squamous-cell carcinoma of the head and neck. *Cancer Chemother. Pharmacol.* **31**, 167–169 (1992).

[CAS](#) [Google Scholar](#)

21. 21.

Maroun, J. et al. Multicenter phase II study of brequinar sodium in patients with advanced lung cancer. *Cancer Chemother. Pharmacol.* **32**, 64–66 (1993).

[CAS](#) [Google Scholar](#)

22. 22.

Lei, G. et al. The role of ferroptosis in ionizing radiation-induced cell death and tumor suppression. *Cell Res.* **30**, 146–162 (2020).

[CAS](#) [PubMed](#) [PubMed Central](#) [Google Scholar](#)

23. 23.

Gout, P. W., Buckley, A. R., Simms, C. R. & Bruchovsky, N. Sulfasalazine, a potent suppressor of lymphoma growth by inhibition of the  $x_c^-$  cystine transporter: a new action for an old drug. *Leukemia* **15**, 1633–1640 (2001).

[CAS](#) [Google Scholar](#)

24. 24.

Zou, Y. et al. A GPX4-dependent cancer cell state underlies the clear-cell morphology and confers sensitivity to ferroptosis. *Nat. Commun.* **10**, 1617 (2019).

[ADS](#) [PubMed](#) [PubMed Central](#) [Google Scholar](#)

25. 25.

Soula, M. et al. Metabolic determinants of cancer cell sensitivity to canonical ferroptosis inducers. *Nat. Chem. Biol.* **16**, 1351–1360 (2020).

[CAS](#) [Google Scholar](#)

26. 26.

Gao, M. et al. Role of mitochondria in ferroptosis. *Mol. Cell* **73**, 354–363.e3 (2019).

[CAS](#) [Google Scholar](#)

27. 27.

Lee, H. et al. Energy-stress-mediated AMPK activation inhibits ferroptosis. *Nat. Cell Biol.* **22**, 225–234 (2020).

[CAS](#) [PubMed](#) [PubMed Central](#) [Google Scholar](#)

28. 28.

Wang, W. et al. CD8<sup>+</sup> T cells regulate tumour ferroptosis during cancer immunotherapy. *Nature* **569**, 270–274 (2019).

[ADS](#) [CAS](#) [PubMed](#) [PubMed Central](#) [Google Scholar](#)

29. 29.

Lang, X. et al. Radiotherapy and immunotherapy promote tumoral lipid oxidation and ferroptosis via synergistic repression of SLC7A11. *Cancer Discov.* **9**, 1673–1685 (2019).

[CAS](#) [PubMed](#) [PubMed Central](#) [Google Scholar](#)

30. 30.

Ye, L. F. et al. Radiation-induced lipid peroxidation triggers ferroptosis and synergizes with ferroptosis inducers. *ACS Chem. Biol.* **15**, 469–484 (2020).

[CAS](#) [PubMed](#) [PubMed Central](#) [Google Scholar](#)

31. 31.

Zhang, Y., Koppula, P. & Gan, B. Regulation of H2A ubiquitination and SLC7A11 expression by BAP1 and PRC1. *Cell Cycle* **18**, 773–783 (2019).

[CAS](#) [PubMed](#) [PubMed Central](#) [Google Scholar](#)

32. 32.

Chauhan, A. S. et al. STIM2 interacts with AMPK and regulates calcium-induced AMPK activation. *FASEB J.* **33**, 2957–2970 (2019).

[CAS](#) [Google Scholar](#)

33. 33.

Liu, X. et al. Cystine transporter regulation of pentose phosphate pathway dependency and disulfide stress exposes a targetable metabolic vulnerability in cancer. *Nat. Cell Biol.* **22**, 476–486 (2020).

[CAS](#) [PubMed](#) [PubMed Central](#) [Google Scholar](#)

34. 34.

Heinrich, P. et al. Correcting for natural isotope abundance and tracer impurity in MS-, MS/MS- and high-resolution-multiple-tracer-data from stable isotope labeling experiments with IsoCorrectoR. *Sci. Rep.* **8**, 17910 (2018).

[ADS](#) [CAS](#) [PubMed](#) [PubMed Central](#) [Google Scholar](#)

35. 35.

Koppula, P., Zhang, Y., Shi, J., Li, W. & Gan, B. The glutamate/cystine antiporter SLC7A11/xCT enhances cancer cell dependency on glucose by exporting glutamate. *J. Biol. Chem.* **292**, 14240–14249 (2017).

[CAS](#) [PubMed](#) [PubMed Central](#) [Google Scholar](#)

36. 36.

Liu, X. & Gan, B. lncRNA NBR2 modulates cancer cell sensitivity to phenformin through GLUT1. *Cell Cycle* **15**, 3471–3481 (2016).

[CAS](#) [PubMed](#) [PubMed Central](#) [Google Scholar](#)

37. 37.

Dai, F. et al. BAP1 inhibits the ER stress gene regulatory network and modulates metabolic stress response. *Proc. Natl Acad. Sci. USA* **114**, 3192–3197 (2017).

[CAS](#) [Google Scholar](#)

38. 38.

Zhang, Y. et al. H2A monoubiquitination links glucose availability to epigenetic regulation of the endoplasmic reticulum stress response and cancer cell death. *Cancer Res.* **80**, 2243–2256 (2020).

[CAS](#) [PubMed](#) [PubMed Central](#) [Google Scholar](#)

39. 39.

Fang, J. et al. Dihydro-orotate dehydrogenase is physically associated with the respiratory complex and its loss leads to mitochondrial dysfunction. *Biosci. Rep.* **33**, e00021 (2013).

[PubMed](#) [PubMed Central](#) [Google Scholar](#)

40. 40.

Nagase, M., Yamamoto, Y., Mitsui, J. & Tsuji, S. Simultaneous detection of reduced and oxidized forms of coenzyme Q10 in human cerebral spinal fluid as a potential marker of oxidative stress. *J. Clin. Biochem. Nutr.* **63**, 205–210 (2018).

[CAS](#) [PubMed](#) [PubMed Central](#) [Google Scholar](#)

41. 41.

Zhang, Y. et al. Imidazole ketone erastin induces ferroptosis and slows tumor growth in a mouse lymphoma model. *Cell Chem. Biol.* **26**, 623–633.e9 (2019).

[CAS](#) [PubMed](#) [PubMed Central](#) [Google Scholar](#)

42. 42.

Liu, X. et al. LncRNA NBR2 engages a metabolic checkpoint by regulating AMPK under energy stress. *Nat. Cell Biol.* **18**, 431–442 (2016).

[CAS](#) [PubMed](#) [PubMed Central](#) [Google Scholar](#)

43. 43.

Lee, H. et al. BAF180 regulates cellular senescence and hematopoietic stem cell homeostasis through p21. *Oncotarget* **7**, 19134–19146 (2016).

[PubMed](#) [PubMed Central](#) [Google Scholar](#)

44. 44.

Lin, A. et al. The FoxO-BNIP3 axis exerts a unique regulation of mTORC1 and cell survival under energy stress. *Oncogene* **33**, 3183–3194 (2014).

[CAS](#) [Google Scholar](#)

45. 45.

Lin, A. et al. FoxO transcription factors promote AKT Ser473 phosphorylation and renal tumor growth in response to pharmacologic inhibition of the PI3K-AKT pathway. *Cancer Res.* **74**, 1682–1693 (2014).

[CAS](#) [PubMed](#) [PubMed Central](#) [Google Scholar](#)

46. 46.

Gan, B. et al. FoxOs enforce a progression checkpoint to constrain mTORC1-activated renal tumorigenesis. *Cancer Cell* **18**, 472–484 (2010).

[CAS](#) [PubMed](#) [PubMed Central](#) [Google Scholar](#)

47. 47.

Gan, B. et al. Role of FIP200 in cardiac and liver development and its regulation of TNFalpha and TSC-mTOR signaling pathways. *J. Cell*

*Biol.* **175**, 121–133 (2006).

[CAS](#) [PubMed](#) [PubMed Central](#) [Google Scholar](#)

[Download references](#)

## Acknowledgements

We apologize to the colleagues whose relevant work cannot be cited here owing to space limitations. This research was supported by Institutional Research Fund from The University of Texas MD Anderson Cancer Center, and grants R01CA181196, R01CA190370, R01CA244144, R01CA247992 from the National Institutes of Health (to B.G.). PDX generation and annotation were supported by the University of Texas MD Anderson Cancer Center Moon Shots Program, and Specialized Program of Research Excellence (SPORE) grant CA070907. This research was also supported by the National Institutes of Health Cancer Center Support Grant P30CA016672 to The University of Texas MD Anderson Cancer Center.

## Author information

### Affiliations

1. Department of Experimental Radiation Oncology, The University of Texas MD Anderson Cancer Center, Houston, TX, USA

Chao Mao, Xiaoguang Liu, Yilei Zhang, Guang Lei, Yuelong Yan, Hyemin Lee, Pranavi Koppula, Shiqi Wu, Li Zhuang & Boyi Gan

2. The University of Texas MD Anderson UTHealth Graduate School of Biomedical Sciences, Houston, TX, USA

Pranavi Koppula & Boyi Gan

3. Department of Thoracic and Cardiovascular Surgery, The University of Texas MD Anderson Cancer Center, Houston, TX, USA

Bingliang Fang

4. Kadmon Corporation, LLC, New York, NY, USA

Masha V. Poyurovsky & Kellen Olszewski

## Authors

1. Chao Mao

[View author publications](#)

You can also search for this author in [PubMed](#) [Google Scholar](#)

2. Xiaoguang Liu

[View author publications](#)

You can also search for this author in [PubMed](#) [Google Scholar](#)

3. Yilei Zhang

[View author publications](#)

You can also search for this author in [PubMed](#) [Google Scholar](#)

4. Guang Lei

[View author publications](#)

You can also search for this author in [PubMed](#) [Google Scholar](#)

5. Yuelong Yan

[View author publications](#)

You can also search for this author in [PubMed](#) [Google Scholar](#)

6. Hyemin Lee

[View author publications](#)

You can also search for this author in [PubMed](#) [Google Scholar](#)

7. Pranavi Koppula

[View author publications](#)

You can also search for this author in [PubMed](#) [Google Scholar](#)

8. Shiqi Wu

[View author publications](#)

You can also search for this author in [PubMed](#) [Google Scholar](#)

9. Li Zhuang

[View author publications](#)

You can also search for this author in [PubMed](#) [Google Scholar](#)

10. Bingliang Fang

[View author publications](#)

You can also search for this author in [PubMed](#) [Google Scholar](#)

11. Masha V. Poyurovsky

[View author publications](#)

You can also search for this author in [PubMed](#) [Google Scholar](#)

12. Kellen Olszewski

[View author publications](#)

You can also search for this author in [PubMed](#) [Google Scholar](#)

13. Boyi Gan

[View author publications](#)

You can also search for this author in [PubMed](#) [Google Scholar](#)

## Contributions

C.M. performed most of the experiments with assistance from X.L., Y.Z., G.L., Y.Y., H.L., P.K., S.W. and L.Z.; K.O. conducted all metabolomic analyses; B.F. provided PDXs used in this study; M.V.P. provided resources

for the project; B.G., C.M., and K.O. designed the experiments; B.G. supervised the study, established collaborations, allocated funding for this study, and wrote most of the manuscript with assistance from K.O. and C.M.; and all authors commented on the manuscript.

## Corresponding authors

Correspondence to [Kellen Olszewski](#) or [Boyi Gan](#).

## Ethics declarations

## Competing interests

K.O. and M.V.P. are full-time employees of Kadmon Corporation, LLC. B.G., K.O., and M.C. have filed a patent application relating to the use of DHODH inhibitors to target ferroptosis in cancer therapy. Other authors declare no competing financial interests.

## Additional information

**Peer review information** *Nature* thanks Kivanç Birsoy and Navdeep Chandel for their contribution to the peer review of this work. Peer reviewer reports are available.

**Publisher's note** Springer Nature remains neutral with regard to jurisdictional claims in published maps and institutional affiliations.

## Extended data figures and tables

### [Extended Data Fig. 1 Pharmacological inhibition of GPX4 affects intermediate levels in the de novo pyrimidine biosynthesis pathway.](#)

**a–c**, Volcano plots comparing metabolomic profiles from HT-1080 (**a**), A-498 (**b**) or RCC4 (**c**) cells treated with vehicle and the same cells treated

with RSL3 (10  $\mu$ M) or ML162 (10  $\mu$ M) for 2 h. **d, e**, Fold change in C-Asp and uridine induced by RSL3 (10  $\mu$ M) or ML162 (10  $\mu$ M) treatment for 2 h compared with vehicle treatment in A-498 (**d**) or RCC4 (**e**) cells. **f**, Simplified schematic of de novo pyrimidine biosynthesis pathway. **g**, Fold change in intracellular DHO and OA levels upon treatment with vehicle, DHO (100  $\mu$ M) or OA (100  $\mu$ M), respectively, for 48 h in NCI-H226 cells. **h**, Fold change in intracellular C-Asp levels upon treatment with vehicle or C-Asp (100  $\mu$ M) for 48 h in NCI-H226 cells. **i**, DHO activity in HT-1080 cells treated with RSL3 (10  $\mu$ M) for 2 h, following pretreatment with vehicle, OA (100  $\mu$ M) for 24 h, or Lip-1 (10  $\mu$ M) for 48 h. **j**, GPX4 protein levels in different cell lines determined by western blotting. **k**, Cell viability in TK-10, UMRC2, A-498 and RCC4 cells treated with different doses of RSL3 for 4 h, following pretreatment with vehicle, C-Asp (100  $\mu$ M), DHO (100  $\mu$ M), OA (100  $\mu$ M), or uridine (50  $\mu$ M) for 48 h. **l**, Cell viability in SW620, U-87 MG, A549, NCI-H1437, MDA-MB-436 and MDA-MB-231 cells treated with different doses of RSL3 for 4 h, following pretreatment with vehicle, DHO (100  $\mu$ M) or OA (100  $\mu$ M) for 48 h. **m**, GPX4, DHODH, and FSP1 protein levels in different cancer cell lines determined by western blotting. **n**, Cell viability in GPX4<sup>high</sup> (HT-1080, A-498, RCC4, 786-O, and 769-P) and GPX4<sup>low</sup> (HCT-8, UMRC6, TK-10, UMRC2, and NCI-H226) cells treated with different doses of the DHODH inhibitors BQR, leflunomide (LFM), or teriflunomide (TF) for 4 h. Data are presented as mean  $\pm$  s.d.,  $n = 3$  independent repeats; unpaired, two-tailed *t*-test. Western blots are representative of two biological replicates. \* $P < 0.05$ , \*\* $P < 0.01$ , \*\*\* $P < 0.001$ , \*\*\*\* $P < 0.0001$ . ns, not significant. Asp, aspartate; C-P, carbamoyl phosphate; P, phosphate; FMN, flavin mononucleotide; FMNH<sub>2</sub>, reduced flavin mononucleotide; PRPP, phosphoribosyl pyrophosphate; PPi, inorganic pyrophosphate; OMP, orotidine 5'-monophosphate; UMP, uridine 5'-monophosphate. [Source data](#)

## Extended Data Fig. 2 The effect of DHODH inhibitors on inducing ferroptosis in different cancer cells with differential expression of GPX4.

**a, b**, Cell survival fraction and *PTGS2* mRNA levels in NCI-H226 (**a**) and HT-1080 (**b**) cells upon treatment with BQR (500  $\mu$ M for NCI-H226 cells;

5 mM for HT-1080 cells), following pretreatment with vehicle, ZVF (10  $\mu$ M), and/or Lip-1 (10  $\mu$ M) for 24 h. **c**, Cell viability in HT-1080 cells treated with different doses of RSL3 and co-treated with LFM (100  $\mu$ M) or TF (500  $\mu$ M) for 4 h, following pretreatment with vehicle or Lip-1 (10  $\mu$ M) for 24 h. **d**, Cell viability in HT-1080 cells treated with different doses of ML162 and co-treated with BQR (500  $\mu$ M), LFM (100  $\mu$ M), or TF (500  $\mu$ M) for 4 h, following pretreatment with vehicle or Lip-1 (10  $\mu$ M) for 24 h. **e**, Cell survival fraction and *PTGS2* mRNA levels in HT-1080 cells upon treatment with RSL3 (1  $\mu$ M) and/or BQR (500  $\mu$ M) for 4 h, following pretreatment with vehicle or Lip-1 (10  $\mu$ M) for 24 h. **f**, Cell viability in HT-1080 cells treated with different doses of sulfasalazine (SAS) and co-treated with BQR (500  $\mu$ M), LFM (100  $\mu$ M) or TF (500  $\mu$ M) for 4 h, following pretreatment with vehicle or Lip-1 (10  $\mu$ M) for 24 h. **g**, Cell viability in HT-1080 cells treated with different doses of erastin and co-treated with BQR (500  $\mu$ M), LFM (100  $\mu$ M) or TF (500  $\mu$ M) for 4 h, following pretreatment with vehicle or Lip-1 (10  $\mu$ M) for 24 h. **h**, mRNA levels of *SLC7A11*, *GPX4*, or *ACSL4* (bar charts) and their protein expression (western blot), were measured in HT-1080 cells treated with BQR (500  $\mu$ M), LFM (100  $\mu$ M), or TF (500  $\mu$ M) for 4 h. **i**, GSH level measurement in HT-1080 cells upon treatment with BQR (500  $\mu$ M), LFM (100  $\mu$ M), or TF (500  $\mu$ M) for 2 h. Data are presented as mean  $\pm$  s.d.,  $n = 3$  independent repeats; unpaired, two-tailed *t*-test. Western blot is representative of two biological replicates. \* $P < 0.05$ , \*\* $P < 0.01$ , \*\*\* $P < 0.001$ , \*\*\*\* $P < 0.0001$ . ns, not significant. [Source data](#)

### Extended Data Fig. 3 *DHODH* deletion sensitizes *GPX4*<sup>high</sup> cancer cells to ferroptosis or induces ferroptosis in *GPX4*<sup>low</sup> cancer cells.

**a**, DHODH protein levels in Cas9 control and *DHODH* KO *GPX4*<sup>high</sup> cancer cell lines. **b**, DHO activity in Cas9 control and *DHODH* KO HT-1080 cells. **c**, Cell survival fraction in Cas9 control and *DHODH* KO HT-1080 cells upon treatment with vehicle or uridine (50  $\mu$ M). **d**, *PTGS2* mRNA levels in Cas9 control and *DHODH* KO HT-1080 cells. **e**, Lipid peroxidation in Cas9 control and *DHODH* KO *GPX4*<sup>high</sup> cell lines as indicated. **f**, Cell viability in Cas9 control and *DHODH* KO HT-1080 cells

treated with different doses of ML162 for 4 h. **g**, Cell survival fraction and *PTGS2* mRNA levels in Cas9 control and *DHODH* KO HT-1080 cells upon treatment with RSL3 (1  $\mu$ M) for 4 h. **h**, Western blot analysis of DHODH and ACSL4 protein levels in HT-1080 cells with indicated genotypes. **i**, Cell viability measurement in HT-1080 cells with indicated genotypes treated with different doses of RSL3 for 4 h. **j**, Measurement of *SLC7A11*, *GPX4*, and *ACSL4* mRNA (bar charts) and protein levels (western blot) in Cas9 control and *DHODH* KO HT-1080 cells. **k**, GSH levels in Cas9 control and *DHODH* KO HT-1080 cells. **l**, DHODH protein levels in Cas9 control and *DHODH* KO *GPX4*<sup>low</sup> cell lines. **m**, DHO activity in Cas9 control and *DHODH* KO NCI-H226 cells. **n**, Cell proliferation of Cas9 control and *DHODH* KO NCI-H226 cells. **o**, *PTGS2* mRNA levels in Cas9 control and *DHODH* KO NCI-H226 cells. **p**, Lipid peroxidation in Cas9 control and *DHODH* KO *GPX4*<sup>low</sup> cells. Cells were grown in medium supplemented with Lip-1 (10  $\mu$ M) (**l**, **m**) and/or uridine (50  $\mu$ M) (**a**, **b**, **d–p**). Data are presented as mean  $\pm$  s.d.,  $n = 3$  independent repeats; unpaired, two-tailed *t*-test. Western blots are representative of two biological replicates. \* $P < 0.05$ , \*\* $P < 0.01$ , \*\*\* $P < 0.001$ , \*\*\*\* $P < 0.0001$ . ns, not significant.

[Source data](#)

## Extended Data Fig. 4 Analyses of genetic interactions between DHODH and GPX4 (or FSP1).

**a**, Western blotting analysis of GPX4 and DHODH protein levels in shControl and sh*GPX4* HT-1080 cells. **b**, Cell proliferation of shControl and sh*GPX4* HT-1080 cells. **c**, Cell viability of shControl and sh*GPX4* HT-1080 cells treated with different doses of LFM or TF for 4 h. **d**, Cell survival fraction and *PTGS2* mRNA levels in shControl and sh*GPX4* HT-1080 cells upon treatment with BQR (500  $\mu$ M) for 4 h. **e**, Western blot analysis of GPX4 and DHODH protein levels in HT-1080 cells with indicated genotypes. **f**, *PTGS2* mRNA levels in HT-1080 cells with indicated genotypes. **g**, Cell proliferation of HT-1080 cells with *DHODH* KO and shControl or sh*GPX4*. **h**, Western blot analysis of DHODH and FSP1 protein levels in HT-1080 cells with indicated genotypes. **i**, Cell viability in Cas9 control or *DHODH* KO HT-1080 cells with indicated genotypes treated with different doses of RSL3 for 4 h, following pretreatment with vehicle or Lip-1 (10  $\mu$ M) for 24 h. **j**, Western blot

analysis of DHODH and FSP1 protein levels in HT-1080 cells with indicated genotypes. **k**, Cell viability in Cas9 control or *DHODH* KO HT-1080 cells with indicated genotypes treated with different doses of RSL3 for 4 h, following pretreatment with vehicle or Lip-1 (10  $\mu$ M) for 24 h. **l**, Cell viability in Cas9 control or *FSP1* KO HT-1080 cells treated with vehicle or BQR (500  $\mu$ M), and different doses of RSL3 for 4 h. **m**, Simplified schematic of DHODH protein and its mutants. **n**, Western blotting showing DHODH protein levels in cytosolic and mitochondrial fractions from *DHODH* KO HT-1080 cells that express the indicated DHODH constructs. **o**, DHO activity in *DHODH* KO HT-1080 cells that express the indicated DHODH constructs. **p**, Cell viability in *DHODH* KO HT-1080 cells that express the indicated DHODH constructs treated with different doses of ML162 for 4 h. **q**, Cell survival fraction, lipid peroxidation and *PTGS2* mRNA levels in *DHODH* KO HT-1080 cells that express the indicated DHODH constructs upon treatment with RSL3 (1  $\mu$ M). Cells were grown in medium supplemented with uridine (50  $\mu$ M) (**e–l**, **n–q**). Data are presented as mean  $\pm$  s.d.,  $n = 3$  independent repeats (**b–d**, **f**, **g**, **i**, **k**, **l**, **o–q**); unpaired, two-tailed *t*-test. Western blots are representative of two biological replicates. \* $P < 0.05$ , \*\* $P < 0.01$ , \*\*\* $P < 0.001$ , \*\*\*\* $P < 0.0001$ . ns, not significant. MTS, mitochondrial targeting sequence; DHOD domain, dihydroorotate dehydrogenase domain.

[Source data](#)

### Extended Data Fig. 5 DHODH cooperates with mitochondrial GPX4 to suppress ferroptosis.

**a**, Western blotting analysis of GPX4 levels in cytosolic and mitochondrial fractions in a panel of cancer cell lines. **b**, Simplified schematic of cytosolic and mitochondrial GPX4 protein constructs. **c**, Western blotting showing GPX4 protein levels in cytosolic and mitochondrial fractions from sh*GPX4* HT-1080 cells that express the indicated GPX4 constructs. **d**, Cell viability in sh*GPX4* HT-1080 cells that express the indicated GPX4 constructs treated with different doses of LFM or TF for 4 h. **e**, Cell survival fraction, lipid peroxidation and *PTGS2* mRNA levels in sh*GPX4* HT-1080 cells that express the indicated GPX4 constructs upon treatment with BQR (500  $\mu$ M). **f**, Western blotting showing GPX4 protein levels in sh*GPX4* cells that express the indicated GPX4 constructs in a variety of cell lines. **g**, Cell

viability measurement in various sh*GPX4* cells that express the indicated GPX4 constructs treated with different doses of BQR for 4 h. Data are presented as mean  $\pm$  s.d.,  $n = 3$  independent repeats (**d, e, g**); unpaired, two-tailed *t*-test. Western blots are representative of two biological replicates. \* $P < 0.05$ , \*\* $P < 0.01$ , \*\*\* $P < 0.001$ , \*\*\*\* $P < 0.0001$ . ns, not significant.

[Source data](#)

## **Extended Data Fig. 6 Inactivation of DHODH and GPX4 induces mitochondrial lipid peroxidation.**

**a**, Western blot showing GPX4 protein levels in cytosolic and mitochondrial fractions from NCI-H226 cells that express the indicated GPX4 constructs. **b**, Cell proliferation of NCI-H226 cells that express the indicated GPX4 constructs. **c**, Cell viability in NCI-H226 cells that express the indicated GPX4 constructs treated with different doses of BQR, LFM or TF for 4 h. **d**, Cell survival fraction, lipid peroxidation and *PTGS2* mRNA levels in NCI-H226 cells that express the indicated GPX4 constructs upon treatment with BQR (500  $\mu$ M). **e**, Cell viability in Cas9 control and *DHODH* KO HT-1080 cells treated with different doses of ML162 for 4 h, following pretreatment with vehicle, TEMPO (10  $\mu$ M), MitoTEMPO (10  $\mu$ M), or Lip-1 (10  $\mu$ M) for 24 h. **f**, Cas9 control and *DHODH* KO HT-1080 cells were treated with RSL3 (1  $\mu$ M) for 2 h, then stained with mito-BODIPY. Oxidized mito-BODIPY (green) indicates mitochondrial lipid peroxidation (scale bar, 5  $\mu$ M). **g**, Mitochondrial lipid peroxidation in Cas9 control and *DHODH* KO HT-1080 cells upon treatment with RSL3 (1  $\mu$ M) for 2 h. **h**, Mitochondrial lipid peroxidation in shControl and sh*GPX4* HT-1080 cells upon treatment with BQR (500  $\mu$ M) for 2 h. **i**, Mitochondrial lipid peroxidation in HT-1080 cells upon treatment with RSL3 (1  $\mu$ M) and/or BQR (500  $\mu$ M), LFM (100  $\mu$ M), or TF (500  $\mu$ M) for 2 h, following pretreatment with vehicle or Lip-1 (10  $\mu$ M) for 24 h. **j**, Mitochondrial lipid peroxidation in HT-1080 cells upon treatment with ML162 (1  $\mu$ M) and/or BQR (500  $\mu$ M), LFM (100  $\mu$ M), or TF (500  $\mu$ M) for 2 h, following pretreatment with vehicle or Lip-1 (10  $\mu$ M) for 24 h. **k**, Mitochondrial lipid peroxidation in *DHODH* KO HT-1080 cells that express the indicated DHODH constructs upon treatment with RSL3 (1  $\mu$ M) for 2 h. **l, m**, Mitochondrial lipid peroxidation in Cas9 control and *DHODH* KO HT-1080 cells with indicated genotypes upon treatment with RSL3 (1  $\mu$ M) for

2 h, following pretreatment with vehicle or Lip-1 (10  $\mu$ M) for 24 h. **n**, Mitochondrial lipid peroxidation in Cas9 control and *FSP1* KO HT-1080 cells upon treatment with RSL3 (1  $\mu$ M) and/or BQR (500  $\mu$ M) for 2 h. **o**, Western blot analysis of DHODH and FSP1 protein levels in cytosolic and mitochondrial fractions of HT-1080 cells with indicated genotypes. **p**, Cell viability in Cas9 control and *DHODH* KO HT-1080 cells with indicated genotypes treated with different doses of RSL3 for 4 h, following pretreatment with vehicle or Lip-1 (10  $\mu$ M) for 24 h. **q**, Mitochondrial lipid peroxidation in Cas9 control and *DHODH* KO HT-1080 cells with indicated genotypes upon treatment with RSL3 (1  $\mu$ M) for 2 h, following pretreatment with vehicle or Lip-1 (10  $\mu$ M) for 24 h. **r**, Mitochondrial lipid peroxidation in sh $GPX4$  HT-1080 cells that express the indicated GPX4 constructs upon treatment with BQR (500  $\mu$ M) for 2 h. **s**, Mitochondrial lipid peroxidation in NCI-H226 cells that express the indicated GPX4 constructs upon treatment with BQR (500  $\mu$ M) for 2 h. Cells were grown in medium supplemented with uridine (50  $\mu$ M) (**e–g**, **k–q**). Data are presented as mean  $\pm$  s.d.,  $n = 3$  independent repeats (**b–e**, **g–n**, **p–s**); unpaired, two-tailed *t*-test. Western blots are representative of two biological replicates. Images are representative of at least  $n = 5$  imaged cells (**f**). \* $P < 0.05$ , \*\* $P < 0.01$ , \*\*\* $P < 0.001$ , \*\*\*\* $P < 0.0001$ . ns. Not significant. Mito-C11, fluorescent mitochondria-targeted lipid peroxidation probe. [Source data](#)

### Extended Data Fig. 7 DHODH regulation of ferroptosis relates to its function to reduce CoQ to CoQH<sub>2</sub> in mitochondria.

**a**, Cell viability in HT-1080 cells treated with different doses of FIN56 and co-treated with BQR (500  $\mu$ M), LFM (100  $\mu$ M) or TF (500  $\mu$ M) for 4 h, following pretreatment with vehicle or Lip-1 (10  $\mu$ M) for 24 h. **b**, Cell survival fraction, mitochondrial lipid peroxidation and *PTGS2* mRNA levels in HT-1080 cells upon treatment with vehicle, FIN56 (50  $\mu$ M) and/or BQR (500  $\mu$ M), following pretreatment with vehicle or Lip-1 (10  $\mu$ M) for 24 h. **c**, Western blot analysis of COQ2 and DHODH protein levels in HT-1080 cells with indicated genotypes. **d**, Total CoQ in Cas9 control and *COQ2* KO HT-1080 cells. **e**, Total CoQ in HT-1080 cells that were treated with vehicle or 4-CBA (5 mM) for 24 h. **f**, Cell viability measurement in Cas9 control and *DHODH* KO HT-1080 cells with indicated genotypes treated with different doses of RSL3 for 4 h, following pretreatment with

vehicle or Lip-1 (10  $\mu$ M) for 24 h. **g**, Cell viability in Cas9 control and *DHODH* KO HT-1080 cells with indicated genotypes treated with different doses of ML162 for 4 h, following pretreatment with vehicle or Lip-1 (10  $\mu$ M) for 24 h. **h**, Cell viability in Cas9 control and *DHODH* KO HT-1080 cells treated with different doses of RSL3 for 4 h, following pretreatment with vehicle, 4-CBA (5 mM), or 4-CBA (5 mM) + Lip-1 (10  $\mu$ M) for 24 h. **i**, Cell viability in Cas9 control and *DHODH* KO HT-1080 cells treated with different doses of ML162 for 4 h, following pretreatment with vehicle, 4-CBA (5 mM) or Lip-1 (10  $\mu$ M) for 24 h. **j**, Mitochondrial lipid peroxidation in Cas9 control and *DHODH* KO HT-1080 cells upon treatment with RSL3 (1  $\mu$ M), following pretreatment with vehicle, 4-CBA (5 mM), or 4-CBA (5 mM) + Lip-1 (10  $\mu$ M) for 24 h. **k**, Simplified schematic showing how DHODH couples the oxidation of DHO to OA to the reduction of CoQ to CoQH<sub>2</sub> in the mitochondrial inner membrane. **l**, CoQ/CoQH<sub>2</sub> ratio in NCI-H226 cells that were treated with BQR (1 mM) for 2 h. **m**, Cell viability in Cas9 control and *DHODH* KO HT-1080 cells treated with different doses of ML162 for 4 h, following pretreatment with vehicle, MitoQ (10  $\mu$ M), MitoQH<sub>2</sub> (10  $\mu$ M), or Lip-1 (10  $\mu$ M) for 24 h. **n**, Mitochondrial lipid peroxidation in Cas9 control and *DHODH* KO HT-1080 cells upon treatment with RSL3 (1  $\mu$ M) for 2 h, following pretreatment with vehicle, MitoQ (10  $\mu$ M), MitoQH<sub>2</sub> (10  $\mu$ M), or Lip-1 (10  $\mu$ M) for 24 h. **o**, Lipid peroxidation in Cas9 control and *DHODH* KO HT-1080 cells upon treatment with RSL3 (1  $\mu$ M) for 2 h, following pretreatment with vehicle, MitoQ (10  $\mu$ M), MitoQH<sub>2</sub> (10  $\mu$ M), or Lip-1 (10  $\mu$ M) for 24 h. Cells were grown in medium supplemented with uridine (50  $\mu$ M) (**c**, **d**, **f–j**, **m–o**). Data are presented as mean  $\pm$  s.d.,  $n = 3$  independent repeats (**a**, **b**, **d–j**, **l–o**); unpaired, two-tailed *t*-test. Western blot is representative of two biological replicates. \**P* < 0.05, \*\**P* < 0.01, \*\*\**P* < 0.001, \*\*\*\**P* < 0.0001. ns, not significant. OCR, oxygen consumption rate; MitoQ, [10-(4,5-dimethoxy-2-methyl-3,6-dioxo-1,4-cyclohexadien-1-yl)decyl] triphenyl-phosphonium, monomethanesulfonate; MitoQH<sub>2</sub>, [10-(2,5-dihydroxy-3,4-dimethoxy-6-methylphenyl)decyl] triphenyl-phosphonium, monomethanesulfonate. [Source data](#)

## Extended Data Fig. 8 The effects of mitoQ and mitoQH<sub>2</sub> on RSL3- and BQR-induced ferroptosis in a variety of cell lines.

**a**, GPX4, DHODH and FSP1 protein levels in indicated cell lines determined by western blotting. **b–j**, Cell viability in 293T (**b**), Hela (**c**), Jurkat (**d**), SW620 (**e**), U-87 MG (**f**), A549 (**g**), NCI-H1437 (**h**), MDA-MB-436 (**i**), and MDA-MB-231 (**j**) cells treated with different doses of RSL3 with vehicle or BQR (500 μM) for 4 h, following pretreatment with vehicle, MitoQ (10 μM), MitoQH<sub>2</sub> (10 μM), or Lip-1 (10 μM) for 24 h. **k**, CoQ/CoQH<sub>2</sub> ratio in HT-1080 cells that were treated with myxothiazol (10 μM) for 2 h. **l**, Cell viability in Cas9 control and *DHODH* KO HT-1080 cells treated with different doses of RSL3 for 4 h, following pretreatment with vehicle or myxothiazol (1 μM) for 24 h. **m**, CoQ/CoQH<sub>2</sub> ratio in A549 cells that were treated with myxothiazol (10 μM) for 2 h. **n**, Cell viability in A549 cells treated with different doses of RSL3 with or without BQR (500 μM) for 4 h, following pretreatment with vehicle or myxothiazol (1 μM) for 24 h. **o**, Western blot analysis of DHODH and *CiAOX* protein levels in HT-1080 cells with indicated genotypes. **p**, Mitochondrial lipid peroxidation in HT-1080 cells with indicated genotypes upon treatment with RSL3 (1 μM) for 2 h. Cells were grown in medium supplemented with uridine (50 μM) (**l**, **o**, **p**). Data are presented as mean ± s.d.,  $n = 3$  independent repeats (**b–n**, **p**); unpaired, two-tailed *t*-test. Western blots are representative of two biological replicates. \* $P < 0.05$ , \*\* $P < 0.01$ , \*\*\* $P < 0.001$ , \*\*\*\* $P < 0.0001$ . ns, not significant. [Source data](#)

## Extended Data Fig. 9 DHODH inhibitor selectively suppresses GPX4<sup>low</sup> tumour growth.

**a**, Weights of shControl and shGPX4 HT-1080 xenograft tumours with the indicated treatments. **b–d**, Representative immunochemical images from shControl and shGPX4 HT-1080 xenograft tumours with the indicated treatments (**b**; scale bars, 20 μM), and staining scores of cleaved-caspase 3 (**c**) and ki67 (**d**). **e**, Weight measurements of NCI-H226 xenograft tumours with the indicated treatments. **f**, Weight measurements of TC632, TC629, or TC494 PDX tumours with the indicated treatments. **g**, Volumes of Cas9 control and *DHODH* KO NCI-H226 xenograft tumours with the indicated treatments at different time points (days). **h**, Weights of Cas9 control and *DHODH* KO NCI-H226 xenograft tumours with the indicated treatments. **i**, Weight measurements of HT-1080 xenograft tumours with the indicated

treatments. **j–l**, Representative immunochemistry images of HT-1080 xenograft tumours with the indicated treatments (**j**; scale bars, 20 µM) and staining scores of cleaved-caspase 3 (**k**) and ki67 (**l**). **m**, Volumes of TC629 PDX tumours with the indicated treatments at different time points (days). **n**, Weights of TC632 and TC629 PDX tumours with the indicated treatments. **o**, Weights of mice for all cell line xenografts or PDXs with different treatments at different time points (days). Box plots indicate median, minima and maxima of the distributions, and with whiskers from minimum to maximum. Data are presented as mean ± s.d.,  $n = 8$  (**a, e, g–i**),  $n = 5$  (**c, d, k, l**) or  $n = 6$  independent tumours (**f, m, n**).  $n = 4$  for nude mouse weights and  $n = 8$  for NSG mouse weights (**o**). Unpaired, two-tailed *t*-test. Images are representative of  $n = 5$  images. \* $P < 0.05$ , \*\* $P < 0.01$ , \*\*\* $P < 0.001$ , \*\*\*\* $P < 0.0001$ . ns, not significant. 4-HNE, 4-hydroxynonenal. [Source data](#)

## Extended Data Fig. 10 Working model depicting how GPX4, FSP1, and DHODH suppress ferroptosis in different subcellular compartments.

See main text for a detailed description. PLOOH, phospholipid hydroperoxide; PLOO·, phospholipid hydroperoxyl radical; GSSH, oxidized glutathione; NAD(P)H, reduced nicotinamide adenine dinucleotide (phosphate); NAD(P)+, oxidized nicotinamide adenine dinucleotide (phosphate).

## Supplementary information

### Supplementary Figure

This file contains a figure exemplifying the gating strategy.

### Reporting Summary

### Supplementary Table 1

A list of sequences and primers used in the study.

## Peer Review File

## **Source data**

[Source Data Fig. 1](#)

[Source Data Fig. 2](#)

[Source Data Fig. 3](#)

[Source Data Fig. 4](#)

[Source Data Extended Data Fig. 1](#)

[Source Data Extended Data Fig. 2](#)

[Source Data Extended Data Fig. 3](#)

[Source Data Extended Data Fig. 4](#)

[Source Data Extended Data Fig. 5](#)

[Source Data Extended Data Fig. 6](#)

[Source Data Extended Data Fig. 7](#)

[Source Data Extended Data Fig. 8](#)

[Source Data Extended Data Fig. 9](#)

## **Rights and permissions**

[Reprints and Permissions](#)

## About this article



## Cite this article

Mao, C., Liu, X., Zhang, Y. *et al.* DHODH-mediated ferroptosis defence is a targetable vulnerability in cancer. *Nature* **593**, 586–590 (2021).  
<https://doi.org/10.1038/s41586-021-03539-7>

### [Download citation](#)

- Received: 25 June 2020
- Accepted: 07 April 2021
- Published: 12 May 2021
- Issue Date: 27 May 2021
- DOI: <https://doi.org/10.1038/s41586-021-03539-7>

## Further reading

- [A mitochondrial gatekeeper that helps cells escape death by ferroptosis](#)
  - Javier Garcia-Bermudez
  - & Kivanç Birsoy

*Nature* (2021)

## Comments

By submitting a comment you agree to abide by our [Terms](#) and [Community Guidelines](#). If you find something abusive or that does not comply with our terms or guidelines please flag it as inappropriate.

[Access through your institution](#)

[Change institution](#)

[Buy or subscribe](#)

## Associated Content

### [A mitochondrial gatekeeper that helps cells escape death by ferroptosis](#)

- Javier Garcia-Bermudez
- Kivanç Birsoy

Nature News & Views 12 May 2021

Advertisement

---

This article was downloaded by **calibre** from <https://www.nature.com/articles/s41586-021-03539-7>

| [Section menu](#) | [Main menu](#) |

- Article
- [Published: 05 May 2021](#)

# Replication stress promotes cell elimination by extrusion

- [Vivek K. Dwivedi](#) ORCID: [orcid.org/0000-0002-0608-1230](#)<sup>1</sup>,
- [Carlos Pardo-Pastor](#) ORCID: [orcid.org/0000-0003-4083-0511](#)<sup>2</sup>,
- [Rita Droste](#)<sup>1</sup>,
- [Ji Na Kong](#)<sup>1</sup>,
- [Nolan Tucker](#)<sup>1</sup>,
- [Daniel P. Denning](#)<sup>1,3</sup>,
- [Jody Rosenblatt](#) ORCID: [orcid.org/0000-0001-9460-5868](#)<sup>2</sup> &
- [H. Robert Horvitz](#) ORCID: [orcid.org/0000-0002-9964-9613](#)<sup>1</sup>

[Nature](#) volume **593**, pages 591–596 (2021) [Cite this article](#)

- 7040 Accesses
- 1 Citations
- 171 Altmetric
- [Metrics details](#)

## Subjects

- [Cell biology](#)
- [Cell death](#)
- [Checkpoints](#)
- [Genetics](#)
- [Tumour-suppressor proteins](#)

## Abstract

Cell extrusion is a mechanism of cell elimination that is used by organisms as diverse as sponges, nematodes, insects and mammals<sup>1,2,3</sup>. During extrusion, a cell detaches from a layer of surrounding cells while maintaining the continuity of that layer<sup>4</sup>. Vertebrate epithelial tissues primarily eliminate cells by extrusion, and the dysregulation of cell extrusion has been linked to epithelial diseases, including cancer<sup>1,5</sup>. The mechanisms that drive cell extrusion remain incompletely understood. Here, to analyse cell extrusion by *Caenorhabditis elegans* embryos<sup>3</sup>, we conducted a genome-wide RNA interference screen, identified multiple cell-cycle genes with S-phase-specific function, and performed live-imaging experiments to establish how those genes control extrusion. Extruding cells experience replication stress during S phase and activate a replication-stress response via homologues of ATR and CHK1. Preventing S-phase entry, inhibiting the replication-stress response, or allowing completion of the cell cycle blocked cell extrusion. Hydroxyurea-induced replication stress<sup>6,7</sup> triggered ATR–CHK1- and p53-dependent cell extrusion from a mammalian epithelial monolayer. We conclude that cell extrusion induced by replication stress is conserved among animals and propose that this extrusion process is a primordial mechanism of cell elimination with a tumour-suppressive function in mammals.

## Access options

Subscribe to Journal

Get full journal access for 1 year

\$199.00

only \$3.90 per issue

[Subscribe](#)

All prices are NET prices.  
VAT will be added later in the checkout.  
Tax calculation will be finalised during checkout.

Rent or Buy article

Get time limited or full article access on ReadCube.

from \$8.99

[Rent or Buy](#)

All prices are NET prices.

### **Additional access options:**

- [Log in](#)
- [Access through your institution](#)
- [Learn about institutional subscriptions](#)

**Fig. 1: Cell-cycle genes control cell extrusion cell autonomously.**

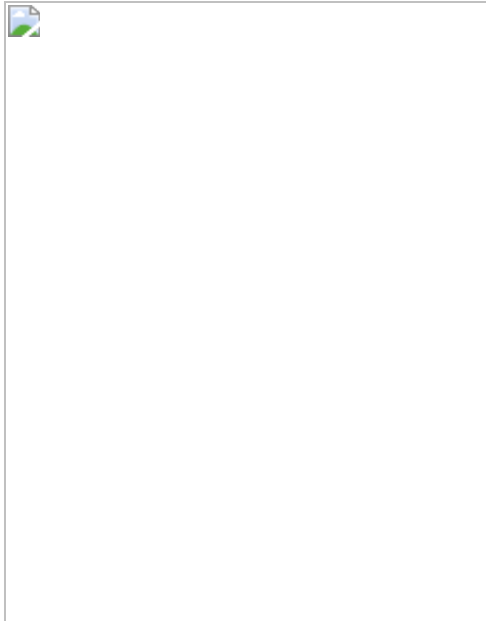


**Fig. 2: Cells undergoing extrusion arrest in S phase.**

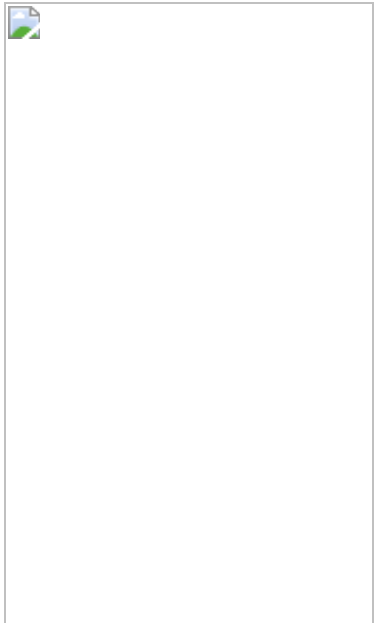


**Fig. 3: Replication stress is coincident with and promotes cell extrusion.**

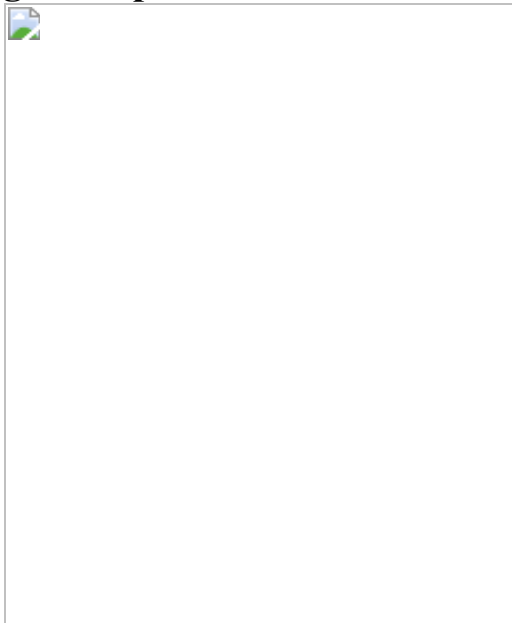
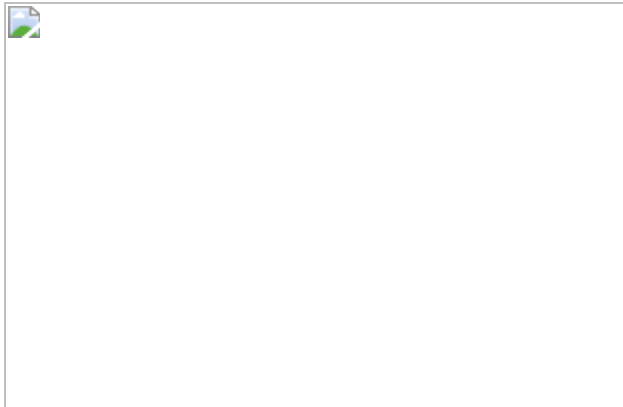


**Fig. 4: Replication stress promotes cell extrusion from a simple mammalian epithelial layer.**



## Data availability

Data supporting all figures are available within the paper and in the associated Source Data files. Raw microscopy data are available upon request from the corresponding author. [Source data](#) are provided with this paper.

## References

1. 1.

Ohsawa, S., Vaughen, J. & Igaki, T. Cell extrusion: a stress-responsive force for good or evil in epithelial homeostasis. *Dev. Cell* **44**, 284–296 (2018).

[CAS](#) [PubMed](#) [PubMed Central](#) [Google Scholar](#)

2. 2.

De Goeij, J. M. et al. Cell kinetics of the marine sponge *Halisarca caerulea* reveal rapid cell turnover and shedding. *J. Exp. Biol.* **212**, 3892–3900 (2009).

[PubMed](#) [Google Scholar](#)

3. 3.

Denning, D. P., Hatch, V. & Horvitz, H. R. Programmed elimination of cells by caspase-independent cell extrusion in *C. elegans*. *Nature* **488**, 226–230 (2012).

[ADS](#) [CAS](#) [PubMed](#) [PubMed Central](#) [Google Scholar](#)

4. 4.

Rosenblatt, J., Raff, M. C. & Cramer, L. P. An epithelial cell destined for apoptosis signals its neighbors to extrude it by an actin- and myosin-dependent mechanism. *Curr. Biol.* **11**, 1847–1857 (2001).

[CAS](#) [PubMed](#) [Google Scholar](#)

5. 5.

Gudipaty, S. A. & Rosenblatt, J. Epithelial cell extrusion: pathways and pathologies. *Semin. Cell Dev. Biol.* **67**, 132–140 (2017).

[CAS](#) [PubMed](#) [Google Scholar](#)

6. 6.

Timson, J. Hydroxyurea. *Mutat. Res.* **32**, 115–132 (1975).

[CAS](#) [PubMed](#) [Google Scholar](#)

7. 7.

Koç, A., Wheeler, L. J., Mathews, C. K. & Merrill, G. F. Hydroxyurea arrests DNA replication by a mechanism that preserves basal dNTP pools. *J. Biol. Chem.* **279**, 223–230 (2004).

[PubMed](#) [Google Scholar](#)

8. 8.

Takeda, D. Y. & Dutta, A. DNA replication and progression through S phase. *Oncogene* **24**, 2827–2843 (2005).

[CAS](#) [PubMed](#) [Google Scholar](#)

9. 9.

Fay, D. S. & Han, M. Mutations in *cye-1*, a *Caenorhabditis elegans* cyclin E homolog, reveal coordination between cell-cycle control and vulval development. *Development* **127**, 4049–4060 (2000).

[CAS](#) [PubMed](#) [Google Scholar](#)

10. 10.

van Rijnberk, L. M., van der Horst, S. E. M., van den Heuvel, S. & Ruijtenberg, S. A dual transcriptional reporter and CDK-activity sensor marks cell cycle entry and progression in *C. elegans*. *PLoS One* **12**, e0171600 (2017).

[PubMed](#) [PubMed Central](#) [Google Scholar](#)

11. 11.

Brauchle, M., Baumer, K. & Gönczy, P. Differential activation of the DNA replication checkpoint contributes to asynchrony of cell division in *C. elegans* embryos. *Curr. Biol.* **13**, 819–827 (2003).

[CAS](#) [PubMed](#) [Google Scholar](#)

12. 12.

Zerjatke, T. et al. Quantitative cell cycle analysis based on an endogenous all-in-one reporter for cell tracking and classification. *Cell Rep.* **19**, 1953–1966 (2017).

[CAS](#) [PubMed](#) [PubMed Central](#) [Google Scholar](#)

13. 13.

Teuliere, J. & Garriga, G. Size matters: how *C. elegans* asymmetric divisions regulate apoptosis. *Results Probl. Cell Differ.* **61**, 141–163

(2017).

[CAS](#) [PubMed](#) [Google Scholar](#)

14. 14.

Stergiou, L., Eberhard, R., Doukoumetzidis, K. & Hengartner, M. O. NER and HR pathways act sequentially to promote UV-C-induced germ cell apoptosis in *Caenorhabditis elegans*. *Cell Death Differ.* **18**, 897–906 (2011).

[CAS](#) [PubMed](#) [Google Scholar](#)

15. 15.

Dinant, C. et al. Activation of multiple DNA repair pathways by sub-nuclear damage induction methods. *J. Cell Sci.* **120**, 2731–2740 (2007).

[CAS](#) [PubMed](#) [Google Scholar](#)

16. 16.

Wu, Y. C., Stanfield, G. M. & Horvitz, H. R. NUC-1, a *Caenorhabditis elegans* DNase II homolog, functions in an intermediate step of DNA degradation during apoptosis. *Genes Dev.* **14**, 536–548 (2000).

[CAS](#) [PubMed](#) [PubMed Central](#) [Google Scholar](#)

17. 17.

Toledo, L. I. et al. ATR prohibits replication catastrophe by preventing global exhaustion of RPA. *Cell* **155**, 1088–1103 (2013).

[CAS](#) [PubMed](#) [Google Scholar](#)

18. 18.

Stevens, H., Williams, A. B. & Michael, W. M. Cell-type specific responses to DNA replication stress in early *C. elegans* embryos. *PLoS One* **11**, e0164601 (2016).

[PubMed](#) [PubMed Central](#) [Google Scholar](#)

19. 19.

Ossareh-Nazari, B., Katsiarimpa, A., Merlet, J. & Pintard, L. RNAi-based suppressor screens reveal genetic interactions between the CRL2LRR-1 E3-ligase and the DNA replication machinery in *Caenorhabditis elegans*. *G3 (Bethesda)* **6**, 3431–3442 (2016).

[CAS](#) [Google Scholar](#)

20. 20.

Sonneville, R. et al. CUL-2<sup>LRR-1</sup> and UBXN-3 drive replisome disassembly during DNA replication termination and mitosis. *Nat. Cell Biol.* **19**, 468–479 (2017).

[CAS](#) [PubMed](#) [PubMed Central](#) [Google Scholar](#)

21. 21.

Dewar, J. M., Low, E., Mann, M., Räschle, M. & Walter, J. C. CRL2<sup>Lrr1</sup> promotes unloading of the vertebrate replisome from chromatin during replication termination. *Genes Dev.* **31**, 275–290 (2017).

[CAS](#) [PubMed](#) [PubMed Central](#) [Google Scholar](#)

22. 22.

Merlet, J. et al. The CRL2LRR-1 ubiquitin ligase regulates cell cycle progression during *C. elegans* development. *Development* **137**, 3857–3866 (2010).

[CAS](#) [PubMed](#) [PubMed Central](#) [Google Scholar](#)

23. 23.

Meek, D. W. Tumour suppression by p53: a role for the DNA damage response? *Nat. Rev. Cancer* **9**, 714–723 (2009).

[CAS](#) [PubMed](#) [Google Scholar](#)

24. 24.

Jones, M. C., Askari, J. A., Humphries, J. D. & Humphries, M. J. Cell adhesion is regulated by CDK1 during the cell cycle. *J. Cell Biol.* **217**, 3203–3218 (2018).

[CAS](#) [PubMed](#) [PubMed Central](#) [Google Scholar](#)

25. 25.

Grieve, A. G. & Rabouille, C. Extracellular cleavage of E-cadherin promotes epithelial cell extrusion. *J. Cell Sci.* **127**, 3331–3346 (2014).

[CAS](#) [PubMed](#) [Google Scholar](#)

26. 26.

Wernike, D., Chen, Y., Mastronardi, K., Makil, N. & Piekny, A. Mechanical forces drive neuroblast morphogenesis and are required for epidermal closure. *Dev. Biol.* **412**, 261–277 (2016).

[CAS](#) [PubMed](#) [Google Scholar](#)

27. 27.

Eisenhoffer, G. T. et al. Crowding induces live cell extrusion to maintain homeostatic cell numbers in epithelia. *Nature* **484**, 546–549 (2012).

[ADS](#) [CAS](#) [PubMed](#) [PubMed Central](#) [Google Scholar](#)

28. 28.

Gaillard, H., García-Muse, T. & Aguilera, A. Replication stress and cancer. *Nat. Rev. Cancer* **15**, 276–289 (2015).

[CAS](#) [PubMed](#) [Google Scholar](#)

29. 29.

Olive, K. P. et al. Mutant p53 gain of function in two mouse models of Li-Fraumeni syndrome. *Cell* **119**, 847–860 (2004).

[CAS](#) [PubMed](#) [Google Scholar](#)

30. 30.

Lang, G. A. et al. Gain of function of a p53 hot spot mutation in a mouse model of Li-Fraumeni syndrome. *Cell* **119**, 861–872 (2004).

[CAS](#) [PubMed](#) [Google Scholar](#)

31. 31.

Singh, S. et al. Mutant p53 establishes targetable tumor dependency by promoting unscheduled replication. *J. Clin. Invest.* **127**, 1839–1855 (2017).

[PubMed](#) [PubMed Central](#) [Google Scholar](#)

32. 32.

Yeo, C. Q. X. et al. p53 maintains genomic stability by preventing interference between transcription and replication. *Cell Rep.* **15**, 132–146 (2016).

[CAS](#) [PubMed](#) [Google Scholar](#)

33. 33.

Karagiannis, G. S. et al. Neoadjuvant chemotherapy induces breast cancer metastasis through a TMEM-mediated mechanism. *Sci. Transl.*

*Med.* **9**, eaan0026 (2017).

[PubMed](#) [PubMed Central](#) [Google Scholar](#)

34. 34.

Brenner, S. The genetics of *Caenorhabditis elegans*. *Genetics* **77**, 71–94 (1974).

[CAS](#) [PubMed](#) [PubMed Central](#) [Google Scholar](#)

35. 35.

Brodigan, T. M., Liu, Ji., Park, M., Kipreos, E. T. & Krause, M. Cyclin E expression during development in *Caenorhabditis elegans*. *Dev. Biol.* **254**, 102–115 (2003).

[CAS](#) [PubMed](#) [Google Scholar](#)

36. 36.

Wu, Y. C. & Horvitz, H. R. *C. elegans* phagocytosis and cell-migration protein CED-5 is similar to human DOCK180. *Nature* **392**, 501–504 (1998).

[ADS](#) [CAS](#) [PubMed](#) [Google Scholar](#)

37. 37.

Hsieh, J. et al. The RING finger/B-box factor TAM-1 and a retinoblastoma-like protein LIN-35 modulate context-dependent gene silencing in *Caenorhabditis elegans*. *Genes Dev.* **13**, 2958–2970 (1999).

[CAS](#) [PubMed](#) [PubMed Central](#) [Google Scholar](#)

38. 38.

Grishok, A., Sinskey, J. L. & Sharp, P. A. Transcriptional silencing of a transgene by RNAi in the soma of *C. elegans*. *Genes Dev.* **19**, 683–696 (2005).

[CAS](#) [PubMed](#) [PubMed Central](#) [Google Scholar](#)

39. 39.

Fischer, S. E. J. et al. Multiple small RNA pathways regulate the silencing of repeated and foreign genes in *C. elegans*. *Genes Dev.* **27**, 2678–2695 (2013).

[CAS](#) [PubMed](#) [PubMed Central](#) [Google Scholar](#)

40. 40.

Boeck, M. E. et al. Specific roles for the GATA transcription factors *end-1* and *end-3* during *C. elegans* E-lineage development. *Dev. Biol.* **358**, 345–355 (2011).

[CAS](#) [PubMed](#) [PubMed Central](#) [Google Scholar](#)

41. 41.

Mello, C. C., Kramer, J. M., Stinchcomb, D. & Ambros, V. Efficient gene transfer in *C. elegans*: extrachromosomal maintenance and integration of transforming sequences. *EMBO J.* **10**, 3959–3970 (1991).

[CAS](#) [PubMed](#) [PubMed Central](#) [Google Scholar](#)

42. 42.

Rual, J.-F. et al. Toward improving *Caenorhabditis elegans* phenome mapping with an ORFeome-based RNAi library. *Genome Res.* **14** (10B), 2162–2168 (2004).

[CAS](#) [PubMed](#) [PubMed Central](#) [Google Scholar](#)

43. 43.

Fraser, A. G. et al. Functional genomic analysis of *C. elegans* chromosome I by systematic RNA interference. *Nature* **408**, 325–330 (2000).

[ADS](#) [CAS](#) [PubMed](#) [Google Scholar](#)

44. 44.

Kamath, R. S. et al. Systematic functional analysis of the *Caenorhabditis elegans* genome using RNAi. *Nature* **421**, 231–237 (2003).

[ADS](#) [CAS](#) [PubMed](#) [Google Scholar](#)

45. 45.

Sulston, J. E., Schierenberg, E., White, J. G. & Thomson, J. N. The embryonic cell lineage of the nematode *Caenorhabditis elegans*. *Dev. Biol.* **100**, 64–119 (1983).

[CAS](#) [PubMed](#) [Google Scholar](#)

46. 46.

Schindelin, J. et al. Fiji: an open-source platform for biological-image analysis. *Nat. Methods* **9**, 676–682 (2012).

[CAS](#) [Google Scholar](#)

47. 47.

Hansson, G. C., Simons, K. & van Meer, G. Two strains of the Madin-Darby canine kidney (MDCK) cell line have distinct glycosphingolipid compositions. *EMBO J.* **5**, 483–489 (1986).

[CAS](#) [PubMed](#) [PubMed Central](#) [Google Scholar](#)

48. 48.

Streichan, S. J., Hoerner, C. R., Schneidt, T., Holzer, D. & Hufnagel, L. Spatial constraints control cell proliferation in tissues. *Proc. Natl Acad. Sci. USA* **111**, 5586–5591 (2014).

[ADS](#) [CAS](#) [PubMed](#) [Google Scholar](#)

49. 49.

Sakaue-Sawano, A. et al. Visualizing spatiotemporal dynamics of multicellular cell-cycle progression. *Cell* **132**, 487–498 (2008).

[CAS](#) [PubMed](#) [Google Scholar](#)

50. 50.

McQuin, C. et al. CellProfiler 3.0: next-generation image processing for biology. *PLoS Biol.* **16**, e2005970 (2018).

[PubMed](#) [PubMed Central](#) [Google Scholar](#)

51. 51.

Kipreos, E. T., Gohel, S. P. & Hedgecock, E. M. The *C. elegans* F-box/WD-repeat protein LIN-23 functions to limit cell division during development. *Development* **127**, 5071–5082 (2000).

[CAS](#) [PubMed](#) [Google Scholar](#)

[Download references](#)

## Acknowledgements

We thank S. van den Heuvel and the CGC, which is funded by NIH Office of Research Infrastructure Programs (P40 OD010440), for providing strains; L. Hufnagel and X. Trepat for providing MDCK-Fucci cells; G. van Meer and the ECACC for providing MDCK-II cells (ECACC 62107); N.

An for strain management; S. Luo, S. R. Sando, E. L. Q. Lee, A. Doi, A. Corrionero and other members of the Horvitz laboratory for helpful discussions; and D. Ghosh, C. L. Pender, M. G. Vander Heiden, P. W. Reddien, and R. O. Hynes for suggestions regarding the manuscript. This work was supported by the Howard Hughes Medical Institute and by NIH grant R01GM024663. V.K.D. was a Howard Hughes Medical Institute International Student Research fellow. C.P.-P. was the recipient of Human Frontiers Science Program postdoctoral fellowship LT000654/2019-L. J.N.K. was supported by NIH grant R01GM024663. N.T. was supported by NIH Pre-Doctoral Training Grant T32GM007287. D.P.D. was supported by postdoctoral fellowships from the Damon Runyon Cancer Research Foundation and from the Charles A. King Trust. J.R. and C.P.-P. were funded by King's College London startup funds. H.R.H. is the David H. Koch Professor of Biology at MIT and an Investigator at the Howard Hughes Medical Institute.

## Author information

### Affiliations

1. Howard Hughes Medical Institute, Department of Biology,  
Massachusetts Institute of Technology, Cambridge, MA, USA

Vivek K. Dwivedi, Rita Droste, Ji Na Kong, Nolan Tucker, Daniel P. Denning & H. Robert Horvitz

2. Randall Centre for Cell & Molecular Biophysics, King's College London, London, UK

Carlos Pardo-Pastor & Jody Rosenblatt

3. Novartis Institutes for BioMedical Research, Cambridge, MA, USA

Daniel P. Denning

### Authors

1. Vivek K. Dwivedi

[View author publications](#)

You can also search for this author in [PubMed](#) [Google Scholar](#)

2. Carlos Pardo-Pastor

[View author publications](#)

You can also search for this author in [PubMed](#) [Google Scholar](#)

3. Rita Droste

[View author publications](#)

You can also search for this author in [PubMed](#) [Google Scholar](#)

4. Ji Na Kong

[View author publications](#)

You can also search for this author in [PubMed](#) [Google Scholar](#)

5. Nolan Tucker

[View author publications](#)

You can also search for this author in [PubMed](#) [Google Scholar](#)

6. Daniel P. Denning

[View author publications](#)

You can also search for this author in [PubMed](#) [Google Scholar](#)

7. Jody Rosenblatt

[View author publications](#)

You can also search for this author in [PubMed](#) [Google Scholar](#)

8. H. Robert Horvitz

[View author publications](#)

You can also search for this author in [PubMed](#) [Google Scholar](#)

## Contributions

H.R.H. supervised the project. V.K.D. and H.R.H. conceptualized the project. V.K.D. and H.R.H. designed the experiments that used *C. elegans*. V.K.D., R.D., J.N.K. and N.T. performed the experiments that used *C. elegans*. V.K.D., R.D. and D.P.D. generated reagents. C.P.-P. and J.R. designed the experiments that used mammalian cells. C.P.-P. performed the experiments that used mammalian cells. V.K.D., D.P.D. and H.R.H. wrote the original and revised manuscript drafts. All authors contributed to data analysis, interpretation, and reviewing and editing of the manuscript.

## Corresponding author

Correspondence to [H. Robert Horvitz](#).

## Ethics declarations

### Competing interests

The authors declare no competing interests.

## Additional information

**Peer review information** *Nature* thanks Joan Brugge and the other, anonymous, reviewer(s) for their contribution to the peer review of this work.

**Publisher's note** Springer Nature remains neutral with regard to jurisdictional claims in published maps and institutional affiliations.

## Extended data figures and tables

[\*\*Extended Data Fig. 1 A genome-wide RNAi screen for the Tex phenotype revealed control of cell extrusion by \*cye-1\* and \*cdk-2\*.\*\*](#)

**a**, Schematic representation of the genome-wide RNAi screen for the Tex phenotype. RNAi using pL4440 empty vector was used as negative control and *pig-1(RNAi)* was used as positive control<sup>3</sup>. **b**, Time-lapse confocal fluorescence micrographs of *ced-3(lf); stIs10026[his-72::GFP]; nIs632[P<sub>egl-1</sub>::mCherry::PH]* embryos after indicated RNAi treatment at the indicated times.  $t_{ve}$ , time point of ventral enclosure. Arrowheads, ABplpappap. Scale bars, 10 μm.

**Extended Data Fig. 2 Genetically mosaic *cye-1(lf); ced-3(lf)* animals with the Tex phenotype lack a *cye-1*-rescuing transgene in ABplpappap.**

**a–i**, Confocal micrographs showing the presence of the *cye-1(+)*-rescuing transgene in the excretory cell but not in ABplpappap (**a–h**) or in neither the excretory cell nor ABplpappap (**i**) of *cye-1(eh10); ced-3(n3692); nIs434[P<sub>pgp-12</sub>::4xNLS-GFP]; nEx3043[cye-1(+); P<sub>sur-5</sub>::RFP]* animals with the Tex phenotype. Scale bars, 10 μm.

**Extended Data Fig. 3 ABplpappap, which is generated by an unequal cell division, arrests in S phase and is extruded.**

**a, b**, Confocal fluorescence micrographs of tDHB–GFP fluorescence in ABplpappap (arrowheads) before (**a**) and after (**b**) ventral enclosure in *heSi192[P<sub>eft-3</sub>::tDHB-GFP]; ced-3(lf); nIs861[P<sub>egl-1</sub>::mCherry::PH]* embryos after the indicated RNAi treatment. Dotted outline, ABplpappap nucleus, as identified by Nomarski optics. **c, d**, Confocal fluorescence micrographs of GFP–PCN-1 fluorescence in ABplpappap (arrowheads) before (**c**) and after (**d**) ventral enclosure in *ced-3(lf); isIs17[P<sub>pie-1</sub>::GFP::pcn-1]; nIs861* embryos after the indicated RNAi treatment. **e**, Time-lapse confocal fluorescence micrographs of GFP–PCN-1 fluorescence in ABplpappap (arrowheads) in a *ced-3(lf); isIs17; nIs861; pig-1(RNAi)* embryo at the indicated times.  $t_{ve}$ , time point of ventral enclosure. **f–h**, Micrographs of virtual lateral section of *ced-3(lf); nIs861; stIs10026* embryos showing either ABplpappap (arrowhead) or its daughter cells (arrowheads) after indicated RNAi treatment. **i–m**, Confocal fluorescence

micrographs of *ced-3(lf)*; *ltIs44*[*P<sub>pie-1</sub>*::*mCherry*::*PH*]; *stIs10026* embryos showing the relative sizes of ABplpappap and its sister cell, ABplpappaa, in embryos after the indicated RNAi treatment. Insets, ABplpappap (**a–d**); ABplpappap or its daughters (**e–h**); magnified view of the region indicated, which includes ABplpappap ( $\dagger$ ) and ABplpappaa (\*) (**i–m**). Scale bars, 10  $\mu$ m.

**Extended Data Fig. 4 All extruded cells display features of cell cycle entry, S-phase arrest, and replication stress.**

**a–d**, tDHB–GFP fluorescence in unidentified extruded cells from the anterior sensory depression (**b**), the ventral pocket (**c**), and the posterior tip (**d**) of a comma stage embryo of the genotype *heSi192*; *ced-3(lf)*; *nIs861* after RNAi against empty vector control. Nuclei of extruded cells, as identified by Nomarski optics, are marked by dotted outlines. **e, f**, Micrographs of GFP–PCN-1 fluorescence in unidentified extruded cells (arrowhead) at the ventral pocket (**e**) or the anterior sensory depression (**f**) from *ced-3(lf)*; *isIs17*; *nIs861* embryos after RNAi against empty vector control (**e**) or no RNAi (**f**). Insets, extruded cells marked by arrowheads in micrographs. **g–j**, RPA-1–YFP fluorescence in unidentified extruded cells from the anterior sensory depression (**h**, **i**) and ventral pocket (**j**) in a *ced-3(lf)*; *ltIs44*; *opIs263*[*P<sub>rpa-1</sub>*::*rpa-1*::*YFP*] embryo after RNAi against empty vector control. Scale bars, 10  $\mu$ m.

**Extended Data Fig. 5 The replication-stress response, probably caused by *lrr-1* and nucleotide insufficiency, promotes cell extrusion.**

**a–d**, Confocal fluorescence micrographs showing the localization of RPA-1–YFP in ABplpappap (arrowheads) in *ced-3(lf)*; *ltIs44*; *opIs263* embryos after the indicated RNAi treatment. Insets, magnified views of ABplpappap. **e**, Genes identified as suppressors of the sterility of *lrr-1(lf)* mutants<sup>19</sup> were tested for suppression of cell extrusion. **f**, Nomarski micrograph showing a cell extruded (arrow) from a wild-type embryo after *gmpr-1*(RNAi) treatment. Scale bars, 10  $\mu$ m.

## Extended Data Fig. 6 Inhibitors of HU-induced replication-stress response and pan-caspase inhibitors do not alter stochastic cell extrusion.

**a, c, d**, Representative micrographs of anti- $\gamma$ H2AX (**a**), anti-pATR (**c**) and anti-p53 immunofluorescence signal (**d**) in vehicle- or HU-treated MDCK-II cells (**c**), and in vehicle-, HU- or Nutlin3-treated MDCK-II cells (**a, d**). DNA is stained with Hoechst. Scale bars, 20  $\mu$ m. **b**, Quantification of extrusions per hour after the indicated treatments.  $n = 13, 6, 5, 5$  and 5 (biological replicates) each for control, PFT, zVAD-FMK, SB 218078 and PF477736 treatments, respectively. Each data point represents a separate experiment. These data were collected and analysed for statistical significance with the data in Fig. 4g.  $P$  values are indicated; n.s., not significant. **e**, Quantification of anti-p53 immunofluorescence signal in MDCK-II cells treated with vehicle, HU, or Nutlin-3.  $n = 9, 7$  and 5 (biological replicates) for vehicle, HU and Nutlin3, respectively. Each data point represents mean fluorescence intensity signal from one image of hundreds of cells. Kruskal–Wallis one-way ANOVA followed by Dunn’s correction was performed.  $P$  values are indicated. Data in **b, e** are represented as mean  $\pm$  s.d. [Source data](#)

### **Extended Data Table 1 Penetrances of the Tex phenotype produced by RNAi against cell cycle genes (and non-cell-cycle cyclins and CDKs) in *ced-3(lf)* animals**

[Full size table](#)

### **Extended Data Table 2 Penetrances of the Tex phenotype produced in wild-type animals by RNAi against cell-cycle genes with potential roles in cell extrusion**

[Full size table](#)

## **Supplementary information**

### Supplementary Information

This file contains the Supplementary Methods, including the sequences of the RNAi constructs - the targets of which affect cell extrusion.

## Reporting Summary

### Video 1

A control embryo extrudes ABplpappap. Time-lapse video of a *ced-3(lf); stIs10026[his-72::GFP]; nIs632[P<sub>egl-1</sub>::mCherry::PH]* embryo after RNAi against empty vector control over a 50-minute period ending in ventral enclosure shows ABplpappap (circled at the beginning and end of video) was extruded from this embryo. All nuclei are labeled with GFP (green) and membranes of *egl-1*-expressing cells are labeled with mCherry (magenta). Time-lapse images used to generate this video were obtained using confocal microscopy. Video playback is at 600x real speed.

### Video 2

A *cye-1(RNAi)* embryo does not extrude ABplpappap. Time-lapse video of a *ced-3(lf); stIs10026[his-72::GFP]; nIs632[P<sub>egl-1</sub>::mCherry::PH]; cye-1(RNAi)* embryo over a 50-minute period ending in ventral enclosure shows ABplpappap (circled at the beginning and end of video) was not extruded from this embryo. All nuclei are labeled with GFP (green) and membranes of *egl-1*-expressing cells are labeled with mCherry (magenta). Time-lapse images used to generate this video were obtained using confocal microscopy. Video playback is at 600x real speed.

### Video 3

A *cdk-2(RNAi)* embryo does not extrude ABplpappap. Time-lapse video of a *ced-3(lf); stIs10026[his-72::GFP]; nIs632[P<sub>egl-1</sub>::mCherry::PH]; cdk-2(RNAi)* embryo over a 50-minute period ending in ventral enclosure shows ABplpappap (circled at the beginning and end of video) was not extruded from this embryo. All nuclei are labeled with GFP and membranes of *egl-1*-expressing cells are labeled with mCherry (magenta). Time-lapse images used to generate this video were obtained using confocal microscopy. Video playback is at 600x real speed.

### Video 4

ABplpappap arrests in S phase and is extruded in a control embryo. Time-lapse video of a *ced-3(lf); isIs17[P<sub>pie-1</sub>::GFP::pcn-1]; nIs861[P<sub>egl-1</sub>::mCherry::PH]* embryo after RNAi against empty vector control over a 35-minute period ending in ventral enclosure shows ABplpappap (circled at the beginning) arrests in S phase and is extruded (circled at the end of video). All cells express GFP-PCN-1 (green) and membranes of *egl-1*-expressing cells are labeled with mCherry (magenta). Time-lapse images used to generate this video were obtained using confocal microscopy. Video playback is at 600x real speed.

## Video 5

ABplpappap completes the cell cycle and is not extruded in a *pig-1(RNAi)* embryo. Time-lapse video of a *ced-3(lf); isIs17[P<sub>pie-1</sub>::GFP::pcn-1]; nIs861[P<sub>egl-1</sub>::mCherry::PH]; pig-1(RNAi)* embryo over an 80-minute period ending in ventral enclosure shows ABplpappap (circled at the beginning) completed the cell cycle and divided to generate daughters (circled at the end of video) that were not extruded. All cells express GFP-PCN-1 (green) and membranes of *egl-1*-expressing cells are labeled with mCherry (magenta). Time-lapse images used to generate this video were obtained using confocal microscopy. Video playback is at 600x real speed.

## Video 6

A vehicle-treated MDCK monolayer extrudes a few cells. A time-lapse video of mammalian MDCK monolayer treated with vehicle control for 21.25 h obtained using phase contrast imaging shows that a few cells are extruded during this period. Extruded cells can be identified as bright, white, rounded spots rising from the epithelial plane. Video playback is at 7200x real speed. Scale bar, 100  $\mu$ m.

## Video 7

A HU-treated MDCK monolayer extrudes a large number of cells. A time-lapse video of mammalian MDCK monolayer exposed to HU for 21.25 h obtained using phase contrast imaging shows that many more cells are

extruded during this period as a result of HU treatment. Extruded cells can be identified as bright, white, rounded spots rising from the epithelial plane. Video playback is at 7200x real speed. Scale bar, 100 µm.

## Source data

[Source Data Fig. 2](#)

[Source Data Fig. 3](#)

[Source Data Fig. 4](#)

[Source Data Extended Data Fig. 6](#)

## Rights and permissions

[Reprints and Permissions](#)

## About this article



Check for  
updates

## Cite this article

Dwivedi, V.K., Pardo-Pastor, C., Droste, R. *et al.* Replication stress promotes cell elimination by extrusion. *Nature* **593**, 591–596 (2021).  
<https://doi.org/10.1038/s41586-021-03526-y>

[Download citation](#)

- Received: 26 December 2019
- Accepted: 09 April 2021

- Published: 05 May 2021
- Issue Date: 27 May 2021
- DOI: <https://doi.org/10.1038/s41586-021-03526-y>

## Further reading

- [Replication stress as a trigger for cell extrusion](#)
  - Paulina Strzyz

*Nature Reviews Molecular Cell Biology* (2021)

## Comments

By submitting a comment you agree to abide by our [Terms](#) and [Community Guidelines](#). If you find something abusive or that does not comply with our terms or guidelines please flag it as inappropriate.

[Access through your institution](#)

[Change institution](#)

[Buy or subscribe](#)

Advertisement

---

This article was downloaded by **calibre** from <https://www.nature.com/articles/s41586-021-03526-y>.

- Article
- [Published: 26 April 2021](#)

# Small-molecule inhibition of METTL3 as a strategy against myeloid leukaemia

- [Eliza Yankova](#) [ORCID: orcid.org/0000-0003-2913-0012](#)<sup>1,2,3 na1</sup>,
- [Wesley Blackaby](#)<sup>3 na1</sup>,
- [Mark Albertella](#)<sup>3</sup>,
- [Justyna Rak](#)<sup>2,4</sup>,
- [Etienne De Braekeleer](#)<sup>2,4</sup>,
- [Georgia Tsagkogeorga](#)<sup>1,3</sup>,
- [Ewa S. Pilka](#) [ORCID: orcid.org/0000-0002-0107-2597](#)<sup>5</sup>,
- [Demetrios Aspris](#)<sup>2,6</sup>,
- [Dan Leggate](#)<sup>3</sup>,
- [Alan G. Hendrick](#) [ORCID: orcid.org/0000-0002-8604-0462](#)<sup>3</sup>,
- [Natalie A. Webster](#)<sup>3</sup>,
- [Byron Andrews](#)<sup>3</sup>,
- [Richard Fosbeary](#)<sup>3</sup>,
- [Patrick Guest](#)<sup>3</sup>,
- [Nerea Irigoyen](#) [ORCID: orcid.org/0000-0001-6346-3369](#)<sup>7</sup>,
- [Maria Eleftheriou](#)<sup>1</sup>,
- [Malgorzata Gozdecka](#)<sup>2</sup>,
- [Joao M. L. Dias](#) [ORCID: orcid.org/0000-0002-8451-3537](#)<sup>8</sup>,
- [Andrew J. Bannister](#) [ORCID: orcid.org/0000-0002-6312-4436](#)<sup>9</sup>,
- [Binje Vick](#) [ORCID: orcid.org/0000-0003-1956-2778](#)<sup>10,11</sup>,
- [Irmela Jeremias](#) [ORCID: orcid.org/0000-0003-1773-7677](#)<sup>10,11,12</sup>,
- [George S. Vassiliou](#) [ORCID: orcid.org/0000-0003-4337-8022](#)<sup>2,4,6</sup>,
- [Oliver Rausch](#) [ORCID: orcid.org/0000-0003-4074-3848](#)<sup>3</sup>,

- [Konstantinos Tzelepis](#)   [ORCID: orcid.org/0000-0002-4865-7648<sup>1,2,4,9</sup>](#) &
- [Tony Kouzarides](#)   [ORCID: orcid.org/0000-0002-8918-4162<sup>1,9</sup>](#)

[\*Nature\*](#) volume **593**, pages 597–601 (2021)[Cite this article](#)

- 14k Accesses
- 1 Citations
- 205 Altmetric
- [Metrics details](#)

## Subjects

- [Acute myeloid leukaemia](#)
- [RNA modification](#)
- [Target validation](#)

## Abstract

$\text{N}^6$ -methyladenosine ( $\text{m}^6\text{A}$ ) is an abundant internal RNA modification<sup>1,2</sup> that is catalysed predominantly by the METTL3–METTL14 methyltransferase complex<sup>3,4</sup>. The  $\text{m}^6\text{A}$  methyltransferase METTL3 has been linked to the initiation and maintenance of acute myeloid leukaemia (AML), but the potential of therapeutic applications targeting this enzyme remains unknown<sup>5,6,7</sup>. Here we present the identification and characterization of STM2457, a highly potent and selective first-in-class catalytic inhibitor of METTL3, and a crystal structure of STM2457 in complex with METTL3–METTL14. Treatment of tumours with STM2457 leads to reduced AML growth and an increase in differentiation and apoptosis. These cellular effects are accompanied by selective reduction of  $\text{m}^6\text{A}$  levels on known leukaemogenic mRNAs and a decrease in their expression consistent with a translational defect. We demonstrate that pharmacological inhibition of METTL3 *in vivo* leads to impaired engraftment and prolonged survival in various mouse models of AML,

specifically targeting key stem cell subpopulations of AML. Collectively, these results reveal the inhibition of METTL3 as a potential therapeutic strategy against AML, and provide proof of concept that the targeting of RNA-modifying enzymes represents a promising avenue for anticancer therapy.

## Access options

Subscribe to Journal

Get full journal access for 1 year

\$199.00

only \$3.90 per issue

[Subscribe](#)

All prices are NET prices.

VAT will be added later in the checkout.

Tax calculation will be finalised during checkout.

Rent or Buy article

Get time limited or full article access on ReadCube.

from \$8.99

[Rent or Buy](#)

All prices are NET prices.

### Additional access options:

- [Log in](#)
- [Access through your institution](#)
- [Learn about institutional subscriptions](#)

**Fig. 1: Characterization of the RNA methyltransferase inhibitor STM2457.**

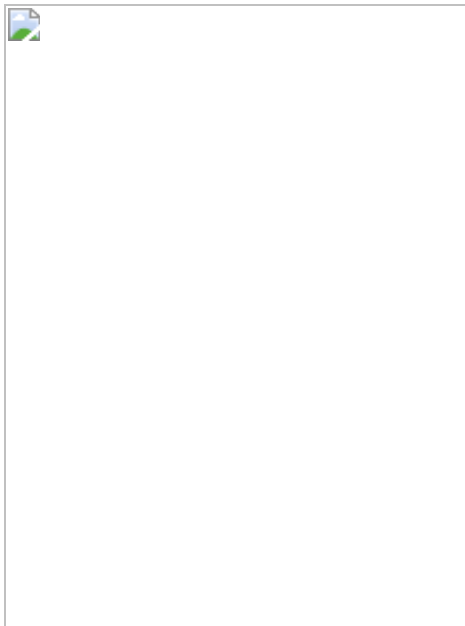


**Fig. 2: Pharmacological inhibition of METTL3 affects AML cells.**

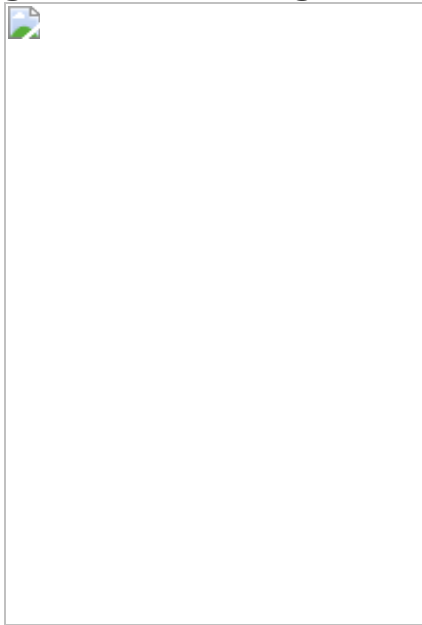
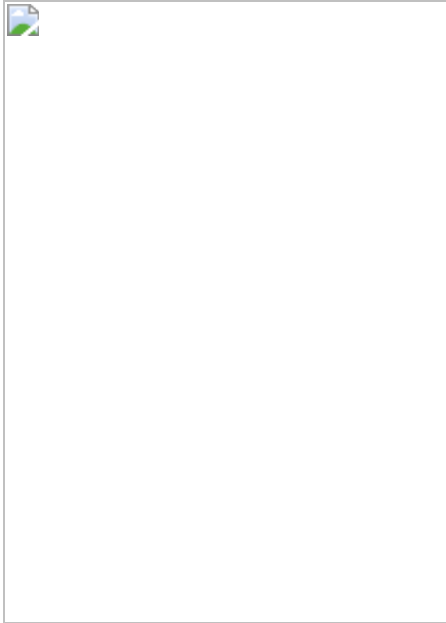


**Fig. 3: STM2457 reduces m<sup>6</sup>A levels and causes mRNA translation defects.**



**Fig. 4: STM2457 prevents AML expansion and reduces the number of key leukaemia stem cells *in vivo*.**



## Data availability

The datasets related to STM2457 used in this study can be accessed from the European Nucleotide Archive under accession [PRJEB41662](#). The previously published datasets from Barbieri et al. can be accessed from the Gene Expression Omnibus database with accession number [GSE94613](#). The

STM2457 structure has been deposited with the PDB as [7O2I](#). Additional details related to the chemical characterization of STM2457 can be found in the relevant published patent (WO2020201773) at World Intellectual Property Organization. [Source data](#) are provided with this paper.

## References

1. 1.

Dominissini, D. et al. Topology of the human and mouse m6A RNA methylomes revealed by m<sup>6</sup>A-seq. *Nature* **485**, 201–206 (2012).

[ADS](#) [CAS](#) [PubMed](#) [Google Scholar](#)

2. 2.

Meyer, K. D. et al. Comprehensive analysis of mRNA methylation reveals enrichment in 3' UTRs and near stop codons. *Cell* **149**, 1635–1646 (2012).

[CAS](#) [PubMed](#) [PubMed Central](#) [Google Scholar](#)

3. 3.

Liu, J. et al. A METTL3–METTL14 complex mediates mammalian nuclear RNA N<sup>6</sup>-adenosine methylation. *Nat. Chem. Biol.* **10**, 93–95 (2014).

[CAS](#) [PubMed](#) [Google Scholar](#)

4. 4.

Wang, X. et al. Structural basis of N<sup>6</sup>-adenosine methylation by the METTL3–METTL14 complex. *Nature* **534**, 575–578 (2016).

[ADS](#) [CAS](#) [PubMed](#) [PubMed Central](#) [Google Scholar](#)

5. 5.

Tzelepis, K. et al. A CRISPR dropout screen identifies genetic vulnerabilities and therapeutic targets in acute myeloid leukemia. *Cell Rep.* **17**, 1193–1205 (2016).

[CAS](#) [PubMed](#) [PubMed Central](#) [Google Scholar](#)

6. 6.

Barbieri, I. et al. Promoter-bound METTL3 maintains myeloid leukaemia by m<sup>6</sup>A-dependent translation control. *Nature* **552**, 126–131 (2017).

[ADS](#) [CAS](#) [PubMed](#) [PubMed Central](#) [Google Scholar](#)

7. 7.

Vu, L. P. et al. The N<sup>6</sup>-methyladenosine (m<sup>6</sup>A)-forming enzyme METTL3 controls myeloid differentiation of normal hematopoietic and leukemia cells. *Nat. Med.* **23**, 1369–1376 (2017).

[CAS](#) [Article](#) [Google Scholar](#)

8. 8.

Schapira, M. Structural chemistry of human RNA methyltransferases. *ACS Chem. Biol.* **11**, 575–582 (2016).

[CAS](#) [PubMed](#) [PubMed Central](#) [Google Scholar](#)

9. 9.

Li, F. et al. A radioactivity-based assay for screening human m<sup>6</sup>A-RNA methyltransferase, METTL3–METTL14 complex, and demethylase ALKBH5. *J. Biomol. Screen.* **21**, 290–297 (2016).

[PubMed](#) [PubMed Central](#) [Google Scholar](#)

10. 10.

Melnyk, S., Pogribna, M., Pogribny, I. P., Yi, P. & James, S. J. Measurement of plasma and intracellular *S*-adenosylmethionine and *S*-adenosylhomocysteine utilizing coulometric electrochemical detection: alterations with plasma homocysteine and pyridoxal 5'-phosphate concentrations. *Clin. Chem.* **46**, 265–272 (2000).

[CAS](#) [PubMed](#) [PubMed Central](#) [Google Scholar](#)

11. 11.

Ripperger, T. et al. The heteromeric transcription factor GABP activates the *ITGAM/CD11b* promoter and induces myeloid differentiation. *Biochim. Biophys. Acta* **1849**, 1145–1154 (2015).

[CAS](#) [PubMed](#) [PubMed Central](#) [Google Scholar](#)

12. 12.

O'Connor, L., Gilmour, J. & Bonifer, C. The role of the ubiquitously expressed transcription factor Sp1 in tissue-specific transcriptional regulation and in disease. *Yale J. Biol. Med.* **89**, 513–525 (2016).

[PubMed](#) [PubMed Central](#) [Google Scholar](#)

13. 13.

Choe, J. et al. mRNA circularization by METTL3–eIF3h enhances translation and promotes oncogenesis. *Nature* **561**, 556–560 (2018).

[ADS](#) [CAS](#) [PubMed](#) [PubMed Central](#) [Google Scholar](#)

14. 14.

Dawson, M. A. et al. Inhibition of BET recruitment to chromatin as an effective treatment for MLL-fusion leukaemia. *Nature* **478**, 529–533 (2011).

[ADS](#) [CAS](#) [PubMed](#) [PubMed Central](#) [Google Scholar](#)

15. 15.

Weng, H. et al. METTL14 inhibits hematopoietic stem/progenitor differentiation and promotes leukemogenesis via mRNA m<sup>6</sup>A modification. *Cell Stem Cell* **22**, 191–205.e9 (2018).

[CAS](#) [PubMed](#) [PubMed Central](#) [Google Scholar](#)

16. 16.

Dominissini, D., Moshitch-Moshkovitz, S., Salmon-Divon, M., Amariglio, N. & Rechavi, G. Transcriptome-wide mapping of N<sup>6</sup>-methyladenosine by m<sup>6</sup>A-seq based on immunocapturing and massively parallel sequencing. *Nat. Protoc.* **8**, 176–189 (2013).

[CAS](#) [PubMed](#) [PubMed Central](#) [Google Scholar](#)

17. 17.

Tzelepis, K., Rausch, O. & Kouzarides, T. RNA-modifying enzymes and their function in a chromatin context. *Nat. Struct. Mol. Biol.* **26**, 858–862 (2019).

[CAS](#) [PubMed](#) [PubMed Central](#) [Google Scholar](#)

18. 18.

Alharbi, R. A., Pettengell, R., Pandha, H. S. & Morgan, R. The role of HOX genes in normal hematopoiesis and acute leukemia. *Leukemia* **27**, 1000–1008 (2013).

[CAS](#) [PubMed](#) [PubMed Central](#) [Google Scholar](#)

19. 19.

Delgado, M. D. & León, J. Myc roles in hematopoiesis and leukemia. *Genes Cancer* **1**, 605–616 (2010).

[CAS](#) [PubMed](#) [PubMed Central](#) [Google Scholar](#)

20. 20.

Liu, J. et al.  $N^6$ -methyladenosine of chromosome-associated regulatory RNA regulates chromatin state and transcription. *Science* **367**, 580–586 (2020).

[ADS](#) [CAS](#) [PubMed](#) [PubMed Central](#) [Google Scholar](#)

21. 21.

Mikutis, S. et al. meCLICK-Seq, a substrate-hijacking and RNA degradation strategy for the study of RNA methylation. *ACS Cent. Sci.* **6**, 2196–2208 (2020).

[CAS](#) [PubMed](#) [PubMed Central](#) [Google Scholar](#)

22. 22.

Xiang, Y. et al. RNA m<sup>6</sup>A methylation regulates the ultraviolet-induced DNA damage response. *Nature* **543**, 573–576 (2017).

[ADS](#) [CAS](#) [PubMed](#) [PubMed Central](#) [Google Scholar](#)

23. 23.

Lin, S., Choe, J., Du, P., Triboulet, R. & Gregory, R. I. The m<sup>6</sup>A methyltransferase METTL3 promotes translation in human cancer cells. *Mol. Cell* **62**, 335–345 (2016).

[CAS](#) [PubMed](#) [PubMed Central](#) [Google Scholar](#)

24. 24.

Iwasaki, M., Liedtke, M., Gentles, A. J. & Cleary, M. L. CD93 marks a non-quiescent human leukemia stem cell population and is required for development of MLL-rearranged acute myeloid leukemia. *Cell Stem Cell* **17**, 412–421 (2015).

[CAS](#) [PubMed](#) [PubMed Central](#) [Google Scholar](#)

25. 25.

Krivtsov, A. V. et al. Transformation from committed progenitor to leukaemia stem cell initiated by MLL–AF9. *Nature* **442**, 818–822 (2006).

[ADS](#) [CAS](#) [PubMed](#) [PubMed Central](#) [Google Scholar](#)

26. 26.

Ellison, R. R. et al. Arabinosyl cytosine: a useful agent in the treatment of acute leukemia in adults. *Blood* **32**, 507–523 (1968).

[CAS](#) [PubMed](#) [PubMed Central](#) [Google Scholar](#)

27. 27.

Daver, N. et al. New directions for emerging therapies in acute myeloid leukemia: the next chapter. *Blood Cancer J.* **10**, 107 (2020).

[PubMed](#) [PubMed Central](#) [Google Scholar](#)

28. 28.

Li, Z. et al. FTO plays an oncogenic role in acute myeloid leukemia as a  $N^6$ -methyladenosine RNA demethylase. *Cancer Cell* **31**, 127–141 (2017).

[Google Scholar](#)

29. 29.

Huang, Y. et al. Small-molecule targeting of oncogenic FTO demethylase in acute myeloid leukemia. *Cancer Cell* **35**, 677–691.e10 (2019).

[CAS](#) [PubMed](#) [PubMed Central](#) [Google Scholar](#)

30. 30.

Moroz-Omori, E. V. et al. METTL3 inhibitors for epitranscriptomic modulation of cellular processes. Preprint at <https://doi.org/10.1101/2020.09.25.311803> (2020).

31. 31.

Śledź, P. & Jinek, M. Structural insights into the molecular mechanism of the m<sup>6</sup>A writer complex. *eLife* **5**, e18434 (2016).

[PubMed](#) [PubMed Central](#) [Google Scholar](#)

32. 32.

Evans, P. R. & Murshudov, G. N. How good are my data and what is the resolution? *Acta Crystallogr. D* **69**, 1204–1214 (2013).

[CAS](#) [PubMed](#) [PubMed Central](#) [Google Scholar](#)

33. 33.

McCoy, A. J. et al. Phaser crystallographic software. *J. Appl. Crystallogr.* **40**, 658–674 (2007).

[CAS](#) [PubMed](#) [PubMed Central](#) [Google Scholar](#)

34. 34.

Winn, M. D., Murshudov, G. N. & Papiz, M. Z. Macromolecular TLS refinement in REFMAC at moderate resolutions. *Methods Enzymol.* **374**, 300–321 (2003).

[CAS](#) [PubMed](#) [PubMed Central](#) [Google Scholar](#)

35. 35.

Emsley, P. & Cowtan, K. Coot: model-building tools for molecular graphics. *Acta Crystallogr. D* **60**, 2126–2132 (2004).

[PubMed](#) [Google Scholar](#)

36. 36.

Wlodek, S., Skillman, A. G. & Nicholls, A. Automated ligand placement and refinement with a combined force field and shape potential. *Acta Crystallogr. D* **62**, 741–749 (2006).

[CAS](#) [PubMed](#) [PubMed Central](#) [Google Scholar](#)

37. 37.

Lee, B. H. et al. FLT3 mutations confer enhanced proliferation and survival properties to multipotent progenitors in a murine model of chronic myelomonocytic leukemia. *Cancer Cell* **12**, 367–380 (2007).

[CAS](#) [PubMed](#) [PubMed Central](#) [Google Scholar](#)

38. 38.

Vick, B. et al. An advanced preclinical mouse model for acute myeloid leukemia using patients' cells of various genetic subgroups and in vivo bioluminescence imaging. *PLoS ONE* **10**, e0120925 (2015).

[PubMed](#) [PubMed Central](#) [Google Scholar](#)

39. 39.

Panda, A. C., Martindale, J. L. & Gorospe, M. Polysome fractionation to analyze mRNA distribution profiles. *Bio Protoc.* **7**, e2126 (2017).

[PubMed](#) [PubMed Central](#) [Google Scholar](#)

40. 40.

Li, H. et al. The Sequence Alignment/Map format and SAMtools. *Bioinformatics* **25**, 2078–2079 (2009).

[PubMed](#) [PubMed Central](#) [Google Scholar](#)

41. 41.

Kim, D., Paggi, J. M., Park, C., Bennett, C. & Salzberg, S. L. Graph-based genome alignment and genotyping with HISAT2 and HISAT-genotype. *Nat. Biotechnol.* **37**, 907–915 (2019).

[CAS](#) [PubMed](#) [PubMed Central](#) [Google Scholar](#)

42. 42.

Quinlan, A. R. & Hall, I. M. BEDTools: a flexible suite of utilities for comparing genomic features. *Bioinformatics* **26**, 841–842 (2010).

[CAS](#) [PubMed](#) [PubMed Central](#) [Google Scholar](#)

43. 43.

Cui, X. et al. MeTDiff: A novel differential RNA methylation analysis for MeRIP-Seq data. *IEEE/ACM Trans. Comput. Biol. Bioinformatics* **15**, 526–534 (2018).

[CAS](#) [Google Scholar](#)

44. 44.

Cui, X. et al. Guitar: An R/Bioconductor package for gene annotation guided transcriptomic analysis of rna-related genomic features. *Biomed. Res. Int.* **2016**, 8367534 (2016).

[PubMed](#) [PubMed Central](#) [Google Scholar](#)

45. 45.

Heinz, S. et al. Simple combinations of lineage-determining transcription factors prime *cis*-regulatory elements required for macrophage and B cell identities. *Mol. Cell* **38**, 576–589 (2010).

[CAS](#) [PubMed](#) [PubMed Central](#) [Google Scholar](#)

46. 46.

Yu, G., Wang, L. G., Han, Y. & He, Q. Y. clusterProfiler: an R package for comparing biological themes among gene clusters. *OMICS* **16**, 284–287 (2012).

[CAS](#) [PubMed](#) [PubMed Central](#) [Google Scholar](#)

47. 47.

Ewels, P. A. et al. The nf-core framework for community-curated bioinformatics pipelines. *Nat. Biotechnol.* **38**, 276–278 (2020).

[CAS](#) [PubMed](#) [PubMed Central](#) [Google Scholar](#)

48. 48.

Love, M. I., Huber, W. & Anders, S. Moderated estimation of fold change and dispersion for RNA-seq data with DESeq2. *Genome Biol.* **15**, 550 (2014).

[PubMed](#) [PubMed Central](#) [Google Scholar](#)

[Download references](#)

## Acknowledgements

T.K. was supported by grants from Cancer Research UK (grant reference RG17001) and ERC (project number 268569), in addition to benefiting from core support from the Wellcome Trust (Core Grant reference 092096), Cancer Research UK (grant reference C6946/A14492) and Kay Kendall Leukaemia Fund project grant (grant reference RG88664). K.T. was funded by a Wellcome Trust Sir Henry Wellcome Fellowship (grant reference RG94424). K.T and M.E. were funded by Leukaemia UK (G108148). I.J. was funded by ERC (Consolidator Grant 681524). I.J. and K.T. were funded by Cambridge-LMU Strategic Partnership Award. G.S.V. was funded by a Cancer Research UK Senior Cancer Fellowship (C22324/A23015). We thank B. L. Ng, J. Graham, S. Thompson and C. Hall for help with flow cytometry and the Cambridge Blood and Stem Cell Biobank for human AML and cord blood sample processing; the staff of the Sanger Institute

Core Sequencing facility for sequencing and the staff of the Sanger Institute Research Support Facility for help with mouse experiments; D. Hardick, B. Thomas, Y. Ofir-Rosenfeld and A. Sapetschnig at Storm Therapeutics for comments and advice; and K. Danker, M. Ridgill, C. Hoareau and their colleagues at Evotec for drug discovery services and lead optimization support.

## Author information

### Author notes

1. These authors contributed equally: Eliza Yankova, Wesley Blackaby

### Affiliations

1. Milner Therapeutics Institute, University of Cambridge, Cambridge, UK

Eliza Yankova, Georgia Tsagkogeorga, Maria Eleftheriou, Konstantinos Tzelepis & Tony Kouzarides

2. Haematological Cancer Genetics, Wellcome Trust Sanger Institute, Cambridge, UK

Eliza Yankova, Justyna Rak, Etienne De Braekeleer, Demetrios Aspis, Malgorzata Gozdecka, George S. Vassiliou & Konstantinos Tzelepis

3. Storm Therapeutics Ltd, Cambridge, UK

Eliza Yankova, Wesley Blackaby, Mark Albertella, Georgia Tsagkogeorga, Dan Leggate, Alan G. Hendrick, Natalie A. Webster, Byron Andrews, Richard Fosbeary, Patrick Guest & Oliver Rausch

4. Wellcome-MRC Cambridge Stem Cell Institute, University of Cambridge, Cambridge, UK

Justyna Rak, Etienne De Braekeleer, George S.  
Vassiliou & Konstantinos Tzelepis

5. Evotec (UK) Ltd, Abingdon, UK

Ewa S. Pilka

6. The Center for the Study of Hematological Malignancies/Karaiskakio Foundation, Nicosia, Cyprus

Demetrios Aspris & George S. Vassiliou

7. Division of Virology, Department of Pathology, University of Cambridge, Cambridge, UK

Nerea Irigoyen

8. MRC Cancer Unit, University of Cambridge, Hutchison/MRC Research Centre, Cambridge, UK

Joao M. L. Dias

9. The Gurdon Institute and Department of Pathology, University of Cambridge, Cambridge, UK

Andrew J. Bannister, Konstantinos Tzelepis & Tony Kouzarides

10. Research Unit Apoptosis in Hematopoietic Stem Cells, Helmholtz Zentrum München, German Research Center for Environmental Health (HMGU), Munich, Germany

Binje Vick & Irmela Jeremias

11. German Consortium for Translational Cancer Research (DKTK), Munich, Germany

Binje Vick & Irmela Jeremias

12. Department of Pediatrics, Dr. von Hauner Children's Hospital, Ludwig Maximilians University München, Munich, Germany

Irmela Jeremias

## Authors

1. Eliza Yankova

[View author publications](#)

You can also search for this author in [PubMed](#) [Google Scholar](#)

2. Wesley Blackaby

[View author publications](#)

You can also search for this author in [PubMed](#) [Google Scholar](#)

3. Mark Albertella

[View author publications](#)

You can also search for this author in [PubMed](#) [Google Scholar](#)

4. Justyna Rak

[View author publications](#)

You can also search for this author in [PubMed](#) [Google Scholar](#)

5. Etienne De Braekeleer

[View author publications](#)

You can also search for this author in [PubMed](#) [Google Scholar](#)

6. Georgia Tsagkogeorga

[View author publications](#)

You can also search for this author in [PubMed](#) [Google Scholar](#)

7. Ewa S. Pilka

[View author publications](#)

You can also search for this author in [PubMed](#) [Google Scholar](#)

8. Demetrios Aspris

[View author publications](#)

You can also search for this author in [PubMed](#) [Google Scholar](#)

9. Dan Leggate

[View author publications](#)

You can also search for this author in [PubMed](#) [Google Scholar](#)

10. Alan G. Hendrick

[View author publications](#)

You can also search for this author in [PubMed](#) [Google Scholar](#)

11. Natalie A. Webster

[View author publications](#)

You can also search for this author in [PubMed](#) [Google Scholar](#)

12. Byron Andrews

[View author publications](#)

You can also search for this author in [PubMed](#) [Google Scholar](#)

13. Richard Fosbary

[View author publications](#)

You can also search for this author in [PubMed](#) [Google Scholar](#)

14. Patrick Guest

[View author publications](#)

You can also search for this author in [PubMed](#) [Google Scholar](#)

15. Nerea Irigoyen

[View author publications](#)

You can also search for this author in [PubMed](#) [Google Scholar](#)

16. Maria Eleftheriou

[View author publications](#)

You can also search for this author in [PubMed](#) [Google Scholar](#)

17. Malgorzata Gozdecka

[View author publications](#)

You can also search for this author in [PubMed](#) [Google Scholar](#)

18. Joao M. L. Dias

[View author publications](#)

You can also search for this author in [PubMed](#) [Google Scholar](#)

19. Andrew J. Bannister

[View author publications](#)

You can also search for this author in [PubMed](#) [Google Scholar](#)

20. Binje Vick

[View author publications](#)

You can also search for this author in [PubMed](#) [Google Scholar](#)

21. Irmela Jeremias

[View author publications](#)

You can also search for this author in [PubMed](#) [Google Scholar](#)

22. George S. Vassiliou

[View author publications](#)

You can also search for this author in [PubMed](#) [Google Scholar](#)

23. Oliver Rausch

[View author publications](#)

You can also search for this author in [PubMed](#) [Google Scholar](#)

24. Konstantinos Tzelepis

[View author publications](#)

You can also search for this author in [PubMed](#) [Google Scholar](#)

25. Tony Kouzarides

[View author publications](#)

You can also search for this author in [PubMed](#) [Google Scholar](#)

## Contributions

K.T., T.K. and O.R. conceived the study and designed the experiments; K.T., W.B., E.Y., M.A., E.S.P., D.A., J.R., E.D.B., M.G., D.L., A.G.H., B.A., B.V., N.A.W., R.F., P.G. and M.E. conducted chemical, biochemical and molecular experiments. K.T., E.Y., J.R., E.D.B. and M.G. performed mouse experiments. G.T. and J.M.L.D. performed bioinformatics analyses. E.S.P. performed X-ray crystallography, assisted by W.B. in data analysis and interpretation. E.Y. and D.A. performed polysome profiling with help and supervision from N.I. and K.T. A.J.B., I.J. and G.S.V. helped with data analysis, interpretation and direction. K.T., T.K., E.Y., M.E. and O.R. wrote the manuscript with help from all authors. All authors discussed the results and commented on the manuscript.

## Corresponding authors

Correspondence to [Oliver Rausch](#) or [Konstantinos Tzelepis](#) or [Tony Kouzarides](#).

## Ethics declarations

## Competing interests

T.K. is a co-founder of Abcam Plc and Storm Therapeutics Ltd, Cambridge, UK and Scientific Advisor to Foghorn Therapeutics and EpiVario. E.Y. is

funded by Storm Therapeutics Ltd, Cambridge, UK. W.B., M.A., G.T., D.L., B.A., R.F., A.G.H., N.A.W., P.G. and O.R. are employees of Storm Therapeutics Ltd, Cambridge, UK. E.S.P. is an employee of Evotec (UK) Ltd, Abingdon, UK. George S. Vassiliou is a consultant for Kymab, Cambridge, UK. Storm Therapeutics Ltd is the owner of a patent application (WO2020201773) covering the development of METTL3 RNA methyltransferase inhibitors.

## Additional information

**Peer review information** *Nature* thanks Richard Gregory and the other, anonymous, reviewer(s) for their contribution to the peer review of this work. Peer reviewer reports are available.

**Publisher's note** Springer Nature remains neutral with regard to jurisdictional claims in published maps and institutional affiliations.

## Extended data figures and tables

### [Extended Data Fig. 1 STM2457 is a specific small molecule inhibitor of METTL3 with no evidence of off-target effects.](#)

**a**, Chemical structures of STM1760 and STM2120. **b**, Biochemical activity assay showing inhibition of the METTL3/METTL14 enzyme complex using a dose-range of STM1760. **c**, Surface plasmon resonance (SPR) sensorgram showing the binding of STM2457 to the METTL3/METTL14 protein complex. **d**, SPR sensorgram showing reduced binding of STM2457 to the METTL3/METTL14 protein complex in the presence of 50  $\mu$ M SAM, illustrating that STM2457 is SAM competitive. **e**, SPR assay showing single-cycle binding kinetics of STM2457. **f**, Biochemical activity assay showing no inhibition of METTL16, NSUN1 and NSUN2 RNA methyltransferases using a dose-range of STM2457. **g**, Methyltransferase dendograms showing that 10  $\mu$ M STM2457 has selective inhibitory activity for METTL3/METTL14 over the indicated RNA and protein methyltransferases. **h**, Treatment with 10  $\mu$ M STM2457 did not inhibit (that

is, result in less than 50% control activity) any of the 468 kinases in the ScanMax (DiscoverX) kinase panel tested (marked by green dots).

### **Extended Data Fig. 2 Binding of STM2457 to the SAM pocket of METTL3.**

**a**, Overlay of crystal structures of METTL3/METTL14 in complex with STM2457 (carbon atoms in cyan) and METTL3/14 in complex with SAM (carbon atoms in magenta, PDB code 7O2I). The position of K513 is shown in lines of the corresponding colour for each structure. **b**, Cellular thermal shift target engagement assay measuring binding affinity of STM2457 against human and mouse METTL3 proteins expressed in HeLa cells. The IC<sub>50</sub> represents the concentration of STM2457 at which 50% of METTL3 is bound to STM2457. (mean +/– s.d., n = 3). **c**, Quantification of m<sup>6</sup>A levels on poly-A<sup>+</sup>-enriched RNA using RNA-mass spectrometry after 48 h of in vitro treatment of MOLM-13 with 1 μM of STM2457 or vehicle (DMSO). (mean +/– s.d., n = 3). **d**, Quantification of m<sup>6</sup>A<sub>m</sub>, m<sup>6</sup><sub>2</sub>A and m<sup>7</sup>G levels on poly-A<sup>+</sup>-enriched RNA 24 h of treatment of MOLM-13 with the indicated STM2457 concentrations (mean +/– s.d., n = 3). **e**, STM2457 in vivo pharmacokinetic profile in mouse blood and brain tissue using a dose of 50 mg/kg. **f**, STM2457 in vivo PK/PD relationship in non-tumour bearing animals from the PK study shown in **e**, demonstrating inhibition of m<sup>6</sup>A in spleen tissue over a range of STM2457 blood concentrations (n = 3). two-tailed Student's t-test. [Source data](#)

### **Extended Data Fig. 3 Treatment with STM2457 triggers colony forming deficiency and apoptosis in AML cells.**

**a**, Colony-forming efficiency of CD34+ human cord blood cells (n = 3) in the presence of 1, 5, or 10 μM STM2457 (mean ± s.d., n = 3). These changes are not significant at the 95% confidence level according to one-way Anova on repeated measures. Error bars refer to variation across 3 different individuals (blue, brown and red square). **b**, Proliferation assay in MOLM-13 cells after treatment with the indicated doses of STM2457 and STM2120, illustrating no sensitivity to the latter at any tested dose (mean ± s.d., n = 3). **c**, Colony forming efficiency of primary murine *MLL*-

*ENL/Flt3<sup>ITD/+</sup>* and *NPM1c/NRAS-G12D* AML cells treated with 1  $\mu$ M STM2457 showing decreased clonogenic potential compared with vehicle-treated (DMSO) controls (mean  $\pm$  s.d.,  $n = 3$ ). **d**, Mac1 levels were used to assess differentiation of non-leukaemic haemopoietic cell line HPC7. Flow cytometry comparison on day 4 post-treatment between vehicle (DMSO) and 1  $\mu$ M STM2457. **e**, Selective increased apoptosis in AML cells but not in non-leukaemic haematopoietic cells, following treatment with 1  $\mu$ M of STM2457 at the presented time points (mean  $\pm$  s.d.,  $n = 3$ ). **f**, Western blot for SP1 and ACTIN in MOLM-13 cells transduced with plasmids expressing *SP1* cDNA or an empty control ( $n = 3$ ). **g**, Dose–response curves of MOLM-13 cells to STM2457 after transduction with vectors expressing *SP1* cDNA or an empty control, showing selective decrease of drug sensitivity upon ectopic expression the former. The dose–response curve of parental MOLM-13 (WT, light blue) shown in Fig. [2a](#) is illustrated for comparison purposes. (mean  $\pm$  s.d.,  $n = 3$ ). d, days; two-tailed Student’s *t*-test; \* $P < 0.05$ , \*\* $P < 0.01$ .

#### **Extended Data Fig. 4 Differential expression analysis of AML cells after treatment with STM2457.**

**a**, Volcano plot for MOLM13 cells treated with 1  $\mu$ M STM2457 versus control samples after 48 h of treatment, showing significantly dysregulated genes in red ( $P_{adj} \leq 0.01$ ). **b**, Extended GO analysis of the differentially expressed genes post-treatment with 1  $\mu$ M STM2457 in MOLM-13 cells. **c**, Representative GO signatures of the differentially expressed genes post-treatment with STM2457 in MOLM-13 cells. LFC, Log Fold Change.

#### **Extended Data Fig. 5 Pharmacological inhibition of METTL3 significantly reduces m<sup>6</sup>A on leukaemia-associated substrates.**

**a**, Overlap between METTL3-dependent m<sup>6</sup>A poly-A<sup>+</sup> RNAs in MOLM-13 cells either treated with 1  $\mu$ M STM2457 or with genetic downregulation of METTL3 from Barbieri et al.<sup>[7](#)</sup>. **b**, Overlap between differential downregulated m<sup>6</sup>A peaks in MOLM-13 cells either treated with 1  $\mu$ M STM2457 or with genetic downregulation of METTL3 from Barbieri et al.<sup>[7](#)</sup>. **c**, Genomic visualization of the m<sup>6</sup>A-meRIP normalized signal in

MOLM13 cells following treatment with vehicle (DMSO) or 1  $\mu$ M STM2457 for the METTL3-dependent m<sup>6</sup>A substrates *BRD4* and *HNRNPL* (red stars indicate loss of m<sup>6</sup>A signal). **d**, m<sup>6</sup>A-meRIP-qPCR analysis of METTL3-dependent and METTL3-independent m<sup>6</sup>A substrates normalized to input in MOLM-13 cells treated for 24 or 48 h with either vehicle (DMSO) or 1  $\mu$ M STM2457 (mean  $\pm$  s.d.,  $n = 3$ ). **e**, GO analysis of differentially m<sup>6</sup>A-methylated mRNAs upon treatment with 1  $\mu$ M STM2457. **f**, RT-qPCR quantification of *METTL3* and *DICER1* in total RNA samples from MOLM-13 cells treated with vehicle or STM2457 (mean  $\pm$  s.d.,  $n = 3$ ). **g**, Western blot for METTL3, METTL14, DDX3X, DICER1 and ACTIN in MOLM-13 cells treated with 10, 5 and 1  $\mu$ M of STM2457 or vehicle (DMSO) for 72 h ( $n = 3$ ). two-tailed Student's *t*-test; n.s., not significant; KD, knockdown.

### Extended Data Fig. 6 STM2457 shows high efficacy and strong target engagement in PDX models.

**a**, Quantification of luminescence for the animal experiment depicted in Fig. 4a (mean  $\pm$  s.d.,  $n = 5$ ). **b**, Bioluminescence imaging of mice transplanted with AML PDX-3 (*MLL-AF10*) treated with vehicle or 50 mg/kg STM2457 ( $n = 5$ ). **c**, Kaplan–Meier survival of AML PDX-3 (*MLL-AF10*) following 12 consecutive treatments with vehicle or 50 mg/kg STM2457 at indicated times ( $n = 5$ ). **d**, Quantification of luminescence for the animal experiment depicted in Extended Data Fig. 4c (mean  $\pm$  s.d.,  $n = 5$ ). **e**, Quantification of luminescence for the animal experiment depicted in Fig. 4c (mean  $\pm$  s.d.,  $n = 5$ ). **f**, Body weight for the animal experiment depicted in Fig. 4a ( $n = 5$ ). Statistical significance was determined by two-tailed Mann–Whitney U test and box plots showing median, IQR and extremes. **g**, Western blot for SP1, BRD4, HNRNPL, BCL2, METTL3 and ACTIN protein levels in AML PDX-3 (*MLL-AF10*) treated with vehicle or 50 mg/kg STM2457 ( $n = 4$ ). **h**, RNA-mass spectrometry quantification of m<sup>6</sup>A levels on poly-A<sup>+</sup>-enriched RNA from bone marrow of AML PDX-3 (*MLL-AF10*) treated in vivo with vehicle, 30 mg/kg STM2457 or 50 mg/kg STM2457 (mean  $\pm$  s.d.,  $n = 4$ ). D, day; n.s. not significant; two-tailed Student's *t*-test; Log-rank (Mantel–Cox) test was used for survival comparisons. [Source data](#)

## Extended Data Fig. 7 STM2457 treatment is efficacious and targeted in primary murine AML.

**a**, Percentage of YFP<sup>+</sup> *MLL-AF9/Flt3<sup>Itd/+</sup>* cells in the bone marrow of mice treated with vehicle or 30 mg/kg STM2457 (mean ± s.d.,  $n = 4$ ). **b**, Spleen weight of *MLL-AF9/Flt3<sup>Itd/+</sup>* murine AML models following treatment with vehicle or 30 mg/kg STM2457 (mean ± s.d.,  $n = 4$ ). **c**, Western blot showing SP1, BRD4, HNRNPL, BCL2, METTL3 and ACTIN protein levels in murine AML (*MLL-AF9/Flt3<sup>Itd/+</sup>*) models treated with either vehicle or 30 mg/kg STM2457 ( $n = 4$ ). **d**, RNA-mass spectrometry quantification of m<sup>6</sup>A levels on poly-A<sup>+</sup>-enriched RNA in vivo from AML murine models (*MLL-AF9/Flt3<sup>Itd/+</sup>*) treated with vehicle, 30 mg/kg STM2457 or 50 mg/kg STM2457 (mean ± s.d.,  $n = 4$ ). **e**, Percentage of CD93<sup>+</sup> cells in the bone marrow of *MLL-AF9/Flt3<sup>Itd/+</sup>* murine models following treatment with either vehicle or 30 mg/kg STM2457 (mean ± s.d.,  $n = 5$ ). **f**, Percentage of L-GMP cells in the bone marrow of *MLL-AF9/Flt3<sup>Itd/+</sup>* murine models following treatment with either vehicle or 30 mg/kg STM2457 (mean ± s.d.,  $n = 5$ ). **g**, CD48 levels of L-GMP cells in the bone marrow of *MLL-AF9/Flt3<sup>Itd/+</sup>* murine models following treatment with either vehicle or 30 mg/kg STM2457 (mean ± s.d.,  $n = 5$ ). **h**, Kaplan–Meier survival after re-transplantation of cells isolated from primary transplanted animals with *MLL-AF9/Flt3<sup>Itd/+</sup>* treated and treated with either vehicle or 30 mg/kg STM2457 ( $n = 5$ ). **i**, Percentage of YFP<sup>+</sup> cells in the peripheral blood 12 days after re-transplantation with *MLL-AF9/Flt3<sup>Itd/+</sup>* (mean ± s.d.,  $n = 5$ ). D, day; BM, bone marrow; PBC, peripheral blood count; n.s. not significant; two-tailed Student's *t*-test; Log-rank (Mantel–Cox) test was used for survival comparisons. [Source data](#)

## Extended Data Fig. 8 Pharmacological inhibition of METTL3 has no lasting effects on normal haematopoiesis.

**a–c**, Quantification of LSK (Lin-/Ska1<sup>+</sup>/c-Kit<sup>+</sup>) and HSC (LSK/CD150<sup>+</sup>/CD34<sup>-</sup>) compartments in bone marrow from WT C57BL/6J mice following 14 consecutive daily treatments with either vehicle or 50 mg/kg STM2457 (mean ± s.d.,  $n = 5$ ). **d**, Blood count results from animal

experiments related to **a–c**. **e**, Body weight of mice from animal experiments related to **a–d** ( $n = 5$ ). Statistical significance was determined by two-tailed Mann–Whitney U test and box plots showing median, IQR and extremes. **f**, RNA-mass spectrometry quantification of m<sup>6</sup>A levels on poly-A<sup>+</sup>-enriched RNA from healthy bone marrow related to the animal experiments in **a–d**, following 14 days of consecutive treatments with either vehicle or 50 mg/kg STM2457 (mean ± s.d.,  $n = 5$ ). HSC, haematopoietic stem cells; two-tailed Student's *t*-test; n.s., not significant. [Source data](#)

## Supplementary information

### [Supplementary Information](#)

This file contains Supplementary Figures 1-2 (the uncropped western blots and gating strategy for FACS experiments), and Supplementary Notes 1-2 (a description of the STM2457 X-ray crystallography results and chemical synthesis of STM2457).

### [Reporting Summary](#)

### [Supplementary Table 1](#)

Differential expression analysis using DESeq2 from RNAseq data.

### [Supplementary Table 2](#)

GSEA of differential downregulated genes from RNAseq.

### [Supplementary Table 3](#)

Differential analysis of m<sup>6</sup>A substrates using meRIP-seq data.

### [Supplementary Table 4](#)

Overlap of differential downregulated m<sup>6</sup>A peaks between pharmacological and genetic inhibition of METTL3.

## **Supplementary Table 5**

Gene Ontology (GO) enrichment of genes differentially m<sup>6</sup>A modified according to meRIP-seq.

## **Supplementary Table 6**

Information for all primer sequences used.

## **Supplementary Table 7**

Data collection and refinement statistics for X-ray crystallography.

## **Peer Review File**

## **Source data**

### **Source Data Fig. 4**

### **Source Data Extended Data Fig. 2**

### **Source Data Extended Data Fig. 6**

### **Source Data Extended Data Fig. 7**

### **Source Data Extended Data Fig. 8**

## **Rights and permissions**

### **Reprints and Permissions**

## About this article



## Cite this article

Yankova, E., Blackaby, W., Albertella, M. *et al.* Small-molecule inhibition of METTL3 as a strategy against myeloid leukaemia. *Nature* **593**, 597–601 (2021). <https://doi.org/10.1038/s41586-021-03536-w>

### [Download citation](#)

- Received: 18 December 2020
- Accepted: 12 April 2021
- Published: 26 April 2021
- Issue Date: 27 May 2021
- DOI: <https://doi.org/10.1038/s41586-021-03536-w>

## Further reading

- [\*\*Mining for METTL3 inhibitors to suppress cancer\*\*](#)
  - Jiazh Li
  - & Richard I. Gregory

*Nature Structural & Molecular Biology* (2021)

- [\*\*METTLing with RNA methylation in leukaemia\*\*](#)
  - Megan Cully

## Comments

By submitting a comment you agree to abide by our [Terms](#) and [Community Guidelines](#). If you find something abusive or that does not comply with our terms or guidelines please flag it as inappropriate.

[Access through your institution](#)

[Change institution](#)

[Buy or subscribe](#)

## Associated Content

### [Mining for METTL3 inhibitors to suppress cancer](#)

- Jiazh Li
- Richard I. Gregory

Nature Structural & Molecular Biology News & Views 26 May 2021

Advertisement

---

This article was downloaded by **calibre** from <https://www.nature.com/articles/s41586-021-03536-w>

- Article
- [Published: 05 May 2021](#)

# Global miRNA dosage control of embryonic germ layer specification

- [Yingzi Cui<sup>1</sup>](#), <sup>na1</sup>,
- [Xuehui Lyu](#) [ORCID: orcid.org/0000-0002-6185-1170](#)<sup>2</sup>, <sup>na1</sup>,
- [Li Ding<sup>1</sup>](#),
- [Lan Ke<sup>3,4,5</sup>](#),
- [Dechang Yang<sup>3,4,5</sup>](#),
- [Mehdi Pirouz](#) [ORCID: orcid.org/0000-0002-7439-6066](#)<sup>6,7</sup>,
- [Ye Qi<sup>2</sup>](#),
- [Jennie Ong<sup>1,2</sup>](#),
- [Ge Gao](#) [ORCID: orcid.org/0000-0001-6470-8815](#)<sup>3,4,5</sup>,
- [Peng Du](#) <sup>1,2</sup> &
- [Richard I. Gregory](#) [ORCID: orcid.org/0000-0001-8090-8673](#)<sup>6,7,8,9,10</sup>

[Nature](#) volume 593, pages 602–606 (2021) [Cite this article](#)

- 4302 Accesses
- 36 Altmetric
- [Metrics details](#)

## Subjects

- [Embryonic stem cells](#)
- [Non-coding RNAs](#)

# Abstract

MicroRNAs (miRNAs) have essential functions during embryonic development, and their dysregulation causes cancer<sup>1,2</sup>. Altered global miRNA abundance is found in different tissues and tumours, which implies that precise control of miRNA dosage is important<sup>1,3,4</sup>, but the underlying mechanism(s) of this control remain unknown. The protein complex Microprocessor, which comprises one DROSHA and two DGCR8 proteins, is essential for miRNA biogenesis<sup>5,6,7</sup>. Here we identify a developmentally regulated miRNA dosage control mechanism that involves alternative transcription initiation (ATI) of *DGCR8*. ATI occurs downstream of a stem-loop in *DGCR8* mRNA to bypass an autoregulatory feedback loop during mouse embryonic stem (mES) cell differentiation. Deletion of the stem-loop causes imbalanced DGCR8:DROSHA protein stoichiometry that drives irreversible Microprocessor aggregation, reduced primary miRNA processing, decreased mature miRNA abundance, and widespread de-repression of lipid metabolic mRNA targets. Although global miRNA dosage control is not essential for mES cells to exit from pluripotency, its dysregulation alters lipid metabolic pathways and interferes with embryonic development by disrupting germ layer specification in vitro and in vivo. This miRNA dosage control mechanism is conserved in humans. Our results identify a promoter switch that balances Microprocessor autoregulation and aggregation to precisely control global miRNA dosage and govern stem cell fate decisions during early embryonic development.

## Access options

Subscribe to Journal

Get full journal access for 1 year

\$199.00

only \$3.90 per issue

[Subscribe](#)

All prices are NET prices.  
VAT will be added later in the checkout.  
Tax calculation will be finalised during checkout.

Rent or Buy article

Get time limited or full article access on ReadCube.

from \$8.99

[Rent or Buy](#)

All prices are NET prices.

### **Additional access options:**

- [Log in](#)
- [Access through your institution](#)
- [Learn about institutional subscriptions](#)

**Fig. 1: ATI of *DGCR8* links dynamic Microprocessor autoregulation to altered DGCR8: DROSHA stoichiometry and aggregation.**

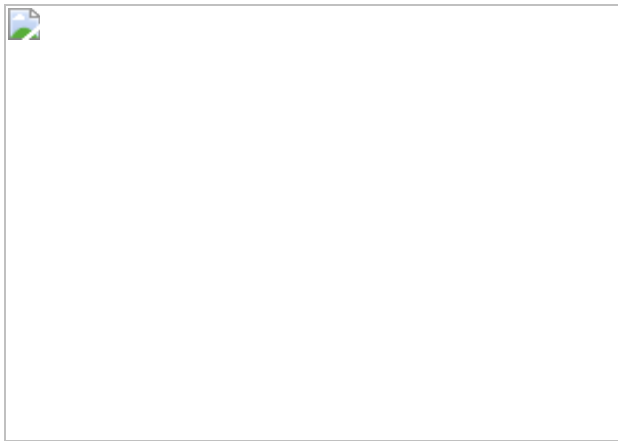


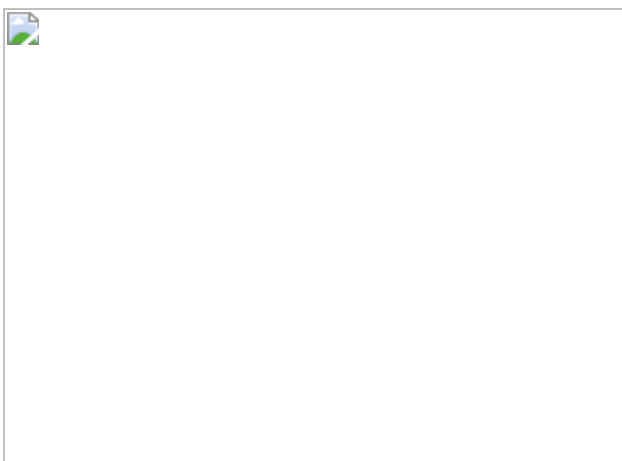
**Fig. 2: Microprocessor aggregation reduces the efficiency of miRNA processing and global miRNA dosage, leading to de-repression of lipid metabolic genes.**



**Fig. 3: ATI-mediated miRNA dosage control determines germ layer specification during mES cell differentiation.**



**Fig. 4: ATI-mediated miRNA dosage control mechanism is conserved in human cells and tissues.**



## Data availability

The RNA-seq and small RNA-seq data that support the findings of this study have been deposited in GEO with accession number [GSE165017](#). Published polyA(+) RNA-seq data for mES cell differentiation is from the

GEO database under accession number GSE112334<sup>14</sup>. The published polyA(+) RNA-seq for EpiS cells and cells of the three germ layers reported in this paper is available on ArrayExpress (<https://www.ebi.ac.uk/arrayexpress/>) with accession E-MTAB-4904<sup>27</sup>. [Source data](#) are provided with this paper.

## Code availability

Perl scripts are available from <https://github.com/lyuxuehui/ATI-of-DGCR8>.

## References

1. 1.

Lin, S. & Gregory, R. I. MicroRNA biogenesis pathways in cancer. *Nat. Rev. Cancer* **15**, 321–333 (2015).

[CAS](#) [Article](#) [Google Scholar](#)

2. 2.

Bartel, D. P. Metazoan MicroRNAs. *Cell* **173**, 20–51 (2018).

[CAS](#) [Article](#) [Google Scholar](#)

3. 3.

Lu, J. et al. MicroRNA expression profiles classify human cancers. *Nature* **435**, 834–838 (2005).

[ADS](#) [CAS](#) [Article](#) [Google Scholar](#)

4. 4.

Landgraf, P. et al. A mammalian microRNA expression atlas based on small RNA library sequencing. *Cell* **129**, 1401–1414 (2007).

[CAS](#) [Article](#) [Google Scholar](#)

5. 5.

Lee, Y. et al. The nuclear RNase III Drosha initiates microRNA processing. *Nature* **425**, 415–419 (2003).

[ADS](#) [CAS](#) [Article](#) [Google Scholar](#)

6. 6.

Denli, A. M., Tops, B. B., Plasterk, R. H., Ketting, R. F. & Hannon, G. J. Processing of primary microRNAs by the Microprocessor complex. *Nature* **432**, 231–235 (2004).

[ADS](#) [CAS](#) [Article](#) [Google Scholar](#)

7. 7.

Gregory, R. I. et al. The Microprocessor complex mediates the genesis of microRNAs. *Nature* **432**, 235–240 (2004).

[ADS](#) [CAS](#) [Article](#) [Google Scholar](#)

8. 8.

Kwon, S. C. et al. Structure of human DROSHA. *Cell* **164**, 81–90 (2016).

[CAS](#) [Article](#) [Google Scholar](#)

9. 9.

Partin, A. C. et al. Cryo-EM structures of human Drosha and DGCR8 in complex with primary MicroRNA. *Mol. Cell* **78**, 411–422.e4 (2020).

[CAS](#) [Article](#) [Google Scholar](#)

10. 10.

Ha, M. & Kim, V. N. Regulation of microRNA biogenesis. *Nat. Rev. Mol. Cell Biol.* **15**, 509–524 (2014).

[CAS](#) [Article](#) [Google Scholar](#)

11. 11.

Han, J. et al. Posttranscriptional crossregulation between Drosha and DGCR8. *Cell* **136**, 75–84 (2009).

[CAS](#) [Article](#) [Google Scholar](#)

12. 12.

Triboulet, R., Chang, H. M., Lapierre, R. J. & Gregory, R. I. Post-transcriptional control of DGCR8 expression by the Microprocessor. *RNA* **15**, 1005–1011 (2009).

[CAS](#) [Article](#) [Google Scholar](#)

13. 13.

Du, P., Wang, L., Sliz, P. & Gregory, R. I. A biogenesis step upstream of Microprocessor controls miR-17~92 expression. *Cell* **162**, 885–899 (2015).

[CAS](#) [Article](#) [Google Scholar](#)

14. 14.

Du, P. et al. An intermediate pluripotent state controlled by microRNAs is required for the naive-to-primed stem cell transition. *Cell Stem Cell* **22**, 851–864.e5 (2018).

[CAS](#) [Article](#) [Google Scholar](#)

15. 15.

Bernstein, E. et al. Dicer is essential for mouse development. *Nat. Genet.* **35**, 215–217 (2003).

[CAS](#) [Article](#) [Google Scholar](#)

16. 16.

Wang, Y., Medvid, R., Melton, C., Jaenisch, R. & Blelloch, R. DGCR8 is essential for microRNA biogenesis and silencing of embryonic stem cell self-renewal. *Nat. Genet.* **39**, 380–385 (2007).

[CAS](#) [Article](#) [Google Scholar](#)

17. 17.

Zhang, B. et al. A dosage-dependent pleiotropic role of Dicer in prostate cancer growth and metastasis. *Oncogene* **33**, 3099–3108 (2014).

[CAS](#) [Article](#) [Google Scholar](#)

18. 18.

Lambo, S. et al. The molecular landscape of ETMR at diagnosis and relapse. *Nature* **576**, 274–280 (2019).

[Article](#) [Google Scholar](#)

19. 19.

Alberti, S., Gladfelter, A. & Mittag, T. Considerations and challenges in studying liquid-liquid phase separation and biomolecular condensates. *Cell* **176**, 419–434 (2019).

[CAS](#) [Article](#) [Google Scholar](#)

20. 20.

Maharana, S. et al. RNA buffers the phase separation behavior of prion-like RNA binding proteins. *Science* **360**, 918–921 (2018).

[ADS](#) [CAS](#) [Article](#) [Google Scholar](#)

21. 21.

Case, L. B., Zhang, X., Ditlev, J. A. & Rosen, M. K. Stoichiometry controls activity of phase-separated clusters of actin signaling proteins. *Science* **363**, 1093–1097 (2019).

[ADS](#) [CAS](#) [Article](#) [Google Scholar](#)

22. 22.

Patel, A. et al. A liquid-to-solid phase transition of the ALS protein FUS accelerated by disease mutation. *Cell* **162**, 1066–1077 (2015).

[CAS](#) [Article](#) [Google Scholar](#)

23. 23.

Lin, Y., Protter, D. S., Rosen, M. K. & Parker, R. Formation and maturation of phase-separated liquid droplets by RNA-binding proteins. *Mol. Cell* **60**, 208–219 (2015).

[CAS](#) [Article](#) [Google Scholar](#)

24. 24.

Hayashi, K., Ohta, H., Kurimoto, K., Aramaki, S. & Saitou, M. Reconstitution of the mouse germ cell specification pathway in culture by pluripotent stem cells. *Cell* **146**, 519–532 (2011).

[CAS](#) [Article](#) [Google Scholar](#)

25. 25.

Sladitschek, H. L. & Neveu, P. A. A gene regulatory network controls the balance between mesendoderm and ectoderm at pluripotency exit. *Mol. Syst. Biol.* **15**, e9043 (2019).

[CAS](#) [Article](#) [Google Scholar](#)

26. 26.

Greve, T. S., Judson, R. L. & Blelloch, R. microRNA control of mouse and human pluripotent stem cell behavior. *Annu. Rev. Cell Dev. Biol.* **29**, 213–239 (2013).

[CAS](#) [Article](#) [Google Scholar](#)

27. 27.

Xie, D. et al. Phase separation of SERRATE drives dicing body assembly and promotes miRNA processing in *Arabidopsis*. *Nat. Cell Biol.* **23**, 32–39 (2021).

[CAS](#) [Article](#) [Google Scholar](#)

28. 28.

Yao, X. et al. CRISPR/Cas9-mediated targeted integration *in vivo* using a homology-mediated end joining-based strategy. *J. Vis. Exp.* **133**, 56844 (2018).

[Google Scholar](#)

29. 29.

Mori, M. et al. Hippo signaling regulates microprocessor and links cell-density-dependent miRNA biogenesis to cancer. *Cell* **156**, 893–906 (2014).

[CAS](#) [Article](#) [Google Scholar](#)

30. 30.

Langmead, B., Trapnell, C., Pop, M. & Salzberg, S. L. Ultrafast and memory-efficient alignment of short DNA sequences to the human genome. *Genome Biol.* **10**, R25 (2009).

[Article](#) [Google Scholar](#)

31. 31.

Griffiths-Jones, S., Saini, H. K., van Dongen, S. & Enright, A. J. miRBase: tools for microRNA genomics. *Nucleic Acids Res.* **36**, D154–D158 (2008).

[CAS](#) [Article](#) [Google Scholar](#)

32. 32.

Bolger, A. M., Lohse, M. & Usadel, B. Trimmomatic: a flexible trimmer for Illumina sequence data. *Bioinformatics* **30**, 2114–2120 (2014).

[CAS](#) [Article](#) [Google Scholar](#)

33. 33.

Kim, D., Paggi, J. M., Park, C., Bennett, C. & Salzberg, S. L. Graph-based genome alignment and genotyping with HISAT2 and HISAT-genotype. *Nat. Biotechnol.* **37**, 907–915 (2019).

[CAS](#) [Article](#) [Google Scholar](#)

34. 34.

Liao, Y., Smyth, G. K. & Shi, W. featureCounts: an efficient general purpose program for assigning sequence reads to genomic features. *Bioinformatics* **30**, 923–930 (2014).

[CAS](#) [Article](#) [Google Scholar](#)

35. 35.

Chen, J., Bardes, E. E., Aronow, B. J. & Jegga, A. G. ToppGene Suite for gene list enrichment analysis and candidate gene prioritization. *Nucleic Acids Res.* **37**, W305–W311 (2009).

[CAS](#) [Article](#) [Google Scholar](#)

36. 36.

Subramanian, A. et al. Gene set enrichment analysis: a knowledge-based approach for interpreting genome-wide expression profiles. *Proc. Natl Acad. Sci. USA* **102**, 15545–15550 (2005).

[ADS](#) [CAS](#) [Article](#) [Google Scholar](#)

37. 37.

Jiang, S. et al. An expanded landscape of human long noncoding RNA. *Nucleic Acids Res.* **47**, 7842–7856 (2019).

[CAS](#) [Article](#) [Google Scholar](#)

[Download references](#)

## Acknowledgements

We thank N. Kim, P. Li, Y. Qi, and X. Fu for discussions; the Biopolymer Facility at Harvard Medical School for RNA-seq and small RNA-seq Illumina high-throughput sequencing; the Core Facilities of the School of Life Sciences at Peking University, particularly S. Qin, C. Shan, L. Fu and S. Huang, for technical help with confocal imaging and radiolabelling assays; and the flow cytometry Core at National Center for Protein Sciences at Peking University, particularly H. Lyu and H. Yang, for technical help. Some work on protein purification was performed in N. Gao's laboratory (Peking University); we thank them for assistance. We thank J. Xiao's laboratory for providing the pFastBac-Dual vector, Sf21 cells and their assistance; H.-Y. Lee's laboratory and Y. Wang's laboratory for providing the K562 cells and *DGCR8<sup>-/-</sup>* cells, respectively; and F. Guo for providing

the pFastBac-HTb-His<sub>6</sub>-DROSHA<sup>390–1374</sup> vector. This work was supported by grants to P.D. from the Natural Science Foundation of China (32050214 and 32090012) and the National Key Research and Development Program of China (2019YFA0110000), M.P. was supported by the National Institute of Diabetes and Digestive and Kidney Diseases (NIDDK) (K01DK121861), and a grant to R.I.G. from the US National Institute of General Medical Sciences (NIGMS) (R01GM086386).

## Author information

### Author notes

1. These authors contributed equally: Yingzi Cui, Xuehui Lyu

### Affiliations

1. MOE Key Laboratory of Cell Proliferation and Differentiation, School of Life Sciences, Peking University, Beijing, China  
Yingzi Cui, Li Ding, Jennie Ong & Peng Du
2. Peking-Tsinghua Center for Life Sciences, Academy for Advanced Interdisciplinary Studies, Peking University, Beijing, China  
Xuehui Lyu, Ye Qi, Jennie Ong & Peng Du
3. Biomedical Pioneering Innovation Center, Beijing Advanced Innovation Center for Genomics, Peking University, Beijing, China  
Lan Ke, Dechang Yang & Ge Gao
4. Center for Bioinformatics, School of Life Sciences, Peking University, Beijing, China  
Lan Ke, Dechang Yang & Ge Gao

5. State Key Laboratory of Protein and Plant Gene Research, School of Life Sciences, Peking University, Beijing, China

Lan Ke, Dechang Yang & Ge Gao

6. Stem Cell Program, Division of Hematology/Oncology, Boston Children's Hospital, Boston, MA, USA

Mehdi Pirouz & Richard I. Gregory

7. Department of Biological Chemistry and Molecular Pharmacology, Harvard Medical School, Boston, MA, USA

Mehdi Pirouz & Richard I. Gregory

8. Harvard Stem Cell Institute, Cambridge, MA, USA

Richard I. Gregory

9. Department of Pediatrics, Harvard Medical School, Boston, MA, USA

Richard I. Gregory

10. Harvard Initiative for RNA Medicine, Boston, MA, USA

Richard I. Gregory

## Authors

1. Yingzi Cui

[View author publications](#)

You can also search for this author in [PubMed](#) [Google Scholar](#)

2. Xuehui Lyu

[View author publications](#)

You can also search for this author in [PubMed](#) [Google Scholar](#)

3. Li Ding

[View author publications](#)

You can also search for this author in [PubMed](#) [Google Scholar](#)

4. Lan Ke

[View author publications](#)

You can also search for this author in [PubMed](#) [Google Scholar](#)

5. Dechang Yang

[View author publications](#)

You can also search for this author in [PubMed](#) [Google Scholar](#)

6. Mehdi Pirouz

[View author publications](#)

You can also search for this author in [PubMed](#) [Google Scholar](#)

7. Ye Qi

[View author publications](#)

You can also search for this author in [PubMed](#) [Google Scholar](#)

8. Jennie Ong

[View author publications](#)

You can also search for this author in [PubMed](#) [Google Scholar](#)

9. Ge Gao

[View author publications](#)

You can also search for this author in [PubMed](#) [Google Scholar](#)

10. Peng Du

[View author publications](#)

You can also search for this author in [PubMed](#) [Google Scholar](#)

11. Richard I. Gregory  
[View author publications](#)

You can also search for this author in [PubMed](#) [Google Scholar](#)

## Contributions

Y.C. performed all phase-separation-related experiments (with some help from Y.Q. and X.L.), 5' RACE experiments, and the teratoma assay. Y.C. and P.D. performed Microprocessor cleavage assays. Y.C. performed EB and neural differentiation with help from X.L. and M.P. P.D. performed the miRNA reporter assay and constructed the ΔSL1 mES cell line; other cell lines were constructed by Y.C. and X.L. X.L. and P.D. carried out qRT–PCR, western blot, and RNA-seq bioinformatic analysis. L.D. performed small RNA-seq bioinformatic analysis. L.K. and D.Y. performed bioinformatic analysis on GTEx datasets under the supervision of G.G. P.D. and R.I.G. designed all experiments, analysed data, and wrote the manuscript with input from J.O., Y.C., and X.L.

## Corresponding authors

Correspondence to [Peng Du](#) or [Richard I. Gregory](#).

## Ethics declarations

## Competing interests

The authors declare no competing interests. R.I.G is a co-founder and scientific advisory board member of 28/7 Therapeutics and Theon Therapeutics.

## Additional information

**Peer review information** *Nature* thanks Hannele Ruohola-Baker and the other, anonymous, reviewer(s) for their contribution to the peer review of this work.

**Publisher's note** Springer Nature remains neutral with regard to jurisdictional claims in published maps and institutional affiliations.

## Extended data figures and tables

### Extended Data Fig. 1 ATI of *DGCR8* links dynamic Microprocessor autoregulation to altered *DGCR8:DROSHA* stoichiometry.

**a**, Ratio of splicing events covering different exons based on RNA-seq data during mES cell-to-EB differentiation over a 13-day time course (Fig. 1a). **b**, Agarose gel analysis of 5' RACE products (left) and summary of Sanger sequencing of 5' RACE colonies (right). PCR products outlined by red arrows were purified and further processed for cloning and Sanger sequencing. The numbers indicate the proportion of all sequenced clones that map to a particular nucleotide. Stem-loop 1 (SL1) sequence in 5' UTR is highlighted in red (Fig. 1b). **c**, Stem-loop structures (SL1 and SL2) in the 5' UTR and CDS region of *DGCR8* mRNA. Green arrowheads indicate CRISPR–Cas9 design for SL1 deletion. **d**, PCR analysis of genomic DNA for SL1 knockout ( $\Delta$ SL1) in mES cells. **e**, qRT–PCR analysis of *DGCR8* and *DROSHA* mRNA expression in wild-type and  $\Delta$ SL1 mES cells. Data were normalized to *GAPDH*, and error bars indicate s.d. ( $n = 3$ , technical replicates). **f**, Western blots of *DGCR8* and *DROSHA* proteins in wild-type and  $\Delta$ SL1 mES cells transfected with corresponding siRNAs. Experiments were repeated three times with similar results (Methods).

### Extended Data Fig. 2 SL1 depletion drives irreversible Microprocessor aggregation in mouse ES cells.

**a**, Immunofluorescence (IF) followed by confocal imaging of *DGCR8* and *DROSHA* proteins in wild-type and  $\Delta$ SL1 mES cells. Fluorescence signals of *DGCR8* and *DROSHA* are shown in red and green, respectively, and DAPI stain is shown in blue. The merged signals are also shown. **b**, Western blot of *DGCR8* and *DROSHA* proteins in wild-type and reporter mES cells expressing endogenous mCherry–*DGCR8* fusion protein. **c**, Images of endogenous mCherry–*DGCR8* fusion protein in the wild-type

and  $\Delta$ SL1 reporter ES cells. **d**, Representative time-lapse images of two proximate assemblies of Microprocessor in living  $\Delta$ SL1 mES cells transfected with plasmids expressing tagged mCherry–DGCR8 and eGFP–DROSHA. **e**, Images of Microprocessor aggregates before and after treatment with 10% 1,6-hexanediol for 3 min in living  $\Delta$ SL1 mES cells. **f**, Representative images of FRAP analysis of Microprocessor aggregates in living  $\Delta$ SL1 mES cells transfected with plasmids expressing tagged mCherry–DGCR8 and eGFP–DROSHA. Targeted region is highlighted in a white box, and DGCR8 (red), DROSHA (green) and merged (yellow) signals are shown. Normalized fluorescence intensity of DGCR8 and DROSHA are shown. Data are represented as mean  $\pm$  s.d. ( $n = 6$ , independent observations in six separated aggregates). **g**, Images of Microprocessor aggregates in  $\Delta$ SL1 mES cells transfected with plasmids expressing tagged mCherry–DGCR8 and eGFP–DROSHA before and after microinjection with RNase. All experiments were repeated at least three times with similar results ([Methods](#)).

### **Extended Data Fig. 3 Imbalanced DGCR8:DROSHA stoichiometry drives irreversible Microprocessor aggregation in vitro.**

**a**, Top, prediction of disordered regions in DGCR8 protein by PONDR (<http://pondr.com/>). Bottom, schematic diagram showing the domains of DGCR8. **b**, Coomassie blue staining of purified rDGCR8 and rDROSHA proteins at different concentrations, as well as two mutant versions of rDGCR8 proteins with deletion of  $\Delta$ CTT and  $\Delta$ Rhed domains. **c**, Representative images of phase separation of rDGCR8, rDGCR8- $\Delta$ CTT, rDGCR8- $\Delta$ Rhed and rDROSHA at different concentrations in physiological buffer. **d**, Representative images of the aggregates of labelled rDGCR8 (30  $\mu$ M) before and after treatment with 10% 1,6-hexanediol for 5 min. **e**, Representative images of FRAP analysis of rDGCR8 puncta. Targeted region is highlighted in a white box. Normalized fluorescence intensity of rDGCR8 in FRAP analysis is represented as mean  $\pm$  s.d. ( $n = 6$ , independent observations in six separated aggregates). **f**, **g**, Representative confocal images of pre-formed Microprocessor aggregates (32  $\mu$ M rDGCR8:8  $\mu$ M rDROSHA) under conditions of dilution and high salt (1 M NaCl). rDGCR8 (red), rDROSHA (green) and merged (yellow) signals are

shown. **h, i**, Images of pre-formed Microprocessor aggregates (32  $\mu$ M rDGCR8:8  $\mu$ M rDROSHA) followed by the addition of extra rDROSHA to achieve a 2:1 ratio or treatment with 10% 1,6-hexanediol for 10 min. **j**, Representative time-lapse images of two proximate Microprocessor aggregates for the times indicated. rDGCR8 (red), rDROSHA (green) and merged (yellow) signals are shown. **k**, FRAP analysis of Microprocessor aggregates in vitro. Targeted droplet region is highlighted in a white box, and rDGCR8 (red), rDROSHA (green) and merged (yellow) signals are shown. Right, normalized fluorescence intensities. Data are represented as mean  $\pm$  s.d. ( $n = 7$ , independent observations in seven separated aggregates). All experiments were repeated at least three times with similar results ([Methods](#)).

#### [Extended Data Fig. 4 Microprocessor aggregation reduces the efficiency of pri-miRNA processing and global miRNA dosage, which leads to the de-repression of lipid metabolic genes.](#)

**a**, Microprocessor in vitro cleavage assay of mouse pri-mir-125b using whole-cell lysate from wild-type and  $\Delta$ SL1 mES cells. Microprocessor purified by immunoprecipitation from Flag–DROSHA-293T cells was used as a control. The pri-mir125b without lysate was the CK sample. **b**, Quantification of pri-miRNA cleavage activity calculated based on the density of pre-miRNA bonds in the assays shown in Fig. [2b](#) and Extended Data Fig. [4a](#). **c**, Luciferase reporter in vivo cleavage assay of pri-mir-125b in wild-type,  $DGCR8^{-/-}$ , and  $\Delta$ SL1 mES cells. Data are represented as mean  $\pm$  s.d. ( $n = 3$ , technical replicates). \*\*\* $P < 0.0001$ , two-sided Student's *t*-test. **d**, Scatter plot of global miRNA expression based small RNA-seq data in wild-type and  $\Delta$ SL1 mES cells. The small RNA-seq data were normalized on the basis of spike-in RNAs. Differentially expressed miRNAs are represented by coloured circles, and the number of up- and downregulated miRNAs is shown. FC, fold change; two-sided Student's *t*-test. **e**, Heat map of the expression of common up- or downregulated genes in  $\Delta$ SL1 and  $DGCR8^{-/-}$  mES cells compared to wild-type mES cells. The enrichment of Gene Ontology (GO) terms and the number of genes in each group are shown. Two-sided Student's *t*-test. **f**, Venn diagram of mRNAs with expression changes in  $\Delta$ SL1 and  $DGCR8^{-/-}$  cells compared to wild-

type mES cells. Number of genes in each group is shown. Two-sided Student's *t*-test. **g**, GSEA analyses of lipid metabolic gene sets by comparing  $\Delta$ SL1 and  $DGCR8^{-/-}$  cells with wild-type mES cells. NES, normalized enrichment score. *P* values calculated by GSEA software. FDR, false discovery rate. **h**, Network of miRNAs and lipid metabolic genes. **i**, miRNA target sites on *PDK4*, *LCLAT1* and *GPCPD1* mRNAs, and luciferase miRNA target reporter assay in wild-type,  $\Delta$ SL1 and  $DGCR8^{-/-}$  mES cells. Data are represented as mean  $\pm$  s.d. ( $n = 3$ , technical replicates). \*\*\*\* $P < 0.0001$ , two-sided Student's *t*-test. Mutations introduced into the miRNA target sites on *PDK4* and *LCLAT1*, and the mutation sequences are shown in red font. Exact *P* values are provided in the Source Data (**c, i**) and Supplementary Table (**d–f**). Details of statistics replications are given in 'Statistics and reproducibility' in Methods. [Source data](#)

## **Extended Data Fig. 5 Imbalanced DGCR8:DROSHA stoichiometry during EB differentiation drives Microprocessor aggregation.**

**a**, Box plots of the relative expression of naive and primed genes during EpiLC differentiation of wild-type,  $\Delta$ SL1 and  $DGCR8^{-/-}$  mES cells. The number of naive and primed genes is shown and representative markers are listed. For box plots, centre line is median; box limits are 25th and 75th percentiles; whiskers extend to  $1.5 \times$  IQR from the 25th and 75th percentiles. **b**, PCA of the wild-type and  $\Delta$ SL1 cells by all expressed mRNAs during mES cell-to-EpiLC differentiation. **c, d**, The relative expression and calculated ratio of *DGCR8* and *DROSHA* mRNA based on RNA-seq data during EB differentiation over a 13-day time course. **e**, Western blot of DGCR8 and DROSHA at different time points during wild-type mES cell-to-EB differentiation. The densities of the DROSHA and DGCR8 bands were normalized to the ACTINB band to calculate the relative protein ratios. **f**, Western blot of DGCR8 and DROSHA in differentiated EB cells (day 8) before and after treatment with a proteasome inhibitor MG132 (10  $\mu$ M) for 2 h. The densities of the DROSHA and DGCR8 bands were normalized to the ACTINB band to calculate the relative protein ratios. **g**, Representative images of Microprocessor aggregates in differentiated EB cells (day 8) derived from dual-reporter ES

cells endogenously expressing both mCherry–DGCR8 and eGFP–DROSHA fusion proteins. All experiments were repeated at least twice with similar results ([Methods](#)).

**Extended Data Fig. 6 ATI-mediated miRNA dosage control determines germ layer specification during mES cell differentiation in vitro.**

**a**, Ratios of splicing events covering different exons based on RNA-seq data from various germ layer cells. Ep, EpiS cell; Ec, ectoderm; Me, mesoderm; En, endoderm. **b**, The relative expression of pluripotent genes in wild-type and  $\Delta$ SL1 cells during neural and EB differentiation. NP, neural progenitor. **c**, Heat maps of the relative expression of genes that are up- or downregulated in  $\Delta$ SL1 cells compared with wild-type cells during EB differentiation. The enrichment of Gene Ontology (GO) terms and the number of genes in each group are shown. **d**, Heat maps of gene expression showing up- or downregulation in  $\Delta$ SL1 mES cells compared with wild-type mES cells during neural differentiation. The enrichment of GO terms and the number of genes in each group are shown. **e**, Heat map of the relative expression of marker genes for three germ layers during neural differentiation. Representative markers are listed on the right. **f**, Scatter plot of global miRNA expression based small RNA-seq data in mES cells and neuronal progenitor cells (day 5). All experiments were repeated at least twice with similar results ([Methods](#)).

**Extended Data Fig. 7 miRNA dosage control affects germ layer specification during teratoma formation in mouse.**

**a**, Histology of teratomas stained with haematoxylin and eosin (HE). Left, low-power view of teratoma; differentiated areas are shown with different colours (black, ectoderm; red, endoderm). Right, representative images of ectoderm (neural tube) and endoderm (glandular structure) tissues. **b**, Comparison of the relative areas of ectoderm and endoderm tissues between wild-type and  $\Delta$ SL1 teratomas, showing the area of each tissue divided by the total area according to HE staining. Data are represented as mean  $\pm$  s.e.m. (WT ectoderm,  $n = 68$ ;  $\Delta$ SL1 ectoderm,  $n = 58$ ; WT

endoderm,  $n = 65$ ;  $\Delta$ SL1 endoderm,  $n = 17$  independent observations). Sixteen (wild-type: 8,  $\Delta$ SL1: 8) sections of eight (wild-type: 4,  $\Delta$ SL1: 4) teratomas from four mice were used for analysis. \*\* $P < 0.01$ , \*\*\* $P < 0.0001$ , two-sided Student's  $t$ -test. **c**, Immunofluorescence of GATA4 protein (endoderm marker) in sections of teratomas derived from wild-type and  $\Delta$ SL1 mES cells. Fluorescence signals of GATA4 are shown in pink, and DAPI staining is shown in blue. **d**, Comparison of the relative area of GATA4<sup>+</sup> cells in teratomas derived from wild-type and  $\Delta$ SL1 mES cells. Data are represented as mean  $\pm$  s.e.m. ( $n = 439$  independent observations), according to the immunofluorescence of 34 (wild-type: 17,  $\Delta$ SL1: 17) sections of 18 (wild-type: 9,  $\Delta$ SL1: 9) teratomas from nine mice. **e**, GATA4<sup>+</sup> cell numbers relative to the total area in teratomas derived from wild-type and  $\Delta$ SL1 mES cells according to the staining in **c**. Exact  $P$  values are provided in the Source Data. Details of statistical replications are given in the Methods. [Source data](#)

### **Extended Data Fig. 8 Inhibition of lipid metabolism affects germ layer specification during EB differentiation in vitro.**

**a**, Heat map of the relative expression of lipid metabolic genes, which is controlled by miRNA dosage in mES cells, during mES cell-to-EB differentiation over a 13-day time course. **b**, Protocol of mES cell-to-EB differentiation including treatment with lipid metabolic inhibitor GW9662. **c**, Heat map of the relative expression of lipid metabolic genes suppressed by GW9662 in differentiated EB cells. Gene number and representative genes are listed. The lipid metabolic genes are from the GO term ‘lipid metabolic process’. **d**, qRT–PCR analysis of the relative expression of germ layer marker genes during EB differentiation with GW9662 treatment. Data are normalized to *GAPDH* and represented as mean  $\pm$  s.d. ( $n = 3$  technical replicates). **e**, Heat map of the relative expression of germ layer marker genes during mES cell-to-EB differentiation under DMSO or GW9662 treatment. All experiments were repeated at least twice with similar results ([Methods](#)).

### **Extended Data Fig. 9 ATI-mediated miRNA dosage control mechanism is conserved in human cells and tissues.**

**a**, Ratios of splicing events covering different exons based on RNA-seq data in different human cell lines (Fig. 4a). **b**, ChIP-seq signals for various transcription factors (TFs) at *DGCR8* 5' UTR are shown in GM12878, MCF-7 and HepG2 cells, and representative transcription factors are listed in red. Histograms show the number of transcription factors that bind to the two distinct promoters (Fig. 4a). **c**, 5' RACE experiment for *DGCR8* mRNA in H1299 and K562 cells. Agarose gel analysis of 5' RACE products (left) and summary of Sanger sequencing of 5' RACE colonies (right). Red arrows indicate PCR products that were purified and further processed for cloning and Sanger sequencing. The numbers indicate the proportion of all sequenced clones that map to a particular nucleotide. SL1 sequence in 5' UTR is shown in red (Fig. 4b). **d**, Imaging of tagged mCherry–DGCR8 and eGFP–DROSHA in living RPE1, HepG2, and K562 cells transfected with corresponding plasmids. **e**, FRAP analysis of Microprocessor aggregates in HepG2 cells transfected with plasmids expressing tagged mCherry–DGCR8 and eGFP–DROSHA. Targeted region is highlighted in a white box. DGCR8 (red), DROSHA (green) and merged (yellow) signals are shown. Normalized fluorescence intensity of DGCR8 and DROSHA in FRAP analysis. Data are presented as mean ± s.d. ( $n = 6$ , independent observations in six separated aggregates). **f**, Representative images of Microprocessor aggregates in HepG2 cells transfected with plasmids expressing tagged mCherry–DGCR8 and eGFP–DROSHA before and after treatment with 10% 1,6-hexanediol (1,6-Hex) for 3 min. **g**, qRT–PCR analysis of *DGCR8* and *DROSHA* mRNA expression in wild-type and  $\Delta$ SL1 H1299 cells. Data are normalized to *GAPDH* and represented as mean ± s.d. ( $n = 3$  technical replicates). **h**, qRT–PCR analysis of mature miRNA expression. Data were normalized to *U2* snoRNA. Data are represented as mean ± s.d. ( $n = 3$  technical replicates). **i**, Formula used to calculate the ATI ratio (representing ATI appearance) and exon ratio based on sequencing coverage of RNA-seq data. **j**, Box plot shows the ATI of *DGCR8* mRNA appearance in different human tissues based on RNA-seq from GTEx dataset. Number of samples analysed is shown in purple. Tissues mainly derived from embryonic endoderm are highlighted in red. For box plots, centre line is median; box limits are 25th and 75th percentiles; whiskers extend to  $1.5 \times$  IQR from the 25th and 75th percentiles. All experiments were repeated at least twice with similar results (Methods).

# **Supplementary information**

## **Supplementary Figure 1**

This file contains the original source images of Western blot, Microprocessor assay.

## **Reporting Summary**

## **Supplementary Table 1**

Global miRNA expression and P-value calculated by two-sided Student's t-test in WT mESCs and  $\Delta$ SL1 mESCs, corresponding to Fig. 2c and Extended Data Fig. 4d.

## **Supplementary Table 2**

Genes with expressional changes and P-value calculated by two-sided Student's t-test in  $\Delta$ SL1 and DGCR8<sup>-/-</sup> ESCs compared with WT ESCs, corresponding to Figs. 2d, Extended Data Fig. 4e, 4f.

## **Supplementary Table 3**

Naive and primed genes expression in WT,  $\Delta$ SL1 and DGCR8<sup>-/-</sup> mESCs during EpiLC differentiation, corresponding to Extended Data Fig. 5a.

## **Supplementary Table 4**

Genes with expressional changes in  $\Delta$ SL1 compared with WT mESCs during EB and neural differentiation, corresponding to Extended Data Fig. 6b-6d.

## **Supplementary Table 5**

The expression of three germ layers marker genes in WT and  $\Delta$ SL1 mESCs during neural and EB differentiation, corresponding to Fig. 3b, Extended Data Fig. 6e.

### **Supplementary Table 6**

Global miRNA expression during neural differentiation, corresponding to Extended Data Fig. 6f.

### **Supplementary Table 7**

The expression of lipid metabolic genes and three germ layer genes during EB differentiation treatment with lipid metabolic inhibitor GW9662, corresponding to Extended Data Figs. 8a, 8c, 8e.

### **Supplementary Table 8**

Global miRNA expression in human cell lines, corresponding to Fig.4c.

### **Supplementary Table 9**

List of primers and siRNA sequences used in the study.

## **Source data**

### **Source Data Fig. 2**

### **Source Data Fig. 3**

### **Source Data Fig. 4**

### **Source Data Extended Data Fig. 4**

### **Source Data Extended Data Fig. 7**

# Rights and permissions

[Reprints and Permissions](#)

## About this article



## Cite this article

Cui, Y., Lyu, X., Ding, L. *et al.* Global miRNA dosage control of embryonic germ layer specification. *Nature* **593**, 602–606 (2021).  
<https://doi.org/10.1038/s41586-021-03524-0>

[Download citation](#)

- Received: 21 January 2020
- Accepted: 08 April 2021
- Published: 05 May 2021
- Issue Date: 27 May 2021
- DOI: <https://doi.org/10.1038/s41586-021-03524-0>

## Comments

By submitting a comment you agree to abide by our [Terms](#) and [Community Guidelines](#). If you find something abusive or that does not comply with our terms or guidelines please flag it as inappropriate.

[Access through your institution](#)

[Change institution](#)

[Buy or subscribe](#)

Advertisement

---

This article was downloaded by **calibre** from <https://www.nature.com/articles/s41586-021-03524-0>

| [Section menu](#) | [Main menu](#) |

- Article
- [Published: 21 April 2021](#)

# Gasdermin D pore structure reveals preferential release of mature interleukin-1

- [Shiyu Xia](#) ORCID: orcid.org/0000-0001-9024-0689<sup>1,2</sup>,
- [Zhibin Zhang](#) ORCID: orcid.org/0000-0003-1349-2713<sup>1,3</sup>,
- [Venkat Giri Magupalli](#)<sup>1,2</sup>,
- [Juan Lorenzo Pablo](#)<sup>4,5</sup>,
- [Ying Dong](#)<sup>1,2</sup>,
- [Setu M. Vora](#)<sup>1,2</sup>,
- [Longfei Wang](#)<sup>1,2</sup>,
- [Tian-Min Fu](#) ORCID: orcid.org/0000-0002-6281-1752<sup>1,2,6,7</sup>,
- [Matthew P. Jacobson](#) ORCID: orcid.org/0000-0001-6262-655X<sup>8</sup>,
- [Anna Greka](#) ORCID: orcid.org/0000-0001-5697-7791<sup>4,5</sup>,
- [Judy Lieberman](#) ORCID: orcid.org/0000-0002-6200-4715<sup>1,3</sup>,
- [Jianbin Ruan](#) ORCID: orcid.org/0000-0001-5843-8273<sup>1,2,9</sup> &
- [Hao Wu](#) ORCID: orcid.org/0000-0002-7281-8579<sup>1,2</sup>

[Nature](#) volume 593, pages 607–611 (2021) [Cite this article](#)

- 9006 Accesses
- 1 Citations
- 59 Altmetric
- [Metrics details](#)

## Subjects

- [Cryoelectron microscopy](#)
- [Innate immunity](#)

## Abstract

As organelles of the innate immune system, inflammasomes activate caspase-1 and other inflammatory caspases that cleave gasdermin D (GSDMD). Caspase-1 also cleaves inactive precursors of the interleukin (IL)-1 family to generate mature cytokines such as IL-1 $\beta$  and IL-18. Cleaved GSDMD forms transmembrane pores to enable the release of IL-1 and to drive cell lysis through pyroptosis<sup>1,2,3,4,5,6,7,8,9</sup>. Here we report cryo-electron microscopy structures of the pore and the prepore of GSDMD. These structures reveal the different conformations of the two states, as well as extensive membrane-binding elements including a hydrophobic anchor and three positively charged patches. The GSDMD pore conduit is predominantly negatively charged. By contrast, IL-1 precursors have an acidic domain that is proteolytically removed by caspase-1<sup>10</sup>. When permeabilized by GSDMD pores, unlysed liposomes release positively charged and neutral cargoes faster than negatively charged cargoes of similar sizes, and the pores favour the passage of IL-1 $\beta$  and IL-18 over that of their precursors. Consistent with these findings, living—but not pyroptotic—macrophages preferentially release mature IL-1 $\beta$  upon perforation by GSDMD. Mutation of the acidic residues of GSDMD compromises this preference, hindering intracellular retention of the precursor and secretion of the mature cytokine. The GSDMD pore therefore mediates IL-1 release by electrostatic filtering, which suggests the importance of charge in addition to size in the transport of cargoes across this large channel.

## Access options

Subscribe to Journal

Get full journal access for 1 year

\$199.00

only \$3.90 per issue

[Subscribe](#)

All prices are NET prices.

VAT will be added later in the checkout.

Tax calculation will be finalised during checkout.

Rent or Buy article

Get time limited or full article access on ReadCube.

from \$8.99

[Rent or Buy](#)

All prices are NET prices.

### **Additional access options:**

- [Log in](#)
- [Access through your institution](#)
- [Learn about institutional subscriptions](#)

**Fig. 1: GSDMD architecture and conformational changes.**

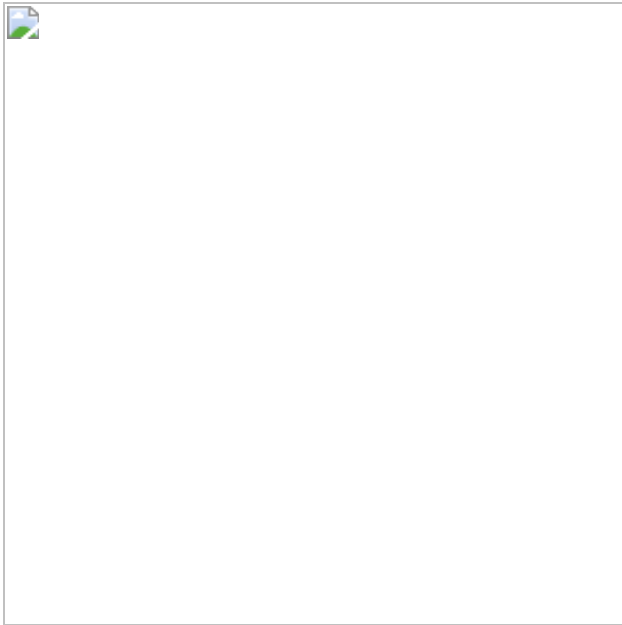


**Fig. 2: Membrane interaction by multiple contact sites.**

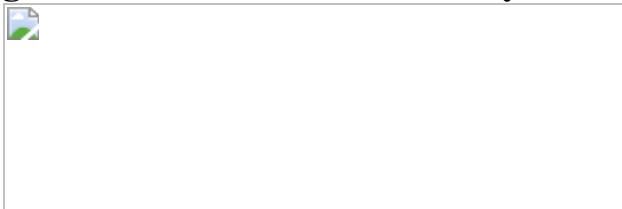


**Fig. 3: Pore conduit and cargo transport.**

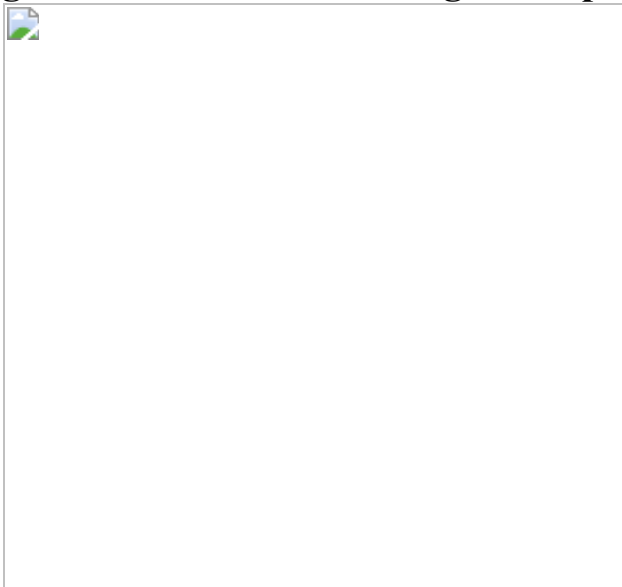
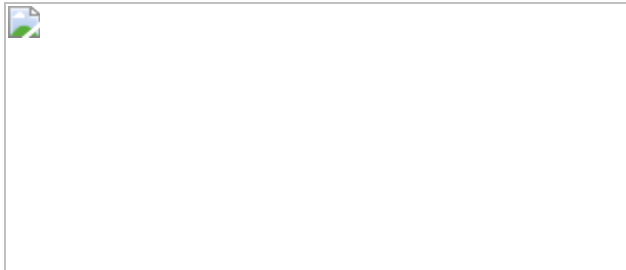


**Fig. 4: Preferential IL-1 $\beta$  release from macrophages.**



## Data availability

Atomic coordinates of the 33-fold symmetric human GSDMD pore structure have been deposited in the PDB under accession number [6VFE](#). The cryo-EM density maps of the 33-fold symmetric pore and the prepore have been deposited in the Electron Microscopy Data Bank under accession numbers [EMD-21160](#) and [EMD-21161](#), respectively. All other data are available from the corresponding authors upon reasonable request.

## References

1. 1.

Kayagaki, N. et al. Caspase-11 cleaves gasdermin D for non-canonical inflammasome signalling. *Nature* **526**, 666–671 (2015).

[ADS](#) [CAS](#) [PubMed](#) [Google Scholar](#)

2. 2.

Shi, J. et al. Cleavage of GSDMD by inflammatory caspases determines pyroptotic cell death. *Nature* **526**, 660–665 (2015).

[ADS](#) [CAS](#) [PubMed](#) [PubMed Central](#) [Google Scholar](#)

3. 3.

Ding, J. et al. Pore-forming activity and structural autoinhibition of the gasdermin family. *Nature* **535**, 111–116 (2016).

[ADS](#) [CAS](#) [PubMed](#) [PubMed Central](#) [Google Scholar](#)

4. 4.

Liu, X. et al. Inflammasome-activated gasdermin D causes pyroptosis by forming membrane pores. *Nature* **535**, 153–158 (2016).

[ADS](#) [CAS](#) [PubMed](#) [PubMed Central](#) [Google Scholar](#)

5. 5.

Aglietti, R. A. et al. GsdmD p30 elicited by caspase-11 during pyroptosis forms pores in membranes. *Proc. Natl Acad. Sci. USA* **113**, 7858–7863 (2016).

[CAS](#) [PubMed](#) [Google Scholar](#)

6. 6.

Sborgi, L. et al. GSDMD membrane pore formation constitutes the mechanism of pyroptotic cell death. *EMBO J.* **35**, 1766–1778 (2016).

[CAS](#) [PubMed](#) [PubMed Central](#) [Google Scholar](#)

7. 7.

Evavold, C. L. et al. The pore-forming protein gasdermin D regulates interleukin-1 secretion from living macrophages. *Immunity* **48**, 35–44.e6 (2018).

[CAS](#) [PubMed](#) [Google Scholar](#)

8. 8.

Heilig, R. et al. The gasdermin-D pore acts as a conduit for IL-1 $\beta$  secretion in mice. *Eur. J. Immunol.* **48**, 584–592 (2018).

[CAS](#) [PubMed](#) [Google Scholar](#)

9. 9.

Kayagaki, N. et al. NINJ1 mediates plasma membrane rupture during lytic cell death. *Nature* **591**, 131–136 (2021).

[ADS](#) [CAS](#) [PubMed](#) [Google Scholar](#)

10. 10.

Monteleone, M. et al. Interleukin-1 $\beta$  maturation triggers its relocation to the plasma membrane for gasdermin-D-dependent and -independent secretion. *Cell Rep.* **24**, 1425–1433 (2018).

[CAS](#) [PubMed](#) [Google Scholar](#)

11. 11.

Liu, X., Xia, S., Zhang, Z., Wu, H. & Lieberman, J. Channelling inflammation: gasdermins in physiology and disease. *Nat. Rev. Drug Discov.* (2021).

12. 12.

Orning, P. et al. Pathogen blockade of TAK1 triggers caspase-8-dependent cleavage of gasdermin D and cell death. *Science* **362**, 1064–1069 (2018).

[ADS](#) [CAS](#) [PubMed](#) [PubMed Central](#) [Google Scholar](#)

13. 13.

Sarhan, J. et al. Caspase-8 induces cleavage of gasdermin D to elicit pyroptosis during *Yersinia* infection. *Proc. Natl Acad. Sci. USA* **115**, E10888–E10897 (2018).

[CAS](#) [PubMed](#) [Google Scholar](#)

14. 14.

Burgener, S. S. et al. Cathepsin G inhibition by Serpinb1 and Serpinb6 prevents programmed necrosis in neutrophils and monocytes and reduces GSDMD-driven inflammation. *Cell Rep.* **27**, 3646–3656.e5 (2019).

[CAS](#) [PubMed](#) [PubMed Central](#) [Google Scholar](#)

15. 15.

Zhang, Z. et al. Gasdermin E suppresses tumour growth by activating anti-tumour immunity. *Nature* **579**, 415–420 (2020).

[ADS](#) [CAS](#) [PubMed](#) [PubMed Central](#) [Google Scholar](#)

16. 16.

Zhou, Z. et al. Granzyme A from cytotoxic lymphocytes cleaves GSDMB to trigger pyroptosis in target cells. *Science* **368**, eaaz7548 (2020).

[CAS](#) [PubMed](#) [Google Scholar](#)

17. 17.

Sollberger, G. et al. Gasdermin D plays a vital role in the generation of neutrophil extracellular traps. *Sci. Immunol.* **3**, eaar6689 (2018).

[PubMed](#) [Google Scholar](#)

18. 18.

Wang, Q. et al. A bioorthogonal system reveals antitumour immune function of pyroptosis. *Nature* **579**, 421–426 (2020).

[ADS](#) [CAS](#) [PubMed](#) [Google Scholar](#)

19. 19.

Chen, K. W. et al. Noncanonical inflammasome signaling elicits gasdermin D-dependent neutrophil extracellular traps. *Sci. Immunol.* **3**, eaar6676 (2018).

[PubMed](#) [Google Scholar](#)

20. 20.

Ruan, J., Xia, S., Liu, X., Lieberman, J. & Wu, H. Cryo-EM structure of the gasdermin A3 membrane pore. *Nature* **557**, 62–67 (2018).

[ADS](#) [CAS](#) [PubMed](#) [PubMed Central](#) [Google Scholar](#)

21. 21.

Mulvihill, E. et al. Mechanism of membrane pore formation by human gasdermin-D. *EMBO J.* **37**, e98321 (2018).

[PubMed](#) [PubMed Central](#) [Google Scholar](#)

22. 22.

Liu, Z. et al. Crystal structures of the full-length murine and human gasdermin D reveal mechanisms of autoinhibition, lipid binding, and oligomerization. *Immunity* **51**, 43–49.e4 (2019).

[CAS](#) [PubMed](#) [PubMed Central](#) [Google Scholar](#)

23. 23.

Rühl, S. et al. ESCRT-dependent membrane repair negatively regulates pyroptosis downstream of GSDMD activation. *Science* **362**, 956–960 (2018).

[ADS](#) [PubMed](#) [Google Scholar](#)

24. 24.

Lee, I. H., Kai, H., Carlson, L. A., Groves, J. T. & Hurley, J. H. Negative membrane curvature catalyzes nucleation of endosomal sorting complex required for transport (ESCRT)-III assembly. *Proc. Natl Acad. Sci. USA* **112**, 15892–15897 (2015).

[ADS](#) [CAS](#) [PubMed](#) [Google Scholar](#)

25. 25.

Davis, M. A. et al. Calpain drives pyroptotic vimentin cleavage, intermediate filament loss, and cell rupture that mediates immunostimulation. *Proc. Natl Acad. Sci. USA* **116**, 5061–5070 (2019).

[CAS](#) [PubMed](#) [Google Scholar](#)

26. 26.

Rogers, C. et al. Gasdermin pores permeabilize mitochondria to augment caspase-3 activation during apoptosis and inflammasome activation. *Nat. Commun.* **10**, 1689 (2019).

[ADS](#) [PubMed](#) [PubMed Central](#) [Google Scholar](#)

27. 27.

van Pee, K. et al. CryoEM structures of membrane pore and prepore complex reveal cytolytic mechanism of Pneumolysin. *eLife* **6**, e23644 (2017).

[PubMed](#) [PubMed Central](#) [Google Scholar](#)

28. 28.

Tapia, V. S. et al. The three cytokines IL-1 $\beta$ , IL-18, and IL-1 $\alpha$  share related but distinct secretory routes. *J. Biol. Chem.* **294**, 8325–8335 (2019).

[CAS](#) [PubMed](#) [PubMed Central](#) [Google Scholar](#)

29. 29.

Martín-Sánchez, F. et al. Inflammasome-dependent IL-1 $\beta$  release depends upon membrane permeabilisation. *Cell Death Differ.* **23**, 1219–1231 (2016).

[PubMed](#) [PubMed Central](#) [Google Scholar](#)

30. 30.

Batista, S. J. et al. Gasdermin-D-dependent IL-1 $\alpha$  release from microglia promotes protective immunity during chronic *Toxoplasma gondii* infection. *Nat. Commun.* **11**, 3687 (2020).

[ADS](#) [CAS](#) [PubMed](#) [PubMed Central](#) [Google Scholar](#)

31. 31.

Scheres, S. H. RELION: implementation of a Bayesian approach to cryo-EM structure determination. *J. Struct. Biol.* **180**, 519–530 (2012).

[CAS](#) [PubMed](#) [PubMed Central](#) [Google Scholar](#)

32. 32.

Zheng, S. Q. et al. MotionCor2: anisotropic correction of beam-induced motion for improved cryo-electron microscopy. *Nat. Methods* **14**, 331–332 (2017).

[CAS](#) [PubMed](#) [PubMed Central](#) [Google Scholar](#)

33. 33.

Rohou, A. & Grigorieff, N. CTFFIND4: Fast and accurate defocus estimation from electron micrographs. *J. Struct. Biol.* **192**, 216–221 (2015).

[PubMed](#) [PubMed Central](#) [Google Scholar](#)

34. 34.

Kucukelbir, A., Sigworth, F. J. & Tagare, H. D. Quantifying the local resolution of cryo-EM density maps. *Nat. Methods* **11**, 63–65 (2014).

[CAS](#) [PubMed](#) [PubMed Central](#) [Google Scholar](#)

35. 35.

Pettersen, E. F. et al. UCSF Chimera—a visualization system for exploratory research and analysis. *J. Comput. Chem.* **25**, 1605–1612 (2004).

[CAS](#) [PubMed](#) [PubMed Central](#) [Google Scholar](#)

36. 36.

Emsley, P. & Cowtan, K. Coot: model-building tools for molecular graphics. *Acta Crystallogr. D* **60**, 2126–2132 (2004).

[PubMed](#) [Google Scholar](#)

37. 37.

Adams, P. D. et al. PHENIX: a comprehensive Python-based system for macromolecular structure solution. *Acta Crystallogr. D* **66**, 213–221 (2010).

[CAS](#) [PubMed](#) [Google Scholar](#)

38. 38.

Roy, A., Kucukural, A. & Zhang, Y. I-TASSER: a unified platform for automated protein structure and function prediction. *Nat. Protoc.* **5**, 725–738 (2010).

[CAS](#) [PubMed](#) [PubMed Central](#) [Google Scholar](#)

39. 39.

Baker, N. A., Sept, D., Joseph, S., Holst, M. J. & McCammon, J. A. Electrostatics of nanosystems: application to microtubules and the ribosome. *Proc. Natl Acad. Sci. USA* **98**, 10037–10041 (2001).

[ADS](#) [CAS](#) [PubMed](#) [Google Scholar](#)

40. 40.

Xia, S., Ruan, J. & Wu, H. Monitoring gasdermin pore formation in vitro. *Methods Enzymol.* **625**, 95–107 (2019).

[CAS](#) [PubMed](#) [PubMed Central](#) [Google Scholar](#)

41. 41.

Schneider, C. A., Rasband, W. S. & Eliceiri, K. W. NIH Image to ImageJ: 25 years of image analysis. *Nat. Methods* **9**, 671–675 (2012).

[CAS](#) [PubMed](#) [PubMed Central](#) [Google Scholar](#)

42. 42.

Sanjana, N. E., Shalem, O. & Zhang, F. Improved vectors and genome-wide libraries for CRISPR screening. *Nat. Methods* **11**, 783–784 (2014).

[CAS](#) [PubMed](#) [PubMed Central](#) [Google Scholar](#)

[Download references](#)

## Acknowledgements

We thank B. Honig, T. Rapoport, F. Shao, J. Kagan, D. Golenbock, S. Blacklow, A. Kruse and M. Liao for discussions. For structural data collection, we thank R. Walsh, S. Sterling, S. Rawson and Z. Li at the Harvard Cryo-EM Center for Structural Biology and K. Song, K. Lee and C. Xu at the Cryo-EM Core Facility at University of Massachusetts Medical School. This work was supported by US National Institutes of Health grants

R01AI139914 (H.W. and J.L.), DP1HD087988 (H.W.), R01AI124491 (H.W.), R01CA240955 (J.L.), R01DK095045 (A.G.), R01DK099465 (A.G.) and 5T32HL066987-18 (T.-M.F.). S.X. received an Albert J. Ryan fellowship. J.R. and Z.Z. received postdoctoral fellowships from the Charles A. King Trust.

## Author information

### Affiliations

1. Program in Cellular and Molecular Medicine, Boston Children's Hospital, Boston, MA, USA

Shiyu Xia, Zhibin Zhang, Venkat Giri Magupalli, Ying Dong, Setu M. Vora, Longfei Wang, Tian-Min Fu, Judy Lieberman, Jianbin Ruan & Hao Wu

2. Department of Biological Chemistry and Molecular Pharmacology, Harvard Medical School, Boston, MA, USA

Shiyu Xia, Venkat Giri Magupalli, Ying Dong, Setu M. Vora, Longfei Wang, Tian-Min Fu, Jianbin Ruan & Hao Wu

3. Department of Pediatrics, Harvard Medical School, Boston, MA, USA

Zhibin Zhang & Judy Lieberman

4. Department of Medicine, Brigham and Women's Hospital, Boston, MA, USA

Juan Lorenzo Pablo & Anna Greka

5. Broad Institute of MIT and Harvard, Cambridge, MA, USA

Juan Lorenzo Pablo & Anna Greka

6. Department of Biological Chemistry and Pharmacology, The Ohio State University, Columbus, OH, USA

Tian-Min Fu

7. The Ohio State University Comprehensive Cancer Center, Columbus, OH, USA

Tian-Min Fu

8. Department of Pharmaceutical Chemistry, School of Pharmacy, University of California San Francisco, San Francisco, CA, USA

Matthew P. Jacobson

9. Department of Immunology, University of Connecticut Health Center, Farmington, CT, USA

Jianbin Ruan

## Authors

1. Shiyu Xia

[View author publications](#)

You can also search for this author in [PubMed](#) [Google Scholar](#)

2. Zhibin Zhang

[View author publications](#)

You can also search for this author in [PubMed](#) [Google Scholar](#)

3. Venkat Giri Magupalli

[View author publications](#)

You can also search for this author in [PubMed](#) [Google Scholar](#)

4. Juan Lorenzo Pablo

[View author publications](#)

You can also search for this author in [PubMed](#) [Google Scholar](#)

5. Ying Dong

[View author publications](#)

You can also search for this author in [PubMed](#) [Google Scholar](#)

6. Setu M. Vora

[View author publications](#)

You can also search for this author in [PubMed](#) [Google Scholar](#)

7. Longfei Wang

[View author publications](#)

You can also search for this author in [PubMed](#) [Google Scholar](#)

8. Tian-Min Fu

[View author publications](#)

You can also search for this author in [PubMed](#) [Google Scholar](#)

9. Matthew P. Jacobson

[View author publications](#)

You can also search for this author in [PubMed](#) [Google Scholar](#)

10. Anna Greka

[View author publications](#)

You can also search for this author in [PubMed](#) [Google Scholar](#)

11. Judy Lieberman

[View author publications](#)

You can also search for this author in [PubMed](#) [Google Scholar](#)

12. Jianbin Ruan

[View author publications](#)

You can also search for this author in [PubMed](#) [Google Scholar](#)

13. Hao Wu

[View author publications](#)

You can also search for this author in [PubMed](#) [Google Scholar](#)

## Contributions

H.W., J.R. and S.X. conceived the study. S.X. and J.R. reconstituted and optimized GSDMD assemblies and determined the cryo-EM structures. S.X., Z.Z. and V.G.M. performed cellular experiments. S.X., J.L.P., Y.D., S.M.V., L.W. and T.-M.F. performed biochemical experiments. H.W., J.L., A.G. and M.P.J. supervised the project. All authors organized and analysed data. H.W. and S.X. wrote the paper with input from all authors.

## Corresponding authors

Correspondence to [Jianbin Ruan](#) or [Hao Wu](#).

## Ethics declarations

## Competing interests

H.W. and J.L. are co-founders of Ventus Therapeutics. The other authors declare no competing interests.

## Additional information

**Peer review information** *Nature* thanks Helen Saibil and the other, anonymous, reviewer(s) for their contribution to the peer review of this work. Peer reviewer reports are available.

**Publisher's note** Springer Nature remains neutral with regard to jurisdictional claims in published maps and institutional affiliations.

## Extended data figures and tables

## Extended Data Fig. 1 Reconstitution and purification of GSDMD assemblies.

**a**, Optimized construct for human GSDMD, referred to as wild-type (WT) GSDMD for convenience. The N-terminal MBP tag and the TEV-cleavable linker between MBP and GSDMD-NT are not shown. **b**, Schematic of GSDMD pore and prepore reconstitution. **c**, Reduced, but not abolished, activity of the GSDMD(L192E) mutant shown by Tb<sup>3+</sup> leakage assay ( $n = 3$  biological replicates). En, activating enzyme. **d**, **e**, Size-exclusion chromatography profiles (**d**) and an enlargement of the boxed region (**e**). The box encloses the fractions containing the majority of wild-type GSDMD or GSDMD(L192E) assemblies. The shaded fractions containing well-dispersed particles (**e**) were used for electron microscopy data collection. **f**, SDS-PAGE showing wild-type GSDMD-NT at around 30 kDa from the corresponding fractions in **e**. **g**, Detergent screen. A group of non-ionic detergents with commercial shorthand C<sub>x</sub>E<sub>y</sub> (C<sub>x</sub>, x number of carbons in the alkyl chain; E<sub>y</sub>, y number of ethylene glycol repeats) yielded stable GSDMD pores. C<sub>12</sub>E<sub>8</sub> was chosen as the final solubilizing agent. Scale bars, 200 nm. **h**, GSDMD pores extracted by 1% C<sub>12</sub>E<sub>8</sub> from liposomes containing different types and amounts (%) of acidic lipids. Liposomes containing 20% PA were chosen. Scale bars, 200 nm. **i**, Sizes of GSDMD and GSDMA3 assemblies reconstituted on liposomes containing different acidic lipids (20%) and extracted by different types of detergent (1% C<sub>x</sub>E<sub>y</sub>, or 50 mM cholate), shown by outer diameters measured under negative-stain electron microscopy (from left to right,  $n = 64, 42, 77, 73, 14, 34, 45, 23, 21$  and 18 particles). Data shown in **c** and **i** are mean  $\pm$  s.d. Data shown in **f-h** are representative of three independent experiments.

## Extended Data Fig. 2 Cryo-EM data processing for the wild-type GSDMD dataset.

**a**, A cryo-EM image of the wild-type GSDMD sample. Data are representative of three independent experiments. Scale bar, 100 nm. **b**, Processing of the wild-type GSDMD cryo-EM dataset. Initial 2D classes showed a ring-stacking phenomenon, which added to structural

heterogeneity and posed challenges for symmetry determination. Density subtraction was therefore performed, followed by 3D reconstruction of each ring without assumption of symmetry, after which particle symmetry could be determined for certain 3D classes. These classes were then refined with their respective symmetry imposed to yield final cryo-EM maps.

### **Extended Data Fig. 3 Cryo-EM data processing for the GSDMD(L192E) dataset.**

**a**, A cryo-EM image of the GSDMD(L192E) sample. Data are representative of three independent experiments. Scale bar, 100 nm. **b**, Processing of the GSDMD(L192E) cryo-EM dataset. This dataset was first processed following the procedures for the wild-type dataset. Cryo-EM maps obtained from 3D refinement with symmetry imposed were further classified without alignment to remove heterogeneous particles. Then, the best 3D classes were refined again to improve resolutions. A 3D reconstruction at 7.3 Å was further improved by symmetry expansion, 3D classification without alignment, 3D local refinement, and per-particle CTF refinement to reach the final map at 3.9 Å resolution. **c**, Similarity of cryo-EM maps generated from the wild-type and L192E datasets. Owing to the higher resolutions, maps from the L192E dataset were chosen for model building.

### **Extended Data Fig. 4 Analysis of cryo-EM densities and models.**

**a**, Half-map-to-half-map and model-to-map FSC for the 33-fold symmetric GSDMD pore and prepore from the L192E dataset. Horizontal dashed lines represent FSC cut-offs at 0.5 and 0.143. **b**, **c**, Pore-form (**b**) and prepore-form (**c**) GSDMD subunits fitted into their respective cryo-EM density. Arrows indicate secondary structural elements specified by residue numbers. **d**, Close-up views of the pore-form GSDMD structure fitted into its cryo-EM density at six representative locations denoted by residue numbers.

## Extended Data Fig. 5 β-hairpin extension and prepore-to-pore transition.

**a**, Comparison between autoinhibited, prepore-form and pore-form GSDMD. The autoinhibited GSDMD-NT was obtained from the crystal structure of full-length GSDMD (PDB: 6N9O). The  $\beta$ 4 strand and  $\alpha$ 4 helix are invisible in the crystal structure and were modelled on the basis of the crystal structure of full-length GSDMA3 (PDB: 5B5R). **b**, Formation of  $\beta$ -hairpins. The  $\beta$ 3– $\beta$ 4– $\beta$ 5 region constitutes the first extension domain (ED1), which transforms into hairpin (HP) 1 by refolding. The  $\beta$ 7– $\alpha$ 4– $\beta$ 8 region represents ED2 and becomes HP2. **c**, Sequence alignment of human and mouse GSDMD, with secondary structures and key residues denoted. Blue highlighting indicates residues responsible for lipid binding, through either hydrophobic or charged interactions; green highlighting indicates residues at inter-subunit interfaces; and underlining indicates residues that are important for membrane insertion. **d**, Conserved rigid-body movement of the globular domain ('palm') towards the membrane-distal direction during GSDM pore formation, shown by alignment of the GSDMA3 pore structure (PDB: 6CB8) and prepore model at their central axes.

## Extended Data Fig. 6 Hydrophobic anchor and basic patches of GSDMs.

**a**, Effects of mutations in the hydrophobic anchor on GSDMD pore formation assessed by  $Tb^{3+}$  leakage from liposomes ( $n = 3$  biological replicates). **b**, GSDM sequences aligned at the hydrophobic anchor and BPs. Blue highlighting indicates basic residues at BPs; green highlighting indicates hydrophobic residues of the anchor; and dashes indicate gaps. **c**, The GSDMA3 prepore model with the  $\beta$ 1– $\beta$ 2 loop highlighted in green and BP1 shown in blue. A GSDMA3 prepore subunit is also shown in two orientations. **d**, A side view of pore-form GSDMA3 (PDB: 6CB8), with electrostatic surface shown around the  $\beta$ 1– $\beta$ 2 loop. The anchor and BP2 are boxed in green. **e**, Impairment of the pore-forming ability of GSDMA3 by mutations in the hydrophobic anchor, shown by  $Tb^{3+}$  leakage assay ( $n = 3$  biological replicates). 'Anchor' indicates that L47, F48 and W49 are mutated to E. **f**, A cryo-EM density blob that probably represents heads of

phospholipids near BP3. Basic residues in BP3 point towards the blob. **g**, Effects of mutations in BP1 (R7, R10 and R11 mutated to E), BP2 (R42, K43, K51 and R53 mutated to E) and BP3 (K204 or R174 mutated to E) on GSDMD activity evaluated by  $Tb^{3+}$  leakage assay ( $n = 3$  biological replicates). **h**, Importance of BP2 for GSDMA3 pore formation, shown by  $Tb^{3+}$  leakage assay ( $n = 3$  biological replicates). Here, in BP2, R41, K42, R43 and K44 are mutated to E. **i**, Exposure of the hydrophobic anchor and BP2 upon removal of the inter-domain linker between GSDMD-NT and GSDMD-CT. Surface representations are shown for autoinhibited GSDMD (PDB: 6N9O) with and without the inferred linker (cyan curve connecting Q241 and T284). Purple, GSDMD-NT; black: GSDMD-CT; green, anchor-BP2 region; yellow, two ends of the linker. Data shown in **a**, **e**, **g** and **h** are mean  $\pm$  s.d.

### **Extended Data Fig. 7 GSDM acidic patches and their mutations.**

**a**, Locations of APs shown by aligned GSDM sequences. Dots, strings of omitted uncharged residues; red highlighting, acidic residues; blue, basic residues. Of note, the basic residues near the APs may face the membrane (such as those in BP3) and therefore do not necessarily weaken the acidity of the pore conduit. **b**, Assessment of alanine mutations of GSDMD APs 1–4 by  $Tb^{3+}$  leakage assay ( $n = 3$  biological replicates). **c**, Assessment of alanine mutations of GSDMA3 AP1 and AP2 by  $Tb^{3+}$  liposome leakage assay ( $n = 3$  biological replicates). **d**, Negative-staining electron microscopy images of wild-type and AP-mutant GSDMD and GSDMA3 assemblies, solubilized from liposomes using  $C_{12}E_8$  and cholate, respectively. Data shown are representative of three independent experiments. Scale bars, 100 nm. **e**, Outer diameters of wild-type or AP-mutant GSDMD and GSDMA3 assemblies, measured under negative-staining electron microscopy ( $n = 50$  particles per group). Data shown in **b**, **c** and **e** are mean  $\pm$  s.d.

### **Extended Data Fig. 8 Liposome experiments and electrostatics analysis.**

**a**, Unlysed liposomes (25–75% PS) demonstrate that LDH release is minimal when GSDMD is added at a sub-lytic concentration ( $1\times = 0.5 \mu\text{M}$ ) ( $n = 3$  biological replicates). **b**, Release of cyt *c*, CRYGD and OCM from liposomes permeabilized by GSDMD shown by immunoblotting. **c**, Similar rates of GSDMD pore formation on liposomes of various acidic lipid contents (25–75% PS), according to  $\text{Tb}^{3+}$  release assay ( $n = 3$  biological replicates). **d**, Preferential IL-1 $\beta$  release from liposomes (50% and 75% PS) perforated by GSDMD shown by immunoblotting. **e**, Release of pro-IL-18 and IL-18 from liposomes permeabilized by GSDMD shown by immunoblotting. **f**, Minimal LDH release when GSDMA3 was activated at a sub-lytic concentration ( $1\times = 0.5 \mu\text{M}$ ) ( $n = 3$  biological replicates), demonstrating that the liposomes are intact. **g**, Release of pro-IL-1 $\beta$  and mature IL-1 $\beta$  from liposomes perforated by GSDMA3 shown by immunoblotting. **h**, Release rates of IL-1 $\beta$  cargoes through GSDMD pores shown by fitted hyperbolic functions. **i**, Initial release rates ( $r$ ) extrapolated from **h**. **j**, Charge differences among the cargoes ( $\Delta q$ ) and rate ratios ( $R$ ). **k**, Plot of  $\ln(R)$  against  $\Delta q$  to estimate the electrostatic potential ( $E$ ) of the GSDMD pore conduit. **l**, A lack of release of encapsulated bulky FITC-labelled dextrans (2 MDa) when SLO or PFO was added at a sub-lytic concentration ( $1\times = 0.1 \mu\text{M}$ ) ( $n = 3$  biological replicates), demonstrating that the liposomes are intact. **m**, Similar release of pro-IL-1 $\beta$  and mature IL-1 $\beta$  from liposomes permeabilized by PFO. **n**, Electrostatic surfaces of the modelled PFO pore conduit. Data shown in **a**, **c**, **f** and **l** are mean  $\pm$  s.d. Data are representative of three (**b**) or two (**d**, **e**, **g**, **m**) independent experiments.

## Extended Data Fig. 9 Macrophage experiments.

**a**, Comparable expression of wild-type and charge-mutant GSDMD in GSDMD-knockout iBMDMs, and of wild-type and charge-mutant pro-IL-1 $\beta$  in IL-1 $\beta$ -knockout iBMDMs, shown by immunoblotting. **b**, **c**, Similar sensitivity of knockout iBMDMs reconstituted with wild-type or charge-mutant GSDMD or pro-IL-1 $\beta$  to pyroptosis and death evasion by glycine protection (**b**) or low-dose nigericin treatment (**c**), shown by LDH release ( $n = 3$  biological replicates). **d**, Cleavage of engineered GSDMA3 chimera (A3chim) by caspase-1 (C1), shown by SDS-PAGE of proteolysis reactions using purified proteins. **e**, Comparable expression of A3chim (Flag-tagged)

and its AP mutants in GSDMD-knockout cells. AP1, 4 D/E to A; AP2, 2 D/E to A. **f**, **g**, Preferential release of mature IL-1 $\beta$  from glycine-protected living iBMDMs permeabilized by A3chim, shown by immunoblotting (**f**) and LDH release ( $n = 3$  biological replicates) (**g**). **h**, **i**, IL-1 $\beta$  release from GSDMD-knockout iBMDMs expressing wild-type or AP-mutant A3chim under glycine protection, shown by immunoblotting (**h**) and LDH release ( $n = 3$  biological replicates) (**i**). **j–l**, IL-1 $\beta$  release from living GSDMD-knockout iBMDMs expressing A3chim stimulated by low-dose nigericin, characterized by immunoblotting (**j**), LDH release ( $n = 3$  biological replicates) (**k**) and ELISA ( $n = 3$  biological replicates) (**l**). **m**, **n**, IL-1 $\beta$  release from low-dose nigericin-stimulated GSDMD-knockout iBMDMs expressing wild-type or AP-mutant A3chim, evaluated by immunoblotting (**m**), LDH release ( $n = 3$  biological replicates) (**n**) and ELISA ( $n = 3$  biological replicates) (**o**). Data shown in **b**, **c**, **g**, **i**, **k**, **l**, **n** and **o** are mean  $\pm$  s.d. Data shown in **a**, **d–f**, **h**, **j** and **m** are representative of two independent experiments.

**Extended Data Table 1 Cryo-EM data collection, refinement and validation statistics**  
[Full size table](#)

## Supplementary information

### [Supplementary Figure 1](#)

Uncropped SDS-PAGE gels and immunoblots. Relative positions of the scans within a panel (black box) follow those in the figures. Blue boxes indicate cropped areas. Molecular weight markers are shown in kDa.

### [Reporting Summary](#)

### [Peer Review File](#)

### [Video 1](#)

The GSDMD prepore-to-pore transition The morph simulation was generated by overlaying structures of the 33-subunit prepore and pore at their  $\alpha$ 1 helices. During pore formation, the globular domain rotates away from the membrane while the  $\beta$ -barrel inserts into the membrane.

## Video 2

Conformational changes of a single GSDMD subunit In addition to the formation and insertion of the  $\beta$ -hairpins, a rotational movement away from the membrane of the whole globular domain can be observed.

## Rights and permissions

### Reprints and Permissions

## About this article



Check for  
updates

## Cite this article

Xia, S., Zhang, Z., Magupalli, V.G. *et al.* Gasdermin D pore structure reveals preferential release of mature interleukin-1. *Nature* **593**, 607–611 (2021). <https://doi.org/10.1038/s41586-021-03478-3>

### Download citation

- Received: 03 January 2020
- Accepted: 19 March 2021
- Published: 21 April 2021
- Issue Date: 27 May 2021

- DOI: <https://doi.org/10.1038/s41586-021-03478-3>

## Further reading

- **NLRP3 inflammasomes that induce antitumor immunity**
  - Dania Zhivaki
  - & Jonathan C. Kagan

*Trends in Immunology* (2021)

## Comments

By submitting a comment you agree to abide by our [Terms](#) and [Community Guidelines](#). If you find something abusive or that does not comply with our terms or guidelines please flag it as inappropriate.

[Access through your institution](#)

[Change institution](#)

[Buy or subscribe](#)

Advertisement

---

This article was downloaded by **calibre** from <https://www.nature.com/articles/s41586-021-03478-3>

| [Section menu](#) | [Main menu](#) |

# Amendments & Corrections

- [\*\*Author Correction: Auto-aggressive CXCR6+ CD8 T cells cause liver immune pathology in NASH\*\*](#) [ 10 May 2021]  
Author Correction •
- [\*\*Publisher Correction: Whole-genome doubling confers unique genetic vulnerabilities on tumour cells\*\*](#) [ 11 May 2021]  
Publisher Correction •
- [\*\*Retraction Note: Endoperoxide formation by an  \$\alpha\$ -ketoglutarate-dependent mononuclear non-haem iron enzyme\*\*](#) [ 19 May 2021]  
Retraction •

Author Correction: Auto-aggressive CXCR6<sup>+</sup> CD8 T cells cause liver immune pathology in NASH

[Download PDF](#)

- Author Correction
- [Published: 10 May 2021](#)

# Author Correction: Auto-aggressive CXCR6<sup>+</sup> CD8 T cells cause liver immune pathology in NASH

- [Michael Dudek](#)<sup>1</sup>,
- [Dominik Pfister](#) ORCID: [orcid.org/0000-0002-0542-2638](https://orcid.org/0000-0002-0542-2638)<sup>2</sup>,
- [Sainitin Donakonda](#) ORCID: [orcid.org/0000-0003-3216-8759](https://orcid.org/0000-0003-3216-8759)<sup>1,3</sup>,
- [Pamela Filpe](#)<sup>4</sup>,
- [Annika Schneider](#)<sup>1</sup>,
- [Melanie Laschinger](#)<sup>5</sup>,
- [Daniel Hartmann](#)<sup>5</sup>,
- [Norbert Hüser](#)<sup>5</sup>,
- [Philippa Meiser](#)<sup>1</sup>,
- [Felix Bayerl](#)<sup>1</sup>,
- [Donato Inverso](#) ORCID: [orcid.org/0000-0003-0987-3345](https://orcid.org/0000-0003-0987-3345)<sup>6,7</sup>,
- [Jennifer Wigger](#)<sup>4</sup>,
- [Marcial Sebode](#)<sup>4</sup>,
- [Rupert Öllinger](#)<sup>8</sup>,
- [Roland Rad](#) ORCID: [orcid.org/0000-0002-6849-9659](https://orcid.org/0000-0002-6849-9659)<sup>8</sup>,
- [Silke Hegenbarth](#)<sup>1</sup>,
- [Martina Anton](#) ORCID: [orcid.org/0000-0001-5290-5213](https://orcid.org/0000-0001-5290-5213)<sup>1</sup>,

- [Adrien Guillot](#) [ORCID: orcid.org/0000-0002-6002-9986<sup>9</sup>](#),
- [Andrew Bowman](#) [ORCID: orcid.org/0000-0002-7609-8687<sup>10</sup>](#),
- [Danijela Heide<sup>2</sup>](#),
- [Florian Müller<sup>2</sup>](#),
- [Pierluigi Ramadori<sup>2</sup>](#),
- [Valentina Leone<sup>11,12</sup>](#),
- [Cristina Garcia-Caceres<sup>13</sup>](#),
- [Tim Gruber<sup>13</sup>](#),
- [Gabriel Seifert](#) [ORCID: orcid.org/0000-0003-3771-2186<sup>14</sup>](#),
- [Agnieszka M. Kabat](#) [ORCID: orcid.org/0000-0003-1916-5983<sup>15</sup>](#),
- [Jan-Philipp Mallm](#) [ORCID: orcid.org/0000-0002-7059-4030<sup>16</sup>](#),
- [Simon Reider](#) [ORCID: orcid.org/0000-0002-0578-9843<sup>17,18</sup>](#),
- [Maria Effenberger](#) [ORCID: orcid.org/0000-0002-0499-9953<sup>17</sup>](#),
- [Susanne Roth<sup>19</sup>](#),
- [Adrian T. Billeter<sup>19</sup>](#),
- [Beat Müller-Stich<sup>19</sup>](#),
- [Edward J. Pearce](#) [ORCID: orcid.org/0000-0003-1001-9656<sup>15</sup>](#),
- [Friedrich Koch-Nolte<sup>20</sup>](#),
- [Rafael Käser<sup>21</sup>](#),
- [Herbert Tilg](#) [ORCID: orcid.org/0000-0002-4235-2579<sup>17</sup>](#),
- [Robert Thimme](#) [ORCID: orcid.org/0000-0003-1417-4135<sup>21</sup>](#),
- [Tobias Boettler](#) [ORCID: orcid.org/0000-0002-1195-055X<sup>21</sup>](#),
- [Frank Tacke<sup>9</sup>](#),
- [Jean-Francois Dufour](#) [ORCID: orcid.org/0000-0002-8062-1346<sup>22</sup>](#),
- [Dirk Haller](#) [ORCID: orcid.org/0000-0002-6977-4085<sup>23</sup>](#),
- [Peter J. Murray<sup>1,24</sup>](#),
- [Ron Heeren](#) [ORCID: orcid.org/0000-0002-6533-7179<sup>10</sup>](#),
- [Dietmar Zehn](#) [ORCID: orcid.org/0000-0003-1393-8527<sup>25</sup>](#),
- [Jan P. Böttcher](#) [ORCID: orcid.org/0000-0002-8163-8107<sup>1</sup>](#),
- [Mathias Heikenwälder](#) [ORCID: orcid.org/0000-0002-3135-2274<sup>2</sup>](#) &
- [Percy A. Knolle](#) [ORCID: orcid.org/0000-0003-2983-0414<sup>1,3,25</sup>](#)

[Nature](#) volume **593**, page E14 (2021) [Cite this article](#)

- 660 Accesses

- 2 Altmetric
- [Metrics details](#)

## Subjects

- [Chronic inflammation](#)
- [Lymphocyte activation](#)

The [Original Article](#) was published on 24 March 2021

[Download PDF](#)

Correction to: *Nature* <https://doi.org/10.1038/s41586-021-03233-8>  
Published online 24 March 2021

In this Article, the surname of Tobias Boettler was incorrectly shown as ‘Böttler’, and the surname of author Jan-Philipp Mallm was incorrectly shown as ‘Malm’. The original Article has been corrected online.

## Author information

### Affiliations

1. Institute of Molecular Immunology and Experimental Oncology,  
School of Medicine, Technical University of Munich (TUM), Munich,  
Germany

Michael Dudek, Sainitin Donakonda, Annika Schneider, Philippa  
Meiser, Felix Bayerl, Silke Hegenbarth, Martina Anton, Peter J.  
Murray, Jan P. Böttcher & Percy A. Knolle

2. Institute of Chronic Inflammation and Cancer, German Cancer  
Research Center, Heidelberg, Germany

Dominik Pfister, Danijela Heide, Florian Müller, Pierluigi Ramadori & Mathias Heikenwälder

3. German Center for Infection Research, Munich, Germany

Sainitin Donakonda & Percy A. Knolle

4. Department of Medicine, University Medical Centre Hamburg-Eppendorf, Hamburg, Germany

Pamela Filpe, Jennifer Wigger & Marcial Sebode

5. Department of Surgery, University Hospital München rechts der Isar, TUM, Munich, Germany

Melanie Laschinger, Daniel Hartmann & Norbert Hüser

6. Division of Vascular Oncology and Metastasis, German Cancer ResearchCenter Heidelberg (DKFZ-ZMBH Alliance), Heidelberg, Germany

Donato Inverso

7. European Center of Angioscience (ECAS), Medical Faculty Mannheim, Heidelberg University, Mannheim, Germany

Donato Inverso

8. Institute of Molecular Oncology and Functional Genomics, TUM, Munich, Germany

Rupert Öllinger & Roland Rad

9. Department of Hepatology and Gastroenterology, Charité Universitätsmedizin, Berlin, Germany

Adrien Guillot & Frank Tacke

10. Maastricht MultiModal Molecular Imaging (M4I) Institute, Division of Imaging Mass Spectrometry, Maastricht University, Maastricht, the Netherlands

Andrew Bowman & Ron Heeren

11. Institute of Virology, Technical University Munich and Helmholtz Zentrum Munich, Munich, Germany

Valentina Leone

12. Research Unit of Radiation Cytogenetics, Helmholtz Zentrum Munich, Neuherberg, Germany

Valentina Leone

13. Institute for Diabetes and Obesity, Helmholtz Diabetes Center, Helmholtz Zentrum München, Neuherberg, Germany

Cristina Garcia-Caceres & Tim Gruber

14. Department of General and Visceral Surgery, Faculty of Medicine, University of Freiburg, Freiburg, Germany

Gabriel Seifert

15. Max Planck Institute of Immunobiology and Epigenetics, Freiburg, Germany

Agnieszka M. Kabat & Edward J. Pearce

16. Division of Chromatin Networks, Single-cell Open Lab, German Cancer Research Center, Heidelberg, Germany

Jan-Philipp Mallm

17. Department of Internal Medicine I, Gastroenterology, Hepatology, Endocrinology and Metabolism, Medical University Innsbruck, Innsbruck, Austria

Simon Reider, Maria Effenberger & Herbert Tilg

18. Christian Doppler Labor for Mucosal Immunology, Innsbruck, Austria

Simon Reider

19. Department of General, Visceral and Transplantation Surgery,  
Heidelberg University, Heidelberg, Germany

Susanne Roth, Adrian T. Billeter & Beat Müller-Stich

20. Institute of Immunology, University Medical Center Hamburg-Eppendorf, Hamburg, Germany

Friedrich Koch-Nolte

21. Department of Medicine II, University Medical Center Freiburg,  
Faculty of Medicine, University of Freiburg, Freiburg, Germany

Rafael Käser, Robert Thimme & Tobias Boettler

22. University Clinic for Visceral Surgery and Medicine, Inselspital,  
University of Bern, Bern, Switzerland

Jean-Francois Dufour

23. Chair of Nutrition and Immunology, School of Life Sciences  
Weihenstephan, TUM, Freising, Germany

Dirk Haller

24. Max Planck Institute for Biochemistry, Martinsried, Germany

Peter J. Murray

25. Division of Animal Physiology and Immunology, School of Life Sciences Weihenstephan, TUM, Freising, Germany

Dietmar Zehn & Percy A. Knolle

## Authors

1. Michael Dudek

[View author publications](#)

You can also search for this author in [PubMed](#) [Google Scholar](#)

2. Dominik Pfister

[View author publications](#)

You can also search for this author in [PubMed](#) [Google Scholar](#)

3. Sainitin Donakonda

[View author publications](#)

You can also search for this author in [PubMed](#) [Google Scholar](#)

4. Pamela Filpe

[View author publications](#)

You can also search for this author in [PubMed](#) [Google Scholar](#)

5. Annika Schneider

[View author publications](#)

You can also search for this author in [PubMed](#) [Google Scholar](#)

6. Melanie Laschinger

[View author publications](#)

You can also search for this author in [PubMed](#) [Google Scholar](#)

7. Daniel Hartmann

[View author publications](#)

You can also search for this author in [PubMed](#) [Google Scholar](#)

8. Norbert Hüser

[View author publications](#)

You can also search for this author in [PubMed](#) [Google Scholar](#)

9. Philippa Meiser

[View author publications](#)

You can also search for this author in [PubMed](#) [Google Scholar](#)

10. Felix Bayerl

[View author publications](#)

You can also search for this author in [PubMed](#) [Google Scholar](#)

11. Donato Inverso

[View author publications](#)

You can also search for this author in [PubMed](#) [Google Scholar](#)

12. Jennifer Wigger

[View author publications](#)

You can also search for this author in [PubMed](#) [Google Scholar](#)

13. Marcial Sebode

[View author publications](#)

You can also search for this author in [PubMed](#) [Google Scholar](#)

14. Rupert Öllinger

[View author publications](#)

You can also search for this author in [PubMed](#) [Google Scholar](#)

15. Roland Rad

[View author publications](#)

You can also search for this author in [PubMed](#) [Google Scholar](#)

16. Silke Hegenbarth

[View author publications](#)

You can also search for this author in [PubMed](#) [Google Scholar](#)

17. Martina Anton

[View author publications](#)

You can also search for this author in [PubMed](#) [Google Scholar](#)

18. Adrien Guillot

[View author publications](#)

You can also search for this author in [PubMed](#) [Google Scholar](#)

19. Andrew Bowman

[View author publications](#)

You can also search for this author in [PubMed](#) [Google Scholar](#)

20. Danijela Heide

[View author publications](#)

You can also search for this author in [PubMed](#) [Google Scholar](#)

21. Florian Müller

[View author publications](#)

You can also search for this author in [PubMed](#) [Google Scholar](#)

22. Pierluigi Ramadori

[View author publications](#)

You can also search for this author in [PubMed](#) [Google Scholar](#)

23. Valentina Leone

[View author publications](#)

You can also search for this author in [PubMed](#) [Google Scholar](#)

24. Cristina Garcia-Caceres

[View author publications](#)

You can also search for this author in [PubMed](#) [Google Scholar](#)

25. Tim Gruber

[View author publications](#)

You can also search for this author in [PubMed](#) [Google Scholar](#)

26. Gabriel Seifert

[View author publications](#)

You can also search for this author in [PubMed](#) [Google Scholar](#)

27. Agnieszka M. Kabat

[View author publications](#)

You can also search for this author in [PubMed](#) [Google Scholar](#)

28. Jan-Philipp Mallm

[View author publications](#)

You can also search for this author in [PubMed](#) [Google Scholar](#)

29. Simon Reider

[View author publications](#)

You can also search for this author in [PubMed](#) [Google Scholar](#)

30. Maria Effenberger

[View author publications](#)

You can also search for this author in [PubMed](#) [Google Scholar](#)

31. Susanne Roth

[View author publications](#)

You can also search for this author in [PubMed](#) [Google Scholar](#)

32. Adrian T. Billeter

[View author publications](#)

You can also search for this author in [PubMed](#) [Google Scholar](#)

33. Beat Müller-Stich

[View author publications](#)

You can also search for this author in [PubMed](#) [Google Scholar](#)

34. Edward J. Pearce

[View author publications](#)

You can also search for this author in [PubMed](#) [Google Scholar](#)

35. Friedrich Koch-Nolte

[View author publications](#)

You can also search for this author in [PubMed](#) [Google Scholar](#)

36. Rafael Käser

[View author publications](#)

You can also search for this author in [PubMed](#) [Google Scholar](#)

37. Herbert Tilg

[View author publications](#)

You can also search for this author in [PubMed](#) [Google Scholar](#)

38. Robert Thimme

[View author publications](#)

You can also search for this author in [PubMed](#) [Google Scholar](#)

39. Tobias Boettler

[View author publications](#)

You can also search for this author in [PubMed](#) [Google Scholar](#)

40. Frank Tacke

[View author publications](#)

You can also search for this author in [PubMed](#) [Google Scholar](#)

41. Jean-Francois Dufour

[View author publications](#)

You can also search for this author in [PubMed](#) [Google Scholar](#)

42. Dirk Haller

[View author publications](#)

You can also search for this author in [PubMed](#) [Google Scholar](#)

43. Peter J. Murray

[View author publications](#)

You can also search for this author in [PubMed](#) [Google Scholar](#)

44. Ron Heeren

[View author publications](#)

You can also search for this author in [PubMed](#) [Google Scholar](#)

45. Dietmar Zehn

[View author publications](#)

You can also search for this author in [PubMed](#) [Google Scholar](#)

46. Jan P. Böttcher

[View author publications](#)

You can also search for this author in [PubMed](#) [Google Scholar](#)

47. Mathias Heikenwälder

[View author publications](#)

You can also search for this author in [PubMed](#) [Google Scholar](#)

48. Percy A. Knolle

[View author publications](#)

You can also search for this author in [PubMed](#) [Google Scholar](#)

## Corresponding author

Correspondence to [Percy A. Knolle](#).

## Rights and permissions

[Reprints and Permissions](#)

## About this article



Check for  
updates

## Cite this article

Dudek, M., Pfister, D., Donakonda, S. *et al.* Author Correction: Auto-aggressive CXCR6<sup>+</sup> CD8 T cells cause liver immune pathology in NASH. *Nature* **593**, E14 (2021). <https://doi.org/10.1038/s41586-021-03568-2>

[Download citation](#)

- Published: 10 May 2021
- Issue Date: 27 May 2021
- DOI: <https://doi.org/10.1038/s41586-021-03568-2>

## Comments

By submitting a comment you agree to abide by our [Terms](#) and [Community Guidelines](#). If you find something abusive or that does not comply with our terms or guidelines please flag it as inappropriate.

[Download PDF](#)

## Advertisement

---

This article was downloaded by **calibre** from <https://www.nature.com/articles/s41586-021-03568-2>

| [Section menu](#) | [Main menu](#) |

Publisher Correction: Whole-genome doubling confers unique genetic vulnerabilities on tumour cells

[Download PDF](#)

- Publisher Correction
- [Published: 11 May 2021](#)

# Publisher Correction: Whole-genome doubling confers unique genetic vulnerabilities on tumour cells

- [Ryan J. Quinton](#)<sup>1</sup>,
- [Amanda DiDomizio](#)<sup>1</sup>,
- [Marc A. Vittoria](#)<sup>1</sup>,
- [Kristýna Kotýnková](#)<sup>1</sup>,
- [Carlos J. Ticas](#)<sup>1</sup>,
- [Sheena Patel](#)<sup>1</sup>,
- [Yusuke Koga](#)<sup>2</sup>,
- [Jasmine Vakhshoorzadeh](#)<sup>1</sup>,
- [Nicole Hermance](#)<sup>3</sup>,
- [Taruho S. Kuroda](#)<sup>4</sup>,
- [Neha Parulekar](#)<sup>2</sup>,
- [Alison M. Taylor](#)<sup>5,6,7</sup>,
- [Amity L. Manning](#)<sup>3</sup>,
- [Joshua D. Campbell](#) ORCID: [orcid.org/0000-0003-0780-8662](https://orcid.org/0000-0003-0780-8662)<sup>2,6</sup> &
- [Neil J. Ganem](#) ORCID: [orcid.org/0000-0003-0269-6585](https://orcid.org/0000-0003-0269-6585)<sup>1,2</sup>

[Nature](#) volume 593, page E15 (2021) [Cite this article](#)

- 389 Accesses
- 1 Altmetric
- [Metrics details](#)

## Subjects

- [Cancer genetics](#)
- [Mitosis](#)

The [Original Article](#) was published on 27 January 2021

[Download PDF](#)

Correction to: *Nature* <https://www.nature.com/articles/s41586-020-03133-3>  
Published online 27 January 2021

In this Article, owing to an error in the production process, the abbreviation TGCT in the legend of Fig. 1a was incorrectly defined as ‘tenosynovial giant cell tumour’. The correct definition is ‘testicular germ cell tumour’. The original Article has been corrected online.

## Author information

### Affiliations

1. Department of Pharmacology & Experimental Therapeutics, Boston University School of Medicine, Boston, MA, USA

Ryan J. Quinton, Amanda DiDomizio, Marc A. Vittoria, Kristýna Kotýnková, Carlos J. Ticas, Sheena Patel, Jasmine Vakhshoorzadeh & Neil J. Ganem

2. Department of Medicine, Boston University School of Medicine, Boston, MA, USA

Yusuke Koga, Neha Parulekar, Joshua D. Campbell & Neil J. Ganem

3. Department of Biology and Biotechnology, Worcester Polytechnic Institute, Worcester, MA, USA

Nicole Hermance & Amity L. Manning

4. Department of Molecular Pathobiology and Cell Adhesion Biology, Mie University Graduate School of Medicine, Mie, Japan

Taruho S. Kuroda

5. Department of Medical Oncology, Dana-Farber Cancer Institute, Boston, MA, USA

Alison M. Taylor

6. Cancer Program, Broad Institute, Cambridge, MA, USA

Alison M. Taylor & Joshua D. Campbell

7. Department of Pathology and Cell Biology, Columbia University Medical Center, Member, Herbert Irving Comprehensive Cancer Center, New York, NY, USA

Alison M. Taylor

## Authors

1. Ryan J. Quinton

[View author publications](#)

You can also search for this author in [PubMed](#) [Google Scholar](#)

2. Amanda DiDomizio

[View author publications](#)

You can also search for this author in [PubMed](#) [Google Scholar](#)

3. Marc A. Vittoria

[View author publications](#)

You can also search for this author in [PubMed](#) [Google Scholar](#)

4. Kristýna Kotýnková

[View author publications](#)

You can also search for this author in [PubMed](#) [Google Scholar](#)

5. Carlos J. Ticas

[View author publications](#)

You can also search for this author in [PubMed](#) [Google Scholar](#)

6. Sheena Patel

[View author publications](#)

You can also search for this author in [PubMed](#) [Google Scholar](#)

7. Yusuke Koga

[View author publications](#)

You can also search for this author in [PubMed](#) [Google Scholar](#)

8. Jasmine Vakhshoorzadeh

[View author publications](#)

You can also search for this author in [PubMed](#) [Google Scholar](#)

9. Nicole Hermance

[View author publications](#)

You can also search for this author in [PubMed](#) [Google Scholar](#)

10. Taruho S. Kuroda

[View author publications](#)

You can also search for this author in [PubMed](#) [Google Scholar](#)

11. Neha Parulekar

[View author publications](#)

You can also search for this author in [PubMed](#) [Google Scholar](#)

12. Alison M. Taylor

[View author publications](#)

You can also search for this author in [PubMed](#) [Google Scholar](#)

13. Amity L. Manning

[View author publications](#)

You can also search for this author in [PubMed](#) [Google Scholar](#)

14. Joshua D. Campbell

[View author publications](#)

You can also search for this author in [PubMed](#) [Google Scholar](#)

15. Neil J. Ganem

[View author publications](#)

You can also search for this author in [PubMed](#) [Google Scholar](#)

## **Corresponding author**

Correspondence to [Neil J. Ganem](#).

## **Rights and permissions**

[Reprints and Permissions](#)

## **About this article**



Check for  
updates

## Cite this article

Quinton, R.J., DiDomizio, A., Vittoria, M.A. *et al.* Publisher Correction: Whole-genome doubling confers unique genetic vulnerabilities on tumour cells. *Nature* **593**, E15 (2021). <https://doi.org/10.1038/s41586-021-03591-3>

### [Download citation](#)

- Published: 11 May 2021
- Issue Date: 27 May 2021
- DOI: <https://doi.org/10.1038/s41586-021-03591-3>

## Comments

By submitting a comment you agree to abide by our [Terms](#) and [Community Guidelines](#). If you find something abusive or that does not comply with our terms or guidelines please flag it as inappropriate.

### [Download PDF](#)

Advertisement

---

This article was downloaded by **calibre** from <https://www.nature.com/articles/s41586-021-03591-3>

Retraction Note: Endoperoxide formation by an  $\alpha$ -ketoglutarate-dependent mononuclear non-haem iron enzyme

[Download PDF](#)

- Retraction Note
- [Published: 19 May 2021](#)

# Retraction Note: Endoperoxide formation by an $\alpha$ -ketoglutarate-dependent mononuclear non-haem iron enzyme

- [Wupeng Yan<sup>1</sup>](#) na1,
- [Heng Song<sup>2</sup>](#) na1,
- [Fuhang Song<sup>3</sup>](#),
- [Yisong Guo<sup>6</sup>](#),
- [Cheng-Hsuan Wu<sup>2</sup>](#),
- [Ampon Sae Her<sup>2</sup>](#),
- [Yi Pu<sup>2,4</sup>](#),
- [Shu Wang<sup>2</sup>](#),
- [Nathchar Naowarojna<sup>2</sup>](#),
- [Andrew Weitz<sup>6</sup>](#),
- [Michael P. Hendrich<sup>6</sup>](#),
- [Catherine E. Costello<sup>2,4</sup>](#),
- [Lixin Zhang<sup>3</sup>](#),
- [Pinghua Liu<sup>2</sup>](#) &
- [Yan Jessie Zhang<sup>1,5</sup>](#)

[Nature](#) volume 593, page 612 (2021) [Cite this article](#)

- 2154 Accesses
- 2 Altmetric
- [Metrics details](#)

## Subjects

- [Biocatalysis](#)
- [Enzyme mechanisms](#)
- [X-ray crystallography](#)

The [Original Article](#) was published on 02 November 2015

[Download PDF](#)

Retraction to: *Nature* <https://doi.org/10.1038/nature15519> Published online 02 November 2015

*Nature* is retracting this Article because after extensive consultation with peer reviewers, it has come to our attention that the data contained within do not support its central conclusions about the mechanism of fumitremorgin B endoperoxidase (FtmOx1) and the central role of Tyr224 in catalysis. Further expert review of the crystal structure 4ZON, which was alleged to show fumitremorgin B bound to FtmOx1 (Fig. 2f of the original Article), noted that the substrate density can also be assigned to bound MES buffer and a cluster of water molecules. We have notified the Protein Data Bank about entry 4ZON. The catalytically competent binding mode of fumitremorgin B therefore remains undefined. Biochemical data on Tyr224 mutants do not conclusively support either the assignment of the observed transient radical to Tyr224 or its mechanistic role in catalysis. Author Yan Jessie Zhang has agreed with the Retraction of this Article, whereas the other authors stand by their data and disagree with this Retraction.

## Author information

## Author notes

1. These authors contributed equally: Wupeng Yan, Heng Song

## Affiliations

1. Department of Molecular Biosciences, University of Texas at Austin, Austin, 78712, Texas, USA

Wupeng Yan & Yan Jessie Zhang

2. Department of Chemistry, Boston University, Boston, 02215, Massachusetts, USA

Heng Song, Cheng-Hsuan Wu, Ampon Sae Her, Yi Pu, Shu Wang, Nathchar Naowarojna, Catherine E. Costello & Pinghua Liu

3. CAS Key Laboratory of Pathogenic Microbiology and Immunology, Institute of Microbiology, Chinese Academy of Sciences, Beijing, 100101, China

Fuhang Song & Lixin Zhang

4. Center for Biomedical Mass Spectrometry, Boston University School of Medicine, Boston, 02118, Massachusetts, USA

Yi Pu & Catherine E. Costello

5. Institute for Cellular and Molecular Biology, University of Texas at Austin, Austin, 78712, Texas, USA

Yan Jessie Zhang

6. Department of Chemistry, Carnegie Mellon University, 4400 Fifth Avenue, Pittsburgh, 15213, Pennsylvania, USA

Yisong Guo, Andrew Weitz & Michael P. Hendrich

## Authors

1. Wupeng Yan

[View author publications](#)

You can also search for this author in [PubMed](#) [Google Scholar](#)

2. Heng Song

[View author publications](#)

You can also search for this author in [PubMed](#) [Google Scholar](#)

3. Fuhang Song

[View author publications](#)

You can also search for this author in [PubMed](#) [Google Scholar](#)

4. Yisong Guo

[View author publications](#)

You can also search for this author in [PubMed](#) [Google Scholar](#)

5. Cheng-Hsuan Wu

[View author publications](#)

You can also search for this author in [PubMed](#) [Google Scholar](#)

6. Ampon Sae Her

[View author publications](#)

You can also search for this author in [PubMed](#) [Google Scholar](#)

7. Yi Pu

[View author publications](#)

You can also search for this author in [PubMed](#) [Google Scholar](#)

8. Shu Wang

[View author publications](#)

You can also search for this author in [PubMed](#) [Google Scholar](#)

9. Nathchar Naowarojna

[View author publications](#)

You can also search for this author in [PubMed](#) [Google Scholar](#)

10. Andrew Weitz

[View author publications](#)

You can also search for this author in [PubMed](#) [Google Scholar](#)

11. Michael P. Hendrich

[View author publications](#)

You can also search for this author in [PubMed](#) [Google Scholar](#)

12. Catherine E. Costello

[View author publications](#)

You can also search for this author in [PubMed](#) [Google Scholar](#)

13. Lixin Zhang

[View author publications](#)

You can also search for this author in [PubMed](#) [Google Scholar](#)

14. Pinghua Liu

[View author publications](#)

You can also search for this author in [PubMed](#) [Google Scholar](#)

15. Yan Jessie Zhang

[View author publications](#)

You can also search for this author in [PubMed](#) [Google Scholar](#)

## **Corresponding authors**

Correspondence to [Lixin Zhang](#) or [Pinghua Liu](#) or [Yan Jessie Zhang](#).

# Rights and permissions

[Reprints and Permissions](#)

## About this article



## Cite this article

Yan, W., Song, H., Song, F. *et al.* Retraction Note: Endoperoxide formation by an  $\alpha$ -ketoglutarate-dependent mononuclear non-haem iron enzyme. *Nature* **593**, 612 (2021). <https://doi.org/10.1038/s41586-021-03527-x>

[Download citation](#)

- Published: 19 May 2021
- Issue Date: 27 May 2021
- DOI: <https://doi.org/10.1038/s41586-021-03527-x>

## Comments

By submitting a comment you agree to abide by our [Terms](#) and [Community Guidelines](#). If you find something abusive or that does not comply with our terms or guidelines please flag it as inappropriate.

[Download PDF](#)

Advertisement

| [Section menu](#) | [Main menu](#) |

# Nature Index